PRINTED ISSN: 1308-9080 / OLINE ISSN: 1308-9099

Volume: 20 / Number: 1 / Year: 2025

TURKISH JOURNAL OF SCIENCE & TECHNOLOGY

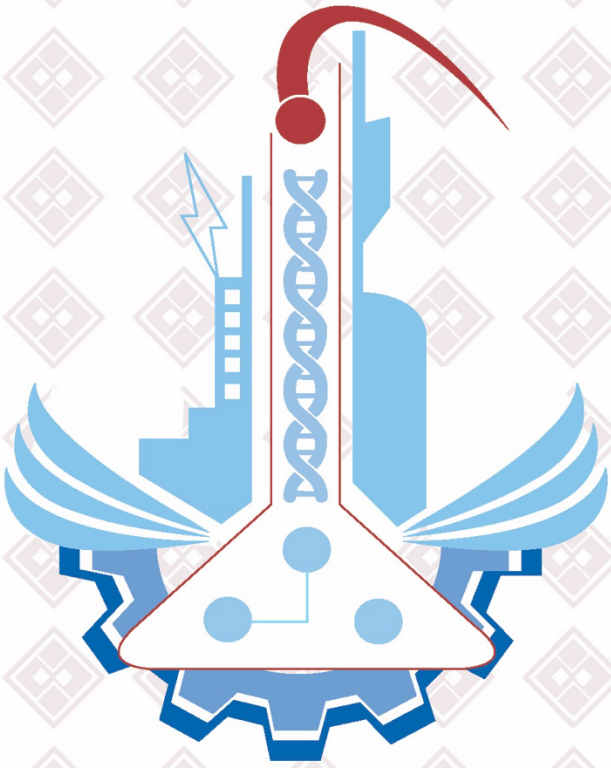

TURKISH JOURNAL OF SCIENCE AND TECHNOLOGY (TJST)

Year: 2025 Vol: 20 Number: 1

Address:
Fırat Universitesi
Fen Bilimleri Enstitüsü
23119, Elazig - TURKEY

Tel: 0 424 212 27 07
Fax: 0 424 236 99 55
e-mail: fenbilim@firat.edu.tr

New ISSN
Online: 1308-9099
Printed: 1308-9080

Old ISSN
Online: 1306 – 8555
Printed: 1306 – 8547

Refereed journal. Published twice a year

https://dergipark.org.tr/tr/pub/tjst

TURKISH JOURNAL OF SCIENCE & TECHNOLOGY (TJST)

Published by Firat University

ADVISORY BOARD

Fırat University Turkish Journal of Science & Technology (TJST)
20-1, 2025

CONTENTS / İÇİNDEKİLER

Turkish Journal of Science & Technology
20(1), 1-6, 2025

Research Paper
https://doi.org/10.55525/tjst.1441856

On the Convergence Analysis of Bernstein Operators

Ayse BUGATEKIN[1*]
[1] Department of Statistics, Faculty of Science, Fırat University, Elazıg, TURKEY
[*] aturan@firat.edu.tr

(Geliş/Received: 23/02/2024; Kabul/Accepted: 4/10/2024)

Abstract: In recent years, many studies have been conducted to emphasize the convergence criteria of the q-Bernstein polynomial and their importance. A point often overlooked in the literature is that the kernels of these polynomials depend on the probabilities of the variable parameter binomial distribution. Taking advantage of this property, we develop a simplified form of this polynomial for the binomial variable with variable parameters. This approach not only simplifies the computational processes but also sheds light on the convergence properties of this polynomial. By examining this reduced form, an upper bound for convergence is determined. The findings highlight the versatility and power of the q-Bernstein polynomial in approximation theory and provide a deeper understanding of the mathematical foundations and potential applications of the polynomial.

Key words: Approximation theory, Bernstein polynomial, Bernoulli process, convergence, expected value.

Bernstein Operatörlerinin Yakınsama Analizi Üzerine

Öz: Son yıllarda, q-Bernstein polinomları yaklaşım teorisinde önemli bir konu olarak ortaya çıkmıştır. Çok sayıda çalışma bu polinomun yakınsama kriterlerini incelemiş, bunların önemini ve kullanışlılığını vurgulamıştır. Literatürde sıklıkla göz ardı edilen bir nokta, bu polinomların çekirdeklerinin değişken parametreli binom dağılımının olasılıklarına bağlı olmasıdır. Bu özellikten yararlanarak, binom bağımlılığına ilişkin bu polinomun basitleştirilmiş bir formunu geliştirdik; bu, değişken parametreli bir binom değişkeni için momentlerinin hesaplanmasını kolaylaştırmıştır. Bu yaklaşım yalnızca hesaplama süreçlerini basitleştirmekle kalmaz, aynı zamanda bu polinomun yakınsama özelliklerine de ışık tutar. Bu indirgenmiş formu inceleyerek yakınsama için bir üst sınır belirlenir. Bulgular, q-Bernstein polinomunun yaklaşım teorisindeki çok yönlülüğünü ve gücünü vurgular ve polinomun matematiksel temelleri ve potansiyel uygulamaları hakkında daha derin bir anlayış sağlar.

Anahtar kelimeler: Yaklaşım teorisi, Bernstein polinom, bernoulli süreci, yakınsaklık, beklenen değer.

1. Introduction

Polynomials have a wide range of applications in today's technological age. For instance, they are extensively used in fields such as physics, engineering, economics, and computer programming. In physics, polynomials can describe various physical phenomena, such as motion, force, and energy relations. In engineering, they are crucial in designing and analyzing systems and structures, from bridges to electronic circuits. Economists use polynomials to model economic growth, trends, and other financial data. In computer programming, polynomials are used in algorithms, graphics, and data interpolation [1-5].

In essence, polynomials are fundamental tools for modeling and solving numerous problems across different disciplines. One of the key advantages of polynomials is their ease of differentiation and integration, which simplifies the processing of mathematical functions. This makes them particularly useful in various studies and practical applications.

This study focuses on Bernstein polynomials, a special class of polynomials known for their significant applications. Bernstein polynomials are widely used due to their simple structure and valuable properties. They are particularly important in approximation theory, which deals with approximating complex functions using simpler and more manageable functions. This theory is crucial because working directly with functions with unknown or complicated properties can be challenging. By approximating these functions with well-known, simpler functions, researchers can derive useful results more easily.

Approximation theory addresses whether it is possible to convert complex functions into polynomial functions and how closely such approximations can represent the original functions. This process of approximation is vital in various fields, providing a way to work with functions that are otherwise difficult to handle. By using polynomial approximations, researchers and practitioners can simplify their analyses and obtain more tractable solutions to complex problems. It can be said that approximation by polynomials is perhaps the most important

[*] Corresponding author: aturan@firat.edu.tr. ORCID Number of authors: [1] 0000-0001-8949-8367

branch of approximation theory. Today, Bernstein polynomials are mostly applied in the field of approximation theory [6,7].

Recent studies on the approximation properties of blending-type modified Bernstein–Durrmeyer operators have demonstrated that these operators possess strong approximation characteristics [8]. In a recent study, a new type of coupled Bernstein operators for Bezier basis functions was introduced, demonstrating their approximation properties, including the establishment of a local approximation theorem and a convergence theorem for Lipschitz continuous functions [9]. In a recent study, a novel method for approximating the Koopman operator using Bernstein polynomials was proposed. This approach provides a finite-dimensional approximation and characterizes approximation errors with upper bounds expressed in the uniform norm, covering various contexts including univariate and multivariate systems [10]. In a recent study, a new class of Bernstein polynomials based on Bézier basic functions with a shape parameter $\lambda \in [-1,1]$ was examined. The study provides a Korovkin-type approximation theorem and demonstrates improvements in error estimation in some cases by comparing these operators with classical Bernstein operators [11]. In 2024, Aslan investigated some approximation properties of the mixture-type univariate and bivariate Schurer-Kantorovich operators based on shape parameters $\lambda \in [-1, 1]$ [12]. In 2023, Su [13] studied various approximation properties of the Durrmeyer variant of q-Bernstein operators based on the Bézier basis with shape parameters.

Most of the recent work on achievement studies in the Bernoulli trials is in Feller's [14] basic book. Let S_n be the total number of successes in the Bernoulli trials of n independents. When the trials are the same, most of the properties of the S_n distribution and the related theorems are well known and discussed in many books and studies on statistics. Charalambides [15] showed that the probability mass function has a very important place in q-Bernstein polynomial. He calculated the expected value and variance based on this probability function.
In the Bernoulli process, the experiment takes place once and has two possible outcomes. Occurrence of the desired situation is considered a success and the occurrence of the undesired situation is considered a failure. Let k be the number of successes in n independent Bernoulli experiments.

$$p_{n,k}(x) = \binom{n}{k} x^k (1-x)^{n-k}, \quad k = 0,1,\dots,n. \tag{1}$$

where x is the probability of success in a single Bernoulli trial as given in Eq. 1. $p_{n,k}(x)$ is the probability of k successes in n trials [16].

The approximation of real-valued continuous functions has attracted attention of researchers for years. The Weierstrass Approximation Theorem is one of the fundamental theorems that is frequently used in functional analysis. According to this approximation theory, polynomials can uniformly approximate any function that is merely continuous over a closed interval. Bernstein proved this approximation theorem in its simplest form in 1912 [17].

Since Bernstein operators are simpler and have very different approach properties, they have become the operators preferred by researchers. Lupaş [18] presented the q-Bernstein theory as a contribution to science in 1987. Acu [19] has studied different generalizations of Bernstein operators. The q-generalization of these operators was examined by Cárdenas-Morales [20] presented the new sequence of linear Bernstein-type operators. It is also useful to say that the Benstein operators have many more generalizations that can contribute to science.

2. Positive Operators Obtained with the Help of the Binomial Distribution

Bernstein polynomials are given in 1912 in the proof of the Weierstrass theorem by Bernstein and were later used in the proof of many theorems. The Korovkin theorem is a typical example. The Bernstein polynomial can be expressed as in Eq. 2.

Let $f: [0,1] \to R$. The Bernstein polynomial of f is

$$B_n(f;x) = \sum_{k=0}^{n} f\left(\frac{k}{n}\right)\binom{n}{k} x^k (1-x)^{n-k} = \sum_{k=0}^{n} f\left(\frac{k}{n}\right) p_{n,k}(x). \tag{2}$$

Here $B_n(f;x)$ is called Bernstein operators of order n for f [21].

Some Korovkin type approximation theorems were proved in [22] by using statistical convergence, lacunary statistical convergence and statistical summability $(C,1)$, respectively. Now, let's introduce the Korovkin approximation theorem [23].

Theorem 2.1. Let (T_n) be a sequence of positive linear operators from $C[a,b]$, into $C[a,b]$. Then $\lim_n \|T_n(f,x)-f(x)\|_\infty = 0$, for all $f \in C[a,b]$ if and only if $\lim_n \|T_n(f_i,x)-f_i(x)\|_\infty = 0$, for $i = 0,1,2$ where $f_0(x)=1$, $f_1(x)=x$ and $f_2(x)=x^2$ [24].

3. Convergence Criteria

Definition 3.1. Let the function f be continuous in the interval $[a,b]$. The $\omega(\delta)$ function defined by the equation

$\omega(\delta) = sup_{|x_1-x_2|\le\delta}|f(x_1)-f(x_2)|$

with $x_1, x_2 \in [a,b]$ for the real number $\delta > 0$, is the modulus of continuity of the function f [25].

This function will take values based on f, the interval $[a,b]$ and the chosen $\delta > 0$. Let's continue the features of $\omega(\delta)$ modulus of continuity.

3.1. For $0 < \delta_1 < \delta_2$, $\omega(\delta_1) \le \omega(\delta_2)$.

3.2. $\lim_{\delta\to 0} \omega(\delta) = 0$, when function f is continuous in the interval $[a,b]$.

3.3. $\omega(\lambda\delta) \le (1+\lambda)\,\omega(\delta)$**,** for the real number $\lambda > 0$.

Let us express the theorem that enables to evaluate the difference $|B_n(f;x)-f(x)|$ with the help of the modulus of continuity.

3.1. Approximation Theorem

Let $\{X_n : n = 1,2,\dots\}$be a sequence of independent random variables where X_n has a distribution with parameters (n,x). where, n represents the number of trials, and x represents the probability of success. Let f be the real-valued function defined on the real interval [a, b] such that $f^{(m)} \in C[a,b]$ and $L_n(f,x) = Ef(X_n) < \infty$. Then for any $x \in [a,b]$ and any $\delta > 0$

$$\left|L_n(f,x) - \sum_{k=0}^{m} \frac{f^{(k)}(x)}{k!} b_k\right| \le \begin{cases} \frac{1}{m!}(\sqrt{b_{2m}} + \delta b_{m+1})\omega_m(\frac{1}{\delta}) & ,if\ m\ is\ odd \\ \frac{1}{m!}(b_m + \delta\sqrt{b_2 b_{2m}})\omega_m(\frac{1}{\delta}) & ,if\ m\ is\ even \end{cases} \quad (3)$$

where $b_k = b_k(n,x) = E(X_n - x)^k$ for $k = 0,1,\dots,m$ is k th moment of random variable X_n around x, $\omega_m(\frac{1}{\delta})$ is the modulus of continuity of $f^{(m)}$ [26].

4. Reduced Form of q- Bernstein Polynomials and Probabilistic Interpretation

Philips [27] gave a generalization of the Bernstein polynomial q in 1996, which changes depending on the integer values of q. After this stage, this issue has been handled by many authors from different angles. Since q-Bernstein polynomials are positive linear operators on *C [0,1]*, the case of *0 <q <*1 is generally investigated. For each positive integer n, $B_n(f,q;x)$ q- Bernstein polynomials as For each positive integer n, $B_n(f,q;x)$ q-Bernstein polynomials are as in Eq. 4.

$$B_n(f,q;x) = \sum_{k=0}^{n} f\left(\frac{[k]}{[n]}\right)\begin{bmatrix} n \\ k \end{bmatrix} x^k \prod_{s=0}^{n-k-1}(1-q^s x). \quad (4)$$

When $q = 1$, $B_n(f,q;x)$ is the classical Bernstein operator. The q- Bernstein polynomial shares the shape-preserving properties of the classical Bernstein polynomial.

Let $q > 0$. As in eq. 5, for each nonnegative integer l, the q- integer $[l]$, q- factorial $[l]!$ and q- binomial $\begin{bmatrix} n \\ r \end{bmatrix}$, $(n \ge l \ge 0)$ are defined by

$$[l] := [l]_q := \begin{cases} (1-q^l)/(1-q) & q \ne 1 \\ l & q = 1 \end{cases}$$

$$[l]! := \begin{cases} [l][l-1]\dots[1] & q \ne 1 \\ l! & q = 1 \end{cases} \qquad \begin{bmatrix} n \\ l \end{bmatrix} := [n]!/([n-l]!\,[l]!) \quad (5)$$

respectively [28]. Additionally, $[0]! \coloneqq 1$.

Theorem 4.1. *Let a sequence* $\{q_n\}$ *satisfy* $0 < q_n < 1$ *and* $q_n \to 1$ *as* $n \to \infty$. *If* $f \in C[0,1]$ *then* $B_n(f, q_n; x) \rightrightarrows f(x)$ *for* $x \in [0,1]$ *as* $n \to \infty$ [29].

Direct calculations show that for $0 < q < 1$

$B_n(t^2, q; x) \rightrightarrows x^2 + (1-q)x(1-x) \neq x^2,\ x \in [0,1]$ as $n \to \infty$.

Therefore in general, the sequence $\{B_n(f, q; x)\}$ is not an approximating one for the function f [16].

4.1. Probabilistic properties of *q*- Bernstein polynomials

Considering probability problems, it is always possible to talk about the probability of a desired situation or event. If two results such as successful or unsuccessful occur for a trial and this trial can be repeated under the same conditions, this experiment is called Bernoulli test. The Bernoulli trial is the basis for discrete distributions. Here, let *k* be the number of successes in *n* independent Bernoulli experiments.

Let's express it as the sum of the events of Bernoulli such that $S_n = X_1 + X_2 + \cdots + X_n$. Since the sum of the Bernoulli trials will give the binomial distribution, $S_n \sim p_{n,k}(x)$ can be written. Therefore, the following Eq. 6 can be written for S_n

$$P(S_n = k) = \binom{n}{k} x^k (1-x)^{n-k} \tag{6}$$

Since the kernel of the Bernstein polynomial provides the properties $p_{n,k}(x) \geq 0$ and $\sum_{k=0}^{n} p_{n,k}(x) = 1$ for $0 < x < 1$, it can be regarded as the probability function of a random variable. From the equation $P(S_n = k) = p_{n,k}(x), k = 0,1, \dots, n$, the Bernstein polynomial can be written in the form of the expected value of the S_n random variable with the help of the expected value operator *E* (Eq. 7)

$$B_n(f; x) = Ef\left(\frac{S_n}{n}\right). \tag{7}$$

4.2. Main results

If the Bernstein polynomial is shown as in (2), the term *q* must be added on success possibilities of $X_1, X_2, \dots, X_n$ Bernoulli in order to express the *q*- Bernstein polynomials in the same way. Accordingly,

$$P\left(X_j^* = 1\right) = q^s x$$

$$P\left(X_j^* = 0\right) = 1 - q^s x \tag{8}$$

to define the number of *j* experiments can be written as Eq. 8. Also *s* denotes the number of unsuccessful attempts in trials up to *j-1*.

Now let's show that $P(S_n^* = k) = \begin{bmatrix} n \\ k \end{bmatrix} x^k \prod_{s=0}^{n-k-1}(1 - q^s x)$ using the method of mathematical induction. For *n = 1, k* values are *0* and *1*, respectively.

$$P(S_1^* = 0) = (1 - x)$$

$$P(S_1^* = 1) = x$$

Let's assume that $P(S_n^* = k) = \begin{bmatrix} n \\ k \end{bmatrix} x^k \prod_{s=0}^{n-k-1}(1 - q^s x)$ (9)
for *n = k.*

As ,n Eq. 10, now let's show that for *n = k+1,*

$$P(S_{n+1}^* = k) = \begin{bmatrix} n+1 \\ k \end{bmatrix} x^k \prod_{s=0}^{n-k}(1 - q^s x).$$

$$P(S_{n+1}^* = k) = P(S_{n+1}^* = k | S_n^* = k-1).P(S_n^* = k-1) + P(S_{n+1}^* = k | S_n^* = k).P(S_n^* = k)$$

$$= q^{n-k+1}x\left(\begin{bmatrix} n \\ k-1 \end{bmatrix} x^{k-1}\prod_{s=0}^{n-k}(1-q^s x)\right)n + (1-q^{n-k}x)\left(\begin{bmatrix} n \\ k \end{bmatrix} x^k \prod_{s=0}^{n-k-1}(1-q^s x)\right)$$

$$= \frac{[n]![n+1]}{[k]![n-k+1]!}x^k\prod_{s=0}^{n-k}(1-q^s x) = \begin{bmatrix} n+1 \\ k \end{bmatrix} x^k \prod_{s=0}^{n-k}(1-q^s x). \quad (10)$$

Thus it is proven that Eq. 9 is true.

To obtain an approximate value, it is necessary to calculate the $E(X_n^* - x)^2$. In this case Eq. 11 is obtained.

$$E(X_n^* - x)^2 = b_2(n,x) = E(\tfrac{S_n}{n} - x)^2 = \tfrac{1}{n^2}E(S_n^2 - 2nxS_n + n^2x^2) = b_2(n,x) = \tfrac{1}{n}xq \quad (11)$$

In approximation theorem (Eq.3), if *m = 0* is taken specially Eq. 12 is obtained.

$$|L_n(f,x) - f(x)| \leq (1 + \delta\sqrt{b_2})\omega(\tfrac{1}{\delta}) \quad (12)$$

is given. According to this, when $L_n = B_{n,q}$ and $\delta = \sqrt{n}$ are taken, Eq. 13 is obtained.

$$|B_n(f,q;x) - f(x)| \leq \left(1 + \delta\sqrt{\frac{1}{n}xq}\right)\omega(\frac{1}{\delta})$$

$$B_n(f,q;x) = f(x) + o\left(\tfrac{1}{n}\right), n \to \infty \quad (13)$$

5. Conclusion

In this paper, q-Bernstein polynomials based on q integers are introduced. These polynomials are constructed in a different form and an upper bound for the approximation of operators is obtained by the approximation theorem. It follows that all operators with kernel-part probability functions can be used in different variations in approximation theory.

References

[1] Kingora K, Sadat-Hosseini H. A novel interpolation-free sharp-interface immersed boundary method. J Comput Phys 2022; 453, 110933.

[2] Tu S, Yang H, Dong L, Huang Y. A stabilized moving Kriging interpolation method and its application in boundary node method. Eng Anal Boundary Elem 2019; 100: 14-23.

[3] Kochurin E. A Simulation of the Wave Turbulence of a Liquid Surface Using the Dynamic Conformal Transformation Method. JETP Letters 2023; 118(12): 893-898.

[4] Christodoulou KN, Scriven LE. Discretization of free surface flows and other moving boundary problems. J Comput Phys 1992; 99(1): 39-55.

[5] Yang X, Zhang X, Li Z, He GW. A smoothing technique for discrete delta functions with application to immersed boundary method in moving boundary simulations. J Comput Phys 2009; 228(20): 7821-7836.

[6] Cetin E, Applications of Bernstein polynomials. Master Thesis, Uludağ Uni., Graduate School of Natural and Applied Sciences, Bursa, 2011.

[7] Kılın BK, Bernstein-Chlodowsky Type Polynomials and Some Applications. Master Thesis, Gaziantep Uni., Graduate School of Natural and Applied Sciences, Gaziantep, 2019.

[8] Liu YJ, Cheng WT, Zhang WH, Ye PX. Approximation Properties of the Blending-Type Bernstein–Durrmeyer Operators. Axioms 2022; 12(1): 5.

[9] Ayman-Mursaleen M, Nasiruzzaman M, Rao N, Dilshad M, Nisar KS. Approximation by the modified λ-Bernstein-polynomial in terms of basis function. AIMS Math 2024; 9(2): 4409-4426.

[10] Yadav R, Mauroy A. Approximation of the Koopman operator via Bernstein polynomials. 2024, arXiv preprint arXiv:2403.02438.

[11] Aslan R, Mursaleen M. Some approximation results on a class of new type λ-Bernstein polynomials. J Math Inequal 2022; 16(2): 445-462.

[12] Aslan R. Rate of approximation of blending type modified univariate and bivariate λ-Schurer-Kantorovich operators. Kuwait J Sci 2024; 51(1): 100168.

[13] Su LT, Aslan R, Zheng FS, Mursaleen M. On the Durrmeyer variant of q-Bernstein operators based on the shape parameter λ. J Inequal Appl 2023; 2023(1): 56.

[14] Feller W. An Introduction to Probability Theory and Its Applications. New York, Wiley, 1968.
[15] Charalambides CA. The q-Bernstein basis as a q-binomial distribution. J Stat Plann Inference 2010; 140(8): 2184-2190.
[16] II'inskii A, Ostrovska S. Convergence of generalized Bernstein polynomials based on the q-integers. Constructive theory of functions 2003; 309-313.
[17] Bernstein S. Demonstration du theoreme de Weierstrass Fondee Sur le Calcul des Probabilities. Communications of the Kharkov Mathematical Society 1912; 13: 1-2. IP: 88.236.115.136.
[18] Lupaş A. A q-analogue of the Bernstein Operator. Seminar on Numerical and Statistical Calculus 1987; 9: 85-92.
[19] Acu MA. Stancu–Schurer–Kantorovich Operators Based on q-integers. Appl Math Comput 2015; 259: 896–907.
[20] Cárdenas-Morales D, Garrancho P, Rasa I. Bernstein-type Operators which Preserve Polynomials. Comput Math Appl 2011; 62(1): 158–163.
[21] Ostrovska S. On the Lupaş q-analogue of the Bernstein operator. The Rocky Mountain J Math 2006;1615-1629.
[22] Patterson RF, Savas E. Korovkin and Weierstrass approximation via lacunary statistical sequences. J Math Stat 2005; 1(2): 165-167.
[23] Korovkin PP. Linear Operators and Approximation Theory. Delhi, Hindustan Publ. Co., 1960.
[24] Kim T. A note on q-Bernstein polynomials, Russ J Math Phys 2011; 18(1): 73-82.
[25] Rıvlin JP. An Introduction to the Approximation of Functions, New York, Bronx, 1978.
[26] Gurcan M, Colak C. Generalization of Korovkin Type Approximation by Appropriate Random Variables and Moments and an Application in Medicine. Pak J Statist 2011; 27(3): 283-297.
[27] Phillips GM. On generalized Bernstein polynomials. In Numerical Analysis 1996; 263-269.
[28] Dalmanoglu O. Approximation by Kantorovich type q-Bernstein operators, In Proceedings of the 12th WSEAS International Conference on Applied Mathematics 2007; 113-117.
[29] Gupta V, Heping W. The rate of convergence of q-Durrmeyer operators for 0<q< 1. Math Methods Appl Sci 2008; 31(16): 1946-1955.

Turkish Journal of Science & Technology
20(1), 7-16, 2025

Research Paper
https://doi.org/10.55525/tjst.1474164

The Hydrogen Potential Assessment based on Wind and Solar Energy in Elazig Province, Türkiye

Abuzer ÇALISKAN[1], Hasan Bektas PERCIN[2*]
[1] Department of Electrical and Electronics Engineering, Firat University, Elazig, Türkiye
[2] Graduate School of Natural and Applied Sciences, Firat University, Elazig, Türkiye
[1] acaliskan@firat.edu.tr,[*2] hbpercin@firat.edu.tr

(Geliş/Received: 26/04/2024 Kabul/Accepted: 07/01/2025)

Abstract: This study investigates the feasibility of hydrogen production potential using the available renewable energy source potentials in the province of Elazig, Türkiye. The study aims to create a potential assessment of each district in Elazig, based on wind and solar sources and Proton Exchange Membrane (PEM) electrolyzer technology. It aims not only to evaluate the green hydrogen potential but also to outline the feasibility of implementing this alternative energy source at a localized level. In this way, an alternative energy source can be assessed for production, storage, and the scarcity of energy in emergency conditions such as earthquakes or other cases. The comprehensive analysis integrates a multitude of parameters, including geographic variations and technological considerations, supported by detailed illustrations to present a holistic view of the hydrogen potential in Elazig. The study's outcomes suggest that districts with high energy potential and minimal geographical and topological constraints have a significant potential for hydrogen production.

Key words: Green Hydrogen, Wind Energy, Solar Energy, PEM Electrolyzer.

Türkiye'nin Elazığ İlinde Rüzgar ve Güneş Enerjisine Dayalı Hidrojen Potansiyelinin Değerlendirilmesi

Öz: Bu çalışma, Türkiye'nin Elâzığ ilinde mevcut yenilenebilir enerji kaynaklarının potansiyeline dayanarak hidrojen üretim potansiyelinin fizibilitesini araştırmaktadır. Çalışma, rüzgâr ve güneş kaynaklarına ve Proton Değişim Membranlı (PEM) elektrolizör teknolojisine dayalı olarak Elazığ'daki her bir ilçenin potansiyel değerlendirmesini oluşturmayı amaçlamaktadır. Sadece yeşil hidrojen potansiyelini değerlendirmeyi değil, aynı zamanda bu alternatif enerji kaynağının yerel düzeyde uygulanmasının fizibilitesini de ortaya koymayı amaçlamaktadır. Bu şekilde, alternatif bir enerji kaynağı üretim, depolama ve deprem gibi çeşitli acil durumlarda enerji kıtlığı için değerlendirilebilir. Kapsamlı analiz, Elazığ'daki hidrojen potansiyelinin bütüncül bir görünümünü sunmak için ayrıntılı görsellerle desteklenen coğrafi varyasyonlar ve teknolojik hususlar da dahil olmak üzere çok sayıda parametreyi içermektedir. Çalışmanın sonuçları, yüksek enerji potansiyeline ve minimum coğrafi ve topolojik kısıtlamalara sahip ilçelerin hidrojen üretimi için önemli bir potansiyele sahip olduğunu göstermektedir.

Anahtar kelimeler: Yeşil Hidrojen, Rüzgâr Enerjisi, Güneş Enerjisi, PEM Elektrolizör.

1. Introduction

Reliance on fossil fuels is insufficient to meet persistent long-term energy demands, particularly in light of the depletion of these resources. Consequently, several key factors are driving the transition to renewable energy sources. These include their abundant availability, declining system costs, and the extensive development of electricity infrastructure [1]. Their intermittent nature, notably solar and wind energy, poses challenges for sustainability and operational efficiency. Consequently, there is a growing need for alternative sources such as hydrogen to mitigate these inherent challenges and reduce reliance on fossil fuels [2,3]. Hydrogen offers advantages like high energy density, abundance, long-distance transportability, storability, and zero-carbon emission. Based on these features, it is anticipated that hydrogen will be abundantly utilized in different sectors in the future. It is estimated that by 2050, nearly 20% of global energy demand will be met by hydrogen. Aligned with Türkiye's 2053 net-zero emissions targets and considering on-site consumption and industrial demands, the Turkish government has set an ambitious goal to achieve an electrolyzer capacity of 5.0 GW by 2035. This initiative reflects the nation's commitment to advancing hydrogen production as a key component of its sustainable energy strategy [4,5].

Hydrogen can be generated through various methods. Each method offers distinct processes and efficiencies, catering to different resource availability and application requirements. The feasibility and potential of hydrogen

* Corresponding author: hbpercin@firat.edu.tr ORCID Number of authors: [1] 0000-0001-8262-7912, [2] 0000-0001-8968-969X

production from renewable energy sources have been widely analyzed in several studies. Mostafaeipour et al. [6] explored the hydrogen generation potential in Iran by utilizing wind energy. Certain wind turbines were identified as capable of meeting both the required energy load and the hydrogen fuel demand. Nematollahi et al. [7] conducted a techno-economic evaluation of hydrogen production by assessing the solar energy potential in Iran. Al-Sharafi et al. [8] investigated the hydrogen production potential in Saudi Arabia, analyzing different regions based on renewable capacity. These regions were compared primarily through the hydrogen production costs. Similarly, Iqbal et al. [9] assessed the hydrogen production potential across eight different sites in Pakistan, using wind energy. The evaluation was conducted based on technical and economic parameters. Rezaei et al. [10] focused on the hydrogen production potential using renewable energy and seawater aiming to enhance hydrogen production by ensuring easy access to water resources. Ayodele et al. [11] evaluated wind and hydrogen energy potential at different locations across South Africa. Katsigiannis et al. [12] examined the feasibility of hydrogen production using wind turbines, gas turbines, and solar systems. Bekele et al. [13] conducted a study to explore the general aspects and feasibility of wind energy utilization for hydrogen production. Several studies have investigated the hydrogen production potential in Türkiye from different energy sources, including solar [14], wind [15], hydroelectric [16], and other renewable resources. Arat et al. [17] focused on hydrogen-related studies conducted in Türkiye, analyzing academic and technical projects to provide guidance for future research. Dincer et al. [18] evaluated Türkiye's hydrogen potential from renewable sources in various selected locations. These studies aimed to assess the green hydrogen production potential of each resource being evaluated based on data provided by official institutions. Although numerous studies have been conducted on renewable energy and hydrogen at both national and international levels, research evaluating the hydrogen potential as an alternative energy source, particularly for emergency conditions, remains limited.

This paper presents an assessment of the hydrogen potential in the province of Elazig, Türkiye. The idea is to assess different parts of Elazig for hydrogen potential by renewable energy sources. The novelty of this paper lies in its integrated assessment of hydrogen potential in Elazig, Türkiye, against the backdrop of recent seismic events in 2023 that caused significant disruptions in fuel and energy supplies. The study strategically identifies safe zones of Elazig with high hydrogen production potential. This innovative approach not only aims to address energy scarcity during emergencies but also proposes a solution for energy transportation and storage by utilizing hydrogen from surplus electricity to aid areas in need. The paper offers meaningful insights into the potential of hydrogen production and contributes to the national hydrogen strategies and objectives of Türkiye.

2. Material and Method

The generation of hydrogen through the renewable energy sources, combined with the electrolysis process, represents one of the cleanest methods of hydrogen production. Figure 1 offers a visual illustration of the hydrogen generation process.

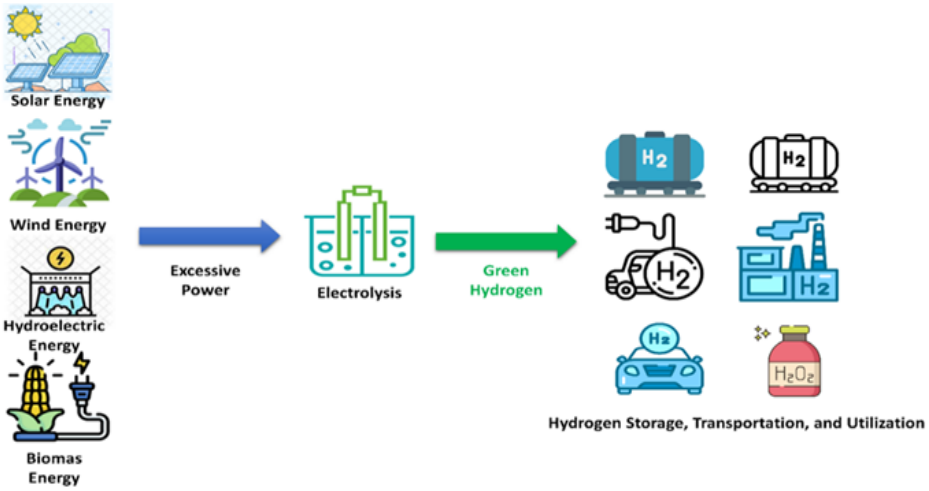

Figure 1. Renewable energies based green hydrogen production.

As illustrated in Figure 1, the diagram emphasizes the flexibility of electrolysis in capturing energy from renewable sources such as solar, wind, and other clean energy technologies for hydrogen production. Excess

renewable energy is channeled into the electrolysis process, which is a highly efficient method of producing hydrogen [19]. This chemical process is referred to as green hydrogen production. The hydrogen generated through this process has various applications, including transportation, industrial, residential, commercial, chemical, and agricultural sectors. For the production of 1 kg of hydrogen, approximately 9 liters of water are required for the electrolysis process. Different electrolyzer configurations exist, such as Alkaline (AEL), Polymer Electrolyte Membrane (PEM), and Solid Oxide Electrolyzers (SOE) [20]. PEM electrolyzers, in particular, are noted for their high efficiency rapid response times, operating at lower temperatures, and higher current densities, positioning them as leading technologies for green hydrogen production [21].

2.1. Potential assessment

The research conducted in this study centers the geographical area of Elazig, Türkiye. Situated within coordinates of 38° 38′ N latitude and 39° 20′ E longitude, this region encompasses a notable altitude of approximately 1067 m (3501 ft). The unique geographical layout of Elazig is characterized by its geographical resemblance to an inland peninsula, encircled by Lake Hazar and reservoirs formed by the Keban and Karakaya Dams. Figure 2 provides a visual representation of the map view detailing the geographical layout of Elazig, highlighting its distinctive topographical features and the spatial relationships of its districts within this province.

Figure 2. The general view of Elazig province.

The province offers a diverse range of renewable energy opportunities across its area. This study primarily focuses on evaluating the hydrogen production potential from wind and solar energy. The assessment involves analyzing various locations within the province to determine their viability for hydrogen generation. Figure 3 provides a detailed map that illustrates the wind energy potential across the different regions of the province.

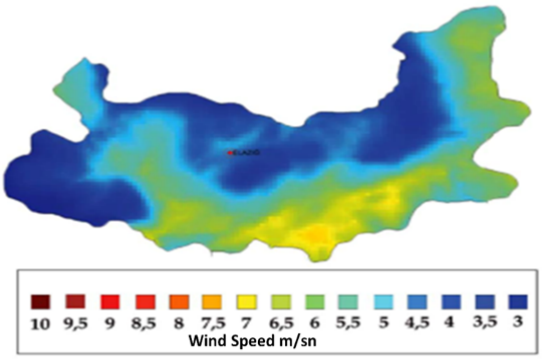

Figure 3. The wind potential map of Elazig province

Figure 3 highlights specific areas within Elazig that display varying levels of wind energy potential. The data for wind energy potential in this study were sourced from the State Meteorology Service, with wind speed

measurements taken at a height of 50 meters above ground level These assessments are essential for identifying optimal sites for wind energy projects. By selecting the locations with elevated wind potential, wind energy systems can generate electricity more efficiently, thereby enhancing the potential for hydrogen production [22]. In Elazig, the southern and southeastern regions exhibit higher wind energy potential compared to other parts of the province. To estimate the total wind energy potential, the overall area of the province was calculated using official data. The average wind speed at 50 meters in Elazig is recorded at 4.4 m/s.

Solar energy is abundant, widely available, and most importantly, freely accessible. These characteristics make it particularly beneficial for use in rural areas and off-grid locations, where access to the conventional electric grid can be limited or nonexistent [23]. The solar energy potential of the province is depicted in Figure 4, which illustrates a relatively uniform distribution of solar potential across the region. Solar radiation data were obtained from official Ministry resources and solar energy databases.

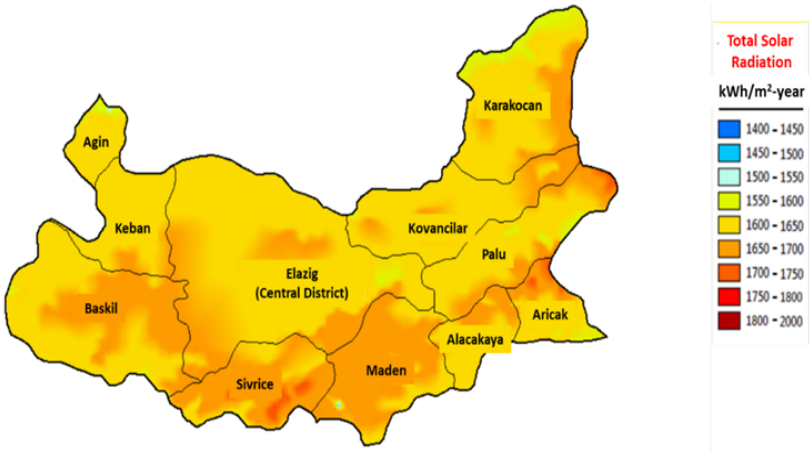

Figure 4. The solar potential of Elazig province.

As shown in Figure 4, there is a high potential for solar energy, particularly in the southern areas of the province. The presented data shows that the average solar potential in these regions varies significantly, ranging between 1550 and 1750 kWh/m² per year.

2.2. Component specifications

When evaluating the potential for hydrogen, it is necessary to consider the characteristics of the components to be used for both electricity and hydrogen production. These characteristics are crucial in comprehending the performance of the components, which contributes to the calculations related to hydrogen potential assessment within the study. Table 1 provides a comprehensive summary of the specifications associated with the selected electrolyzer technology.

Table 1. The specifications PEM electrolyzer [24].

Model Name	H-TEC PEM Electrolyzer ME450
Net Production Rate (Nm3/h)	42 – 210 Nm^3/h
Production Capacity Range (%)	20 – 100 %
Power Consumption at Stack (kWh/Nm3)	4.7 kWh/Nm^3 | 53 kWh/kg
H_2 Purity	5.0
Ambient Temperature (C)	-20°C to +40°C
System efficiency	75 %

Proton Exchange Membrane (PEM) electrolyzers operate on the same fundamental principles as other water electrolysis technologies, where water is electrochemically split into hydrogen and oxygen using electrical energy. The working principle is shown in the Figure 5.

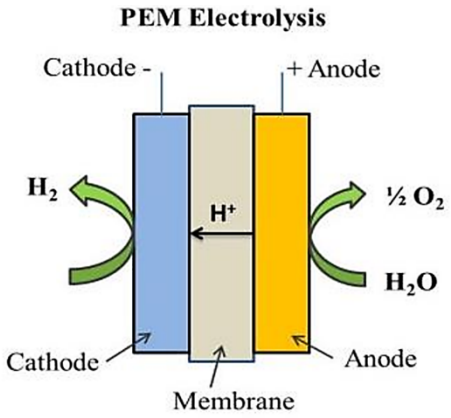

Figure 5. The working principle of a PEM electrolyzer.

For the electrolyzer, a defined quantity electricity is required to be applied to both electrodes. These electrodes are isolated from each other by an electrolyte characterized by high ionic conductivity. This application facilitates the decomposition of water into its elements, hydrogen, and oxygen in the electrolysis process. This process is described by the following equations [25].

$$Anode: H_2O \rightarrow 2H^+ + \frac{1}{2}O_2 + 2e^- \quad (1)$$

$$Cathode: 2H^+ + 2e^- \rightarrow H_2 \quad (2)$$

$$Overall\ reaction: H_2O \rightarrow H_2 + \frac{1}{2}O_2 \quad (3)$$

The expressions in Equations (1-3) are utilized to carry out the necessary modeling and analysis for the conversion of hydrogen into electricity.

PV panels generate electricity by converting sunlight into electrical energy through the solar cells. The method produces electricity without emitting pollutants, contributing to cleaner and greener energy generation [25]. In this study, mono-facial monocrystalline PV panels were employed for harnessing solar energy. The specific characteristics of the chosen PV panels are systematically presented in Table 2.

Table 2. The PV panel specifications [26].

Model Name	Canadian solar HiKu6 Mono PERC 400MS
Cell Type	Mono-crystalline
Nominal Max. Power (Pmax)	400 W
Max. System Voltage	1500V (IEC/UL)
Module Efficiency	20.5%
Operating Temperature	-40°C ~ +85°C

The electrical output of PV panels P_{PV} is given in Equation (4).

$$P_{PV} = Y_{PV} \times f_{PV}\left(\frac{G_T}{G_{T,SC}}\right) \times [1 + a_f(T_C - T_{C,SC})] \quad (4)$$

Where:
Y_{PV}: Rated power value of PV panels under standard conditions (SC) (kW)
f_{PV}: PV panels derating factor (%)
G_T: Solar irradiation value on PV panels (kWh/m^2)
$G_{T,SC}$: Standart irradiation value (1 kWh/m^2)
a_f: PV panel temperature coefficient (% °C)
T_C: PV cell temperature (°C)
$T_{C,SC}$: PV cell standard temperature (25 °C)

If the local wind velocity is denoted as V, with air density represented by ρ, and A as the swept area of the rotating blades of the wind turbine, the potential wind energy can be mathematically expressed as follows:

$$W = \frac{1}{2} \times \rho \times A \times V^3 \quad (5)$$

The potential for a given wind speed is expressed as described above. Wind speeds vary with altitude levels. The Hellmann Equation serves as a common method for estimating wind speeds at different altitudes of a wind turbine. [27]. The equation can be expressed as in Equation (6).

$$\frac{V}{V_0} = (\frac{H}{H_0})^{\propto} \quad (6)$$

Where:
H_0 is the reference height,
V_0 is the wind speed at the reference height,
H is the height at which the wind speed is to be calculated,
V is the wind speed at height
$\propto$ is the friction coefficient, a value that varies according to the topology of the area exposed to the wind. The power captured by a wind turbine can be quantitatively described using fundamental aerodynamic principlesThis relationship can generally be expressed in the form of the power equation of a wind turbine in Equation (7).

$$P = \frac{1}{2} \times C_P \times p \times A \times {V_W}^3 \quad (7)$$

Where:
P is the power extracted from the wind (watts),
ρ is the air density (kg/m³),
A is the swept area of the turbine blades (m²),
V_W is the wind speed at the turbine level(m/s),
C_P (λ, β) is the power coefficient, which depends on the tip speed ratio (λ) and the blade pitch angle (β). This parameter represents the energy conversion efficiency of a turbine. C_P is critical to wind turbine design and efficiency, influenced by blade aerodynamics, rotor integrity, and control strategies. The theoretical maximum, known as the Betz Limit, is 59.3%. Under normal conditions, this value can be maintained between 45% and 55% with effective control strategies, ensuring efficient operation. The proposed study utilizes onshore-type wind turbines featuring horizontal axis turbines as the chosen wind energy conversion system. The usage of these types aligns with specific considerations and requirements, and the turbine specifications are tabulated as Table 3.

Table 3. Wind turbine specifications [28].

Model Name	EWT DW 54
Rotor diameter (meters)	50
Rated Power (kW)	900
Cut-in wind speed (m/s)	3
Cut-out wind speed (m/s)	25

The power curves, which details the relationship between power output and wind speed, play a pivotal role in the analysis of the selected turbine's generation potential under varying atmospheric conditions. Characteristic curves for the selected model are shown in Figure 6.

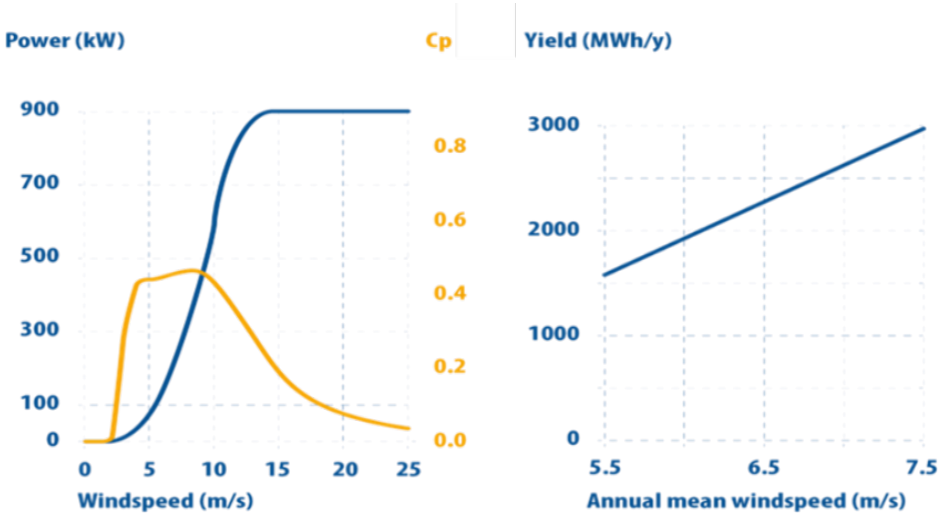

Figure 6. The solar potential of Elazig province.

As depicted in Figure 6, wind speeds exceeding the minimum threshold initiate electricity generation. The variation of the power coefficient (C_P) between 0.45 and 0.55 (yellow curve) highlights the critical role of adaptive control systems. These controls adjust operational parameters in real-time to ensure that C_P remains within this optimal range, thereby maximizing energy output and contribute to effective electricity generation. The power (Yield) curve relative to wind speed values is derived from measurements taken at the tower hub level. With the annual average wind speed, it is estimated that approximately 1000 MWh/year of electricity can be generated in the selected province.

The geographical restrictions are the excluded areas in different parts of the province. These limitations are crucial in identifying the specific areas where energy conversion systems will be implemented. The territory gets more rugged in the south and southeast districts (Sivrice, Maden Alacakaya, Aricak, Palu) [17]. Approximately 80% of the province's territory is utilized, considering topological constraints and other relevant factors. To account for these variations, the study introduces the topological coefficient parameter (α). This coefficient provides a systematic approach to evaluating the suitability of the terrain for energy conversion projects. The topological coefficient is determined through a detailed analysis of geographic maps and comprehensive evaluations of all designated areas [20]. The specific topological coefficients for each district are provided in Table 4, offering a quantitative representation of the topological considerations inherent in the study's analysis.

Table 4. The topological coefficients for Elazig province.

	Area (km2)	The topological coefficients
Elazig (Central District)	2243	0.47
Agin	242	0.05
Alacakaya	318	0.06
Arıcak	354	0.07
Baskil	1318	0.28
Karakocan	1049	0.22
Keban	641	0.121
Kovancılar	960	0.2
Maden	819	0.17
Palu	730	0.156
Sivrice	710	0.15
Total	8343	

The yearly electricity consumption of the whole province was obtained from the energy distribution company and other institutes. Although the electricity consumption is calculated as Wh, the hydrogen production based on renewable energy sources expressed as megatons (Mt). To ensure equivalence between different units, these values are converted to an equal unit of electricity, produced as Mt of hydrogen. According to these assumptions, the yearly electricity consumption of the province is about 0.02 Mt/per year [18].

3. Results and discussions

Solar energy, changes in various districts according to different solar radiation and insulation values. For the city center and the districts, monofacial PV panels are assessed with an efficiency of 20.5% The other option, bifacial PV arrays, are commonly utilized for floating (on-water) applications. For wind turbines, hub height for a wind turbine can be adjusted based on population distribution and geographical conditions. Horizontal-bladed high tower turbines are utilized in scarcely populated districts. This type turbines are not applicable in densely populated and agricultural areas [1]. Theoretically, 1 kg of hydrogen production requires 117650 kJ of energy for the production process. The efficiency of the selected electrolyzer is regarded as 75%. Therefore, the required energy for hydrogen production (W_{actual}) is approximately calculated as:

$$W_{actual} = \frac{117{,}650}{0.75} = 158866\ kJ \tag{8}$$

As described in Equation (8), the selection of the electrolyzer type determines the production characteristics. In this analysis, it is assumed that 60% of the total potential power (90000 kj) will be generated by wind turbines, while the remaining 40% (68866 kj) will be supplied by the reference solar panels. The evaluation of hydrogen potential can be conducted in the city center and other districts by using the energy equivalent of 1 kg hydrogen. Based on the average wind speed and solar potential across the province, the estimated hydrogen production potential is approximately 11.9 Mt for 1 kg H_2. Hydrogen potential based on this value can be mapped by assessing each district's hydrogen potential. This involves a comprehensive evaluation of factors such as renewable energy availability, topological constraints, and other relevant parameters for each district. By conducting this, a spatial representation can be generated to visually depict the varying degrees of hydrogen potential across the entire province [6]. In light of this information, Figure 7 provides a colorized map of the province showing total hydrogen potential based on the available renewable power.

Figure 7. Hydrogen production potential of Elazig from excess power.

In Figure 7, each color represents potential variation, ranging from light to dark tones. The produced energy is firstly provided for load demand from different parts of the province and the excess power is utilized for electrolyzer systems. Districts with more available land and higher altitudes tend to have greater hydrogen production potential. Dark-colored areas, such as Elazig (central district), Baskil, and Kovancilar, demonstrate higher potential compared to other districts. Although Karakocan exhibits substantial potential, the presence of topographical challenges, as outlined in Table 4, reduces the hydrogen potential for this district. Similarly, other districts face diminished potential due to a combination of topographical limitations and various environmental factors. Notably, districts located near water reservoirs, particularly in the northern and western parts of the province, exhibit significantly greater potential for hydrogen production compared to other regions. Figure 8 provides a graphical representation of the relative contributions of each district to the overall hydrogen potential.

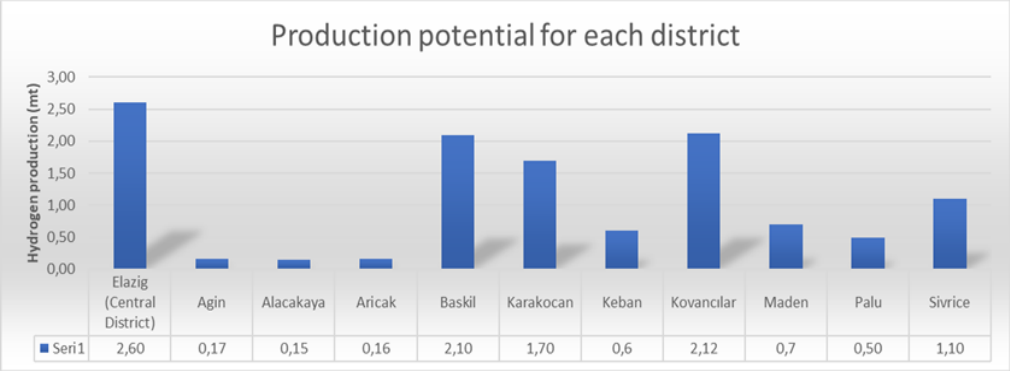

Figure 8. Hydrogen potential graph for each district.

Figure 8 highlights the proportional hydrogen production across different districts, offering insights into regional variations in production efficiency and capacity. Furthermore, it enables researchers, policymakers, and stakeholders to comprehend and analyze the distribution and magnitude of hydrogen potential for the area. The number of components required per kilogram of hydrogen is another critical parameter for evaluating production potential. Table 5 presents values derived from the selected wind turbine and solar panel data.

Table 5. The number of components required per kilogram of hydrogen.

Components	Required power for per component (kJ)	Numbers* Selected Model
Wind Turbine	90000	1* EWT DW 54
Solar Panel	68866	50*PERC 400MS

To determine the number of energy conversion components required per unit of hydrogen production, the study considered the average wind speed and solar radiation values of Elazığ, along with the efficiency values of the selected components. The overall efficiency of the solar panel was assumed to be 20%, as determined by its standard characteristic value. The wind turbine's general efficiency, depicted in Figure 6, was estimated to be approximately 40% based on average wind speed values. Calculations were performed based on the power contributions from wind turbines and solar panels, expressed relative to the energy demand for producing one kilogram of hydrogen in kilojoules. For the selected electrolyzer technology, it was determined that the required energy could be supplied by combining 1 wind turbine and 50 solar panels.

4. Conclusions

Hydrogen can become an important means of renewable energy storage and transportation over long distances and a long period. The main idea related to hydrogen is to create a promising clean, and more durable energy source and an essential component for further development. Due to its geopolitical location, Türkiye is rich in retaining various types of renewable energy resources. By using these sources, the utilization of fossil fuels could decrease and provide clean sustainable energy for different parts of Türkiye. This study provides an in-depth analysis of the potential for hydrogen production in various districts of Elazig, Türkiye. The available renewable potentials for each district are discussed comprehensively, shedding light on the unique factors that influence hydrogen production in the region. The study presents innovative ideas to deal with the fossil fuel usage, and energy scarcity problems for the province, as well as the region. It has been observed that districts with high energy potential and low restrictions have a high potential for hydrogen production. The results prove that renewable energy potential for the province is convincing for hydrogen productibility. In this way, greenhouse gas emissions will be reduced and a carbon-free province and eco-friendly hydrogen production will be possible. Furthermore, the results fulfill a concise guide to enable different sectors to use renewable energy potentials for hydrogen production. Future research will involve conducting various simulations and real-time experimental studies using different configurations of renewable energy sources for the province. These studies will be based on real-time meteorological data and on-site assessments to enhance the accuracy and applicability of the findings.

References

[1] Harrouz A, Temmam A, Abbes, M. Renewable energy in algeria and energy management systems. IJESG 2018; 2(1): 34-39.

[2] Dincer I, Javani N. Karayel GK. Sustainable city concept based on green hydrogen energy. Sustainable Cities Soc 2022; 87, 104154.

[3] Bayrak ZU, Bayrak G, Ozdemir MT. Gencoglu MT, Cebeci M. A low-cost power management system design for residential hydrogen & solar energy-based power plants. Int J Hydrogen Energy 2016; 41(29), 12569–12581.

[4] T.C. Enerji ve Tabii Kaynaklar Bakanlığı, Türkiye Hidrojen Teknolojileri Stratejisi ve Yol Haritası 2023.

[5] Caliskan A, Percin HB. Techno-economic analysis of a campus-based hydrogen-producing hybrid system. Int J Hydrogen Energy 2024; 75: 428-437

[6] Mostafaeipour A, Khayyami M, Sedaghat A, Mohammadi K, Shamshirband S, Sehati, MA, Gorakifard. E. Evaluating the wind energy potential for hydrogen production: A case study. Int J Hydrogen Energy 2016; 41: 6200–6210.

[7] Nematollahi O, Alamdari P, Jahangiri M, Sedaghat A, Alemrajabi AA. A techno-economical assessment of solar/wind resources and hydrogen production: A case study with GIS maps. Energy 2019; 175: 914–930.

[8] Al-Sharafi A, Sahin AZ, Ayar T, Yilbas BS. Techno-economic analysis and optimization of solar and wind energy systems for power generation and hydrogen production in Saudi Arabia. Renewable Sustainable Energy Rev 2017; 69: 33–49.

[9] Iqbal W, Yumei H, Abbas Q, Hafeez M, Mohsin, M, Fatima A, et al. Assessment of Wind Energy Potential for the Production of Renewable Hydrogen in Sindh Province of Pakistan. Processes 2019; 7:196.

[10] Rezaei M, Naghdi-Khozani N, Jafari N. Wind energy utilization for hydrogen production in an underdeveloped country: An economic investigation. Renewable Energy 2020; 147: 1044–1057.

[11] Ayodele TR., Munda JL. Potential and economic viability of green hydrogen production by water electrolysis using wind energy resources in South Africa. Int J Hydrogen Energy 2019; 44(33): 17669-17687.

[12] Katsigiannis YA, Georgilakis PS, Karapidakis ES. Multiobjective genetic algorithm solution to the optimum economic and environmental performance problem of small autonomous hybrid power systems with renewables. IET Renewable Power Gener 2010; 4:404-19.

[13] Bekele G, Tadesse G. Feasibility study of small Hydro/PV/ Wind hybrid system for off-grid rural electrification in Ethiopia. Appl Energy 2012; 97 :5-15.

[14] Karayel GK, Javani N, Dincer, I. Green hydrogen production potential for Türkiye with solar energy. Int J Hydrogen Energy 2022; 47(45): 19354-19364.

[15] Karayel GK, Javani N, Dincer I. Green hydrogen production potential in Türkiye with wind power Int J Hydrogen Energy 2023; 20(2): 129-138.

[16] Karayel GK, et al. Hydropower for green hydrogen production in Türkiye, Int J Hydrogen Energy 2022; 48(60): 22806-17.

[17] Arat HT, Baltacioglu MK, Tanç B, Sürer MG, Dincer I. A perspective on hydrogen energy research, development and innovation activities in Türkiye. Int J Energy Res 2020; 44(2): 588-593.

[18] Dincer I, Javani N, Karayel GK. Hydrogen farm concept: A Perspective for Türkiye. Int J Energy Res 2021; 45(13): 18309–18317.

[19] Razi F, Dincer I. Challenges, opportunities and future directions in hydrogen sector development in Canada. Int J Hydrogen Energy 2022; 47(15): 9083-9102.

[20] Yilmaz C, Kanoglu M. Thermodynamic evaluation of geothermal energy powered hydrogen production by PEM water electrolysis. Energy J 2014; 69: 592–602.

[21] Bilhan AK. Integrated solar-based PEMWEs for green electricity production. Int J Hydrogen Energy 2024; 75: 415–427.

[22] Emeksiz C, Demirci B. The determination of offshore wind energy potential of Türkiye by using novelty hybrid site selection method. Sustainable Energy Technol Assess 2019; 36: 100562.

[23] Ural Z, Gencoglu MT. Design and simulation of a solar-hydrogen system for different situations. Int J Hydrogen Energy 2014; 39(16): 8833-8840.

[24] PEM Electrolyzer ME450: H-TEC SYSTEMS products. https://www.h-tec.com/en/products/detail/h-tec-pem-electrolyser-me450/me450/.

[25] Dagteke SE, Unal S. Design of an Electric Vehicle Charging System Consisting of PV and Fuel Cell for Historical and Tourist Regions. World Electric Vehicle Journal 2024; 15(7): 288-8.

[26] HiKu6 Mono PERC specification datasheet. https://static.csisolar.com/wp content/uploads/sites/9/2023/09/26103727/CS-Datasheet-HiKu6_CS6R-MS_v2.3C25_EN-25-years-product-warranty-1.pdf.

[27] Çelikdemir S, Özdemir, MT. Türkiye's Offshore Hybrid Energy Potential and Cost Estimation in the Eastern Mediterranean. Türk Doğa ve Fen Dergisi 2023; 12(1): 99-107.

[28] Directwind 54 specification datasheet, https://ewtdirectwind.com/products/dw54/.

Turkish Journal of Science & Technology
20(1), 17-27, 2025

Research Paper
https://doi.org/10.55525/tjst.1481794

Investigation of the Effect of Grain Size and Wire Size on the Mechanical and Structural Properties of Polycrystalline Ni Nano Wire Using Molecular Dynamics Simulation

Sefa KAZANÇ[1], Canan AKSU CANBAY[2*]
[1] Mathematics and Science Education, Faculty of Education, Fırat University, Elazig, Türkiye
[2] Department of Physics, Faculty of Science, Fırat University, Elazig, Türkiye
[1] skazanc@firat.edu.tr, [*2] caksu@firat.edu.tr

(Geliş/Received: 10/05/2024; Kabul/Accepted: 14/09/2024)

Abstract: The effect of grain size and length-to-diameter ratio (LDR) on the mechanical properties of polycrystalline Ni nanowire was examined by molecular dynamics simulation as a result of uniaxial tensile deformation applied at a temperature of 300 K. The Embedded Atom Method (EAM) was used to determine the forces acting on the nanowire atoms. Elastic modulus (E), yield strength and fracture stress values were determined from the stress-strain relationship determined as a result of the deformation process. Microstructural changes resulting from plastic deformation were examined from the atomic positions determined using the common neighbor analysis method (CNA). It was determined that grain size and LDR had a significant effect on the deformation behavior of Ni nanowire, and plastic deformation and breaks resulted from the rearrangement of atomic positions by surface effect and also the nanowires with small grain size and LDR exhibited superplasticity behavior. The grain size in the modeled polycrystalline nanowire system affected the movement mechanisms of the grains, grain boundaries, and the relationship between grain size and flow force was investigated. From this relationship, the Hall-Petch effect and the reverse Hall-Petch effect were observed after a certain critical grain size.

Key words: Polycrystal, nanowire, superplastic, molecular dynamics, Hall-Petch effect.

Tane Büyüklüğü ve Tel Boyutunun Polikristal Ni Nano Telinin Mekanik ve Yapısal Özelliklerine Etkisinin Moleküler Dinamik Benzetimi ile İncelenmesi

Öz: Polikristal Ni nano telinin mekanik özelliklerine tane büyüklüğü ve uzunluk-çap oranının (Length-to-Diameter-Ratio-LDR) etkisi, 300 K sıcaklık değerinde uygulanan tek eksenli çekme deformasyonu sonucu moleküler dinamik benzetimi ile incelendi. Gömülmüş Atom Metodu (GAM) nano tel atomları üzerine etki eden kuvvetlerin belirlenmesinde kullanıldı. Deformasyon işlemi sonucu tespit edilen zor-zorlanma ilişkisinden Elastiklik modülü (E), akma dayanımı, kopma gerilmesi değerleri belirlendi. Ortak komşu analiz yöntemi (Common Neighbor Analysis-CNA) kullanılarak tespit edilen atomik konumlardan plastik deformasyon sonucu meydana gelen mikro yapısal değişimler incelendi. Tane büyüklüğü ve LDR'nin Ni nano telinin deformasyon davranışları üzerinde önemli bir etkiye sahip olduğu ve plastik şekil değişimi ve kopmaların, atomik konumların yüzey etkisi ile yeniden düzenlenmesinden kaynaklandığı belirlendi. Küçük tane boyutuna ve LDR'ye sahip nanotellerin süper plastiklik davranış sergilediği tespit edildi. Modellenen polikristal nano tel sistemde tane boyutunun, tanelerin hareket mekanizmalarını, tane sınırlarını ve tane boyutu ile akma zoru arasındaki ilişkiyi etkilediği tespit edildi. Bu ilişkiden Hall-Petch etkisi ve belirli bir kritik tane büyüklüğünden sonra ters Hall-Petch etkisi gözlemlendi.

Anahtar kelimeler: Polikristal, nano tel, süper plastik, moleküler dinamik, Hall-Petch etkisi.

1. Introduction

The studies on the mechanical properties of nanowires are becoming an increasingly important area of materials science and also nanowires have been extensively studied in recent years for their use as building blocks in nano-electromechanical devices due to their superior thermal, mechanical, electronic and optical properties resulting from their nanoscale scale [1-5]. The use of metallic nanowires as building blocks and connectors in electronic and optical devices as well as chemical and biological sensors requires an understanding of their structure and mechanical properties [6].

The properties of nanostructured materials can vary depending on the intrinsic microstructure size and extrinsic sample size [7]. An important property of metallic nanowires is the surface effects resulting from their large surface/volume ratio. Internal stresses resulting from surface tension in nanowires lead to mechanical properties that are quite different from bulk structures [8]. As a result of experimental studies, it has been determined that the grain boundaries of metallic nanowires significantly affect their mechanical properties [9-11]. Reducing the sample size to nanoscale reduces the formation and probability of defects in the material. The size, shape, number of grains in the sample, crystal orientations and boundary structures in the grains have a significant impact on the thermodynamic, mechanical and electrical properties of materials. Although there are many theories

[*] Corresponding author: caksu@firat.edu.tr. ORCID Number of authors: [1] 0000-0002-8896-8571, [2] 0000-0002-5151-4576

explaining how these parameters affect large grains, this number is quite small at the nanoscale [12]. If metal nanowires are used in practice, the most important elements to know are their elastic behavior and durability during tensile deformation [13,14]. Young's modulus, yield stress and fracture stress are determined as a result of tensile deformation tests applied to the sample [15]. Although it is easy to perform these tests at macro scale to determine mechanical properties, they are quite difficult at nano dimensions.

Due to the difficulty and time-consuming processes of experimental studies at the nanoscale, the computer simulations were used to establish a connection between theory and experiment. There are effective simulation techniques used in modeling systems at the atomic level. One of these techniques is the Molecular Dynamics (MD) simulation method. MD simulation method is widely used to investigate the physical and thermodynamic properties of alloy systems, glassy structures, polymers, semiconductors and nanomaterials [16-18]. However, MD simulations are a powerful modeling tool used to examine the structure, mechanical properties and deformation behaviors of metallic nanowires under different strain conditions, especially at the atomic level [19-21]. However, studies on the mechanical properties of polycrystalline nanowires are still not sufficient.

In this study, the uniaxial tensile deformation process applied to polycrystalline Ni nanowires with different LDR and grain sizes at a temperature of 300 K and a strain rate of $1x10^{10}$ s^{-1} was examined with the MD simulation software package LAMMPS (Large-scale Atomic/Molecular Massively Parallel Simulator). Calculation of forces between Ni atoms was performed with the EAM potential function. The main advantage of EAM is that the calculation time is short and it provides the opportunity to work with a large number of particles. The effect of grain number and LDR on the mechanical properties of the model polycrystal was tried to be determined from the strain curves and the atomic-sized deformation mechanism of the nanowire during strain from the CNA analysis obtained from the OVITO program. In addition, the development processes of dislocations in the nanowire within the structure during the tensile deformation process were detected by Dislocation Extraction Algorithm (DXA) analysis method.

1. Material and Method

The extent to which the results obtained from MD simulation are in agreement with the experimental results depends on the correct selection of the interatomic potential. EAM, proposed by Daw and Baskes [22] and whose validity has been proven by many studies, produces very effective results in determining the mechanical properties of materials. The general structure of EAM as a semi-empirical potential energy function is defined as Eq.1;

$$E_{top} = \sum_i^N F_i\,(\rho_i) + \frac{1}{2}\sum_{i\neq j} \Phi\left(r_{ij}\right) \tag{1}$$

In this function, which includes many-body interactions, N is the number of atoms in the model system, $F_i(\rho_i)$, corresponds to the embedding energy and $\Phi(r_{ij})$ corresponds to the binary interaction energy [23]. Details of EAM and its potential parameters for the Ni element can be found in the literature [24]. The expression of force in the tensile or compression strain to be applied in MD studies is calculated by the microscopic force tensor given as Eq.2 [25,26].

$$\boldsymbol{\sigma} = V^{-1}\left[\sum_{i=1}^{N} m_i \vartheta_i \vartheta_i - \sum_{i=1}^{N}\sum_{j>i}^{N} \frac{F_{ij}}{r_{ij}} \mathbf{r}_i.\,\mathbf{r}_j\right] \tag{2}$$

The difficult tensor with nine components is expressed as Eq.3;

$$\sigma_{ij} = \begin{pmatrix} \sigma_{11} & \sigma_{12} & \sigma_{13} \\ \sigma_{21} & \sigma_{22} & \sigma_{23} \\ \sigma_{31} & \sigma_{32} & \sigma_{33} \end{pmatrix} \tag{3}$$

Positive values of the normal components of the force tensor correspond to tensile force, and negative values correspond to compression force [27].

One of the algorithms used to analyze the details of the atomic configurations in the system to be modeled in the MD simulation method is CNA analysis [28]. The basis of this method is to assign 4 characteristic integers (*i, j, k, l*) to a selected reference atom to define a structure and analyze its surrounding neighbors. Details of this method can be found in the literature [29]. In the study, CNA analysis was performed with the OVITO program and atomic positions were determined [30].

The effects of grain size and LDR on the deformation behavior of polycrystalline Ni nanowire were examined by MD simulation under a strain rate of $1x10^{10}s^{-1}$ at 300 K temperature. In this study, grains were created in the

nanowire with the Voronoi tessellation algorithm by the Atomsk program [31]. To determine the average grain size d in the model system, the expression $n = [6V / (\pi d^3)]$ was used, where n is the grain number and V is the MD cell volume [32]. The points where the grains would grow were determined randomly and the grains grew by focusing on these points. The study consists of three parts. In the first part, basic mechanical properties were determined for the model nanowire from the strain curves obtained as a result of the applied tensile deformation for LDR values 1, 1.5, 2, 3 and 4. The base cross-sectional area of all nanowires used in the study is 70.4Åx70.4Å, the number of atoms in the nanowire is N and the average grain size is d, respectively: 32000-3.21 nm for LDR=1, 48000-3.68 nm for LDR=1.5, LDR=2. It was determined as 64000-4.05 nm for LDR=3, 96000-4.64 nm for LDR=3 and 128000-5.1 nm for LDR=4. In the second part, the effect of grain size on the mechanical properties of the nanowire was tried to be determined by creating 10, 12, 15, 20, 30, 50, 70 and 80 grains in the nanowire for LDR = 4 value. Hall-Petch and reverse Hall-Petch effect were determined from the relationship between grain size and flow strain. In the last part, the change in mechanical properties was examined by creating grains of fixed size (d = 5.1 nm) in nanowires for different LDR ratios, as in the first part.

In the polycrystalline Ni nanowire system modeled in this study, atoms were placed at fcc lattice points with a lattice parameter of 3.52 Å. Periodic boundary conditions were applied only along the x direction of the nanowire. However, the y and z directions of the nanowire are freed. The initial velocities were assigned to the atoms randomly, taking into account the Maxwell-Boltzman velocity distribution. The velocity form of the Verlet algorithm was used for the numerical solution of the equations of motion at 1 fs time intervals. The NVT statistical ensemble was used to ensure that all model polycrystalline nanowires reached equilibrium at target temperature and pressure values before applying the drawing process.

2. Results and Discussion

In this study, the changes in mechanical properties and the plastic deformation mechanism that occurred as a result of $1x10^{10}$ s^{-1} tensile strain applied along the x-axis under a constant temperature of 300 K and a pressure of 0 GPa on polycrystalline Ni nanowires with different initial structures and grain sizes were tried to be examined by MD simulation method.

2.1. Effect of LDR variation on mechanical properties of constant grain number polycrystalline Ni nanowire

Figure 1 shows the different initial structure obtained from the (001) plane section of the 12-grain Ni nanowire from the OVITO program. In the atomic configuration obtained from CNA analysis, green atoms indicate fcc unit cell structures. However, the white atoms represent the irregularly structured atoms at the grain boundary, which are not defined as any unit cell structure by CNA, and the surface atoms of the nanowire, where periodic boundary conditions are not applied.

In this study, first of all, the changes in the mechanical properties of nanowires with different LDR values as a result of uniaxial tensile stress was tried to determine. To reduce the effect of the random nature of sample generation throughout the entire study, the number of grains in the nanowires was fixed and set at 20. The fixed number of grains caused the formation of grains of different sizes in the nanowire system, depending on the LDR ratio. The strain curve obtained as a result of the tensile deformation applied to the polycrystalline Ni nanowire with LDR change is given in Fig. 2. In all nanowires, it is clearly seen that the stress-strain curve, where the elastic properties of the sample are determined, changes almost linearly up to a certain value of the applied strain. The elastic modulus of Ni polycrystalline nanowires was determined by linearly fitting the elastic region of the stress curve up to 2 strain value. The first maximum point on the stress-strain curve where plastic deformation begins is expressed as the yield force. It is thought that the zig-zag changes seen in Fig. 2 arise from the atomic arrangements within the structure [33]. Parameters expressing the mechanical properties of the polycrystalline Ni nanowire such as elastic modulus, yield strain, and fracture stress depending on the LDR values are given in Table 1. It has been determined that as the grain size decreases, the elastic modulus and yield force value decrease. Experimental results show that the elastic modulus of nanowires increases with decreasing wire diameter [34,35].

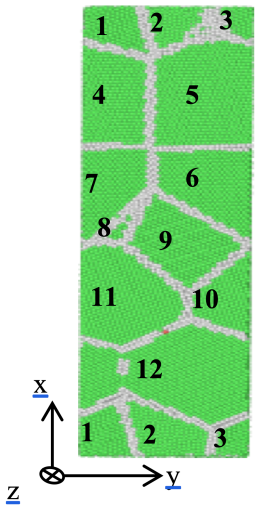

Figure 1. Initial structure of the polycrystalline Ni nanowire system containing 12 grains for LDR = 4.

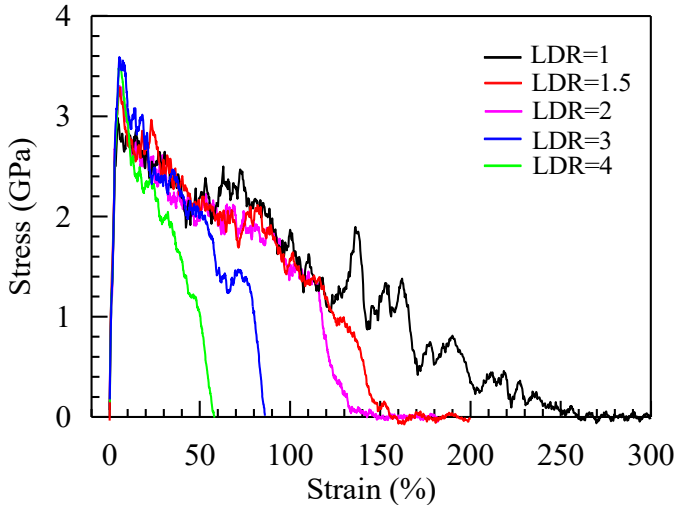

Figure 2. Stress-strain curves of polycrystalline Ni nanowire for different LDR values.

A softening of the material is observed with decreasing grain size. It is thought that this softening occurs because the grain boundaries occupy a larger part of the total volume in samples with smaller grain sizes and grain boundary sliding becomes easier [36]. The elastic weakness of grain boundaries and triple junctions at small grain size significantly affects the elastic properties of polycrystalline nanowires. Looking at the fracture percentage values given in Table 1, it can be seen that two deformation behaviors occur in the model nanowire sample: plastic and superplastic. At LDR values of 1, 1.5 and 2, the fracture strain value for nanowires was over 100% and superplastic deformation was observed. Especially for LDR=1, the percentage of fracture strain is quite high. Super plasticity is known as the ability of the sample to change shape greatly without bending at certain temperatures and strain rates. In superplastic materials, the deformation area can increase from 100% to 1000% without giving way. It is accepted that superplastic deformation will occur mostly with grain boundary sliding. The idea that grain boundary shifting will be effective in superplastic deformation arises from the fact that these materials have a small-grained structure [37]. Fig. 3 shows the atomic positions obtained from CNA analysis for different strain percentages, from the initial state ε=0%, where no strain is applied, for LDR value 1, to the value ε=259%, where fracture occurs in the sample. Plastic deformation is observed without any neck formation up to ε=100% of the tensile stress applied to the sample. At ε=20% value and beyond, hcp unit cell structures, indicated by red atoms, are formed in almost all grains. These structures are known as stacking defects that occur as a result of the nucleation of Shockley partial dislocations in the model nanowire [38,39].

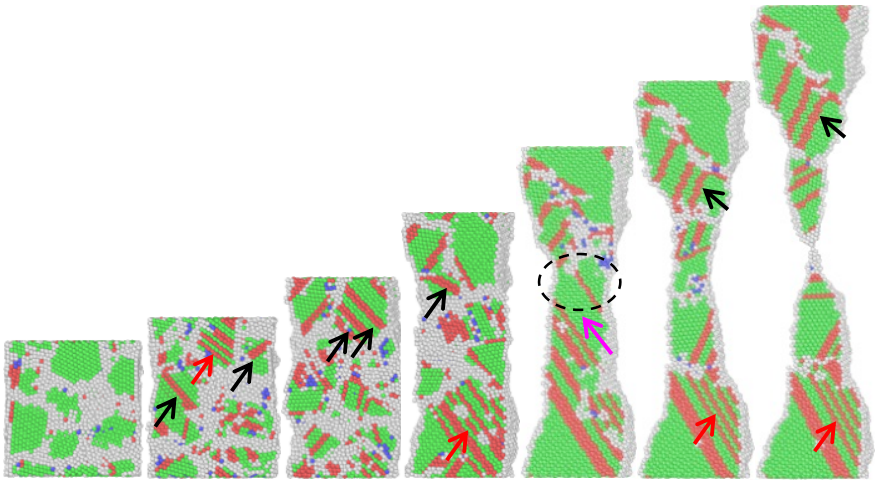

Figure 3. Atomic images obtained at different strain percentages of the polycrystalline Ni nanowire system with d = 3.21nm grain size for LDR = 1 at a strain rate of $1x10^{10}$ s^{-1}.

Table 1. Parameters of some elastic and plastic properties of polycrystalline Ni nanowires with different LDR and grain sizes containing 20 grains.

LDR	1	1.5	2	3	4
Grain size (nm)	3.21	3.68	4.05	4.64	5.10
E (GPa)	68.2	71.1	78.6	78.9	79.2
Yield strength (GPa)	2.96	3.28	3.29	3.58	3.58
Fracture strain (%)	259	155	148	86.0	59.0

As the strain increases, accumulation defects increase as a result of the nucleation and propagation of new dislocations. Two side by side atomic layers consisting of hcp unit cells are defined as internal stacking defects, the structure with an fcc atom layer between two hcp atomic layers is defined as external stacking defect, and the structure consisting of many fcc unit cells between two hcp layers is defined as deformation twins [40,41]. Accordingly, internal stacking defect formation was detected in the places marked with black arrows in Fig. 3, and external stacking defects were detected in the places marked with red arrows. However, deformation twins were detected in the area indicated by the pink arrow. It can be seen that at ε=150%, the nanowire begins to neck in the region indicated by the dotted circle, at ε=200%, the neck area gradually becomes thinner with increasing strain, and at ε=259%, fracture occurs. In an experimental study conducted by Lu, it was observed that excessive elongation (ε=5000%) occurred in the Cu nanowire synthesized in high purity under tensile deformation [42]. For the strain percentages from ε=0% to ε=259% given in Fig. 3, the percentage changes obtained from the CNA analysis of the atoms called "other" were determined as 50, 50.6, 46.3, 36.8, 28.4, 27.8 and 27.3, respectively. Accordingly, it is thought that the decrease in the percentage of surface atoms and "other" atoms representing grain boundaries due to periodic boundary conditions with increasing strain occurs as a result of the grains in the nanowire coalescing with increasing strain and the grain boundaries disappear.

2.2. Effect of grain size on mechanical properties of polycrystalline Ni nanowire

In Figure 4, for the fixed initial structure of the MD calculation cell (LDR = 4), polycrystalline Ni nanowires containing 10, 12, 15, 20, 30, 50, 70 and 80 grains are applied with a strain rate of $1x10^{10}$ s^{-1} along the x-axis direction. The stress-strain curves obtained as a result of tensile deformation are seen. The grain numbers used in the study were chosen randomly to determine the effects of grain size on the mechanical properties of the nanowire. The elastic modulus, yield strength and fracture strain percentages obtained from the stress-strain curves determined as a result of the uniaxial drawing process applied to nanowires with different grain sizes are given in Table 2. From Figure 4, it is clearly seen that the strain-strain curve changes almost linearly up to a certain value of the applied strain in all nanowires with different grain numbers. The elastic modulus values obtained from the

regression analysis of this change, known as the elastic deformation region, are given in Table 2. It is clearly seen that the elastic modulus is affected by grain size. As the number of grains increases, in other words, as the grain size decreases, the elastic modulus decreases. When the strain applied to the nanowires reaches the value corresponding to the yield strength, which is the maximum point of the stress-strain curve, the mechanisms required for plastic deformation begin to take effect and permanent deformations begin. When Table 2 is examined, increasing the number of grains in nanowires with 10, 12 and 15 grain numbers caused an increase in the yield strength values. Polycrystals are stronger than single crystals, and the increase in flow force as the number of grains increases, in other words as the grain size decreases, causes an increase in the strength of the material due to the "smaller is stronger" effect [7].

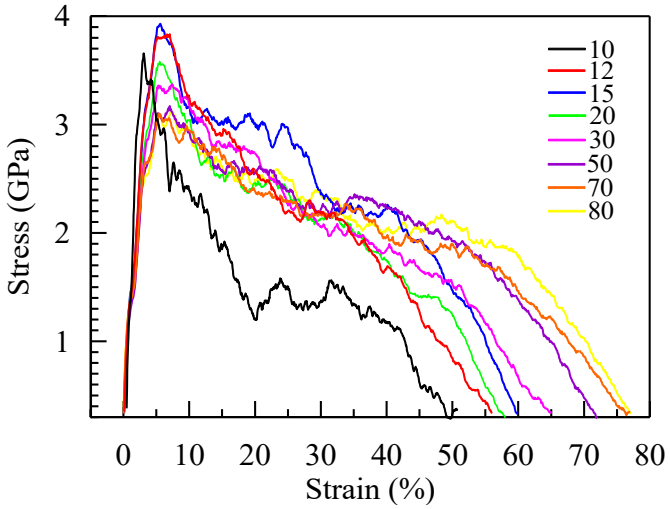

Figure 4. Strain curves of polycrystalline Ni nanowire containing different numbers of grains for a constant value of LDR = 4.

Table 2. Parameters of some elastic and plastic properties of polycrystalline Ni nanowires with different grain numbers for the constant value of LDR = 4.

The number of grain	Grain size (nm)	E (GPa)	Yield strength (GPa)	Fracture strain (%)
10	6.43	88.87	3.68	49
12	6.05	88.84	3.82	56
15	5.62	86.49	3.91	60
20	5.10	79.20	3.58	59
30	4.46	65.61	3.38	66
50	3.76	66.55	3.18	72
70	3.36	61.03	3.10	77
80	3.21	54.95	3.08	78

However, the flow forces of nanowires containing 20, 30, 50, 70 and 80 grains decrease as the number of grains increases. Hall [43] and Petch [44] determined the Hall-Petch expression, which gives the relationship between flow force and grain size, from the data they obtained as a result of their experimental studies. This relationship states that a small grain size corresponds to a high material strength. Thus, reducing the grain size has become an effective method to change the strength of materials [45-47]. The difficulty of dislocation movement along grain boundaries and the concentration of force resulting from dislocation accumulation are expressed as the physical basis of this behavior. Reducing the grain size to the nanoscale level results in a significant increase in the volume fraction of grain boundaries. As a result, grain boundary-mediated processes such as grain boundary sliding and grain boundary transformation become more important [48, 49]. However, reducing the grain size has a limited effect on the strength of the material [A5 and else]. When the grain size decreases below a certain critical value, the strength of the material decreases and a situation called the reverse Hall-Petch effect occurs. Yip suggested that the highest plastic resistance occurs in polycrystalline materials at grain sizes of approximately 20

nm [36]. Schiotz et al. They determined a softening process at small grain sizes with their simulation studies for nanocrystal Cu [51]. This grain softening phenomenon has also been reported in studies on various nanowires such as Ni and Pt [52-54].

The relationship between flow force and grain size for Ni nanowire is given in Fig.5. It is seen that when the average grain size is larger than d = 5.62 nm, that is, smaller than $d^{-1/2}$ = 0.422 nm, the flow force of the model polycrystalline nanowires increases with the decrease in d. This result is compatible with the Hall-Petch relationship (Eq. 4).

$$\sigma_S = \sigma_0 + k.d^{-1/2} \quad (4)$$

In this equation, σ_0 is the lattice friction force required to move individual dislocations, σ_S is the flow force, k is a constant that varies depending on the material and is known as the Hall-Petch slope, and d is the average grain size [50]. Hall-Petch equation from the fit process using points with $d^{-1/2}$ value less than 0.422 nm, is obtained by the Eq.5;

$$\sigma_S = 0.33 + 8.49.d^{-1/2} \quad (5)$$

It has been determined that when the grain size is smaller than 5.62 nm, that is, the $d^{-1/2}$ value is greater than 0.422 nm, the flow force of the model nanowire system decreases with the decrease of d. This result was first reported by Chokshi et al. It is compatible with the inverse Hall-Petch effect determined by . The inverse Hall-Petch equation for the Ni nanowire system was obtained by fitting the points with $d^{-1/2}$ values greater than 0.422 nm as follows (Eq. 6).

$$\sigma_S = 6.13 - 5.61.d^{-1/2} \quad (6)$$

Nanowire structures with grain sizes larger than 6.43 nm and fewer than 10 grains were not included in the study because no size effect was observed.

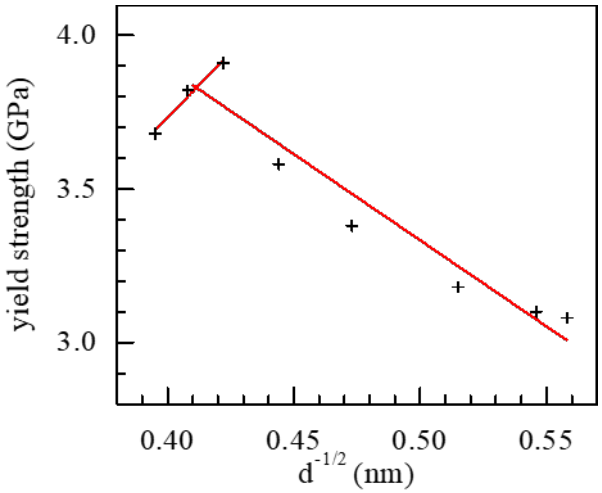

Figure 5. Relationship between grain size and yield-strenght of polycrystalline Ni nanowire.

In crystal structures, grain boundaries act as a barrier against dislocations moving on slip planes. Increasing the orientation angles of the atoms in the grains also increases the strength of this barrier. In Figure 6, in the images of the atomic positions of the nanowire containing 15 grains taken from the elastic deformation region before the plastic deformation started, it is clearly seen that dislocations accumulate at the grain boundaries and the transition of other grains to the slip planes is prevented by these boundaries. In DXA analysis, green color shows 1/6<112> Shockley dislocations, blue color shows 1/2<110> perfect dislocations, and red color shows dislocations that are not defined in DXA analysis and are called “other”.

From Table 2, it can be seen that as the grain size decreases, the strain values at which fracture occurs in the nanowire increase. Li et al. reported that there was an increase in the fracture stress value with decreasing grain size for Mo nanowire [37] determined in their study. In addition to having high strength, small-grained structures also break more slowly due to their high elongation.

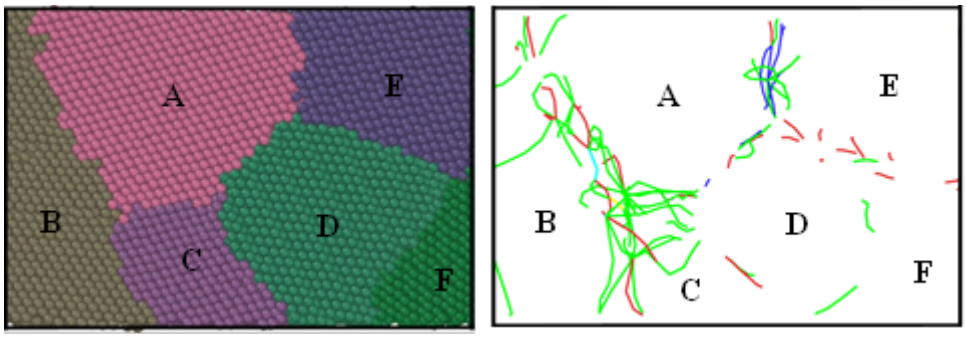

Figure 6. Grain structures in atomic configuration and dislocation distributions at grain boundaries taken from a specific cross-section of the polycrystalline Ni nanowire.

2.3. Effect of LDR change on mechanical properties in polycrystalline Ni nanowire with constant grain size

In this section, the effect of LDR variation of the MD calculation cell with fixed grain size (d = 5.1 nm) on the mechanical properties of polycrystalline Ni nanowire was tried to be examined. The stress-strain curves obtained as a result of the tension deformation applied to the model nanowire system with a strain rate of $1x10^{10}$ s^{-1} along the x-axis direction for different LDR values are shown in Fig. 7. The parameters of the mechanical properties obtained from the figure are given in Table 3. Although the grain size is larger than 4.05 nm, superplastic deformation behavior is still observed in the nanowire at LDR values of 1 and 1.5. LDR affects the deformation behavior and fracture stress percentage, and with increasing LDR, the fracture stress of the sample tends to be small due to the surface effect. It can be seen that the elasticity modulus is almost unaffected by the LDR change. In addition, it has been determined that the yield strength values at which plastic deformation begins are almost unaffected by the LDR change, except for LDR = 3.

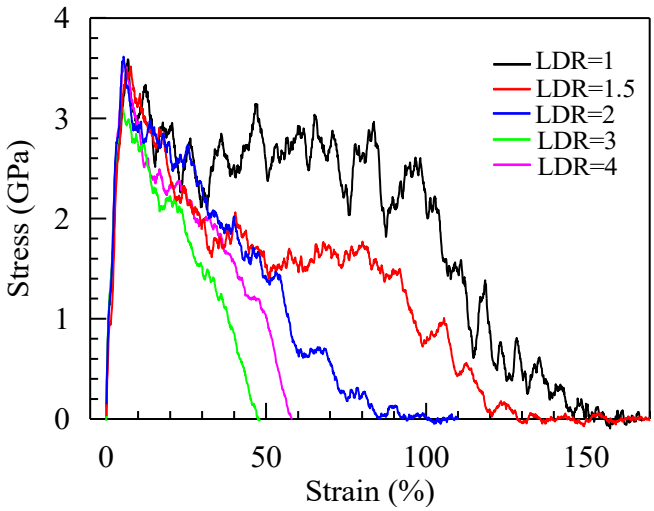

Figure 7. Stress-Strain curves of polycrystalline Ni nanowire for fixed grain size and different LDR values.

Table 3. Parameters of some elastic and plastic properties of polycrystalline Ni nanowires with different LDR for fixed grain size (d = 5.1 nm).

LDR	1	1.5	2	3	4
The number of grain	5	8	10	16	20
E (GPa)	73.2	72.9	74.1	73.9	79.2
Yield strength (GPa)	3.60	3.52	3.61	3.17	3.58
Fracture strain (%)	151	120	85	48	59

Figure 8 shows the atomic positions obtained from CNA analysis for different strain percentages, from ε=%0 initial state, where no strain is applied, to ε=151%, where fracture occurs in the sample, for LDR=1, which contains 5 grains and has a grain size of 5.1 nm. It is seen that no neck formation occurs up to the tension strain value applied to the model system, ε = 100%. However, at ε = 7%, which is the yield strenght at which plastic deformation begins, it has been determined that the atoms in grains 4 and 5 are rearranged and have the same orientation, as a result of which the boundary between them disappears, these grains come together, and hcp unit cell structures shown with red atoms begin to form. These stacking defects occurring in hcp unit cells, known as alignment errors of fcc structures, are thought to occur as a result of the nucleation of Shockley partial dislocations [38,39]. It is clearly seen that as the strain increases, many accumulation defects occur as a result of new dislocations nucleating and spreading within the structure. The black, red and pink arrows in Fig. 8 point to the places where deformation twins with internal and external stacking defects are formed within the nanostructure, respectively. However, it has been determined that as the strain applied to the nanowire increases, the grain boundaries disappear and the grains coalesce. It is seen that at ε=110%, the nanowire begins to yield in the region indicated by the dotted circle, and at ε=151%, fracture occurs in this region. The fact that the percentages of atoms representing free surfaces and grain boundaries atoms, called "other", obtained from CNA analysis, decreased from 36.5% before the strain was applied to 22.3% when the fracture occurred, which is evidence that the different atomic orientations in different grains disappear and the coalescence of the grains occurs.

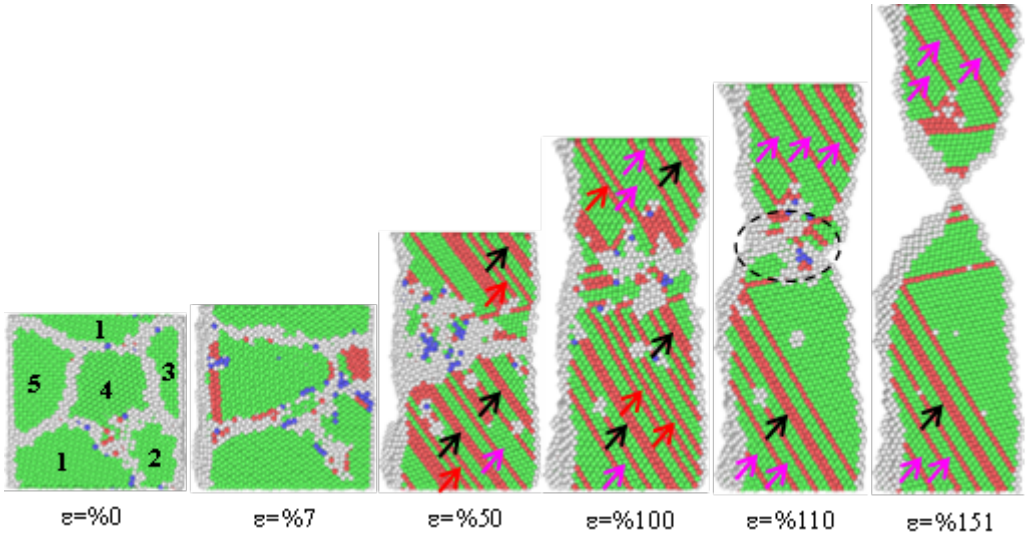

Figure 8. Atomic images obtained at different strain percentages of the polycrystalline Ni nanowire system with d = 5.1 nm grain size for LDR = 1 at a strain rate of $1x10^{10}$ s^{-1}.

4. Conclusion

This study, in which the interactions between Ni atoms are modeled with the EAM potential function, consists of three parts. In the first part, the changes in mechanical and microstructural properties as a result of tension deformation applied to nanowires containing 20 grains and with different LDR values were examined. At LDR values of 1, 1.5 and 2, the nanowire exhibits superplastic deformation behavior. At LDR=1, the fracture percentage of the nanowire reaches its highest value. It has been determined that increasing LDR values cause a decrease in the elastic modulus, which gives the elastic properties of the nanowire, and the flow strain value at which plastic deformation begins. During the superplastic deformation of the nanowire, the formation of deformation twins as well as internal and external stacking defects was observed in the structure. In the second part, nanowires with different grain numbers were subjected to tension deformation for a constant value of LDR = 4. When the average grain size was larger than 5.62 nm, it was determined that the nanowire showed a Hall-Petch relationship from the change in flow force with grain size. However, when the grain size was smaller than 5.62 nm, an inverse Hall-Petch relationship was observed. When the critical grain size of 5.62 nm is reached, the ability of interfacial atoms to resist dislocation transfer and grain rotation is strongest. In the last part, tension deformation was applied to nanowires with different LDR starting structures with a fixed grain size of 5.1 nm. Although the number of grains is large, the structure undergoes superplastic deformation at LDR values of 1 and 1.5. In addition, the elastic

modulus is almost close to each other at all LDR values. It was determined that the grains coalesced during superplastic deformation and many stacking defects formed in the nanostructure.

References

[1] Lu W, Lieber CM. Semiconductor nanowires. J Phys Appl Phys 2006; 39(21): 387.
[2] Rurali R. Colloquium: Structural, electronic, and transport properties of silicon nanowires. Rev Mod Phys 2010; 82(1): 427, 2010.
[3] Park HS, Zimmerman JA. Modeling inelasticity and failure in gold nanowires. Physical Review B 2005; 72: 054106.
[4] Veerababu J, Nagesha A, Shankar V. Slip to twinning to slip transition in polycrystalline BCC-Fe: Effect of grain size. Physica B: Condensed Matter 2024; 694: 416465.
[5] Niu Y, Jia Y, Lv X, Zhu Y, Wang Y. Molecular dynamics simulations of polycrystalline titanium mechanical properties: Grain size effect. Materials Today Communications. 2024; 40: 109558.
[6] Suryavanshi AP, Yu MF. Probe-based electrochemical fabrication of freestanding Cu nanowire array. Appl Phys Lett 2006; 88: 083103.
[7] Zhu Y, Li Z,Huang M. Coupled effect of sample size and grain size in polycrystalline Al nanowires. Scripta Materialia 2013; 68: 663–666.
[8] Diao J, Gall K, Dunn ML. Yield strength asymmetry in metal nanowires. Nano Lett 2004; 4(10): 1863-1867.
[9] Wu W, Brongersma SH, Hove MV, Maex K. Influence of surface and grain-boundary scattering on the resistivity of copper in reduced dimensions. Appl Phys Lett 2004; 84: 2838-2840.
[10] Klinger L, Rabkin E. Thermal stability and creep of polycrystalline nanowires. Acta Mater 2006; 54: 305-311.
[11] Molares MET, Balogh AG, Cornelius TW, Neumann R, Trautmann C. Fragmentation of nanowires driven by Rayleigh instability. Appl Phys Lett 2004; 85: 5337-5339.
[12] Philips R, Crystals, Defects and Microstructures. Cambridge University Press, 2001.
[13] Golovnev IF, Golovneva EI, Fomin VM. The influence of a nanocrystal size on the results of molecular-dynamics modeling. Comp Matter Sci 2006; 36: 176-179.
[14] Niu JJ, Zhang JY, Liu G, Zhang P, Lei SY, Zhang GJ, Sun J. Size- dependent deformation mechanisms and strain-rate sensitivity in nanostructured Cu/X (X = Cr, Zr) multilayer films, Acta Materialia 2012; 60: 3677-3689.
[15] Smith WF. Principles of Materials Science and Engineering, McGraw-Hill Inc. 1996; New York, USA.
[16] Zhang XJ, Chen CL. Phonon dispersion in the fcc metals Ca, Sr and Yb. J Low Temp Phys 2012; 169 : 40-50.
[17] Tolpin KA, Bachurin VI, Yurasova VE. Features of energy dependence of NiPd sputtering for various ion irradiation angles. Nucl Instrum Methods Phys Res B 2012; 273: 76-79.
[18] Louail L, Maouche D, Roumili A, Hachemi A. Pressure effect on elastic constants of some transition metals. Mat Chem Phys 2005; 91: 17-20.
[19] Cao AJ, Wei YG. Formation of fivefold deformation twins in nanocrystalline face-centered-cubic copper based on molecular dynamics simulations. Appl Phys Lett 2006; 89: 041919.
[20] Fu B, Chen N, Xie Y, Ye X. Size and orientation dependent melting properties and behavior of wurtzite CdSe nanowires. Comput Mater Sci 2014; 84: 293–300.
[21] Mandal T, Strain induced phase transition in CdSe nanowires: Effect of size and temperature. Appl Phys Lett 2012; 101(2): 021906.
[22] Daw MS, Baskes MI. Semiempirical, quantum mechanical calculation of hydrogen embrittlement in metals. Phys Rev Lett 1983; 50: 1285–1295.
[23] Guellil AM, Adams JB. The application of the analytic embedded atom method to bcc metals and alloys. J Mater Res 1992; 7: 639-652.
[24] Foiles SM, Baskes MI, Daw MS. Embedded-atom-method functions for the fcc metals Cu, Ag, Au, Ni, Pd, Pt, and their alloys. Phys Rev B Condens Matter 1986; 33(12): 7983-7991.
[25] Kazanc S. The effects on the lattice dynamical properties of the temperature and pressure in random NiPd alloy. Canadian Journal of Physics 2013; 91: 833-838.
[26] Kazanc S, Ozgen S, Adiguzel O. Pressure effects on martensitic transformation under quenching process in a molecular dynamics model of NiAl alloy. Physica B 2003; 334: 375-381.
[27] Jacobus K, Sehitoglu H, Balzer M. Effect of stress state on the stress-induced martensitic transformation in polycrystalline Ni-Ti alloy. Metallurgical and Materials Transactions A 1996; 27(A): 3066-3073.
[28] Bonny G, Castin N, Terentyev D, Interatomic potential for studying ageing under irradiation in stainless steels: the FeNiCr model alloy. Model Simul Mater Sci Eng 2013; 21: 085004.
[29] Stukowski A. Structure identification methods for atomistic simulations of crystalline materials. Modelling and Simulation in Materials Science and Engineering 2012; 20: 045021.
[30] Stukowski A. Visualization and analysis of atomistic simulation data with OVITO-the Open Visualization Tool. Modelling and Simulation in Materials Science and Engineering 2010; 18(1): 015012.
[31] Hirel P. Atomsk: A tool for manipulating and converting atomic data files. Comput Phys Commun 2015; 197: 212-219.
[32] Zhang Y, Li J, Hu Y, Ding S, Du F, Xia R. Mechanical properties and scaling laws of polycrystalline CuZr shape memory alloy. J Appl Phys 2021; 130: 155106.
[33] Koh SJA, Lee HP, Lu C, Cheng QH. Molecular dynamics simulation of a solid platinum nanowire under uniaxial tensile strain: Temperature and strain-rate effects. Cheng, Phys Rev B 2005; 72: 085414.

[34] McDowell MT, Leach AM, Gall K. Bending and tensile deformation of metallic nanowires. Model Simul Mater Sci Eng 2008; 16; 045003.
[35] Bhatt JC, Kholiya K. Effect of size on the elastic and thermodynamic properties of nanomaterials. Indian Journal of Pure & Applied Physics 2014; 52: 604-608.
[36] Schiøtz J, Tolla FDD, Jacobsen KW. Softening of nanocrystalline metals at very small grain sizes. Nature 1998; 391: 561-563.
[37] Li X, Hu W, Xiao S, Huang WQ. Molecular dynamics simulation of polycrystalline molybdenum nanowires under uniaxial tensile strain: Size effects. Physica E 2008; 40: 3030–3036.
[38] Wen YH, Zhang Y, Wang Q, Zheng JC, Zhu ZZ. Orientation-dependent mechanical properties of Au nanowires. Computational Materials Science 2010; 48: 513-519.
[39] Wu HA. Molecular dynamics study of the mechanism of metal nanowires at finite temperature. European Journal of Mechanics A/Solids 2006; 25: 370-377.
[40] Wu B. Heidelberg A, Boland JJ. Mechanical properties of ultrahigh-strength gold nanowires. Nature Materials 2005; 4(7): 525-529.
[41] Hou Z, Xiao Q, Wang Z, Wang J, Liu R, Wang C. Effect of twin boundary spacing on the deformation behaviour of Au nanowire. Physica B 2020; 581: 411952.
[42] Lu L, Sui ML, Lu K. Superplastic extensibility of nanocrystalline copper at room temperature. Science 2000; 287: 1463-1466.
[43] Hall EO. The Deformation and Ageing of Mild Steel: III Discussion and Results. Proceed Phys Soc Lond Sect B 1951; 64:747–752.
[44] Petch NJ. The Cleavage Strength of Polycrystals. J Iron Steel Inst 1953; 174:25–28.
[45] Hughes GD, Smith SD, Pande CS, Johnson HR, Armstrong RW. Hall-Petch strengthening for the microhardness of twelve nanometer grain diameter electrodeposited nickel. Scr Metall 1986; 20: 93–97.
[46] Jang JSC, Koch CC. The Hall–Petch relationship in nanocrystalline iron produced by ball milling. Scr Metall Mater 1990; 24: 1599–1604.
[47] Knapp JA, Follstaedt DM. Hall–Petch relationship in pulsed-laser deposited nickel films. J Mater Res 2004; 19: 218–227.
[48] Zhang L, Lu C, Tieu K. A review on atomistic simulation of grain boundary behaviors in face-centered cubic metals. Comput Mater Sci 2016; 118: 180-191.
[49] Zhang L, Shibuta Y, Huang X, Lu C, Liu M. Grain boundary induced deformation mechanisms in nanocrystalline Al by molecular dynamics simulation: From interatomic potential perspective. Comput Mater Sci 2019; 156: 421-433.
[50] Jia H, Liu X,Li Z,Sun S,Li M. The effect of grain size on the deformation mechanisms and mechanical properties of polycrystalline TiN: A EAM molecular dynamics study. Computational Materials Science 2018; 143: 189–194.
[51] Yip S. The strongest size. Nature 1998; 391: 532–533.
[52] Shan ZW, Stach EA, Wiezorek JMK, Knapp JA, Follstaedt DM. Grain boundary-mediated plasticity in nanocrystalline nickel. S.X. Mao, Science 2004; 305: 654–657.
[53] Wang LH,Han XD, Liu P, Yue YH, Zhang Z, Ma E. In situ observation of dislocation behavior in nanometer grains. Phys Rev Lett 2010; 105: 135501.
[54] Wang LH, Teng J, Liu , Hirata A, Ma E, Zhang Z, Chen MW, Han XD. Grain rotation mediated by grain boundary dislocations in nanocrystalline platinum. Nat Commun 2014; 5: 4402.

Turkish Journal of Science & Technology
20(1), 29-40, 2025

Research Paper
https://doi.org/10.55525/tjst.1483617

Early Diagnosis of Invasive Ductal Carcinoma Breast Cancer using Deep Learning Framework

Hakan GÜLER[1*], Yunus SANTUR[2], Mustafa ULAŞ[3]
[1] Software Engineering, Faculty of Technology, Fırat University, Elazig, Türkiye
[2,3] Artificial Intelligence and Data Engineering, Faculty of Engineering, Fırat University, Elazig, Türkiye
[*1] hakanguler@firat.edu.tr, [2] ysantur@firat.edu.tr, [3] mustafaulas@firat.edu.tr

(Geliş/Received: 13/05/2024; Kabul/Accepted: 24/10/2024)

Abstract: This study is aimed to be conducted on invasive ductal carcinoma breast cancer, which is a type of cancer that is common around the world and found in women. Early diagnosis of this disease can be lifesaving. It was aimed to conduct the study to determine the early diagnosis of breast cancer due to its early detection feature. In addition to deep learning techniques, image processing techniques were also used in the study. A dataset consisting of breast cancer images was used. The images in the data set may be complicated or time-consuming when evaluated using traditional diagnostic methods. This is where deep learning models come into play. The models used in the study analyzed breast cancer cells. As a result of the analysis, cells were classified as cancerous or cancer-free. Five different models were used in this study: CNN, SVM, Random Forest, DenseNet and MobileNet. When the results were examined, it was analyzed that the proposed method showed better performance than other methods. The accuracy rates of the models were: CNN (95.1%), SVM (89.87%), Random Forest (93.21%), DenseNet (94.31%), and MobileNet (94.6%). In conclusion, this study reveals the differences between models used in breast cancer diagnosis. In this period when the importance of artificial intelligence increases, it is predicted that it will be an important step in saving breast cancer patients. If the methods are used efficiently and effectively, the rate of early diagnosis will increase and diseases will be prevented.

Key words: Artificial Intelligence, Breast Cancer, Deep Learning, Image Processing, Invasive Ductal Carcinoma.

Derin öğrenme çerçevesini kullanarak invazif duktal karsinom meme kanserinin erken tanısı

Öz: Bu çalışma, dünya genelinde kadınlarda yaygın olarak görülen invazif duktal karsinom meme kanseri üzerine odaklanmaktadır. Erken teşhis, hayat kurtarıcı olabilecek bu kanser türü için kritiktir. Çalışmanın amacı, meme kanserinin erken teşhisini belirlemek için derin öğrenme ve görüntü işleme tekniklerini kullanmaktır. Meme kanseri adlı bir veri seti, geleneksel tanı yöntemleriyle değerlendirildiğinde karmaşık veya zaman alıcı olabilen görüntüler içermektedir. Derin öğrenme modelleri, bu zorlukları aşmak için kullanılmıştır. Çalışmada kullanılan modeller, meme kanseri hücrelerini analiz etmiş ve kötü hücrelere sahip olanları kanserli, iyi hücrelere sahip olanları kansersiz olarak sınıflandırmıştır. Beş farklı model (CNN, SVM, Random Forest, DenseNet ve MobileNet) kullanılmıştır. Sonuçlar incelendiğinde, önerilen yöntemin diğer metodlara göre daha iyi performans gösterdiği görülmüştür. Modellerin doğruluk oranları sırasıyla şu şekildedir: CNN (%95,1), SVM (%89,87), Random Forest (%93,21), DenseNet (%94,31) ve MobileNet (%94,6). Bu çalışma, meme kanseri tanısında kullanılacak modeller arasındaki farklılıkları ortaya koymaktadır. Yapay zekanın önemi göz önüne alındığında, bu çalışmanın meme kanseri hastalarının kurtarılmasında önemli bir adım olabileceği öngörülmektedir. Yöntemlerin etkin ve verimli bir şekilde kullanılması durumunda, erken tanı oranının artması ve hastalıkların önlenmesi sağlanabilir.

Anahtar kelimeler: Yapay Zeka, Meme Kanseri, Derin Öğrenme, Görüntü İşleme, İnvazif Duktal Karsinom.

1. Introduction

Various types of cancer are common worldwide. Breast cancer is among the most common ones. This type of cancer occurs when the cells in the breast turn into harmful cells. There are tools used to diagnose breast cancer and these include mammography. Mammography performs a special X-ray scan and provides detailed examination of the tissues in the breast. It is seen that breast cancer is present if an individual has an abnormal cyst in her breast. Certain symptoms can indicate the presence of breast cancer. Changes seen in the nipple or skin disorders are some of these [1]. Shah and her colleagues also expressed their opinions, claiming that some factors increase the potential of breast cancer [2]. Early diagnosis is crucial as breast cancer can be fatal. After early diagnosis, the correct treatment method is among the major factors in eradicating the disease.

There are many types of breast cancer. One of these types appears to be invasive ductal carcinoma [3]. The type of cancer that we encounter as invasive ductal carcinoma occurs in breast tissues. There are milk ducts in the

[*] Corresponding author: hakanguler@firat.edu.tr. ORCID Number of authors: [1] 0000-0002-7599-5431, [2] 0000-0002-8942-4605, [3] 0000-0002-0096-9693

breast tissue. This cancer, as shown in Figure 1, called Invasive Ductal Carcinoma (IDC), is a type that occurs by contacting these tissues as well as the surrounding tissues. IDC is known as the most harmful type of breast cancer. Harmful cells begin to spread into tissues. It occurs when it infiltrates other cells other than the cell in which it is located. Therefore, accurately identifying and classifying IDC plays a vital role in determining treatment options and assembling comprehensive checkups as shown in Figure 1.

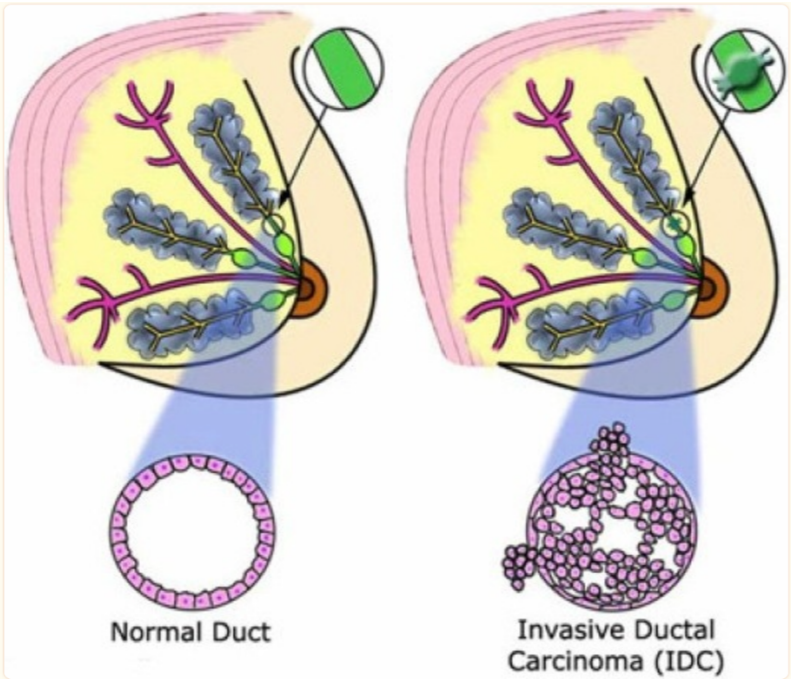

Figure 1. Normal duct and Invasive Ductal Carcinoma (IDC) [4].

Today, diagnosis and classification of breast cancer is usually done manually by pathologists. However, it has great endurance for pathologists who ensure accurate recognition of an aggressive strain such as IDC. Therefore, IDC has a large collection capacity to obtain computer-aided analysis results to accelerate diagnostic support. Therefore, developing a model to recognize IDC using deep learning methods and evaluating its effectiveness by applying this model to large data sets has become an important role. Additionally, it is necessary to explain why these techniques are so important in clinical practice, highlighting the potential impact of deep learning methods in the field of breast cancer diagnosis and classification. This study has the potential to open a new path in the field of breast cancer diagnosis and classification, providing pathologists and clinicians with the opportunity to provide faster and more accurate diagnoses. The unique values of this study or its unique contributions to the literature are described as follows.

Compared to literature studies, a faster approach was presented and results close to the literature were obtained. It can be seen that the study covers the detection and success rate of breast cancer in detail. Inspired by deep learning models, a wide range of investigations and studies have been carried out. The literature review goes beyond previous studies to re-evaluate the effectiveness of pioneering architectures such as Convolutional Neural Network (CNN), Densely Connected Convolutional Networks (DenseNet), and Efficient Convolutional Neural Networks for Mobile Vision Applications (MobileNet) in breast cancer diagnosis and offers a new perspective on this field. Deep learning has become an important technique in artificial intelligence in almost all fields. Its importance was also emphasized in the study and similar studies. It played a helpful role in detecting breast cancer in the study. Thus, it has been seen that it has an important place in the health sector and cancer diagnoses.

2. Background

Studies have been conducted on breast cancer, its diagnosis or classification. In this section, we will examine the studies and approaches. We will examine the proposed methods and what they are, along with their results.

Janowczyk and his colleagues proposed to analyze images and analyze bad cells in breast cancer using deep learning methods. They called the bad cells in breast cancer pathology. While they said that deep learning methods performed well in some cases, they claimed that in some cases it was the opposite. They said that the results were obtained from studies conducted in similar fields and the deep learning methods used in these studies. They proposed and used some techniques to achieve better performing results than these results. They focused on deep learning methods. By talking about a singular network architecture structure, they talked about the framework of this architecture. If we examine the framework in some detail: nucleus segmentation (over 12,000 nuclei, it appeared with an F_1 score of 0.83), epithelial segmentation (1735 regions showed a 0.84 F_1 Score cross score), tubule segmentation (0.83 F_1 score was obtained in 795 tubules).), lymphocyte detection (0.90 F_1 score was obtained in 3064 lymphocytes), mitosis detection (0.53 F_1 score was observed in 550 mitotic events), (f) invasive ductal carcinoma detection (0.7648 F_1 score was seen in 50k test field) and lymphoma classification (0.97 accuracy rate in a total of 374 images). Janowczyk and his colleagues actively used design learning methods and claimed that their study on more than 1200 images was an effective and large study [5].

Shahidi and colleagues conducted a study on the classification of breast cancer histopathology images. They used deep learning methods while carrying out their studies. They made comparisons between the methods they used. In their study, they aimed to investigate the performance of the latest models in this field, which have been little or not studied in the literature, and to offer a new perspective on existing studies. Shahidi and his colleagues claimed that they took important steps in the diagnosis of breast cancer in their studies. They emphasized that deep learning methods and comparisons will help future research [6].

Houssein and his colleagues focused on revealing the current knowledge of machine and deep learning technologies used in detailing and categorizing breast cancer and providing a general evaluation of the developments in this field of research. The focus of the study is to ensure the classification of breast studies with multiple study medical imaging. It has been observed that tumors are presented in some detail to facilitate the classification of non-tumor lesions and dense masses. In addition to the machine learning used in the proposed method, it was seen that different perspectives, different techniques and different thoughts were also included. Following these stages, the breast cancer detection process begins and follows specific architectures in the change process. Provides an overview of different imaging methods. The classification of breast cancers and their detected distributions in this analysis are summarized and summarized [7].

In the literature review, one of the studies on breast cancer diagnosis is the study focused on by Zahoor et al. Zahoor and his colleagues aimed to provide better options and a safer source in the study. They used different techniques in the stages of Computer-Aided Diagnosis (CAD) systems (such as pre-processing, segmentation, feature extraction and classification). They presented a report on the detection of breast masses, microcalcifications and malignant cells, including detailed analysis and the use of various techniques. When all these are brought together and examined, it is seen how important early diagnosis is in this type of cancer, as in every type of cancer. By emphasizing this importance, they emphasized the development of the necessary techniques and solutions. They made a brief criticism and said that the segmentation and classification stages have no disadvantages or convenience levels. They said that there would be more optimized and flexible techniques to get accurate results [8].

Zhang and his colleagues also conducted a study on breast cancer. They proceeded by dividing their work into 4 parts. In the first part, they focused on the detection of breast cancer. They then processed the images they obtained. In the next part, pre-processing was done on the images. Then the results were obtained. They discussed the effects of different methods on breast cancer. In addition to supervised and unsupervised learning methods, they also received help from deep learning methods. They evaluated the performance rates of the methods they applied. They evaluated whether the results were breast cancer or not. They emphasized that these studies will guide future studies [9].

Kanojia et al. focused on the early diagnosis and diagnosis of breast cancer and emphasized its importance. They said that breast cancer is very common worldwide and the risk level is high. They said that making a diagnosis on a normal patient takes too much time under normal conditions and in a hospital environment. They said that this waste of time would be prevented with automatic diagnosis systems. They stated that if this type of cancer is diagnosed early, its treatment will be faster and the recovery rate will increase. When these reasons come together, they said that the importance of systems increases even more, considering the concept of time is an important factor in the detection and prevention of cancer. In this context, Kanojia and his colleagues examined breast tissues in their study. They have conducted comprehensive and detailed research on breast cancer with the help of image processing techniques. The main point that Kanojia and his colleagues emphasize is early diagnosis. They aim to make this diagnosis by using relevant techniques [10].

According to Rezaei's study, it was determined that the disease that most threatens the life of women is breast cancer. Rezaei states that in the face of this threat, they stated that this type of cancer will be prevented and the chance of survival will be high. In this context, it is possible to state that various studies have been carried out covering the development of diagnoses and methods for the early diagnosis of breast cancer. In this study, examinations for the diagnosis of breast cancer are carried out with automatic and semi-automatic image-based approaches. The limitation of the research was the image-based diagnosis application journals published between 2016 and 2020 [11].

In their study, Lu and colleagues believe that there is no way to effectively treat breast cancer risk yet. In this context, the point emphasized by Lu et al. is early diagnosis. They point out the importance of correct diagnosis and analysis in breast cancer and say that early detection and diagnosis are the key to reducing the risk of death. Based on medical imaging methods commonly used in the diagnosis of breast cancer, some approaches have been examined to detect breast cancer using computer vision and machine learning techniques. As a result, the data were analyzed by comparing the performances of different methods on histological images and mammography images [12].

In their study, Mashekova and her colleagues, unlike others, predicted that breast cancer is the most common fatal disease in women and that this disease can also affect men. They agreed that the best way to get a quick response during the treatment process of the disease is early diagnosis. Although the screenings for breast cancer today vary, these screenings also have various advantages and disadvantages. Thermography, one of the breast cancer screening methods, is considered safe compared to other methods. This method attracts attention with its smart classification feature and new image processing features. This method has great potential in terms of its low cost, use of contactless technology, and mass screening and continuous monitoring of patients for early diagnosis. This study by Mashekova and her friends emphasized the importance of deep learning fields as well as numerical simulation. It allows a more detailed examination of the studies in the literature covering these areas. It also touches upon the importance of early diagnosis of breast cancer [13].

The literature review focused on comparing and examining the methods used in the research. In addition to these researches, deep learning models are examined and their effects in studies are shown. By combining all these, their effects on the relevant cancer type have been revealed. Its effects and suggestions on current studies are also included. It is thought that it will be an important resource that can support other studies.

3. Material and Methods

Machine learning methods were used in the study. In addition, image processing techniques were also used to make diagnoses. Its further examination and explanation is described in detail.

3.1. Dataset

The dataset moving through the receiver focuses on "IDC", one of the most common subtypes of breast cancer. The dataset includes all cross-sectional images of a total of 162 breast sections scanned with a magnification factor of 40x. 277,524 50x50 segmented patches were extracted from these cross-sectional images. Of these patches, 198,738 represent IDC- negative samples and 78,786 represent IDC+ positive samples as given in Table 1.

Table 1. Detailed View of Number of Datasets.

Class	Magnification	Number of Patches
Invasive Ductal Carcinoma Negative (IDC-)	40x	198,738
Invasive Ductal Carcinoma Positive (IDC+)	40x	78,786
Total	40x	277,524

The filename of each patch is "u_xX_yY_classC.png;" It is formatted as follows. Here, u represents the patient ID, X and Y represent where the patches broke, and C represents the class. Class 0, IDC-; class 1 means IDC+. The figure below describes separating the images in the breast cancer dataset according to their classes and then visualizing randomly selected examples as shown in Figure 2.

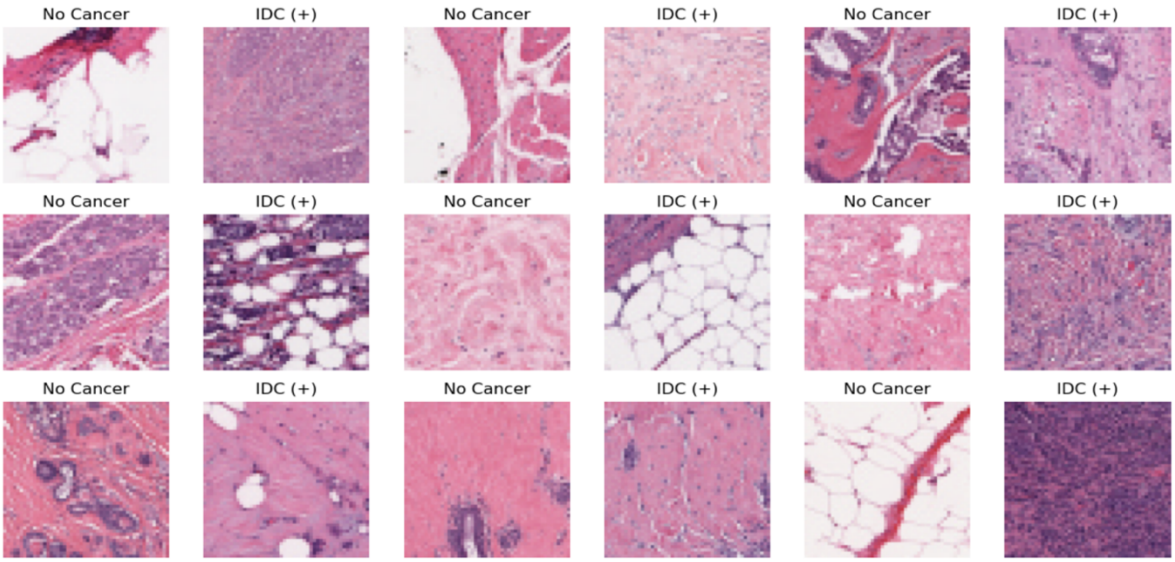

Figure 2. Visualization of IDC+/IDC- (negative and positive) samples.

3.2. Data Preprocessing

Before feeding images to machine learning models, it is critical to pre-process the data for better model performance. Let's examine the data preprocessing stages.

First, images of the IDC+ and IDC- classes were uploaded, then resized and added to the relevant lists to be used in training the model. Additionally, the class label (0 or 1) of each image was determined and this information was added to the relevant list. First, images of the IDC- and IDC+ classes were processed. In both cases, images were first read in color and then resized to 50x50 pixels. The resized images were added to their respective lists along with their tags.

These steps aim to bring the data set into a suitable format that the model can learn from. In other words, a data structure containing images and labels was created, so it was ready to be used for the training process.

Let's see the numbers of data added to the relevant lists during this process. We can see examples of numbers and total numbers belonging to IDC- and IDC+ classes in the chart below.

After this section, a selected subset of the data added to the relevant lists in the previous step was taken and combined. By mixing this data, X and Y data sets were created to be used for training. For each sample, its features (images) were added to dataset x and its labels were added to dataset y. This process enabled him to create a list containing the features and labels of the samples that make up the data set.

Finally, this data set was processed more effectively. The X array contains the image features, while the Y array contains the corresponding class labels. Thus, the data set was brought to a format suitable for training the model and was made ready to be used in the learning process of the model. Our data set after the operations was as shown in Figure 3.

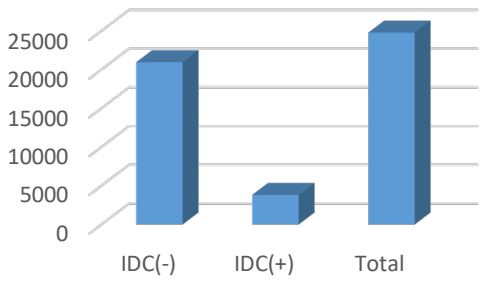

Figure 3. IDC-, IDC+ and total values.

3.3. Analyzing the Performance of Machine Learning Models in Breast Cancer Diagnosis

As for this part of the study, we will focus on the methods used in the diagnosis and diagnosis of breast cancer. The most important of these methods are machine learning and models. Machine learning was used in the study. In addition, different deep learning techniques were also benefited from. It has been observed that techniques such as machine learning and deep learning have been applied in many areas and success has been achieved [14-18]. With the preparation of the data set, the packages were set up step by step. At this stage of the study, both traditional machine learning methods and deep learning models were observed. First, traditional machine learning models such as Support Vector Machines (SVM) and Random Forest (RF) were used to classify the dataset.

SVM a classification algorithm used to separate data into two classes, is considered one of the new supervised machine generator techniques. These models can be accessed by classical multilayer perceptron neural networks. SVMs revolve around a hyperplane that separates two classes of data. This revolves around the term "margin", which creates the largest possible distance between the hyperplane separated by variants in both regions. This has proven effective in reducing the upper bound of expected generalization error [19].

In breast cancer diagnosis, SVMs offer a powerful option for samples belonging to different categories. The ability to define a distinct margin between different classes makes SVMs particularly effective in scenarios involving parts that are not between data classes.

RF a combinatorial machine learning algorithm, is an ensemble method created by combining multiple decision trees. First, RF is combined into classifying a set of trees, yielding the unit to the most popular class. Then, the obtained data are combined to obtain the final ranking result. RF not only has high classification accuracy but also manages to eliminate noise by detecting inappropriate values. RF is preferred as one of the most popular research methods in data mining and biological fields. RF has a wide range of applications in classification tasks and regression analysis. Since each tree is trained on a subset of the dataset, its generalization capabilities are also high. Additionally, the contributions of each tree are combined to improve the overall performance of the model. This method is especially useful for obtaining effective results on complex and noisy data sets. Advantages of RF include resistance to overfitting, the ability to understand relationships between features, and automatic feature selection. Therefore, using RF to analyze complex medical data sets, such as breast cancer diagnosis, has significant potential for accuracy and reliability [20].

The literature was evaluated on prominent points in the field of deep learning. In this context, deep learning models such as CNN, DenseNet and MobileNet were also investigated. These models have complex architectures that are especially effective in image classification tasks.

In CNN, which is called a type of artificial neural network, the output of each layer is used as the input of the next detailed range. To transform the layer results in a non-linear manner, multi-layer convolution is used and this process continues until the output channel [21].

DenseNet uses denser connections by connecting one layer between connections to previous ones. These dense connections not only alleviate the learning problem but also enable feature reuse. In this context, it is recommended to use various deep learning approaches with denser connections after DenseNet [22].

MobilNet, a network developed to increase the real-time performance of deep learning, provides connections under limited hardware conditions. The most important feature of this network is that it has a very high accuracy rate and can reduce the number of parameters [23].

Each model was tested against the validation dataset for performance evaluation. To measure model performance, measurements were made based on accuracy, precision, recall and F_1 score. It is thought that the performance and prominent features of these models will be a guide for the application of machine learning in the diagnosis of breast cancer.

4. Results and Discussion

The aim of this study is to compare machine learning and deep learning models for classification of breast cancer tissues. As a result of experiments using different models such as SVM, CNN, RF, MobileNet and DenseNet, the results of the research were supported as to which model gives more effective results in breast cancer diagnosis.

During the training and evaluation phase of each model, the performance criteria include accuracy rate, sensitivity, freedom and F_1 scores. Additionally, the performance of the models was examined in detail through loss functions and confusion matrices. The analysis in this study allowed us to identify the strengths and weaknesses of each model and find the appropriate model for the categorization task.

As a result of the research, it was determined that the deep learning models MobileNet and DenseNet showed superior performance even under limited hardware conditions. However, it should be noted that each model should be evaluated in the context of its advantages and application. Based on these results, it is predicted that the models developed for the diagnosis of breast cancer can be used as an auxiliary tool that can be preferred in clinical applications.

Let's examine the results obtained in more detail, focusing on the detailed performance analysis of each model. An evaluation was made on the performance of the CNN model. In the evaluation, the model was subjected to test accuracy separately in each period in the training phase, in the graph showing the success. Additionally, the loss graph showing the learning process of the model was also examined. The training accuracy graph shows that the model is achieving increasing accuracy on the training data. The test accuracy graph represents the generalization ability of the model. The similarity between the model's training process and test accuracy shows that the model avoids overfitting and can generalize. When the loss graph was examined, a decrease in training and testing losses was observed. This reduction demonstrates the model's ability to effectively learn and parse data. As a result, we can say that the CNN model has a successful performance in breast cancer diagnosis. The high accuracy values obtained by the model during the training process show its usability as a potential auxiliary tool for breast cancer diagnosis as shown in Figure 4a and Figure 4b.

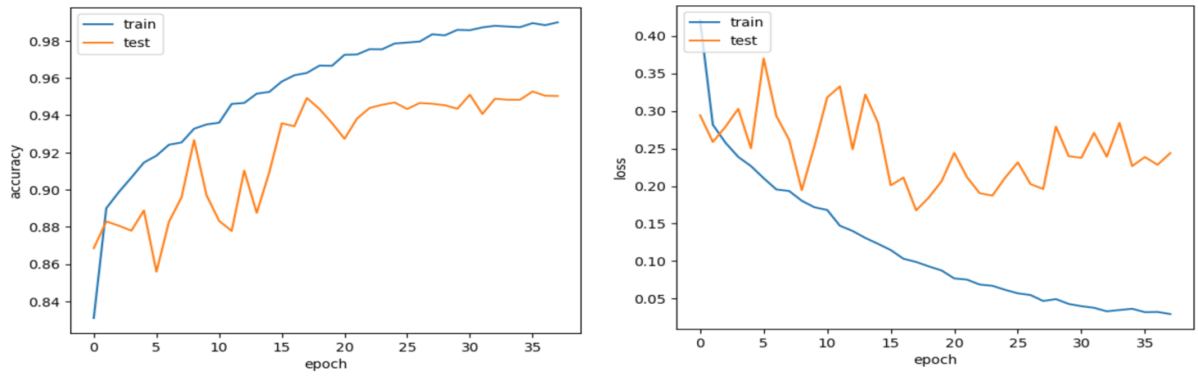

(a) CNN model accuracy (b) CNN model loss

Figure 4. CNN model a) Model accuracy b) Model loss.

If we talk about the performance of the MobileNet model, as a result of the evaluation, it can be said that the model can achieve a successful result in breast cancer diagnosis as shown in Figure 5a and Figure 5b. The high accuracy values obtained by the model during the training process show its usability as a potential auxiliary tool for breast cancer diagnosis.

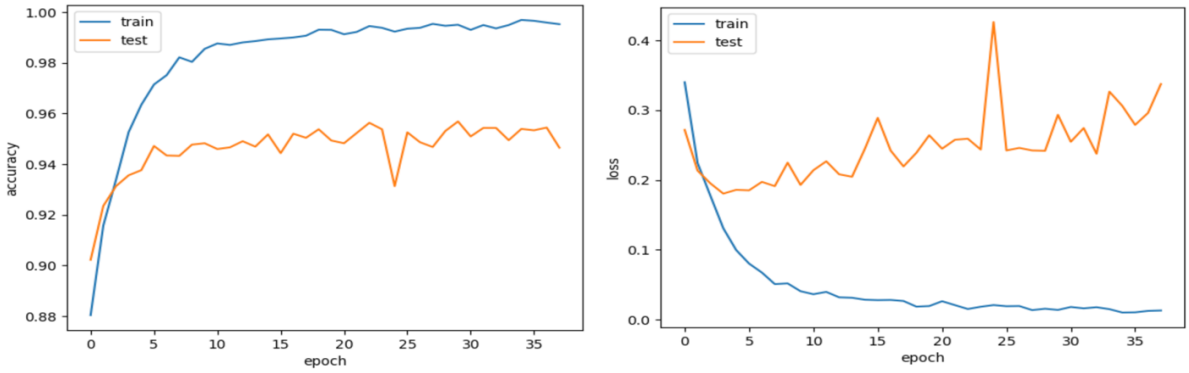

(a) MobileNet model accuracy (b) MobileNet model loss

Figure 5. MolineNet model a) Model accuracy b) Model loss.

It can be said that the DenseNet model has an impressive performance in breast cancer diagnosis. The high accuracy values obtained by the model during the training process show that it can be used as a reliable tool for breast cancer diagnosis as shown in Figure 6a and Figure 6b.

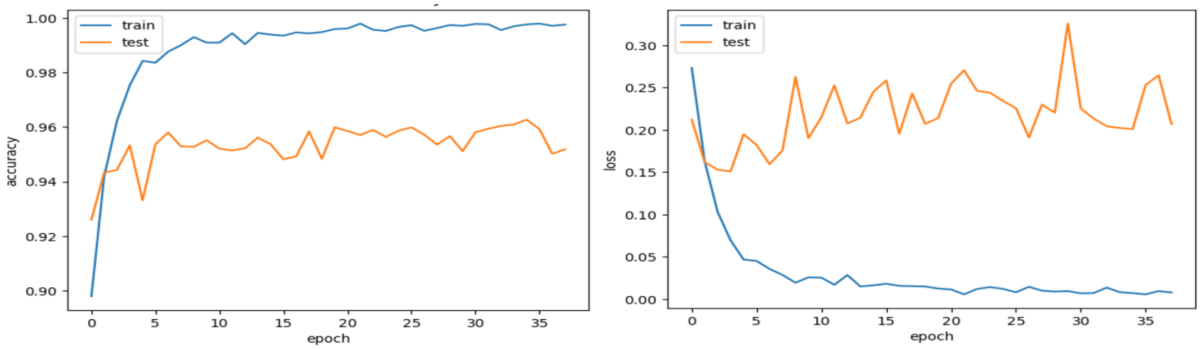

(a) DenseNet model accuracy (b) DenseNet model loss

Figure 6. DenseNet model a) Model accuracy b) Model loss.

One of the methods used in the study is SVM. A study was conducted to detect the type of cancer related to the SVM model. SVM results were evaluated. ROC analysis was used to demonstrate its performance. When looking at ROC analysis, is a tool that shows the relationship between the sensitivity and specificity of the model and turns it into a graph. The results obtained with SVM are expressed in orange color on the graph. The part under the curve represents the classification success of the model used. As the value remaining in this section increases, the performance results of the model also increase and are directly proportional. The blue line represents random classification. The fact that the model tested for training is above this line indicates that it achieved a better result than the one tested. As can be seen from Figure 7, the accuracy of the model showed better performance than the accuracy of a randomly selected class.

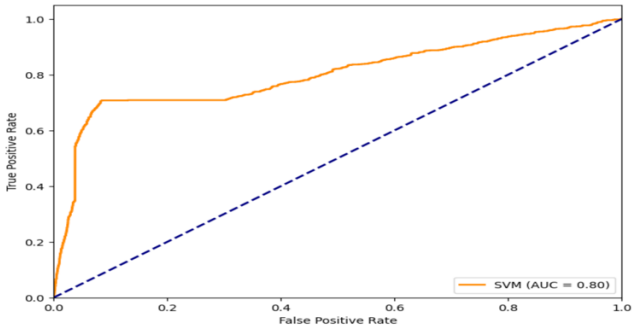

Figure 7. SVM roc curve.

Let's move on to the confusion matrix analysis of the models we used in our study. Confusion matrix analysis means that it shows the confusions between classes of each model as shown in Figure 8. These analyses allowed us to perceive and better understand the advantages and disadvantages of the models. The analyses and percentage equivalents of these models are shown below, respectively.

The study evaluated the performance of deep learning models used in breast cancer diagnosis and treatment. Various models such as CNN, SVM, RF, DenseNet and MobileNet have been trained and subjected to various tests. The analysis results are as follows as shown in Table 2:

- CNN Model: It has a 95.1% accuracy rate. F_1-Score, Recall and Precision values were measured as 0.95, 0.95 and 0.95, respectively.
- SVM Model: It has a 89.87% accuracy rate. F_1-Score, Recall and Precision values were measured as 0.89, 0.90 and 0.89, respectively.

- Random Forest Model: It has a 93.21% accuracy rate. F_1-Score, Recall and Precision values were measured as 0.93, 0.93 and 0.94, respectively.
- DenseNet Model: It has a 94.31% accuracy rate. F_1-Score, Recall and Precision values were measured as 0.95, 0.95 and 0.95, respectively.
- MobileNet Model: It has a 94.6% accuracy rate. F_1-Score, Recall and Precision values were measured as 0.94, 0.95 and 0.95, respectively.

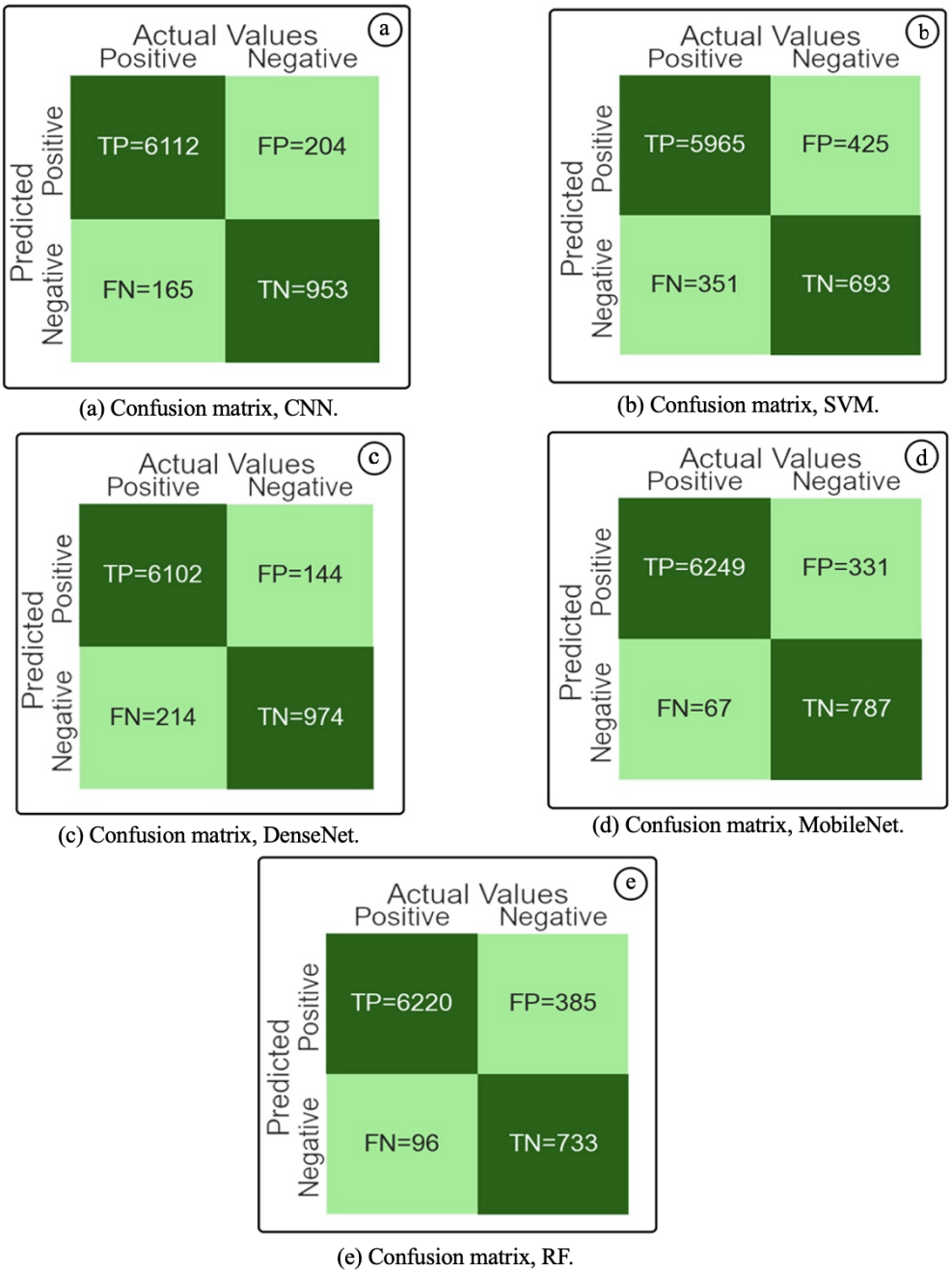

(a) Confusion matrix, CNN.

(b) Confusion matrix, SVM.

(c) Confusion matrix, DenseNet.

(d) Confusion matrix, MobileNet.

(e) Confusion matrix, RF.

Figure 8. (a) CNN, (b) SVM, (c) DenseNet, (d) MobileNet, (e) RF Confusion matrices.

The results are shown in a detailed analysis covering the performances of various deep learning models used in the diagnosis and treatment of breast cancer. Different models such as CNN, SVM, RF, DenseNet and

MobileNet were evaluated based on accuracy rates and classification metrics. The findings reveal the advantages and limitations of each model; It has been observed that models such as CNN and DenseNet have high accuracy rates and balanced F_1-Score, Recall and Precision values.

These results shed important light on understanding and improving the effectiveness of deep learning models for breast cancer diagnosis and treatment. However, other models such as SVM also appear to be effective in certain situations. The analysis can guide future research and clinical practices and inspire studies to obtain more precise and reliable results in disease detection and treatment planning.

Table 2. Experimental results.

Model	Accuracy (%)	F_1-Score	Recall	Precision
CNN	**95.1**	0.950712	0.950363	**0.951150**
SVM	89.8	0.894132	0.895615	**0.892930**
Random Forest	93.2	0.931609	0.933818	**0.935169**
DenseNet	94.3	0.952440	0.951843	**0.953322**
MobileNet	**94.6**	**0.943427**	**0.946462**	**0.945463**

This study provides an in-depth evaluation on a wide range of models, including various machine learning models. The results obtained were compared with the performance rates in different studies. The table below provides a comprehensive evaluation of the various metrics used when measuring the performance of these models as presented in Table 3.

Table 3. Comparison results.

Article	Model	Accuracy (%)
Proposed approach	CNN	**95.1**
	SVM	89.8
	Random Forest	93.2
	DenseNet	94.3
	MobileNet	94.6
A Dataset for Breast Cancer Histopathological Image Classification [24]	1-NN	91.5
A Dataset for Breast Cancer Histopathological Image Classification [24]	Random Forest	92.3
Convolutional Neural Network for Classification of Histopathology Images for Breast Cancer Detection [25]	CNN	93.5
Detection of Breast Cancer Using Histopathological Image Classification Dataset with Deep Learning Techniques [26]	SVM	86.1
Detection of Breast Cancer Using Histopathological Image Classification Dataset with Deep Learning Techniques [26]	K-NN	76.1
BRACS: A Dataset for BReAst Carcinoma Subtyping in H&E Histology Images [27]	WSI	70.3
An SVM approach towards breast cancer classification from H&E-stained histopathology images based on integrated features [28]	SVM	91.0
An SVM approach towards breast cancer classification from H&E-stained histopathology images based on integrated features [28]	Random Forest	85.0
Breast cancer detection from histopathology images with deep inception and residual blocks [29]	ResNet	79.0
Breast cancer detection from histopathology images with deep inception and residual blocks [29]	SVM	83.0

Since the highest accuracy rate was obtained with the CNN algorithm, the training and hyperparameters of this algorithm are given in Table 4 as follows.

Table 4. Selected hyperparameters for CNN model.

Layers	Dropout	optimizer	Learning rate	Loss function	Early stop	Activation function	Test split	Total params
10	.3	Adam	1e-4	Binary crossentropy	5 epochs	Relu - softmax	.3	3.36e6

The table above shows the models used in studies conducted on similar data sets regarding breast cancer and their success rates. In this article, the performances of the used models were analyzed in detail by comparing them with the results of previous studies in the literature. The results obtained reveal important similarities and differences between the prominent models of this study and the models in other literature. This comparison serves as an important resource for the current evaluation in the development of models for breast cancer diagnosis and treatment.

In this context, the analysis results show that deep learning models have the power to be used effectively in the diagnosis of breast cancer. Especially CNN and DenseNet models stand out with their high accuracy rates and classification metrics. The findings encourage further exploration of deep learning models in clinical applications.

5. Conclusion

This study focuses on the early diagnosis of invasive ductal carcinoma (IDC), the most common and aggressive type of breast cancer found in women globally. IDC poses a significant threat to women's health, and early detection is critical to improving survival rates and reducing mortality. Traditional diagnostic methods, such as mammography, often face challenges in accurately detecting early-stage cancer due to the complexity and time required for image interpretation. To address these limitations, this research leverages deep learning techniques, which have the potential to provide faster and more accurate diagnostics through automated image processing.

The primary objective of this study is to explore the effectiveness of deep learning models in the classification of IDC-positive and IDC-negative breast cancer cells. A dataset comprising thousands of breast cancer histopathology images was used, and image processing techniques were applied to prepare the data for model training. Five state-of-the-art deep learning models were utilized: Convolutional Neural Network (CNN), Support Vector Machine (SVM), Random Forest, DenseNet, and MobileNet. Each model was trained to analyze and classify the breast cancer images, distinguishing cancerous cells from non-cancerous cells.

The results of the analysis demonstrated that all models performed well, but some outperformed others in terms of accuracy and efficiency. CNN and DenseNet emerged as the top-performing models, with accuracy rates of 95.1% and 94.31%, respectively. MobileNet also exhibited strong performance with an accuracy rate of 94.6%, followed by Random Forest with 93.21% and SVM with 89.87%. These findings highlight the strength of deep learning models in accurately diagnosing breast cancer compared to traditional machine learning models. The superior performance of CNN and DenseNet, in particular, suggests that they have the potential to be integrated into clinical practice to assist pathologists in making faster and more accurate diagnoses. In addition, comparisons were made with models in studies conducted with artificial intelligence in the field of health [30], further validating the robustness and applicability of these models in medical diagnostics.

In conclusion, this study provides a comprehensive evaluation of multiple deep learning models in the context of breast cancer diagnosis. The comparative analysis of these models offers valuable insights into their strengths and weaknesses. CNN and DenseNet, with their high accuracy and robust classification metrics, show significant promise for clinical applications, especially in assisting with early diagnosis where time and precision are of utmost importance. This research underscores the potential of artificial intelligence to revolutionize cancer diagnosis, offering more reliable and efficient diagnostic tools that can significantly impact patient outcomes. Future research should focus on optimizing these models for real-time clinical use, expanding the dataset to include more diverse samples, and exploring ways to reduce the computational complexity of deep learning models to facilitate their integration into everyday medical practice. If these methods are applied efficiently, they could lead to earlier detection, more effective treatment planning, and ultimately, a reduction in breast cancer mortality worldwide.

References

[1] Waks AG, Winer EP. Breast cancer treatment. JAMA 2019; 321(3): 316-316.

[2] Shah R, Rosso K, Nathanson SD. Pathogenesis, prevention, diagnosis and treatment of breast cancer. World J Clin Oncol 2014; 5(3): 283.

[3] Barroso-Sousa R, Metzger-Filho O. Differences between invasive lobular and invasive ductal carcinoma of the breast: results and therapeutic implications. Ther Adv Med Oncol 2016; 8(4): 261-266.

[4] Sharma GN, Dave R, Sanadya J, Sharma P. Various types and management of breast cancer: an overview. J Adv Pharm Technol Res 2010; 1(2): 109.

[5] Janowczyk A, Madabhushi A. Deep learning for digital pathology image analysis: a comprehensive tutorial with selected use cases. J Pathol Inform 2016; 7(1): 29.

[6] Shahidi F, Daud SM, Abas H, Ahmad NA, Maarop N. Breast cancer classification using deep learning approaches and histopathology images: a comparison study. IEEE Access 2020; 8: 187531-187552.
[7] Houssein EH, Emam MM, Ali AA, Suganthan PN. Deep and machine learning techniques for medical imaging-based breast cancer: a comprehensive review. Expert Syst Appl 2021; 167: 114161.
[8] Zahoor S, Lali IU, Khan MA, Javed K, Mehmood W. Breast cancer detection and classification using traditional computer vision techniques: a comprehensive review. Curr Med Imaging 2020; 16(10): 1187-1200.
[9] Zhang YN, Xia KR, Li CY, Wei BL, Zhang B. Review of breast cancer pathological image processing. Biomed Res Int 2021; 2021: 1-7.
[10] Kanojia MG, Ansari MAMH, Gandhi N, Yadav SK. Image processing techniques for breast cancer detection: A review. In: Intelligent Systems Design and Applications: 19th International Conference on Intelligent Systems Design and Applications (ISDA 2019) held December 3-5, 2019. Springer International Publishing; 2019. p. 649-660.
[11] Rezaei Z. A review on image-based approaches for breast cancer detection, segmentation, and classification. Expert Syst Appl 2021; 182: 115204.
[12] Lu Y, Li JY, Su YT, Liu AA. A review of breast cancer detection in medical images. In: 2018 IEEE Visual Communications and Image Processing (VCIP); 2018. p. 1-4.
[13] Mashekova A, Zhao Y, Ng EY, Zarikas V, Fok SC, Mukhmetov O. Early detection of breast cancer using infrared technology: A comprehensive review. Thermal Sci Eng Progress 2022; 27: 101142.
[14] Zhang L, Tan J, Han D, Zhu H. From machine learning to deep learning: progress in machine intelligence for rational drug discovery. Drug Discov Today 2017; 22(11): 1680-1685.
[15] Sharma N, Sharma R, Jindal N. Machine learning and deep learning applications: a vision. Global Transitions Proceedings 2021; 2(1): 24-28.
[16] Ahmad Z, Shahid Khan A, Wai Shiang C, Abdullah J, Ahmad F. Network intrusion detection system: A systematic study of machine learning and deep learning approaches. Trans Emerg Telecommun Technol 2021; 32(1): e4150.
[17] Bharti R, Khamparia A, Shabaz M, Dhiman G, Pande S, Singh P. Prediction of heart disease using a combination of machine learning and deep learning. Comput Intell Neurosci 2021; 2021: 1-8.
[18] Dushyant K, Muskan G, Annu G, Pramanik S. Utilizing Machine Learning and Deep Learning in Cybersecurity: An Innovative Approach. Cyber Security and Digital Forensics 2022; 1: 271-293.
[19] Osisanwo FY, Akinsola JET, Awodele O, Hinmikaiye JO, Olakanmi O, Akinjobi J. Supervised machine learning algorithms: classification and comparison. Int J Comput Trends Technol 2017; 48(3): 128-138
[20] Liu Y, Wang Y, Zhang J. New machine learning algorithm: Random forest. In: Information Computing and Applications: Third International Conference, ICICA 2012; 2012. p. 246-252. Springer Berlin Heidelberg
[21] Wang Z, Qu Z. Research on web text classification algorithm based on improved CNN and SVM. In: 2017 IEEE 17th International Conference on Communication Technology (ICCT); 2017. p. 1958-1961.
[22] Li T, Jiao W, Wang LN, Zhong G. Automatic DenseNet sparsification. IEEE Access 2020; 8: 62561-62571.
[23] Li Y, Huang H, Xie Q, Yao L, Chen Q. Research on a surface defect detection algorithm based on MobileNet-SSD. Appl Sci 2018; 8(9): 1678.
[24] Spanhol FA, Oliveira LS, Petitjean C, Heutte L. A dataset for breast cancer histopathological image classification. IEEE Trans Biomed Eng 2015; 63(7): 1455-1462.
[25] Narayanan BN, Krishnaraja V, Ali R. Convolutional neural network for classification of histopathology images for breast cancer detection. In: 2019 IEEE National Aerospace and Electronics Conference (NAECON); 2019. p. 291-295.
[26] Reshma VK, Arya N, Ahmad SS, Wattar I, Mekala S, Joshi S, Krah D. Detection of breast cancer using histopathological image classification dataset with deep learning techniques. Biomed Res Int 2022; 2022: 1-8.
[27] Brancati N, Anniciello AM, Pati P, Riccio D, Scognamiglio G, Jaume G, Frucci M. BRACS: A dataset for breast carcinoma subtyping in H&E histology images. Database 2022; 2022: baac093.
[28] Aswathy MA, Jagannath M. An SVM approach towards breast cancer classification from H&E-stained histopathology images based on integrated features. Med Biol Eng Comput 2021; 59(9): 1773-1783.
[29] Singh S, Kumar R. Breast cancer detection from histopathology images with deep inception and residual blocks. Multimedia Tools Appl 2022; 81(4): 5849-5865.
[30] Güler H, Santur Y, Ulaş M. Comparison of machine learning algorithms to predict cardiovascular heart disease risk level. Int J Adv Nat Sci Eng Res 2023; 7(10): 42-49.

Turkish Journal of Science & Technology
20(1), 41-53, 2025

Research Paper
https://doi.org/10.55525/tjst.1561165

Ontology of Stochastic Differential Equations

Muharrem Tuncay GENÇOĞLU[1*],
[1]Technical Science Vocational School, Fırat University, Elazig, Türkiye
mt.gencoglu@firat.edu.tr

(Geliş/Received: 04/10/2024; Kabul/Accepted:16/11/2024)

Abstract: This study provides a comprehensive examination of the mathematical formulations, ontological foundations, and application domains of stochastic differential equations (SDEs). SDEs play a critical role in modeling complex phenomena such as uncertainty and randomness and can be applied across a wide range of fields from financial markets to biological systems. The paper contrasts the mathematical approaches of Itô and Stratonovich calculus, detailing the solution methods and theoretical foundations of SDEs. Additionally, the ontological foundations of SDEs and their applications in various scientific and engineering fields are explored. Emphasis is placed on their use in finance, biology, cryptology, and blockchain technology. The results highlight the significance of SDEs in mathematical modeling and their impact across numerous application areas.

Key words: Stochastic Differential Equations, Itô Integral, Stratonovich Integral, Mathematical Modeling.

Stokastik Diferansiyel Denklemlerin Ontolojisi

Öz: Bu çalışma, stokastik diferansiyel denklemlerin (SDE'ler) matematiksel formülasyonları, ontolojik temelleri ve uygulama alanlarının kapsamlı bir incelemesini sunmaktadır. SDE'ler, belirsizlik ve rastgelelik gibi karmaşık olguların modellenmesinde kritik bir rol oynar ve finansal piyasalardan biyolojik sistemlere kadar çok çeşitli alanlarda uygulanabilir. Makale, Itô ve Stratonovich hesabının matematiksel yaklaşımlarını karşılaştırarak SDE'lerin çözüm yöntemlerini ve teorik temellerini ayrıntılı olarak açıklamaktadır. Ek olarak, SDE'lerin ontolojik temelleri ve çeşitli bilimsel ve mühendislik alanlarındaki uygulamaları incelenmektedir. Finans, biyoloji, kriptoloji ve blok zinciri teknolojisindeki kullanımlarına özel vurgu yapılmaktadır. Sonuçlar, SDE'lerin matematiksel modellemedeki önemini ve çok sayıda uygulama alanındaki etkilerini vurgulamaktadır.

Anahtar kelimeler: Stokastik Diferansiyel Denklemler, Itô İntegrali, Stratonovich İntegrali, Matematiksel Modelleme.

1. Introduction

Stochastic Differential Equations (SDEs) play a critical role in mathematical and applied sciences for modeling complex phenomena such as uncertainty and randomness. These equations, which span a wide spectrum in mathematical analysis and applications, play a significant role in various fields from financial markets to biological systems. Studies on the mathematical formulations and ontological foundations of SDEs allow for a profound understanding of these equations both theoretically and practically.

SDEs provide a robust foundation for understanding and modeling uncertainties and stochastic processes. Typically, these equations are formed by adding a random component to a deterministic system, thereby offering an opportunity to examine the effects of uncertainty mathematically. Mathematically, SDEs are often addressed using various methods such as Itô calculus or Stratonovich calculus. The structural analysis of these equations focuses particularly on solution methods and the properties of these solutions. Itô's work provides a fundamental framework for stochastic calculations [1], while Stratonovich's approach offers an important alternative in the analysis of stochastic processes [2]. These mathematical approaches enable a deep understanding of stochastic process analysis [3].

From an ontological perspective, SDEs are seen to mathematically express concepts of uncertainty and randomness. In this context, studies on the ontological foundations of SDEs provide an in-depth understanding of how these equations structure uncertainty and randomness. They focus on how SDEs model real-world systems and the philosophical foundations of these models. Additionally, the relationships between SDEs and various mathematical structures, and the effects of these relationships in scientific applications, constitute a significant research area.

In the application domain, SDEs are used across a broad range of fields from financial markets to biological systems. Notably, the contributions of the Black-Scholes model in financial markets for risk management and option pricing highlight the importance of these equations in economic and financial theories. Moreover, the use of SDEs in biological systems has been proposed as an important tool for understanding the dynamics of biological processes [4].

* Corresponding author: mt.gencoglu@firat.edu.tr. ORCID Number of authors: [1] 0000-0002-8784-9634

This study aims to provide a comprehensive analysis of the mathematical and ontological aspects of SDEs. Initially, the mathematical structure and solution methods of SDEs will be detailed. The comparison of Itô's and Stratonovich's approaches will aid in understanding the place of these equations in mathematical theory. Subsequently, the ontological framework of these equations and their application in various scientific fields will be discussed. The relationships of SDEs with other mathematical structures and future research directions will also be addressed. This study aims to offer a thorough assessment of the mathematical and ontological foundations of SDEs by referencing the existing literature.

SDEs hold a significant place in the field of mathematical modeling. These equations are fundamental tools used to understand and model the dynamics of stochastic processes. The mathematical theory of SDEs is derived from the integration of stochastic processes and differential equations theory, expanding the boundaries of mathematical modeling [5].

Concepts such as Itô's Lemma and the Wiener process form the foundation of stochastic calculus, offering wide applications for analyzing complex systems. In this context, the mathematical analysis of SDEs strengthens the theoretical foundations of these equations and facilitates the development of new mathematical methods.

The importance of SDEs in applied sciences and engineering arises from their ability to model randomness and uncertainty. Applications such as the Black-Scholes option pricing model in financial markets, epidemiological models in biological systems, and molecular dynamics in physical systems demonstrate the broad effectiveness of SDEs [6].

SDEs also play a significant role in cryptology and blockchain technologies. In these fields, the mathematical structures of SDEs are used for security and randomness analysis.

- **Cryptology**: Stochastic processes and SDEs are used to evaluate the security of cryptographic algorithms. For instance, analyzing the security of encryption algorithms and stochastic key generation is crucial for determining the robustness of these algorithms. For example, the analysis of the security of the RSA encryption algorithm uses mathematical models based on randomness and number theory, with SDEs playing a critical role [7].
- **Blockchain Technologies**: The security and accuracy of data structures in blockchains can be modeled using stochastic processes. Various algorithms used to ensure the security of blockchains employ the mathematical tools of randomness and SDEs. Additionally, SDEs can be used for optimization and performance analysis of blockchain technologies. For example, algorithms used to model the security and performance of Bitcoin and other cryptocurrencies incorporate the mathematical properties of stochastic processes [8].

The role of SDEs in social sciences, intelligence, and national security stems from their impact on analyzing randomness and uncertainties. In these fields, the use of SDEs allows for the analysis of complex social dynamics and security threats.

- **Social Sciences**: Dynamics in social systems often involve uncertainty and randomness. SDEs are used to model and analyze these dynamics. Topics such as social interactions, behavioral models, and social network analyses can be studied with SDEs. For example, modeling social interactions and forecasting societal trends demonstrate how SDEs can be used to analyze random effects and dynamics in social networks [9].
- **Intelligence**: In intelligence gathering and analysis, SDEs can model random events and data flows, enhancing the accuracy of intelligence analyses and facilitating risk prediction. The analysis of intelligence data using SDEs can model potential threats and security vulnerabilities.
- **National Security**: In national security strategies and threat analysis, SDEs can be used for the mathematical modeling of potential risks and uncertainties. This enables the more effective development of security strategies. The ability of SDEs to model randomness and uncertainty can enhance the effectiveness of security measures and strategies in national security threat analysis and strategic planning.

Understanding the place of SDEs in scientific thought and their role in mathematical modeling processes requires ontological analysis. Studies on how mathematical models represent real-world systems and the accuracy of these representations contribute to the development of scientific thought.

In this context, the ontological foundations of SDEs are crucial for understanding the scientific and philosophical basis of mathematical models. Studies on the representation of mathematical models and their accuracy explain the evolution of scientific thought and the real-world applications of mathematical models [10,16].

The motivation for this study includes:

- How are SDEs mathematically formulated and analyzed?

- What are the ontological foundations of SDEs, and how are these foundations applied in various scientific fields?
- How can the relationships between SDEs and other mathematical structures be understood?

With this motivation, the study aims to:

- Detail the mathematical formulations and conceptual structures of SDEs
- Explain how SDEs can be evaluated within an ontological framework
- Examine how SDEs are used in various application areas and their relationships with other mathematical structures

In the 2nd and 3rd sections of this study, the mathematical and ontological foundations of SDEs are explained in detail, respectively. In the 4th section, the findings and discussions are given, and in the last section, the conclusion section is given, emphasizing the effects of SDEs in modeling randomness and uncertainty.

2. Mathematical Foundations of SDEs

2.1. Definition

Stochastic Differential Equations can be thought of as differential equations with added stochastic (random) terms. These equations are typically used within a modeling framework that includes a stochastic process and exhibits randomness (Equation 1).

$$dX(t) = f(t,X)dt \tag{1}$$

Ordinary Differential Equation 2 with Initial Condition $X(0) = X_0$

$$X(t) = X_0 + \int_0^t f\big(s.X(s)\big)ds, \tag{2}$$

When solved with the initial condition, is obtained. $X(t) = X(t,X_0,t_0) \rightarrow X(t_0) = X_0$

$$dX(t) = a(t)X(t)dt, \quad (X(0) = X_0)$$

Let us assume that $a(t)$ in Equation (2) is a non-deterministic, stochastic parameter. In this case, the equation transforms into a stochastic differential equation (Equation 3).
For $a(t) = f(t) + h(t)\xi(t)$, is obtained.

$$X(t) = f(t)X(t)dt + h(t)X(t)\xi(t)dt. \tag{3}$$

Here, the differential form of Brownian motion.
Given $dW(t) = \xi(t)dt$ in Equation (3):

$$dX(t) = f(t)X(t)dt + h(t)X(t)dW(t). \tag{4}$$

the stochastic differential equation is obtained.
when the equation is rewritten with new notations;

$$dX(t) = \mu(X(t),t)dt + \sigma(X(t),t)dW(t). \tag{5}$$

The general form of the stochastic differential equation is obtained (Equation 5).
Where;

- $X(t)$: Represents the system state.
- $\mu(X(t),t)$: Function representing the deterministic component.
- $\sigma(X(t),t)$: Function representing the stochastic component.
- $W(t)$: The stochastic process known as the Wiener process or Brownian motion.

SDEs are classified as Linear and Nonlinear SDEs [1].

I. Lineer SDE

- **Scalar Lineer SDE**

In the equation

$$dX(t) = f\big(t, X(t)\big)dt + g\big(t, X(t)\big)dW(t). \quad (6)$$

a one-dimensional stochastic process $X(t)$ is called a Scalar Linear SDE if and only if the functions $f\big(t, X(t)\big)$ and $g\big(t, X(t)\big)$ in Equation 6 are affine functions of $X(t) \in R$.

- **Vector Value Linear SDE**

$$dX(t) = \big(A(t)X(t) + a(t)\big)dt + \sum_{i=1}^{m}(B_i(t)X(t) + b_i)\, dW_i(t). \quad (7)$$

II. Non-Linear SDE

In Equation 7, where $A(t), a(t)$ and $B(t)$ are real scalars:

$$\begin{matrix} f\big(t,X(t)\big) = A(t)X(t) + a(t) \\ g\big(t,X(t)\big) = B(t)\sqrt{X(t)} \end{matrix} \quad (8)$$

the equation becomes a Nonlinear SDE (Equation 8) [13].

2.2. Basic Concepts

Wiener Process (Brownian Motion): The Wiener process is a continuous stochastic process and is mathematically expressed as follows (Equation 9): [14,15]

$$W(t) = \int_0^t \xi(s)ds. \quad (9)$$

Drift and volatilize: Drift (μ) and volatility (σ) measure the average trend and randomness in stochastic processes [14,15].

2.3. Solution Methods

2.3.1. Itô Approach

2.3.1.1. Itô Integral

- **Definition**: The Itô integral is a method used for integration in stochastic differential equations and is typically defined with respect to the Wiener process (Brownian motion (Equation 10)).

$$\int_0^t f(X(s))dW(s)\,. \quad (10)$$

- **Properties**: The Itô integral follows differentiation rules according to Itô's Lemma and differs from classical calculus rules. The Itô integral uses the values at the endpoints of integration, making it a "stricter" method. It is commonly used in financial mathematics and stochastic processes, considering the variance-related properties of integration.

2.3.1.2. Itô's Lemma

- **Definition**: Itô's Lemma is used to calculate the derivative of a function in stochastic differential equations (Equation 11).

If $X(t)$ is defined by an Itô SDE and $f(X(t),t)$ is a function, then:

$$df(X(t),t) = \left(\frac{\partial t}{\partial f} + \mu\frac{\partial X}{\partial f} + \frac{1}{2}\sigma^2\frac{\partial^2 f}{\partial X^2}\right)dt + \sigma\frac{\partial f}{\partial X}dW(t). \quad (11)$$

- **Properties**: Itô's Lemma extends classical differentiation rules in stochastic differential equations and involves integration with the Itô integral [17].

2.3.2. Stratonovich Approach

2.3.2.1. Stratonovich Integral

- **Definition**: The Stratonovich integral is a version of stochastic integration that is closer to classical integration rules (Equation 12).

$$\int_0^t f\big(X(s)\big)\ \mathrm{o}\ \mathrm{dW(s)}. \quad (12)$$

- **Properties**: The Stratonovich integral provides results that are more aligned with classical differentiation rules and often yields more natural results in physical and engineering problems. The "o" notation indicates that the Stratonovich integration uses the midpoint values of the function $f(X(s))$ over the integration interval. This means that during integration, the values at the midpoint of the interval are used.

2.3.2.2. Stratonovich Lemma

- **Definition**: Stratonovich's Lemma enables differentiation using the Stratonovich integral (Equation 13).

If $X(t)$ is defined by a Stratonovich SDE and $f(X(t),t)$ is a function, then:

$$df(X(t),t) = \left(\frac{\partial t}{\partial f} + \frac{1}{2}\sigma^2\frac{\partial^2 f}{\partial X^2}\right)dt + \sigma\frac{\partial f}{\partial X}dW(t). \quad (13)$$

- **Properties**: Stratonovich's Lemma conforms more closely to classical differentiation rules and provides results like classical formulas for stochastic integration [18].

2.3.3. General Numerical Solution Methods

2.3.3.1. Euler-Maruyama Method

- **Definition**: The Euler-Maruyama method is a simple technique used for the numerical solution of stochastic differential equations (Equation 14).

$$X(t) + \Delta t = X(t) + \mu(X(t),t)\Delta t + \sigma(X(t),t)\Delta W(t). \quad (14)$$

- **Properties**: This method is commonly used for Itô SDEs and is a fundamental technique in numerical simulations.

2.3.3.2. Milstein Method

- **Definition**: The Milstein method extends the Euler-Maruyama method by including second-order terms (Equation 15).

$$\mathrm{X(t+\Delta t) = X(t) + \mu(X(t),t)\Delta t + \sigma(X(t),t)\Delta W(t) + \frac{1}{2}\sigma(X(t),t)\sigma'(X(t),t)((\Delta W(t))^2 - \Delta t)}. \quad (15)$$

- **Properties**: This method provides more accurate results and generally offers better accuracy.

2.3.3.3. Runge-Kutta Methods

- **Definition:** Runge-Kutta methods provide advanced numerical techniques with various orders of accuracy for stochastic differential equations.
    - **Second-Order Runge-Kutta:** Second-order Runge-Kutta methods offer more precise solutions for stochastic differential equations.
    - **Fourth-Order Runge-Kutta:** Fourth-order Runge-Kutta methods provide higher accuracy but are more complex.

2.3.3.4. Girsanov's Theorem: Girsanov's Theorem facilitates simpler modeling by altering the measure of a stochastic process. It is particularly useful for understanding how the distributions arising from changes in stochastic processes are altered.

2.3.3.5. Monte Carlo Simulations: Monte Carlo simulations are used to understand the statistical properties of solutions to stochastic differential equations by sampling many random instances to predict the distribution of solutions.

2.3.3.6. Feynman-Kac Formula: The Feynman-Kac Formula relates the solutions of stochastic differential equations to partial differential equations. This formula is commonly used in financial mathematics and physics problems.

2.3.4. Application Fields

2.3.4.1. Financial Mathematics

- **Option Pricing:** The Black-Scholes model, based on an SDE, is used to calculate option prices.
- **Portfolio Management:** Stochastic models are used for risk and return analysis.
- **Credit Risk Management:** SDEs are employed to model the likelihood of default and associated risks.
- **Volatility Modeling:** Models like GARCH use stochastic processes to understand asset price variability.

2.3.4.2. Physics and Engineering

- **Thermodynamics:** Used to model the random movement of molecules and energy distributions.
- **Stochastic Resonance:** Helps in understanding signal detection at low noise levels.
- **Control Theory:** Evaluates the impact of stochastic processes in controlling systems.

2.3.4.3. Biology

- **Population Dynamics:** Models the growth and decline of biological populations, such as interspecies interactions in ecosystems.
- **Genetics:** Models genetic variations and evolution using stochastic processes.
- **Epidemiology:** Analyzes disease spread models and infection dynamics.

2.3.4.4. Economics

- **Macroeconomic Models:** Uses stochastic processes to model economic variables like growth, unemployment, and inflation.
- **Monetary Policy:** Understands the effects of central bank policies using stochastic models.

2.3.4.5. Signal Processing

- **Noise Modeling:** Analysis and filtering of random noise in signals.
- **Signal Prediction:** Forecasting future signal values.

2.3.4.6. Machine Learning and Artificial Intelligence

- **Stochastic Optimization:** Uses stochastic processes in optimizing learning algorithms.
- **Data Analysis:** Applies stochastic methods to large datasets.

2.3.4.7. Insurance

- **Actuarial Science:** Calculates risks and sets premiums for life insurance and retirement plans.
- **Natural Disasters:** Assesses risks from events such as floods and earthquakes.

2.3.4.8. Chemistry

- **Reaction Dynamics:** Models the rates and mechanisms of chemical reactions using stochastic processes.

2.3.4.9. Computer Science

i. Stochastic Algorithms

- **Random Walks:** Utilizes random walks in data structures and algorithms, such as in graph algorithms.
- **Stochastic Optimization:** Uses stochastic methods for solving problems, especially in large datasets and complex systems.

ii. Artificial Intelligence and Machine Learning

- **Noise and Data Cleaning:** Employs stochastic models in data cleaning and improvement processes.
- **Advanced Learning Techniques:** Utilizes stochastic processes in deep learning and other machine learning algorithms.

2.3.4.10. Cybersecurity

i. Security Protocols and Encryption

- **Security Analysis:** Uses stochastic processes to evaluate the security of protocols and analyze vulnerabilities.
- **Encryption Algorithms:** Employs stochastic processes and algorithms for generating secure random numbers.

ii. Attack and Defense Strategies

- **Attack Models:** Models various types of attacks using stochastic models.
- **Defense Methods:** Develops stochastic defense strategies against cyber-attacks.

2.3.4.11. Cryptology

i. Encryption and Key Management

- **Random Key Generation:** Uses stochastic processes and algorithms to generate strong and secure keys.
- **Crypto Analysis:** Analyzes the security of cryptographic systems and identifies vulnerabilities using stochastic methods.

ii. Encryption Protocols

- **Stochastic Encryption Methods:** Utilizes stochastic methods in developing new encryption techniques.

2.3.4.12. Blockchain

i. Consensus Algorithms

- **Proof of Work (PoW):** PoW algorithms incorporate stochastic processes in the mining process for adding new blocks to the blockchain.
- **Proof of Stake (PoS):** PoS algorithms model block creation processes with randomly selected validators based on stake amounts.

ii. Security and Transparency

- **Transaction Modeling:** Uses stochastic processes to ensure the security and transparency of blockchain transactions and data validations.
- **Risk Management:** Analyzes potential risks and security vulnerabilities in blockchain networks.

iii. Smart Contracts

- **Error Analysis:** Tests for potential errors and security vulnerabilities in smart contract operations using stochastic processes.

2.3.4.13. Social Sciences

- **Behavior Analysis:** Analyzes human behavior and social interactions using stochastic models.
- **Social Networks:** Models dynamics in social media and communication networks.

3. Ontological Foundations of SDEs

The ontological foundations of SDEs concern the deeper philosophical question of whether randomness and uncertainty are intrinsic to the systems being modeled or if they are merely a reflection of incomplete knowledge.

3.1. Ontological Status of Mathematical Models: Investigates how mathematical models, including SDEs, represent real-world systems and assesses the accuracy of these representations [10,16].

3.2. Randomness as an Intrinsic Feature

One view suggests that SDEs reflect true randomness in nature. This perspective is supported by fields such as quantum mechanics, where uncertainty and probabilistic behavior are fundamental. For example, in quantum systems, the behavior of particles cannot be predicted with certainty, and SDEs capture this inherent randomness.

3.3. SDEs as Approximation Tools

An alternative view is that SDEs serve as approximation tools for modeling complex, deterministic systems. In this framework, randomness arises due to our inability to fully describe the underlying dynamics of a system. For instance, in biological systems, random fluctuations in population sizes may result from environmental factors that are not explicitly modeled.

3.3.1. Existential Framework: Examines the existence of SDEs as mathematical models and how these models represent real-world systems, evaluating the accuracy of these representations and their implications in various applications.

3.3.2. Functional Framework: Analyzes the role and impact of SDEs in various scientific and engineering applications. The functional framework explains how SDEs model system dynamics and random variations.

3.4. Applications of SDEs

SDEs have become indispensable in various fields due to their ability to model uncertainty and stochastic processes. Below, we highlight some key applications:

- **Financial Applications:** SDEs play a critical role in modeling risk and volatility in financial markets. The Black-Scholes model, a classical stochastic model used for option pricing, demonstrates how SDEs are applied to model randomness in financial risk and return [9]. Studies on the accuracy of this model have explored its effects on financial markets [12].
- **Biological Applications:** In epidemiological and population dynamics models, SDEs help understand random changes in biological systems, aiding in better comprehension and prediction of biological processes [4].
- **Physical Applications**: SDEs are used to analyze random effects in molecular dynamics and other physical processes [11].
- Cryptology and Blockchain Technology: In cryptology, SDEs contribute to secure communication by modeling noise-based encryption methods. Furthermore, blockchain technology, with its decentralized structure, can benefit from SDEs in optimizing transaction throughput and ensuring security in unpredictable environments. For example, stochastic models can be used to predict the behavior of blockchain systems under varying levels of network traffic and external disturbances.

3.5. Ontological Analysis with Examples

A. Black-Scholes Model

Ontological Representation: The Black-Scholes model represents the pricing of options through a stochastic process, if the underlying asset's price follows a geometric Brownian motion. This model operates under specific assumptions, such as constant volatility and a log-normal distribution of asset prices. However, real financial markets do not always adhere to these assumptions. For instance, market volatility can change over time, and price distributions can deviate from the log normal. Thus, while the Black-Scholes model provides a foundational framework for option pricing, its assumptions limit its ability to fully capture the complexities of real market dynamics. This discrepancy illustrates the model's potential limitations in representing actual financial market behavior accurately.

B. Lotka-Volterra Model

Ontological Representation: The Lotka-Volterra model, also known as the predator-prey model, describes the dynamics of biological populations through stochastic differential equations. It assumes that the growth rates of predator and prey populations follow specific mathematical rules with random perturbations. However, real-world ecosystems are influenced by a multitude of factors beyond the model's scope, such as environmental changes, genetic variations, and interactions with other species. These additional complexities mean that while the Lotka-Volterra model provides useful insights into population dynamics, it may not fully capture the intricate realities of actual ecological systems. This limitation highlights the model's ontological constraints in representing comprehensive biological dynamics.

C. Molecular Dynamics

Ontological Representation: Molecular dynamics (MD) simulations model the movement of molecules using stochastic processes to account for random thermal fluctuations and interactions between particles. The simulations typically involve detailed modeling of atomic interactions based on physical laws, such as Newtonian mechanics, coupled with random noise to represent thermal energy. However, real molecular systems involve additional complexities, such as quantum effects and complex environmental interactions, which are not always fully accounted for in MD simulations. Consequently, while MD provides valuable insights into molecular behavior, its ability to represent all aspects of molecular interactions and environmental influences is limited. This demonstrates the ontological limitations of MD simulations in capturing the complete range of real-world molecular phenomena.

3.6. Scientific and Applied Representation: Evaluates the effects and uses of SDEs in various scientific and applied contexts, understanding their role in representing scientific theories and real-world phenomena

3.6.1. Ontological Analysis of Scientific and Applied Representation of SDEs

A. Financial Mathematics: Black-Scholes Model

Scientific Representation: The Black-Scholes model is a cornerstone of financial mathematics that employs SDEs to model the evolution of stock prices over time. It represents asset price dynamics as a geometric Brownian motion with constant volatility. Scientifically, the model simplifies the complex reality of financial markets into a tractable mathematical framework, allowing for the theoretical pricing of options and other derivatives.

Ontological Perspective: Ontologically, the Black-Scholes model abstracts financial market dynamics into a set of stochastic processes that follow specific mathematical rules. This abstraction enables the model to provide valuable insights and predictive capabilities within its defined parameters. However, the model's reliance on assumptions like constant volatility and log-normal price distribution limits its ability to fully represent the complexities and anomalies observed in actual financial markets. For instance, phenomena like market crashes or volatility clustering are not adequately captured by the model, demonstrating the ontological gap between the simplified representation and the multifaceted nature of real-world financial systems.

B. Ecology: Lotka-Volterra Model

Scientific Representation: The Lotka-Volterra model, or predator-prey model, uses SDEs to describe the population dynamics of predator and prey species. It captures the fluctuations in population sizes through stochastic processes, representing the inherent randomness in ecological interactions and environmental factors.

Ontological Perspective: From an ontological standpoint, the Lotka-Volterra model offers a simplified yet insightful representation of ecological dynamics by focusing on the core interactions between predators and prey. The model's stochastic elements account for random variations in population growth rates and interactions. However, the ontological limitations become apparent when considering the full complexity of natural ecosystems. Real-world ecosystems involve additional layers of complexity, such as the effects of climate change, habitat destruction, and species interactions beyond predator-prey relationships. The model's simplifications reflect an ontological abstraction that, while useful, may not fully capture the broader ecological realities.

C. Molecular Dynamics: Simulation of Protein Folding

Scientific Representation: Molecular dynamics (MD) simulations use SDEs to model the movement of atoms and molecules, including the folding process of proteins. These simulations incorporate stochastic forces to represent thermal fluctuations and interactions between molecules, providing insights into molecular behavior at the atomic level.

Ontological Perspective: Ontologically, MD simulations represent molecular systems through mathematical models that account for random thermal motions and interactions. This representation is valuable for understanding the dynamics of molecular processes, such as protein folding, and provides predictions about molecular configurations and interactions. However, MD simulations face ontological limitations in capturing all relevant physical phenomena. For instance, quantum mechanical effects and complex solvent interactions might not be fully represented in the classical simulations. This ontological gap highlights the constraints of the models in reflecting the complete range of real-world molecular interactions and behaviors.

D. Epidemiology: Disease Spread Modeling

Scientific Representation: SDEs are used in epidemiology to model the spread of infectious diseases within populations. These models incorporate stochastic elements to represent the randomness in disease transmission rates, contact patterns, and other factors influencing the spread of disease.

Ontological Perspective: From an ontological perspective, SDE-based epidemiological models provide a simplified representation of disease dynamics by focusing on stochastic processes that capture the inherent randomness of disease transmission. These models offer valuable insights into the probabilistic nature of disease spread and help in predicting potential outbreaks. However, the ontological limitations arise when considering additional factors such as public health interventions, behavioral changes, and genetic variations. The model's abstraction may not fully encompass the complexity of real-world epidemiological scenarios, illustrating the gap between the simplified mathematical representation and the multifaceted nature of actual disease dynamics.

4. Result and Discussion

The analysis reveals that the choice between Itô and Stratonovich calculus depends on the specific application domain. Itô's calculus is ideal for financial models that require non-anticipative properties, whereas Stratonovich calculus is better suited for physical systems with feedback between state and noise.
Ontologically, SDEs can either be seen as tools that approximate complex deterministic systems or as representations of genuine randomness. In either case, their importance in both theoretical and applied mathematics cannot be overstated.

This study evaluates the mathematical and ontological structures of stochastic differential equations (SDEs) and their place within scientific thought. It provides an in-depth exploration of the role of SDEs in mathematical modeling processes and their impact on both theoretical and applied sciences.

4.1. Mathematical Structures

4.1.1. Role in Modeling Randomness and Uncertainty: SDEs are essential tools for capturing and modeling the inherent randomness and uncertainty present in complex systems. These equations extend traditional deterministic models by incorporating stochastic elements, which allow for the analysis of systems where uncertainty plays a critical role. Mathematically, SDEs provide a framework to understand and analyze the dynamics of random processes, such as financial markets, biological systems, and physical phenomena.

4.1.2. Key Mathematical Tools:

- **Ito's Lemma:** This fundamental result in stochastic calculus enables the differentiation of functions of stochastic processes. It is crucial for deriving the dynamics of functions of random variables and plays a central role in the application of SDEs to financial mathematics and other fields.
- **Wiener Process:** Also known as Brownian motion, the Wiener process is a cornerstone of stochastic processes. It models continuous random motion and is used to describe the random component of SDEs. Its properties, such as independent increments and Gaussian distribution, are pivotal for the theoretical foundation of stochastic differential equations.

4.1.3. Expanding Mathematical Boundaries: The inclusion of stochastic processes in mathematical models pushes the boundaries of traditional modeling approaches. SDEs enable the exploration of systems where uncertainty is a fundamental aspect, leading to new insights and methodologies. The integration of SDEs with other mathematical structures, such as partial differential equations and optimization techniques, further enhances the analytical capabilities and application scope of mathematical modeling.

4.2. Ontological Structures

4.2.1. Representation of Real-World Systems: Ontologically, SDEs offer a nuanced representation of real-world systems by modeling the randomness and variability inherent in these systems. They bridge the gap between theoretical models and empirical observations by providing a probabilistic framework to understand complex phenomena. The ability of SDEs to incorporate randomness and uncertainty enhances their capacity to represent scientific realities more accurately.

4.2.2. Impact on Scientific Theories: SDEs play a significant role in validating and refining scientific theories by offering a robust mathematical framework to model real-world processes. Their application extends across various disciplines, including finance, biology, physics, and engineering, demonstrating their versatility and relevance. By modeling the stochastic nature of these processes, SDEs contribute to a deeper understanding of theoretical concepts and their alignment with empirical data.

4.2.3. Enhancing Model Validity and Accuracy: The ontological significance of SDEs lies in their ability to enhance the validity and accuracy of mathematical models. By incorporating stochastic elements, SDEs address the limitations of deterministic models and provide a more comprehensive view of the systems under study. This capability is crucial for developing reliable predictions and insights in applied fields, where the impact of randomness and uncertainty cannot be ignored.

4.2.4 Evolution of Scientific Thought: The role of SDEs in the evolution of scientific thought reflects their contribution to advancing theoretical and applied sciences. As mathematical tools, SDEs have expanded the scope

of analysis and understanding in various domains. Their continued development and application signify the ongoing evolution of scientific methodologies and the increasing recognition of the importance of stochastic processes in modeling complex systems.
The role of SDEs in mathematical modeling processes continues to be significant in the evolution of science and in applied fields.

4.3. Future Research

Future research could explore the potential developments in the mathematical structures and applications of SDEs in greater detail. In this context, focusing on the following areas could be fruitful for future studies:

4.3.1. Integration with Other Mathematical Structures

Integration and Relationships: Investigating the integration of SDEs with other mathematical structures and the implications of such integration could represent a significant step in mathematical modeling. For example, studies could focus on the relationships between SDEs and differential equations, integral equations, and functional analysis. This could enhance the understanding of mathematical theories and provide new solutions for applied problems.

4.3.2. New Application Areas

Scientific and Engineering Applications: Exploring potential applications of SDEs in new scientific and engineering fields could reveal significant opportunities. Specifically, the use of SDEs in artificial intelligence and machine learning holds considerable potential for developing data analysis and prediction models. Additionally, modeling environmental and climate changes, optimizing energy systems, and analyzing risk in healthcare could benefit from SDE applications.

4.3.3. Applications in Social Sciences and Security

Social Dynamics and Security Analyses: Broadening the investigation of SDEs in social sciences and national security could lead to new methods for modeling social interactions and security threats. This would enhance the understanding of social behavior and security strategies.

4.4. Scientific and Applied Contributions

This study has thoroughly examined the mathematical and ontological structures of SDEs and their applications across various disciplines. Future research, through in-depth investigations, is expected to further develop the mathematical theory and application areas of SDEs. The applications of SDEs in various scientific and engineering fields will continue to play a critical role in modern mathematical modeling processes.

5. Conclusion

Stochastic differential equations (SDEs) offer a versatile mathematical framework for understanding and modeling complex systems that are inherently random and uncertain. In fields such as finance, biology, cryptology, and blockchain, SDEs provide insights that go beyond traditional modeling methods, enabling a deeper analysis and an intuitive understanding of unpredictable events in the real world. By modeling how systems evolve randomly over time, SDEs introduce significant innovations in forecasting and analyzing phenomena characterized by uncertainty.

One of the key innovations of SDEs is their ability to model random movements in detail, directly account for uncertainty within a system, and quantify the effects of this randomness on outcomes. The choice between Itô and Stratonovich calculus is crucial for creating models that align with the physical reality of the processes being studied. For instance, Itô calculus is more suitable for domains like finance, where discrete, instantaneous changes are common, while Stratonovich calculus is often preferred in natural sciences, especially for biological processes. This flexibility allows SDEs to adapt to various applications and significantly enhances their accuracy.

Beyond their practical applications, SDEs also raise intriguing ontological questions. There is an ongoing debate among mathematicians and philosophers about whether SDEs are merely tools for modeling random changes or if they reveal something fundamental about the randomness of nature itself. In areas like quantum mechanics and cryptology, the ontological status of SDEs touches upon foundational questions in information

theory, suggesting that these equations open profound inquiries into the nature of reality, rather than just offering a means of modeling.

In recent years, SDEs have found new applications in emerging fields like blockchain technology, where they contribute to data privacy and security solutions. These equations are now being used to analyze dynamics that ensure system security, anticipate vulnerabilities and build more resilient cybersecurity frameworks. This diversity of applications has expanded the reach of SDEs, indicating that as research continues, SDEs will remain indispensable across a growing array of fields, cementing their status as a key tool in scientific inquiry and innovation.

Funding

This study is supported by TÜBİTAK [223N142] (CHISTERA-Di4SPDS).

References

[1] Ito K. On Stochastic Differential Equations. Mem Amer Math Soc, 1951; 4: 1-51.
[2] Stratonovich RL. A New Representation for Stochastic Integrals and Equations. SIAM Journal on Control, 1966; 4: 362-371.
[3] Karatzas SE, Shreve SE. Brownian Motion and Stochastic Calculus. 2nd Ed. USA: Springer-Verlag; 1991.
[4] Allen LJS. An Introduction to Stochastic Processes with Applications to Biology, USA: Springer; 2008.
[5] Itô K, McKean HP. Diffusion Processes and their Sample Paths, USA: Springer; 1965.
[6] Rivest RL, Adleman L, Deaouzos ML. On Data Banks and Privacy Homomorphism. In: DeMillo, RA, editors. Foundations of Secure Computation, USA: Academic Press, 1978: 169-179.
[7] Nakamoto S. Bitcoin: A Peer-to-Peer Electronic Cash System; 2008. https://bitcoin.org/bitcoin.pdf
[8] Kang H, Chang X, Mišić J, Mišić VB, Yao Y, Chen Z. Stochastic modeling approaches for analyzing blockchain: A survey. *arXiv preprint arXiv:2009.05945*, 2020.
[9] Black F, Scholes M. The pricing of options and corporate liabilities. Journal of Political Economy, 1973; 81(3): 637-654.
[10] Frigg R, Hartmann S. Models and Fiction. In The Philosophy of Model-Based Science, USA: Springer, 2012; 49-97.
[11] Gardiner CW. Handbook of Stochastic Methods, USA: Springer, 2004.
[12] Hull JC. Options, Futures, and Other Derivatives, AUSTRALIA: Pearson 2015.
[13] Van Kampen NG. Stochastic differential equations, Physics Reports, 1976; 24(3): 171-228.
[14] Merton RC. Theory of rational option pricing. Bell J Econ Manage Sci, 1973; 4(1): 141-183.
[15] Nelkin D. Stochastic Processes and Applications. USA: Academic Press, 1983.
[16] Norton JD. Mathematical Models in the Sciences: The Role of Simulation anda Computation. MIT Press, 2019.
[17] Øksendal B. Stochastic Differential Equations, USA: Springer-Verlag, 2000.
[18] Kuznetsov DF. Mean-Square Approximation of Iterated Itˆo and Stratonovich Stochastic Integrals: Method of Generalized Multiple Fourier Series. Application to Numerical Integration of Itˆo SDEs and Semilinear SPDEs. Differential Equations and Control Processes, 2021; 4: 4-14.

Turkish Journal of Science & Technology
20(1), 55-61, 2025

Research Paper
https://doi.org/10.55525/tjst.1528213

PCG-Generated Randomness: A NIST Analysis of 100-Million Bits

Zülfiye Beyza METİN[1*], Fatih ÖZKAYNAK[2]
[1,2] Department of Software Engineering, Faculty of Tecnology, Fırat University, Elazığ, Turkey
[*1] zbmetin@firat.edu.tr, [2] ozkaynak@firat.edu.tr

(Geliş/Received: 05/08/2024; Kabul/Accepted: 20/11/2024)

Abstract: The generation of random numbers is crucial for various applications, including cryptography, simulation, sampling, and statistical analysis. Cryptography utilizes random numbers to secure communication through the generation of encryption keys, thereby safeguarding sensitive information from unauthorized access. This study aims to evaluate the randomness and suitability of the Permuted Congruential Generator (PCG) algorithm for cryptography applications, through testing its generated random numbers using the National Institute of Standards and Technology (NIST) statistical tests. A novel method is proposed for generating 100 million bits using the PCG algorithm. The generated random numbers are then subjected to NIST testing. The results indicate that the PCG-generated random numbers pass most relevant statistical tests and comply with the standards of randomness necessary for cryptography. In conclusion, the PCG algorithm is demonstrated to be a robust, dependable, and appropriate random number generator for cryptography and other applications requiring random numbers.

Key words: Randomness, PCG, NIST, Security.

PCG Tarafından Oluşturulan Rastgelelik: 100 Milyon Bitlik Bir NIST Analizi

Öz: Rastgele sayıların üretilmesi kriptografi, simülasyon, örnekleme ve istatistiksel analiz gibi çeşitli uygulamalar için çok önemlidir. Kriptografi, şifreleme anahtarlarının oluşturulması yoluyla iletişimi güvence altına almak için rastgele sayıları kullanır ve böylece hassas bilgileri yetkisiz erişime karşı korur. Bu çalışma, Permuted Congruential Generator (PCG) algoritmasının kriptografi uygulamaları için rastgeleliğini ve uygunluğunu, üretilen rastgele sayıları Ulusal Standartlar ve Teknoloji Enstitüsü (NIST) istatistiksel testlerini kullanarak test ederek değerlendirmeyi amaçlamaktadır. PCG algoritmasını kullanarak 100 milyon bit üretmek için yeni bir yöntem önerilmiştir. Üretilen rastgele sayılar daha sonra NIST testine tabi tutulmuştur. Sonuçlar, PCG tarafından üretilen rastgele sayıların ilgili istatistiksel testlerin çoğunu geçtiğini ve kriptografi için gerekli rastgelelik standartlarına uygun olduğunu göstermektedir. Sonuç olarak, PCG algoritmasının kriptografi ve rastgele sayı gerektiren diğer uygulamalar için sağlam, güvenilir ve uygun bir rastgele sayı üreteci olduğu gösterilmiştir.

Anahtar kelimeler: Rastgelelik, PCG, NIST, Güvenlik.

1. Introduction

Encryption refers to the process of converting plain text into a coded format that is unreadable to anyone except those who possess the decryption key [1]. This process utilizes mathematical algorithms to scramble the data, making it unreadable to anyone without the corresponding decryption key. Encryption is a crucial component of modern computer security and is employed in a variety of applications, such as online shopping, banking, and government communications [2]. Additionally, it is utilized to protect data in transit, such as when it is transmitted over the internet or through a network. In recent years, encryption has become increasingly important as an increasing amount of personal and sensitive information is stored and transmitted online. As a result, governments and organizations worldwide have implemented encryption policies to protect their data and communications [3].

There are various types of encryption, such as symmetric and asymmetric encryption. Symmetric encryption uses the same key for both encryption and decryption processes, while asymmetric encryption involves a public key for encryption and a private key for decryption. The effectiveness of an encryption system relies on the keys being genuinely random and distinct. Predictable or reused keys compromise the encryption's security [4].

Random numbers are crucial for generating encryption keys used in both symmetric and asymmetric encryption [5]. In symmetric encryption, a random key encrypts and decrypts data [6]. Predictable or reused keys weaken encryption [7]. Asymmetric encryption uses mathematically related public and private keys. The private key decrypts what the public key encrypts, ensuring security [8]. Random numbers also support digital signature and key agreement protocols by creating unique values for authentication [9].

* Corresponding author: zbmetin@firat.edu.tr. ORCID Number of authors: [1]0000-0003-4376-7319, [2]0000-0003-1292-8490

Random numbers are generated through a process known as random number generation [10]. There are several methods for generating random numbers, including pseudorandom number generation, hardware random number generation, True Random Number Generation, and Permuted Congruential Generators (PCG).

PCG is a family of random number generators that employs a combination of a linear congruential generator (LCG) and a permutation function to produce a sequence of high-quality random numbers [11]. LCG is a simple and efficient method for generating pseudorandom numbers. It utilizes a mathematical formula to generate a sequence of numbers based on an initial value (seed) and a set of parameters (multiplier, increment, and modulus) [12]. However, LCGs are known to have certain weaknesses, such as poor statistical properties and a limited period of repetition. To overcome these limitations, PCG employs a permutation function to scramble the output of the LCG, creating a new sequence of numbers that possess superior statistical properties and an extended period of repetition. The permutation function can be a simple operation, such as a bitwise shift, or a more complex operation, such as a cryptographic hash function. PCG also incorporates a feature called "streams" which allows for the generation of multiple independent sequences of random numbers from the same seed without interference. This can be useful in applications requiring multiple random numbers, such as the generation of random keys for encryption or the simulation of random events in a computer game [13]. One of the key advantages of PCG over other random number generators is its ability to produce high-quality random numbers that pass various statistical tests and have a long period of repetition [14]. Additionally, it has a small memory footprint, making it suitable for embedded systems and other resource-constrained environments.

The NIST is applied to numbers produced by PCG as it is a widely accepted set of statistical tests for evaluating the randomness and quality of random numbers. The NIST is designed to assess the suitability of a random number generator for cryptographic purposes the statistical properties of the numbers generated by the generator [14]. The NIST includes a variety of tests that cover different aspects of random number generation, such as tests for uniformity, independence, and patterns in the numbers. These tests are designed to detect any biases or weaknesses in the random number generator that could potentially be exploited by an attacker [15]. By applying the NIST to numbers generated by PCG, it is possible to obtain a quantitative measure of the quality of the random numbers produced by the generator. The results of the tests can be used to determine if the numbers produced by PCG meet the standards for cryptographic use and to identify any potential weaknesses or biases that need to be addressed.

In this study, we analyze the random numbers generated by the PCG algorithm to determine how many of the NIST statistical tests they pass and to what extent they meet the randomness standards required for cryptographic applications. To achieve this, 100 random bit strings, each consisting of one million bits, were generated using the PCG method. In order to apply the NIST test to these generated bit strings, a method based on changing the stream values has been proposed.

The main cont are as follows:

- The examination of the application of the NIST to numbers generated by PCG, a widely-used random number generator.
- The proposal of a method for applying the NIST test to bit strings generated by the PCG method by changing the stream values.
- The assessment of the quality of random numbers generated by the PCG method through the application of the NIST and the identification of any potential biases or weaknesses in the generator.
- The demonstration of the suitability of PCG for cryptographic purposes based on the results of the NIST.

2. Materials and Methods

In this study, the seed and stream values of the PCG algorithm are defined as parameters and 32-bit coins and rolls are produced in the output. In the binary conversion process, ‘T’ variables are assigned a value of 0 and ‘H’ variables are assigned a value of 1. As a result of this binary conversion process, random numbers are obtained. The proposed method is illustrated in a block diagram representation in Figure 1.

2.1. The Proposed Method

The proposed method generates a single-bit random number each time it is executed. In this study, we obtained a series of 100 one million-bit random numbers. The algorithm steps used to achieve this are as follows:

1. Define the PCG function with seed=42 and stream=21 values. (This choice was made because we obtained the most successful results as a result of trying all possible combinations.)

2. Generate one million random numbers with the specified parameters.
3. After each one million random numbers are generated, change the stream value.
4. Repeat Step 2 (100 times).

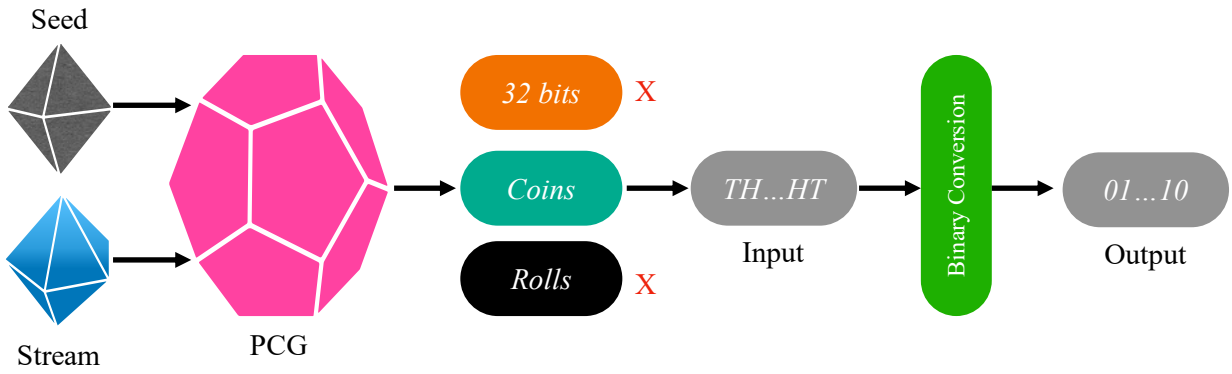

Figure 1. Block diagram of the recommended method.

2.2. Evaluating Randomness

Random and pseudo-random numbers are necessary for many cryptographic applications. Before using random numbers as inputs in various cryptographic protocols, it is important to verify that they conform to the definition of randomness. The NIST family of tests, developed by the US National Institute of Standards and Technology, is commonly used to evaluate the reliability of random number generators. NIST SP 800-22 includes 15 individual tests [16]. In this study, the NIST statistical test suite was used to assess the randomness of 100 one-million-bit random number sequences generated using the PCG algorithm. The NIST statistical test suite includes 15 different tests, as described below [17].

- The frequency test is a method for measuring whether the number of occurrences of the values 0 and 1 in a sequence are approximately equal, which is an expected characteristic in a real random number generator. The values 0 and 1 in the bit string should be relatively close to one another. If the value generated using the test equations, p, is greater than 0.01, the sequence is considered to be random.
- The block frequency test evaluates the proportion of 0s and 1s within blocks of m bits in a sequence. It focuses on observing the frequency of 1s in each block of m bits.
- The runs test analyzes the total number of runs in a sequence, where a run is a continuous series of the same bit. This test assesses the transitions between 0s and 1s to determine if the bit sequence changes states too slowly or too quickly.
- The longest runs of ones test focuses on observing the longest consecutive sequence of 1s in a string. The only parameter of the test is the block length (m). The array is divided into n blocks of m bits and the longest sequence of 1s in each block is checked. The frequencies of the obtained values are compared to expected values and a deviation is checked for. The block length and the number of blocks are decided by considering the length of the array.
- The rank test assesses the ranks of smaller submatrices extracted from the entire sequence. The objective of this test is to determine if there is any linear dependence among the subsequences of the original sequence.In the test, the sequence is split into M x M-bit matrices and the rank of each generated matrix is calculated. The frequencies of the ranks of the matrices formed in order are calculated, compared to the expected frequency and checked for a significant deviation.
- The discrete Fourier transform test is used to test whether there is any dominant harmonic in the sequence that would prevent randomness. It identifies periodic patterns in the sequence that differ from what would be expected in a truly random sequence.

- The overlapping template of all ones test is based on observing the frequency of occurrence of a predefined target sequence. An m-bit window is used to search for an m-bit sample. If the searched sample is not found, scanning continues by shifting the window one bit.
- Maurer's Universal Statistical Test checks whether the given array is sufficiently compressed. Excessive compression of the array indicates that the array is far from random.
- The non-overlapping template matching test is employed to detect non-periodic samples generated by a generator. In this test, as well as in the subsequent Overlapping Pattern Matching Test, an m-bit window is utilized to search for an m-bit sample. If the sample is not found, the window is shifted by one bit and the search continues. In the event that the sample is located, the window is repositioned to the first bit following the identified sample and the search continues.
- The serial test centers on the frequency of potential m-bit overlapping samples in the entire array.
- The approximate entropy test, similar to the Serial Test, focuses on the occurrence frequency of possible m-bit overlapping patterns within the sequence. This test aims to compare the observed frequency of overlapping blocks of two consecutive lengths with the expected frequency in a truly random sequence.
- The cumulative sum test aims to determine whether the cumulative sums of partial subsequences in the tested sequence are disproportionately small or large in comparison to the expected value of a known random sequence. This test can be considered as a cumulative total random walk, with random walk excursions in random sequences typically around zero.
- The random excursions test focuses on the number of precisely K visit cycles in the cumulative total random walk. The cumulative sum is obtained from the partial sums of the random walk, after arranging the sequence of (0,1) as (-1, +1). A random walk cycle consists of a sequence of steps of a certain length, beginning at a location that is considered random, until it becomes a complete cycle. The purpose of this test is to determine the number of visits to a particular state resulting from the expected bias in the random sequence during this cycle.
- The random excursions variant test evaluates the frequency of specific states being visited during a cumulative random walk. The goal is to identify deviations in the number of visits to these states from what is expected in a typical random walk.
- The linear complexity test examines the complexity of the bit string by examining the length of the Linear Feedback Shift Register (LFRS). The test assesses whether the array is sufficiently complex for randomness. Arrays are considered Linear Feedback Shift Register (LFSR) outputs, and the array is deemed not complex enough to be random if the smallest LFSR capable of forming the array is small.

Statistical tests of randomness are commonly known as hypothesis tests. The results of the tests are concluded as successful or unsuccessful based on the acceptance or rejection of the hypothesis. In NIST tests, the hypothesis is typically set to α=0.01 [18]. It is desired that the calculated p-values for each statistical test are greater than the value of α.

3. Experimental Setup

In this study, 100 sequences of one million bits of random numbers were generated utilizing the PCG algorithm. Each of these sequences underwent NIST testing, with a significance level of α=0.01. The methodology employed for testing the random number generation method based on PCG is depicted in Figure 2.

The NIST statistical test suite was chosen because it is a widely recognized standard for evaluating the randomness and quality of random number generators, especially in cryptographic contexts. The 15 tests it includes assess various statistical properties of randomness, such as uniformity, independence, and the absence of patterns. These properties are crucial for cryptographic applications, where predictable patterns could lead to vulnerabilities. By using the NIST suite, we ensure a comprehensive evaluation that addresses both short-term randomness and long-term unpredictability.

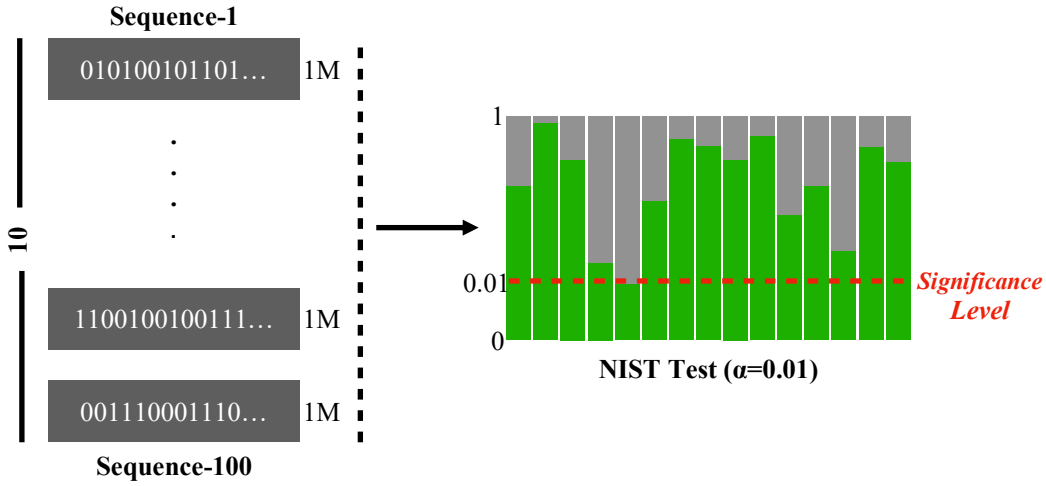

Figure 2. The testing structure utilized in the study.

3.1. NIST Results

In the NIST test, the p-value is used to express the likelihood of a hypothesis being true. In the context of hypothesis testing, the p-value is a numerical value between 0 and 1, and its magnitude is crucial in determining the validity of the hypothesis [19]. In this study, 100 random number sequences of 1 million bits were generated using the PCG algorithm, and each of these sequences underwent NIST testing. The significance level was set at α=0.01. The p-values obtained from each test are presented in Table 1, for samples randomly selected from the 1-million-bit random number sequences.

Table 1. Results from NIST tests on random numbers generated.

Test	Sequence-1 (P)	Sequence-2 (P)	Sequence-3 (P)	Sequence-4 (P)	Sequence-5 (P)
Frequency	0.525815	0.025124	0.487777	0.158261	0.618781
Block Frequency	0.378385	0.848552	0.132612	0.748528	0.237045
Runs	0.278555	0.572323	0.653277	0.234722	0.372731
Longest Runs Of Ones	0.311016	0.575607	0.532123	0.658764	0.142112
Rank	0.348308	0.402712	0.548777	0.570032	0.6401218
Dft	0.281435	0.445888	0.225511	0.488345	0.220654
Overlapping Template Of All Ones	0.126013	0.606571	0.165242	0.524711	0.207075
Universal Statistical	0.727131	0.167532	0.473012	0.513728	0.725812
Non Overlapping Template Matching	0.286852	0.005787	0.121352	0.116552	0.003462
Serial	0.464433	0.224327	0.351381	0.575431	0.721515
Approximate Entropy	0.6165204	0.232114	0.833664	0.428243	0.161452
Cumulative Sums	0.8202184	0.018425	0.862662	0.077256	0.583116
Random Excursions	0.226583	0.122675	0.113715	0.124321	0.235313
Random Excursions Variant	0.446532	0.382112	0.275228	0.105312	0.318621
Linear Complexity	0.286852	0.135210	0.253642	0.751383	0.613712

The NIST test results of 100 1 million-bit random numbers generated with the PCG algorithm indicate that the numbers are highly random and suitable for cryptographic use. The results demonstrate that the numbers pass most of the statistical tests in the NIST suite, which include tests for randomness, uniformity, and independence. The p-values for many tests were well above the commonly used significance level of 0.01, indicating that the numbers are highly unlikely to be non-random. Overall, these results indicate that the PCG algorithm is a reliable and efficient method for generating high-quality random numbers for cryptographic applications. The performance

of the generated 100 random number sequences of 1 million for each test in the NIST suite is presented in Figure 3. In Figure 3, those indicated in gray represent the random number sequences that passed the test, while those in red represent the sequences of numbers that failed the test.

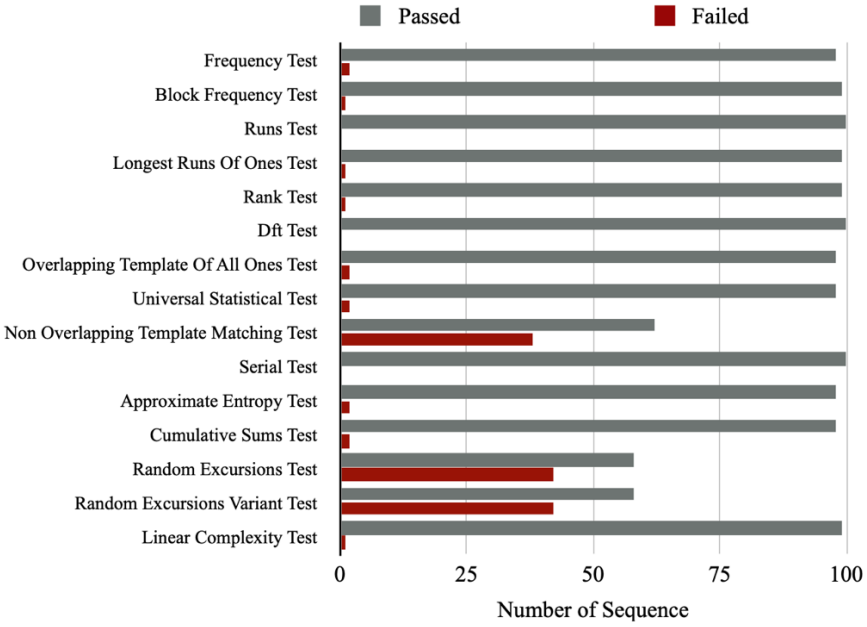

Figure 3. Performance of the nist tests on 100 million random numbers.

4. Discussion

The evaluation of random number sequences generated by the PCG algorithm using the NIST test suite revealed an overall success rate of 90.94%. However, three tests—the Non-Overlapping Template Matching Test, Random Excursions Test, and Random Excursions Variant Test—showed noticeably weaker performance. These failures could be linked to specific characteristics of the PCG algorithm, such as its structure or periodicity, which may not align well with the statistical patterns these tests are designed to detect.

The Non-Overlapping Template Matching Test, which looks for specific bit patterns within the sequence, highlighted potential limitations in the algorithm's bit generation process. This failure could indicate that the PCG algorithm occasionally produces predictable patterns, which may be detrimental in applications requiring high levels of randomness, such as cryptography. Similarly, the Random Excursions and Random Excursions Variant Tests, which analyze the number of state visits within a random walk, exposed possible deficiencies in long-range dependencies or correlations in the sequences generated by PCG. This suggests that while the algorithm performs well in the short term, it may exhibit periodic behavior or correlations over longer sequences, which is undesirable for cryptographic applications where long-term unpredictability is essential.

While 30 out of the 100 sequences passed all 15 NIST tests, the failures in these specific tests raise important questions about the algorithm's suitability for cryptographic purposes. For cryptography, the randomness quality must be exceptionally high to avoid vulnerabilities. These results suggest that the PCG algorithm, in its current form, may not yet provide the level of randomness required for secure cryptographic applications without further refinement. The PCG algorithm demonstrates several advantages, such as efficiency and good performance in the majority of other statistical tests. These benefits indicate that with targeted improvements, it may still be a viable candidate for cryptographic use. Future work will focus on addressing the identified weaknesses, particularly in relation to the failed tests, and further investigating the security implications. Additionally, we plan to support the analysis with alternative test suites, such as TestU01, to provide a broader evaluation of the algorithm's performance and ensure its robustness for cryptographic applications.

5. Conclusion

This study presents an approach for generating 100 random numbers of 1 million bits using the PCG algorithm. The numbers were tested using the NIST, and the results indicate that the numbers with high p-values. While some test results were quite low, like Non-Overlapping Template Matching Test, Random Excursions Test and Random Excursions Variant Tests. However, 90.94% success rate was obtained on the NIST test of random numbers generated by the proposed method. This approach has several advantages over existing methods for generating random numbers. The PCG algorithm is relatively simple and easy to implement, yet it produces high-quality random numbers that are suitable for cryptographic applications. Furthermore, the PCG algorithm has a small memory footprint and can generate a large number of random numbers quickly. In conclusion, this approach can be a valuable tool for researchers and practitioners in fields that require high-quality random numbers, such as cryptography and computer simulations. The results of this study support the use of the PCG algorithm for generating random numbers and provide a solid foundation for further research in this area.

Acknowledgments

This work was supported in part by Fırat University Scientific Research Projects Coordination Unit with project number TEKF.24.27 and. The Scientific and Technological Research Council of Turkey under Grant 121E600 and 122E337.

References

[1] Akashi N, Nakajima K, Shibayama M, Kuniyoshi Y. A mechanical true random number generator. New J Phys 2022; 24(1): 249-252.
[2] Basharat I, Azam F, Muzaffar AW. Database security and encryption: A survey study. Int J Comput Appl 2012; 47(12): 28-34.
[3] Bouillaguet C, Martinez F, Sauvage J. Practical seed-recovery for the PCG pseudo-random number generator. IACR Trans Symmetric Cryptol 2020; 2020(3): 175-196.
[4] Dong L, Chen K. Cryptographic protocol. Security analysis based on trusted freshness. Springer, 2012.
[5] Johnston D. Random number generators—principles and practices. In Random Number Generators—Principles and Practices. De Gruyter Press, 2018.
[6] Kohlbrenner P, Gaj K. An embedded true random number generator for FPGAs. Proc ACM SIGDA Int Symp Field Program Gate Arrays 2004; 71–78.
[7] Naik RB, Singh U. A review on applications of chaotic maps in pseudo-random number generators and encryption. Ann Data Sci 2022; 1-26.
[8] O'Neill ME. PCG: A family of simple fast space-efficient statistically good algorithms for random number generation. ACM Trans Math Softw, 2014.
[9] Paar C, Pelzl J. Understanding cryptography: a textbook for students and practitioners. Springer Sci Bus Media, 2009.
[10] Panda M. Performance analysis of encryption algorithms for security. In Proc Int Conf Signal Process Commun Power Embed Syst (SCOPES). IEEE, 2016; 278-284.
[11] Pareschi F, Rovatti R, Setti G. Second-level NIST randomness tests for improving test reliability. In Proc IEEE Int Symp Circuits Syst (ISCAS) 2007; 1437-1440.
[12] Patnala TR, Jayanthi D, Majji S, Valleti M, Kothapalli S, Karanam SR. A modernistic way for key generation for highly secure data transfer in ASIC design flow. In Proc Int Conf Adv Comput Commun Syst (ICACCS). IEEE, 2020; 892-897.
[13] Ponuma R, Amutha R. Compressive sensing based image compression-encryption using novel 1D-chaotic map. Multimed Tools Appl 2018; 77: 19209-19234.
[14] Sharma S, Gupta Y. Study on cryptography and techniques. Int J Sci Res Comput Sci Eng Inf Technol 2017; 2(1): 249–252.
[15] Soto J. Statistical testing of random number generators. In Proc Natl Inf Syst Secur Conf 1999; 12.
[16] Thambiraja E, Ramesh G, Umarani DR. A survey on various most common encryption techniques. Int J Adv Res Comput Sci Softw Eng 2012; 2(7).
[17] Zaman JKMS, Ghosh R. Review on fifteen statistical tests proposed by NIST. J Theor Phys Cryptogr 2012; 1: 18-31.
[18] Zaru A, Khan M. General summary of cryptography. J Eng Res Appl 2018; 8(02): 68-71.
[19] Zhu S, Ma Y, Lin J, Zhuang J, Jing J. More powerful and reliable second-level statistical randomness tests for NIST SP 800-22. In Adv Cryptol – ASIACRYPT. Springer 2016; 307-329.

Turkish Journal of Science & Technology
20(1), 63-76, 2025

Research Paper
https://doi.org/10.55525/tjst.1571845

A Novel Car Interior Sound Classification Method based on Multileveled Local Binary Four Patterns and Iterative ReliefF

Erhan AKBAL[1*], Sengul DOGAN[2], Turker TUNCER[3]
[1,2,3] Department of Digital Forensics Engineering, Technology Faculty, Firat University, Elazig, Turkey

[*1] erhanakbal@firat.edu.tr, [2] sdogan@firat.edu.tr, [3] turkertuncer@firat.edu.tr

(Geliş/Received: 22/10/2024; Kabul/Accepted: 23/12/2024)

Abstract: Sound classification is one of the crucial study areas in machine learning and sound forensics. However, there are limited studies on sound forensics or sound-based crime investigations in the digital forensics literature. In this work, a novel area of sound forensics is presented: car interior sound classification (CISC). The main aim of CISC is to identify a car using its interior environmental sound. A car interior sound dataset was collected using 10 car models. This CISC model includes feature generation using the local binary four pattern and one-dimensional multilevel discrete wavelet transform (DWT), iterative ReliefF-based feature selection, and classification. k-nearest neighbors (kNN) and support vector machine (SVM) were utilized as classifiers to demonstrate the general success of the proposed learning model for CISC. The accuracy rates were calculated as 93.72% ± 0.37 and 95.04% ± 0.30 with kNN and SVM, respectively. These results demonstrate the success of the proposed method.

Key words: Car interior sound classification, Iterative ReliefF, Local Binary Four Pattern, Environmental sound classification, Sound forensics Analysis, Cyber Crime.

Çok Seviyeli Yerel İkili Dört Desenler ve İteratif ReliefF Tabanlı Yeni Bir Araç İçi Ses Sınıflandırma Yöntemi

Öz: Ses sınıflandırması, makine öğrenimi ve ses adli bilişiminde önemli çalışma alanlarından biridir. Ancak, dijital adli bilişim literatüründe ses adli bilişimi veya ses tabanlı suç soruşturmaları üzerine sınırlı sayıda çalışma bulunmaktadır. Bu çalışmada, ses adli bilişiminde yeni bir alan sunulmaktadır: araç içi ses sınıflandırması (CISC). CISC'nin temel amacı, araçların iç ortam seslerini kullanarak tanımlanmasıdır. Bu amaçla, 10 farklı araç modeli kullanılarak bir araç içi ses veri seti oluşturulmuştur. CISC modeli, yerel ikili dört desen ve tek boyutlu çok seviyeli ayrık dalgacık dönüşümü (DWT) ile özellik çıkarımını, iteratif ReliefF tabanlı özellik seçimini ve sınıflandırmayı içermektedir. Modelin genel başarısını göstermek için k-en yakın komşu (kNN) ve destek vektör makinesi (SVM) sınıflandırıcıları kullanılmıştır. kNN ve SVM ile elde edilen doğruluk oranları sırasıyla %93,72 ± 0,37 ve %95,04 ± 0,30 olarak hesaplanmıştır. Bu sonuçlar, önerilen yöntemin başarısını ortaya koymaktadır.

Anahtar kelimeler: Araba iç ses sınıflandırması, döngüsel rölyef, yerel ikili dört desen, çevresel ses sınıflandırması, ses adli bilişimi analizi, siber suç.

1. Introduction

In recent years, many environmental sound classification (ESC) methods have been presented for signal processing and digital forensics. There are many studies in the literature for determining environmental sounds. Studies generally cover topics such as environment monitoring [1, 2], health applications [3], diagnostic systems [4-8], environment recognition [9], cyber security [10, 11], fault detection [12, 13] and different ambient sounds [14, 15]. Generally, common studies are in the field of ESC [16-20]. In digital forensics, many sound data are obtained from the digital storage device [10, 21, 22]. The sounds are listened by the examiner for a detailed understanding of the sounds obtained. The frequency values that the human ear can hear are limited. Human auditory system cannot detect some evidence in sound format [23]. While law enforcement officers follow criminals, they usually use ways such as listening to the environment and listening to the phone. Obtaining information such as the location and environment of the criminal from a sound data can provide great convenience in terms of following the suspect. For instance, when there is no information about the suspect, law enforcement officers have difficulties following up [24]. Follow-up can be made easier with the predict of the crime scene.

* Corresponding author: erhanakbal@firat.edu.tr. ORCID Number of authors: [1] 0000-0002-5257-7560, [2] 0000-0001-9677-5684, [3] 0000-0002-5126-6445

Automatic sound classification methods aim to achieve fast results by minimizing human errors. Thus, at the moment of the incident, fast and error-free information about the crime is obtained [25, 26].

There are many classification studies in the literature using local binary pattern. Some of them are given as follows. Güner et al. [27] showed that LBP can be used to classification of different modulation types. Gupta et al. [28] used an optimized binary pattern algorithm to classify white blood cells. Hu et al. [29] demonstrated the performance of LBP for the classification of pump vibrations for IoT systems.

Classification of environmental sounds is a subject of signal processing [30, 31]. Many different methods have been used in signal processing, such as deep learning, machine learning, and artificial neural networks [32-37]. The aim of all studies is to present high accurate sound classification method for sound signals [38]. There are different studies in the literature on sound classification/detection using artificial intelligence methods and some of these are; Fan et al. [39] proposed a model for classification different environmental sounds for use in hearing aids. It is aimed to automatically classification 5 different environmental sounds (bus, subway, street, indoor and car) using deep neural networks. They proposed algorithm has achieved a classification rate of 98.8%. Jaber et al. [40] suggested a classification algorithm for disease detection using lung sounds. Random Forest, AdaBoost, Gradient Boosting algorithms are used. The dataset consists of 5 classes and 99.04% accuracy classification rate is shown. Shen et al. [41] proposed a system for classification of sound events obtained from real environments. The proposed system uses Gaussian mixture models and Mel-Frequency Cepstral Coefficients (MFCCs). Accuracy rate was calculated as 91.36% for 8 classes. Saki and Kehtarnavaz [42] proposed a method for real-time classification of sound signals obtained from hearing aids. The three-level model is intended to distinguish music, speech and noise. With their model, it was demonstrated that traditional classification models could be reached high accuracies. Abdoli et al. [16] presented a classification model based on 1D Convolution Neural Network (CNN). Their model resulted 89% accuracy on UrbanSound8k dataset [43]. Medhat et al. [44] applied the deep CNN method of the spectrograms of the used sound signals. Masked ConditionaL Neural Network (MCLNN) model was applied on ESC-10 and ESC-50 datasets [22]. Chen et al. [45] emphasized that the CNN model used in ESC caused information loss during pooling. In their study, a model to eliminate data loss during pooling was presented. Souli et al. [46] presented an approach to the classification of environmental sounds. Scatter transform and principal component analysis (PCA) were used to extract the feature vectors of the sound signals. It achieved 92.22% classification performance using SVM classifier. López-Pacheco et al. [47] suggested a method for classification of urban sounds. Orthogonal Matching Pursuit (OMP) algorithm was used as a feature generation method. The results obtained showed that it was successful in determining the dominant sounds in urban dataset. Tuncer et al. [48] presented a model for disease detection in sound signals. Their model consisted of feature extraction with 1D-LBPNet, informative feature selection with NCA and classification using 1NN. Sounds were classified with an accuracy of 98.83%. AlQahtani [49] presented a model to facilitate forensic investigations. Experimental studies showing the problems of sound recognition environments about the model were presented. The K-Nearest Neighbors classifier was utilized as classifier. Muhammad and Alghathbar [10] presented an experimental study on sound media detection in digital forensics. MFCCs algorithm was employed as feature generator. In addition, MPEG-7 audio dataset was proposed. Their dataset contained 10 classes and they reached to 75% from 90% classification accuracies.

1.1. Motivation of this work

In this paper, our main aims are to define a sub-branch of ESC and develop a novel sound forensics method. Therefore, we used car interior sounds, and a novel CISC method is presented. We collected a sound dataset, which contains 700 sounds with 10 classes. To accurately classify this dataset, a novel learning model is presented in this work.

1.2. Our Method

In this study, a novel CISC method is proposed using sounds obtained from the 10 most commonly used C-class cars in the world market. This dataset contains 10 different car models, and each class has 70 sound signals, totaling 700 sounds. Our method is multileveled and includes multileveled feature generation with LBFP, iterative feature selection with ReliefF, and classification phases. Our fundamental goals are outlined as follows. We used a 7-level one-dimensional discrete wavelet transform to generate low, medium, and high-level features. LBFP uses four variable patterns to comprehensively generate features, with 544 features extracted at each level. A total of 544 x 8 = 4352 features are generated (LBFP is applied to the raw sound signal and 7 low-pass filters of it). The most valuable features are selected using IRF, and the selected features are then forwarded to classifiers.

1.3. Contributions

Our contributions are given as below.

- In this paper, we define a novel ESC-like study area, which can be considered a sub-branch of ESC. The study area we present is car interior sound classification (CISC). CISC is directly dependent on the automotive industry, digital forensics, signal processing, and machine learning. To propose a novel model for CISC, we collected a car interior sounds (CIS) dataset.
- A novel multileveled feature generation method is presented using a new feature generation approach. The proposed LBFP uses four variable patterns to comprehensively extract features from CIS. ReliefF faces an optimal feature selection problem; therefore, iterative ReliefF is introduced to choose the optimal number of features. SVM and kNN were utilized as classifiers. The proposed LBFP and IRF-based method achieved high success rates using conventional classifiers. This demonstrates the discriminative strength of the LBFP and IRF-based feature extraction and selection processes. A classification accuracy of 95.86% was achieved using this method for CISC.

2. Materials

We curated CIS from YouTube point-of-view (PoV) drive videos [50]. Road conditions are given as follows. The sounds of these cars were collected on dry and asphalt roads. We selected 10 widely preferred car models, and the acoustics of these cars were recorded using the Windows audio recorder in m4a format. These sounds were segmented into 3–5-second frames, and their frequency is 48 KHz. The segmentation of the sounds into 3–5-second frames was deliberately chosen to balance the need to capture meaningful audio information. Variations in segment length accommodate differences in the acoustic events captured in each recording. For example, longer segments can include transitions or continuous sounds necessary for context, while shorter segments ensure that isolated or discrete sounds are not lost in the analysis. The interval also aligns with the duration of steady-state in-car sounds under consistent conditions (e.g., driving on a paved road). This approach minimizes the risk of introducing noise or losing important details due to excessively short or excessively long segments. By defining a flexible yet controlled segmentation interval, the dataset is designed to maintain high quality for feature extraction and classification of the in-car sound environment. Additionally, this approach helps create a balanced dataset. In some cars, the collected interior sounds are longer than in others. Therefore, sound segments of varying lengths were used.

The attributes of the collected CIS dataset are listed in Table 1. These cars use petrol (gasoline) engines and manual transmissions.

Table 1. Attributes of the collected CIS dataset.

No	Model	Observation	No	Model	Observation
1	Clio 4 - 2018	70	6	Meganne 4 - 2018	70
2	Fiat Egea 1.4 - 2018	70	7	Passat B8 - 2018	70
3	Ford Focus Mk4- 2018	70	8	Peugeot 308 - 2019	70
4	Golf VII - 2019	70	9	Skoda Octavia - 2019	70
5	Honda Civic - 2018	70	10	Toyota Corolla XI - 2018	70

As seen in Table 1, the collected CIS dataset has 700 sounds. This dataset named as CISC10. The graphical demonstration of the samples of the CISC10 is shown in Figure 1.

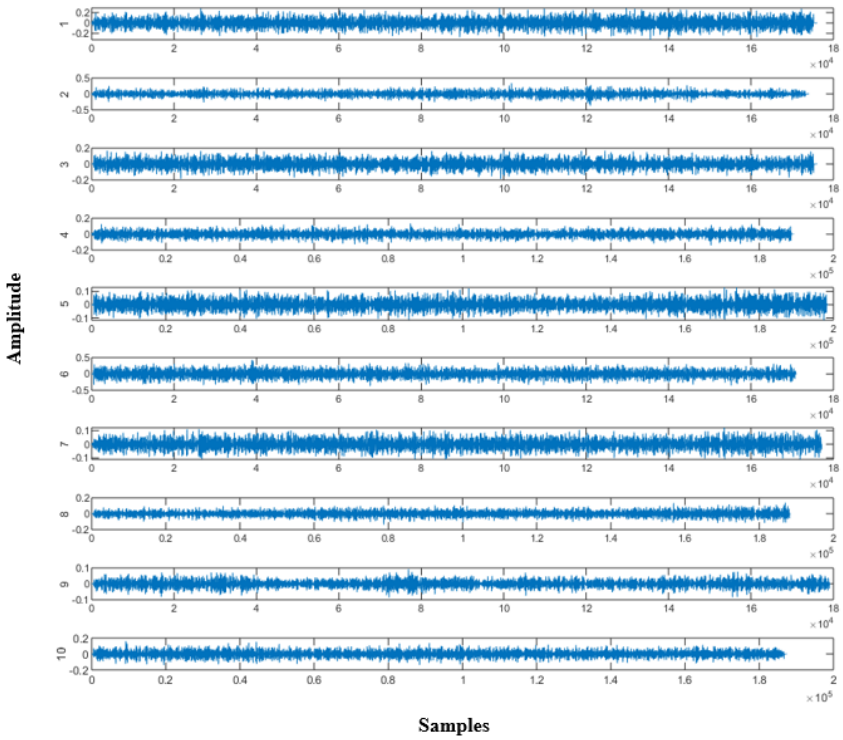

Figure 1. Graphical demonstration of the samples of CISC10 dataset according to classes.

3. The proposed CISC model

A novel learning model is presented in this paper. Our model uses the proposed LBFP for feature generation, IRF to select meaningful features and SVM [51], kNN [52, 53] for classification. The used feature generation phase is multileveled. In order to achieve, low, medium and high features should be generated. Therefore, we used one dimensional multilevel DWT [54] for decomposition. Multileveled DWT is applied on CIS and seven low pass coefficients are obtained. LBFP extracts 544 features from each low pass coefficients and raw CIS. These features are concatenated and 4352 features are generated. IRF selects 693 most valuable from the generated 4352 features. These 693 features are utilized as input of the kNN and SVM classifiers and predictive results are calculated. The proposed LBFP and IRCA based CISC method is summarized as Figure 2.

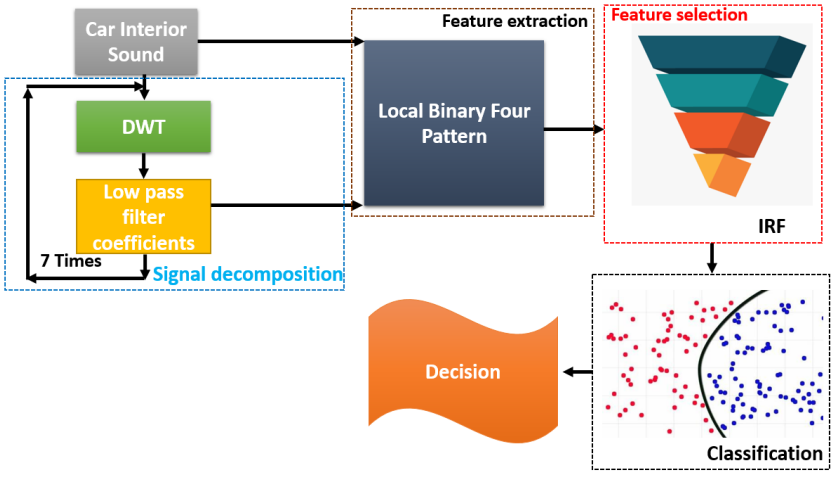

Figure 2. Demonstration of the block diagram of our proposed CISC method.

The used phases and steps of the proposed method are explained in subsections.

3.1. The proposed LBFP based multileveled feature generation

Our first phase is LBFP based multileveled feature generation. In this phase, multilevel DWT decomposition [55, 56], feature extraction with LBFP and feature concatenation processes are used. Details of LBFP also in this section.

Step 0: Load CIS.
Step 1: Apply multilevel 1D-DWT on the loaded CIS. As it can be seen from Equations 1-2.

$$[low_1\ high_1] = dwt(CIS, sym4) \tag{1}$$

$$[low_{k+1}\ high_{k+1}] = dwt(low_k, sym4), k = \{1,2,\dots,6\} \tag{2}$$

where low_k and $high_k$ denote k[th] leveled low pass filter and high pass filter coefficients, $sym4$ represnets symlets 4 filter. This filter has been mostly preferred signal processing application for decomposition and noise reduction. Therefore, $sym4$ filter is chosen and this filter is one of the commonly used noise reduction wavelet filters. The selection of level 7 in DWT decomposition is aimed at obtaining the most optimal level of features and frequency content of in-car audio signals in accordance with the sound dimension. Higher decomposition levels effectively capture low-frequency, steady-state sounds specific to vehicle interiors by separating frequency components in greater detail. At level 7, the approximation coefficients retain sufficient detail to represent these low-frequency components while discarding irrelevant high-frequency noise. Although detail coefficients are widely used in signal classification and feature engineering, in this study, the approximation coefficients are utilized to focus on the salient acoustic features critical for in-car audio classification. This selection also minimizes noise originating from the nature of the signal. Furthermore, experiments have demonstrated that the level 7 approximation coefficients combined with the proposed LBFP method provide the highest classification performance among various parameter configurations.

Step 2: Extract 544 features from CIS and low pass filter coefficients by using LBFP.

$$feat^1 = LBFP(CIS) \tag{3}$$

$$feat^t = LBFP(low_{t-1}), t = \{2,3,\dots,8\} \tag{4}$$

$feat^t$ is t[th] feature vector.

As it can be seen Equations 3-4, the fundamental function of the feature generation is LBFP. LBFP is a LBP like feature extractor. It uses four variable patterns and these patterns extract 256, 256, 32 and 32 features respectively. Finally, these features are fussed and 544 features are obtained. LBFP procedure is explained in below steps.

Step 2.1: Divide CIS into 9 sized overlapping windows. As it can be seen from Equation 5.

$$window^h = CIS(i: i+8), i = \{1,2,\dots,L\}, h = \{1,2,\dots,L-8\} \tag{5}$$

where $window^h$ h[th] 9 sized overlapping windows, L represents length of the CIS.

Step 2.2: Generate binary features using signum function and the defined 4 patterns. The used patterns are shown in Figure 3.

These patterns (See Figure 2) are used to generate features with signum function. Equation of signum function is shown in Equation 6.

$$sgnm(P_N, P_C) = \begin{cases} 0, P_N - P_C < 0 \\ 1, Otherwise \end{cases} \tag{6}$$

where $sgnm(.,.)$ is signum function, P_N and P_C denote first and second parameters of the signum function respectively. Explanation of the bit generation procedure of the proposed LBFP is shown in Equations 7-10.

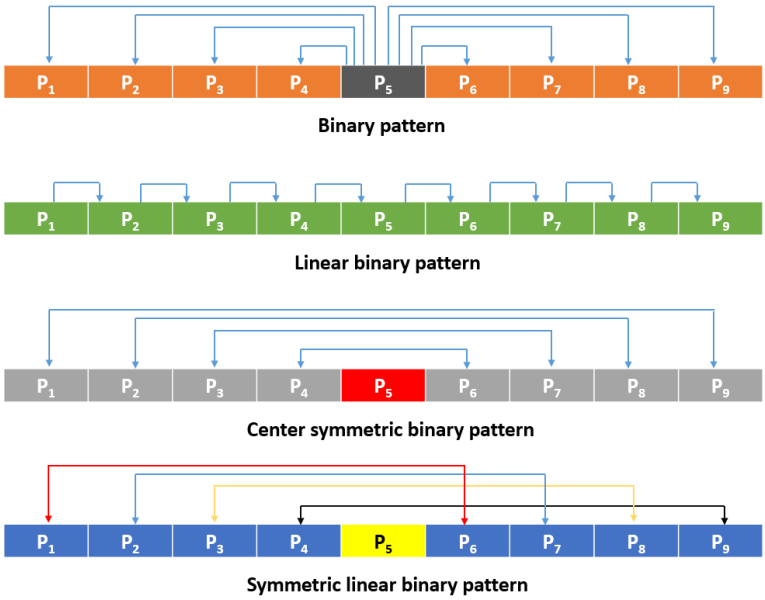

Figure 3. The used patterns in the proposed LBFP.

$$bit^1(i) = sgnm\big(window(i), window(5)\big), i = \{1,2,\dots,9\}, i \notin \{5\} \quad (7)$$

$$bit^2(j) = sgnm\big(window(j), window(j+1)\big), i = \{1,2,\dots,8\} \quad (8)$$

$$bit^3(g) = sgnm\big(window(g), window(10-g)\big), g = \{1,2,3,4\} \quad (9)$$

$$bit^4(g) = sgnm\big(window(g), window(g+5)\big) \quad (10)$$

where bit^1, bit^2, bit^3 and bit^4 denote extracted bits with binary pattern (BP) [57], linear binary pattern (LiBP), center symmetric binary pattern (CSBP) and symmetric linear binary pattern (SLBP) respectively. i, j and g values represent index values. As it can be seen from Equations 7-10, BP, LiBP, CSBP and SLBP extracts 8, 8, 4 and 4 bits respectively.

Step 2.3: Construct four map values using the extracted bits and binary to decimal value conversion. As it can be seen from Equations 11-14.

$$mv^1(h) = \sum_{i=1}^{8} bit^1(i) * 2^{8-i} \quad (11)$$

$$mv^2(h) = \sum_{i=1}^{8} bit^2(i) * 2^{8-i} \quad (12)$$

$$mv^3(h) = \sum_{i=1}^{4} bit^3(i) * 2^{4-i} \quad (13)$$

$$mv^4(h) = \sum_{i=1}^{4} bit^4(i) * 2^{4-i} \quad (14)$$

where mv^k is kth map values.

Step 2.4: Generate histograms of the map values. In this step, four histograms are calculated. The length of these histograms are calculated as $2^8, 2^8, 2^4$ and 2^4 for BP, LiBP, CSBP and SLBP values respectively. Therefore, four

arrays with size of 256, 256, 16 and 16 are defined and initial values of them are assigned as 0. Histograms are generated by using Equations 15-17.

$$histo^t\left(mv^t(h)\right) = histo^t\left(mv^t(h)\right) + 1, t = \{1,2,\dots,4\} \quad (15)$$

where $histo^t$ defines histogram of t[th] map value.

Step 2.5: Concatenate the generated four histograms to obtain feature vector ($featvec$) with length of 544.

$$featvec = histo^1 \cup histo^2 \cup histo^3 \cup histo^4 \quad (16)$$

where ∪ denotes concatenation operator.

Step 3: Concatenate feature vector.

$$X = feat^1 \cup feat^1 \cup \dots \cup feat^8 \quad (17)$$

where X is concatenated feature vector with size of 4352.

Step 1-3 have been defined the recommended multilevel feature extraction method. This feature extraction method is designed to capture the distinct features of in-car sounds. The MDWT decomposes audio signals into multiple levels, enabling the extraction of frequency components while reducing the noise ratio at each level. As a result, features are obtained in both spatial and frequency domains. Additionally, DWT serves as both a preprocessing and a multilevel feature extraction function, creating a multilevel feature extraction method similar to deep learning approaches. In this phase, LBFP is employed as the main feature extractor.

The presented LBFP method is inspired by local binary patterns (LBP) and is specifically designed to extract robust and distinctive features. By utilizing four unique patterns—binary pattern (BP), linear binary pattern (LiBP), center-symmetric binary pattern (CSBP), and symmetric linear binary pattern (SLBP)—LBFP captures hidden patterns in overlapping signal windows. Each pattern provides a different perspective on the signal structure, enabling the extraction of nuanced, texture-like features from a 1D audio signal. For instance, BP captures local differences between sample points, while CSBP and SLBP extract more global and symmetric relationships.

The proposed method leverages the complementary strengths of both approaches by combining DWT with LBFP. DWT performs multi-resolution analysis, filtering out noise and focusing on meaningful frequency components, while LBFP extracts descriptive features from the processed signals. Experimental results demonstrate that integrating DWT and LBFP in this manner achieves optimal performance.

3.2. Iterative ReliefF feature selector

Relief [58] has been mostly used feature selector in the literature and improved version of the Relief is named as ReliefF. Both Relief and ReliefF [59] generates weights. Relief uses Euclidean distance-based fitness function but ReliefF uses Manhattan distance-based fitness function to calculate optimal weights of each features. In this work, ReliefF is selected as feature selector. The generated negative weighted features can be assigned as redundant feature. However, number of optimal features has been selected parametrically. To automatically select number of optimal features, iterative ReliefF (IRF) is chosen as feature selector. To calculate error values, we need a classifier. kNN is selected as error value calculator in this work. Steps of our IRF based feature selection are given as below.

Step 4: Apply IRF function to generated features (X) for selecting final features use Equation 18.

$$feat^S = IRF(X, y) \quad (18)$$

where $feat^S$ represents selected features, $IRF(.,.)$ defines the used supervised feature selection function and y denotes target.
Steps of the IRF function are;

Step 4.1: Apply ReliefF function to features (X) for calculation weights and sorted indices of the weights. Equation 19 showed below.

$$[weight\ index] = RF(X, y) \quad (19)$$

where RF is ReliefF function, $weight$ ReliefF weights and $index$ is sorted indices.

Step 4.2: Set lower and upper bounds for number of features. This step is applied to decrease time cost of the IRF. In this work, lower and upper bounds are selected as from 100 to 1100 respectively.

Step 4.3: Calculate error values iteratively used to Equations 20,21.

$$feature^{t-99}(i) = X\big(index(i)\big), t = \{100,101, \dots ,1100\}, i = \{1,2, \dots , t\} \quad (20)$$

$$error(t-99) = kNN(feature^{t-99}, y, 1, 10, MD) \quad (21)$$

The parameters of the kNN functions are given as follows. These are features, target, k value, cross validation parameter (10-fold CV is used), and distance metric (MD is manhattan distance).

Step 4.4: Calculate minimum error value and index of it with Equation 22.

$$[minimum, index^{min}] = min\ (error) \quad (22)$$

Step 4.5: Select optimal number of features by using index of minimum error ($index^{min}$) used Equation 23.

$$feat^{S}(i) = X\big(index(i)\big), i = \{1,2, \dots , index^{min} + 99\} \quad (23)$$

In this work, IRF selected 693 features. The plotting of the calculated error values with IRF is shown in Figure 4.

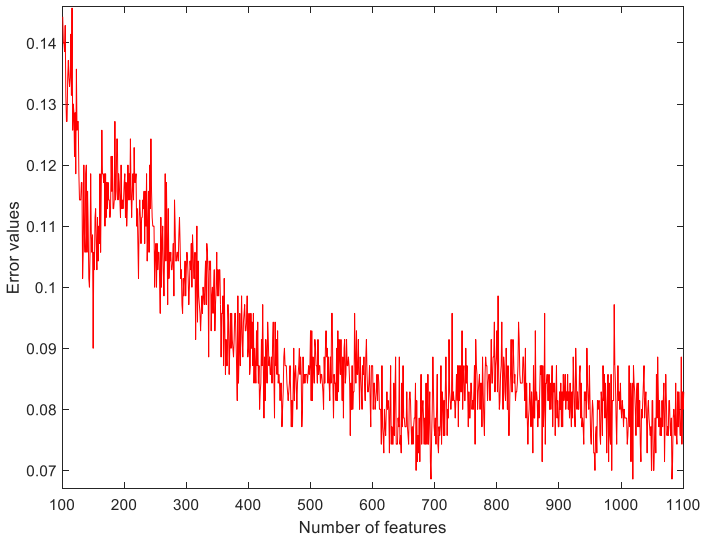

Figure 4. Error values of the IRF by using kNN classifier.

3.3. Classification

The classification phase is the final phase of the proposed method. The numerical performance metrics are calculated using classifiers. In this section, kNN and SVM classifiers are employed. The attributes of these classifiers are as follows: the kNN classifier used is the 1NN classifier, which uses the Manhattan distance for classification. The other classifier is SVM, which has various mathematical kernels. In this work, we used a second-degree polynomial kernel to obtain classification results. The constraint level (C) is set to 2, and the one-vs-all method is chosen for multiclass classification. 10-fold cross-validation (CV) is one of the most preferred training and testing strategies in the literature, and therefore, it is used to obtain the results.

Step 5: Classify selected 693 features with kNN or SVM classifiers with 10-fold CV.

4. Experimental results

Results were shown in this section. We used two classifiers to calculate numerical results. In the classification papers, F1-score ($F1$), geometric mean ($gmean$) and classification accuracy (CA) have been widely used to obtain numerical results of the used classifiers. To calculate these values, number of true positives (ntp), true negatives (ntn), false positives (nfp) and false negatives (nfn) values should be used. We implemented the proposed multileveled LBFP and IRF on a desktop computer by using MATLAB2018a programming environment. By using MATLAB Classification Learner Tool (MCLT), kNN and SVM were executed and we generated code of the used classifiers and $F1$, $gmean$ and CA codes were added these classifiers codes. Explanation of these evaluation criteria were given as Equations 24-26 [60].

$$F1 = \frac{2ntp}{2ntp + nfn + nfp} \tag{24}$$

$$gmean = \sqrt{\frac{ntp * ntn}{(ntp + nfn)(ntn * nfp)}} \tag{25}$$

$$CA = \frac{ntp + ntn}{ntp + ntn + nfp + nfs} \tag{26}$$

The calculated performance criteria for each classifier were listed in Table 2. To calculate general success rates (average value ± standard deviation of the value), test process of each classifier was executed 1000 times.

Table 2. F1-score (%), geometric mean (%) and accuracy scores of the used classifiers.

Classifier	Evaluation Type	F1-score	Geometric mean	Accuracy
kNN	General	93.90±0.36	93.57±0.39	93.72±0.37
	Maximum	94.75	94.47	94.57
SVM	General	95.10±0.29	94.96.10±0.30	95.04±0.30
	Maximum	95.92	95.80	95.86

Confusion matrices of the best results were shown in Figure 5.

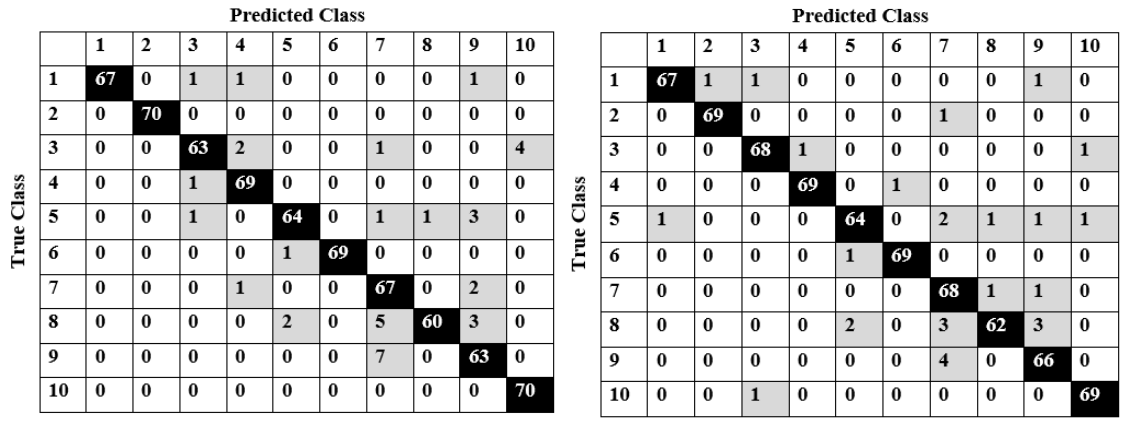

Figure 5. a) Confusion matrix of the best result of the kNN b) Confusion matrix of the best result of the SVM.

5. Discussions and conclusions

In this work, we presented a novel research area called CISC, which can be defined as a sub-branch of ESC. ESC is crucial for digital forensics, signal processing, and machine learning. The main aim of CISC is to identify a car using its cabin sound. To achieve this, we collected a novel CIS dataset. This dataset contains 700 sounds from 10 widely preferred car models. To demonstrate the feasibility of CISC, we introduced novel methods: the LBFP feature extractor and the IRF feature selector. Multilevel DWT and LBFP were used together to generate

low, medium, and high-level features. The most discriminative ones were selected using IRF, and the selected features were forwarded to kNN and SVM classifiers. Classification accuracies of 95.86% and 94.57% were achieved using SVM and kNN classifiers, respectively. The confusion matrices of the best results were also presented. As shown in these matrices, while the best result for kNN is lower than that of SVM, kNN achieved 100.0% classification accuracy for two classes. Other widely used performance criteria were also employed. The general success rates (%) of kNN were calculated as 93.90±0.36, 93.57±0.39, and 93.72±0.37 for F1-score, geometric mean, and accuracy, respectively. For SVM, the values were 95.10±0.29, 94.96±0.30, and 95.04±0.30 for F1-score, geometric mean, and accuracy, respectively. The statistical analysis of the results has been given Figure 6.

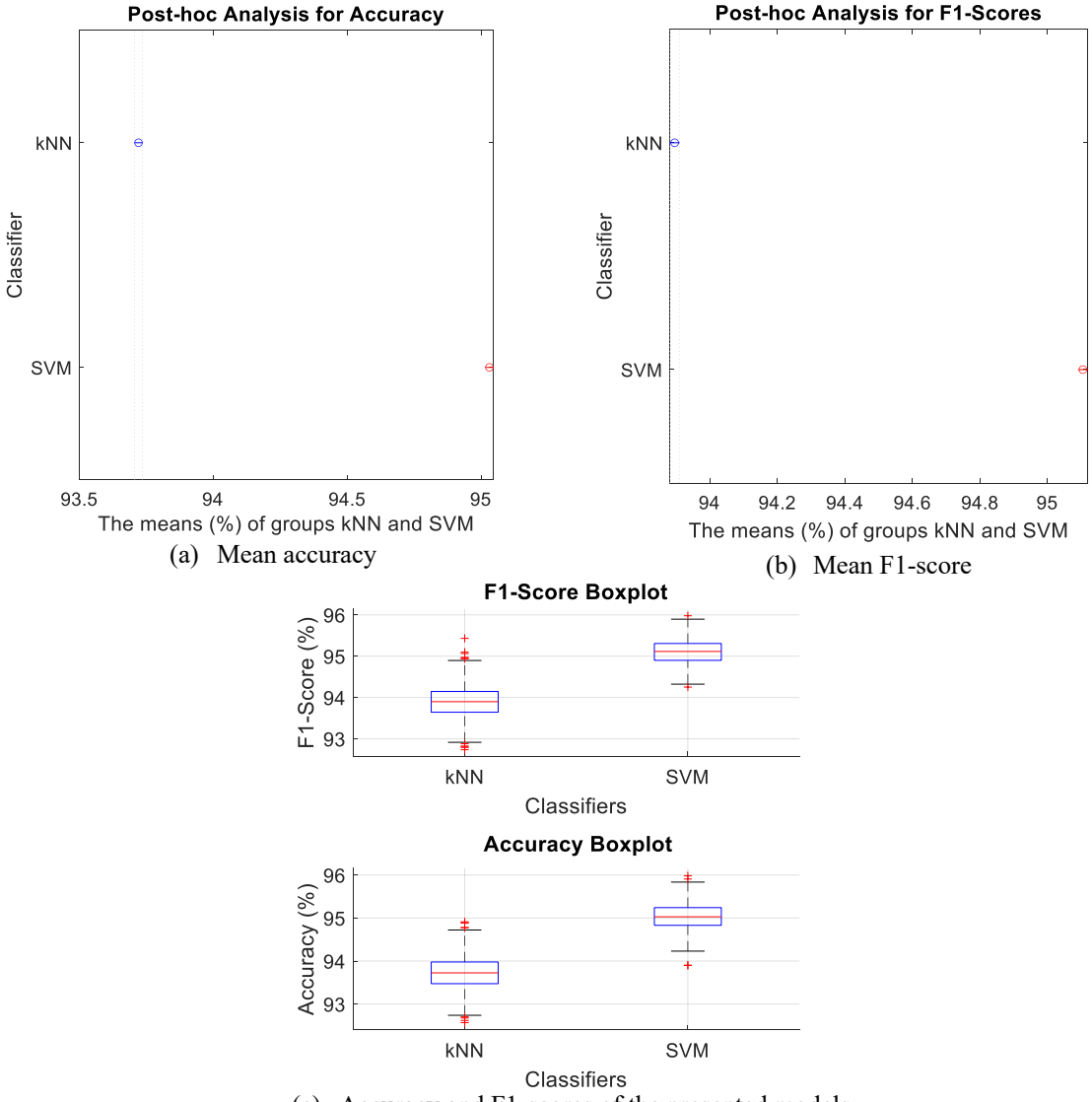

(a) Mean accuracy

(b) Mean F1-score

(c) Accuracy and F1-scores of the presented models

Figure 6. The statistical analysis of the computed classification accuracies and F1-scores.

The p-value for both F1-score and accuracy in the ANOVA test is 0.0003 (approximated to a very small value due to numerical precision limits). This indicates that the differences in the performance metrics between the kNN and SVM classifiers are significant.

To clearly demonstrate the success of the proposed LBFP and IRF-based sound classification method, comparative results are listed in Table 3.

Table 3. Comparison of the proposed classification method with other sound classification methods.

Method	Aim and Methods	Performance	Number of class
[27]	Automatic digital modulation classification using LBP	95%	6 classes
[39]	ESC for implementation on hearing aid app using deep neural network	98.8%	5 classes
[29]	Classification of pumps vibration and sounds using varying classifier and feature extractors	99.47%	3 classes
[40]	Lung sounds classification using ensemble classifier algorithms	99.04%	7 classes
[45]	ESC using dilated convolutions	78%	10 classes
[16]	ESC using 1D CNN	89%	10 classes
[46]	Audio sound classification for medical surveillance using SVM	92.22%	10 classes
[10]	Environment recognition for audio forensics using MFCCs	96%	4 classes
[6]	Acoustic-based fault diagnosis of roller bearings using a deep graph convolutional network	92%	4 classes
[12]	Termite detection system based on acoustic using various ML algorithms	93.83%	2 classes
[13]	Fault diagnosis of bearing and stator faults using acoustic signals using Nearest Neighbor, Nearest Mean classifier and GMM	95.3%	3 classes
Our Method	Car interior sound classification by using LBFP and IRF	95.92%	10 classes

As seen in Table 3, previously presented 10-class classification methods achieved classification accuracies of 78%, 89%, and 92.22%, respectively. In contrast, our method achieved a 95.92% success rate on a new dataset with 10 classes.

The key points of the recommended model are:

- The SVM classifier achieved higher general and maximum performance metrics compared to kNN. Specifically, SVM's maximum accuracy reached 95.86%, compared to 94.57% for kNN.
- Both classifiers show strong diagonal dominance in the confusion matrices (Figure 5), indicating accurate predictions for most classes.
- SVM showcases fewer misclassifications overall compared to kNN, particularly for classes with more complex patterns, such as classes 8 and 9.
- Certain classes, such as Class 10, achieved perfect classification accuracy in kNN (70/70 correct classifications). Similarly, SVM also yielded high precision for Class 10 but with a single misclassification.
- For challenging classes like Class 8, SVM showed better performance with fewer misclassifications (3 errors compared to 5 in kNN).
- The low standard deviations across multiple runs (±0.36 for kNN and ±0.29 for SVM in F1-score) indicate that both classifiers are robust and provide consistent results across multiple test iterations.
- The multilevel feature extraction and iterative feature selection contributed significantly to high classification performance. The integration of approximation coefficients from DWT and descriptive features from LBFP provides meaningful feature representation.
- While SVM performs better in terms of overall metrics and generalization, kNN demonstrated strong performance for certain classes, especially those with less variation in features, such as Classes 1, 6, and 10.
- For higher accuracy and robustness, SVM is preferable, whereas kNN may be sufficient for less computationally intensive tasks.
- The hierarchical extraction of features through DWT and LBFP significantly boosts the discriminative power of the classifiers.

- Misclassifications often occur between similar classes (e.g., Classes 5 and 6 or Classes 7 and 8), likely due to overlapping or less distinct features in these cases. Future work could focus on enhancing inter-class separability by incorporating additional feature extraction techniques or using ensemble models.

These results clearly demonstrate the general success of the proposed method and the feasibility of CISC. The benefits and novelties of the proposed LBFP and IRF-based CISC method are listed below.

- A novel sound classification area was defined.
- The feasibility of CISC was demonstrated using a novel learning model.
- A new one-dimensional feature extractor, called LBFP, was introduced.
- The optimal feature selection problem of ReliefF was solved using IRF.
- A highly accurate CISC method was proposed, and its success was demonstrated using two classifiers.

6. Future directions

Our proposals for future works are;

- People spend a significant amount of time in cars. Therefore, the car interior is crucial for digital forensics and crime investigation, as it can also be considered a crime scene. Consequently, many methods and datasets can be developed for CISC.
- LBFP is a one-dimensional feature extractor. By using LBFP, other signal-related problems can also be addressed.
- Other branches of sound forensics or ESC can be defined.
- Novel sound forensics tools and applications can be implemented using the proposed LBFP and INCA-based methods for crime investigators.
- In the near future, autonomous cars and vehicles will likely become common in traffic. These cars will be intelligent, and to authenticate them, novel intelligent CISC methods can be developed.

References

[1] Lou SC, Chao RM, Ko SH, Lin KM and Zhong JX. A simplified signal analysis algorithm for the development of a low cost underwater echo-sounder. Measurement 2011; 44(9):1572-1581.

[2] Liu S. Measurement and analysis of vibration and noise in the ambient environment of metro. Measurement 2020; 107998.

[3] Amarnath M, Sugumaran V and Kumar H. Exploiting sound signals for fault diagnosis of bearings using decision tree. Measurement 2013; 46(3):1250-1256.

[4] Lara R, Jimenez-Romero R, Perez-Hidalgo F and Redel-Macias M D. Influence of constructive parameters and power signals on sound quality and airborne noise radiated by inverter-fed induction motors. Measurement 2015; 73:503-514.

[5] Ye S, Zhang J, Xu B, Song W, and Zhu S. Experimental studies of the vibro-acoustic characteristics of an axial piston pump under run-up and steady-state operating conditions. Measurement 2019; 133: 522-531.

[6] Zhang D, Stewart E, Entezami M, Roberts C and Yu D. Intelligent acoustic-based fault diagnosis of roller bearings using a deep graph convolutional network. Measurement 2020; 156:107585.

[7] Xiang M, Zang J, Wang J, Wang H, Zhou C, Bi R and Xue C. Research of heart sound classification using two-dimensional features. Biomed Signal Proces 2023; 79:104190.

[8] Chen J, Guo Z, Xu X, Zhang L B, Teng Y, Chen Y and Wang W. A robust deep learning framework based on spectrograms for heart sound classification. IEEE/ACM Trans Comput Biol Bioinform 2023; 21(4): 936-947

[9] Petošić A, Djurek I, Suhanek M and Grubeša S. Interlaboratory comparisons' measurement uncertainty in the field of environmental noise. Measurement 2019; 148: 106932.

[10] Muhammad G and Alghathbar K. Environment recognition for digital audio forensics using MPEG-7 and mel cepstral features. J Electr Eng 2011; 62(4):199-205.

[11] Ratcliffe JH, Lattanzio M, Kikuchi G, Thomas K. A partially randomized field experiment on the effect of an acoustic gunshot detection system on police incident reports. J Exp Criminol 2019; 15(1):67-76.

[12] Nanda MA, Seminar KB, Nandika D, Maddu A. Development of termite detection system based on acoustic and temperature signals. Measurement 2019; 147: 106902.

[13] Glowacz A, Glowacz W, Glowacz Z, Kozik J. Early fault diagnosis of bearing and stator faults of the single-phase induction motor using acoustic signals. Measurement 2018; 113:1-9.

[14] Kane P and Andhare A. Critical evaluation and comparison of psychoacoustics, acoustics and vibration features for gear fault correlation and classification. Measurement 2020;107495.

[15] Mohaimenuzzaman M, Bergmeir C, West I T, Meyer B. Environmental Sound Classification on the Edge: A Pipeline for Deep Acoustic Networks on Extremely Resource-Constrained Devices. Pattern Recognit 2023;133:109025.

[16] Abdoli S, Cardinal P, Koerich AL. End-to-end environmental sound classification using a 1d convolutional neural network. Expert Syst Appl 2019; 136:252-263.

[17] Ahmad S, Agrawal S, Joshi S, Taran S, Bajaj V, Demir F, Sengur A. Environmental sound classification using optimum allocation sampling based empirical mode decomposition. Phys A Stat 2020; 537: 122613.
[18] Bardou D, Zhang K, Ahmad SM. Lung sounds classification using convolutional neural networks. Artif Intell Med 2018; 88: 58-69.
[19] Beltrán J, Chávez E, Favela J. Scalable identification of mixed environmental sounds, recorded from heterogeneous sources. Pattern Recognit Lett 2015;68:153-160.
[20] İnik Ö, CNN hyper-parameter optimization for environmental sound classification. Appl Acoust 2023; 202:109168.
[21] Khunarsal P, Lursinsap C, Raicharoen T. Very short time environmental sound classification based on spectrogram pattern matching. Inf Sci 2013; 243:57-74.
[22] Piczak, KJ. ESC: Dataset for environmental sound classification. In: Proceedings of the 23rd ACM international conference on Multimedia; 2015; New York, NY, USA, pp. 1015-1018.
[23] Muhammad G and Alghathbar K. Environment Recognition for Digital Audio Forensics Using MPEG-7 and Mel Cepstral Features. Int Arab J Inf Technol 2013; 10(1).
[24] Kraetzer C, Oermann A, Dittmann J, Lang A. Digital audio forensics: a first practical evaluation on microphone and environment classification. In: 9th workshop on Multimedia & security; 2007; pp.63-74.
[25] Oermann A, Lang A and Dittmann J. Verifier-tuple for audio-forensic to determine speaker environment. In: 7th workshop on Multimedia and security; 2005; pp.57-62.
[26] Serizel R, Bisot V, Essid S, Richard G. Machine listening techniques as a complement to video image analysis in forensics. In: IEEE International Conference on Image Processing; 2016; IEEE, pp. 948-952.
[27] Güner A, Alçin ÖF Şengür A. Automatic digital modulation classification using extreme learning machine with local binary pattern histogram features. Measurement 2019;145: 214-225.
[28] Gupta D, Arora J, Agrawal U, Khanna A, Albuquerque VHC. Optimized Binary Bat algorithm for classification of white blood cells. Measurement 2019; 143:180-190.
[29] Hu Q, Ohata EF, Silva FH, Ramalho GL, Han T, Reboucas Filho PP. A new online approach for classification of pumps vibration patterns based on intelligent IoT system. Measurement 2020;151: 107138.
[30] Ma C, An Y, Shen E, Yu D, Zhang J. Car Interior Sound Field Zoning Using Optimal Loudspeaker Array and Double Iteration Method. J Audio Eng Soc 2024; 72(4): p. 247-256.
[31] Zaman K, Sah M, Direkoglu C, Unoki M. A survey of audio classification using deep learning. IEEE Access 202;11: 106620-106649.
[32] Li F, Pang X, Yang Z. Motor current signal analysis using deep neural networks for planetary gear fault diagnosis. Measurement 2019; 145:45-54.
[33] Xue Y, Dou D, Yang J, Multi-fault diagnosis of rotating machinery based on deep convolution neural network and support vector machine. Measurement 2020; 156:107571.
[34] Lu Y, Wang M, Wu W, Han Y, Zhang Q, Chen S, Dynamic entropy-based pattern learning to identify emotions from EEG signals across individuals. Measurement 2020; 150: 107003.
[35] Sudhagar S, Sakthivel M, Ganeshkumar P. Monitoring of friction stir welding based on vision system coupled with Machine learning algorithm. Measurement 2019; 144:135-143.
[36] Navarro JM and Pita A. Machine Learning Prediction of the Long-Term Environmental Acoustic Pattern of a City Location Using Short-Term Sound Pressure Level Measurements. Appl Sci 2023; 13(3):1613.
[37] Mollah A, Mahanta TK, Balide V., Intelligent Classification of Automotive Horn Sound Quality 2024; SAE Tech Pap, No: 2024-26-0204.
[38] Nasim F, Masood S, Jaffar A, Ahmad U, Rashid M. Intelligent Sound-Based Early Fault Detection System for Vehicles. Comput Syst Sci Eng 2023; 46(3).
[39] Fan X, Sun T, Chen W, Fan Q. Deep neural network based environment sound classification and its implementation on hearing aid app. Measurement 2020;107790.
[40] Jaber MM, Abd SK, Shakeel PM, Burhanuddin MA, Mohammed MA, Yussof S. A telemedicine tool framework for lung sounds classification using ensemble classifier algorithms. Measurement 2020; 107883.
[41] Shen G, Nguyen Q, Choi J, An environmental sound source classification system based on Mel-frequency cepstral coefficients and Gaussian mixture models. IFAC Proc Vol 2012; 45(6): 1802-1807.
[42] Saki F, Kehtarnavaz N. Real-time hierarchical classification of sound signals for hearing improvement devices. Appl Acoust 2018;132: 26-32.
[43] Salamon J, Jacoby C, Bello JP. A dataset and taxonomy for urban sound research. In: 22nd ACM international conference on Multimedia 2014;1041-1044.
[44] Medhat F, Chesmore D, Robinson J, Masked Conditional Neural Networks for sound classification. Appl Soft Comput 2020; 90: 106073.
[45] Chen Y, Guo Q, Liang X, Wang J, Qian Y. Environmental sound classification with dilated convolutions. Appl Acoust 2019;148:123-132.
[46] Souli S, Lachiri Z. Audio sounds classification using scattering features and support vectors machines for medical surveillance. Appl Acoust 2018;130: 270-282.
[47] López-Pacheco MG, Sánchez-Fernández LP, Molina-Lozano H, Sánchez-Pérez LA. Predominant environmental noise classification over sound mixing based on source-specific dictionary. Appl Acoust 2016; 112: 171-180.
[48] Tuncer T, Dogan S, Ertam F. Automatic voice based disease detection method using one dimensional local binary pattern feature extraction network. Appl Acoust 2019; 155: 500-506.

[49] AlQahtani MO. Environment Sound recognition for digital audio forensics using linear predictive coding features. In: International Conference on Digital Information Processing and Communications. 2011; Berlin, Heidelberg: Springer Berlin Heidelberg, pp.301-309.
[50] Black J. Youtube Channel. [cited 05.04.2024; Available from: https://www.youtube.com/channel/UCRT3s4cWpEKyu2U9xPtmOiw.
[51] Keerthi SS, Shevade SK, Bhattacharyya C, Murthy KR. A fast iterative nearest point algorithm for support vector machine classifier design. IEEE Trans Neural Netw Learn Syst 2000; 11(1): 124-136.
[52] Kar S, Sharma KD, Maitra M, Gene selection from microarray gene expression data for classification of cancer subgroups employing PSO and adaptive K-nearest neighborhood technique. Expert Syst Appl 2015; 42(1):612-627.
[53] Liao Y, Vemuri VR, Use of k-nearest neighbor classifier for intrusion detection. Comput Secur 2002; 21(5): 439-448.
[54] Patel JR, Patel JM, Medical image fusion technique using singlelevel and multilevel DWT, Int J Eng Res Technol ESRSA Publications 2014; 3(1).
[55] Hasan KK, Ngah UK, Salleh MFM. Multilevel decomposition Discrete Wavelet Transform for hardware image compression architectures applications. In: 2013 IEEE International Conference on Control System, Computing and Engineering 2013;pp.315-320.
[56] Tian H and Ji W. A digital video watermarking scheme based on 1D-DWT. In: 2013 IEEE International Conference on Control System, Computing and Engineering IEEE, 2013;pp.315-320.
[57] Ojala T, Pietikäinen M, Mäenpää T. A generalized local binary pattern operator for multiresolution gray scale and rotation invariant texture classification. In: Advances in Pattern Recognition—ICAPR 2001: Second International Conference; Rio de Janeiro, Brazil; March 11–14, 2001; 2. Springer Berlin Heidelberg, 2001; pp. 399-408.
[58] Sun Y, Lou X, Bao B, A novel relief feature selection algorithm based on mean-variance model. J Inf Comput Sci 2011; 8(16): 3921-3929.
[59] Robnik-Šikonja M and Kononenko I. Theoretical and empirical analysis of ReliefF and RReliefF. Mach Learn. 2003;53(1-2):23-69.
[60] Tuncer T, Dogan S, Pławiak P, Acharya UR. Automated arrhythmia detection using novel hexadecimal local pattern and multilevel wavelet transform with ECG signals. Knowl Based Syst 2019;186:104923.

Turkish Journal of Science & Technology
20(1), 77-90, 2025

Research Paper
https://doi.org/10.55525/tjst.1572382

Machine Learning Models for Accurate Prediction of Obesity: A Data-Driven Approach

Ali DEĞİRMENCİ[1*]

[1] Department of Electrical and Electronics Engineering, Faculty of Engineering and Natural Sciences, Ankara Yıldırım Beyazıt University, Ankara, Türkiye

[*1] alidegirmenci@aybu.edu.tr

(Geliş/Received: 23/10/2024; Kabul/Accepted: 03/12/2024)

Abstract: The number of people affected by obesity is rising steadily. Diagnosing obesity is crucial due to its harmful impacts on human health and it has become one of the world's most important global health concerns. Therefore, it is crucial to develop methods that can enable early prediction of obesity risk and aid in mitigating the increasing prevalence of obesity. In the literature, some methods rely solely on Body Mass Index (BMI) for the prediction and classification of obesity may result in inaccurate outcomes. Additionally, more accurate predictions can be performed by developing machine learning models that incorporate additional factors such as individuals' lifestyle and dietary habits, alongside height and weight used in BMI calculations. In this study, the potential of three different machine learning methods (naive Bayes, decision tree, and Random Forest (RF)) in predicting obesity levels were investigated. The best performance among the compared methods was obtained with RF (accuracy=0.8892, macro average F1-score=0.8618, Macro Average Precision (MAP)=0.8350, Macro Average Recall (MAR)=0.9122,). In addition, feature selection was also performed to determine the features that are significant for the estimation of the obesity level. According to the experimental results with feature selection, the RF method resulted in the highest score (accuracy=0.9236, MAP=0.9232, MAR=0.9358, macro average F1-score=0.9269) with fewer features. The results demonstrate that the performance of machine learning models on the same dataset can be enhanced through detailed hyperparameter tuning. Furthermore, applying feature selection can improve performance by mitigating the adverse effects of irrelevant or redundant features that may degrade the model's effectiveness.

Key words: Obesity, machine learning, feature selection, mutual information.

Obezitenin Doğru Tahmini için Makine Öğrenimi Modelleri: Veri Odaklı Yaklaşım

Öz: Obezitenin insan sağlığı üzerindeki zararlı etkileri ve obeziteden etkilenen bireylerin sayısı giderek artışı nedeniyle bu sorunun teşhis edilmesi büyük bir önem taşımaktadır. Obezitenin yaygınlaşması küresel sağlık açısından en önemli sorunlardan biri haline gelmesine yol açmıştır. Bu nedenle, obezite riskinin erken tespitini sağlayacak, ayrıca obezitenin artan yaygınlığını azaltmaya yardımcı olacak yöntemlerin geliştirilmesi elzemdir. Obezitenin öngörülmesi ve sınıflandırılması için yalnızca Beden Kitle İndeksine (BKİ) güvenmek hatalı sonuçlara yol açabilir. BKİ hesaplamalarında kullanılan boy ve kilonun yanı sıra bireylerin yaşam tarzı ve beslenme alışkanlıkları gibi ek faktörleri de içeren makine öğrenimi modelleri geliştirilerek daha doğru tahminler elde edilebilir. Bu çalışmada, üç farklı makine öğrenimi yönteminin (naive Bayes, karar ağacı ve Rasgele Orman (RF)) obezite seviyelerini tahmin etme potansiyeli araştırılmıştır. Karşılaştırılan yöntemler arasında en iyi performans RF ile elde edilmiştir (doğruluk=0,8892, makro ortalama F1-skor=0,8618, Makro Ortalama Kesinlik (MAP)=0,8350, Makro Ortalama Duyarlılık (MAR)=0,9122). Ayrıca, obezite seviyesini tahmin etmede etkili olan öznitelikleri belirlemek için öznitelik seçimi de yapılmıştır. Öznitelik seçimi ile elde edilen deneysel sonuçlara göre, RF yöntemi daha az öznitelik ile en yüksek skoru (doğruluk=0,9236, MAP=0,9232, MAR=0,9358, makro ortalama F1-skor=0,9269) elde etmiştir. Sonuçlar, makine öğrenimi modellerinin aynı veri kümesi üzerindeki performansının ayrıntılı hiperparametre ayarlamasıyla artırılabileceğini göstermektedir. Ayrıca, öznitelik seçimi uygulamak, modelin etkinliğini azaltabilecek ilgisiz veya gereksiz özniteliklerin olumsuz etkilerini azaltarak performansı artırabilir.

Anahtar kelimeler: Obezite, makine öğrenmesi, öznitelik seçimi, karşılıklı bilgi.

1. Introduction

The rising prevalence of obesity has emerged as a major concern in global public health. Obesity is a complex, multifactorial health issue that can affect individuals of any age, regardless of location, ethnicity, or socioeconomic status, and has thus become a global epidemic [1]. In recent years, factors such as easy transportation, decreased physical activity, long screen time, increased consumption of processed foods, as well as sedentary lifestyles have led to an increase in obesity. Moreover, it is well known phenomenon that obesity is linked to various health conditions, including heart disease, type 2 diabetes, and certain cancers (such as colorectal, endometrial, liver, pancreatic, and kidney cancers). It also increases the risk of surgical procedures, metabolic abnormalities, joint problems, and other chronic diseases [2]. There is a strong connection between obesity and diabetes (especially type 2 diabetes). Obesity causes insulin resistance, making it harder for the body to use insulin effectively. When

* Corresponding author: alidegirmenci@aybu.edu.tr. ORCID Number of authors: [1] 0000-0001-9727-8559

this happens, blood sugar levels rise, and the pancreas tries to produce more insulin to keep blood sugar levels under control. Over time, the pancreas cannot sustain this excessive production and Type 2 diabetes can develop. Recently, studies focusing on determining blood glucose through non-invasive methods have gained significant attention [3]. Obesity accounts for a significant proportion of health expenditure and imposes a substantial burden on society. Therefore, both direct and indirect costs of obesity have an important place in the health system expenditures of countries. For this reason, measures should be taken to prevent obesity. This can be possible by raising public awareness of the factors that cause obesity and the health problems caused by obesity and taking action accordingly [4,5].

The World Health Organization (WHO) defines obesity as excessive fat accumulation in the body to the extent that it impairs health. Obesity arises from the fact that the energy intake from daily food is more than the energy expended, and this excess is stored as fat in the body. Body Mass Index (BMI) is a straightforward and widely adopted tool employed to assess and classify obesity based on a person's height and weight [6,7]. BMI is defined as in Equation (1).

$$BMI = \frac{Weight\ in\ kilograms}{Height\ in\ meters^2} \quad (1)$$

BMI categories defined by the WHO are given in Table 1. According to Table 1, weight status is categorized into four main groups, with obesity further classified into three subcategories based on BMI. Within these categories, the risk of developing health problems increases, except for individuals with normal weight, and the severity of these risks escalates with the level of obesity.

Table 1. BMI categories based on WHO.

Category	**Obesity class**	$\boldsymbol{BMI}\ (\boldsymbol{kg/m^2})$
Underweight	-	< 18.5
Normal weight	-	$18.5 - 24.9$
Overweight	-	$25.0 - 29.9$
Obese	Class I	$30.0 - 34.9$
	Class II	$35.0 - 39.9$
	Class III	> 40.0

Although BMI is widely adopted as a measure of obesity, it is insufficient as a stand-alone metric due to its inherent limitations and inaccuracies. BMI fails to discriminate between body fat and muscle mass. Consequently, individuals such as weightlifters and athletes can be categorized as overweight or obese, while those with low muscle mass but high fat levels may be misclassified as healthy. BMI also does not take into account other health indicators such as cholesterol levels, blood pressure, and metabolic health. Body composition can vary between different ethnic groups, age ranges, and genders, so using the same index for everyone can lead to inaccurate assessments. The BMI also fails to consider body fat distribution; studies have shown that fat around the abdomen (visceral fat) has been shown to better predict health risks than fat stored elsewhere [8].

Machine learning-supported approaches have been widely adopted in many fields, such as outlier detection [9,10], medicine [11-13], and biology [14]. Machine learning based approaches have also been adopted in obesity prediction. Previous reports showed that different hypotheses and models were developed for the estimation and classification of obesity using various machine learning techniques. For instance, Cheng et al. employed a recurrent neural network-based model, specifically Long Short-Term Memory (LSTM), to estimate BMI in children [15]. The data set was obtained from the Obesity Prediction in Early Life (OPEL) database. It consists of children aged 0 to 4 years, 2, 3, 5, and 8 clinic visits according to the electronic health record. According to the findings, five visits were adequate for accurate forecasts, the performance results of the LSTM model showed a mean absolute error of 0.98 and R^2 of 0.72. Solomon et al. presented a majority voting-based ensemble learning model that includes an eXtreme Gradient Boosting (XGBoost), a gradient-boosting classifier, and a Multi-Layer Perceptron (MLP) to predict and classify obesity [16]. The dataset has 17 features, including eating habits and physical conditions, from 2111 people in Colombia, Mexico, and Peru. To demonstrate the effectiveness of the model, it was compared with different machine learning algorithms (Naive Bayes (NB), XGBoost, Decision Tree (DT), Support Vector Machine (SVM), Gradient Boosting (GB), K-Nearest Neighbor (KNN), MLP, and Random Forest (RF)). While their model achieved the highest accuracy of 97.16%, the closest result was obtained using XGBoost at 96.37%. Another study using the same dataset was conducted by Kaur et al. [17]. Six different machine learning methods (GB, Bagging Meta-Estimator (BME), XGBoost, RF, SVM, and KNN) were used. Different train/test

ratios (90:10, 80:20, 70:30, 60:40) were examined. The highest accuracy in each train/test ratio was achieved by GB at 90:10 ratio (98.11%), GB and XGboost at 80:20 ratio (97.87%), and XGboost at 70:30 ratio (97.79%). In addition, meal recommendations were made according to calorie and macronutrient needs with the nearest neighbor learning method. Wang et al. used 9 different machine learning methods (Logistic Regression (LR), NB, KNN, DT, SVM, Light Gradient Boosting Machine (LGBM), RF, GB Machine (GBM), and XGBoost) for overweight or obesity risk prediction in Chinese preschool-aged children [18]. The dataset includes a total of 9478 children, 1250 of whom were overweight or obese. With the training-test ratio of 6:4, the SVM algorithm achieved the highest accuracy (0.9457). The top 5 most influential features were identified through $\chi 2$-based Scikit-learn feature selection and Shapley additive explanation. Liu et al. utilized different machine learning algorithms to measure the relationship between obesity status and BMI values [19]. Gut microbiota metagenomics and phenotype information data were gathered from 2262 Chinese volunteers to investigate microbiota-obesity interaction. The best prediction accuracy of BMI groups among Gradient Boosting DT (GBDT), RF, SVM, logistic regression methods was obtained with SVM (0.716). Wong et al. compared the performance of 4 methods, XGBoost, RF, LR, and SVM, to identify overweight or obesity status among working adults in Malaysia [20]. The dataset consists of 16,860 individuals, of which 7048 were overweight or obese. 70% of the data is utilized for training and the remaining 30% for testing, with the data being randomly split. The Area Under the Receiver Operating Characteristic (ROC-AUC) curve results for the methods are XGBoost = 0.81, RF and SVM = 0.80, and LR = 0.78. The results indicate that the performances of the compared models are not significantly different from each other. Calderón-Díaz et al. classified Chilean youth into two categories: normal weight and overweight/obese [21]. The dataset consists of 13 biomedical and 8 lipid features obtained from 40 university students between the ages of 20-30. XGBoost was applied to this dataset and a ROC-AUC score of 0.818 was obtained. Köklü and Sulak categorized the Turkish people as underweight, normal, overweight, and obese [22]. The dataset in their study consists of 14 features obtained from 1610 individuals. They compared the performance of Artificial Neural Network (ANN), KNN, RF, and SVM methods. The accuracies of the compared methods are 74.96% for ANN, 74.03% for SVM, 80.62% for KNN, and 87.82% for RF.

Predicting the individuals' obesity is of great interest because it affects the quality of life. As can be seen in the literature review, studies on obesity level prediction using machine learning methods are generally carried out on a country level and/or for specific age groups. Studies on predicting obesity in Turkey using machine learning are quite limited. It is of great importance to determine the factors affecting obesity on a national level. In this study, obesity levels were predicted by using three different machine learning methods: random forest, naive Bayes, and decision tree. To achieve the best performance among these methods, hyperparameter optimization was performed using the brute force grid search method, covering a specified range of method-specific hyperparameters. Then, most prominent features that have the effect of the estimation are analyzed with the Mutual Information (MI) feature selection method. To train the machine learning methods compared from the hyperparameters that achieve the best performance using all samples in the data set, different subsets of the data were created from the highest to the lowest according to the MI score. In this process, one feature was added at a time and the performance of the algorithms was assessed with each subset. In this way, the subset with the highest success rate was determined by using the minimum number of attributes. According to the experimental results, the best results obtained with the RF method using the entire data set are accuracy: 0.8892, macro average F1-score= 0.8618, Macro Average Precision (MAP)=0.8350, and Macro Average Recall (MAR)=0.9122. Using feature selection, the highest scores were obtained with 9 features and the performance scores were accuracy=0.9236, macro average F1-score=0.9269, MAP=0.9232, and MAR=0.9358. These results highlight that feature selection can improve the performance of machine learning algorithms.

The structure of the study is defined as follows. Section 2 introduces the dataset used in the study, provides a description of the machine learning methods compared and the feature selection method. Section 3 presents the performance of the machine learning algorithms, the MI scores of the features in the dataset, and the analysis of results obtained using fewer features based on their MI scores. Section 4 provides concluding remarks and outlines future directions for the study.

2. Materials and Methods

This study conducts a comparative analysis of three different machine learning methods used to predict obesity levels from an online questionnaire. The machine learning methods employed are NB, DT, and RF. In these methods, hyperparameter tuning was performed with the brute force grid search method to achieve the best performance. Then, the importance of each feature in the dataset was determined through MI. Using the best-performing method and its optimized hyperparameters, features were sequentially added from the highest to the lowest MI score. The positive and negative effects of adding each feature on the model's performance were then

examined. In all these analyses, k-fold cross-validation was employed to increase the reliability of the machine learning algorithms. The structure of the study is presented in Figure 1. The subsequent subsections outline the employed machine learning methods and feature selection technique, offering a thorough explanation of the methodology used in the study.

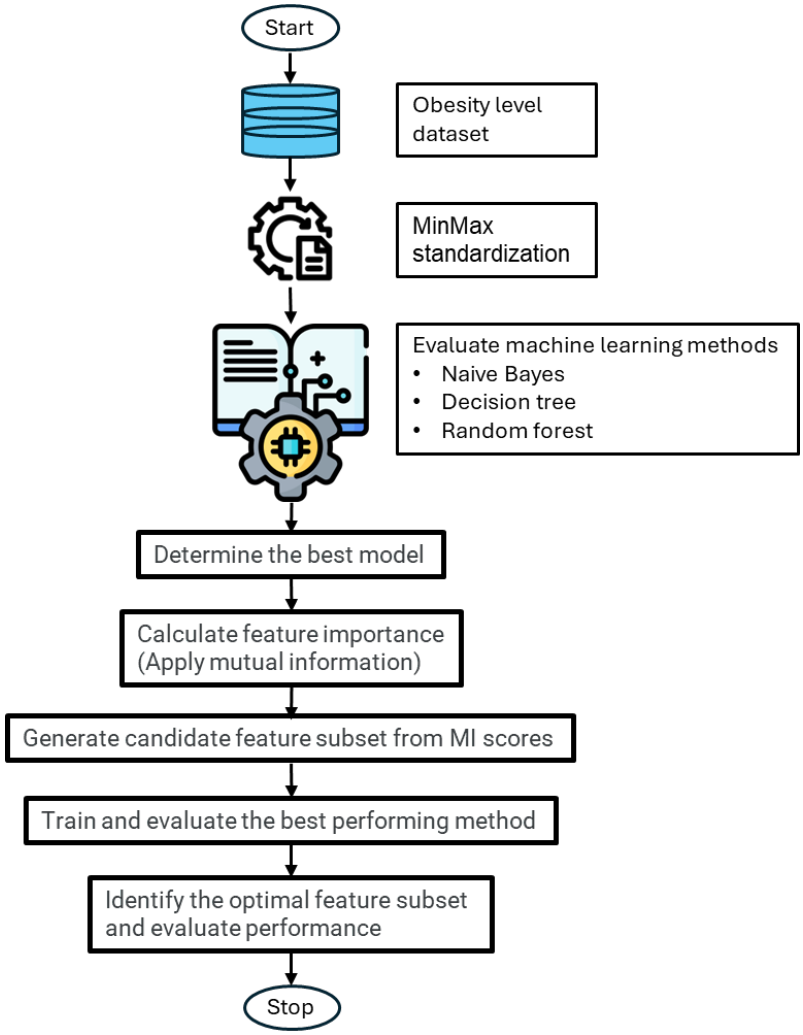

Figure 1. The flowchart of the study.

2.1. Data set

The data set employed in this study was acquired from a Kaggle repository named "Obesity" [22,23]. It was gathered through an online questionnaire from individuals residing in Turkey. The purpose of the data set was to determine the obesity levels of individuals based on the characteristics identified as influencing obesity in literature. Individuals were divided into four different classes: underweight, normal, overweight, and obese. The dataset consists of 1610 instances and 14 features. The dataset exhibits a skewed class distribution, as the proportions of each class are unequal. The class distributions are as follows: underweight (4.5%), normal (40.8%), overweight (36.8%), and obesity (17.8%). Details of the features, including brief descriptions, are given in Table 2.

Table 2. Explanations of the features in the Obesity data set.

Feature	Explanation	Measurement	Range
Age	Age of individual	Years	[18,...,54]
Sex	Male / Female	Boolean	0,1
Height	Height of individual	cm	[150,...193]
Overweight/Obese family	Overweight/Obese history in the family	Boolean	0,1
Fastfood	Fast food consumption	Boolean	0,1
Vegetable consumption	Frequency of vegetable consumption	Categorical	Rarely, Sometimes, Always
Main meals	Number of daily main meals	Categorical	1-2, 3, 3+
Interval meal	Intermeal food consumption	Categorical	Rarely, Sometimes, Usually, Always
Smoking	Smoking habit	Boolean	0,1
Liquid consumption	Daily liquid consumption	Categorical	<1 liter 1-2 liters > 2 liters
Calorie calculation	Calculation of daily calorie consumption	Boolean	0,1
Physical activity	Physical activity per week	Categorical	No activity 1-2 days 3-4 days 5-6 days 6+ days
Screen exposure	Duration of screen exposure	Categorical	0 - 2 hours 3 - 5 hours > 5 hours
Transportation type	Mode of transportation utilized	Categorical	Automobile, Motorbike, Bike, Public transportation, Walking

2.2. Naive Bayes (NB)

The NB classifier is a probabilistic classifier that employs Bayes' theorem to classify samples. In this method, the assumption is made that the features in the dataset are independent of each other. Bayes' rule is based on the fundamental concept of conditional probability, enabling users to calculate the probability of event *C* occurring given that event *X* has also occurred *p(C|X)* [24]. It is defined as in Equation (2).

$$p(C|X) = \frac{p(X|C)p(C)}{p(X)} \tag{2}$$

where *p(X|C)* is probability of *X* occurring, given *C* has occurred, *p(C)* equals probability of *C* occurring, and *p(X)* is probability of *X* occurring.

Assume $X = \{x_1, x_2, \dots, x_n\}$ to be a set of feature vectors of a new sample to be classified, where $x_1, x_2, \dots, x_n$ corresponds to the features of the sample, and $C = \{c_1, c_2, \dots, c_M\}$ is the target of possible classes. Here, *M* denotes the number of classes in the data set. Equation (2) can be expressed for *n* number of events x_i to be occurred, as shown in Equation (3).

$$p(c_j|x_1, x_2, \dots, x_n) = \frac{p(x_1,x_2,\dots,x_n|c_k)p(c_j)}{p(x_1,x_2,\dots,x_n)} \tag{3}$$

where c_j is the j^{th} class. Posterior probability $p(x_i|y)$ estimation increases model complexity and requires to need of excessive training data. Hence, in NB, it is assumed that all the features are conditionally independent. Additionally, $p(x_1, x_2, \dots, x_n)$ is constant for a sample and equal across classes in the data set. NB classifier can be defined as in Equation (4).

$$p(c_j|x_1, x_2, \dots, x_n) \propto \prod_{i=1}^{n} p(x_i|c_j)\, p(c_j) \tag{4}$$

The classification of the sample can be defined as in Equation (5).

$$\hat{y}_i = \arg\max_{c_j \in C} \left[p(c_j) \prod_{i=1}^{n} p(x_i|c_j) \right] \quad (5)$$

where y_i is the estimated class with maximum a posteriori probability, and $p(x_i|c_j)$ is the distribution of the i^{th} attribute for the given class c_j.

2.3. Decision tree (DT)

A DT is a tree-like structured model and a nonparametric method, meaning it does not rely on any assumptions about the distribution of the input data. It is a top-down approach that predicts the class of the unseen sample using decision rules. DT consists of root node, internal nodes, and leaf nodes. The root node is the top node of the tree where branching begins. Internal nodes reside between the root node and the leaf nodes, representing the conditions that determine how the tree splits into branches. Leaf nodes are also known as terminal nodes and determine the class of the query instance. In splitting, the aim is to decrease the impurity (or uncertainty) in the dataset corresponding to the class at a later stage. Commonly used techniques to select the splitting criteria include information gain and the Gini index [25].

To determine the optimal cut-off feature, features that have a lower Gini index are preferred in the DT method. The Gini index is computed as shown in Equation (6).

$$Gini\ \ Index = 1 - \sum_{i=1}^{n} p_i^2 \quad (6)$$

where p_i is the probability of the i^{th} class in the dataset and n is the number of classes in the data set. Sample schematic of the DT is shown in Figure 2.

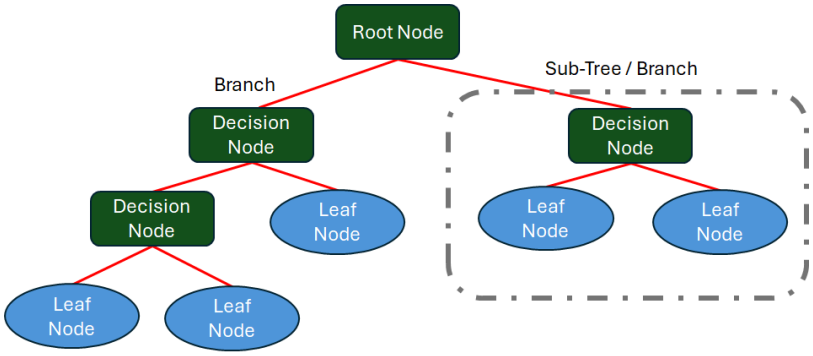

Figure 2. Schematic of the decision tree.

2.4. Random forest (RF)

RF is an ensemble learning algorithm that combines the concept of bootstrapping and aggregation, abbreviated as bagging. The intuition behind ensemble learning algorithms is that by combining a group of models, the performance and robustness of predictions can be improved compared to individual models. This is because a group of models, also defined as weak learners, can produce a powerful model that outperforms any individual model when aggregated. In bootstrapping, a new data set is created with replacement and samples are randomly selected from the original data set. The size of the training data set and the bootstrapped data set are equal. In aggregation, model predictions are averaged in regression problems, whereas in classification problems, the final decision is determined by majority voting. It is defined as in Equation (7).

$$\hat{y} = \arg\max_{m \in \{1,2,\ldots,M\}} \sum_{i=1}^{P} I(C_i = m) \quad (7)$$

where M is the number of classes, C_i equals the prediction of the i^{th} classifier, P is the number of classifiers, $\hat{y}$ denotes the final class prediction.

The DT method is used as a weak learner in RF. Each tree model in the RF method is created with bootstrapped data sets. In RF, randomness is added to the bagging. To grow a tree in RF, instead of using the best split of features in the DT method, it employs the best split among the random subset of features in the division of each node. Although this process weakens the strength of each tree, it also reduces the correlation and generalization error between the trees [26]. In the RF classification, the final prediction on unseen samples is determined by a majority vote of the prediction made by each of the tree models built from the bootstrapped data. The workflow of RF can be visualized in Figure 3. Nodes are split using a random subset of features, and branches terminate at leaf nodes, which contribute to the final decision based on the path followed in each tree.

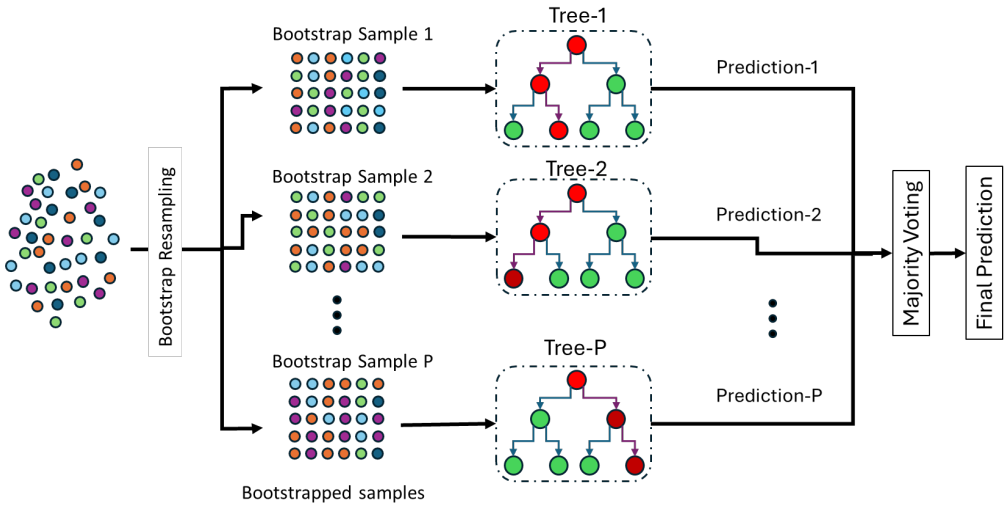

Figure 3. Workflow of the random forest.

2.5. Mutual information (MI)

Information theory enables the quantification of the linear and nonlinear relationships between variables [27, 28]. Information entropy, proposed by Shannon, is a measure of the uncertainty of a random variable. As the value of entropy increases, the uncertainty of the random variable also increases. Information entropy of a random variable $X = (x_1, x_2, \dots, x_N)$ is denoted as $H(X)$ and defined as shown in Equation (8).

$$H(X) = -\sum_{i=1}^{N} p(x_i)\, log\big(p(x_i)\big) \tag{8}$$

where $p(x_i)$ equals the probability of observing outcome x_i for variable X. The joint entropy of the two random variables $X = (x_1, x_2, \dots, x_n)$ and $Y = (y_1, y_2, \dots, y_m)$ can be calculated as in Equation (9).

$$H(X,Y) = -\sum_{i=1}^{n}\sum_{j=1}^{m} p\big(x_i, y_j\big) log\big(x_i, y_j\big) \tag{9}$$

where $p\big(x_i, y_j\big)$ are the probabilities of $n = i$ and $m = j$, respectively. If the value of variable Y is known, the conditional probability of X can be expressed mathematically as shown in Equation (10).

$$I(X;Y) = H(X) - H(X|Y) \tag{10}$$

Using the Equations (8) and (9), Equation (10) can be described as in Equation (11).

$$I(X;Y) = -\sum_{i=1}^{n}\sum_{j=1}^{m} p\big(x_i, y_j\big) \frac{p(x_i|y_j)}{p(x_i)} \tag{11}$$

When $I(X;Y)$ is high, it means that X and Y are closely related to each other. If X and Y are independent, $I(X;Y)$ becomes 0, which indicates that knowledge of one variable does not give any information about the other.

3. Results and Discussion

This section presents experimental evaluations of benchmarked machine learning methods in obesity level prediction. Initially, the performance metrics utilized to evaluate the success of machine learning methods are described in detail. The performance of each method is then analyzed and visualized for method-specific hyperparameter ranges. The importance of the features was determined by the MI method and the effect of the features on machine learning was analyzed with the method with the best performing method among the compared methods.

3.1. Performance metrics

Performance metrics have been developed to assess the success of machine learning methods and to compare methods with each other. Confusion matrix, also known as contingency table, provides information about the correct and incorrect predictions of the machine learning model. The standard structure of a confusion matrix for a multi-class classification task is given in Table 3. In Table 3, the classes are labeled as $C_1, C_2, \dots, C_M$ and N_{ij} denotes the number of samples where the true class is C_i but is predicted as class C_j, where $i, j = 1,2, \dots, M$ and M is the number of classes.

Table 3. Confusion matrix for a classification task involving M classes.

		Predicted Class		
		C_1	$\cdots C_j \cdots$	C_M
Actual Class	C_1	N_{11}	N_{1j}	N_{1M}
	$\vdots$		$\vdots$	
	C_i	N_{i1}	$\cdots N_{ij} \cdots$	N_{iM}
	$\vdots$		$\vdots$	
	C_M	N_{M1}	N_{Mj}	N_{MM}

Various performance measures are generated from the confusion matrix. For imbalanced multi-class classification datasets, macro-averaged metrics are commonly employed. In the calculation of the macro-averaged metrics, the desired metric is computed for each class individually, and then the average is obtained by summing the results for all classes and dividing by the total number of classes. This approach assigns equal weight to each class, regardless of the sample size in each class. Widely adopted performance metrics for multi-class classification are accuracy, MAR, MAP, and macro-average F1-score.

Accuracy is described as the ratio of the total number of correctly classified samples in all classes to the number of samples in the dataset. It is defined as in Equation (12).

$$Accuracy = \frac{\sum_{i=1}^{M} N_{ii}}{\sum_{i=1}^{M} \sum_{j=1}^{M} N_{ij}} \tag{12}$$

MAR assesses the model's capability to accurately classify instances within each class. MAR is computed as in Equation (13).

$$Macro\ average\ recall\ (MAR) = \frac{1}{M} \sum_{i=1}^{M} \frac{N_{ii}}{N_{i.}} \tag{13}$$

where

$N_{i.} = \sum_{j=1}^{M} N_{ij} \quad \forall\, i \in \{1,2,..,M\}$

MAP evaluates the model's capacity to generate accurate correct predictions for every class. MAP is calculated as in Equation (14).

$$Macro\ average\ precision\ (MAP) = \frac{1}{M} \sum_{i=1}^{M} \frac{N_{ii}}{N_{.i}} \tag{14}$$

where
$N_{.i} = \sum_{j=1}^{M} N_{ji} \quad \forall\, i \in \{1,2,..,M\}$

The macro average F1-score considers both false positive and false negative predictions when computing the metric, enables a balanced evaluation of the model's overall performance. Macro average F1-score can be expressed mathematically as shown in Equation (15).

$$Macro\ average\ F1-score = 2 \times \frac{MAP \times MAR}{MAP + MAR} \tag{15}$$

3.2. Experimental results

Obesity level was predicted by three different machine learning methods: NB, DT, and RF. These methods receive user-specified hyperparameters and the setting of these hyperparameters affects the performance of the methods. Therefore, in order to achieve the highest performance, method-specific hyperparameters need to be tuned to the dataset in each method. In the tuning of hyperparameters, determination is made using the brute-force grid search technique. The hyperparameters of each compared method, along with their corresponding ranges, are given in Table 4. To obtain more reliable performance estimation, k-fold cross validation is used. In the experiments, a *k* value of 10 was selected for the k-fold cross validation method, and the process was iterated 10 times. In the study, the average of 10 iterations obtained in the experimental results is given.

Table 4. Method specific hyperparameter range of the compared methods.

Method	Hyperparameter	Value
Naive Bayes	var_smoothing	$10^{-12}, 10^{-11}, \ldots, 10^{0}$
Decision Tree	Minimum samples split Maximum depth	2, 3, … ,17 1, 2, … , 20
Random Forest	Number of trees Maximum depth	$2^{0}, 2^{1}, \ldots, 2^{11}$ 1, 2, … , 20

The accuracy results of the method-specific hyperparameters of the compared methods are shown in Figure 4. The results of the NB method with the varying values of *var_smoothing* hyperparameter is shown in Figure 4(a). The accuracy of the methods increases as the value of *var_smoothing* approaches 10^{-1}; beyond that point, it starts to decrease. The highest accuracy is achieved at a *var_smoothing* value of 10^{-1}. The results of the DT method for the hyperparameter pair (*max_depth, number_of_trees*) are shown in Figure 4(b). The accuracy value increases with the increase of the *maximum_depth* hyperparameter. However, at low *max_depth* values (1 - 8), changes in the *min_samples_split* hyperparameter at the same *max_depth* values have little effect on the result. The highest values are obtained in the hyperparameter range where *max_depth* is high and *min_samples_split* is low. The performance of the RF algorithm concerning the *number_of_trees* and *max_depth* hyperparameters is illustrated in Figure 4(c). In the RF model, the highest accuracy values for the examined *max_depth* and *number_of_trees* hyperparameters were observed within the ranges 12–20 and 2^{6}-2^{11}, respectively. At values outside this range, the accuracy value begins to decrease gradually. The lowest accuracy is obtained when both *max_depth* and *number_of_trees* hyperparameters are at their minimum values.

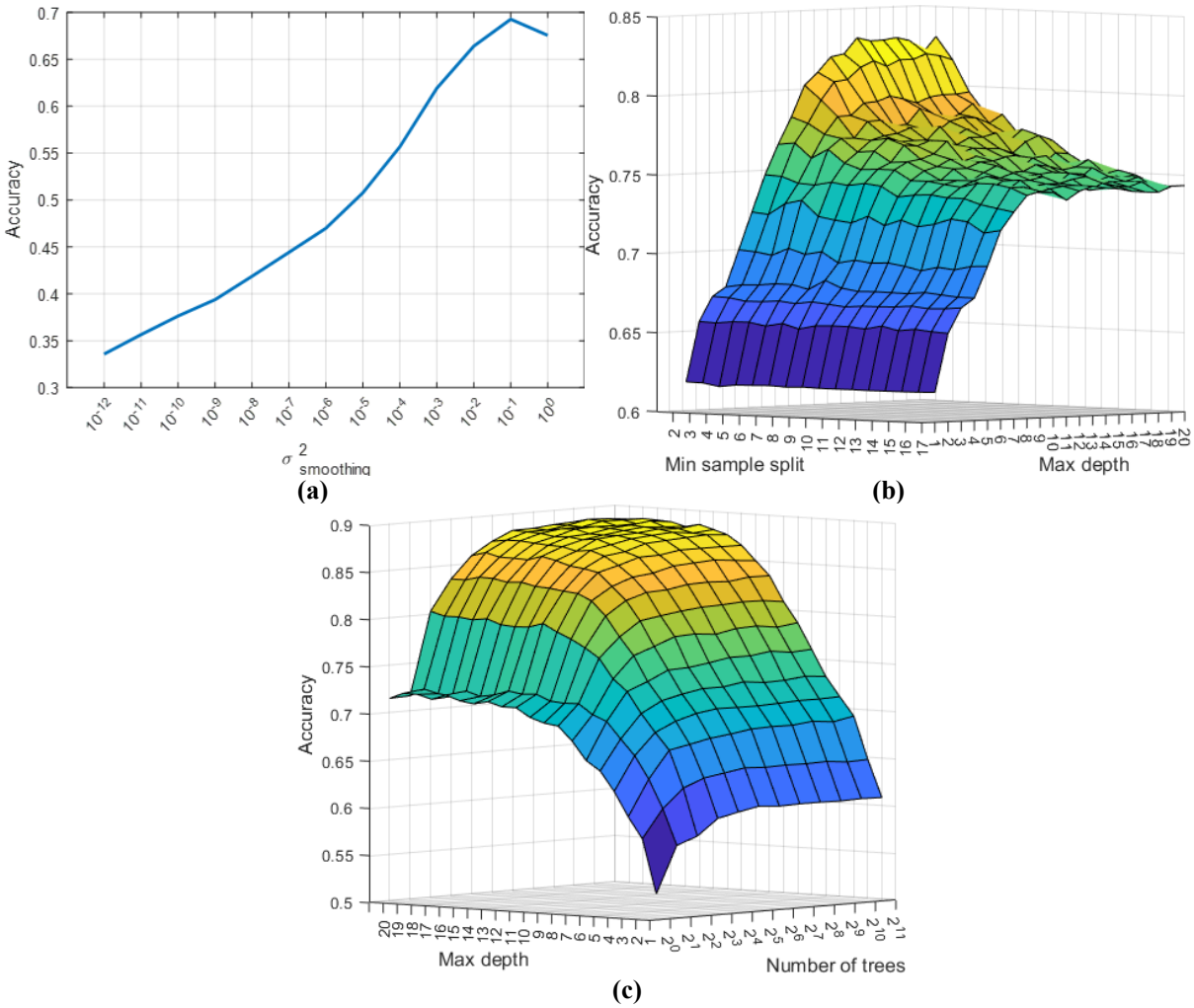

Figure 4. Accuracy results of the machine learning methods a) NB, b) DT, c) RF.

3.3. Feature selection

With the development of technology, data collection has become very easy. In this way, a large number of attributes can be easily collected for a specific problem. Although it is generally thought that increasing the number of features will better define the problem and increase the performance of machine learning algorithms, this may not always be the case. A large number of features increase the complexity of the machine learning algorithms and the processing time. For this reason, determining the most prominent features in the collected data set and building the machine learning model according to these features will both reduce the required processing power and the complexity. In this study, the importance of the features in the dataset was determined using the MI method and they are ranked in descending order in Figure 5. As can be seen from Figure 5, age, vegetable consumption, and main meals are the most prominent features, while screen exposure, liquid consumption, and overweight/obese family are the least effective.

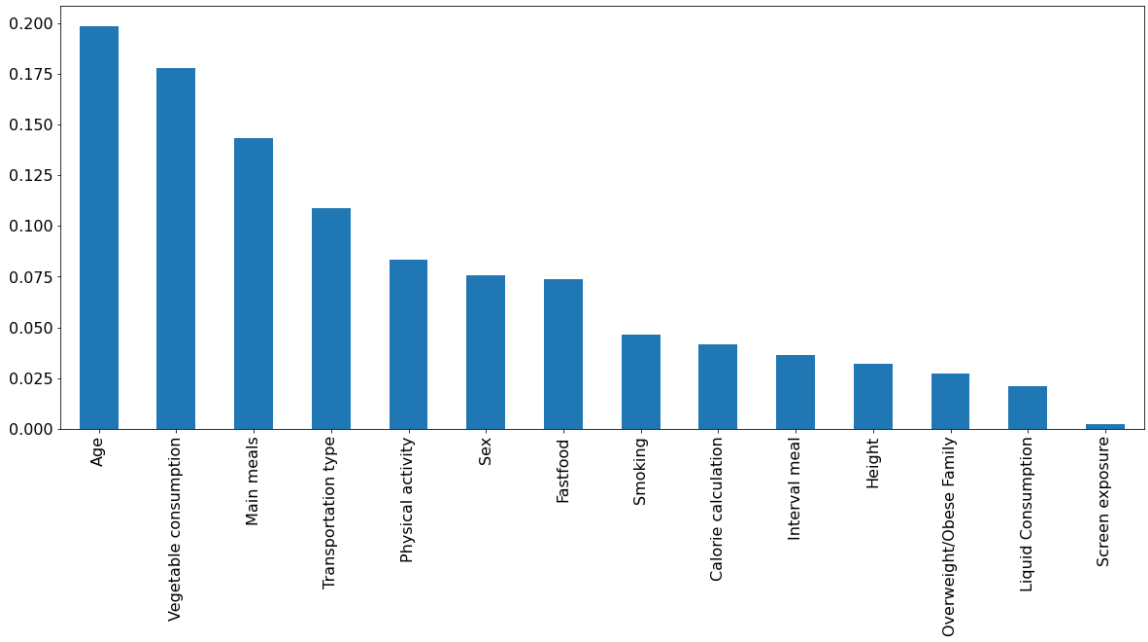

Figure 5. MI score of the features.

In order to observe the effect of the features in the dataset, the MI scores of the features were added one by one starting from the highest to the lowest, and data subsets were created. In the compared machine learning methods, models were created from these data subsets by using the hyperparameters that provided the best performance with all features in the data set. The results of these models were then evaluated with 4 different performance metrics to observe the effectiveness of each added feature. In this way, it will be possible to identify the subset of data with the highest performance using the minimum number of features. The experimental results obtained by the methods depending on the increasing number of features are shown in Figure 6.

In Figure 6(a), performance results of the NB method are presented. In NB, the highest results are obtained by using 12 features. Despite using 2 fewer features than the number of features in the entire dataset, higher results are obtained. Figure 6(b) shows the results of the DT method. The highest performance metric results for DT are obtained when the number of features is equal to 9. As can be seen in Figure 6(b), as the number of features increases from 1 to 9, the performance of the method increases by 47.03% in the accuracy performance metric. However, when comparing the results obtained with feature selection with the results obtained when all features are added, a performance improvement of 8.05% is obtained despite using 35.71% fewer features. Figure 6(c) demonstrates the performance results of the RF method. The highest results in the RF method were obtained by using the 10 features with the highest MI scores. After the highest values were obtained with 10 features, it was seen that increasing the number of features caused a slight decrease in performance.

Table 5 presents the performance results (accuracy, macro average F1-score, MAP, and MAR) of the compared methods with the determined hyperparameters, using both the entire set of features and a subset of features from the dataset. The hyperparameters of the methods were determined based on the values that achieved the highest results in the accuracy performance metric. In the remaining performance metrics, the results corresponding to these hyperparameters are given. In the table, the number of features for which the highest values were obtained by feature selection is given in the columns corresponding to the row named “Feature”. When the NB method results in Table 5 are analyzed, it is seen that by using fewer features, a 3.03% increase in accuracy, a 3.34% increase in macro average F1-score, a 0.34% increase in MAP, and a 6.54% increase in MAR is achieved. The 4th column in Table 5 presents the results of the DT method. The highest percentage increase in performance with feature selection is observed for the DT method. The results of the RF method are given in the last column of Table 5. As in the other methods, higher results are obtained with feature selection in this method as well. Additionally, the highest performance results in all cases were achieved using the RF method with 10 features selected through the MI feature selection technique.

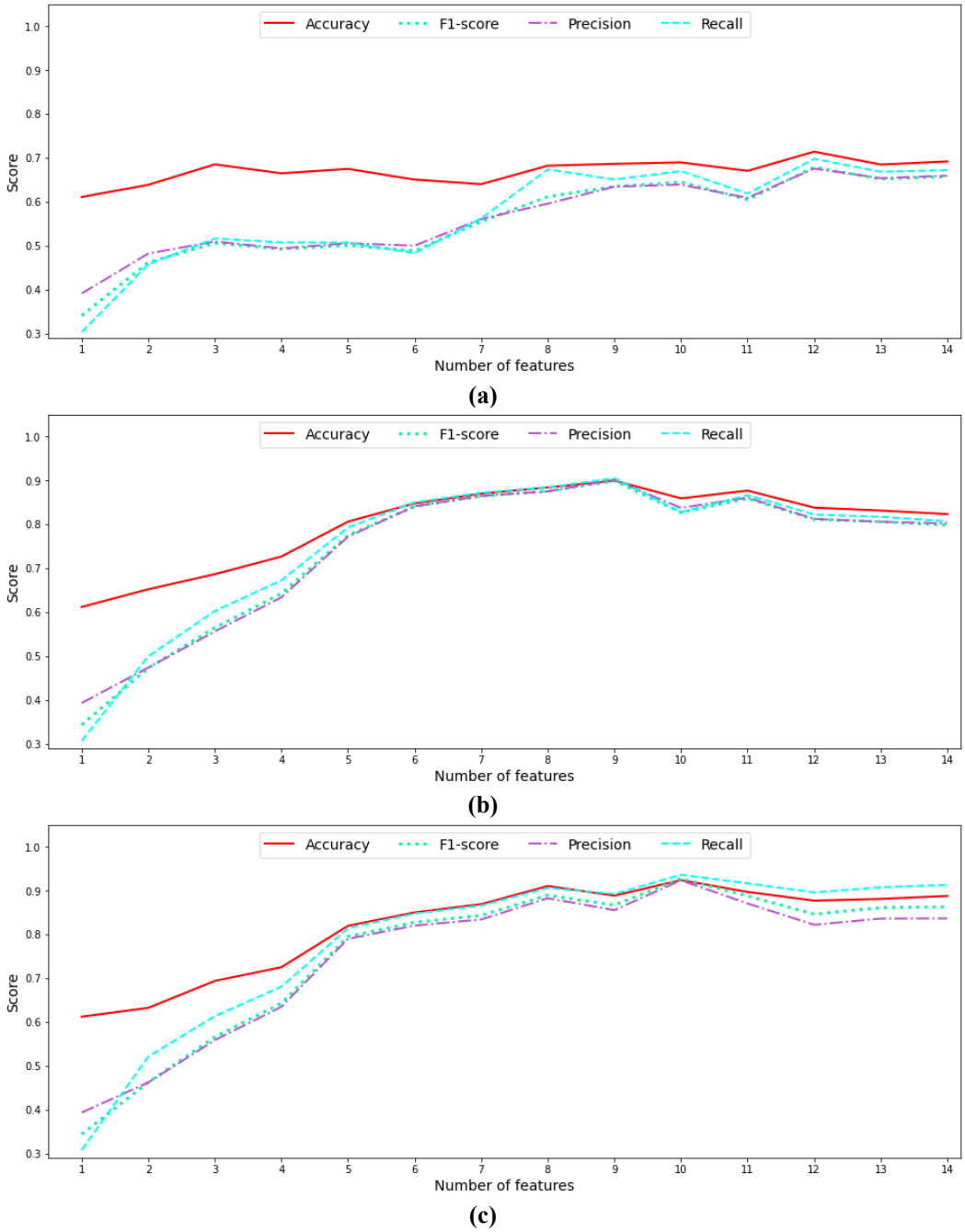

Figure 6. Performance results of the compared methods based on the increasing number of features **a)** NB, **b)** DT, **c)** RF

The only study in the literature using same data set was conducted by Köklü and Sulak [22]. In their study, the performances of three different machine learning methods, namely KNN, RF, and SVM, were compared. According to the results obtained, the highest accuracy was achieved with RF, similar to the presented study. However, the accuracy was improved by 1.25% in the current study. Furthermore, feature selection was performed with MI, which improved accuracy by 5.17% while reducing the number of features by 28.57%.

Table 5. Best performance results of the compared methods with/without feature selection.

Method	Metric	Naive Bayes	Decision Tree	Random Forest
Hyperparameter		var_smoothing=10^{-1}	maks_depth=14 min_samp_split = 2	maks_depth=19 number_of_trees=2^9
Features		12	9	10
All Features	**Accuracy**	0.6927	0.8321	0.8892
	F1-score	0.6563	0.8041	0.8618
	MAP	0.6730	0.8090	0.8350
	MAR	0.6546	0.8121	0.9122
Feature Selection	**Accuracy**	0.7137	0.8991	0.9236
	F1-score	0.6782	0.8986	0.9269
	MAP	0.6753	0.9009	0.9232
	MAR	0.6974	0.9047	0.9358

To summarize, in all the compared machine learning methods, better performance was achieved using fewer features when feature selection was applied. The highest performance was achieved with the RF method both through features from the whole dataset and through feature selection. However, when comparing the performance results using all features in the dataset with those obtained through feature selection, the greatest improvement was observed in the DT method, with 8.05% in accuracy, 11.75% in macro average F1-score, 11.36% in MAP, and 11.40% in MAR. Although there is a 6.86% difference in accuracy performance metric between the DT and RF methods in the results of the experiments using all attributes, this difference decreased to 2.72% in the results after feature selection.

4. Conclusion

In this study, a detailed analysis of the performance of three different machine learning methods—NB, DT, and RF—was conducted to determine obesity levels. To achieve optimal performance, method-specific hyperparameter tuning was carried out using a brute-force grid search. Additionally, to enhance the reliability of the results, k-fold cross-validation ($k = 10$) was employed and repeated 10 times with the average results reported. According to the results, the RF method outperformed the others across four different performance metrics. Moreover, the most influential features for predicting obesity levels were identified using the MI method. Data subsets were then generated based on MI scores, and the performance of the methods, using the best hyperparameters identified from the entire dataset, was analyzed. While the DT method exhibited the greatest performance improvement, the RF method consistently achieved the highest overall performance. Considering both the smallest subset of features and the accuracy of predictions, RF was proven to be the most effective method for predicting obesity levels. When the results of two different experiments are examined together, by applying feature selection, a performance increase of 3.87% was achieved in the same method by using 28.57% fewer features.

The current study presented promising information for obesity determination. Thus, in the future, the presented study is open to improvements in the following aspects. Different deterministic features may be added to enhance the performance while removing the less relevant ones. Furthermore, explainable machine learning methods can be implemented to learn the decisions behind the constructed machine learning models. Hence, the trustworthiness of the model predictions can be enhanced.

References

[1] World Obesity Federation. “World Obesity Atlas 2023.” Available: https://data.worldobesity.org/publications/?cat=19
[2] Włodarczyk M, Nowicka G. Obesity, DNA damage, and development of obesity-related diseases. Int J Mol Sci 2019; 20(5): 1146.
[3] Mohajan D, Mohajan HK. Obesity and its related diseases: a new escalating alarming in global health. J Innov Med Res 2023; 2(3): 12-23.
[4] Göktaş ÖF, Çankaya İ, Ermeydan EŞ. Determination of the Optimum Test Conditions for Measurement of Glucose Level in Liquids. TJST 2024; 19(1): 45-53.
[5] Okunogbe A, Nugent R, Spencer G, Powis J, Ralston J, Wilding J. Economic impacts of overweight and obesity: current and future estimates for 161 countries. BMJ Glob Health 2022; 7(9): e009773.
[6] World Health Organization. (2024). Obesity and overweight. https://www.who.int/news-room/fact-sheets/detail/obesity-and-overweight

[7] Nuttall FQ. Body mass index: obesity, BMI, and health: a critical review. Nutr Today 2015; 50(3): 117-128.
[8] De Koning L, Merchant AT, Pogue J, Anand SS. Waist circumference and waist-to-hip ratio as predictors of cardiovascular events: meta-regression analysis of prospective studies. Eur Heart J 2007; 28(7): 850-856.
[9] Degirmenci A, Karal O. iMCOD: Incremental multi-class outlier detection model in data streams. Knowledge-Based Syst 2022; 258: 109950.
[10] Degirmenci A, Karal O. Efficient density and cluster based incremental outlier detection in data streams. Inf Sci 2022; 607: 901-920.
[11] Özbay FA, Özbay E. An NCA-based hybrid cnn model for classification of Alzheimer's disease on grad-cam-enhanced brain MRI images. TJST 2023; 18(1): 139-155.
[12] Degirmenci A. Performance comparison of kNN, random forest and SVM in the prediction of cervical cancer from behavioral risk. Int J Innov Sci Res Technol 2022; 7(10): 71-79.
[13] Peeyada P, Cholamjiak W. A new projection algorithm for variational inclusion problems and its application to cervical cancer disease prediction. J Comput Appl Math 2024: 441, 115702.
[14] Goktas OF, Demiray E, Degirmenci A, Cankaya I. Real time non-invasive monitoring of glucose and nitrogen sources with a novel window sliding based algorithm. Eng Sci Technol Int J 2024; 58: 101845.
[15] Cheng ER, Steinhardt R, Ben Miled Z. Predicting childhood obesity using machine learning: Practical considerations. BioMedInformatics 2022; 2(1): 184-203
[16] Solomon DD, Khan S, Garg S, Gupta G, Almjally A, Alabduallah BI, Alsagri HS, Ibrahim MM, Abdallah AMA. Hybrid Majority Voting: Prediction and Classification Model for Obesity. Diagnostics 2023; 13(15): 2610.
[17] Kaur R, Kumar R, Gupta M. Predicting risk of obesity and meal planning to reduce the obese in adulthood using artificial intelligence. Endocrine 2022; 78(3): 458-469.
[18] Wang Q, Yang M, Pang B, Xue M, Zhang Y, Zhang Z, Niu W. Predicting risk of overweight or obesity in Chinese preschool-aged children using artificial intelligence techniques. Endocrine 2022; 77(1): 63-72.
[19] Liu W, Fang X, Zhou Y, Dou L, Dou T. Machine learning-based investigation of the relationship between gut microbiome and obesity status. Microbes Infect 2022; 24(2): 104892.
[20] Wong JE, Yamaguchi M, Nishi N, Araki M, Wee LH. Predicting overweight and obesity status among Malaysian working adults with machine learning or logistic regression: retrospective comparison study. JMIR Format Res 2022; 6(12): e40404.
[21] Calderón-Díaz M, Serey-Castillo LJ, Vallejos-Cuevas EA, Espinoza A, Salas R, Macías-Jiménez MA. Detection of variables for the diagnosis of overweight and obesity in young Chileans using machine learning techniques. Procedia Comput Sci 2023; 220: 978-983.
[22] Koklu N, Sulak SA. Using Artificial Intelligence Techniques for the Analysis of Obesity Status According to the Individuals' Social and Physical Activities. Sinop Uni J Nat Sci 2024; 9(1): 217-239.
[23] Koklu N, Sulak SA. Obesity Dataset. Kaggle. https://www.kaggle.com/datasets/suleymansulak/obesity-dataset: 2024.
[24] Kim T, Lee JS. Maximizing AUC to learn weighted naive Bayes for imbalanced data classification. Expert Syst Appl 2023; 217: 119564.
[25] Tokgöz N, Değirmenci A, Karal Ö. Machine Learning-Based Classification of Turkish Music for Mood-Driven Selection. J Adv Res Nat Appl Sci 2024; 10(2): 312-328.
[26] Rodriguez-Galiano VF, Ghimire B, Rogan J, Chica-Olmo M, Rigol-Sanchez JP. An assessment of the effectiveness of a random forest classifier for land-cover classification. ISPRS J Photogramm Remote Sens 2012; 67: 93-104.
[27] Shannon CE. A mathematical theory of communication. Bell Syst Tech J 1948; 27(3): 379-423.
[28] Cover TM. Elements of information theory. John Wiley & Sons.

Turkish Journal of Science & Technology
20(1), 91-100, 2025

Research Paper
https://doi.org/10.55525/tjst.1589545

AHP and GRA-Based Decision Support Model for Classified Ad Websites: A Case Study on Vehicle Selection

Çağrı UYSAL[1*], Ömer GİRAN[2]
[1,2] Department of Civil Engineering, Faculty of Engineering, Istanbul University-Cerrahpasa, Istanbul, Turkey
[*1] cagri.uysal@ogr.iuc.edu.tr, [2] omer.giran@iuc.edu.tr

(Geliş/Received: 22/11/2024; Kabul/Accepted: 18/12/2024)

Abstract: This study proposes an application for scoring and ranking vehicles selected from classified ads based on criteria defined by decision-makers. The approach aims to reduce the time wasted in commonly encountered decision-making situations. The criteria weights were determined using the Analytic Hierarchy Process based on relative comparison data separately defined by two decision-makers. The degree and ranking data for the alternatives were obtained through Grey Relational Analysis. For Decision Maker A, the highest-ranking vehicle was a hybrid car with a C-segment, sedan body type, automatic transmission, and a 1.8-liter engine capacity, scoring 91%. For Decision Maker B, the result was a D-segment vehicle with a sedan body type, automatic transmission, and a 1.5-liter engine capacity, ranking first with 85%. In situations where the comparison matrix could not be completed due to time constraints, an analysis based on the assumption of equal weights indicated that the hybrid car with a C-segment, sedan body type, automatic transmission, and a 1.8-liter engine capacity ranked first with a Grey Relational Degree of 81%.

Keywords: Multi-criteria decision making, analytic hierarchy process, grey relational analysis, classified ad websites, vehicle selection.

İlan Sitelerine Yönelik AHP ve GİA Temelli Karar Destek Modeli: Araç Seçimi Problemi Uygulaması

Öz: Bu çalışmada, karar vericiler tarafından tanımlanan kriterlere dayalı olarak ilan sitelerinden seçilen araçların puanlandırılması ve sıralanmasına yönelik bir uygulama önerilmiştir. Bu yaklaşım, sıkça karşılaşılan karar verme durumlarında kaybedilen zamanı azaltmayı amaçlamaktadır. Kriter ağırlıkları, iki karar vericinin ayrı ayrı tanımladığı rölatif karşılaştırma verileri kullanılarak Analitik Hiyerarşi Prosesi ile belirlenmiştir. Alternatiflere ait derece ve sıralama verileri Gri İlişki Analizi kullanılarak elde edilmiştir. Karar verici A'nın kullanım profili, beklenti ve ihtiyaçları doğrultusunda ilk sırayı %91'lik bir puanla C segment, sedan, otomatik şanzıman, 1,8 litre motor hacmine sahip hibrid araç almıştır. Karar verici B için ise sonuç, sedan gövde tipine, otomatik şanzımana ve 1,5 litre motor hacmine sahip D-segment araç olup, %85'lik bir puanla birinci sırada yer almıştır. Karar vericilerin zaman kısıtından dolayı karşılaştırma matrisinin tamamlanamadığı durumlarda, eşit ağırlıklar varsayımına dayalı yapılan analizlerde, yine C segment, sedan, otomatik, 1,8 litre motor hacmine sahip hibrid araç %81'lik bir Gri İlişki Derecesi ile birinci sırada yer almıştır.

Anahtar kelimeler: Çok kriterli karar verme, analitik hiyerarşi prosesi, gri ilişkisel analiz, ilan siteleri, araç seçimi.

1. Introduction

In today's world, where online shopping methods have become an essential part of our lives, customers conduct extensive research to obtain the best product at the most suitable cost. As it becomes increasingly difficult to choose among hundreds of brands and models, e-commerce websites have developed various filtering, sorting, and comparison algorithms to assist users in the decision-making process. While selecting from only a few criteria and alternatives can be easily achieved with the help of these applications, situations involving dozens of alternatives and criteria transform the decision-making process into a complex problem that goes beyond human cognitive abilities. This decision problem can be simplified by grounding it on a scientific basis through Multi-Criteria Decision Making (MCDM) techniques.

In today's world, with technological advancements, consumers' shopping habits have undergone a profound transformation. In particular, large-scale purchases, such as housing or vehicles, are often made online. In this context, listing websites play a crucial role in such acquisitions, emerging as significant shopping platforms for consumers.

This study develops a comprehensive decision support model based on the Analytic Hierarchy Process (AHP) and Grey Relational Analysis (GRA) methods to solve the vehicle selection problem on listing websites. Although listing sites generally serve to rank, compare, and list vehicles within specific criteria ranges, they do not provide

[*] Corresponding author: cagri.uysal@ogr.iuc.edu.tr. ORCID Number of authors: [1] 0000-0003-3617-8049, [2] 0000-0003-4135-393X

the necessary importance or ranking information required for users to make their final decisions. This model is designed to help users overcome these challenges when purchasing a vehicle and to assist them in selecting the most suitable option based on their personal preferences and expectations.

The decision-making process is multi-staged and complex. The process involves the evaluation of information obtained from analyses based on alternatives and the criteria necessary for selecting among these alternatives. To effectively manage this structure, it is modeled and analyzed, and relevant data are evaluated using MCDM techniques [1].

The emergence of MCDM applications is driven by the fact that as the number of criteria increases, the task of selecting among alternatives goes beyond human cognitive capabilities. In this study, rating and ranking applications for selecting e-commerce products can be used to assist consumers in choosing products from these platforms and to minimize the time spent in the selection process.

In recent years, there have been numerous studies in the literature where AHP and GRA methods have been used integratively in various fields. Pophali et al. [2] integrated AHP and GRA methods for the optimal selection of tannery wastewater treatment plants. This approach, based on real data and considering economic, technical, and administrative factors, provides significant advantages in identifying areas for further improvement within the existing treatment options. Gülçiçek Tolun and Tümtürk [3] aimed to manage a complex decision-making process for agricultural machinery manufacturing companies by selecting the most suitable machine from various alternatives with differing criteria such as cost, speed, quality, and after-sales service, using AHP. Additionally, the selection of the most appropriate machine from the alternatives identified using the GRA method was supported by considering the diversity of managerial priorities. In a study by Samvedi et al. [4], the integrated use of AHP and GRA methods for selecting the most suitable machine tool for a manufacturing facility was examined. In the study, the priorities of criteria such as cost, flexibility, efficiency, and safety were determined using AHP, and the GRA method was then applied to select the most suitable machine tool. Tayyar et al. [5] aimed to evaluate the financial performance of companies operating in the technology and IT sectors listed on the Istanbul Stock Exchange. In this study, AHP and GRA methods were used to compare the financial performance of companies based on financial criteria such as profitability, and the most successful company in the sector was determined. Wang et al. [6] developed a mathematical model using GRA and AHP theories for optimizing the necessary machinery systems to convert biomass resources, such as straw, into biomass briquette fuel. The optimal approach for selecting a biomass briquette fuel system schema aims to meet multiple objectives, including cleanliness, economy, environmental protection, product quality, production capacity, and production stability. There are also studies in the literature related to vehicle selection and the application of various decision-making techniques. Ballı et al. [7] evaluated seven selected vehicles based on criteria such as price, fuel consumption, performance, and safety. They demonstrated that the PROMETHEE method, which processes linguistic values through fuzzy logic, provides a more flexible evaluation, thereby simplifying the resolution of complex problems. Yavaş et al. [8] scaled a set of primary criteria and twenty sub-criteria using AHP and the Analytic Network Process (ANP) methods. The analysis results prioritized criteria such as interior design, safety equipment, and engine capacity, and ranked alternative car brands, showing that these methods could positively impact customer satisfaction and sales volume. In a study by Ghadikolaei and Esbouei [9], a hybrid approach incorporating accounting and economic value measures was proposed to assess the financial performance of automotive companies listed on the Tehran Stock Exchange. Using fuzzy AHP (FAHP), criteria weights were determined, and companies were ranked using grey-VIKOR, ARAS-F, and grey-COPRAS methods. It was found that economic value measures were more important than accounting measures. Gnanasekaran et al. [10] proposed two models for selecting the best car among five alternatives based on criteria such as safety, performance, economy, exterior design, comfort, dealership services, warranty, and emissions. In the first model, FAHP was integrated with the PROMETHEE technique, and in the second model, FAHP was integrated with the hierarchical GRA technique. In both models, FAHP was used to analyze the structure of the car selection problem and determine the weights of criteria, while hierarchical GRA and PROMETHEE techniques were employed to obtain the final ranking of the cars.

1.1. Analytical Hierarchy Process (AHP)

The Analytical Hierarchy Process (AHP) is an approach developed by Thomas L. Saaty in the first half of the 1970s. The method allows for the hierarchical organization of criteria, the evaluation of their weights, and, in this context, the ranking or comparison of alternatives [11].

AHP utilizes expert opinions to conduct pairwise comparisons. This process simplifies decision-making by eliminating complexity and making the selection process more straightforward [12].

AHP is commonly used in various fields, such as planning processes, resource allocation, and conflict management, to select the best alternative among several [13]. In decision-making processes where objective data

is insufficient, AHP is frequently applied. This method incorporates subjective data, such as the decision maker's personal opinions, along with objective data in the decision process [14].

This study aims to determine the criteria weights using AHP. After identifying the criteria that will form the basis for selecting alternatives, a pairwise comparison matrix is constructed. The purpose of pairwise comparisons among criteria is to convert non-numerical expressions into a numerical scale. In Table 1, all criteria are evaluated relatively using the comparison scale defined by Saaty [15].

Table 1. AHP comparison scale.

Importance Degree	Definition	Explanation
1	Equal Importance	Two criteria contribute equally to the goal
3	Moderately Important	The decision-maker slightly prioritizes one element over the other.
5	Significantly Important	The decision-maker strongly prefers one element over the other.
7	Highly Important	One criterion is very strongly preferred over the other — in a practically demonstrable way.
9	Critically Important	One criterion is superior to the other in a highly verifiable manner, supported by strong evidence.
2,4,6,8	Transition Values	Can be used to express intermediate values.

As a result of the relative evaluations, the comparison matrix A_{nxn} given in Equation 1 is obtained. Here, n represents the number of criteria.

$$A = [A_{ij}] = \begin{bmatrix} 1 & a_{12} & a_{13} & \dots & a_{1n} \\ a_{21} & 1 & a_{23} & \dots & a_{2n} \\ a_{31} & a_{32} & 1 & \dots & a_{3n} \\ \dots & \dots & \dots & \dots & \dots \\ a_{n1} & a_{n2} & a_{n3} & \dots & 1 \end{bmatrix} \quad (1)$$

Equation 2 normalizes the comparison matrix by dividing each column element by its total. The sum of each column in the normalized matrix must be equal to 1.

$$b_{ij} = \frac{a_{ij}}{\sum_{i=1}^{n} a_{ij}} \quad (2)$$

The average of the row elements of the normalized matrix is calculated by using Equation 3. The obtained w_i values represent the criteria weights. The eigenvalue calculation used in the consistency ratio calculation is provided in Equation 4.

$$w_i = \frac{\sum_{j=1}^{n} b_{ij}}{n} \quad (3)$$

$$\lambda = \frac{\sum_{i=1}^{n} \frac{a_{ij} w_i}{w_i}}{n} \quad (4)$$

In Equation 5, CR represents the consistency ratio, which is a random index that changes based on the size of the comparison matrix (the value of n). The RI values, created by Saaty [16], are provided in Table 2.

$$CR = \frac{\lambda - n}{RI(n-1)} \quad (5)$$

Table 2. Random index table.

N	3	4	5	6	7	8	9	10	11	12	13	14	15
RI	0.58	0.90	1.12	1.24	1.32	1.41	1.45	1.49	1.51	1.48	1.56	1.57	1.59

1.2. Grey Relational Analysis (GRA)

The method we now use as GRA is based on the concept of "grey theory", which was introduced by Julong D. in 1982 [17]. Grey theory offers advantages in solving problems involving limited data and uncertainty, without requiring a statistical distribution.

GRA is a quantitative analysis that shows the similarity and difference between the reference series and the alternative series. The alternative series that shows the closest similarity to the reference series is the best alternative for the given problem.

GRA is more efficient than deterministic methods when analyzing decision-making problems under uncertainty. If the data is sufficient, it allows the use of statistical analyses such as clustering analysis and regression analysis. Additionally, multi-criteria decision-making (MCDM) methods such as AHP, ANP, Data Envelopment Analysis (DEA), TOPSIS, and ELECTRE can also be used [18].

The term "grey" in the method refers to the lack of information within the system. The state of complete information is represented by the color 'white,' while complete lack of information is represented by the color "black". The goal of grey theory is to grey the black data within the system.

The application of the GRA method begins with an mxn decision matrix consisting of m alternatives and n criteria, as shown in Equation 6.

$$X = \begin{bmatrix} x_1(1) & x_1(2) & \cdots & x_1(m) \\ x_2(1) & x_2(2) & \cdots & x_2(m) \\ \vdots & \vdots & \vdots & \vdots \\ x_n(1) & x_n(2) & \cdots & x_n(m) \end{bmatrix} \qquad \text{i=1,2,…,n ve j=1,2,…,m} \tag{6}$$

The reference series is derived from the column values of the matrix in Equation 1, based on benefit, cost, or optimal criteria. For example, if the vehicle price is to be minimized, the lowest price of the alternatives is added to the series as the reference value.

In the normalization of the decision matrix, if the data set is in the benefit case, Equation 7 is used, and if it is in the cost case, Equation 8 is used.

$$x'_i(j) = \frac{x_i(j) - min_{i=1}^{n} x_i(j)}{max_{i=1}^{n} x_i(j) - min_{i=1}^{n} x_i(j)} \tag{7}$$

$$x'_i(j) = \frac{max_{i=1}^{n} x_i(j) - x_i(j)}{max_{i=1}^{n} x_i(j) - min_{i=1}^{n} x_i(j)} \tag{8}$$

As a result of normalization, a standardized decision matrix is obtained. The largest values of the columns of the decision matrix constitute the reference series specified in Equation 9. The highest value of the jth criterion among the normalized values is represented by $x'_0(j)$.

$$x'_0 = x'_0(1), x'_0(2), \ldots, x'_0(m) \qquad \text{i=1,2,…,n ve j=1,2,…,m} \tag{9}$$

The absolute value matrix is created by subtracting the reference series from the standardized decision matrix via Equation 10.

$$\Delta_{0i}(j) = |x'_0(j) - x'_i(j)| \qquad \text{i=1,2,…,n ve j=1,2,…,m} \tag{10}$$

The grey relational coefficient is calculated for all values in the difference matrix. The calculation of the grey relational coefficient is shown in Equation 11. The grey relational coefficient is used to determine how close $x_i(j)$ is to $x_0(j)$. The larger the grey relational coefficient, the closer the $x_i(j)$ and $x_0(j)$ series are for criterion j.

$$\gamma_{0i}(j) = \frac{\Delta_{min} + \xi\Delta_{max}}{\Delta_{0i}(j) + \xi\Delta_{max}} \tag{11}$$

The "ξ" (distinguish) coefficient specified in Equation 11 takes values in the range of [0,1], and it is typically set to 0.5 in applications [19]. Δ_{max} and Δ_{min} are selected from all elements in the $\Delta_{0i}(j)$ matrix.

The determination of grey relational degrees can be calculated for cases where the criteria weights are either equal or different. Γ_{0i}, given in Equation 12, represents the grey relational degree of element i.

$$\Gamma_{0i} = \sum_{j=1}^{m} [w(j) \times \gamma_{oi}(j)] \ , \sum_{j=1}^{m} w(j) = 1 \tag{12}$$

2. Material and Methods

In this study, the AHP and GIA methods are used together to address the vehicle selection problem from online advertisement sites. Considering the necessity of taking personal preferences and expectations into account when purchasing a vehicle, it is believed that weighting the criteria will produce more realistic solutions [20].

Therefore, while the AHP method is used for weighting the criteria, the GIA method is applied for ranking the vehicle listings. For the application, 10 cars published on a widely used advertisement site in Turkey were evaluated based on 13 predefined criteria.

2.1. Determination of criteria

In this study, in addition to the site data, objective data that could influence vehicle selection were used when determining the criteria. The user profile, expectations, and needs are outlined below.

- High security features
- Large trunk space and living area
- High long-distance capability
- Automatic transmission for ease of use
- Fuel-efficient
- Advanced in terms of equipment features
- High performance on hills
- Suitable for generally calm driving
- Low repair, maintenance, and parts costs
- Suitable for use by a family of three

The user has selected ten vehicles from the list based on their own defined criteria, such as price, model, and mileage range. In this way, subjective evaluations such as vehicle design, color, and body type have been left to the individual's personal judgments, while the analysis is primarily based on numerical or quantifiable data. Table 3 presents the site data for the selected alternatives.

Table 3. General information about the alternatives, listing site data.

VEHICLE ID	BODY TYPE	SEGMENT	MODEL YEAR	ENGINE DISPLACEMENT	ENGINE POWER	FUEL TYPE	FUEL CONSUMPTION	TRANSMISSION TYPE	COLOR	MILEAGE	PRICE	ACCELERATION (0-100 km)	MAXIMUM SPEED
A1	SEDAN	C	2017	1.6	125	PETROL	6.7	AUTOMATIC	GREY	122000	800000	11.6	196
A2	HATCHBACK	B	2017	1.4	90	DIESEL	3.5	AUTOMATIC	WHITE	129000	725000	10.9	184
A3	SEDAN	C	2019	1.8	122	HYBRID	3.5	AUTOMATIC	GREY	110600	841000	11.0	180
A4	SUV	B	2020	1.0	115	PETROL	5.2	AUTOMATIC	BLUE	134000	935000	11.8	180
A5	SUV	H	2019	1.6	120	DIESEL	5.0	AUTOMATIC	BLACK	105000	965000	10.2	178
A6	HATCHBACK	C	2017	1.6	116	DIESEL	3.9	AUTOMATIC	WHITE	110000	900000	10.4	202
A7	SEDAN	D	2018	1.5	152	PETROL	5.8	AUTOMATIC	BLACK	108000	1100000	8.60	210
A8	SUV	B	2018	1.4	100	PETROL	6.9	AUTOMATIC	WHITE	77452	840000	13.7	176
A9	SEDAN	C	2018	1.5	120	PETROL	5.0	MANUAL	RED	93000	850000	10.1	195
A10	HATCHBACK	B	2017	1.4	100	PETROL	6.2	AUTOMATIC	WHITE	122250	725000	12.9	170

The following assumptions and quantifications were made when determining the criteria to be included in the decision matrix:

- **Body type and vehicle color criteria:** These criteria are based on individual preferences and are assumed to have no impact on the analysis outcome. Therefore, they are excluded." avoids redundancy.
- **Model year:** Model year values were converted into vehicle age relative to 2024.
- **Fuel consumption:** The fuel consumption criterion, in Turkish Lira (TL), was included in the analysis based on the ceiling prices of the top 8 companies with the highest transaction volume for the period of June 2024, published on the EPDK [21] website.
- **Transmission type:** According to the May bulletin from ODMD [22], automatic transmission vehicles account for 89.6% of total sales, while manual transmission vehicles account for 10.4%. Based on user preferences outlined in the article, the transmission type criterion was weighted as 9 for automatic and 1 for manual transmissions.

- **Engine capacity:** It was directly included in the numerical analysis based on the assumption that engine capacity affects the vehicle's long-distance capability.
- **Engine power:** Given the environmental factors where the vehicle will be used, the engine power criterion, which affects climbing ability, was directly included in the analysis.
- **Acceleration and top speed values:** Due to customer expectations for generally calm usage, the 0-100 km/h acceleration time and maximum speed values were excluded from the analysis.
- **Vehicle safety:** The vehicle safety criterion was included in the analysis based on the Euro NCAP [23] test results, which provide a final rating between 1 and 5 for the model year.
- **Mileage, price, and trunk capacity:** These numerical values were directly included in the analysis.
- **Segment values (B, C, D, and H):** Since the B, C, D, and H segment values are part of a classification system used in the automotive industry to categorize vehicles based on certain features and usage purposes, a suitability scoring scale, as shown in Table 4, was created for their quantification.

Table 4. Suitability scores according to vehicle segments.

Segment	Interior Space	Trunk Space	Comfort	Safety	Fuel Economy	Average Suitability Score
B	5	4	6	7	8	6.0
C	7	7	7	8	7	7.2
D	8	8	9	9	6	8.0
H	9	9	9	9	5	8.2

- **Repair-maintenance costs:** Ten-year total repair-maintenance cost values, published by Consumer Reports [24] in April 2024, were included in the analysis in relation to the user's expectations regarding repair-maintenance and parts costs. The analysis incorporated breakdown rates per 100 vehicles, derived from the 2024 J.D. Power Vehicle Dependability Study [25].
- **Equipment features:** The equipment features criterion varies in terms of brand and model, so it was possible to quantify the selected alternatives based on their level of meeting the technical specifications provided on the site. Each alternative was assigned a numerical value based on the number of equipment features it satisfies, as listed in Table 5.

Table 5. Equipment features matrix of the alternatives.

ABS braking system	Tire pressure monitoring System	Fatigue detection system	Heated front seats	Steering wheel audio controls	LED rear stop lights
Electronic stability control system	Rearview camera	Parking sensors (rear or front/rear)	Electric windows (front and rear)	360-degree bird's-eye view camera	Alloy wheels
Multiple airbags	Lane-keeping assist	Automatic emergency braking system	Electrically foldable side mirrors	Keyless entry and start	Start-stop system
Traction control System	Adaptive cruise control	Parking assistant	Touchscreen multimedia system	Automatic headlights	Panoramic sunroof
Electronic brakeforce distribution	Traffic sign recognition system	Automatic climate control	Bluetooth connection	Rain-sensing wipers	Traction control system
Hill-start assist	Blind spot warning system	Leather steering wheel and gear shift	USB and AUX ports	LED daytime running lights	Eco-driving assistance system

As a result of the assumptions and quantifications explained above, the criteria and data for the alternatives determined are presented in Table 6. The abbreviations for the criteria are as follows: K1: Segment, K2: Vehicle Age, K3: Engine Volume, K4: Engine Power, K5: Fuel Consumption, K6: Ncap Test Result, K7: Transmission Type, K8: Trunk Capasity, K9: Vehicle Mileage, K10: Price, K11: Number of Breakdowns, K12: Repair Cost, K13: Features. Table 6 presents the initial data set consisting of given alternatives and criteria values.

Table 6. Initial data set consisting of alternatives and criteria values.

	K1	K2	K3	K4	K5	K6	K7	K8	K9	K10	K11	K12	K13
A1	7.2	7	1.6	125	274.05	4	9	440	122000	800000	206	5835	26
A2	6.0	7	1.4	90	142.34	5	9	280	129000	725000	267	6530	25
A3	7.2	5	1.8	122	143.16	5	9	471	110600	841000	147	4900	27
A4	6.0	4	1.0	115	212.69	5	9	422	134000	935000	199	5700	28
A5	8.2	5	1.6	120	203.35	3	9	351	105000	965000	190	6400	26
A6	7.2	7	1.6	116	158.61	5	9	380	110000	900000	275	9890	26
A7	8.0	6	1.5	152	237.24	5	9	380	108000	1100000	245	9285	29
A8	6.0	6	1.4	100	282.23	3	9	352	77452	840000	187	5850	26
A9	7.2	6	1.5	120	204.51	5	1	419	93000	850000	185	5800	25
A10	6.0	7	1.4	100	253.60	4	9	301	122250	725000	198	5640	9

2.2. Determining criterion weights using AHP

In this study, the AHP method has been applied to determine the weights of the criteria. Evaluating only the upper diagonal matrix requires 78 comparisons. Assuming that the decision maker has sufficient time, it is possible for them to evaluate each criterion relatively using a 78 question survey.

Table 7. Criteria expectations of decision-makers for vehicles and their relative importance levels.

Decision Maker A			Decision Maker B		
HIGH EXPECTATION LEVEL (9)	**MEDIUM EXPECTATION LEVEL (3)**	**LOW EXPECTATION LEVEL (1)**	**HIGH EXPECTATION LEVEL (9)**	**MEDIUM EXPECTATION LEVEL (3)**	**LOW EXPECTATION LEVEL (1)**
Trunk Capasity	Low Mileage	Package Completeness	Safety	Breakdown Rate	Trunk Capasity
Fuel Consumption	Automatic Transmission	Performance	Automatic Trasnsmission	Repair Cost	Fuel Consumption
Engine Volume	Segment			Package Completeness	Engine Volume
Safety	Investment Cost			Segment	Low Mileage
Breakdown Rate	Vehicle Age			Vehicle Age	Performance
Repair Cost					Investment Cost

Ensuring the decision support model is both realistic and applicable to practical scenarios involved tasking two decision-makers with categorizing the criteria into three main groups. Table 7 illustrates the grouping of customer expectations and the corresponding importance levels assigned to these groups. For decision-maker A, pairwise comparisons reveal, for example, that luggage volume is three times more important than the vehicle segment, while vehicle age is considered only one-third as important as fuel consumption.

Table 8. Pairwise comparison matrix.

	K1	**K2**	**K3**	**K4**	**K5**	**K6**	**K7**	**K8**	**K9**	**K10**	**K11**	**K12**	**K13**
	SEGMENT	**VEHICLE AGE**	**ENGINE VOLUME**	**ENGINE POWER**	**FUEL CONSUMPTION**	**NCAP TEST RESULT**	**TRANSMISSION TYPE**	**TRUNK CAPASITY**	**VEHICLE MILEAGE**	**PRICE**	**NUMBER OF BREAKDOWNS**	**REPAIR COST**	**FEATURES**
K1	1.00	1.00	0.33	3.00	0.33	0.33	1.00	0.33	1.00	1.00	0.33	0.33	3.00
K2	1.00	1.00	0.33	3.00	0.33	0.33	1.00	0.33	1.00	1.00	0.33	0.33	3.00
K3	3.00	3.00	1.00	9.00	1.00	1.00	3.00	1.00	3.00	3.00	1.00	1.00	9.00
K4	0.30	0.33	0.11	1.00	0.11	0.11	0.33	0.11	0.33	0.33	0.11	0.11	1.00
K5	3.00	3.00	1.00	9.00	1.00	1.00	3.00	1.00	3.00	3.00	1.00	1.00	9.00
K6	3.00	3.00	1.00	9.00	1.00	1.00	3.00	1.00	3.00	3.00	1.00	1.00	9.00
K7	1.00	1.00	0.33	3.00	0.33	0.33	1.00	0.33	1.00	1.00	0.33	0.33	3.00
K8	3.00	3.00	1.00	9.00	1.00	1.00	3.00	1.00	3.00	3.00	1.00	1.00	9.00
K9	1.00	1.00	0.33	3.00	0.33	0.33	1.00	0.33	1.00	1.00	0.33	0.33	3.00
K10	1.00	1.00	0.33	3.00	0.33	0.33	1.00	0.33	1.00	1.00	1.00	1.00	3.00
K11	3.00	3.00	1.00	9.00	1.00	1.00	3.00	1.00	3.00	1.00	1.00	0.33	9.00
K12	3.00	3.00	1.00	9.00	1.00	1.00	3.00	1.00	3.00	1.00	3.00	1.00	1.00
K13	0.30	0.33	0.11	1.00	0.11	0.11	0.33	0.11	0.33	0.33	0.11	1.00	1.00
Toplam	**23.67**	**23.67**	**7.89**	**71.00**	**7.89**	**7.89**	**23.67**	**7.89**	**23.67**	**19.67**	**10.56**	**8.78**	**63.00**

Since the criteria of luggage volume and fuel consumption belong to the same expectation level group and have equal relative importance, their comparison coefficient is assigned a value of 1. Additionally, Table 7 includes the relative evaluation of the criteria defined by decision-maker B. The analyses presented in the subsequent sections of this study focus on decision-maker A. However, the same methodology can be applied to derive results for decision-maker B.

It should be noted that in cases where there is no time constraint for the decision maker, they may be required to fill in the pairwise comparison matrix provided in Table 8 based on the comparison scale data in Table 1. In this study, the analysis will proceed with the importance degree coefficients (9-3-1) assigned to the expectation levels divided into three groups. Based on the data obtained from the decision maker, the pairwise comparison matrix provided in Table 8 has been created.

The created pairwise comparison table was normalized with the formulas given in Equations 2 and 3. The criterion weights (w) were found and shown in Table 9. Eigenvalues for the consistency ratio calculation were calculated with Equation 4. The consistency ratio was calculated using Equation 5 with the weights obtained from the normalized matrix.

Tablo 9. Normalized matrix and criteria weights (w_i).

	K1	K2	K3	K4	K5	K6	K7	K8	K9	K10	K11	K12	K13	w	AW	AW/W
K1	0.04	0.04	0.04	0.04	0.04	0.04	0.04	0.04	0.04	0.05	0.03	0.04	0.05	**0.04**	0.58	13.68
K2	0.04	0.04	0.04	0.04	0.04	0.04	0.04	0.04	0.04	0.05	0.03	0.04	0.05	**0.04**	0.58	13.68
K3	0.13	0.13	0.13	0.13	0.13	0.13	0.13	0.13	0.13	0.15	0.09	0.11	0.14	**0.13**	1.73	13.68
K4	0.01	0.01	0.01	0.01	0.01	0.01	0.01	0.01	0.01	0.02	0.01	0.01	0.02	**0.01**	0.19	13.68
K5	0.13	0.13	0.13	0.13	0.13	0.13	0.13	0.13	0.13	0.15	0.09	0.11	0.14	**0.13**	1.73	13.68
K6	0.13	0.13	0.13	0.13	0.13	0.13	0.13	0.13	0.13	0.15	0.09	0.11	0.14	**0.13**	1.73	13.68
K7	0.04	0.04	0.04	0.04	0.04	0.04	0.04	0.04	0.04	0.05	0.03	0.04	0.05	**0.04**	0.58	13.68
K8	0.13	0.13	0.13	0.13	0.13	0.13	0.13	0.13	0.13	0.15	0.09	0.11	0.14	**0.13**	1.73	13.68
K9	0.04	0.04	0.04	0.04	0.04	0.04	0.04	0.04	0.04	0.05	0.03	0.04	0.05	**0.04**	0.58	13.68
K10	0.04	0.04	0.04	0.04	0.04	0.04	0.04	0.04	0.04	0.05	0.09	0.11	0.05	**0.05**	0.73	13.89
K11	0.13	0.13	0.13	0.13	0.13	0.13	0.13	0.13	0.13	0.05	0.09	0.04	0.14	**0.11**	1.54	13.67
K12	0.13	0.13	0.13	0.13	0.13	0.13	0.13	0.13	0.13	0.05	0.28	0.11	0.02	**0.12**	1.68	13.57
K13	0.01	0.01	0.01	0.01	0.01	0.01	0.01	0.01	0.01	0.02	0.01	0.11	0.02	**0.02**	0.30	13.83

As a result of the calculations, $\lambda = 13.69$; $CI = 0.058$ has been found, and RI for 13 criteria has been selected as 1.56 from Table 1. Since the consistency ratio $CR = 0.0371 < 0.1$, it has been determined that the criteria weights are consistent.

2.3. Alternative Selection with GRA

The problem, for which the criteria weights have been determined using the AHP method, will be resolved through GRA. The dataset, comprising the criteria and alternatives presented in Table 6, serves as the initial matrix for the analysis. The identified criteria are listed in Table 10, where they are categorized according to their nature as either maximization or minimization criteria, depending on whether they represent benefits or costs.

The reference series has been determined by selecting the maximum values for benefit criteria (e.g., a higher NCAP score is preferred) and the minimum values for cost criteria (e.g., a lower vehicle price is preferred).

Table 10. Dataset and reference series.

	K1	K2	K3	K4	K5	K6	K7	K8	K9	K10	K11	K12	K13
	MAK	**MİN**	**MAK**	**MAK**	**MİN**	**MAK**	**MAK**	**MAK**	**MİN**	**MİN**	**MİN**	**MİN**	**MAK**
RS	**8.2**	**4**	**1.8**	**152**	142.34	**5**	**9**	**471**	**77452**	**725000**	**147**	**4900**	**29**
A1	7.2	7	1.6	125	274.05	4	9	440	122000	800000	206	5835	26
A2	6.0	7	1.4	90	142.34	5	9	280	129000	725000	267	6530	25
A3	7.2	5	1.8	122	143.16	5	9	471	110600	841000	147	4900	27
A4	6.0	4	1	115	212.69	5	9	422	134000	935000	199	5700	28
A5	8.2	5	1.6	120	203.35	3	9	351	105000	965000	190	6400	26
A6	7.2	7	1.6	116	158.61	5	9	380	110000	900000	275	9890	26
A7	8.0	6	1.5	152	237.24	5	9	380	108000	1100000	245	9285	29
A8	6.0	6	1.4	100	282.23	3	9	352	77452	840000	187	5850	26
A9	7.2	6	1.5	120	204.51	5	1	419	93000	850000	185	5800	25
A10	6.0	7	1.4	100	253.60	4	9	301	122250	725000	198	5640	9

The normalization method based on the ratio was used for benefit criteria according to Equation 7 and for cost criteria according to Equation 8.

By obtaining the data from the normalization matrix, the differences between the values and the reference series were calculated, and the coefficient differences were determined. From the absolute value matrix data, $\Delta_{max} = 1$ and $\Delta_{min} = 0$ were found. The distinguishing coefficient ζ was selected as 0.5. The Grey Relational Grade, indicating the closeness of the alternatives to the reference series, was calculated using Equation 12.

The Grey Relational Coefficients, computed with the weights obtained from AHP, were multiplied, and the weighted Grey Relational Coefficients for each alternative were summed up to obtain the Grey Relational Grade. Table 11 shows the Grey Relational Grades and the ranking based on these grades.

Table 11. Grey relational grades and alternative ranking for decision-maker A.

	K1	K2	K3	K4	K5	K6	K7	K8	K9	K10	K11	K12	K13	Γ_1	$RANK_1$
	0.04	**0.04**	**0.13**	**0.01**	**0.13**	**0.13**	**0.04**	**0.13**	**0.04**	**0.05**	**0.11**	**0.12**	**0.02**		
A1	0.52	0.33	0.67	0.53	0.35	0.50	1.00	0.75	0.39	0.71	0.52	0.73	0.77	**0.59**	**6**
A2	0.33	0.33	0.50	0.33	1.00	1.00	1.00	0.33	0.35	1.00	0.35	0.60	0.71	**0.63**	**4**
A3	0.52	0.60	1.00	0.51	0.99	1.00	1.00	1.00	0.46	0.62	1.00	1.00	0.83	**0.91**	**1**
A4	0.33	1.00	0.33	0.46	0.50	1.00	1.00	0.66	0.33	0.47	0.55	0.76	0.91	**0.63**	**3**
A5	1.00	0.60	0.67	0.49	0.53	0.33	1.00	0.44	0.51	0.44	0.60	0.62	0.77	**0.57**	**8**
A6	0.52	0.33	0.67	0.46	0.81	1.00	1.00	0.51	0.46	0.52	0.33	0.33	0.77	**0.61**	**5**
A7	0.85	0.43	0.57	1.00	0.42	1.00	1.00	0.51	0.48	0.33	0.40	0.36	1.00	**0.58**	**7**
A8	0.33	0.43	0.50	0.37	0.33	0.33	1.00	0.45	1.00	0.62	0.62	0.72	0.77	**0.53**	**9**
A9	0.52	0.43	0.57	0.49	0.53	1.00	0.33	0.65	0.65	0.60	0.63	0.73	0.71	**0.65**	**2**
A10	0.33	0.33	0.50	0.37	0.39	0.50	1.00	0.36	0.39	1.00	0.56	0.77	0.33	**0.53**	**10**

In cases where the comparison matrix cannot be created due to the decision-maker's time constraints, it is still possible to determine the ranking of alternatives using GRA. In such instances, it is assumed that the criteria weights are equal, and the Grey Relational Grades are calculated accordingly. Table 12 presents not only the ranking obtained with equal criteria weights but also the Grey Relational Grades and alternative rankings for Decision-Maker A and Decision-Maker B.

Table 12. Grey relational grades in all cases.

	A1	A2	A3	A4	A5	A6	A7	A8	A9	A10
Γ_{equal}	0.6	0.6	**0.81**	**0.64**	0.62	0.59	**0.64**	0.58	0.6	0.53
$RANK_{eq}$	7	5	**1**	**3**	4	8	**2**	9	6	10
Γ_A	0.59	0.63	**0.91**	0.63	0.57	0.61	0.58	0.53	0.65	0.53
$RANK_A$	6	4	**1**	3	8	5	7	9	2	10
Γ_A	0.64	0.67	**0.77**	0.68	0.67	**0.70**	**0.85**	0.54	0.60	0.55
$RANK_B$	7	6	**2**	4	5	**3**	**1**	10	8	9

3. Conclusion

In this study, a decision support model for classified advertisement websites was examined. Using criteria based on the expectations of decision-makers, the vehicle selection problem was analyzed by evaluating 10 vehicles from a widely used classified ad website in Turkey through the AHP and GRA methods.

As a result of the analysis, for Decision-Maker A, who had expectations suitable for family use, a C-segment hybrid vehicle with a sedan body type, automatic transmission, and a 1.8 engine volume ranked first with a weight of 91%. In cases where the decision-maker faced time constraints and was unable to complete the comparison matrix, assuming equal weights for all criteria, the same alternative still ranked first with a score of 81%.

For Decision-Maker B, who determined criteria for a person new to driving, Alternative 7, a D-segment vehicle with a sedan body type, automatic transmission, and a 1.5 engine volume, ranked first with a score of 85%.

The decision support model developed for classified advertisement websites was evaluated as an innovative approach, as it can generate results solely based on the criteria data available within the website infrastructure, regardless of whether detailed or limited data is provided by the user.

This study presents a unique and adaptable methodology, offering a solution that can be applied to all online sales or classified advertisement websites, even in cases where very limited data is available.

References

[1] Kul Y, Şeker A, Yurdakul M. Bulanık çok kriterli karar verme yöntemlerinin alışılmamış imalat yöntemlerinin seçiminde kullanılması. Gazi Univ Müh Mim Fak Derg 2014; 29(3).

[2] Pophali GR, Chelani AB, Dhodapkar RS. Optimal selection of full-scale tannery effluent treatment alternative using integrated AHP and GRA approach. Expert Syst Appl 2011; 38(9): 10889-10895.

[3] Gülçiçek Tolun B, Tümtürk A. AHP ile bütünleşik gri ilişkisel analiz yöntemi ile makine seçimi: Tarım makinaları üretim işletmesinde bir uygulama. Yön ve Ekon Derg 2020; 27(1): 21-34.

[4] Samvedi A, Jain V, Chan FTS. An integrated approach for machine tool selection using fuzzy analytical hierarchy process and grey relational analysis. Int J Prod Res 2011; 50(12): 3211-3221.

[5] Tayyar N, Akcanlı F, Genç E, Erem I. BİST'e kayıtlı bilişim ve teknoloji alanında faaliyet gösteren işletmelerin finansal performanslarının analitik hiyerarşi prosesi (AHP) ve gri ilişkisel analiz (GİA) yöntemiyle değerlendirilmesi. Muh ve Fin Derg 2014; 61: 19-40.
[6] Wang Z, Lei T, Chang X, Shi X, Xiao J, Li Z, et al. Optimization of a biomass briquette fuel system based on grey relational analysis and analytic hierarchy process: A study using cornstalks in China. Appl Energy 2015; 157: 10.1016/j.apenergy.2015.04.079
[7] Ballı S, Karasulu B, Korukoğlu S. En uygun otomobil seçimi problemi için bir bulanık PROMETHEE yöntemi uygulaması. Dokuz Eylul Univ Ikt Id Bil Fak Derg 2016; 22(1): 139-147.
[8] Yavaş M, Ersöz T, Kabak M, Ersöz F. Otomobil seçimine çok kriterli yaklaşım önerisi. Isl ve Ikt Cal Derg 2014; 2(4): 110-118.
[9] Ghadikolaei S, Esbouei K, Antucheviciene J. Applying fuzzy MCDM for financial performance evaluation of Iranian companies. Technol Econ Dev Econ 2014; 20: 10.3846/20294913.2014.913274
[10] Gnanasekaran S, Ilangkumaran M, Govindan N, Raja A, Ragunadhan PM, Prakash J. A hybrid MCDM approach for evaluating an automobile purchase model. Int J Inf Decis Sci 2013; 5: 50-85.
[11] Hu J, Peng J. Application of supplier selection based on the AHP theory. Knowl Acquis Model Worksh (Int Symp) 2008: 1095-1097.
[12] Punniyamoorty M, Ponnusamy M, Lakshmi G. A combined application of structural equation modeling (SEM) and analytic hierarchy process (AHP) in supplier selection. Bench Int J 2012; 19(1): 70-92.
[13] Kannan V. Benchmarking the service quality of ocean container carriers using AHP. Bench Int J 2010; 17(5): 637-656.
[14] Yılmaz S. Uçak seçim kriterlerinin değerlendirilmesinde AHP ve bulanık AHP uygulaması. MSc, Yıldız Teknik Üniversitesi, İstanbul, Türkiye, 2006.
[15] Saaty TL. Decision making with the Analytic Hierarchy Process. Int J Serv Sci 2008; 1: 83-98.
[16] Saaty TL. Theory and Applications of the Analytic Network Process. USA: RWS Publications; 2005.
[17] Deng JL. Introduction to grey system theory. J Grey Syst 1989; 1(1): 1-24.
[18] Feng CM, Wang RT. Performance evaluation for airlines including the consideration of financial ratios. J Air Transp Manage 2000; 6: 133-142.
[19] Ecer F, Günay F. Borsa İstanbul'da işlem gören turizm şirketlerinin finansal performanslarının gri ilişkisel analiz yöntemiyle ölçülmesi. Anatolia 2014; 25(1): 35-48.
[20] Güngör İ, İşler DB. Analitik hiyerarşi yaklaşımı ile otomobil seçimi. Ulus Yön Ikt İsb Derg 2005; 1(2): 21-33.
[21] "Energy Market Regulatory Authority (EPDK). Monthly Bulletins." https://bildirim.epdk.gov.tr/bildirim-portal/faces/pages/tarife/petrol/yonetim/bultenSorgulaAylik.xhtml (accessed May 03, 2024).
[22] "Euro NCAP. The Ratings Explained." https://www.euroncap.com/en/car-safety/the-ratings-explained/(accessed May 03, 2024).
[23] "Consumer Reports. The Cost of Car Ownership." https://www.consumerreports.org/cars/car-maintenance/the-cost-of-car-ownership-a1854979198/(accessed May 03, 2024).
[24] "J.D. Power 2024 U.S. Vehicle Dependability Study." https://www.jdpower.com/business/press-releases/2024-us-vehicle-dependability-study-vds (accessed May 03, 2024).

Turkish Journal of Science & Technology
20(1), 101-108, 2025

Research Paper
https://doi.org/10.55525/tjst.1600893

Packaging Waste Recycling: A Pathway to Climate Change Mitigation in Türkiye

Berna CAPAR[1*], Martin KRANERT[2], Bulent TOPKAYA[3]
[1,3] University of Stuttgart, Faculty of Civil and Environmental Engineering, Institute for Sanitary Engineering, Water Quality, and Solid Waste Management, Stuttgart, Germany
[2] University of Akdeniz, Faculty of Engineering, Department of Environmental Engineering, Antalya, Türkiye
[*1] bernacapar@gmail.com, [2]martin.kranert@iswa.uni-stuttgart.de [3] bulenttopkaya@gmail.com

(Received: 13/12/2024; Accepted: 28/02/2025)

Abstract: Climate change has significantly affected numerous aspects of our planet, with weather patterns being one of the most visibly impacted. The growing concentration of greenhouse gases (GHGs) in the atmosphere traps more heat, leading to disruptions in weather systems and amplifying the challenges posed by climate change. The main sources of greenhouse gas (GHG) emissions are fossil fuels, with the largest contributors being the power generation, transportation, and industrial combustion sectors. Additional significant sources include agriculture, fuel extraction, buildings, and waste management both globally and in Türkiye. Recycling packaging waste plays a vital role in mitigating climate change by reducing GHG emissions and conserving energy. It minimizes waste sent to landfills and promotes a circular economy, enabling the continual reuse and recycling of materials. This process decreases the reliance on new raw materials, further reducing environmental impacts and contributing to a more sustainable future.

Key words: Climate change, Greenhouse Gas (GHG), Recycling, Packaging waste.

Ambalaj Atığı Geri Dönüşüm: Türkiye'de İklim Değişikliğiyle Mücadele için Bir Yol

Özet: İklim değişikliği, gezegenimizin birçok yönünü önemli ölçüde etkilemiş olup, hava olayları en görünür şekilde etkilenen alanlardan biridir. Atmosferde artan sera gazı (GHG) yoğunluğu, daha fazla ısının tutulmasına neden olarak hava sistemlerinde bozulmalara yol açmakta ve iklim değişikliğinin yarattığı zorlukları artırmaktadır. Sera gazı (GHG) emisyonlarının başlıca kaynakları fosil yakıtlar olup, en büyük katkıyı enerji üretimi, ulaşım ve endüstriyel yanma sektörleri sağlamaktadır. Ayrıca, tarım, yakıt çıkarma, binalar ve atık yönetimi hem dünya genelinde hem de Türkiye'de önemli diğer önemli kaynaklar arasında yer almaktadır. Ambalaj atıklarının geri dönüşümü, sera gazı emisyonlarını azaltarak ve enerji tasarrufu sağlayarak iklim değişikliğiyle mücadelede hayati bir rol oynamaktadır. Bu süreç, depolama alanlarına gönderilen atık miktarını azaltmakta ve malzemelerin sürekli olarak yeniden kullanılıp geri dönüştürülmesini sağlayan döngüsel bir ekonomiyi teşvik etmektedir. Böylece yeni ham maddelere olan bağımlılık azalmakta, çevresel etkiler en aza indirilmekte ve daha sürdürülebilir bir geleceğe katkı sağlanmaktadır.

Anahtar kelimeler: İklim değişikliği, Sera gazı, Geri dönüşüm, Ambalaj atığı.

1. Introduction

Climate change has profoundly affected various aspects of our planet, with the weather being one of the most impacted. The increasing concentration of greenhouse gases in the atmosphere traps more heat, disrupting weather patterns and intensifying climate-related challenges [1].

Greenhouse gases (GHGs) in the atmosphere trap infrared radiation emitted by the earth, helping to retain heat-a phenomenon known as the greenhouse effect. Human activities have significantly increased GHG emissions, contributing to a global temperature rise of approximately 1.1°C. Greenhouse gases effects are categorized into two categories which are natural and enhanced effects. The natural greenhouse effect arises from naturally occurring greenhouse gases and is essential for sustaining life on Earth. The enhanced greenhouse effect, on the other hand, refers to the additional warming caused by increased concentrations of greenhouse gases (GHGs) due to human activities [2].

Since the start of the 21st century, global greenhouse gas (GHG) emissions have been on a steady upward trend, largely driven by contributions from China and other emerging economies. As of 2023, global GHG emissions reached a record high of 53 Gt CO_2 eq (excluding emissions from Land Use, Land Use Change, and Forestry). This marks a 1.9% increase or an additional 994 Mt CO_2 eq compared to 2022 levels [3]. According to

[*] Corresponding author: bernacapar@gmail.com. ORCID Number of authors: [1] 0009-0006-0834-9241, [2] 0000-0003-3614-7920 [3]0000-0003-3082-7415.

research, the average global temperature has risen 1.1°C above pre-industrial levels and already exceeded the 1.5°C threshold at the beginning of 2024. During the same period, annual global greenhouse gas (GHG) emissions reached 59 billion tons of CO_2 eq. At this critical juncture, it is imperative to adopt a decisive stance to mitigate the GHG emissions driving climate change [4].

The primary sources of greenhouse gas (GHG) emissions are fossil fuels, with the power industry, transportation, and industrial combustion sectors being the largest contributors. Other significant sources include agriculture, fuel extraction, buildings, and waste management [5]. Globally, the primary greenhouse gases (GHGs) released by human activities are carbon dioxide (CO_2), methane (CH_4), nitrous Oxide (N_2O), and fluorinated gases. CO_2 emissions mainly arise from the combustion of fossil fuels. Additionally, deforestation, land clearing for agriculture, and soil degradation contribute to CO_2 release from the landscape. CH_4 emissions mainly result from agricultural activities, waste management, energy production and consumption, and biomass burning. N_2O emissions predominantly originate from agricultural practices, particularly fertilizer use while Fluorinated gases are released through industrial processes, refrigeration, and various consumer products. These include hydrofluorocarbons (HFCs), perfluorocarbons (PFCs), and sulfur hexafluoride (SF_6) [6].

Energy efficiency and transitioning to renewable energy can address only 55% of global emissions. Achieving net-zero requires transforming how we produce and consume products, materials, and food. By incorporating the three principles of the circular economy into the design of products, services, and systems, it can tackled the GHG emissions linked to industry, agriculture, and land use emissions that the energy transition alone cannot resolve. Greenhouse gas emissions are reduced across the value chain by eliminating waste and pollution, energy is preserved in products and materials by keeping them in circulation, and carbon is sequestered in soil and products through nature regeneration [7].

2. Climate Change

Climate change is caused by human activities and threatens life on Earth. With increasing greenhouse gas emissions, climate change is occurring much faster than expected**.** Action must be dramatically increased at all levels to address climate change. While many measures are being taken worldwide such as increasing investment in renewable energy more must be done. The world needs to transform its energy, industry, transportation, food, waste management, agriculture, and forestry systems to limit global temperature increases to well below 2°C, and possibly even below 1.5°C [8].

To combat climate change, the United Nations Framework Convention on Climate Change (UNFCCC) was adopted in 1992, followed by the Kyoto Protocol in 1997, and the Paris Agreement in 2015 on a global scale. Türkiye continues its efforts to reduce greenhouse gas emissions and adapt to the adverse effects of climate change, in line with the "common but differentiated responsibilities and respective capabilities" principle of the UNFCCC, to which it became a party in 2004. Furthermore, Turkey has demonstrated its commitment to combating climate change by setting a net-zero emission targets and becoming a party to the Paris Agreement [4].

The Paris Agreement which is a legally binding international treaty on climate change is adopted by 196 parties at the UN Climate Change Conference (COP21) in Paris, France, by 2015. The primary goal of the agreement is to limit the increase in global average temperature to well below 2°C above pre-industrial levels and to pursue efforts to limit the temperature increase to 1.5°C above pre-industrial levels. To achieve this, greenhouse gas emissions must peak no later than 2025 and decrease by 43% by 2030 [9].

2.1. Greenhouse Gas Emissions (GHGs)

Greenhouse gases (GHGs) warm the earth by absorbing energy and slowing the rate at which the energy escapes to space; they act like a blanket insulating the earth. The main greenhouse gases are carbon dioxide (CO_2), methane (CH_4), nitrous oxide (N_2O), hydro fluorocarbons (HFCs), perfluorocarbons (PFCs), and Sulphur hexafluoride (SF_6). Different GHGs can have different effects on the earth's warming. Two key ways in which these gases differ from each other are their ability to absorb energy (their "radioactive efficiency"), and how long they stay in the atmosphere (also known as their "lifetime") (Table 1) [10].

Table 1. Global Warming Potential (GWP) and Atmospheric Lifetime of Main GHGs [11].

Greenhouse Gases	Chemical Formula	Global Warming Potential *AR5 (GWP-100 year)	Atmospheric Lifetime (years)
Carbon dioxide	CO_2	1	*
Methane	CH_4	28	12.4
Nitrous Oxide	N_2O	265	121
Chlorofluorocarbons (CFC11)	CCl_3F	4,660	45
Hydrofluorocarbons (HFCs)	Various	12-12,400	<1-222
Perfluorocarbons (PFCs)	Various	6,630-11,100	2,600-50,000
Sulphur hexafluoride	SF_6	23,500	3,200

* No single lifetime can be given
AR5 refers to the IPCC Fifth Assessment Report (2014)

The waste sector is not only responsible for GHG emissions but also contributes to avoiding GHG emissions. In the waste sector, GHG emission reduction is achieved through material (reuse, recycling, composting, etc.) and energy (biogas, electricity, and heat generation) recovery and thus an environmental benefit accounted for as avoided emissions [12].

2.1.1. Greenhouse Gas Emissions (GHGs) by Sectors: A Global and Türkiye Overview

Global GHG emission reached 53 Gt (billion tons) CO_2 eq in 2023. The power industry was the largest contributor, responsible for 15.1 Gt CO_2 eq (28.5%) of the total emissions, followed by transportation sector with 8.4 Gt CO_2 eq (15.8%). The agriculture sector emitted 6.5 Gt CO_2 eq (12.3%), while industrial combustion and fuel exploitation accounted for 6.4 Gt CO_2 eq (12.1%) and 5.9 Gt CO_2 eq (11.1%), respectively. The processes sector contributed 4.9 Gt CO_2 eq (9.2%) of the total emissions, and buildings were responsible for 3.8 Gt CO_2 eq (7.2%). Waste management had the smallest share, emitting 2 Gt CO_2 eq (3.8%) (Fig.1). This distribution highlights the significant role of energy production, transportation, and agriculture in overall GHG emissions [5].

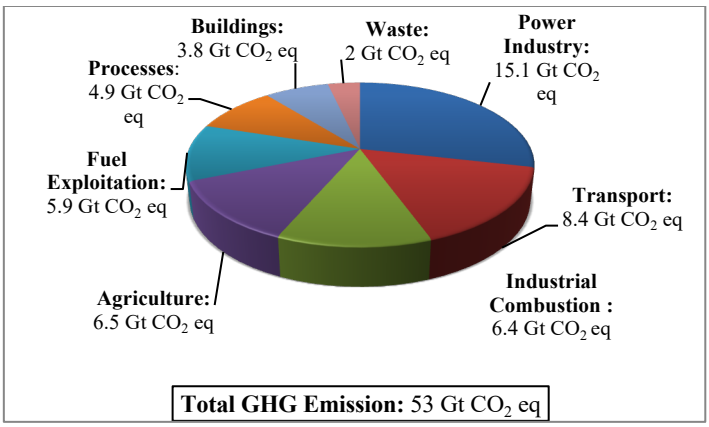

Figure 1. Global GHG Emissions by Sector, 2023 [5].

In 2022, Türkiye's total greenhouse gas (GHG) emissions amounted to 553 Mt (million tons) CO_2 eq (equivalent). The energy sector was the largest contributor, accounting for 400.6 Mt CO_2 eq (71.8%), followed by the agriculture sector with 71.5 Mt CO_2 eq (12.8%). Emissions from industrial processes and product use were 69.9 Mt CO_2 eq (12.5%), while the waste sector contributed the smallest share at 16.3 Mt CO_2 eq (2.9%) (Fig. 2) [13]. The data highlights the dominance of the energy sector in Türkiye's GHG emissions, followed by significant contributions from agriculture and industrial processes.

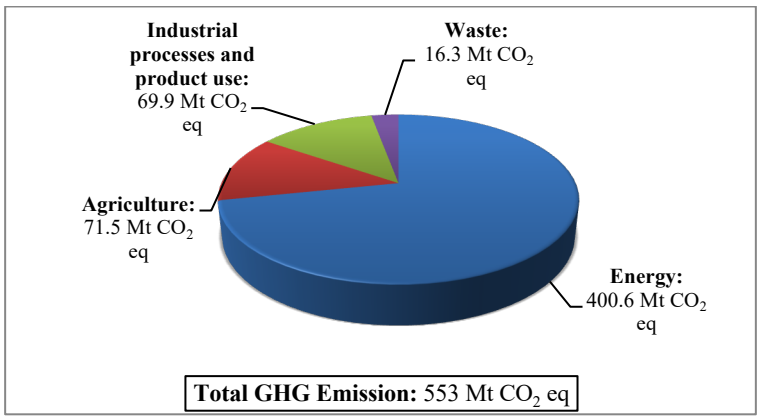

Figure 2. GHG Emissions in Türkiye by Sector, 2023 [13].

3. Material and Method

In Türkiye separately collected packaging waste including graphic paper mainly consists of paper-cardboard (e.g., newspapers, magazines, books, and packaging boxes), plastic (e.g., PET bottles, plastic bags, plastic packaging), glass (e.g., glass bottles and jars), and metal (e.g., aluminum beverage cans and tin cans). This study examines the avoided impacts specifically avoided GHG emissions and energy savings associated with the recycling of packaging waste, including paper-cardboard, plastic, and glass waste. To achieve this, data on municipal solid waste (MSW) production and composition were obtained from the literature. The avoided GHG emissions and energy savings data used in the analysis were sourced from [14], [15], [16]. Using these references, the avoided GHG emissions and energy savings from packaging waste recycling in Türkiye were calculated.

109.2 million tons of MSW were generated in Türkiye by 2022 [17]. According to Türkiye's waste characterization data, biowaste accounted for 55.54% of the total waste, paper-cardboard made up 8.11%, glass constituted 3.38%, metal represented 1.37%, and hazardous waste comprised 0.43%. The remaining 8.03% consisted of other types of waste [18].

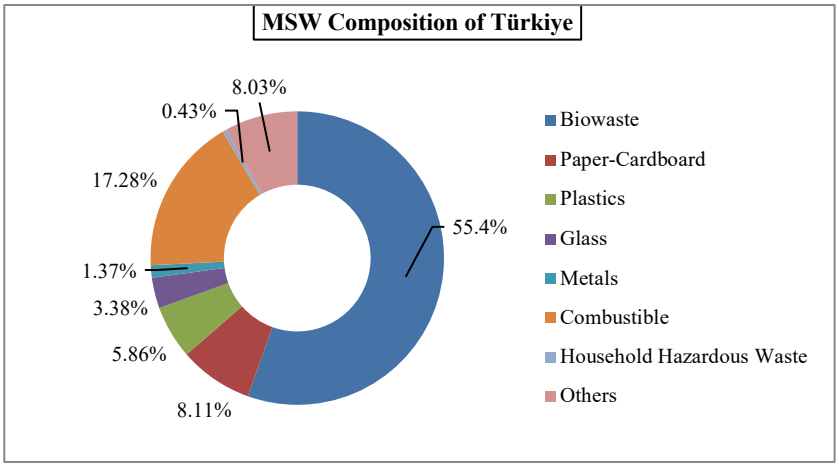

Figure 3. MSW Composition of Türkiye, 2016 [18].

Based on the MSW composition data in Fig. 3, the compositions of paper-cardboard, plastics, and glass waste were 8.11%, 5.86%, and 3.38% repectively. These packaging waste values constitute 17.35% of the total MSW (Table 2). These values of each recyclable in the table are multiplied by 100 and divided by the total packaging waste to calculate the amount in the total packaging waste.

Table 2. Calculation of Recyclable Waste in Total MSW and Packaging Waste.

Recyclable waste	**(%)**
Paper-Cardboard$_{(a)}$	8.11
Plastic$_{(a)}$	5.86
Glass$_{(a)}$	3.38
Total packaging waste	17.35

Secondly, the data on avoided GHG emissions and energy savings were obtained from the literature (Table 3). The percentage of materials used in primary and secondary production, as well as the cumulative energy consumption (CEC), GHG emissions, avoided energy, and avoided GHG emissions values associated with the primary and secondary production of recyclables, were used in the calculations.

Table 3. Savings (CEC and GHG emissions) through secondary production of marketable intermediate products from secondary raw materials compared to primary production [14], [15], [16].

	Primary Raw Material	**Secondary Raw Material**	**CEC**	**GHG Emissions**	**Avoided Energy**	**Avoided GHG**
	(%)		**(MJ/Mg)**	**(kg CO_2 eq)/Mg**	**(MJ/Mg)**	**(kg CO_2 eq/Mg)**
GLASS						
Primary production of green container glass	95		10.670	921		
Secondary production of green container glass		80% Broken Glass	7.270	506	3.400	415
PLASTICS						
PET beverage bottles, primary production	100		105.700	3.495		
PET beverage bottles, secondary production		30	78.700	2.685	27.000	810
PAPER-CARDBOARD						
Primary fibre paper	100		18.000	-		
Recycled Paper		100	7.200	-	10.800	160

The avoided GHG and avoided energy values for each type of recyclable waste were calculated by multiplying the avoided GHG and energy values from Table 2 by the corresponding amounts of glass, plastic, and paper-cardboard.

4. Results

Based on the MSW composition data in Table 2, packaging waste consisting of paper-cardboard, plastics, and glass accounts for 17.35% of the total waste. This corresponds to 18.96 million tons of packaging waste, including 8.86 million tons of paper-cardboard, 6.4 million tons of plastic, and 3.7 million tons of glass (Table 4).

Table 4. Amount of Recyclable Waste in MSW of Türkiye, 2022.

Recyclable Waste	Calculation	Result
Paper-Cardboard $_{(b)}$	(Paper-Cardboard$_{(a)}$ x Total MSW)/100	(8.11 x 109.2 Mt)/100 = 8.86 Mt
Plastic$_{(b)}$	(Plastic$_{(a)}$ x Total MSW)/100	(5.86 x 109.2 Mt)/100 = 6.4 Mt
Glass$_{(b)}$	(Glass$_{(a)}$ x Total MSW)/100	(3.38 x 109.2 Mt)/100 = 3.7 Mt
Total packaging waste	Paper-Cardboard$_{(b)}$ + Plastic$_{(b)}$ + Glass$_{(b)}$	8.86 Mt + 6.4 Mt + 3.7 Mt = 18.96 Mt

The values of each recyclable material in Table 4 are multiplied by 100 and divided by the total packaging waste to calculate their percentage in the total packaging waste. Based on these calculations, paper-cardboard comprises 46.73%, plastic comprises 33.75%, and glass comprises 19.52% of the total packaging waste (Table 5).

Table 5. Amount of Recyclable Waste in Total Packaging Waste of Türkiye, 2022.

Recyclable Waste	Calculation	Result
Paper-Cardboard	(Paper-Cardboard $_{(b)}$ x 100)/Total Packaging waste	(8.86 Mt x100)/18.96 Mt = 46.73%
Plastic	(Plastic$_{(b)}$ x 100)/Total Packaging waste	(6.4 Mt x100)/18.96 Mt = 33.75%
Glass	(Glass$_{(b)}$ x 100)/Total Packaging waste	(3.7 Mt x100)/18.96 Mt = 19.52%
Total packaging waste	Paper-Cardboard + Plastic + Glass	100%

The avoided greenhouse gas (GHG) emissions and energy savings were calculated by multiplying the values in Table 3 by the quantities of each recyclable material, as determined through inventory analysis. Based on these calculations, recycling 1 ton of packaging waste in Türkiye leads to a reduction of 419.1 kg CO_2 eq in GHG emissions and saves 13,540.7 MJ (3,764.3 kWh) of energy (Table 6).

Avoided GHG emission and energy savings are calculated by multiplying the total avoided GHG and energy values by the total packaging waste, as follow:

Avoided GHG Emissions and Energy Values of Packaging Waste of Türkiye by 2022:

- **Avoided GHG =** (Avoided GHG emissions per ton of packaging waste x total packaging waste)/1 ton

  = (419.1 kg CO_2 eq x 10^{-3} tons/kg) x (18.96 x 10^6 tons/year)/1ton

  = 7,946 x 10^3 tons CO_2 eq = 7.9 x 10^6 tons CO_2 eq/year

• **Avoided Energy =** (Avoided energy per ton of packaging waste x Total packaging waste)/1 ton

= (3,764.3 kWh) x (18.96 x 10^6 tons/year)/1ton

= 71,371 x 10^6 kWh/year

Based on these calculations, recycling 1 ton of packaging waste in Türkiye resulted in a reduction of 7.9 x 10^6 tons of CO_2 eq GHG emissions and saved of 71,371 x 10^6 kWh of energy by 2022 (Table 7).

Table 6. Avoided GHG and Energy of Recyclable Waste.

Recycled Materials (1 ton)	Avoided GHG (kg CO_2 eq)	Avoided Energy (MJ)
Glass	0.415 (kg CO_2 eq/kg) x 195.2 kg = 81.1	3.4 (MJ/kg) x 195.2 kg = 663.7
Plastic	0.78 (kg CO_2 eq/kg) x 337.5 kg = 263.2	23.2 (MJ/kg) x 337.5 kg = 7,830
Paper-Cardboard	0.16 (kg CO_2 eq/kg) x 467.3 kg = 74.8	10.8 (MJ/kg) x 467.3 kg = 5,047
Total	419.1 kg CO_2 eq	13,540.7 MJ = 3,764.3 kWh

Table 7. GHG Emissions and Energy Values of Packaging Waste of Türkiye by 2022

GHG and Energy	Value
Total GHG (from Waste sector)	16.3 x 10^6 tons CO_2 eq/year
Avoided GHG	7.9 x 10^6 tons CO_2 eq/year
Avoided Energy	71,371 x 10^6 kWh/year

5. Conclusions

Waste management is closely linked to climate change, as the way waste is managed has significant effects on greenhouse gas (GHG) emissions and the broader environment. In particular, effective waste management through practices such as recycling, composting, and diverting waste from landfills can play a crucial role in reducing GHG emissions and supporting global efforts to combat climate change.

Addressing GHG emissions in these key sectors will be essential for climate mitigation efforts. Based on the findings in this study, global GHG emissions amounted to 53 Gt (billion tons) CO_2 eq in 2023. The power industry was the largest contributor, responsible for 15.1 Gt CO_2 eq (28.5%) of the total emissions, followed by transportation sector with 8.4 Gt CO_2 eq (15.8%). The agriculture sector emitted 6.5 Gt CO_2 eq (12.3%), while industrial combustion and fuel exploitation accounted for 6.4 Gt CO_2 eq (12.1%) and 5.9 Gt CO_2 eq (11.1%), respectively. The processes sector contributed 4.9 Gt CO_2 eq (9.2%) of the total emissions, and buildings were responsible for 3.8 Gt CO_2 eq (7.2%). Waste management had the smallest share, emitting 2 Gt CO_2 eq (3.8%). This distribution highlights the significant role of energy production, transportation, and agriculture in overall GHG emissions

Total GHG emissions amounted to 553 Mt (million tons) CO_2 eq in Türkiye by 2022. The energy sector was the largest contributor, accounting for 400.6 Mt CO_2 eq (71.8%), followed by the agriculture sector with 71.5 Mt

CO_2 eq (12.8%). Emissions from industrial processes and product use totaled 69.9 Mt CO_2 eq (12.5%), while the waste sector contributed the smallest share at 16.3 Mt CO_2 eq (2.9%). 109.2 million tons of MSW were generated, with packaging waste comprising paper-cardboard, plastic, and glass making up 17,35% of the total MSW. Recycling 1 ton of packaging waste saves 419.1 kg CO_2 eq in GHG emissions and 13,540.7 MJ (3,764.3 kWh) of energy. These values correspond to a reduction of 7.9 Mt CO_2 eq GHG and a recovery of 71,371 million kWh of energy, if all 18.96 Mt of packaging waste produced in 2022 were to be recycled.

Recycling packaging waste helps mitigate climate change by reducing greenhouse gas emissions and conserving energy. It also decreases the amount of waste sent to landfills, fostering a circular economy where materials are continually reused and recycled. This reduces the demand for new raw materials and the associated environmental impacts, including GHG emissions.

References

[1] Rajak J. A Preliminary Review on Impact of Climate Change and Our Environment With Reference to Global Warming, International Journal of Environmental Sciences, 2021; 10(1): 11-14.

[2] WMO (World Meteorological Organization), All Topics/Greenhouse Gases. Available at: https://wmo.int/topics/greenhouse-gases [Accessed: 4.12.2024].

[3] EDGAR (Emissions Database for Global Atmospheric Research), GHG Emissions of All World Countries, EC (European Comission), JRC (Joint Research Centre), 2024.

[4] Climate Change Mitigation Strategy and Action Plan, 2024-2030, Ministry of Environment and Urbanization, Climate Change Directorate, 2024.

[5] Statista, Annual Greenhose Gas (GHG) Emissions Worldwide from 1990-2023, by Sector," 2024. Available at: https://www.statista.com/statistics/1423179/global-ghg-emissions-by-sector-annual/ [Accessed.1 12.2024].

[6] (USEPA) United States Environmental Protection Agency. Global Greenhouse Gas Overview, Global Emissions and Removals by Gas, September 2024. Available at: https://www.epa.gov/ghgemissions/global-greenhouse-gas-overview [Accessed: 26.02.2025].

[7] EMF (Ellen Macarthur Foundation), Fixing the Economy to Fix Climate Change. Available at: https://www.ellenmacarthurfoundation.org/topics/climate/overview [Accessed: 3.12.2024].

[8] UN (United Nations) Climate Change, What is Goal 13 - Climate Action?, 2023. Available at: https://www.un.org/sustainabledevelopment/wp-content/uploads/2023/09/Goal-13_Fast-Facts.pdf [Accessed: 5.12.2024].

[9] UNFCC (United Nations Framework Convention on Climate Change), The Paris Agreement. Available at: https://unfccc.int/process-and-meetings/the-paris-agreement [Accessed: 6.12.2024].

[10] USEPA (United States Environmental Protection Agency), Understanding Global Warming Potentials. Greenhouse Gas (GHG) Emissions, Sources of GHG Emissions and Removals, 2012. Available at: https://www.epa.gov/ghgemissions/understanding-global-warming-potentials#Learn%20why [Accessed: 28.11.2024].

[11] Pachauri RK, (Chairman IPCC) and Meyer L (Head, Technical Support Unit IPCC). Core Writing Team (Synthesis Report IPCC), IPCC (International Panel on Climate Change), Climate Change, 2014.

[12] GHG (Greenhouse Gas) Protocol, Protocol for the Quantification of Greenhouse Gas Emissions from Waste Management Activities. Version 5.0. EPE (Entreprises pour l'Environnement), 2013.

[13] Tuik (Turkish Statistical Institute), Greenhouse Gas Emissions Statistics, 1990-2022, 2024. Available at: https://data.tuik.gov.tr/Bulten/Index?p=Greenhouse-Gas-Emissions-Statistics-1990-2022-53701&dil=2 [Accessed: 15.11.2024].

[14] Probas (Prozessorientierte Basisdaten für Umweltmanagementsysteme), "Prozesskategorien, Materialien und Produkte, Umwelt Bundesamt. Available at: https://www.probas.umweltbundesamt.de/en/einblick/#/ [Accessed: 20.11.2024].

[15] Frischenschlager H, Karigl B, Lampert C, Pölz W, Schindler I, Tesar M, Wiesenberger H, Winter B, Klimarelevanz Ausgewählter Endbericht Recycling-Prozesse in Österreich, Endbericht, Umweltbundesamt, 2010.

[16] Regensburg, "Recycling für den Klimaschutz Ergebnisse der Studie von Fraunhofer Umsicht und Interseroh zur CO_2-Einsparung durch den Einsatz von Sekundärrohstoffen, 2008.

[17] TURKSTAT (Turkish Statistical Institute), Waste Statistics, 2022, 14 November 2022. Available at: https://data.tuik.gov.tr/Bulten/Index?p=Waste-Statistics-2022-49570&dil=2 [Accessed: 10.11.2024].

[18] Kunt M, Gurbuzler D, Erkal IF, Yıldırım K, 6th State of Environment Report for Republic of Turkey, Ministry of Environment and Urbanization Directorate General of Environmental Impact Assessment, Permit and Inspection, Ankara, 2020.

Turkish Journal of Science & Technology
20(1), 109-119, 2025

Research Paper
https://doi.org/10.55525/tjst.1375167

Innovative Decision-Making with VFP-Soft Sets: A Comparative Analysis

Orhan DALKILIÇ[1*]
[1] Department of Mathematics, Faculty of Arts and Science, Mersin University, Mersin, Turkey
[*1] orhandlk952495@hotmail.com

(Geliş/Received: 12/10/2023; Kabul/Accepted: 07/08/2024)

Abstract: This study delves into fundamental set properties within the framework of virtual fuzzy parameterized (VFP-)soft set theory. It provides a comprehensive examination of these properties, offering essential insights and considerations. The study also simplifies the definition of VFP-soft sets to streamline data analysis, making it more accessible and less complex. Furthermore, the paper explores the integration of two distinct approaches for parameter weighting in VFP-soft sets. Notably, the research introduces a novel decision-making algorithm grounded in VFP-soft sets and conducts a comparative analysis to evaluate its effectiveness. This work contributes to the field by enhancing the understanding of VFP-soft sets and their applications, while also providing a practical decision-making tool for real-world scenarios.

Key words: Fuzzy et, soft set, VFP-soft set, algorithm, decision-making.

VFP-Esnek Kümelerle Yenilikçi Karar Verme: Karşılaştırmalı Bir Analiz

Öz: Bu çalışma sanal bulanık parametreli (VFP-)yumuşak küme teorisi çerçevesinde temel küme özelliklerini incelemektedir. Bu özelliklerin kapsamlı bir incelemesini sağlayarak temel içgörüleri ve değerlendirmeleri sunar. Çalışma aynı zamanda veri analizini kolaylaştırmak için VFP-soft kümelerinin tanımını basitleştirerek onu daha erişilebilir ve daha az karmaşık hale getiriyor. Ayrıca makale, VFP-soft kümelerinde parametre ağırlıklandırmaya yönelik iki farklı yaklaşımın entegrasyonunu araştırıyor. Özellikle araştırma, VFP-soft kümelerine dayanan yeni bir karar verme algoritması sunmakta ve bunun etkinliğini değerlendirmek için karşılaştırmalı bir analiz gerçekleştirmektedir. Bu çalışma, VFP-soft kümelerinin ve uygulamalarının anlaşılmasını geliştirerek alana katkıda bulunurken, aynı zamanda gerçek dünya senaryoları için pratik bir karar verme aracı da sağlıyor.

Anahtar kelimeler: Bulanık küme, esnek küme, VFP-esnek küme, algoritma, karar verme.

1. Introduction

Uncertainty is an important feature that must be addressed during data analysis to increase the robustness of the results. However, parsing the uncertainty of the data is generally not that easy. Therefore, many mathematical approaches based on the analysis of specific data may be insufficient to capture this component. Many theories have been introduced to deal with the uncertainty in the data. One of these theories is the fuzzy set (FS) theory, introduced to the literature by Zadeh [1] in 1965. In the following years, another important mathematical model of the effort to cope with uncertainty, the rough set (RS) theory [2] was proposed. However, FS and RS theories are difficult to apply objectively to uncertainty problems. Molodtsov [3], who thinks that the reason for this difficulty is due to the lack of a parameterization tool, proposed the soft set (SS) theory in 1999. Then, Maji et al. [4] defined the basic operations of SSs in order to make a detailed theoretical study on SSs. In addition, in the following years, Maji et al. [5] defined the concept of fuzzy soft sets (FSS) and gave an application based on FSS theory for a decision-making problem in [6]. In addition, Çağman and Enginoğlu [7] have worked on soft decision-making problems and Çağman et al. proposed an application of SS theory for a decision-making problem in [8]. On the other hand, Chen et al. [9] discussed the parameterization reduction and applications of SS. Moreover, an adjustable approach for FSS based on decision-making has been given by Feng et al. [10]. Later, Çağman et al. presented a new perspective on FSSs in their studies [11]. The combination of SS and FSS theories enabled the development of different algorithms for solving uncertainty problems [12-21].

In the following years, Çağman [22] defined the concept of fuzzy parameterized (FP-)soft set (FPSS) in order to achieve near ideal results for uncertainty problems encountered in almost every field. However, FPSSs were insufficient to express this situation when the uncertainty consisted of more than one stage. In order to overcome this deficiency, virtual fuzzy parameterized (VFP)-soft sets (VFPSSs) were proposed by Dalkılıç and Demirtaş [23] in 2021. This set theory [23] consists of lower and upper approximate functions in expressing more than one stage, so three FP-soft sets can be evaluated. This novel set theory incorporated lower and upper approximate

* Corresponding author: orhandlk952495@hotmail.com. ORCID Number of authors: [1]0000-0003-3875-1398

functions, facilitating evaluation across multiple stages of uncertainty, effectively surpassing the limitations of FPSSs. Motivated by the need for a comprehensive approach to uncertainty management, this study revisits VFP-soft sets, aiming to streamline their representation and enhance their utility in decision-making contexts. The primary motivations and contributions of this paper are outlined as follows:

- **Simplification of Complex Structures:** We propose a streamlined representation of VFP-soft sets to tackle complex data, enhancing accessibility and usability.
- **Exploration of Incomplete Operations:** We examine incomplete basic set operations on VFP-soft sets, contributing to the ongoing development of the theory and expanding its applicability.
- **Development of a New Decision-Making Algorithm:** We present a novel decision-making algorithm leveraging fuzzy decision sets. Notably, this algorithm integrates the importance weights of parameters, accommodating two distinct approaches within VFP-soft sets. The most important feature of this algorithm is that it also considers the importance weights of the parameters for VFP-soft sets that focus on two different approaches.

Through this study, we aim to provide a comprehensive overview of VFP-soft sets, elucidating their potential in addressing uncertainty challenges. A short representation is expressed for this analyzed set theory and some new properties and remarks were included. Additionally, we introduce a new algorithm tailored to optimize decision-making processes within this framework, offering a comparative analysis with existing methodologies [23]. By addressing these key points, we endeavor to enhance the understanding and applicability of VFP-soft sets, ultimately contributing to more effective uncertainty management across diverse domains.

2. Preliminaries

In this section, some definitions and results are reminded. Detailed explanations related to VFPSSs can be found in [23].

Throughout this paper, let $U = \{u_1, u_2, \dots\}$ be a universe set, $P = \{p_1, p_2, \dots\}$ be a set of parameters and X be a FS over P. In this case, the lower virtual parameter set and the upper virtual parameter set are expressed as $\underline{P} = \left\{p_1^{\underline{\alpha_1}}, p_2^{\underline{\alpha_2}}, \dots\right\}$ and $\overline{P} = \left\{p_1^{\overline{\alpha_1}}, p_2^{\overline{\alpha_2}}, \dots\right\}$, respectively. Also, let 2^U denote the power set of U and $\emptyset \neq A \subseteq P$.

Definition 1. [1] A FS X over U is a set defined by $\mu_X: U \to [0,1]$. μ_X is called the membership function of X, and the value $\mu_X(u)$ is called the grade of membership of $u \in U$. Thus, as given in Equation (1), a FS X over U can be represented as follows:

$$X = \{(\mu_X(u)/u): u \in U, \mu_X(u) \in [0,1]\}. \tag{1}$$

Definition 2. [3] A pair (F, P) is called a SS over U, where F is a mapping given by $F: P \to 2^U$. In other words, a SS over U is a parameterized family of subsets of U for $p \in P$, $F(p)$ may be considered as the set of p-approximate elements of (F, P).

Definition 3. [22] A FPSS Φ_X on U is defined by the set of ordered pairs, given in Equation (2)

$$\Phi_X = \left\{\left(\frac{\mu_X(p)}{p}, \varphi_X(p)\right): p \in P, \mu_X(p) \in [0,1]\right\}, \tag{2}$$

where the function $\varphi_X: P \to 2^U$ is called approximate function such that $\varphi_X(p) = \emptyset$ if $\mu_X(p) = 0$, and the function $\mu_X: U \to [0,1]$ is called membership function of FPSS Φ_X.

State that the set of all FPSSs over U will be denoted by $FPS(U)$.

Definition 4. [22] Let $\Phi_X \in FPS(U)$. Then a fuzzy decision set of Φ_X, denoted by Φ_X^d, is defined by Equation (3).

$$\Phi_X^d = \left\{\mu_{\Phi_X^d}(u)/u : u \in U\right\} \tag{3}$$

which is a FS over U, its membership function $\mu_{\Phi_X^d}$ is defined by $\mu_{\Phi_X^d}: U \to [0,1]$, given in Equation (4)

$$\mu_{\Phi_X^d}(u) = \frac{1}{|supp(X)|}\sum_{p\in supp(X)} \mu_X(p)\chi_{\varphi_X(p)}(u) \tag{4}$$

where $supp(X)$ is the support set of X, $\varphi_X(p)$ is the crisp subset determined by the parameter p and

$$\chi_{\varphi_X(p)}(u) = \begin{cases} 1, & u \in \varphi_X(p) \\ 0, & u \notin \varphi_X(p) \end{cases}. \tag{5}$$

as given in Equation (5).

Definition 5. [23] Let $\underline{X}$, X, $\overline{X}$ be a FS over $\underline{P}$, P, $\overline{P}$, respectively. Thus, in Equations (6), (7), (8) and (9), a VFPSS Ψ_X over U is defined as follows:

$$\Psi_X = \underline{\Upsilon_X} \cup \Upsilon_X \cup \overline{\Upsilon_X} \tag{6}$$

such that

$$\underline{\Upsilon_X} = \left\{\left(\frac{\mu_X(p)-\underline{\alpha}}{p}, \underline{\psi_X}(p^{\underline{\alpha}})\right) : p^{\underline{\alpha}} \in \underline{P}, p \in P, \mu_X(p) \in [0,1], 0 \le \underline{\alpha} < \mu_X(p)\right\}, \tag{7}$$

$$\Upsilon_X = \left\{\left(\frac{\mu_X(p)}{p}, \psi_X(p)\right) : p \in P, \mu_X(p) \in [0,1]\right\}, \tag{8}$$

$$\overline{\Upsilon_X} = \left\{\left(\frac{\mu_X(p)+\overline{\alpha}}{p}, \overline{\psi_X}(p^{\overline{\alpha}})\right) : p \in P, p^{\overline{\alpha}} \in \overline{P}, \mu_X(p) \in [0,1], 0 \le \overline{\alpha} \le 1-\mu_X(p)\right\}, \tag{9}$$

where the functions $\underline{\psi_X}: \underline{P} \to 2^U$, $\psi_X: P \to 2^U$, $\overline{\psi_X}: \overline{P} \to 2^U$ are called lower approximate function, approximate function, upper approximate function, respectively, and the functions $\mu_X: P \to [0,1]$ is called membership function of the set X. Here $\psi_X(p) = \emptyset$ if $\mu_X(p) = 0$. Moreover, $\underline{\psi_X}(p^{\underline{\alpha}}) = \emptyset$ if $\mu_X(p) - \underline{\alpha} = 0$ and $\overline{\psi_X}(p^{\overline{\alpha}}) = \emptyset$ if $\mu_X(p) + \overline{\alpha} = 0$.

Obviously, each ordinary SSs can be written as VFPSSs.

From now on, $VFPS(U)$ denotes the family of all VFPSSs over U with P as the set of parameters.

Example 1. Let $U = \{u_1, u_2, u_3, u_4, u_5, u_6, u_7\}$ be an universe set, $P = \{p_1, p_2, p_3, p_4\}$ be the set of parameters and $X = \{0.45/p_2, 0.6/p_4\}$ be a FS over P. If $\underline{X} = \{0.32/p_2, 0.24/p_4\}$, $\overline{X} = \{0.8/p_2, 0.92/p_4\}$, and

$$\begin{aligned} \underline{\psi_X}(p_2^{0.13}) &= \{u_2, u_4, u_5, u_6, u_7\}, & \underline{\psi_X}(p_4^{0.36}) &= \{u_1, u_2, u_3, u_5, u_6\}, \\ \psi_X(p_2) &= \{u_2, u_5, u_6, u_7\}, & \underline{\psi_X}(p_4) &= \{u_2, u_3, u_5, u_6\}, \\ \overline{\psi_X}(p_2^{0.35}) &= \{u_5, u_6, u_7\}, & \overline{\psi_X}(p_4^{0.32}) &= \{u_3, u_5, u_6\}, \end{aligned}$$

then the VFPSS Ψ_X is written by

$$\Psi_X = \begin{Bmatrix} (0.32/p_2, \{u_2, u_4, u_5, u_6, u_7\}), (0.24/p_4, \{u_1, u_2, u_3, u_5, u_6\}) \\ (0.45/p_2, \{u_2, u_5, u_6, u_7\}), (0.6/p_4, \{u_2, u_3, u_5, u_6\}) \\ (0.8/p_2, \{u_5, u_6, u_7\}), (0.92/p_4, \{u_3, u_5, u_6\}) \end{Bmatrix}$$

where

$$\underline{Y_X} = \{(0.32/p_2, \{u_2, u_4, u_5, u_6, u_7\}), (0.24/p_4, \{u_1, u_2, u_3, u_5, u_6\})\},$$

$$Y_X = \{(0.45/p_2, \{u_2, u_5, u_6, u_7\}), (0.6/p_4, \{u_2, u_3, u_5, u_6\})\}$$

and

$$\overline{Y_X} = \{(0.8/p_2, \{u_5, u_6, u_7\}), (0.92/p_4, \{u_3, u_5, u_6\})\}.$$

Definition 6. [23] Let $\Psi_X \in VFPS(U)$.

i. If $\underline{\psi_X}(p^{\underline{\alpha}}) = \psi_X(p) = \overline{\psi_X}(p^{\overline{\alpha}}) = \emptyset$ for all $p^{\underline{\alpha}} \in \underline{P}$, $p \in P$, $p^{\overline{\alpha}} \in \overline{P}$, then VFPSS Ψ_X is called an X-empty VFPSS, denoted by $\Psi_{\emptyset_X}$. If $X = \emptyset$, then Ψ_X is called an empty VFPSS, denoted by $\Psi_\emptyset$.

ii. If $\underline{X}$, X, $\overline{X}$ is a crisp subset of $\underline{P}$, P, $\overline{P}$, respectively, and $\underline{\psi_X}(p^{\underline{\alpha}}) = \psi_X(p) = \overline{\psi_X}(p^{\overline{\alpha}}) = U$ for all $p^{\underline{\alpha}} \in \underline{P}$, $p \in P$, $p^{\overline{\alpha}} \in \overline{P}$, then VFPSS Ψ_X is called an X-universal VFPSS, denoted by $\Psi_{\tilde{X}}$. If $X = P$, then the X-universal VFPSS is called universal VFPSS, denoted by $\Psi_{\tilde{P}}$.

Definition 7. [23] Let $\Psi_X, \Psi_Y \in VFPS(U)$. Then, Ψ_X is a VFP-soft subset of Ψ_Y, denoted by $\Psi_X \tilde{\subseteq} \Psi_Y$, if

i. $\mu_X(p) - \underline{\alpha} \leq \mu_Y(p) - \underline{\beta}$ and $\underline{\psi_X}(p^{\underline{\alpha}}) \subseteq \underline{\psi_Y}(p^{\underline{\beta}})$ for all $p^{\underline{\alpha}}, p^{\underline{\beta}} \in \underline{P}$,
ii. $\mu_X(p) \leq \mu_Y(p)$ and $\psi_X(p) \subseteq \psi_Y(p)$ for all $p \in P$,
iii. $\mu_X(p) + \overline{\alpha} \leq \mu_Y(p) + \overline{\beta}$ and $\overline{\psi_X}(p^{\overline{\alpha}}) \subseteq \overline{\psi_Y}\left(p^{\overline{\beta}}\right)$ for all $p^{\overline{\alpha}}, p^{\overline{\beta}} \in \overline{P}$.

Also, Ψ_X is a VFP-soft equal to Ψ_Y, denoted by $\Psi_X = \Psi_Y$, if

i. $\mu_X(p) - \underline{\alpha} = \mu_Y(p) - \underline{\beta}$ and $\underline{\psi_X}(p^{\underline{\alpha}}) = \underline{\psi_Y}(p^{\underline{\beta}})$ for all $p^{\underline{\alpha}}, p^{\underline{\beta}} \in \underline{P}$,
ii. $\mu_X(p) = \mu_Y(p)$ and $\psi_X(p) = \psi_Y(p)$ for all $p \in P$,
iii. $\mu_X(p) + \overline{\alpha} = \mu_Y(p) + \overline{\beta}$ and $\overline{\psi_X}(p^{\overline{\alpha}}) = \overline{\psi_Y}\left(p^{\overline{\beta}}\right)$ for all $p^{\overline{\alpha}}, p^{\overline{\beta}} \in \overline{P}$.

Proposition 1. [23] Let $\Psi_X \in VFPS(U)$. $s\left(\overline{\psi_X}(p^{\overline{\alpha}})\right) \subseteq s(\psi_Y(p)) \subseteq s\left(\underline{\psi_X}(p^{\underline{\alpha}})\right)$ is valid for all $p^{\underline{\alpha}} \in \underline{P}, p \in P, p^{\overline{\alpha}} \in \overline{P}$.

Definition 8. [23] Let $\Psi_X \in VFPS(U)$. Then, complement Ψ_X, denoted by Ψ_X^c, is a VFPSS defined by the approximate and membership functions as

i. $\mu_{X^c}(p) - \tilde{\underline{\alpha}} = 1 - (\mu_X(p) - \underline{\alpha})$ and $\underline{\psi_{X^c}}(p^{\tilde{\underline{\alpha}}}) = U/\underline{\psi_X}(p^{\underline{\alpha}})$ for all $p^{\underline{\alpha}}, p^{\tilde{\underline{\alpha}}} \in \underline{P}$,
ii. $\mu_{X^c}(p) = 1 - \mu_X(p)$ and $\psi_{X^c}(p) = U/\psi_X(p)$ for all $p \in P$,
iii. $\mu_{X^c}(p) + \tilde{\overline{\alpha}} = 1 - (\mu_X(p) + \overline{\alpha})$ and $\overline{\psi_{X^c}}\left(p^{\tilde{\overline{\alpha}}}\right) = U/\overline{\psi_X}(p^{\overline{\alpha}})$ for all $p^{\overline{\alpha}}, p^{\tilde{\overline{\alpha}}} \in \overline{P}$.

Definition 9. [23] Let $\Psi_X, \Psi_Y \in VFPS(U)$. Then, union Ψ_X and Ψ_Y, denoted by $\Psi_X \tilde{\cup} \Psi_Y$, is defined by

i. $\mu_{X \cup Y}(p) - \underline{\gamma} = max\left\{\mu_X(p) - \underline{\alpha}, \mu_Y(p) - \underline{\beta}\right\}$ and $\underline{\psi_{X \cup Y}}(p^{\underline{\gamma}}) = \underline{\psi_X}(p^{\underline{\alpha}}) \cup \underline{\psi_Y}(p^{\underline{\beta}})$ for all $p^{\underline{\alpha}}, p^{\underline{\beta}}, p^{\underline{\gamma}} \in \underline{P}$,
ii. $\mu_{X \cup Y}(p) = max\{\mu_X(p), \mu_Y(p)\}$ and $\psi_{X \cup Y}(p) = \psi_X(p) \cup \psi_Y(p)$ for all $p \in P$,

iii. $\mu_{X\cup Y}(p)+\overline{\gamma}=max\{\mu_X(p)+\overline{\alpha},\mu_Y(p)+\overline{\beta}\}$ and $\overline{\psi_{X\cup Y}}(p^{\overline{\gamma}})=\overline{\psi_X}(p^{\overline{\alpha}})\cup\overline{\psi_Y}\left(p^{\overline{\beta}}\right)$ for all $p^{\overline{\alpha}},p^{\overline{\beta}},p^{\overline{\gamma}}\in\overline{P}$.

Definition 10. [23] Let $\Psi_X,\Psi_Y\in VFPS(U)$. Then, intersection Ψ_X and Ψ_Y, denoted by $\Psi_X\,\widetilde{\sqcap}\,\Psi_Y$, is defined by

i. $\mu_{X\cap Y}(p)-\underline{\gamma}=min\left\{\mu_X(p)-\underline{\alpha},\mu_Y(p)-\underline{\beta}\right\}$ and $\underline{\psi_{X\cap Y}}(p^{\underline{\gamma}})=\underline{\psi_X}(p^{\underline{\alpha}})\cap\underline{\psi_Y}(p^{\underline{\beta}})$ for all $p^{\underline{\alpha}},p^{\underline{\beta}},p^{\underline{\gamma}}\in\underline{P}$,
ii. $\mu_{X\cap Y}(p)=min\{\mu_X(p),\mu_Y(p)\}$ and $\psi_{X\cap Y}(p)=\psi_X(p)\cap\psi_Y(p)$ for all $p\in P$,
iii. $\mu_{X\cap Y}(p)+\overline{\gamma}=min\{\mu_X(p)+\overline{\alpha},\mu_Y(p)+\overline{\beta}\}$ and $\overline{\psi_{X\cap Y}}(p^{\overline{\gamma}})=\overline{\psi_X}(p^{\overline{\alpha}})\cap\overline{\psi_Y}\left(p^{\overline{\beta}}\right)$ for all $p^{\overline{\alpha}},p^{\overline{\beta}},p^{\overline{\gamma}}\in\overline{P}$.

3. On VFP-Soft Sets

In this section; in order to avoid complex representations in data analysis, a simpler representation for VFP-soft sets is proposed. Moreover, some new properties of VFP-soft sets are studied. In addition, a fuzzy decision set is given for the decision-making algorithm built in the next section.

Definition 11. Let $\Psi_X\in VFPS(U)$. The presentation of

$$\Psi_X=\left\{\begin{array}{l}\left(\frac{\mu_X(p)-\underline{\alpha}}{p},\underline{\psi_X}(p^{\underline{\alpha}})\right)\cup\\ \left(\frac{\mu_X(p)}{p},\psi_X(p)\right)\cup\\ \left(\frac{\mu_X(p)+\overline{\alpha}}{p},\overline{\psi_X}(p^{\overline{\alpha}})\right)\end{array}\;:\;\begin{array}{ll}p^{\underline{\alpha}}\in\underline{P} & 0\le\underline{\alpha}<\mu_X(p)\\ p\in P, & \mu_X(p)\in[0,1]\\ p^{\overline{\alpha}}\in\overline{P} & 0\le\overline{\alpha}\le 1-\mu_X(p)\end{array}\right\} \tag{10}$$

is said to be a short representation of VFPSS Ψ_X as given in Equation (10). Here, the internal structure of the set expressed in (10) denotes the union of the sets (7), (8) and (9). It is the same as the definition of VFP-soft set given in Definition 5, but this representation is shorter and clearer. In this way, it is aimed to express indefinite data sets more easily.

Remark 1. $\Psi_X\,\widetilde{\sqsubseteq}\,\Psi_Y$ does not imply that every element of Ψ_X is an element of Ψ_Y. For example, let's consider the VFPSSs Ψ_Y given below and Ψ_X of Example 1,

$$\Psi_X=\left\{\begin{array}{c}(0.32/p_2,\{u_2,u_4,u_5,u_6,u_7\}),(0.24/p_4,\{u_1,u_2,u_3,u_5,u_6\})\\ (0.45/p_2,\{u_2,u_5,u_6,u_7\}),(0.6/p_4,\{u_2,u_3,u_5,u_6\})\\ (0.8/p_2,\{u_5,u_6,u_7\}),(0.92/p_4,\{u_3,u_5,u_6\})\end{array}\right\},$$

$$\Psi_Y=\left\{\begin{array}{c}(0.5/p_2,\{u_1,u_2,u_4,u_5,u_6,u_7\}),(0.4/p_4,\{u_1,u_2,u_3,u_5,u_6,u_7\})\\ (0.65/p_2,\{u_2,u_5,u_6,u_7\}),(0.7/p_4,\{u_1,u_2,u_3,u_5,u_6\})\\ (0.9/p_2,\{u_5,u_6,u_7\}),(0.95/p_4,\{u_2,u_3,u_5,u_6\})\end{array}\right\}.$$

Then, for p_4

i. $0.24=\mu_X(p_4)-0.36\le\mu_Y(p_4)-0.3=0.4$ and $\underline{\psi_X}(p_4^{0.36})\subseteq\underline{\psi_Y}(p_4^{0.3})$ for $p_4^{0.36},p_4^{0.3}\in\underline{P}$,
ii. $0.6=\mu_X(p_4)\le\mu_Y(p_4)=0.7$ and $\psi_X(p)\subseteq\psi_Y(p)$ for all $p\in P$,
iii. $0.92=\mu_X(p_4)+0.32\le\mu_Y(p_4)+0.25=0.95$ and $\overline{\psi_X}(p_4^{0.32})\subseteq\overline{\psi_Y}(p_4^{0.25})$ for $p_4^{0.32},p_4^{0.25}\in\overline{P}$.

It can be shown similarly for p_2. Therefore, $\Psi_X \tilde{\sqsubseteq} \Psi_Y$. It is clear that $(0.24/p_4, \{u_1, u_2, u_3, u_5, u_6\}) \in \Psi_X$ but $(0.24/p_4, \{u_1, u_2, u_3, u_5, u_6\}) \notin \Psi_Y$.

Proposition 2. Let $\Psi_X, \Psi_Y \in VFPS(U)$. Then,

i. $\Psi_\emptyset \tilde{\sqsubseteq} \Psi_X \tilde{\sqsubseteq} \Psi_X \tilde{\sqsubseteq} \Psi_{\tilde{P}}$,
ii. If $\Psi_X \tilde{\sqsubseteq} \Psi_Y$ and $\Psi_Y \tilde{\sqsubseteq} \Psi_Z$, then $\Psi_X \tilde{\sqsubseteq} \Psi_Z$,
iii. If $\Psi_X = \Psi_Y$ and $\Psi_Y = \Psi_Z$, then $\Psi_X = \Psi_Z$,
iv. If $\Psi_X \tilde{\sqsubseteq} \Psi_Y$ and $\Psi_Y \tilde{\sqsubseteq} \Psi_X$, then $\Psi_X = \Psi_Y$.

Proof. They can be proved easily by using the approximate and membership functions of the VFPSSs.

Remark 2. Let $\Psi_X \in VFPS(U)$. If $\Psi_\emptyset \neq \Psi_X \neq \Psi_{\tilde{P}}$, then $\Psi_X \tilde{\sqcup} \Psi_X^c \neq \Psi_{\tilde{P}}$ and $\Psi_X \tilde{\sqcap} \Psi_X^c \neq \Psi_\emptyset$.

Proposition 3. Let $\Psi_X, \Psi_Y \in VFPS(U)$. Then De Morgan's laws are valid

i. $(\Psi_X \tilde{\sqcup} \Psi_Y)^c = \Psi_X^c \tilde{\sqcap} \Psi_Y^c$,
ii. $(\Psi_X \tilde{\sqcap} \Psi_Y)^c = \Psi_X^c \tilde{\sqcup} \Psi_Y^c$.

Proof. For all $p^{\underline{\alpha}} \in \underline{P}$, $p \in P$, $p^{\overline{\alpha}} \in \overline{P}$;

i. $\mu_{(X\cup Y)^c}(p) - \tilde{\underline{\gamma}} = 1 - \left(\mu_{X\cup Y}(p) - \underline{\gamma}\right) = 1 - max\left\{\mu_X(p) - \underline{\alpha}, \mu_Y(p) - \underline{\beta}\right\} = min\left\{1 - \left(\mu_X(p) - \underline{\alpha}\right), 1 - \left(\mu_Y(p) - \underline{\beta}\right)\right\} = min\left\{\mu_{X^c}(p) - \tilde{\underline{\alpha}}, \mu_{Y^c}(p) - \tilde{\underline{\beta}}\right\} = \mu_{X^c\cap Y^c}(p) - \tilde{\underline{\gamma}}$
ii. $\mu_{(X\cup Y)^c}(p) = 1 - \mu_{X\cup Y}(p) = 1 - max\{\mu_X(p), \mu_Y(p)\} = min\{1 - \mu_X(p), 1 - \mu_Y(p)\} = min\{\mu_{X^c}(p), \mu_{Y^c}(p)\} = \mu_{X^c\cap Y^c}(p)$
iii. $\mu_{(X\cup Y)^c}(p) + \tilde{\overline{\gamma}} = 1 - (\mu_{X\cup Y}(p) + \overline{\gamma}) = 1 - max\left\{\mu_X(p) + \overline{\alpha}, \mu_Y(p) + \overline{\beta}\right\} = min\left\{1 - (\mu_X(p) + \overline{\alpha}), 1 - \left(\mu_Y(p) + \overline{\beta}\right)\right\} = min\left\{\mu_{X^c}(p) + \tilde{\overline{\alpha}}, \mu_{Y^c}(p) + \tilde{\overline{\beta}}\right\} = \mu_{X^c\cap Y^c}(p) + \tilde{\overline{\gamma}}$

and

i. $\underline{\psi_{(X\cup Y)^c}}\left(p^{\tilde{\underline{\gamma}}}\right) = U \setminus \underline{\psi_{X\cup Y}}(p^{\underline{\gamma}}) = U \setminus \left(\underline{\psi_X}(p^{\underline{\alpha}}) \cup \underline{\psi_Y}\left(p^{\underline{\beta}}\right)\right) = \left(U \setminus \underline{\psi_X}(p^{\underline{\alpha}})\right) \cap \left(U \setminus \underline{\psi_Y}\left(p^{\underline{\beta}}\right)\right) = \underline{\psi_{X^c}}\left(p^{\tilde{\underline{\alpha}}}\right) \cap \underline{\psi_{Y^c}}\left(p^{\tilde{\underline{\beta}}}\right) = \underline{\psi_{X^c\cap Y^c}}\left(p^{\tilde{\underline{\gamma}}}\right)$
ii. $\psi_{(X\cup Y)^c}(p) = U \setminus \psi_{X\cup Y}(p) = U \setminus \left(\psi_X(p) \cup \psi_Y(p)\right) = \left(U \setminus \psi_X(p)\right) \cap \left(U \setminus \psi_Y(p)\right) = \psi_{X^c}(p) \cap \psi_{Y^c}(p) = \psi_{X^c\cap Y^c}(p)$
iii. $\overline{\psi_{(X\cup Y)^c}}\left(p^{\tilde{\overline{\gamma}}}\right) = U \setminus \overline{\psi_{X\cup Y}}(p^{\overline{\gamma}}) = U \setminus \left(\overline{\psi_X}(p^{\overline{\alpha}}) \cup \overline{\psi_Y}\left(p^{\overline{\beta}}\right)\right) = \left(U \setminus \overline{\psi_X}(p^{\overline{\alpha}})\right) \cap \left(U \setminus \overline{\psi_Y}\left(p^{\overline{\beta}}\right)\right) = \overline{\psi_{X^c}}\left(p^{\tilde{\overline{\alpha}}}\right) \cap \overline{\psi_{Y^c}}\left(p^{\tilde{\overline{\beta}}}\right) = \overline{\psi_{X^c\cap Y^c}}\left(p^{\tilde{\overline{\gamma}}}\right)$

Likewise, the proof of (ii) can be made similarly.
Proposition 4. Let $\Psi_X \in VFPS(U)$. Then,

i. $(\Psi_X^c)^c = \Psi_X$,
ii. $\Psi_\emptyset^c = \Psi_{\tilde{P}}$.

Proof. Straightforward.

Proposition 5. Let $\Psi_X, \Psi_Y, \Psi_Z \in VFPS(U)$. Then,

i. $\Psi_X \sqcup (\Psi_Y \sqcap \Psi_Z) = (\Psi_X \sqcup \Psi_Y) \sqcap (\Psi_X \sqcup \Psi_Z)$,
ii. $\Psi_X \sqcap (\Psi_Y \sqcup \Psi_Z) = (\Psi_X \sqcap \Psi_Y) \sqcup (\Psi_X \sqcap \Psi_Z)$.

Proof. For all $p^{\underline{\alpha}} \in \underline{P}$, $p \in P$, $p^{\overline{\alpha}} \in \overline{P}$

i. $\mu_{X\cup(Y\cap Z)}(p) - \underline{\alpha_{1,2,3}} = max\left\{\mu_X(p) - \underline{\alpha_1}, \mu_{Y\cap Z}(p) - \underline{\alpha_{2,3}}\right\} = max\left\{\mu_X(p) - \underline{\alpha_1}, min\left\{\mu_Y(p) - \underline{\alpha_2}, \mu_Z(p) - \underline{\alpha_3}\right\}\right\} = min\left\{max\left\{\mu_X(p) - \underline{\alpha_1}, \mu_Y(p) - \underline{\alpha_2}\right\}, max\left\{\mu_X(p) - \underline{\alpha_1}, \mu_Z(p) - \underline{\alpha_3}\right\}\right\} = min\left\{\mu_{X\cup Y}(p) - \underline{\alpha_{1,2}}, \mu_{X\cup Z}(p) - \underline{\alpha_{1,3}}\right\} = \mu_{(X\cup Y)\cap(X\cup Z)}(p) - \underline{\alpha_{1,2,3}}$
ii. $\mu_{X\cup(Y\cap Z)}(p) = max\{\mu_X(p), \mu_{Y\cap Z}(p)\} = max\{\mu_X(p), min\{\mu_Y(p), \mu_Z(p)\}\} = min\{max\{\mu_X(p), \mu_Y(p)\}, max\{\mu_X(p), \mu_Z(p)\}\} = min\{\mu_{X\cup Y}(p), \mu_{X\cup Z}(p)\} = \mu_{(X\cup Y)\cap(X\cup Z)}(p)$
iii. $\mu_{X\cup(Y\cap Z)}(p) + \overline{\alpha_{1,2,3}} = max\{\mu_X(p) + \overline{\alpha_1}, \mu_{Y\cap Z}(p) + \overline{\alpha_{2,3}}\} = max\{\mu_X(p) + \overline{\alpha_1}, min\{\mu_Y(p) + \overline{\alpha_2}, \mu_Z(p) + \overline{\alpha_3}\}\} = min\{max\{\mu_X(p) + \overline{\alpha_1}, \mu_Y(p) + \overline{\alpha_2}\}, max\{\mu_X(p) + \overline{\alpha_1}, \mu_Z(p) + \overline{\alpha_3}\}\} = min\{\mu_{X\cup Y}(p) + \overline{\alpha_{1,2}}, \mu_{X\cup Z}(p) + \overline{\alpha_{1,3}}\} = \mu_{(X\cup Y)\cap(X\cup Z)}(p) + \overline{\alpha_{1,2,3}}$

and

i. $\underline{\psi_{X\cup(Y\cap Z)}}(p^{\underline{\alpha_{1,2,3}}}) = \underline{\psi_X}(p^{\underline{\alpha_1}}) \cup \underline{\psi_{Y\cap Z}}(p^{\underline{\alpha_{2,3}}}) = \underline{\psi_X}(p^{\underline{\alpha_1}}) \cup \left(\underline{\psi_Y}(p^{\underline{\alpha_2}}) \cap \underline{\psi_Z}(p^{\underline{\alpha_3}})\right) = \left(\underline{\psi_X}(p^{\underline{\alpha_1}}) \cup \underline{\psi_Y}(p^{\underline{\alpha_2}})\right) \cap \left(\underline{\psi_X}(p^{\underline{\alpha_1}}) \cup \underline{\psi_Z}(p^{\underline{\alpha_3}})\right) = \underline{\psi_{X\cup Y}}(p^{\underline{\alpha_{1,2}}}) \cap \underline{\psi_{X\cup Z}}(p^{\underline{\alpha_{1,3}}}) = \underline{\psi_{(X\cup Y)\cap(X\cup Z)}}(p^{\underline{\alpha_{1,2,3}}})$
ii. $\psi_{X\cup(Y\cap Z)}(p) = \psi_X(p) \cup \psi_{Y\cap Z}(p) = \psi_X(p) \cup \left(\psi_Y(p) \cap \psi_Z(p)\right) = \left(\psi_X(p) \cup \psi_Y(p)\right) \cap \left(\psi_X(p) \cup \psi_Z(p)\right) = \psi_{X\cup Y}(p) \cap \psi_{X\cup Z}(p) = \psi_{(X\cup Y)\cap(X\cup Z)}(p)$
iii. $\overline{\psi_{X\cup(Y\cap Z)}}(p^{\overline{\alpha_{1,2,3}}}) = \overline{\psi_X}(p^{\overline{\alpha_1}}) \cup \overline{\psi_{Y\cap Z}}(p^{\overline{\alpha_{2,3}}}) = \overline{\psi_X}(p^{\overline{\alpha_1}}) \cup \left(\overline{\psi_Y}(p^{\overline{\alpha_2}}) \cap \overline{\psi_Z}(p^{\overline{\alpha_3}})\right) = \left(\overline{\psi_X}(p^{\overline{\alpha_1}}) \cup \overline{\psi_Y}(p^{\overline{\alpha_2}})\right) \cap \left(\overline{\psi_X}(p^{\overline{\alpha_1}}) \cup \overline{\psi_Z}(p^{\overline{\alpha_3}})\right) = \overline{\psi_{X\cup Y}}(p^{\overline{\alpha_{1,2}}}) \cap \overline{\psi_{X\cup Z}}(p^{\overline{\alpha_{1,3}}}) = \overline{\psi_{(X\cup Y)\cap(X\cup Z)}}(p^{\overline{\alpha_{1,2,3}}})$

Likewise, the proof of (ii) can be made in a similar way.

Proposition 6. Let $\Psi_X, \Psi_Y, \Psi_Z \in VFPS(U)$. Then,

i. $\Psi_X \sqcup \Psi_X = \Psi_X$ and $\Psi_X \sqcap \Psi_X = \Psi_X$,
ii. $\Psi_X \sqcup \Psi_\emptyset = \Psi_X$ and $\Psi_X \sqcap \Psi_\emptyset = \Psi_\emptyset$,
iii. $\Psi_X \sqcup \Psi_{\tilde{P}} = \Psi_{\tilde{P}}$ and $\Psi_X \sqcap \Psi_{\tilde{P}} = \Psi_X$,
iv. $\Psi_X \sqcup \Psi_Y = \Psi_Y \sqcup \Psi_X$ and $\Psi_X \sqcap \Psi_Y = \Psi_Y \sqcap \Psi_X$,
v. $(\Psi_X \sqcup \Psi_Y) \sqcup \Psi_Z = \Psi_X \sqcup (\Psi_Y \sqcup \Psi_Z)$ and $(\Psi_X \sqcap \Psi_Y) \sqcap \Psi_Z = \Psi_X \sqcap (\Psi_Y \sqcap \Psi_Z)$.

Proof. The proofs can be easily obtained from Definition 8 and 9.

Definition 12. Let $\Psi_X \in VFPS(U)$. Then a fuzzy decision set of Ψ_X, denoted by Ψ_X^d, is defined by Equations (11), (12), (13), (14) and (15)

$$\Psi_X^d = \left\{\mu_{\Psi_X^d}(u)/u : u \in U\right\} \tag{11}$$

which is a FS over U and $\mu_{\Psi_X^d}$ is defined by $\mu_{\Psi_X^d} : U \to [0,1]$, (as shown in Equation (12), (13), (14) and (15))

$$\mu_{\Psi_X^d}(u) = \frac{1}{3}\left(\sum_{p^{\underline{\alpha}}\in\underline{X}} \frac{(\mu_X(p) - \underline{\alpha})\, \chi_{\underline{\psi_X}(p^{\underline{\alpha}})}(u)}{\underline{w}|\underline{X}|} + \sum_{p\in X} \frac{\mu_X(p)\, \chi_{\psi_X(p)}(u)}{w|X|} + \sum_{p^{\overline{\alpha}}\in\overline{X}} \frac{(\mu_X(p) + \overline{\alpha})\, \chi_{\overline{\psi_X}(p^{\overline{\alpha}})}(u)}{\overline{w}|\overline{X}|}\right) \tag{12}$$

where $\left|\underline{X}\right|$, $|X|$, $\left|\overline{X}\right|$ are the cardinality of $\underline{X}$, X, $\overline{X}$ and

$$\chi_{\underline{\psi_X}(p^{\underline{\alpha}})}(u) = \begin{cases} 1, & u \in \underline{\psi_X}(p^{\underline{\alpha}}) \\ 0, & u \notin \underline{\psi_X}(p^{\underline{\alpha}}) \end{cases} \tag{13}$$

$$\chi_{\psi_X(p)}(u) = \begin{cases} 1, & u \in \psi_X(p) \\ 0, & u \notin \psi_X(p) \end{cases} \tag{14}$$

$$\chi_{\overline{\psi_X}(p^{\overline{\alpha}})}(u) = \begin{cases} 1, & u \in \overline{\psi_X}(p^{\overline{\alpha}}) \\ 0, & u \notin \overline{\psi_X}(p^{\overline{\alpha}}) \end{cases} \tag{15}$$

Here, $\underline{w}, w, \overline{w}$ represent the total weight of objects with membership degrees $\mu_X(p) - \underline{\alpha}$, the total weight of objects with membership degrees $\mu_X(p)$, the total weight of objects with membership degrees $\mu_X(p) + \overline{\alpha}$, respectively, for all $p \in P$ and $\underline{w}, w, \overline{w} \in \mathbb{R}^+$.

Remark 3. As the membership degree of a parameter in Proposition 1 decreases, the number of objects that provide that parameter increases. For this reason, when we increase the membership degree, it is clear that there should be a relationship $\overline{\mathrm{w}} < w < \underline{\mathrm{w}}$ between the total weights in order to highlight the objects that still provide that parameter. So the choice of weights is not random. In this case, if there is a contrary situation between the total weights, it becomes difficult to highlight the best objects that meet the desired parameters.

4. Numerical Example

In this section, a decision-making algorithm is proposed for the selection of the best choice. Moreover, the given algorithm has been analyzed comparatively with an algorithm proposed for VFPSS.

Firstly; let's construct a decision-making method over a fuzzy decision set of Ψ_X by the following algorithm;

Algorithm. The algorithm for the selection of the best choice is given as:

Step 1: Express the uncertainty encountered with the help of a VFPSS Ψ_X.
Step 2: Compute the fuzzy decision set Ψ_X^d.
Step 3: Find r, for which $\mu_{\Psi_X^d}(u_r) = max\left\{\mu_{\Psi_X^d}(u): u \in U\right\}$.

Remark 4. If r has more than one value then any one of them may be chose.

Now, let's consider the uncertainty problem given below to analyze the algorithm.

Example 2. Suppose a school wants to choose the students that best suit its parameters. For this, the school has posted an announcement. According to the announcement, a three-stage exam will be held for candidate students. Participation conditions for these exams are stated as follows:

(A) All student candidates who apply for all three-stage exams held by the school will be able to participate.
(B) The first exam is less decisive than the second exam and is less decisive in the second exam than the third exam.

(C) Increasing decisive in an exam means that the score to be obtained from this exam is higher.

Assume that the set of candidate students applying for admission to the school under these conditions is $U = \{u_1, u_2, u_3, u_4, u_5, u_6, u_7, u_8, u_9, u_{10}\}$ and the set of parameters the school requires from students is $P =$

$\{p_1 = self - confident, p_2 = successful,\}$. Moreover, the difficulty levels of the exams to be made by the school administration to evaluate candidate students are determined as follows:

For each parameter, the difficulty level of the first exam is "0.28, 0.38", the second exam's difficulty level is "0.45, 0.57" and finally, the third exam's difficulty level is "0.68, 0.75", respectively. The difficulty levels of the exams expressed here construct FSs of parameter sets $\underline{P}$, P, $\overline{P}$ and are $\underline{X} = \{0.28/p_1, 0.38/p_2\}$, $X = \{0.45/p_1, 0.57/p_2\}$, $\overline{X} = \{0.68/p_1, 0.75/p_2\}$ respectively.

Remark 5. It should be noted that; changing the difficulty levels for each parameter in the exams can directly affect the success of candidate students in the exams. In order to obtain more detailed information about this stated situation, studies [23-25] can be examined.

Step 1: During the evaluation of candidate students, the data obtained from the school administration are assumed as follows:

$$\underline{\psi_X}(p_1^{0.17}) = \{u_1, u_2, u_3, u_4, u_5, u_7, u_9, u_{10}\}, \qquad \underline{\psi_X}(p_2^{0.19}) = \{u_1, u_4, u_5, u_6, u_8, u_{10}\},$$
$$\psi_X(p_1) = \{u_1, u_2, u_3, u_5, u_7, u_{10}\}, \qquad \psi_X(p_2) = \{u_4, u_5, u_6, u_8\},$$
$$\overline{\psi_X}(p_1^{0.23}) = \{u_7, u_{10}\}, \qquad \overline{\psi_X}(p_2^{0.18}) = \{u_8\},$$

These data can be expressed as a whole with the help of a VFPSS Ψ_X,

$$\Psi_X = \left\{ \begin{matrix} (0.28/p_1, \{u_1, u_2, u_3, u_4, u_5, u_7, u_9, u_{10}\}), (0.38/p_2, \{u_1, u_4, u_5, u_6, u_8, u_{10}\}) \\ (0.45/p_1, \{u_1, u_2, u_3, u_5, u_7, u_{10}\}), (0.57/p_2, \{u_4, u_5, u_6, u_8\}) \\ (0.68/p_1, \{u_7, u_{10}\}), (0.75/p_2, \{u_8\}) \end{matrix} \right\}.$$

Step 2: The fuzzy decision set of Ψ_X can be found as, (for $\underline{w} = 3, w = 2, \overline{w} = 1$)

$$\Psi_X^d = \left\{ \begin{matrix} 0.074/u_1, 0.053/u_2, 0.053/u_3, 0.084/u_4, 0.121/u_5 \\ 0.068/u_6, 0.166/u_7, 0.193/u_8, 0.015/u_9, 0.1875/u_{10} \end{matrix} \right\}.$$

For example; considering the u_2,

$$\mu_{\Psi_X^d}(u_2) = \frac{1}{3}\left(\frac{(0.28 * 1) + (0.38 * 0)}{3 * 2} + \frac{(0.45 * 1) + (0.57 * 0)}{2 * 2} + \frac{(0.68 * 0) + (0.75 * 0)}{1 * 2}\right) = 0.053$$

Here, attention should be paid to the values selected in accordance with the condition $\overline{w} < w < \underline{w}$.

Step 3: We conclude from the values of u that $\mu_{\Psi_X^d}(u_8) = max\left\{\mu_{\Psi_X^d}(u): u \in U\right\} = 0.193$ and hence $r = 8$. Thus u_8 is the optimal choice candidate and so u_8 is the most suitable student candidate for the desired parameters.

A comparison: Only one algorithm has been proposed for VFPSS theory, since it is very new. If we apply the algorithm suggested by Dalkılıç and Demirtaş [4] for the example given above, the results obtained are as follows:

Table 1. Comparison of algorithms for VFPSSs.

Algorithm	u_1	u_2	u_3	u_4	u_5	u_6	u_7	u_8	u_9	u_{10}
[4]	1.11	0.73	0.73	1.23	1.68	0.95	1.41	1.7	0.28	1.79
Suggested	0.074	0.053	0.053	0.084	0.121	0.068	0.166	0.193	0.015	0.1875

According to the scores obtained in Table 1, the ranking among the candidate students is as follows:

For the algorithm [4], $u_{10} > u_8 > u_5 > u_7 > u_4 > u_1 > u_6 > u_2 = u_3 > u_9$.
For the suggested algorithm, $u_8 > u_{10} > u_7 > u_9 > u_5 > u_4 > u_1 > u_6 > u_2 = u_3$.

When the results are examined, it is striking that there is a serious difference. First of all, it should be noted that an error such as the best student u_{10} is avoided. There are two important reasons for the difference between the algorithms given for the VFPSS,

i. Their algorithm is very complex, but the algorithm proposed in this study is so simple. Moreover, their algorithm has more variables and constraints than the algorithm proposed in this study.

ii. In the algorithm proposed by Dalkılıç and Demirtaş [4], the scores obtained from each approximate function were evaluated equally. Therefore, students who passed the more difficult exams were also subjected to an equal score. However, the algorithm proposed in this study eliminated this problem.

For these reasons, it is recommended to use the algorithm given in this study in expressing any uncertainty and in obtaining of the decision-making process in a more ideal way.

5. Conclusion

In conclusion, this study has significantly advanced the field of set theory, particularly within the context of VFP-soft sets, a novel mathematical tool tailored to address uncertainties in data analysis. The research's importance lies in its dual objective of enhancing existing theory while offering practical solutions to complex data analysis challenges. Firstly, the study simplifies the representation of intricate data, making analysis more accessible. By exploring fundamental set operations within the framework of VFP-soft sets, the research contributes to strengthening the theoretical foundation of this mathematical model. A crucial aspect of this research is the examination of parameter importance weights in VFP-soft sets, encompassing three different types of fuzzy parameterized soft sets. This investigation sheds light on nuanced approaches to parameter weighting, a fundamental aspect of the theory, thereby enhancing its applicability. Furthermore, the development of a novel decision-making algorithm based on VFP-soft sets represents a significant practical outcome of this research. This algorithm, derived from theoretical enhancements and insights, holds promise for addressing real-world uncertainty problems effectively. However, it's important to acknowledge certain limitations and challenges associated with the proposed methodology. While VFP-soft sets offer a versatile approach, their implementation may require specialized expertise, and computational complexity could pose challenges for large-scale datasets. Additionally, the effectiveness of the proposed algorithm may vary depending on the specific characteristics of the data and the context of the decision problem. In light of these considerations, future research should focus on refining the methodology to overcome these limitations and explore its applicability across diverse domains. By addressing these challenges and leveraging the advantages of VFP-soft sets, further advancements in data analysis and decision-making can be achieved.

References

[1] Zadeh LA. Fuzzy sets. Inf & Cont 1965; 8: 338-353.
[2] Pawlak Z. Rough sets. Int J Comput Inform Sci 1982; 11: 341-356.
[3] Molodtsov D. Soft set theory-first results. Comput & Math Appl 1999; 37: 19-31.
[4] Maji PK, Roy AR, Biswas R. Soft set theory. Comput & Math Appl 2003; 45(4-5): 555–562.
[5] Maji PK, Roy AR, Biswas R. Fuzzy soft sets. J Fuzzy Math 2001; 9(3): 589-602.
[6] Maji PK, Roy AR, Biswas R. An application of soft sets in a decision-making problem. Comput & Math Appl 2002; 44: 1077-1083.
[7] Çağman N, Enginoglu S. Soft matrices and its decision makings. Comput & Math Appl 2010; 59: 3308-3314.

[8] Çağman N, Çıtak F, Enginoglu S. Fuzzy parameterized fuzzy soft set theory and its applications. Turkish J Fuzzy Syst 2010; 1(1): 21-35.
[9] Chen D, Tsang ECC, Yeung DS, Wang X. The parameterization reduction of soft sets and its applications. Comput & Math Appl 2005; 49: 757-763.
[10] Feng F, Jun YB, Liu X, Li L. An adjustable approach to fuzzy soft set based decision making. J Comput & Appl Math 2010; 234: 10-20.
[11] Çağman N, Enginoglu S, Çıtak F. Fuzzy soft set theory and its applications. Iranian J Fuzzy Syst 2011; 8(3): 137-147.
[12] Demirtaş N, Dalkılıç O. An application in the diagnosis of prostate cancer with the help of bipolar soft rough sets. In: Mathematics and Mathematics Education (ICMME 2019), Konya, 283, 2019.
[13] Dalkılıç O, Demirtaş N. Bipolar soft filter. J Univ Math 2020; 3(1): 21-27.
[14] Demirtaş N, Hussaın S, Dalkılıc O. New approaches of inverse soft rough sets and their applications in a decision making problem. J Appl Math & Inf 2020; 38(3-4): 335-349.
[15] Demirtaş N, Dalkılıç O. Decompositions of soft α-continuity and soft A-continuity. J New Theory 2020; (31): 86-94.
[16] Roy AR, Maji PK. A fuzzy soft set theoretic approach to decision making problems. J Comput & Appl Math 2007; 203(2): 412-418.
[17] Peng X, Jingguo D. Hesitant fuzzy soft decision making methods based on WASPAS, MABAC, and COPRAS with combined weights. J Intell Fuzzy Syst 2017; 33: 1313-1325.
[18] Özlü, Ş. Interval valued q-rung orthopair hesitant fuzzy choquet aggregating operators in multi-criteria decision making problems. Gazi Univ J Sci Part C Des & Technol 2022; 10(4): 1006-1025.
[19] Özlü, Ş. Interval valued bipolar fuzzy prioritized weighted dombi averaging operator based on multi-criteria decision making problems. Gazi Univ J Sci Part C Des & Technol 2022; 10(4): 841-857.
[20] Özlü, Ş. Generalized Dice measures of single valued neutrosophic type-2 hesitant fuzzy sets and their application to multi-criteria decision making problems. Int J Mach Learn & Cybern 2023; 14(1): 33-62.
[21] Özlü, Ş. Multi-criteria decision making based on vector similarity measures of picture type-2 hesitant fuzzy sets. Granular Comput 2023; 8(6): 1505-1531.
[22] Çağman N, Çıtak F, Enginoglu S. FP-soft set theory and its applications. Annals Fuzzy Math & Inf 2011; 2: 219-226.
[23] Dalkılıç O, Demirtas N. VFP-soft sets and its application on decision making problems. J Polytech 2021; 24(4): 1391-1399.
[24] Dalkılıç O. An application of VFPFSS's in decision making problems. J Polytech 2021; 25(2): 491-501.
[25] Dalkılıç O. On topological structures of virtual fuzzy parametrized fuzzy soft sets. Complex & Intell Syst 2022; 8(1): 337-348.

Turkish Journal of Science & Technology
20(1), 121-133, 2025

Research Paper
https://doi.org/10.55525/tjst.1404350

An Integrated MATLAB-ArcGIS Toolbox for Landfill Suitability Mapping Using Neural Networks

Sohaib K. M. ABUJAYYAB[1*], Mohd Sanusi AHAMAD[2]
[1] Department of Geography, Faculty of Letters, Demir Celik Campus, Karabuk University, Karabuk, Turkey
[2] School of Civil Engineering, Universiti Sains Malaysia, Engineering Campus, 14300, Penang, Malaysia.
[*1]sjayyab@karabuk.edu.tr, [2]cesanusi@gmail.com

(Geliş/Received: 13/12/2023; Kabul/Accepted: 01/02/2025)

Abstract: The Neural Network Toolbox for Landfill Suitability Mapping presents a novel approach to enhance solid waste management by automating landfill site selection using a combination of Python-ArcGIS and MATLAB environments. This study addresses the critical need for efficient landfill suitability mapping, which is essential for minimizing environmental risks and optimizing land use. We developed an automated toolbox that integrates the capabilities of MATLAB for neural network modeling with Python scripting in ArcGIS, facilitating a user-friendly workflow for decision-makers. Our methodology was tested in the northern region of Peninsular Malaysia, employing 14 specific criteria to generate training and testing datasets. The results of neural network model achieving an accuracy of 82%. This toolbox streamlines the process by automating various stages, from data preparation to suitability mapping, reducing the likelihood of human errors and minimizing processing time. The flexibility, interoperability, and user-friendly interface of the toolbox make it accessible to users with varying levels of GIS expertise, ensuring its adaptability to different geographic regions and environmental conditions. This research contributes to more efficient, accurate, and sustainable landfill site selection, benefiting decision-makers and supporting broader environmental protection efforts.

Key words: Landfill Suitability Mapping, Neural Networks, ArcGIS, Decision-Makers, Spatial Data.

Sinir Ağı Kullanarak Düzenli Depolama Alanı Uygunluk Haritalaması için Entegre MATLAB-ArcGIS Araç Kutusu

Öz: Atık depolama Sahası Uygunluk Haritalaması için Sinir Ağı Araç Kutusu, Python-ArcGIS ve MATLAB ortamlarının bir kombinasyonunu kullanarak depolama sahası seçimini otomatikleştirerek katı atık yönetimini geliştirmek için yeni bir yaklaşım sunar. Bu çalışma, çevresel risklerin en aza indirilmesi ve arazi kullanımının optimize edilmesi için gerekli olan verimli depolama sahası uygunluk haritalamasına yönelik kritik ihtiyacı ele almaktadır. Karar vericiler için kullanıcı dostu bir iş akışını kolaylaştıran, MATLAB'ın sinir ağı modelleme yeteneklerini ArcGIS'teki Python komut dosyası oluşturma ile birleştiren otomatik bir araç kutusu geliştirdik. Metodolojimiz Malezya Yarımadası'nın kuzey bölgesinde, eğitim ve test veri kümeleri oluşturmak için 14 spesifik kriter kullanılarak test edildi. Sinir ağı modelinin sonuçları %82 doğruluk oranına ulaşmıştır. Bu araç kutusu, veri hazırlamadan uygunluk haritalamasına kadar çeşitli aşamaları otomatikleştirerek, insan hatası olasılığını azaltarak ve işlem süresini en aza indirerek süreci kolaylaştırır. Araç kutusunun esnekliği, birlikte çalışabilirliği ve kullanıcı dostu arayüzü, onu farklı düzeylerde CBS uzmanlığına sahip kullanıcılar için erişilebilir hale getirerek farklı coğrafi bölgelere ve çevre koşullarına uyarlanabilirliğini sağlar. Bu araştırma, daha verimli, doğru ve sürdürülebilir depolama alanı seçimine katkıda bulunarak karar vericilere fayda sağlar ve daha geniş çevre koruma çabalarını destekler.

Anahtar kelimeler: Atık Depolama Sahasına Uygunluk Haritalaması, Sinir Ağı, ArcGIS, Karar Vericiler, Mekansal Veriler.

1. Introduction

Landfills stand as some of the most dangerous locations, posing a profound threat to environment, tourism, and property values [1–3]. The pursuit of suitability mapping has been an enduring concern within environmental planning endeavors, marked by the persistent need to address critical aspects. Aspects such as minimizing risks to public health, mitigating the adverse effects on the natural life, maximizing the services of landuse to communities, and minimizing the overall expenditure associated with the operation of facilities, underscoring the economic aspect of the challenge [4,5]. Numerous commendable efforts have been undertaken towards the enhancement of solid waste management, as underscored by several works [6,7]. Notably, among this research, a notable one transpired in Malaysia, led by [8]. Back in 2005, the Malaysian government took a significant step by publishing the National Strategic Plan (NSP) for Solid Waste Management under the Ministry of Housing and Local Government in Malaysia. Additionally, Japan International Cooperation Agency (JICA) embarked on an evaluation and baseline-setting initiative in 2005. This was supplemented by an array of research projects carried

* Corresponding author:sjayyab@karabuk.edu.tr. ORCID Number of authors:[1]0000-0002-6692-3567, [2]0000-0003-2978-0736

out by various researchers and organizations, including but not limited to [9–14]. These collective efforts saw the emergence of an array of methods for landfill suitability mapping [15–17].

The developed methods in the former works relayed on integration of vector and raster data, which proved the valuable aiding decision-makers operating within defined geographic regions. The integration empowered them to navigate the labyrinth of criteria selection and suitability mapping for landfill sites [18,19]. Such modules operated at the interconnection of Multi-criteria decision analysis (MCDA) and Geographic Information Systems (GIS), underpinned by the principles of these technologies. Additionally, they seamlessly merged diverse processing environments, primarily drawing upon the capabilities of Matlab and Python within the ArcGIS framework. Majumdar develops a Multi-criteria Decision Making (MCDM) tool using the Analytical Hierarchy Process to evaluate the suitability of three proposed landfill sites in Kolkata, considering various criteria such as environmental impact and economic viability. The analysis indicates that the sites are moderately suitable, with scores between 300 and 750 on both the Landfill Site Sensitivity Index (LSSI) and Economic Viability Index (EVI) [20]. Eldrandaly introduces a GIS-based multicriteria evaluation (MCE) tool in ArcGIS 9.3, designed for use by engineers and planners with varying GIS expertise, and demonstrates its application through a case study [21]. Daneshvar customizes ArcMap v8.2 using VBA to develop a user-friendly Landfill Site Selection (LSS) toolbar, aiding engineers of varying GIS expertise in evaluating landfill site suitability based on diverse criteria and scoring schemes [22]. The former studies include potential limitations in terms of scalability, adaptability to changing landscapes, and accessibility to users with varying levels of GIS expertise. Consequently, the development of a new tool is justified to address these limitations by offering a solution that is user-friendly, adaptable to evolving GIS technologies, and accessible to engineers and planners with varying levels of GIS expertise.

In our research, Matlab served as the primary programming environment for the implementation of neural networks (NN) models. The utilization of Matlab offers a multitude of advantages, essentially in its capacity to provide a robust foundation for the creation and refinement of NN models. However, it is worth noting that Matlab is not inherently a spatial software, which gives rise to certain challenges within the integrated model. These challenges manifest in the form of complex processing procedures, as identified by [23], demanding extensive and time-consuming efforts from decision-makers in the production of suitability maps. Consequently, end-users, particularly decision-makers, may cope with a host of difficulties and limitations when attempting to apply the developed model. These limitations encompass the intricacies of importing spatial data, the construction of training data sets from such data, spatial-related issues, the management of voluminous data, the potential for human errors, as well as the need for manual input variable assignment and implementation.

Manual analysis prone to consuming excessive time and possessing reduced accuracy. Furthermore, analysts must undertake the difficult task of assembling the model from scratch with every application. This often results in the dispersion of models due to the use of multiple functions, rendering them impractical and challenging to reproduce. Moreover, previous models lack adaptability to various geographical areas, each having distinct criteria, which necessitates repeated consultation with experts and deep understanding of variables. The earlier methods exhibit limitations in the implementation, prompting a demand to develop of these methods to streamlining landfill suitability mapping. This enhancement aimed at bolstering landfill suitability mapping systems and unifying all tasks into a singular, user-friendly workflow that provides to decision-makers requirements.

To overcome these limitations, an ArcGIS Toolbox has been developed using the Python scripting language. This toolbox provides a solution to improve integrality between the NN-Matlab environment, and ArcGIS-Python environment. Python is an open-source scripting language, offering a wide array of functionalities that facilitate geospatial data processing. This combination of Python and Matlab, realized through the NN toolbox we present in this paper, is specially tailored to accommodate non-specialist users. It provides to individuals with a basic understanding of Matlab and ArcGIS, enabling them to generate the suitability maps of different locations based on NN modeling. The toolbox simplifies and automates the various stages of processing, offering a user-friendly solution that holds the potential to revolutionize solid waste management systems.

2. Methods

1.1 Model Automation

The automated toolbox serve for conducting landfill suitability mapping. These toolboxes dynamically executed through a combination of the ArcGIS-Python and Matlab environment. They form an integral part of our workflow, seamlessly linking the ArcGIS Python toolbox with the sophisticated NN structure within the Matlab environment. Figure 1. illustrated the flowchart of our NN toolbox unfolds across nine distinct toolsets, each

representing crucial stages for data preparation and analysis, as depicted in Figure 2. The toolbox carries several notable benifits as outlined below:

- User-Friendly Interface: It simplifies the end-users experience, particularly decision-makers, by automating various stages, reducing the likelihood of human errors, and minimizing time wastage.
- Flexible Functionality: Our toolbox empowers users to swiftly create both straightforward and complex workflows in a systematic and efficient manner.
- Interoperability: It seamlessly integrates Matlab environment, enhancing the range of functionalities for geospatial modeling.
- Streamlined Criteria Selection: The model facilitates the selection of criteria thus, streamlining the decision-making process.

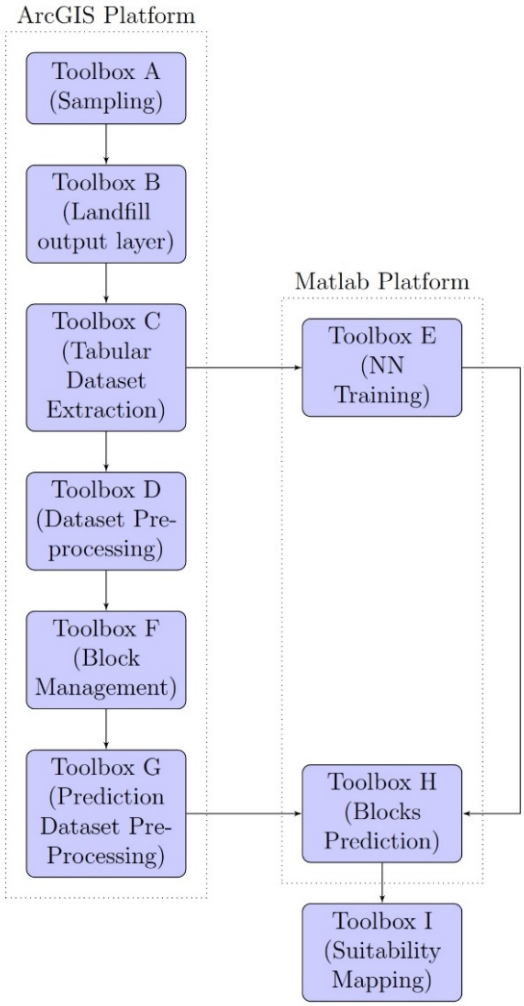

Figure 1. Presents the flowchart detailing the expansion of our Neural Network toolbox across nine distinct toolsets. Each toolset corresponds to essential stages in data preparation and analysis.

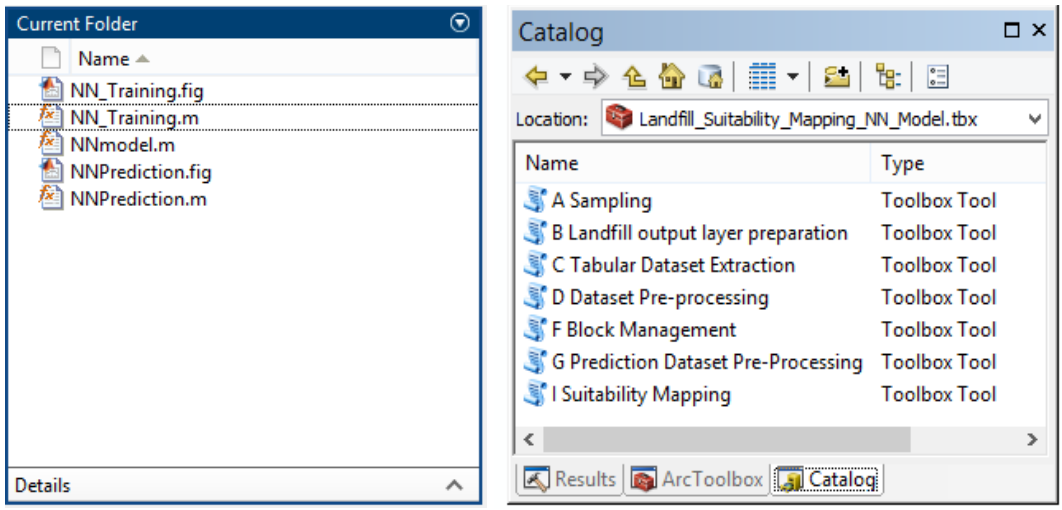

Figure 2. Developed Toolbox in ArcGIS and Matlab Environment.

The developed model designed to import ESRI layers and tabular data in Matlab. The toolboxes descried as the following:

The Python script named (A: Sampling) serves the purpose of generating a spatial sampling framework within a given study area, particularly focusing on areas designated as landfills (see Figure 3. and Annex 1.). It employs ArcPy, the Python site package for ArcGIS, to execute geospatial operations. Initially, it imports necessary modules and sets up the environment, including setting overwrite output to true and checking out the spatial extension license. The script then receives input parameters such as landfill polygons, study area polygons, and coordinate system information. It proceeds to create a fishnet grid within the boundaries of the landfill polygons, using the CreateFishnet function. Subsequently, the grid is clipped to the landfill extents, resulting in a refined grid. This clipped grid is further processed: converted to lines, then to points, and duplicates are removed. Another aspect of the script involves creating random sample points within areas excluding the landfills, achieved by erasing landfill areas from the study area and generating random points constrained within the resulting non-landfill areas. Finally, the script merges the refined grid points with the random sample points to produce a comprehensive set of sampling points for further analysis, facilitating spatial data collection and analysis within the specified study area.

The Python script named (B: Landfill output layer preparation) is designed to prepare an output layer that distinguishes between landfill areas and the rest of the study area (see Figure 3. and Annex 2.). Utilizing ArcPy and ArcGIS Spatial Analyst tools, the script initially imports necessary modules and sets up the environment. It then acquires input parameters such as landfill and study area polygon layers, coordinate system information, and cell size. Following this, the script defines field attributes for indicating landfill presence and absence, and it adds and calculates these fields accordingly to the study area layer. Subsequently, it merges the landfill and study area layers into a single vector layer and converts this merged layer into a raster format. The raster values are then reclassified to assign a value of 1 to landfill areas and 0 to non-landfill areas, resulting in the final output raster layer. Finally, the script refreshes the Table of Contents (TOC) and the Active View in the ArcGIS environment to reflect the updated layers. This process enables the creation of a spatially explicit representation of landfill areas within the study area for further analysis and visualization.

The Python script named (C: Tabular Dataset Extraction) is developed to extract values from raster layers to corresponding sample points and perform data cleanup operations (see Figure 3. and Annex 3.). The script acquires input parameters such as point features and raster layers. The script identifies and drops unnecessary fields from the input point features to streamline the dataset. Following this, it utilizes the ExtractMultiValuesToPoints function to extract values from target raster layers to the points. Additionally, the script extracts values from additional raster layers to the same set of points. This process ensures that the points possess relevant raster values, facilitating subsequent spatial analysis.

The Python script named (D: Dataset Pre-processing) is designed to prepare a dataset for training machine learning models (see Figure 3. and Annex 4.). The script begins by defines the workspace based on the input dataset and creates a feature layer. The script iterates through selected fields to remove rows with missing data, ensuring data integrity. Subsequently, it constructs the dataset by extracting samples and shuffling them to prevent

biases during training. The dataset is divided into input features and target variables, reshaped as necessary. Finally, the script outputs the prepared input and target datasets to specified paths.

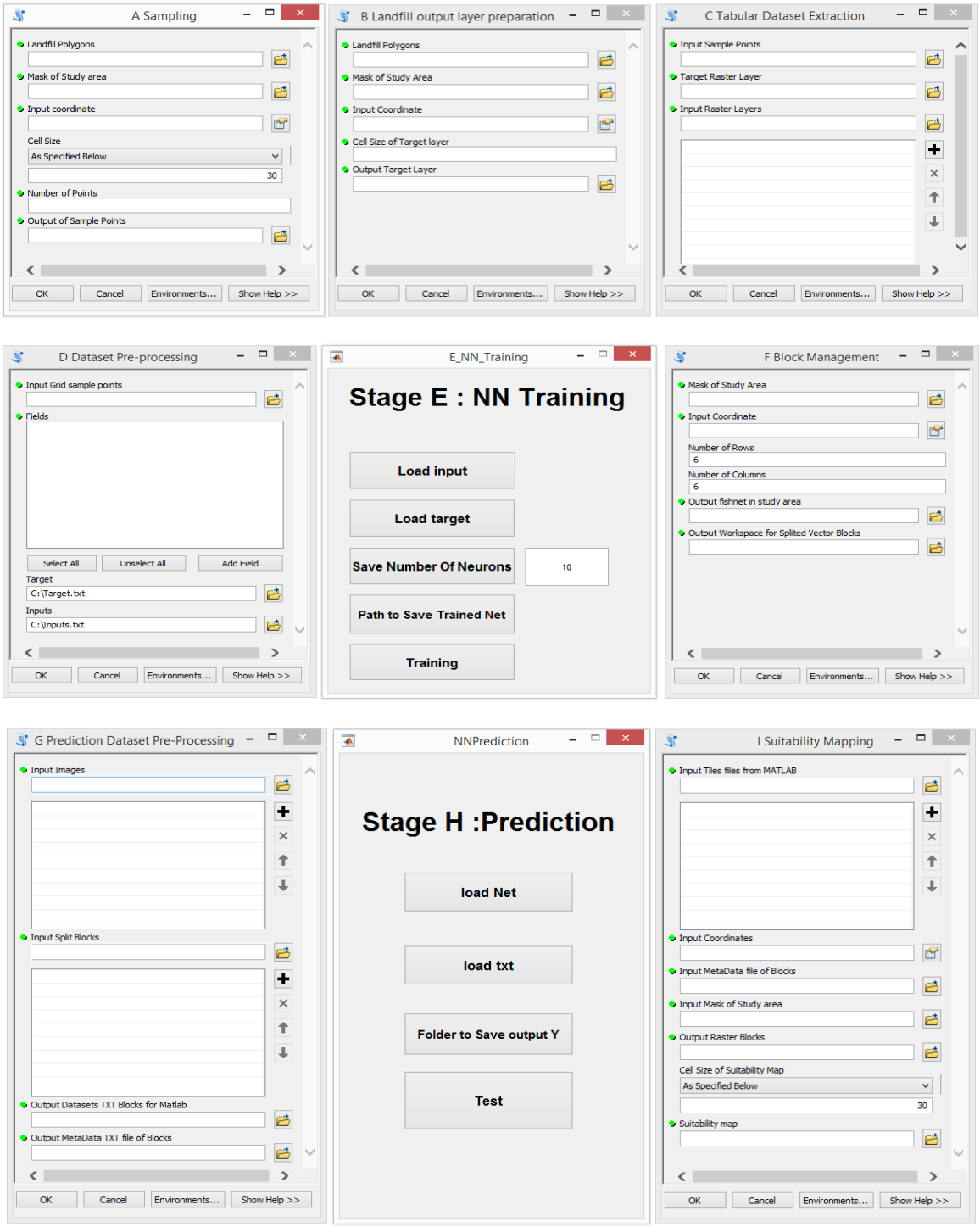

Figure 3. Toolbox Suite for Landfill Site Selection using Neural Networks. This comprehensive toolbox suite comprises nine interconnected Python and MATLAB scripts (A-I) designed for landfill site selection employing neural networks. From spatial sampling, dataset extraction, to neural network training and prediction, these scripts utilize Python, and MATLAB, to streamline processes like block management, dataset preparation, and suitability mapping.

The MATLAB script named (E: NN_Training) serves the purpose of training a neural network model using graphical user interface (GUI) interaction (see Figure 3. and Annex 5.). The script initializes the GUI parameters and handles user interactions, such as loading input and target data files, specifying the path to save the trained network, and setting the number of neurons for the model. Upon user inputs, the script executes the neural network training function "NNmodel" with the provided input, target data, and specified number of neurons. The trained model is then saved to the specified output network path. The trained NN model is encapsulate in (*.m) format for further stages. The MATLAB function "NNmodel" is developed to create and train a neural network model based on provided input and target data. The function utilizes the scaled conjugate gradient backpropagation algorithm for training, denoted by the variable "trainFcn". It initializes a neural network using the "patternnet" function with a specified number of neurons. The data is divided into training, validation, and testing sets using predefined ratios. This methodology streamlines the process of neural network model creation and training, enabling efficient experimentation and analysis with different datasets and model configurations.

1.2 Study area

The Python script named (F: Block Management) aims to generate blocks from a given shapefile and subsequently split them based on a provided mask (see Figure 3. and Annex 6.). The script creates a describe object from the input shapefile to extract its extent, which is used to define the boundary points for block generation. Blocks are generated using the CreateFishnet function, creating a grid within the extent of the shapefile. The script then selects blocks intersecting with the mask shapefile and copies them to an output feature class. Subsequently, it splits the selected blocks based on a specified field, assigning unique identifiers to each split block.

The Python script named (G: Prediction Dataset Pre-Processing) is designed to generate metadata and datasets for each block defined by vector polygons (see Figure 3. and Annex 7.). It retrieves input raster maps and vector polygons along with output folders for metadata and datasets. For each vector polygon, the script extracts its extent and iterates through the raster maps to clip them to the polygon extent. It then converts the clipped raster maps to NumPy arrays and saves them as text files. The script also computes metadata such as minimum x-coordinate (xmin), minimum y-coordinate (ymin), mean cell width, mean cell height, row count, and column count for each block and saves them to a metadata file. This methodology enables the creation of datasets and metadata tailored to each block within the study area, facilitating subsequent analysis and modeling tasks.

The MATLAB script named (H: Block NNPrediction) implements a graphical user interface (GUI) for conducting neural network predictions (see Figure 3. and Annex 8.). It initializes the GUI parameters and handles user interactions such as loading trained network models and input data files. Upon user inputs, specifically loading the trained model and input data files, the script executes the neural network prediction function. For each input data file, the script loads the trained model, performs prediction using the input data, and saves the predicted output (Y) as text files. The predicted values between 0 and 1 as the foundation for predictions. This methodology provides a user-friendly interface for conducting neural network predictions, allowing users to conveniently load models and input data, perform predictions, and save the results for further analysis.

The Python script named (I: Suitability Mapping) is representing the conclusive phase, this stage marks the step in generating the tentative suitability map (see Figure 3. and Annex 9.). The script retrieves input prediction files along with metadata and other parameters such as the study area mask and output folder. For each predicted (Y) text file, the script reshapes the data and saves it as an ASCII file, then converts it to a raster format. The raster paths are collected and used to mosaic them into a single raster image. Additionally, the script clips the mosaic raster based on the study area mask. Finally, the clipped raster is saved as the output suitability map. This methodology enables the conversion, aggregation, and clipping of prediction files to generate a comprehensive raster output tailored to the study area.

The study area was conducted in the northern region of Peninsular Malaysia, specifically encompassing Penang, Perak, Perlis and Kedah, states as illustrated in Figure 4. The area of study area is covers 32,191 square kilometers, constituting roughly 9.75% of Peninsular Malaysia. As of the 2010 demographic data, the region inhabited by a population of 2,258,428 people. Meteorologically, the area is characterized by a warm and sunny climate, experiencing rainfall 3,218 millimeters per year. The topography of the area varies from flat terrain to hilly regions, with elevations spanning from 1 meter above sea level (m AMSL) to 3,978 meters AMSL.

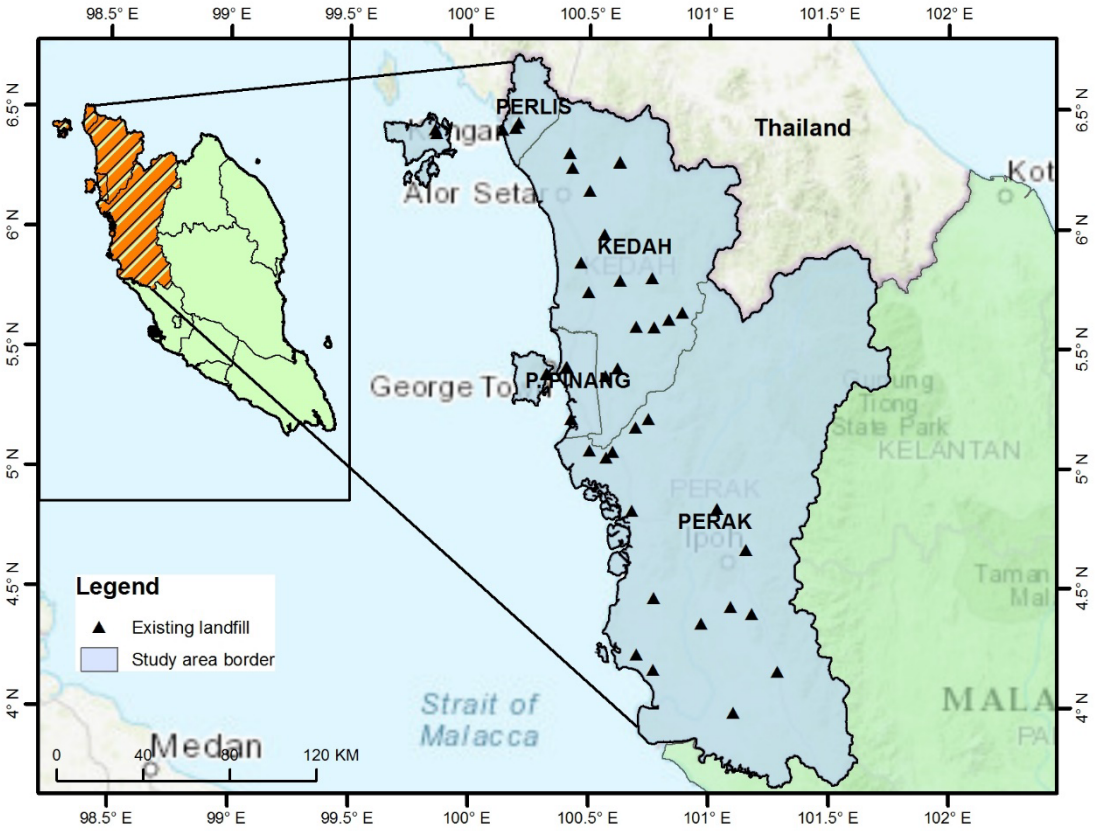

Figure 4. Study Region (Perak, Penang, Kedah, and Perlis).

Spatial data layers corresponding to the chosen criteria were prepared. The existing landfill sites depicted in Figures 4, while the sample points of non-landfill presented in Figure 5. The tabular data extracted using the developed toolbox. Figures 5 and 6 presenting the relevant explanatory 14 parameters, which are distance from district boundaries, secondary roads, federal roads, highways, hospitals, airports, dams, rivers, geological faults, caves, as well as precipitation, slope, elevation, and landuse.

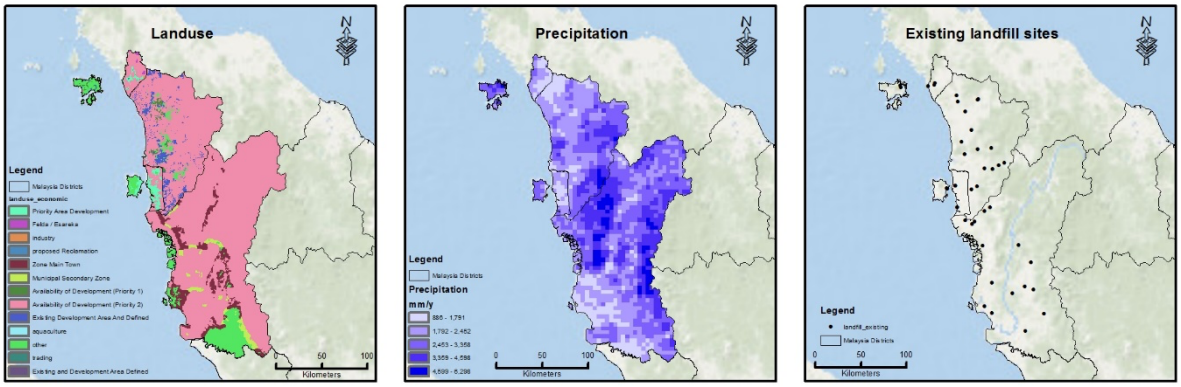

Figure 5. Precipitation, and Landuse, as well as the existing landfill sites.

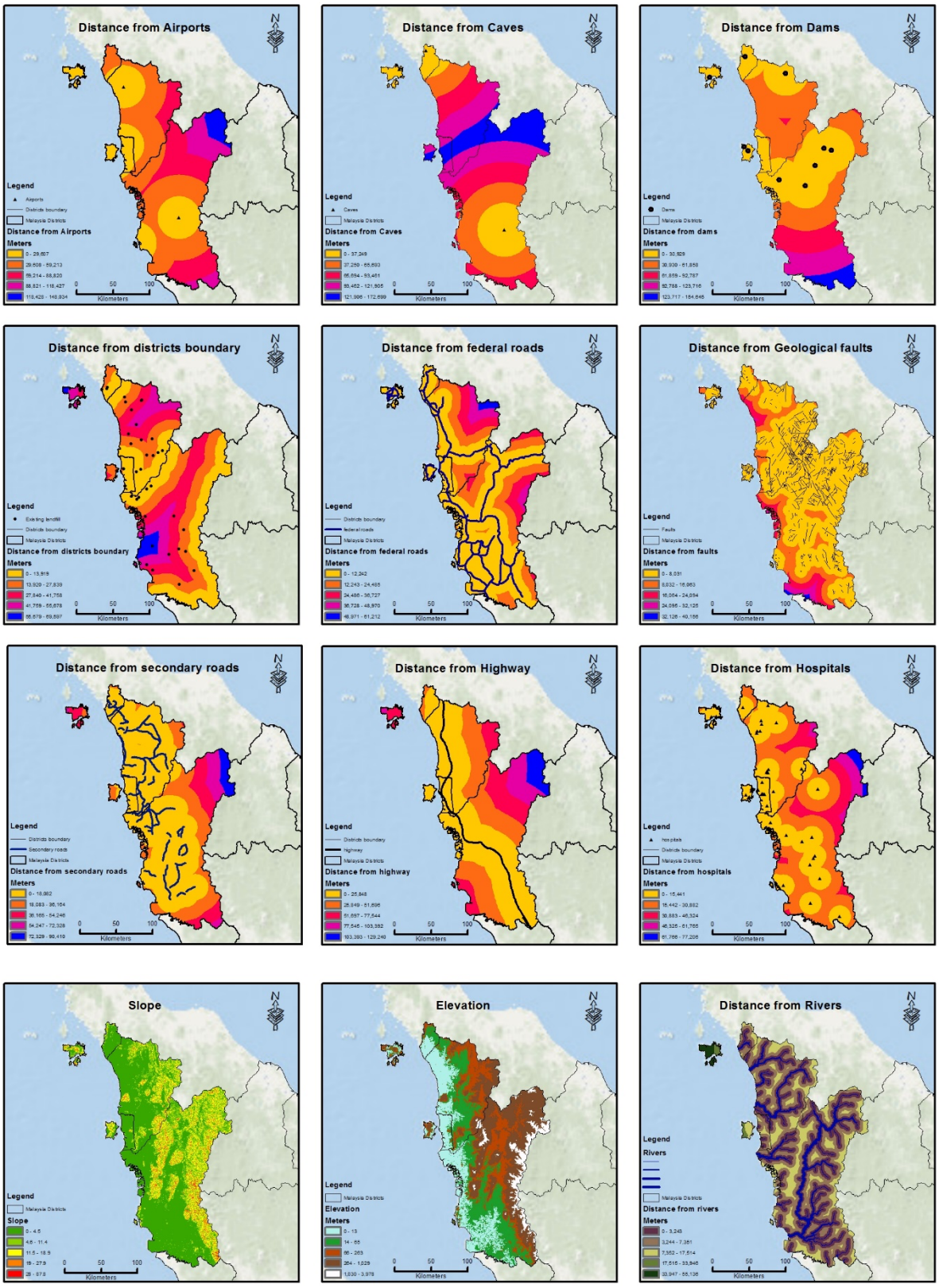

Figure 6. Distance from several variables such as Caves, dams, Geological faults, Secondary roads, federal road, Highway, local boundaries, Airports, Rivers, and hospitals as well as Slope, and Elevation.

3. Results

3.1.Tool implementation for Suitability Mapping

The utilization of the developed toolkit facilitated the systematic generation of a suitability map tailored to our designated study area. In phase A, samples established with spatial resolution of 30 meters, ultimately yielding a 7000 sample points. Moving to phase B, the landfill binary target map produced, drawing it from the pool of collected landfill polygons. Simultaneously, stage C generate the attributes through the 14 variables in conjunction with the binary output map of landfill and non-landfill categories. Phase D undertook the critical task of processing the tabular data associated with the generated points, which was then construct our training dataset. It is worth noting that this process resulted in a final processed dataset housing 5,902 records, after the removing of missing records and outliers. Phase E, the NN model generated and trained as well exhibited remarkable accuracy of 82% during testing. Phase F created of a grid of blocks that effectively partitioned our study area into manageable blocks. Stage G, assembled tabular dataset of blocks. In totality, 19 subsets generated (see figure 7). In stage H, we transitioned into the prediction stage, supported by the trained NN model. The trained NN model processing the 19 subsets, yielding Y values. Phase I, present of the suitability mapping of landfills.

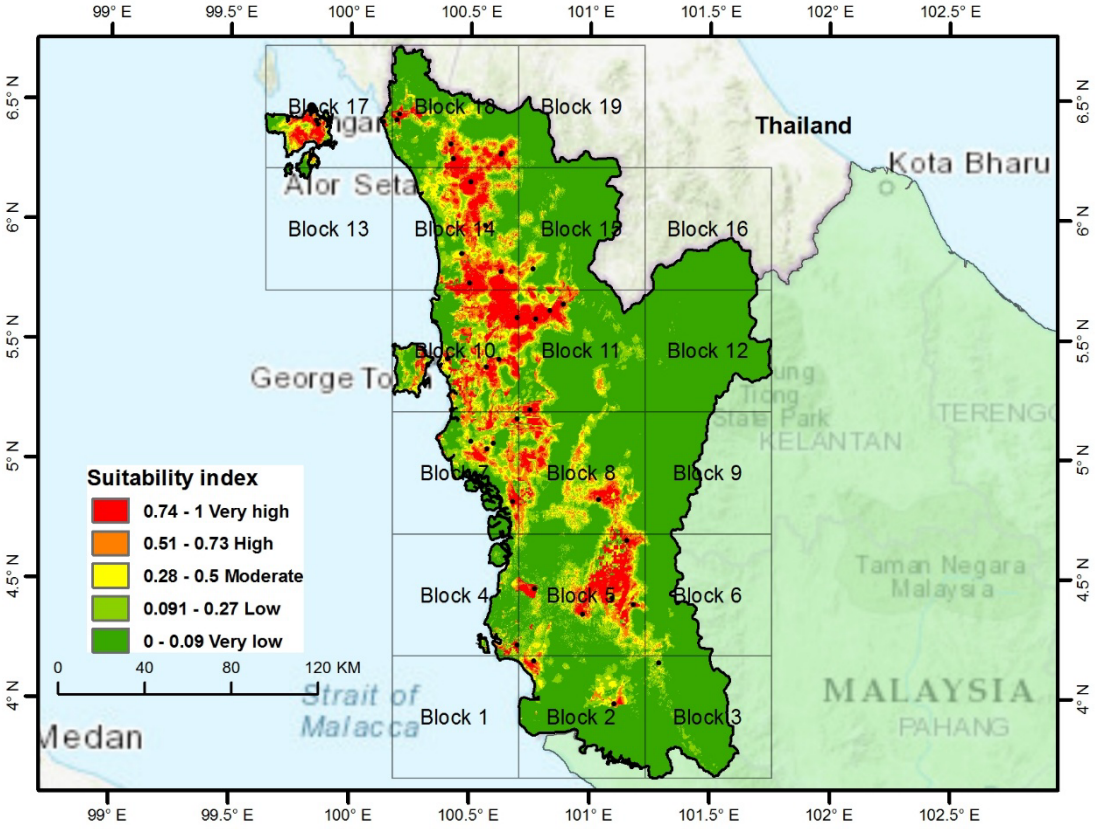

Figure 7. Suitability Map for Solid Waste Landfill Sites Generated Using the Automated and Integrated NN Model.

Figure 7 illustrates the suitability map for the solid waste landfills. This map highlights areas categorized as either suitable or unsuitable for landfill placement. To enhance the map's clarity, a legend provided with the suitability index. Notably, majority of area falls into the low suitability category, encompassing 57.84% of the total area. This distribution includes 26.56% in the low suitability category, 2.89% in the moderate suitability category, and 1.86% in high suitability category. A 10.82% exhibits a very high suitability category.

3.2.NN model performance

The Figure 8. shows a confusion matrix for a machine learning model classifying two classes. The confusion matrix is a table that compares the actual labels of the data with the labels predicted by the model. In this case, the rows represent the actual classes, and the columns represent the predicted classes. Each cell of the table shows the number of instances (5273 for class 0 and 3153 for class 1) and the corresponding percentage (51.3% and 30.7% respectively) of how many instances were correctly classified. For example, the top-left cell (5,273) shows that the model correctly predicted 89.4% of the instances that actually belong to class 0. The bottom right cell (3153) shows that the model incorrectly classified 27.9% of the instances that actually belong to class 1 as class 0. Overall, the model performs better at classifying class 0 with a higher accuracy (89.4%) and a lower error rate (10.6%) compared to class 1 (72.1% accuracy and 27.9% error rate). The overall accuracy metric is 82%.

In addition, the figure shows a Receiver Operating Characteristic (ROC) curve, which is a graph used to visualize the performance of a binary classification model. The ROC curve plots the true positive rate (TPR) on the y-axis against the false positive rate (FPR) on the x-axis. The TPR is the proportion of positive cases that were correctly identified by the model, while the FPR is the proportion of negative cases that were incorrectly classified as positive. A perfect classifier would have a ROC curve that follows the upper left corner of the graph, meaning it has a 100% TPR and a 0% FPR. In the ROC curve depicted in the figure, the AUC (Area Under the Curve) is difficult to determine visually due to the lack of gridlines and specific data points. However, a higher AUC generally indicates a better performing classifier. Overall, the ROC curve in the figure can be used to assess the trade-off between TPR and FPR for the binary classification model.

The F1 score, which balances precision and recall, was calculated as 77.2% for Class 1, indicating a strong but improvable model performance. This suggests that while the model effectively identifies landfill-suitable areas, some misclassification persists. Future improvements could focus on optimizing feature selection and refining classification thresholds to enhance predictive accuracy.

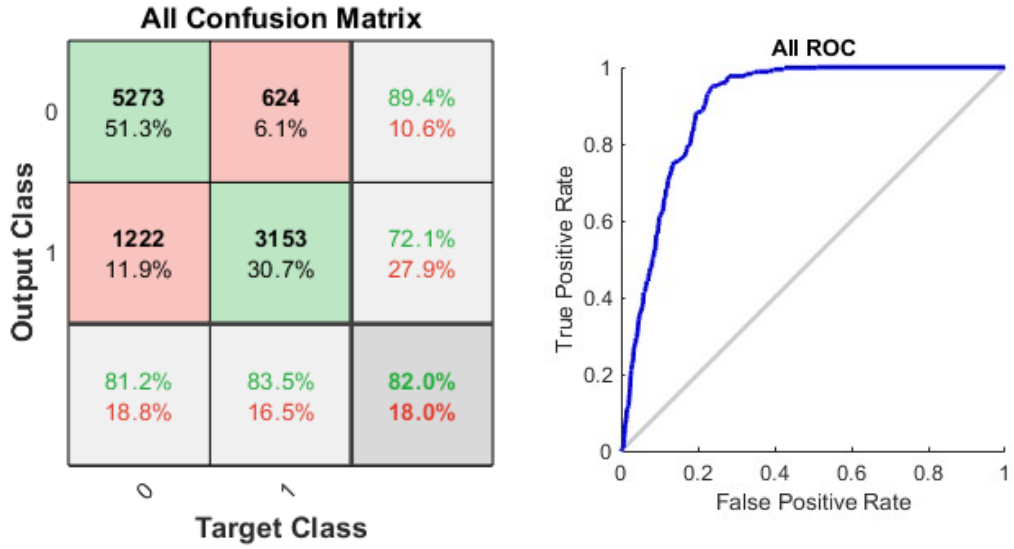

Figure 8. Evaluation Metrics for the Machine Learning Model

4. Discussion

The developed Neural Network Toolbox demonstrably improved the efficiency and accuracy of landfill suitability mapping by automating various stages of the process (See Table.1.). By automating tasks like spatial sampling, data preparation, and suitability map generation (previously completed manually), the toolbox minimizes human error and significantly reduces the time required to generate suitability maps, allowing decision-makers to focus on strategic planning and analysis. The integration of a neural network model within the toolbox facilitates highly accurate suitability assessments, as evidenced by the mentioned 82% accuracy, which surpasses traditional methods that may rely on subjective criteria or less sophisticated modeling techniques. Earlier methodologies, such as those developed by Majumdar, Eldrandaly, and Daneshvar, often struggled with

scalability, adaptability, and accessibility, especially for users with varying levels of GIS expertise [20–22]. By contrast, our toolbox simplifies these challenges through its user-friendly interface, flexible functionality, and seamless interoperability between MATLAB and ArcGIS environments.

Table 1. Comparison of the Developed Toolbox with Existing Methods.

Feature/Criteria	Traditional GIS-Based Approaches	Machine Learning-Based Methods	Proposed Neural Network Toolbox
Automation Level	Manual or semi-automated	Semi-automated	Fully automated
Integration	GIS-based only	Standalone ML models	Seamless integration with GIS & MATLAB
Ease of Use	Requires expert knowledge	Requires coding experience	User-friendly GUI, minimal coding required
Flexibility	Limited to rule-based models	Requires extensive parameter tuning	Adaptive learning with minimal manual intervention
Computational Efficiency	Moderate (depends on GIS software)	High computational cost	Optimized for efficiency with parallel processing
Interpretability	High (rule-based models)	Moderate to low (black-box nature)	Moderate (provides decision layers)
Scalability	Limited to small datasets	Works with large datasets	Optimized for large-scale analysis
Accuracy & Performance	Relies on predefined rules	Performance varies based on training data	High accuracy (82% with F1 score of 77.2%)
Strengths	Simple and interpretable	Can capture complex patterns	Combines GIS & ML for robust, automated decision-making
Weaknesses	Limited adaptability	Requires extensive tuning	Initial setup requires MATLAB & ArcGIS

The utilization of Python scripting within the ArcGIS toolbox creates a user-friendly interface, eliminating the need for in-depth GIS expertise and making the tool accessible to a wider range of decision-makers involved in waste management. The toolbox streamlines the entire workflow by automating various stages and provides flexibility by allowing users to create both simple and complex workflows, tailored to their specific needs and data requirements. The seamless integration of Python and MATLAB environments within the toolbox expands the range of functionalities available for geospatial modeling, leveraging the strengths of both platforms for a more comprehensive approach to landfill suitability mapping. This innovative toolbox, integrating Python-ArcGIS and MATLAB environments, automates the complex process of landfill site selection, addressing several limitations observed in previous models that struggled with scalability, adaptability, and accessibility, especially for users with varying levels of GIS expertise.

The highly promising results, highlighted by a testing accuracy of 82%, underscore the robustness and reliability of our model. The automation of the neural network model not only minimizes human errors but also significantly reduces the time required for data processing and suitability mapping. Moreover, the toolbox's ability to dynamically execute processes across nine distinct stages ensures efficient data handling and streamlined workflows, optimizing internal memory usage and allowing for the integration of diverse datasets, making the model adaptable to various geographic regions and environmental conditions.

Our case study in northern Peninsular Malaysia demonstrates the practical application and effectiveness of the toolbox, with the suitability map generated through our automated process providing a clear and accurate identification of potential landfill sites, crucial for informed decision-making. By overcoming the limitations of previous models and offering a robust, automated solution, our research contributes to more efficient, accurate, and sustainable landfill site selection, benefiting decision-makers and supporting broader environmental protection efforts by optimizing the management of solid waste.

5.Conclusion

In this research, we introduced an innovative approach that addresses the challenges of developing a robust method for landfill suitability mapping through automating a NN model. Through a case study in the northern region of Peninsular Malaysia, we demonstrated effectiveness of our methodology by employing 14 specific criteria to create training and testing datasets.

The results of our study were highly promising, with a remarkable testing dataset accuracy of 82% achieved. This automated toolbox has laid a durable foundation for decision making process of landfill suitability mapping. It has shown great potential for optimizing processes within this critical domain, contributing to enhanced solid

waste management systems and unifying tasks into a user-friendly workflow tailored to the needs of decision-makers.

The significance of our research lies in the simplification and automation of the landfill suitability mapping process, offering a user-friendly interface that minimizes human errors and accelerates decision-making. The flexibility and interoperability of our model enable users to create both simple and complex workflows while integrating various environments. We streamlined criteria selection and facilitated the decision-making process, making it more accessible to a broader audience.

Our research has overcome the limitations of previous models, such as data integration challenges, manual input requirements, and lack of adaptability to different geographical areas. By developing an ArcGIS Toolbox using Python scripting, we have successfully enhanced the performance of the streamlining Landfill suitability mapping workflow, which ultimately benefits solid waste management systems.

The suitability mapping in the study area exemplifies practical application of our model. By automating the entire process, from data preparation to suitability mapping, we achieved an impressive level of accuracy in identifying potential landfill sites. The division of the workflow into nine distinct stages optimizes internal memory usage and ensures efficiency throughout the process.

Future studies should expand the geographic scope of the toolbox, validating its use in diverse regional and global settings. Incorporating additional criteria, such as detailed soil characteristics, groundwater flow, and climate change projections, could improve model accuracy. Enhancing the user interface and automating more processes would simplify decision-making for non-experts. Integrating the toolbox with other decision-making tools and incorporating policy and economic analysis could provide a more comprehensive support system. Real-time data integration and updating capabilities, along with performance optimizations like advanced neural network architectures and parallel processing, can improve efficiency. Validating the model against existing ones and conducting longitudinal studies to assess temporal changes and long-term impacts will ensure the model's reliability and sustainability in landfill suitability mapping and broader environmental planning applications.

References

[1] Demesouka OE, Anagnostopoulos KP, Siskos E. Spatial multicriteria decision support for robust land-use suitability: The case of landfill site selection in Northeastern Greece. Eur J Oper Res 2019; 272:574–86.

[2] Demesouka OE, Vavatsikos AP, Anagnostopoulos KP. Suitability analysis for siting MSW landfills and its multicriteria spatial decision support system: Method, implementation and case study. Waste Management 2013; 33:1190–206.

[3] Owoseni JO. Landfill site suitability mapping for rational development planning: a GIS-based multi-criteria evaluation in Edo State, Nigeria. GeoJournal 2023; 88:4603–24.

[4] Demesouka OE, Vavatsikos AP, Anagnostopoulos KP. GIS-based multicriteria municipal solid waste landfill suitability analysis: A review of the methodologies performed and criteria implemented. Waste Management & Research 2014; 32:270–96.

[5] Karipoğlu F, Koca K, Zeray Öztürk E. GIS-AHP Approach for A Comprehensıve Framework to Determıne the Suıtable Regıons for Geothermal Power Plants in Izmır, Türkiye. Konya Journal of Engineering Sciences [Internet] 2024;12:263–79. Available from: https://doi.org/10.36306/konjes.1381523

[6] Mir MA, Ghazvinei PT, Sulaiman NMN, Basri NEA, Saheri S, Mahmood NZ, et al. Application of {TOPSIS} and {VIKOR} improved versions in a multi criteria decision analysis to develop an optimized municipal solid waste management model. J Environ Manage 2016;166:109–15.

[7] Khan D, Samadder SR. Municipal solid waste management using Geographical Information System aided methods: A mini review. Waste Management & Research 2014;32:1049–62.

[8] Ahmad SZ, Ahamad MSS, Wan Hussin WMA. Application of gis in extracting spatial criteria from existing landfill site a study on pulau burong landfill site. In: 13th International Surveyor Congress. Malaysia: 2011.

[9] Afzali A, Samani JM V, Rashid M. Municipal landfill site selection for Isfahan City by use of fuzzy logic and analytic hierarchy process. Iranian J Environ Health Sci Eng 2011;8:273–84.

[10] Ghobadi MH, Babazadeh R, Bagheri V. Siting MSW landfills by combining AHP with GIS in Hamedan province, western Iran. Environ Earth Sci 2013;70:1823–40.

[11] Javaheri H, Nasrabadi T, Jafarian MH, Rowshan GR, Khoshnam H. Site selection of municipal solid waste landfills using analytical hierarchy process method in a geographical information technology environment in giroft. 2006;3:177–84.

[12] Mahamid, Thawaba S. Multi criteria and landfill site selection using GIS: a case study from Palestine. Open Environmental Engineering Journal 2010;3:33–41.

[13] Pradhan B, Billa L. GIS modeling for selection of a transfer station site for residential solid waste separation and recycling. Pertanika J Sci Technol 2013;21:477–88.

[14] Son LH, Louati A. Modeling municipal solid waste collection: A generalized vehicle routing model with multiple transfer stations, gather sites and inhomogeneous vehicles in time windows. Waste Management 2016;52:34–49.

[15] Günay EE, Dere S. Hazardous Solid Waste Landfill Site Selection for İstanbul, Türkiye using Multi-Criteria Decision-Making Methods and GIS Data. Journal of Advanced Research in Natural and Applied Sciences [Internet] 2024;10:446–63. Available from: https://doi.org/10.28979/jarnas.1416814
[16] Tulun Ş, Gürbüz E, Arsu T. Developing a GIS-based landfill site suitability map for the Aksaray province, Turkey. Environ Earth Sci 2021;80.
[17] Macalam FJT, Arreza KP, Magpantay AT, Rabaño KY. Landfill Site Suitability Assessment Using Geographic Information System (GIS) and Analytic Hierarchy Process (AHP) in Butuan City, Philippines. Journal of Environmental and Earth Sciences 2023;5.
[18] Gupta N, Yadav KK, Kumar V. A review on current status of municipal solid waste management in India. Journal of Environmental Sciences 2015;37:206–17.
[19] Wijesinghe DC. GIS-based AHP and MCDA Modeling for Cropland Suitability Analysis: A Bibliometric Analysis. Gazi University Journal of Science Part A: Engineering and Innovation [Internet] 2024;11:598–621. Available from: https://doi.org/10.54287/gujsa.1510527
[20] Majumdar A, Hazra T, Dutta A. Landfill Site Selection by AHP Based Multi-criteria Decision Making Tool: A Case Study in Kolkata, India. Journal of The Institution of Engineers (India): Series A 2017;98:277–83.
[21] Eldrandaly K. Developing a GIS-based MCE site selection tool in ArcGIS using COM technology. Int. Arab J. Inf. Technol. 2013;10:276–82.
[22] Daneshvar R. Customizing arcmap interface to generate a user-friendly landfill site selection GIS tool. 2004;
[23] Yesilnacar MI, Süzen ML, Kaya BŞ, Doyuran V. Municipal solid waste landfill site selection for the city of Şanliurfa-Turkey: an example using MCDA integrated with GIS. Int J Digit Earth 2011;5:147–64.

Turkish Journal of Science & Technology
20(1), 135-140, 2025

Research Paper
https://doi.org/10.55525/tjst.1421838

Epipsammic Diatoms of Sülük Lake (Ağın/Elazığ, Türkiye)

Metin ÇAĞLAR[1*]
[1]Faculty of Fisheries, Fırat University, Elazığ, Türkiye
[*1] mcaglar@firat.edu.tr

(Geliş/Received: 18/01/2024; Kabul/Accepted: 01/02/2025)

Abstract: In this study, epipsammic diatoms in water sampled from a particular station on Sülük Lake (Ağın/Elazığ) between March-November 2022 were examined. A total of 36 taxa belong to the epipsammic diatoms were identified throughout the investigation. Nitzschia was dominant with 5 taxa, followed by Cymbella and Surirella with 4 taxa. When the water temperature started to rise in the spring and summer, the diatoms reached the highest number. In the summer, water temperature (23.10 °C), dissolved oxygen (8.5 mg/L), and electrical conductivity (331.1 mho/cm) were recorded higher than others. The Sülük Lake is vulnerable to eutrophication because of its coastal structure, small surface area and especially useing as a picnic place in the spring and summer.

Key words: Sülük Lake, Epipsammic, Diatom.

Sülük Gölü Epipsammik Diyatomları (Ağın/Elazığ, Türkiye)

Öz: Bu çalışmada Sülük Gölü (Ağın/Elazığ) üzerindeki belirli bir istasyondan Mart-Kasım 2022 tarihleri arasında örneklenen epipsammik diatomlar incelenmiştir. Araştırma boyunca epipsammik diatomlara ait toplam 36 takson tespit edilmiştir. Nitzschia 5 takson ile baskın olurken, Cymbella ve Surirella 4 takson ile onu takip etmişlerdir. İlkbahar ve yazın su sıcaklığı artışı ile diatomlar en yüksek sayıya erişmiştir. Yaz aylarında göl suyunun sıcaklık (23,10 C), çözünmüş oksijen (8,5 mg/L) ve elektriksel iletkenlik (331,1 mho/cm) değerleri diğer aylara göre daha yüksek seviyelerde gözlemlendi. Sülük Gölü kıyı alanının yapısı, yüzey alanının küçük olması ve özellikle bahar ve yaz aylarında piknik alanı olarak kullanılması nedeniyle ötrofikasyona karşı hassastır.

Anahtar kelimeler: Sülük Gölü, Epipsammik, Diatom.

1. Introduction

Planktonic studies are the ones that initially made algaes existence known. The first link in the food chain and the primary producers of organic materials in aquatic environments are algae. Because they produce their own nutrients through photosynthesis, they are referred to as primary producers.

Diatoms are widespread algae that have significant biological and economic value and are widely distributed around the world [1]. In both fresh and salty water, as well as in benthic areas, diatoms constitute the most significant category of phytoplankton organisms. Those living on mud at the bottom of lakes and rivers is referred to as epipelic, while living on sand is referred to as epipsammic, living on rocks and other natural objects is referred to as epilithic, and dwelling on plants is referred to as epiphytic forms.

Algae are organisms that have high levels of fatty acids, proteins, and carbohydrates. The most significant source of minerals, vitamins, and trace elements for aquatic species is microalgae with high nutritional value. One of the categories that should be studied in order to assess ecosystem biodiversity is microalgae, which are crucial for aquatic ecosystems in terms of the food chain [2].

In recent years, data from research on the identification of Türkiyes freshwater algal flora have been compiled [3]. Studies indicate that the algal flora of a sizable portion of the wetlands in our nation has not been identified yet. The distribution of indicator species, in particular, and research on species diversity can serve as a foundation for assessing the ecological significance of the environment and tracking changes. From this perspective, it is vital to continue the investigations on the identification of the algal flora in all water resources. In terms of species diversity, some small wetlands may include both numerous and unusual species [4]. The importance of studying algae in lotic ecosystems is rising. It is essential to identify the ecological parameters and nutrient content in inland waters in order to assure the efficiency of the aquaculture operations. Therefore, it is important to understand the taxonomy, density, and seasonal variations of the phytoplankton and benthic algae that make up the first link in

* Corresponding author: mcaglar@firat.edu.tr ORCID Number of authors: [1]0000-0002-0442-2281

the food chain, as well as the ecological, physical, and chemical variables influencing the corresponding changes. Phytoplankton exhibits the strongest and most rapid changes in the aquatic ecosystems structure. Some pollution indicator algal species are important criteria for determining the degree of environmental pollution and eutrophication in these environments, in addition to information about productivity provided by the number and species richness of algae in aquatic ecosystems [5]. Since the 1980s, Türkiye has been conducting extensive research on the identification of algae species in lotic and lentic ecosystems (lakes, ponds, dam lakes, and rivers) [6-19].

Algae, which are found all over the world in a variety of habitats (such as water, soil, snow, etc.), contain indicator species that reveal the composition of their surroundings. In order to more effectively utilize the inland waters and transform them into a source of food and money in Türkiye, which has a highly rich supply of inland water resources, it is required to identify the algae present in the environment. Particularly in shallow lakes, benthic algae make up the majority of the algal flora and significantly increase the lakes production. The significance of this work is therefore elevated by the identification of the algae present in the Sülük Lakes bottom region and the clarification of their ecological interactions. The Sülük Lake within the borders of Balkayası Village of Ağın located 77 km away from the center of Elazığ are worth seeing with their natural beauty and surrounding green areas. The recreational areas, picnic sites, camellias and social facilities made of wood on the shores of the Sülük Lake have made it a preferable place in the district. The removal of the lakes reeds and landscaping will both greatly contribute in the growth of tourism in the area. Additionally, a Natural Park could be established here. Determining the epipsammic diatoms of the Sülük Lake and their monthly variations is the goal of this study.

2. Material and Methods

In this study, the epipsammic algae of the Sülük Lake (38° 55 06" N - 38°34 34" E) located in Ağın district of Elazığ were studied (Figure 1).

Figure 1. A satellite view of Sülük Lake (Ağın/Elazığ-Türkiye) [20].

Epipsammic algae were sampled by using the methods [21] from the Sülük Lake between March and November (2022). For this purpose, a glass rod with a diameter of 1 cm and a length of 100 cm was used. Permanent preparations were made from the epipsammic samples in order to be able to diagnose the diatoms accurately. For this purpose, samples taken in a certain volume (10 ml) were treated with 5 ml HNO_3 + 5 ml H_2SO_4 acid and boiled on a heat plate at 120 °C for 15 minutes, thus oxidizing the organic substances inside the diatom cells and only the diatom shells consisting of silicon remained in the beaker. This process was carried out in order

to observe the shell structures of diatoms called frustules in more detail. The boiled samples were placed in Erlenmeyer flasks that were previously sterilized and passed through pure water. In order to eliminate the acidity of the acidic environment in which the diatom shells were located, the acidic water in the beaker was carefully poured and pure water was added to the diatom shells remaining at the bottom of the beaker. This process was continued until the environment was close to neutral [21]. A drop of the sample containing the diatom shells was taken on a coverslip and left to dry at room temperature. Afterwards, the coverslips were lifted with a pair of forceps and closed by turning them upside down on the slide on which entellan had been previously dripped. In order to avoid leaving air bubbles in the preparation, light pressure was applied to the coverslip after the slide and coverslip were glued [21]. Species identification and counting of the diatoms were made by using a Nikon (model Alphaphot-2 YS2-H) inverted microscope. The counting was based on relative density (Eq.1) and the results are given as organism %.

$$\text{Relative density (Rd)} = (\text{NA}/\text{N})\text{x}100 \quad (1)$$

NA =Total number of a species individuals
N= Number of all species individuals [22].

Some studies [23-27] were used for the species identification of the diatoms found in the Sülük Lake. The temperature of the water at the stations was measured by using 1 °C graduated mercury thermometer. Oxygen and electrical conductivity were measured in situ by using a portable YSI 55 DO digital oxygen meter which is calibrated just before of using.

3. Results

Monthly changes in some physical and chemical parameters of the Sülük Lake (Ağın) are shown in Table 1.

Table 1. Monthly changes in some physical and chemical parameters of the Sülük Lake.

Parameters	Mar.	Apr.	May.	Jun.	Jul.	Aug.	Sep.	Oct.	Nov.
Temperature (°C)	20	20	24	26	27	27	27	19	18
Dissolved Oxygen (mgO_2/L)	9.5	9.5	8.0	7.5	7.0	7.1	8.9	9.7	9.7
Electrical Conductivity (µmho/cm)	380	380	307	320	320	321	318	318	316

During the study, the highest temperature (27°C) was recorded in July, August and September; the lowest temperature (18°C) was recorded in November; the highest dissolved oxygen value (9.7mg O_2/L) was recorded in October and November; the lowest dissolved oxygen value (7.0mg O_2/L) was recorded in July; the highest electrical conductivity (380 µmho/cm) was recorded in March and April; and the lowest electrical conductivity (316 µmho/cm) was recorded in November.

The epipsammic diatoms recorded in the Sülük Lake in Ağın (Elazığ) and their relative densities are shown in Table 2. When Table 2 is examined, it can be seen that a total of 36 taxa belonging to the diatoms were recorded in the Sülük Lake: Cymatopleura (1 taxon), Cymbella (4 taxa), Cymbopleura (1 taxon), Delicatophycus (1 taxon), Diatoma (2 taxa), Encyonema (2 taxa), Encyonopsis (1 taxon), Fragilaria (1 taxon), Gomphonema (3 taxa), Lindavia (1 taxon), Mayamaea (1 taxon), Navicula (3 taxa), Nitzschia (5 taxa), Pantocsekiella (1 taxon), Pinnularia (3 taxa), Surirella (4 taxa) and Ulnaria (2 taxa). The maximum number of species belonged to Nitzschia with 5 taxa.

According to Table 2, the highest relative density (5.82%) during the study belonged to *Ulnaria ulna* species. The relative densities of *U. ulna* did not fall below almost 4% during the study. The lowest relative density (0.96%) among the epipsammic diatoms belonged to *Surirella librile*. The relative densities of this diatom were recorded to be below 2% in all months except for August. The relative densities of Encyonema elginense and Navicula gregaria species in November (4.85%) were the second highest relative densities. Furthermore, the recorded relative densities of Cymbella affinis, Cymbella cistula, Cymbella parva, Navicula cryptocephala, Navicula radiosa and Ulnaria ulna never fell below 3% in any of the months. The relative density of Surirella angusta, on the other hand, never reached 2% in any month.

Table 2. Presence and relative densities of the epipsammic diatoms recorded in the Sülük Lake by months.

	Mar.	Apr.	May.	Jun.	Jul.	Aug.	Sep.	Oct.	Nov.
Cymatopleura elliptica Brebisson W.Smith	2.23	1.92	1.83	2.04	1.93	1.84	1.92	1.42	1.94
Cymbella affinis Kützing	3.73	3.84	3.67	3.79	3.62	3.91	3.20	3.31	3.88
Cymbella cistula (Ehrenberg) O.Kirchner	4.47	4.32	3.30	3.49	3.86	3.45	4.80	3.79	3.88
Cymbella helvetica Kützing	2.23	2.40	2.94	2.91	2.65	2.99	2.88	3.31	1.94
Cymbella parva (W.Smith) Kirchner	3.73	3.36	3.30	3.20	3.14	3.22	3.20	3.79	3.88
Cymbopleura amphicephala (Nägeli ex Kützing) Krammer	4.47	3.84	3.30	3.20	3.14	2.76	3.20	3.31	3.88
Delicatophycus delicatulus (Kützing) M.J.Wynne	2.98	2.88	3.30	3.49	3.38	3.68	4.16	3.79	2.91
Diatoma elongata (Lyngbye) C.Agardh	2.98	2.88	2.57	3.20	3.14	2.30	2.56	2.84	1.94
Diatoma vulgaris Bory	3.73	2.40	2.94	2.91	2.65	2.99	2.24	2.36	2.91
Encyonema elginense (Krammer) D.G.Mann	3.73	3.36	2.57	2.91	2.65	2.99	3.20	2.36	4.85
Encyonema ventricosum (C.Agardh) Grunow	4.47	3.84	3.67	2.91	2.89	2.53	2.56	2.84	3.88
Encyonopsis microcephala (Grunow) Krammer	1.49	3.36	2.94	2.62	2.41	2.76	2.24	2.36	0.97
Fragilaria tenera (W.Smith) Lange-Bertalot	1.49	2.40	2.57	2.04	1.93	2.07	2.56	2.84	2.91
Gomphonema acuminatum Ehrenberg	2.98	1.92	2.20	2.33	2.65	2.99	2.88	2.36	1.94
Gomphonema angustatum (Kützing) Rabenhorst	2.98	2.88	2.94	3.20	3.14	3.15	3.20	3.79	2.91
Gomphonema olivaceum (Hornemann) Brébisson	3.73	2.40	2.57	2.62	2.89	3.22	2.88	3.31	2.91
Lindavia comta (Kützing) Nakov, Gullory, Julius, Theriot & Alverson	1.49	2.40	2.57	2.62	3.14	2.99	2.56	1.89	1.94
Mayamaea atomus (Kützing) Lange-Bertalot	2.98	3.36	2.57	2.91	2.65	2.76	2.56	2.84	2.91
Navicula cryptocephala Kützing	4.47	4.32	3.67	3.79	3.86	3.91	4.48	4.26	3.88
Navicula gregaria Donkin	2.98	2.88	4.08	3.49	3.14	2.76	2.88	2.84	4.85
Navicula radiosa Kützing	4.47	3.84	4.08	3.79	3.62	2.53	2.88	1.89	3.88
Nitzschia palea (Kützing) W.Smith	3.73	3.36	3.30	3.20	3.14	3.45	2.88	2.84	2.91
Nitzschia sigma (Kützing) W.Smith	2.23	1.44	1.47	1.45	1.69	2.07	1.92	2.36	2.91
Nitzschia sigmoidea (Nitzsch) W.Smith	2.98	2.40	2.20	2.33	2.41	2.07	2.24	2.36	1.94
Nitzschia tenuis W.Smith	1.49	2.88	3.30	3.20	3.14	3.22	3.20	3.79	2.91
Nitzschia terrestris (J.B.Petersen) Hustedt	1.49	1.92	1.83	2.04	2.17	1.61	1.60	1.42	0.97
Pantocsekiella ocellata (Pantocsek) K.T.Kiss & Ács tella ocellata	0.74	1.44	1.83	2.33	2.17	2.30	2.24	1.89	1.94
Pinnularia divergens W.Smith	1.49	1.92	1.83	2.04	2.41	2.07	2.24	2.36	0.97
Pinnularia nobilis (Ehrenberg) Ehrenberg	2.23	2.40	2.20	2.62	2.65	2.76	2.88	3.31	2.91
Pinnularia viridis (Nitzsch) Ehrenberg	2.98	2.88	2.94	2.33	2.41	2.53	2.56	2.36	1.94
Surirella angusta Kützing	1.49	1.44	1.47	1.16	1.69	1.84	1.92	1.89	1.94
Surirella librile (Ehrenberg) Ehrenberg	1.49	0.96	1.47	1.45	1.69	2.07	1.92	1.42	0.97
Surirella minuta Brébisson ex Kützing nom illeg	1.48	2.88	3.30	3.20	3.14	3.22	2.56	3.31	2.91
Surirella ovalis Brébisson	2.23	2.40	2.94	2.91	2.89	2.53	2.24	2.36	1.94
Ulnaria acus (Kützing) Aboal	1.49	1.92	1.83	2.04	2.24	2.07	1.92	1.89	1.94
Ulnaria ulna (Nitzsch) Compère	4.47	4.80	4.41	4.08	3.62	3.91	4.48	4.73	5.82

4. Discussion and Conclusion

In this study, some physical and chemical data were analyzed along with the benthic samples that were collected from the Sülük Lake on a monthly basis between March and November 2022 in order to identify the epipsammic diatoms. In this investigation, a total of 36 Bacillariophyta taxa were identified.

According to Reynolds [28], the optimum temperature for the development of algae is 25 ºC. Some algae species, though, prefer colder or warmer temperatures. In general, algae can endure temperatures between 10 and 30 °C. Biological, chemical, and physical processes, as well as changes in various concentrations, all have an impact on water activity. The environments species metabolic and respiration rates rise with temperature, which also causes an increase in oxygen consumption. Due of the reduced temperature and sunlight in winter, algaes reproduction rates and biomass decline. In the spring, phytoplanktonic organisms begin to proliferate as a result of the rise in temperature and length of the heating period, which causes the bacterial activity that results in the

breakdown of nutrients into inorganic compounds. The average water temperature of the Sülük Lake was measured as 23.1 ºC which is below the optimum water temperature (25 ºC) required for the development of algae [28]. This prevented the diatoms from reaching high taxa numbers.

Round noted that diatoms developed well in phytoplankton in the spring and early summer and showed less development between July and October [29], contrary to Cox who claimed that light is the most significant component in the seasonal distribution of diatoms [30]. The results of this investigation, which was done in the Sülük Lake, were similar to those previously mentioned. The dissolved oxygen values of the Sülük Lake ranged from 7.0 to 9.7 mgO_2/L. The average amount of dissolved oxygen was 8.5 mg/L. The average electrical conductivity of the lake was 331.1 µmho/cm and the average temperature was measured as 23.1 ºC.

It was found that Bacillariophyta members have to be dominant [31]. It was observed that Navicula gregaria, Navicula rhyncocephala, Nitzschia palea, Amphora ovalis and Cymbella affinis species of these diatoms reached significant numbers.

The majority of the Sülük Lakes algae were diatoms (Bacillariophyta), which were significant in terms of the number of species, frequency of occurrence, and number of individuals. Due to their extreme rarity in terms of emergence frequency and individual number, other algae were overlooked. There were no Centrales diatom taxa found in the lake, and all diatom taxa that were recorded were Pennales. It was noted that the members of the Pennales order were not true planktonic species and that pennate diatoms were mostly found in phytoplankton when lakes were turbulent [32, 32, 34]. The epipsammic diatoms of the Sülük Lake are also composed of only pennate diatoms.

Diatoms were observed over the entire study period, which may suggest that they are cosmopolitan, adaptable to a variety of environments, and have a broad tolerance range. According to Chessman (1986) Navicula and Nitzschia species are widespread in distribution. In this study conducted in the Sülük Lake, the identification of Navicula and Nitzschia species in all months and with more taxa supports the idea that the species belonging to these genera are cosmopolitan [35].

Species belonging to Navicula and Nitzschia were recorded to be dominant in the studies carried out in the Central Anatolia Region [36]. Especially Nitzschia palea, N. sigma, N. sigmoide, N. terrestris and N. tenuis, Navicula cryptocephala, N. gregaria and N. radiosa were identified to be abundant and widespread in the Sülük Lake.

Cox stated that species such as Cymbella amphicephala, C. aspera, C. cymbiformis, C. leptoceros, C. lanceolata, Gomphonema angustum, G. subtile, Eunotia monodon are more common in oligotrophic waters [37]. Similarly, Eunotia, Frustulia, Pinnularia, and Neidium species are generally found in oligotrophic lakes [38]. Only Gomphonema angustatum among these organisms was detected in the Sülük Lake.

In conclusion, as the first algological study conducted in the Sülük Lake (Ağın/Elazığ), this study is expected to contribute to the identification of freshwater algal flora of both the Sülük Lake and Türkiye.

References

[1] Allan JD. Stream Ecology Kluwer Academic Publishers. The Netherlands, 388 pp, 1995.

[2] Atıcı T, Ahıska S. Pollution and algae of Ankara stream. Gazi University Journal of Science. 2005; 18: 51-59.

[3] Gönülol A, Öztürk M, Öztürk M. A check-list of the freshwater algae of Turkey (Turkiye tatlısu algleri), OMÜ Fen Edeb Fak Fen Dergisi. 1996; 7(1): 8-46.

[4] Açıkgöz İ, Baykal T. Karagöl (Çubuk-Ankara) alg florası. SDÜ Eğirdir Su Ür Fak Der. 2005; 1(2): 38-55.

[5] Sezen G. Sarımsaklı Baraj Gölü (Kayseri) fitoplanktonu ve su kalitesi özellikleri, Ankara Üni**ve**rsitesi Fen Bilimleri Enstitüsü Doktota Tezi. 242p, 2008.

[6] Altuner Z, Gürbüz, H. Karasu (Fırat) Nehri Fitoplankton Topluluğu Üzerinde Bir Araştırma. İ.Ü. Su Ürünleri Der. 1989; 3(1-2): 151-176.

[7] Dere US, Sıvacı, R. Kızılırmak (Sivas, Giriş-Çıkış) epipelik, epifitik, epilitik alg florası. XII. Ulusal Biyoloji Kongresi: Hidrobiyoloji Seksiyonu, Edirne, IV, 180-188p, 1995.

[8] Altuner Z, Gürbüz, H. Tercan Baraj Gölü bentik alg florası üzerinde bir araştırma. Tr. J. of Botany. 1996; 20(1): 41-51.

[9] Akköz C, Küçüködük M, Obalı O, Öztürk C, Doğan HH. Beşgöz Gölü (Sarayönü/Konya) alg florası II: Epilitik ve Epifitik Algleri. S.Ü. Fen Fak Der. 2000; 1: 5-11.

[10] Pala G, Çağlar M. Epilithic algae and seasonal changes of Keban Dam Lake. Fırat Üniv Fen Bil Dergisi. 2006; 18(3): 323-329.

[11] Bingöl AN, Özyurt SM, Dayıoğlu H, Solak CN. Yukarı Porsuk Çayı (Kütahya) Epilitik Diyatomeleri, Academia.edu. 2007; 15(62): 23-29.

[12] Pala G, Çağlar M. Epilithic Diatoms and Seasonal Changes of Peri-Stream (Tunceli/ Turkey), Fırat Üniv Fen Bil Dergisi. 2008; 20(4): 557-562.

[13] Kıvrak E, Gürbüz H. Tortum Çayının (Erzurum) epipelik diyatomeleri ve bazı fizikokimyasal özellikleri ile ilişkisi. Ekoloji. 2010; 19(74): 102-109.
[14] Çiçek NL, Kalyoncu H, Akköz C, Ertan ÖO. J FisheriesSciences.com. 2010; 4(1): 78-90.
[15] Fakıoğlu Ö, Atamanalp M, Şenel M, Şensurat T, Arslan H. Pulur Çayı (Erzurum) epilitik ve epifitik diyatomeleri. Eğirdir Su Ürünleri Fakültesi Dergisi. 2012; 8(1): 1-8.
[16] Çağlar M, Pala G. Epiphytic and epipsammic diatom communities of Gölbaşı Lake (Adıyaman/Turkey). EgeJFAS. 2016a; 33(3): 193-199.
[17] Çağlar M, Pala G. Seasonal variations in the epilithic diatoms of Koçan Falls (Erzincan, Turkey). J Surv Fish Sci 2016b; 3(1): 47-59.
[18] Pala G, Çağlar M, Selamoğlu Z. Study on epilithic diatoms in the Kozluk Creek (Arapgir/Malatya, Turkey). Iran J Fish. Sci. 2017; 16(1): 441-450.
[19] Çağlar M, Pala G, Selamoğlu Z. Study on epilithic diatoms in the Balikli Tohma Creek (Darende/Malatya in Turkey). Iran J Fish Sci. 2017; 16(2): 858-868.
[20] URL-1. https://earth.google.com, 2024
[21] Round FE. An ingestion of two benthic algal communities in Malham Tarn, Yorkshire, J Ecol. 1953; 41: 97-174.
[22] Kocataş A. Ecology and Environmental Biology Course Book, Ege University Bornova-İzmir, 564p, 1999.
[23] Germain F. Flora Des Diatomees Diatomophycees. Societye Nouvelle Des Editions Boubee, Paris. 1981.
[24] Patrick R, Reimer CW. The Diatoms of the United States. Volume II. Acad. Sci Phyladelphia. 1975.
[25] Krammer K, Lange-Bertalot H. Bacillariophyceae. I. Teil: Naviculaceae. In: Ettl H, Gerloff J, Heynig H, Mollenhauer D, editors. Süsswasser flora von Mitteleuropa, Band 2/1. Gustav Fischer Verlag: Stuttgart, New York, 876p, 1986.
[26] Krammer K, Lange-Bertalot H. Bacillariophyceae. II. Teil: Bacillariaceae, Epithemiaceae, Surirellaceae. In: Ettl H, Gerloff J, Heynig H, Mollenhauer D, editors. Süsswasser flora von Mitteleuropa, Band 2/2. VEB Gustav Fischer Verlag: Jena. 596p, 988.
[27] Krammer K, Lange-Bertalot H. Süßwasserflora von Mitteleuropa. Bacillariophyceae, Band 2/4, 4. Teil: Achnanthaceae, Kritische Ergänzungen zu Navicula (Lineolatae) und Gomphonema Gesamtliteraturverzeichnis. Gustav Fischer Verlag, Stuttgart, 436p, 1991b.
[28] Reynolds CS. The Ecology of freshwater phytoplankton, Chambridge Univ. 384p, 1993.
[29] Round FE. The Biology of Algae, Edward Arnold, London. 1973.
[30] Cox EJ. Observations on some benthic diatoms from North German Lakes: The effect of substratum and light regime. Verh internat. Verein Limnol. 1984; 22: 924-928.
[31] Soylu EN, Maraşlıoğlu F, Gönülol A. Gıcı Gölü (Samsun-Bafra) epipelik algleri ve mevsimsel değişimi. J FisheriesSciences.com. 2010; 4(4): 437-445.
[32] Round FE. The Ecology of Algae, Cambridge University press. USA. 1981.
[33] Obalı O. Mogan Gölü fitoplanktonunun mevsimsel değişimi. Doğa Bil Der. 1984; A2(8): 91-104.
[34] Kairesalo T, Koskimes I. Vernal succession of littoral and nearshore phytoplankton: significance of interchange between the two communities, Aqua Fennica. 1985; 15(1): 115-126.
[35] Chessman BC. Diatom flora of an Australian River System: spatial Patterns and enviromental relationships. Freshwater Biology. 1986; 16: 805-819.
[36] Obalı O, Gönüol A, Dere Ş. Algal flora in the littoral zone of Lake Mogan. OMÜ, Fen Dergisi. 1989: 3:33-53.
[37] Cox EJ. Identification of Freshwater Diatoms from Live Material, London Chapman and Hall. 158p, 1996.
[38] Round FE. The Epipelic algal flora of some Finnish Lakes. Arch Hydrobiol. 1960; 57(1/2): 161-178.

Turkish Journal of Science & Technology
20(1), 141-158, 2025

Research Paper
https://doi.org/10.55525/tjst.1433935

An Investigative Comparison of Higher-Order Runge-Kutta Techniques for Resolving First-Order Differential Equations

Khadeejah James AUDU[1*], Victor James UDOH[2], Jamiu GARBA[3]
[1,2,3] Department of Mathematics, School of Physical Science, Federal University of Technology, Minna, Nigeria.
[*1.] k.james@futminna.edu.ng, [2] udoh.m1701594@st.futminna.edu.ng, [3]jamiu.garba@st.futminna.edu.ng

(Geliş/Received: 08/02/2024; Kabul/Accepted: 14/07/2024)

Abstract: In the context of solving first-order ordinary differential equations (ODEs), this paper thoroughly compares various higher-order Runge-Kutta methods. Reviewing the effectiveness, precision, and practicality of several Runge-Kutta schemes and highlighting their usage in numerical approximation is the main goal of the research. The study explores traditional approaches, including the fifth-order, six-stage Runge-Kutta (RK56), the sixth-order, seven-stage Runge-Kutta (RK67), and the seventh-order, nine-stage Runge-Kutta (RK79), with the goal of offering a comprehensive comprehension of their individual advantages and disadvantages. In order to help academics and practitioners choose the best approach based on the features of the problem, comparative benchmarks are constructed, utilizing both theoretical underpinnings and real-world implementations. Robustness evaluations and sensitivity analysis complement the comparison research by illuminating how flexible these techniques are in various context. The results of this study provide important new understandings of how higher-order Runge-Kutta methods function and provide a thorough manual for applying them to solve first-order differential problems in a variety of scientific and engineering fields. The study's examination of three higher order Runge-Kutta algorithms reveals that the RK56 is more effective at solving first order ODEs.

Keywords: Runge-Kutta technique, ordinary differential equations, numerical integration, error analysis, computational comparison.

Birinci Dereceden Diferansiyel Denklemlerin Çözümü için Yüksek Dereceli Runge-Kutta Yöntemlerinin Karşılaştırmalı Araştırması

Öz: Birinci dereceden adi diferansiyel denklemlerin (ODE'ler) çözümünde, bu makale çeşitli yüksek dereceli Runge-Kutta yöntemlerini kapsamlı bir şekilde karşılaştırmaktadır. Araştırmanın ana amacı, çeşitli Runge-Kutta şemalarının etkinliğini, doğruluğunu ve uygulanabilirliğini gözden geçirmek ve bunların sayısal yaklaşımlarda kullanımını vurgulamaktır. Çalışma, beşinci dereceli, altı aşamalı Runge-Kutta (RK56), altıncı dereceli, yedi aşamalı Runge-Kutta (RK67) ve yedinci dereceli, dokuz aşamalı Runge-Kutta (RK79) gibi geleneksel yaklaşımları araştırmakta olup, bu yöntemlerin bireysel avantaj ve dezavantajlarına dair kapsamlı bir anlayış sunmayı amaçlamaktadır. Akademisyenler ve uygulayıcıların, problemin özelliklerine göre en uygun yaklaşımı seçmelerine yardımcı olmak için teorik temeller ve gerçek dünya uygulamaları kullanılarak karşılaştırmalı ölçütler oluşturulmuştur. Dayanıklılık değerlendirmeleri ve hassasiyet analizleri, bu tekniklerin farklı bağlamlardaki esnekliğini aydınlatarak karşılaştırma araştırmasını tamamlamaktadır. Bu çalışmanın sonuçları, yüksek dereceli Runge-Kutta yöntemlerinin nasıl çalıştığına dair önemli yeni anlayışlar sunmakta ve bu yöntemlerin çeşitli bilim ve mühendislik alanlarında birinci dereceden diferansiyel problemleri çözmek için uygulanması konusunda kapsamlı bir kılavuz sağlamaktadır. Üç yüksek dereceli Runge-Kutta algoritmasının incelenmesi, RK56'nın birinci dereceden ODE'leri çözmede daha etkili olduğunu ortaya koymaktadır.

Anahtar kelimeler: Runge-Kutta tekniği, adi diferansiyel denklemler, sayısal entegrasyon, hata analizi, hesaplamalı karşılaştırma.

1. Introduction

This study aims to investigate the role those differential equations more specifically, ordinary differential equations, or ODEs have in determining the relationships between functions and their derivatives. When it comes to studying dynamic processes in phenomena like quantum mechanics, population modeling, and ecological

* Corresponding author: k.james@futminna.edu.ng. ORCID Number of authors: [1]0000-0002-6986-3491,[2]0009-0009-9319-6986 [3]0000-0002-2850-7730

interactions, ODEs are essential in many scientific domains, including physics, engineering, and the social sciences. The objective of the research is to categorize and contrast approaches to solving ODEs, highlighting their effectiveness and supporting mathematicians and researchers in making decisions when faced with these equations [1,2].

Higher-order Runge-Kutta techniques play a pivotal role in numerical analysis, particularly in resolving first-order differential equations with precision and efficiency. Despite their widespread use, there exists a need for a comprehensive comparative investigation to discern the performance discrepancies among these techniques. This research aims to bridge this gap by conducting an investigative comparison of various higher-order Runge-Kutta methods. The motivation stems from the critical importance of accurately solving first-order differential equations across diverse scientific and engineering domains. By systematically analyzing the strengths and weaknesses of different methods, this study seeks to identify the most effective approach for achieving accurate numerical solutions. The novelty lies in the comprehensive evaluation of multiple higher-order Runge-Kutta techniques within a unified framework, shedding light on their comparative performance and offering insights into their applicability in real-world scenarios. Ultimately, the contribution of this research lies in advancing the understanding of numerical techniques for solving first-order differential equations, thereby facilitating more informed decision-making in practical problem-solving contexts.

Higher-order Runge-Kutta methods, a particular class of numerical techniques are emphasized for their precision in solving ODEs, offering crucial instruments for comprehending and forecasting actual occurrences [3]. A thorough comparative analysis of higher-order Runge-Kutta techniques for first-order differential problem solving is covered in the study's second section. Although differential equations are widely used in many different contexts, the study highlights the value of numerical solutions, particularly when dealing with complicated real-world systems [4,5]. By assessing and contrasting the performance of several higher-order Runge-Kutta procedures, the study seeks to advance existing knowledge by providing an understanding of their advantages and disadvantages. Important information for academics, practitioners, and educators is provided by highlighting the possible consequences for future numerical analytic applications and improvements. First-order differential problem solving is emphasized because it is important in many areas of science, engineering, and mathematics and because it provides the framework for simulating and interpreting real-world processes in many different domains [6].

Numerous investigations have been undertaken regarding Runge-Kutta methods. [7] conducted a Comparative Analysis of Runge-Kutta Methods for Solving Ordinary Differential Equations, providing insights into their numerical performance and computational efficiency. [8] reviewed Higher-Order Runge-Kutta Methods in Scientific Computing, addressing advancements and challenges in this field. [9] evaluated Runge-Kutta Techniques in Atmospheric Modeling, focusing on their accuracy in capturing atmospheric processes. [10] compared Runge-Kutta Methods for Solving Heat Transfer Equations in Engineering Applications, aiming to model heat transfer phenomena effectively. [11] surveyed Runge-Kutta Methods for Solving Chemical Reaction Kinetics, emphasizing their importance in chemical engineering applications. The authors in [12] introduced a novel approach aimed at tackling Ordinary Differential Equation (ODE) problems. Runge-Kutta methods are also used for solving partial differential equations (PDEs) by numerically integrating them over time. [13-17] show that these methods approximate the solution of the differential equations by iteratively advancing the solution from one time step to the next. By developing a sixth-stage fifth-order method, the solutions achieved notably enhanced accuracy and minimized error levels when dealing with initial value problems. [18] establishes and derives a Runge-Kutta method of the sixth order, employing seven stages to facilitate precise numerical approximation. Utilizing Butcher's table, the researcher constructs a non-linear equation system, which is subsequently solved to determine the values of all relevant parameters. Finally, the reduction formula for the Runge-Kutta seventh order with nine steps method is derived [19]. These studies collectively contribute to understanding the theoretical foundations, numerical properties, and practical applications of Runge-Kutta methods across scientific and engineering disciplines. [20] studied different techniques on resolving linear differential equations.

The purpose of this study is to conduct a comprehensive comparative analysis of higher-order Runge-Kutta techniques for resolving first-order differential equations. This study aims to achieve several objectives in its investigation of higher-order Runge-Kutta techniques for resolving first-order differential equations. Firstly, it seeks to categorize and describe various higher-order Runge-Kutta methods to provide a comprehensive overview of available numerical techniques. Secondly, the study endeavors to conduct numerical experiments to compare the accuracy and stability of these techniques, thus facilitating a thorough assessment of their performance. Thirdly, it aims to evaluate the computational efficiency of each method, considering factors such as runtime and memory requirements. Finally, the study aims to synthesize its findings into actionable recommendations, guiding practitioners in selecting the most suitable higher-order Runge-Kutta technique for resolving first-order differential

equations in diverse scientific and engineering applications. Through these objectives, the study endeavors to contribute to the advancement of numerical methods in the field of differential equations and facilitate informed decision-making among researchers and practitioners.

The study will provide clear recommendations for selecting the most effective higher-order Runge-Kutta technique based on its comparative analysis. Additionally, it aims to highlight innovative insights gleaned from the research process, particularly regarding the performance and applicability of different numerical methods in resolving first-order differential equations. The research study under review focuses on conducting a comparative analysis of higher-order Runge-Kutta techniques for resolving first-order differential equations. It emphasizes the precision of these numerical techniques in solving ordinary differential equations (ODEs) and their significance in understanding real-world phenomena. The study aims to advance existing knowledge by assessing and contrasting the performance of various higher-order Runge-Kutta procedures, providing insights into their advantages and disadvantages. It highlights the importance of numerical solutions, particularly in complex real-world systems, and offers valuable information for academics, practitioners, and educators regarding potential consequences and improvements for future numerical analytic applications.

Comparing this study with similar studies in the literature, it is evident that numerous investigations have been undertaken regarding Runge-Kutta methods in various scientific and engineering disciplines. For instance, previous studies have conducted comparative analyses of Runge-Kutta methods for solving ordinary differential equations, reviewed higher-order Runge-Kutta methods in scientific computing, evaluated their accuracy in capturing atmospheric processes, and compared their effectiveness in modeling heat transfer phenomena and chemical reaction kinetics. Some studies have also introduced novel approaches, such as sixth-stage fifth-order methods and sixth-order Runge-Kutta methods employing seven stages, to enhance accuracy and precision in solving ODE problems. Overall, while previous studies have contributed to understanding the theoretical foundations, numerical properties, and practical applications of Runge-Kutta methods across different domains, the research study under review provides a focused investigation specifically on higher-order Runge-Kutta techniques for resolving first-order differential equations. By synthesizing existing knowledge and conducting a comparative analysis within a unified framework, the study aims to offer valuable insights and recommendations for selecting the most suitable numerical technique for practical problem-solving contexts.

2. Methodology

2.1 The Fifth Order Six-Step Runge-Kutta (RK56) Technique

The fifth-order six-step Runge-Kutta (RK56) Scheme is a numerical method utilized for solving ordinary differential equations (ODEs). It progresses the solution through six stages, where computations are based on derivatives of the function being solved. Notably, RK56 achieves fifth-order accuracy, indicating a significant reduction in global error with each step, typically proportional to the fifth power of the step size. This scheme strikes a balance between accuracy and computational cost, making it suitable for a variety of practical applications. Implementation involves iteratively computing solution values at discrete points using weighted averages of function values at different stages. By carefully selecting weights and stage values, RK56 achieves a desirable balance between accuracy and computational efficiency, rendering it valuable for numerical simulations and analysis [21]. The outlined procedure for obtaining the fifth-order sixth-stage Runge-Kutta formula are;

i. Obtain a sixth-stage, fifth-order method from the general Runge-Kutta approach
ii. Obtain the Taylor series expansion of $k_{i's}$ about the point $(n_c), i = 1,2,\ 3,\ 4,\ 5,\ 6$
iii. Carry out substitution to ensure that all $k_{i's}$ are in terms of k_1 only
iv. Reducing all the $k_{i's}$ in terms of k_1 and substituting into the increment function, $\phi(n_c, d) = \sum_{i=1}^{6} e_i k_i$,
v. By comparing the coefficients of all partial derivatives of y with the fifth-order Taylor series expansion involving only partial derivatives concerning n.

According to [12], a new fifth-order sixth-stage explicit Runge-Kutta formula will be obtained after some simplification, as shown in Equation 1,2.

$$s_{c+1} - s_c = \frac{d}{144}(14k_1 + 48k_2 + 162k_3 + 33k_4 - 125k_5 + 12k_6) \quad (1)$$

Where;

$$k_1 = f(z_c, s_c)$$
$$k_2 = f\left(z_c + \frac{1}{3}d,\ s_c + \frac{1}{3}dk_1\right)$$
$$k_3 = f\left(z_c + \frac{2}{3}d, s_c + \frac{2}{3}dk_2\right)$$
$$k_4 = f\left(z_c + \frac{1}{3}d,\ s_c + d\left(-\frac{167765027}{45900120}k_1 + \frac{43549}{7217}k_2 - \frac{30361}{14840}k_3\right)\right)$$
$$k_5 = f\left(z_c + \frac{3}{5}d, s_c + d\left(-\frac{516388549921283}{28366716018615}k_1 + \frac{35525}{9169}k_2 - \frac{27646}{19955}k_3 - \frac{10643}{155037}k_4\right)\right)$$
$$k_6 = f\left(z_c + d, s_c + d\left(-\frac{9039268043}{1401332565}k_1 + \frac{736810}{53619}k_2 - \frac{28702}{5227}k_3 - \frac{7}{5}k_4 + \frac{3}{5}k_5\right)\right) \quad (2)$$

2.1.1 Implementation Procedure for RK56 Technique

Step 1: Express the function $f(z, s)$ such that $f(z, s) \in (p, q)$.
Step 2: Provide the initial estimate for z_0 and s_0.
Step 3: Choose the desired step size $h = \frac{q-p}{i}$, where i is number of steps.
Step 4: Input $p,\ q,\ z_0,\ s_0,\ i$.

Step 5: for c from 1 to i

Compute $k_1,\ k_2,\ k_3, k_4, k_5\ and\ k_6$ as denoted in the RK56 method.

Step 6: Set $z_{c+d} \rightarrow z_c$, then compute, using Equation 3.

$$s_{c+1} = s_c + \frac{d}{144}(14k_1 + 48k_2 + 162k_3 + 33k_4 - 125k_5 + 12k_6) \quad (3)$$

Step 7: Output z_0 and s_0.

Step 8: End the process if $z_c \geq h$ such that $\|s_{c+1} - s_c\| < \varepsilon$.

2.2 The Sixth Order Seven-Step Runge-Kutta (RK67) Technique

The Sixth Order Seven-Step Runge-Kutta (RK67) Scheme is a highly accurate numerical method for solving ordinary differential equations, progressing the solution through seven stages with sixth-order accuracy and a balance between precision and computational efficiency. Considering the first-order differential equation $z'(s) = \frac{dz}{ds} = f(z, s)$, we introduce the initial value $s(z_0) = s_0$, and prioritize our objectives in this case to finding the absolute solution of $s(z)$, the sixth order with seven stages Runge-Kutta method is employed to evaluate n_{c+1} as an approximation to $s(z_{c+1}) = s(z_c + d)$ without the loss of generality. If the function f does not depend on z but only of s, then by setting $z' = 1$, then, the equation above reduces to the relation shown in Equation 4.

$$s'(z) = f(s(z)), s(z_0) = s_0 \quad (4)$$

The suggested explicit Runge-Kutta method of sixth order with seven stages, denoted by $k_1, \ldots, k_7$ for one step, entails that, following this approach, the solution to equation (3) at the end of the first step can be calculated using Equation 5.

$$s_1 = s_0 + d\sum_{i=1}^{7} e_i k_i \quad (5)$$

And the exact solution of equation (4) can be calculated using Equation 6.

$$S_i = s(z_0 + d\sum_{j=1}^{7} a_{ij}) + O(d^2) \quad (6)$$

Thus, RK67 can be calculated using Equation 7,

$$s_{c+1} = s_c + \frac{d}{200}(13k_1 + 55k_3 + 55k_4 + 32k_5 + 32k_6 + 13k_7) \quad (7)$$

where ;

$$k_1 = f(z_c, s_c)$$
$$k_2 = f\left(z_c + \frac{1}{3}d, s_c + \frac{1}{3}dk_1\right)$$
$$k_3 = f\left((z_0 + \frac{2}{3}d, s_0 + \frac{2}{3}dk_2\right)$$
$$k_4 = f\left((z_0 + \frac{1}{3}d, s_0 + d\left(\frac{1}{12}k_1 + \frac{1}{3}k_2\frac{1}{12}k_3\right)\right)\right)$$
$$k_5 = f\left((z_0 + \frac{5}{6}d, s_0 + d\left(\frac{25}{48}k_1 - \frac{55}{24}k_2 + \frac{35}{48}k_3 + \frac{15}{8}k_4\right)\right)\right)$$
$$k_6 = f\left((z_0 + \frac{1}{6}d, s_0 + d\left(\frac{3}{20}k_1 - \frac{11}{20}k_2 - \frac{1}{8}k_3 + \frac{1}{2}k_4 + \frac{1}{10}k_5\right)\right)\right)$$
$$k_7 = f\left((z_0 + d, s_0 + d\left(-\frac{261}{260}k_1 + \frac{33}{13}k_2 + \frac{43}{156}k_3 + \frac{118}{79}k_4 + \frac{32}{195}k_5 + \frac{80}{39}k_6\right)\right)\right) \quad (8)$$

2.2.1 Implementation Procedure for RK67 Method

Step 1: Express the function $f(z, s)$ such that $f(z, s) \in (p, q)$.

Step 2: Provide the initial estimate for z_0 and s_0.
Step 3: Choose the desired step size $h = \frac{q-p}{i}$, where i is number of steps.
Step 4: Input $p, q,\ z_0,\ s_0,\ i$.

Step 5: for c from 1 to i, compute $k_1,\ k_2,\ k_3,\ k_4,\ k_5, k_6\ and\ k_7$ as denoted in the RK67 method, shown in Equation (8,9).
Step 6: Set $z_{c+d} \rightarrow z_c$, then compute

$$s_{c+1} = s_c + \frac{d}{200}(13k_1 + 55k_3 + 55k_4 + 32k_5 + 32k_6 + 13k_7) \quad (9)$$

Step 7: Output z_0 and s_0

Step 8: End the process if $z_c \geq h$ such that $\|s_{c+1} - s_c\| < \varepsilon$

2.3 The Seventh Order Nine-Step Runge-Kutta (RK79) Technique

Considering the equation $z_{c+1} - z_c = +d\phi(z, s, d)$ and the relations shown in Equations 10, 11 and 12

$$d\phi(z_c,\ s_c,\ d) = \sum_{i=1}^{P} e_i k_i i = 1,2,3,\ldots 6 \quad (10)$$

$$k_1 = f(z_c, s_c),\quad k_i = f\left[z_c + g_i d, s_c + d\sum_{j=1}^{i-1} a_{ij}k_j\right],\ i = 2,3,\ldots.6 \quad (11)$$

$$g_i = \sum_{j=1}^{i-1} a_{ij}, i = 2,3,\ldots.6 \quad (12)$$

as the reduction formula of Runge-Kutta methods, the nine-step seventh order Runge-Kutta is shown in Equation 13,14.

$$s_{c+1} = s_c + \frac{41k_1 + 216k_4 + 27k_5 + 272k_6 + 27k_7 + 216k_8 + 41k_9}{840} \quad (13)$$

Where;

$$
\begin{aligned}
k_1 &= f(z_c, s_c)\\
k_2 &= f\left(z_c + \frac{1}{12}d, s_c + \frac{1}{12}dk_1\right)\\
k_3 &= f\left(z_c + \frac{1}{12}d, s_c + d\left(\frac{-10k_1 + 11k_2}{12}\right)\right)\\
k_4 &= f\left(z_c + \frac{2}{12}d, s_c + \frac{2k_3}{12}d\right)\\
k_5 &= f\left(z_c + \frac{4}{12}d, s_c + d\left(\frac{157k_1 - 318k_2 + 4k_3 + 160k_4}{9}\right)\right)\\
k_6 &= f\left(z_c + \frac{6}{12}d, s_c + d\left(\frac{-322k_1 + 199k_2 + 108k_3 - 131k_5}{30}\right)\right)\\
k_7 &= f\left(z_c + \frac{8}{12}d, s_c + d\left(\frac{3158k_1}{45} - \frac{638k_2}{6} - \frac{23k_3}{2} + \frac{157k_4}{3} + \frac{157k_6}{45}\right)\right)\\
k_8 &= f\left(z_c + \frac{10}{12}d, s_c + d\left(-\frac{53k_1}{14} + \frac{38k_2}{7} - \frac{3k_3}{14} - \frac{65k_5}{72} + \frac{29k_7}{90}\right)\right)\\
k_9 &= f\left(z_c + d, s_c + d\left(\frac{56k_1}{25} + \frac{283k_2}{14} - \frac{119k_3}{6} - \frac{26k_4}{7} - \frac{13k_5}{15} + \frac{149k_6}{32} - \frac{25k_7}{9} + \frac{27k_8}{25}\right)\right)
\end{aligned}
\tag{14}
$$

2.3.1 Implementation Procedure for RK79 Technique

Step 1: Express the function $f(z, s)$ such that $f(z, s) \in (p, q)$.

Step 2: Provide the initial estimate for z_0 and s_0.

Step 3: Choose the desired step size $h = \frac{q-p}{i}$, where i is number of steps.

Step 4: Input $p,\ q,\ z_0,\ s_0, i$.

Step 5: for c from 1 to i,

Compute $k_1,\ k_2,\ k_3, k_4, k_5, k_6, k_7, k_8\ and\ k_9$ as denoted in the RK79 method.

Step 6: Set $z_{c+d} \rightarrow z_c$, then compute, using Equation (15)

$$s_{c+1} = s_c + \frac{41k_1+216k_4+27k_5+272k_6+27k_7+216k_8+41k_9}{840} \tag{15}$$

Step 7: Output z_0 and s_0

Step 8: End the process if $z_c \geq h\ such\ that\ \ \|s_{c+1} - s_c\| < \mathcal{E}$

2.4 Error Analysis

Numerical solutions of ordinary differential equations may encounter two types of errors: rounding errors and truncation errors. Rounding errors arise from the limited precision with which computers can represent integers, leading to discrepancies known as round-off errors. The computers fixed and restricted number of significant figures prevents the exact representation of certain numbers in memory. On the other hand, truncation errors in numerical analysis occur when approximations are employed to estimate a value, with the precision of the solution dependent on the chosen step size, denoted as 'h.' A numerical method is considered convergent when the solution approaches the exact solution as the step size (h) approaches zero [22].

In this investigation, a first-order initial value problem is examined to validate the accuracy of the proposed method. Subsequently, numerical approximations are sought for specific initial value problems using this approach [23]. The Maple software is employed to explore the estimated solutions for three selected numerical algorithms, each with varying step sizes.

The expression $t_c = |s(z_c) - s_c| < \varepsilon$ calculates the convergence of the initial value problems, where $s(z_c)$ signifies the approximate answer and s_c denotes the precise solution, is dependent on the problem and varies from 10^{-15}. These two formulas' faults are specified by the expression $errors = |n(m_c) - n_c|$.

3. Numerical Investigation

To validate the feasibility and performance of the three previously discussed algorithms, we introduce first-order ordinary differential problems for numerical exploration in this section. We compute the numerical solutions and absolute errors and provide a graphical representation of the computational results, which are obtained with the use of the MAPLE 2021 package. The particular numerical issues that are being looked into are detailed below:

Problem 1: Considering the numerical solutions of RK56, RK67 and RK79 for the first-order ordinary differential equation

$\frac{ds}{dz} = z^2 + zs, \quad s(0) = 1$

within interval $0 \le z \le 1, h = 0.1,$ Exact solution: $s(z) = \sqrt{\frac{\pi}{2}} e^{\frac{z^2}{2}} erf\left(\frac{z}{\sqrt{2}} + e^{\frac{z^2}{2}} - z\right)$

Problem 2: Considering the approximate solutions provided by RK56, RK67 and RK79 for a first-order ODE.

$s' = z(1+s), \quad z_0 = 0, \quad s_0 = 1, \quad h = 0.1,$ Exact solution: $s(z) = -1 + 2e^{\frac{z^2}{2}}$

Problem 3: We aim to solve the following non-linear first order ordinary differential equation

$\frac{ds}{dz} = -zs^2, \quad s_0 = 1,\ z_0 = 2,\ h = 0.1,$ Exact solution: $s(z) = e^{\frac{1}{4}z(z^3-6)}$

using RK56, RK67 and RK79.

Problem 4: We intend to address the given ODE by utilizing RK56, RK67 and RK79 techniques

$s' = z^2 - s, \quad s_0 = 1, \quad z_0 = 0, \quad h = 0.1,$ Exact solution: $s(z) = z^2 - 2z + 2 - e^{-z}$

Problem 5: $s' = -zs^2, s_0 = 1, z_0 = 2,\ h = 0.1,$ Exact solution**:** $s(z) = \frac{2}{z^2-2}$

Problem 6: $s' = -2zs^2, s_0 = 1,\ z_0 = 2,\ h = 0.1,$ Exact solution: $s(z) = \frac{1}{1+z^2}$

4. Results

Here, we apply the RK56, RK67, and RK79 methods to solve the starting value problems for a first-order ordinary differential equation. The first order ordinary differential equations discussed in the previous section are treated with these techniques. To demonstrate which of the numerical methods converges to the analytical solution more quickly, the three approaches are applied. The Maple progamming with its 2023 software version is used to compute the numerical solutions and errors. A Laptop of 8GB Ram, 2.7 GHZ processor and storage of 500GB, keyboard and mouse constitute the harware used for the computations.

Table 1. Computational solution for RK56, RK67, RK79 experiment 1.

x	Approx. Values for RK56 (s)	Approx. Values for RK67 (s)	Approx. Values for RK79 (s)	Precise Values(S)
0.0	1.000	1.000	1.000	1.000
0.1	1.005	1.005	1.005	1.005
0.2	1.023	1.023	1.023	1.023
0.3	1.055	1.055	1.054	1.055
0.4	1.105	1.105	1.102	1.105
0.5	1.177	1.177	1.168	1.177
0.6	1.275	1.275	1.258	1.275
0.7	1.404	1.405	1.374	1.404
0.8	1.572	1.574	1.520	1.572
0.9	1.787	1.791	1.703	1.787
1.0	2.059	2.066	1.928	2.059

Table 2. RK56, RK67, RK79 contrast errors for experiment 1.

x	Eror Values for RK56	Error Values for RK67	Error Values for RK79
0.0	0	0	0
0.1	2.092×10^{-6}	3.588×10^{-6}	0.116×10^{-5}
0.2	4.242×10^{-6}	7.026×10^{-6}	0.305×10^{-4}
0.3	6.478×10^{-6}	0.546×10^{-5}	0.134×10^{-3}
0.4	8.821×10^{-6}	0.170×10^{-4}	0.377×10^{-3}
0.5	0.113×10^{-5}	0.397×10^{-4}	0.849×10^{-3}
0.6	0.139×10^{-5}	0.794×10^{-4}	0.017×10^{-2}
0.7	0.166×10^{-5}	0.144×10^{-3}	0.302×10^{-2}
0.8	0.194×10^{-5}	0.246×10^{-3}	0.514×10^{-2}
0.9	0.223×10^{-5}	0.400×10^{-3}	0.835×10^{-2}
1.0	0.251×10^{-5}	0.628×10^{-3}	0.131

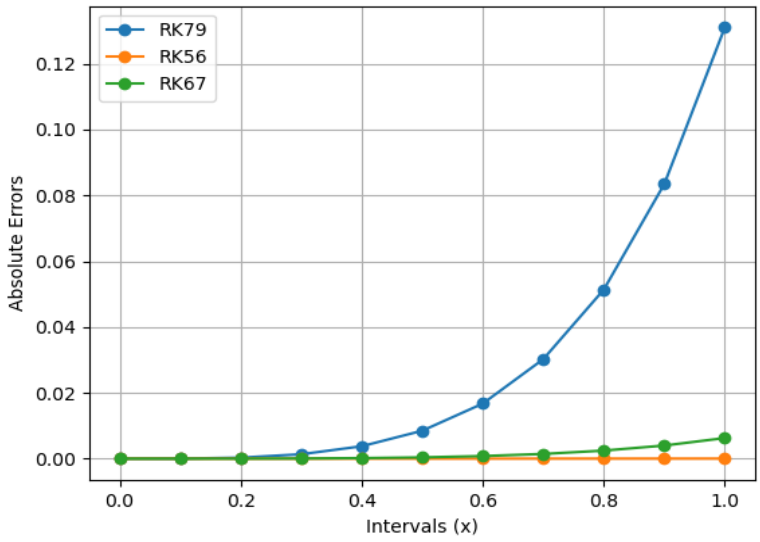

Figure 1. Plot showing contrast errors for experiment 1.

Figure 1 presents a comprehensive evaluation of the RK56, RK67, and RK79 methods as they are employed to solve experiment 1.

Table 3. Computational solution for RK56, RK67 and RK79 experiment 2.

x	Approx. Values for RK56 (s)	Approx. Values for RK67 (s)	Approx. Values for RK79 (s)	Precise Values (S)
0.0	1.0	1.0	1.0	1.0
0.1	1.010	1.010	1.010	1.010
0.2	1.040	1.040	1.040	1.040
0.3	1.092	1.092	1.090	1.092
0.4	1.167	1.167	1.161	1.167
0.5	1.266	1.267	1.254	1.266
0.6	1.394	1.396	1.371	1.394
0.7	1.555	1.557	1.514	1.555
0.8	1.754	1.758	1.687	1.754
0.9	1.999	2.004	1.894	1.999
1.0	2.297	2.305	2.139	2.297

Table 4. RK56, RK67, RK79 contrast errors for experiment 2.

x	Error Values for RK56	Error Values for RK67	Error Values for RK79
0.0	0	0	0
0.1	4.184×10^{-6}	6.097×10^{-6}	0.220×10^{-5}
0.2	8.471×10^{-6}	0.165×10^{-5}	0.548×10^{-4}
0.3	0.129×10^{-5}	0.103×10^{-4}	0.226×10^{-3}
0.4	0.177×10^{-5}	0.293×10^{-4}	0.597×10^{-3}
0.5	0.225×10^{-5}	0.636×10^{-4}	0.127×10^{-2}
0.6	0.277×10^{-5}	0.120×10^{-3}	0.248×10^{-2}
0.7	0.335×10^{-5}	0.207×10^{-3}	0.411×10^{-2}
0.8	0.394×10^{-5}	0.335×10^{-3}	0.669×10^{-2}
0.9	0.460×10^{-5}	0.522×10^{-3}	0.104
1.0	0.531×10^{-5}	0.789×10^{-3}	0.158

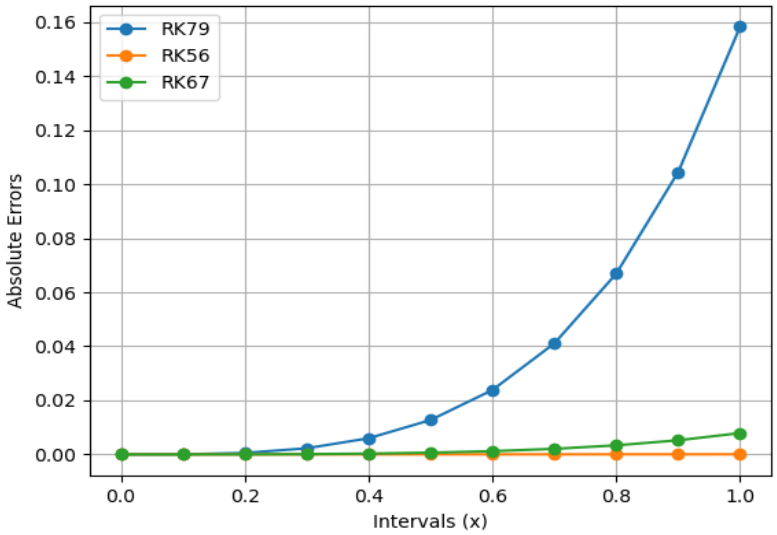

Figure 2. Plot showing contrast errors for experiment 2.

The graphical representation in Figure 2 offers a thorough evaluation of the RK56, RK67, and RK79 methods in their application to solve experiment 2.

Table 5. Computational solution for RK56, RK67 and RK79 experiment 3.

x	Approx. Values for RK56 (s)	Approx. Values for RK67 (s)	Approx. Values for RK79 (s)	Precise Values (S)
0.0	1.0	1.0	1.0	1.0
0.1	0.861	0.863	0.836	0.861
0.2	0.741	0.746	0.699	0.741
0.3	0.639	0.644	0.585	0.639
0.4	0.552	0.559	0.492	0.552
0.5	0.479	0.487	0.416	0.480
0.6	0.419	0.428	0.355	0.420
0.7	0.371	0.380	0.308	0.372
0.8	0.332	0.342	0.272	0.334
0.9	0.303	0.314	0.246	0.305
1.0	0.284	0.296	0.229	0.287

Table 6. RK56, RK67, RK79 contrast errors for experiment 3.

x	Error Values for RK56	Error Values for RK67	Error Values for RK79
0.0	0	0	0
0.1	1.341×10^{-6}	0.261×10^{-3}	0.249×10^{-2}
0.2	0.173×10^{-5}	0.449×10^{-3}	0.423×10^{-2}
0.3	0.710×10^{-5}	0.580×10^{-3}	0.537×10^{-2}
0.4	0.186×10^{-4}	0.668×10^{-3}	0.605×10^{-2}
0.5	0.382×10^{-4}	0.725×10^{-3}	0.639×10^{-2}
0.6	0.668×10^{-4}	0.763×10^{-3}	0.647×10^{-2}
0.7	0.105×10^{-3}	0.794×10^{-3}	0.639×10^{-2}
0.8	0.150×10^{-3}	0.827×10^{-3}	0.621×10^{-2}
0.9	0.203×10^{-3}	0.875×10^{-3}	0.598×10^{-2}
1.0	0.261×10^{-3}	0.950×10^{-3}	0.577×10^{-2}

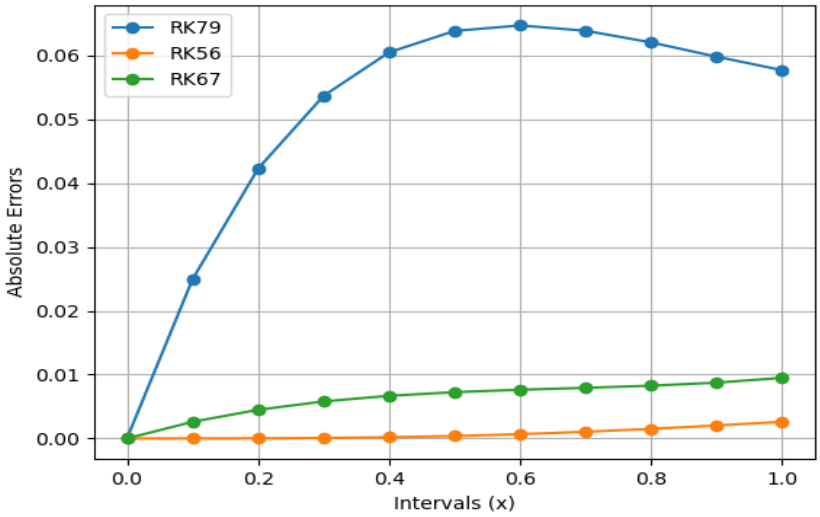

Figure 3. Plot showing contrast errors for experiment 3.

In the assessment of experiment 3, the RK56, RK67, and RK79 methods are comprehensively evaluated through the insights provided in Figure 3.

Table 7. Computational solutions for RK56, RK67 and RK79 experiment 4

x	Approx. Values for RK56 (s)	Approx. Values for RK67 (s)	Approx. Values for RK79 (s)	Precise Values (S)
0.0	1.0	1.0	1.0	1.0
0.1	0.905	0.906	0.893	0.905
0.2	0.821	0.823	0.799	0.821
0.3	0.749	0.751	0.719	0.749
0.4	0.690	0.692	0.655	0.690
0.5	0.643	0.646	0.606	0.643
0.6	0.611	0.614	0.573	0.611
0.7	0.593	0.596	0.557	0.593
0.8	0.591	0.593	0.557	0.591
0.9	0.603	0.606	0.574	0.603
1.0	0.632	0.634	0.609	0.632

Table 8: RK56, RK67, RK79 contrast errors for experiment 4.

x	Error Values for RK56	Error Values for RK67	Error Values for RK79
0.0	0	0	0
0.1	4.083×10^{-6}	0.823×10^{-4}	0.124×10^{-2}
0.2	7.776×10^{-6}	0.149×10^{-3}	0.221×10^{-2}
0.3	0.111×10^{-5}	0.201×10^{-3}	0.294×10^{-2}
0.4	0.141×10^{-5}	0.239×10^{-3}	0.343×10^{-2}
0.5	0.169×10^{-5}	0.264×10^{-3}	0.370×10^{-2}
0.6	0.194×10^{-5}	0.276×10^{-3}	0.377×10^{-2}
0.7	0.216×10^{-5}	0.276×10^{-3}	0.365×10^{-2}
0.8	0.236×10^{-5}	0.264×10^{-3}	0.336×10^{-2}
0.9	0.255×10^{-5}	0.242×10^{-3}	0.291×10^{-2}
1.0	0.271×10^{-5}	0.210×10^{-3}	0.230×10^{-2}

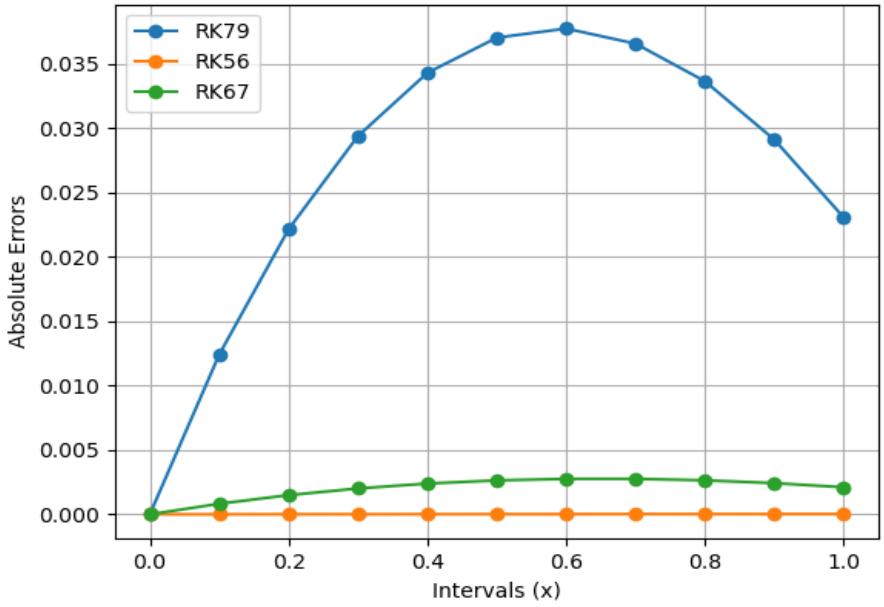

Figure 4. Plot showing contrast errors for experiment 4.

Figure 4 provides a detailed analysis of how the errors of the RK56, RK67, and RK79 methods perform in solving experiment 4.

Table 9. Computational solutions for RK56, RK67 and RK79 experiment 5.

x	Approx. Values for RK56 (s)	Approx. Values for RK67 (s)	Approx. Values for RK79 (s)	Precise Values (S)
2.0	1.0	1.0	1.0	1.0
2.1	0.815	0.818	0.776	0.830
2.2	0.651	0.691	0.634	0.704
2.3	0.511	0.597	0.535	0.608
2.4	0.393	0.524	0.462	0.533
2.5	0.297	0.466	0.405	0.471
2.6	0.221	0.418	0.360	0.420
2.7	0.161	0.378	0.323	0.378
2.8	0.115	0.345	0.291	0.342
2.9	0.081	0.316	0.266	0.312
3.0	0.056	0.291	0.244	0.286

Table 10. RK56, RK67, RK79 contrast errors for experiment 5.

x	Error Values for RK56	Error Values for RK67	Error Values for RK79
2.0	0	0	0
2.1	0.158×10^{-4}	0.489×10^{-3}	0.230
2.2	0.171×10^{-4}	0.583×10^{-3}	0.211
2.3	0.152×10^{-4}	0.549×10^{-3}	0.186
2.4	0.128×10^{-4}	0.479×10^{-3}	0.162
2.5	0.107×10^{-4}	0.405×10^{-3}	0.142
2.6	0.889×10^{-5}	0.336×10^{-3}	0.124
2.7	0.743×10^{-5}	0.277×10^{-3}	0.110
2.8	0.624×10^{-5}	0.227×10^{-3}	0.097
2.9	0.528×10^{-5}	0.186×10^{-3}	0.087
3.0	0.450×10^{-5}	0.152×10^{-3}	0.077

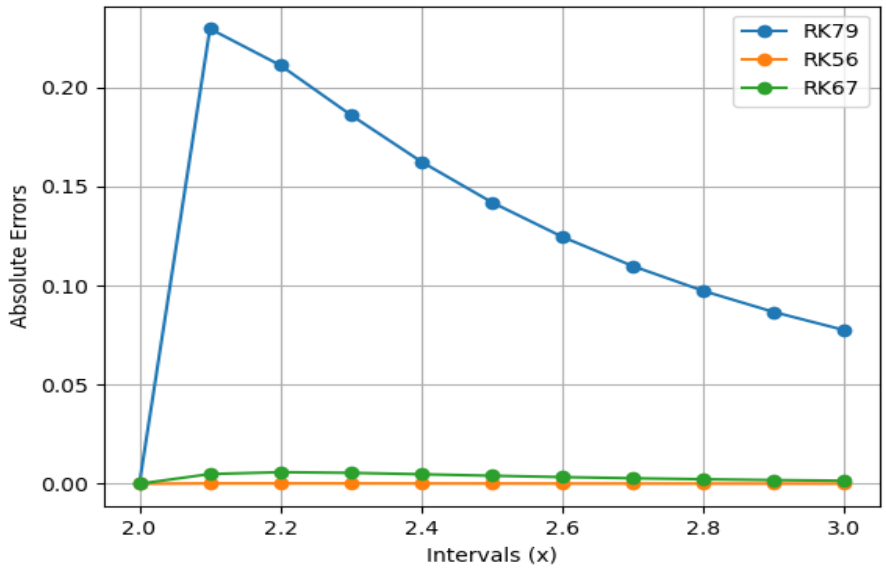

Figure 5. Plot showing contrast errors for experiment 5.

Table 11. Computational solutions for RK56, RK67 and RK79 experiment 6.

x	Approx. Values for RK56 (s)	Approx. Values for RK67 (s)	Approx. Values for RK79 (s)	Precise Values (S)
0.0	1.0	1.0	1.0	1.0
0.1	0.990	0.990	0.990	0.990
0.2	0.962	0.962	0.960	0.962
0.3	0.917	0.918	0.910	0.917
0.4	0.862	0.862	0.846	0.862
0.5	0.780	0.800	0.772	0.800
0.6	0.735	0.736	0.694	0.735
0.7	0.671	0.671	0.619	0.671
0.8	0.610	0.610	0.549	0.610
0.9	0.552	0.553	0.487	0.552
1.0	0.500	0.500	0.432	0.500

Table 12. RK56, RK67, RK79 contrast errors for experiment 6.

x	RK56 Errors	RK67 Errors	RK79 Errors
0.0	0	0	0
0.1	0.165×10^{-5}	0.258×10^{-5}	0.827×10^{-5}
0.2	0.314×10^{-5}	0.175×10^{-5}	0.195×10^{-3}
0.3	0.439×10^{-5}	0.129×10^{-4}	0.725×10^{-3}
0.4	0.530×10^{-5}	0.251×10^{-4}	0.164×10^{-2}
0.5	0.585×10^{-5}	0.329×10^{-4}	0.283×10^{-2}
0.6	0.606×10^{-5}	0.339×10^{-4}	0.409×10^{-2}
0.7	0.598×10^{-5}	0.293×10^{-4}	0.520×10^{-2}
0.8	0.572×10^{-5}	0.215×10^{-4}	0.604×10^{-2}
0.9	0.534×10^{-5}	0.134×10^{-4}	0.656×10^{-2}
1.0	0.489×10^{-5}	0.650×10^{-5}	0.680×10^{-2}

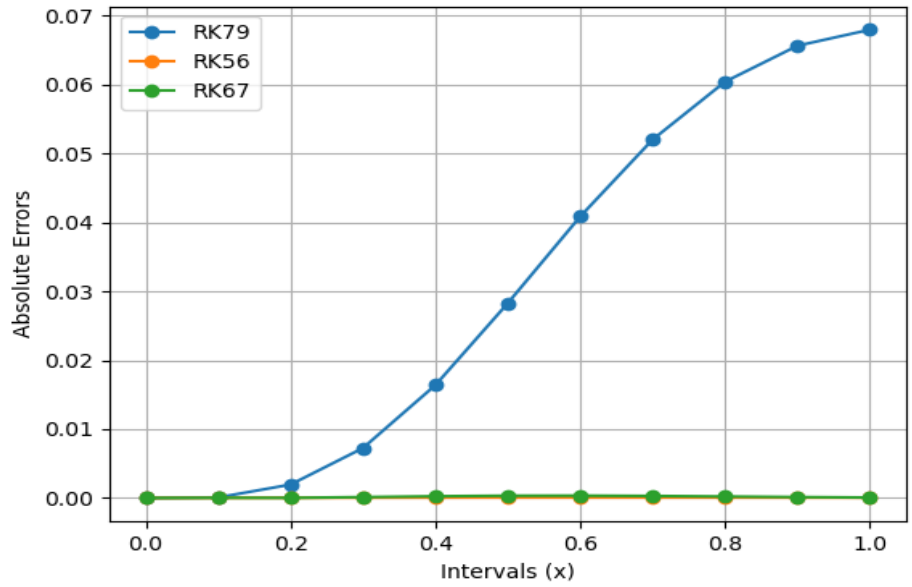

Figure 6. Plot showing contrast errors for experiment 6.

4. 1 Discussion

According to Poornima and Nirmala (2020), a numerical solution is said to be convergent if $\lim_{l\to\infty}|s(z_c) - s_c| = 0$, where c varies from 1 to S and the error is depicted by the relation $rrors = |s(z_c) - s_c|$, where $s(z_c)$ represent the numerical solution and s_c represent the analytical solution. In light of this, a thorough examination of the data from Tables 1, 2, 3, and 4 and a comparison of the numerical solutions obtained by the RK56, RK67, and RK79 methods with the analytical solution for Problems 1-4 provide significant new

information regarding the effectiveness of these numerical techniques. Furthermore, Figures 1-4 offer additional clarification by evaluating the mistakes related to every approach.

Numerical Approximations Comparison (Tables 1, 3, 5, 7, 9 and 11)

i. The tables demonstrate that by employing a consistent step size of 0.1, the RK56, RK67, and RK79 approaches produce numerical solutions for all three problems that closely approximates the analytical answer.
ii. The RK56, RK67, and RK79 solutions deviate somewhat from one another, indicating that these approaches approximate the real answer about equally well.
iii. The outcomes highlight how well the three numerical approaches performed in resolving the given problems.

Error Comparison (Tables 2, 4, 6, 8, 10, 12 and Figures 1-6)

i. A more thorough understanding of the effectiveness of each technique is offered by the tables and graphical representations of errors.
ii. It is obvious that the RK56 approach consistently provides more accurate findings and exhibits lower error values compared to both the RK67 and RK79 procedures.
iii. The RK56 method's error curves graphically show in Figures 1-3 that they approach zero, showing a convergence to the exact solution as long as the step size stays constant.
iv. The RK67 and RK79 approaches, on the other hand, show somewhat larger error numbers, indicating a considerably less precise approximation of the actual solution.

Computational Time (seconds)

Table 13. Computer Simulation Speed of the Problems.

Problem 1	Problem 2	Problem 3	Problem 4	Problem 5	Problem 6
RK56 - 0.5s	RK56 - 0.29s	RK56 - 0.20s	RK56 - 0.28s	RK56 - 0.28s	RK56 - 0.52s
RK67 - 0.92s	RK67 - 0.79s	RK67 - 0.78s	RK67 - 0.73s	RK67 - 0.71s	RK67 - 0.71s
RK79 - 1.26s	RK79 - 1.28s	RK79 - 1.14s	RK79 - 1.04s	RK79 -1.01s	RK79 - 1.15s

Discoveries

i The comparative analysis unequivocally demonstrates the RK56 method's advantage over the other three approaches in solving Problems 1-6.
ii The RK56 technique is noteworthy for its excellent accuracy and efficiency as it constantly converges to the analytical answer with low error.
iii Although the RK67 and RK79 procedures yield dependable outcomes as well, the RK56 method is the most accurate numerical solution for these issues.
iv The RK79 procedure gives higher errors than the other approaches. RK79 is a powerful numerical technique known for its high accuracy and stability in solving differential equations. However, it may yield higher errors compared to other approaches due to its intricate complexity, which can amplify round-off errors and numerical instability. RK79's sensitivity to step size selection and stiffness-induced errors further contribute to this phenomenon. While RK79 offers superior accuracy theoretically, its practical implementation may be challenged by computational overhead and difficulty in balancing accuracy and efficiency. Understanding these limitations is crucial for selecting appropriate numerical methods in scientific and engineering applications.

5. Conclusion

This study thoroughly explored the resolution of first-order ordinary differential equations using RK56, RK67, and RK79 techniques. In the course of this study, extensive numerical exploration has revealed compelling results showcasing the outstanding accuracy achieved by all three methodologies. Based on its smaller error values, RK56 is the most proficient model in the graphical representations (Figures 1–6). Tables 1, 3, 5, 7, 9 and 11's analysis provide more evidence for RK56's improved performance. Regarding the computer simulation speed, we

observe variations in the performance of the RK methods across the tested problems. Generally, the RK56 method demonstrates the fastest computational speed among the tested problems, with execution times ranging from 0.20s to 0.52s. On the other hand, the RK79 method consistently exhibits slower computational speeds, with execution times ranging from 1.01s to 1.28s. These findings suggest that the RK56 method offers superior computational efficiency compared to RK67 and RK79 for the given simulation tasks.

According to the research, RK56 is the best option because of its dependability, efficacy, and efficiency when solving these kinds of problems. By adding insightful new information to the body of knowledge, this contribution helps academics and practitioners choose efficient numerical solutions for related mathematical issues.

References

[1] Lee KC, Senu N, Ahmadian A, Ibrahim SI & Baleanu D. Numerical Study of Third-Order Ordinary Differential Equations Using a New Class of Two Derivative Runge-Kutta Type Methods. Alex Eng J 2020; 59, 2449–2467.

[2] Poornima S, and Nirmala T. Comparative Study of Runge-Kutta Methods of Solving Ordinary Differential Equations. Int J Res in Eng, Sci and Mgt 2020; .3: 557-559.

[3] Jamali N. Analysis and Comparative Study of Numerical Methods to Solve Ordinary Differential Equation with Initial Value Problem. Int J Adv Res 2020; 7(5): 117-128.

[4] Okeke AA, Hambagda BM, & Tumba P. Accuracy Study on Numerical Solutions of Initial Value Problems (IVP) in Ordinary Differential Equations. Int J Math and Stat Invention 2019. 7(2), 2321-4759.

[5] Soliu AA. Comparative Study on Some Numerical Algorithms for First Order Ordinary Differential Equations. B. Tech, Federal University of Technology, Minna, Nigeria. 2023.

[6] Mesa F, Devia-Narvaez DM, Correa-Velez G. Numerical Comparison by Different Methods (Second Order Runge Kutta Methods, Heun Method, fixed Point Method and Ralston Method) to Differential Equations with Initial Condition. Scientia et Technica 2020; 25(2): 299-305

[7] Smith J, & Johnson A. Comparative Analysis of Runge-Kutta Methods for Solving Ordinary Differential Equations. J Comput Math 2019. 45(2), 210-225.

[8] Wang L, & Li HA. Review of Higher-Order Runge-Kutta Methods in Scientific Computing. Applied Numerical Analysis 2020; 35(4): 567-582.

[9] Jones R, Brown M. Performance Evaluation of Runge-Kutta Techniques in Atmospheric Modeling. J Atmosph Sci 2018; 25(3): 410-425.

[10] Garcia P, & Martinez E. Comparative Study of Runge-Kutta Methods for Solving Heat Transfer Equations in Engineering Applications. Heat Trans Eng 2017;, 33(1): 89-104.

[11] Chen Y, & Zhang Q. A Survey of Runge-Kutta Methods for Solving Chemical Reaction Kinetics. Chem Eng. J. 2016; 40(2): 315-330.

[12] Agbeboh GU, Adoghe LO, Ehiemua ME, Ononogbo BC. On the Derivation of a Sixth-Stage-Fifth-Order Runge-Kutta Method for Solving Initial Value Problems in Ordinary Differential Equations. American J Sci Eng Res. 2020; 3(5): 29-41.

[13] Başhan A, Battal S, Karakoç G, and Geyikli T. Approximation of the KdVB Equation by the Quintic B-spline Differential Quadrature method. Kuwait J.Sci 2015; 42(2)**:** 67-92.

[14] Bashan A, Ucar Y, Yagmurlu NM, Esen A. An effective approach to numerical soliton solutions for the Schrodinger equation via modified cubic B-spline differential quadrature method. Article *in* Chaos Solitons & Fractals 2017; 100, 45–56.

[15] Bashan A. An effective application of differential quadrature method based on modified cubic B-splines to numerical solutions of the kdV equation. Turk J Math 2018; 42: 373 – 394.

[16] Bashan A, Ucar Y, Yagmurlu NM, Esen A. Numerical Solutions for the Fourth Order Extended Fisher-Kolmogorov Equation with High Accuracy by Differential Quadrature Method. Sigma J Eng & Nat Sci 2018; 9(3): 273-284.

[17] Ucar Y, Yagmurlu NM, Bashan A. Numerical Solutions and Stability Analysis of Modified Burgers Equation via Modified Cubic B-Spline Differential Quadrature Methods. Sigma J Eng & Nat Sci 2019; 37 (1): 129-142.

[18] Al-Shimmary AF. Solving initial value problem using Runge-Kutta 6th order method. ARPN J Eng Appl Sci 2017; 12(13): 3953-3961.

[19] Trikkaliotis GD & Gousidou-Koutita MCh. Production of the Reduction Formula of Seventh Order Runge-Kutta Method with Step Size Control of an Ordinary Differential Equation. Appl Math 2022; 13, 325-337.

[20] Tuba G. Some Approaches For Solving Mulplicative Second Order Linear Differential Equations with Variable Exponentials and Multiplicative Airy's Equation. Turk J Sci & Tech 2023; 18(2): 301-309.

[21] Audu KJ, Taiwo AR, Soliu AA. Assessment of Numerical Performance of Some Runge-Kutta Methods and New Iteration Method on First Order Differential Problems. Dutse J Pure & Appl Sci 2023; 9(4a): 58-70.

[22] Arora G, Joshi V & Garki I. Developments in Runge–Kutta Method to Solve Ordinary Differential. Recent Advan Math Eng 2020; pp 193-202..

[23] Hetmaniok E, Pleszczynski M. Comparison of the Selected Methods Used for Solving the Ordinary Differential Equations and Their Systems. Mathematics 2022; 10(3): 1-15.

Turkish Journal of Science & Technology
20(1), 159-172, 2025

Research Paper
https://doi.org/10.55525/tjst.1518569

A New Optimization Model for Rotary-Wing Air Vehicle Propeller Design

Ukbe Üsame UÇAR[1*], Burak TANYERİ[2] , Zehra URAL BAYRAK[3]
[1,2] Aircraft Maintenance and Repair Department, School of Aviation, Fırat University, Elazığ, Türkiye
[3] Department of Avionics, School of Aviation, Fırat University, Elazığ, Türkiye
[*1] uucar@firat.edu.tr , [2] btanyeri@firat.edu.tr , [3] zural@firat.edu.tr

(Geliş/Received: 18/07/2024) **Kabul/Accepted: 26/09/2024)**

Abstract: In this study, the propeller characteristics of the aircraft have been optimized in terms of stabilization and manoeuvrability and it has been aimed to find the ideal propeller dimensions for the aircraft. A mathematical modelling has been developed for optimization and four different objectives are simultaneously optimized in the model. The results have been compared with simulation, analysis and real results. Gams and MATLAB programs have been used for developed mathematical model and simulation algorithm, respectively, and ANSYS program has been also used for CFD analysis. It has been observed that CFD analysis and mathematical model results are parallel to each other. As a result of the analysis, thanks to the developed model, a 6.47% improvement has been achieved in efficiency compared to the existing propeller system. In addition, an improvement of 3.93 times in "thrust" and 3.86 times in "total lift force" has been provided. Finally, it has been reported that the total drag force has been successfully minimized.

Key words: Propeller design, aviation, optimization, simulation, aircrafts, CFD analysis.

Döner Kanatlı Hava Aracı Pervanesi Tasarımı için Yeni Bir Optimizasyon Modeli

Öz: Bu çalışmada, uçağın pervane karakteristikleri stabilizasyon ve manevra kabiliyeti açısından optimize edilmiş ve uçak için ideal pervane boyutlarının bulunması amaçlanmıştır. Optimizasyon için yeni bir matematiksel model geliştirilmiş ve modelde dört farklı hedef aynı anda optimize edilmiştir. Elde edilen sonuçlar simülasyon, analiz ve gerçek sonuçlar ile karşılaştırılmıştır. Geliştirilen matematiksel model ve simülasyon algoritması için sırasıyla Gams ve MATLAB programı kullanılmış, CFD analizi için de ANSYS programı kullanılmıştır. CFD analizi ve matematiksel model sonuçlarının birbirine paralel olduğu gözlemlenmiştir. Analiz sonucunda, geliştirilen model sayesinde mevcut pervane sistemine göre verimlilikte %6,47'lik bir iyileşme sağlanmıştır. Ayrıca "itme kuvvetinde" 3,93 kat, "toplam kaldırma kuvvetinde" ise 3,86 kat iyileşme sağlanmıştır. Son olarak toplam sürükleme kuvvetinin başarılı bir şekilde minimize edildiği tespit edilmiştir.

Anahtar kelimeler: Pervane tasarımı, havacılık, optimizasyon, simülasyon, uçaklar, CFD analizi

1. Introduction

Systems consisting of blades designed considering aerodynamic or hydrodynamic criteria on a rotating shaft and moving with pushing or pulling power are called propellers. Propellers are used extensively in many systems, especially in air, sea and land vehicles, wind turbines and air conditioning systems [1].

As the propellers spin, they provide reducing the static pressure by accelerating the air in front of the propellers and increasing the static pressure at the rear of the propellers thanks to pitch. As a result of this operating principle, the vehicle moves forward. While the propellers are turning, they accelerate the air in front of them thanks to their pitch, reducing the static pressure and increasing the static pressure at the rear of the propeller, thus enabling the vehicle to move forward [2].

Propellers, which have different features and blade numbers according to their areas of usage and the vehicles they are used, can rotate clockwise and counter-clockwise in the direction of their leading edges. In addition, due to the Bernoulli Principle, the pressure difference in the front and rear regions of the propeller can resist the drag force of the relevant vehicle and the number of propellers can be determined depending on this situation.

Systems Drone systems contain many components such as engine, body, camera, compass, GPS (Global Positioning System), ESC (Electronic Speed Controller), battery, cable and screws. The most important component is the propeller systems. The efficient movement of rotary-wing unmanned aerial vehicles in the air in the desired formation and direction is possible with a correct propeller design. Propeller systems also contain many parameters, variables and restrictions. Under these constraints, it is not possible to determine the ideal propeller dimensions among many alternatives without using any solution methodology.

* Corresponding author: uucar@firat.edu.tr . ORCID Number of authors: [1] 0000-0002-9872-2890, [2] 0000-0002-3517-9755, [3] 0000-0001-8249-0063

In the literature, there are many methods [3-5] for designing propeller systems and determining their parameters. Gaggero et al., have developed multi-objective numerical optimization approach for design of marine propellers of a high-speed craft [6]. Gur and Rosen, have used a multidisciplinary solution approach for optimal design of propeller system of ultralight aircraft [3]. Zhang et al., have recommended multidisciplinary design optimization of a quadrotor fixed-wing hybrid UAV. The optimization method has been evaluated to design electric propulsion system in terms of flight performance [7]. Zhao et al., have developed a novel airborne electric propulsion measure system for fixed-wing UAV. They have implemented an experimental study to predict the truth of flight test and wind tunnel [8]. Dundar et al., have also used a fixed-wing UAV in terms of power consumption and performance analyses for all flight scenarios. Vertical take-off and landing (VTOL) concept have modelled in Simulink to design multirotor and propeller system for the best endurance [4]. (Bayraktar and Güldaş have one an experimental study using simulation approach based on the statistical methods to determine thrust and torque coefficients of the quadrotors [9]. Foeth and Lafeber, have optimized the parameters related to propeller geometry using NSGA-II Algorithm [10]. Lee et al., have intended to increase of flight time of the fuel cell powered quadcopter UAV. For this purpose, they have used genetic algorithm for weight optimization [11]. Bacciaglia et al., have proposed a solution methodology to optimization of the pitch propeller on the small entertainment ship boats by using Particle Swarm Optimization which is a metaheuristic algorithm [1]. Podsedkowski et al., have realized experimental tests on the pitch propeller of UAV in terms of propulsion system [2]. Magnussen et al., have optimized and designed various features (propeller, motor, power etc.) of UAV that is a multicopter using mathematical modelling [12]. Onay et al., have carried out the design of the two different propellers and have tested by comparing these propellers with the different methods [13]. Sinibaldi and Marino, have done an experimental study on the propulsion system of the mini drones Furthermore, they have examined the different between acoustic signature which is optimized and conventional propellers which is driven by brushless electric motors [14]. Kuantama and Tarca have optimized the thrust system of the quadcopter with ducted-propeller using CFD (Computational Fluid Dynamics) method [15]. Larocca et al., have optimized in terms of topological of the drone propeller which is used on the thrust system of multirotor by commercial CFD code [16]. Mian et al., have simulated a space mapping surrogate modeling to optimization of the UAV propeller shape. The CFD analysis has also used for accuracy of the optimization [17]. Kapsalis et al., have also used CFD method for the optimization of a tactical, fixed-wing UAV. The paper has represented the UAV layout optimization in the early stages of preliminary design with realizing Analysis of Variance (ANOVA) [18]. Dahal et al., have designed the propeller by experimental analyses in line with the goal of optimal thrust for UAVs that can fly altitude range between 3,000 and 5,000m and have used the CFD method to determine the validity of these experimental results [19]. Delbecq et al., have suggested a generic and efficient sizing methodology for electric multirotor drones. They have also performed sizing optimization for different flight phases and payloads [20]. ElGhazali and Dol have done the experimental analyses using ANSYS Fluent 16.1related to the improvement of the propeller system of UAVs which is multirotor [5]. McKay et al., have experimentally examined contra-rotating propellers of the UAV with multi-rotor [21]. Yeong and Dol, 2016 have optimized the aerodynamic performance of micro-drone using Shear Stress Transport K-Omega (SST k-ω) turbulence model [22]. Andria et al., 2018 have modelled and produced the drone propeller and have compared them with other propellers in terms of thrust performance [23]. Iannace et al., have used an artificial neural network to determine faults (unbalanced blades) on drone propellers [24]. Dumitrache et al., have designed drone propellers using Blade Element Momentum Theory (BEMT) and have analysed performance characteristics of them [25]. Wang et al., have used a direct optimal control method for the battery package topology of the small electric UAV. This optimization method has been tested on a small blended wing-body electric aircraft [26].

Studies in the literature generally focus on a single purpose (maximization of thrust) [15,19,23,27]. However, propeller design is not a problem that needs to be addressed unilaterally. Multiple objectives affect the propeller design process. In this article, it is obtained multi-objective propeller design optimization problem and the aircraft propeller has been simultaneously optimized under four different purposes (maximum thrust, maximum efficiency, maximum total lift force and minimum total drag force) in line with specific technical specifications and constraints. The reasons for considering more than one objective are stated as follows.

Among these purposes considered in the article, “thrust” and “total lift force”; it occurs depending on the number of propeller blades, blade angle and engine speed. These parameters that affect “thrust” and “total lift force” need to be optimized. That’s why high propeller angle both positively affects thrust force and increases the drag force. Since the torque created by the motor will increase the pitch when the propeller angle increases, the torque required for rotation will also increase. The increase in torque means that the engine power should remain. The propeller efficiency is also calculated by considering all these data. For that reason, while designing the propeller, it is necessary to meet many objectives simultaneously. A mathematical model based on Multi

Objective-Non-Linear Mixed Integer Programming (MO-NMLP) has been developed to solve the problem in the article. The effectiveness of the proposed solution method has been tested by comparing it with the Simulation Algorithm and the data of the drone propeller used in the market. ANSYS program has been also applied to test efficiency and accuracy of the optimization results.

The contribution of the article to the literature is in two ways. First of all, best knowledge, there is no study in which optimal propeller design has been made considering the stated purposes. As well as, unique solution approach developed for the problem has a generic and dynamic structure and it is discussed for the first time in the literature, as far as known. Due to its generic and dynamic nature, the proposed solution approach can be easily used in all aircraft with propeller systems.

The originality of the article has been analysed in detail with comparisons, taking into account the studies that are closely related to the subject in the literature, and it is shown in Table 1 below.

Table 1. Comparison of this article with studies in the literature.

	Article's Features		
	Vehicle taken into account	*Objectives taken into account*	*Solution Methodology*
This article	Aircraft propeller design.	Maximum thrust, maximum efficiency, maximum total lift force and minimum total drag force	MO-NMLP (Exact solution methodology that guarantees optimal)
Literature	**Article's Features**		
Author(s) Information	*Vehicle taken into account*	*Objectives taken into account*	*Solution Methodology*
[28]	Marine propeller design.	Highest efficiency, the largest thrust, and the smallest maximum stress	NSGA-II
[29]	Marine propeller design.	Maximizing efficiency and minimizing cavitation	Multi-Objective Particle Swarm Optimization
[30]	Ship propeller design.	Efficiency ratio and thrust coefficient	NSGA-II
[31]	Marine propeller design.	The maximization of the efficiency and the minimization of the maximum cavity	Interactive Genetic Algorithms
[32]	Propeller-driven airplane	The maximization the stability of the lateral–directional motion the maximization longitudinal trim condition	Genetic Algorithm
[33]	The Vahana A^3 tilt-wing aircraft	Minimum energy consumption Maximum thrust	Betz Optimum Theory Blade Element Momentum Theory
[34]	Ship propeller design.	Minimum cavitation, maximum efficiency	Genetic Algorithm
[35]	Aircraft propeller design.	Minimization mass and costs	Genetic Algorithm,NSGA-II

Based on Table 1, we can express the differences of our article from the studies in the literature as follows. First of all, our article differs from other studies in the literature in terms of the purposes considered. In this article, the objectives of "total drag force" and "total lift force" are considered, along with thrust and efficiency purposes. As far as is known, it is understood from the results in the table that there is no study that considers these four objectives simultaneously. The second difference is the solution methodology used. The mathematical model developed for the solution of the problem was used for the first time in the literature due to the purposes and constraints considered. In addition, when the results in Table 1 are examined, it is seen that the methods used in other studies are based on metaheuristic algorithms and cannot guarantee the optimal. The method proposed in this article guarantees the optimal. For these reasons, it is thought that the article contributes to the literature.

The importance of the article is explained as follows. In the present situation, it is determined from the information in the literature that rotary-wing aircraft are subject to many accidents on account of adverse weather conditions [35, 36]. The aircraft gets out of control and falls by losing altitude, since suddenly changing air currents reduce the total lift force of propellers. The optimal propeller design depending on engine power requirements will keep under control the aircraft by providing abrupt power increases in such situations. In this article, it can be prevented the aircraft accident due to existing propellers by performing design optimal propellers thanks to proposed solution approaches.

2. Definition of the Problem

There are many parameters, constraints and decision variables that affect the system in the optimization of the drone propeller. While some of these decision variables take discrete values within the specified value range,

some can take continuous values. The non-linear structure of the propeller optimization and mixed type of the variables make the solution of the problem very difficult. In addition, the continuous variable structure means that the relevant variable can take an infinite number of values. It is very difficult and takes time to determine the value range that optimizes the system for different purposes from this infinite range of values and to guarantee the optimal without using operations research techniques. The criteria considered in optimizing the propeller design in this article are shown in the Fig. 1.

As indicated in Fig. 1, the first factor considered in propeller design is technical specifications. In this context, the first variable value to be determined is the number of blades (propellers). The thickness-tightness ratio of the material (material constant) is known as the stretch ratio that the total pulling force on the propeller will create on the blades. If the produced total thrust force causes stretch on the blades, these new angles will directly affect the propeller performance. For this reason, if the required thrust force is higher than the desired elasticity coefficient of the propeller material, the propeller can be designed by increasing the number of blades and decreasing the force per blade.

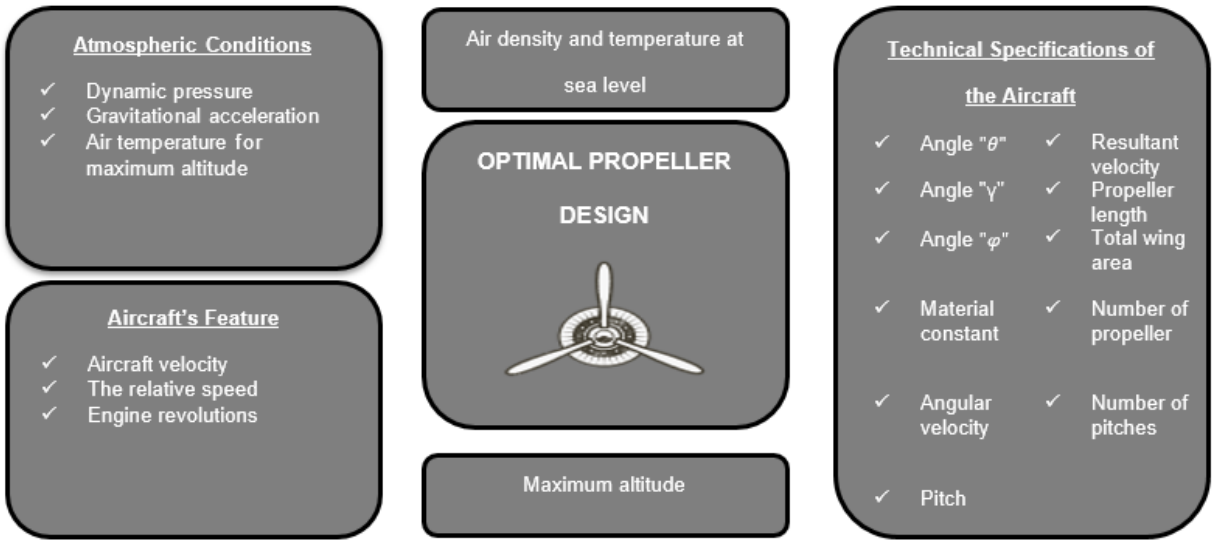

Figure 1. Factors affecting propeller design.

Blade (propeller) length, number of blades and pitch angle are three other technical factors affecting the design process. The number of blades is selected depending on the maximum pulling force needed according to the engine power and aircraft take-off weight. If the force on a knife is outside the strength limits according to the selected knife material, the number of knives is increased. Increasing the number of blades reduces thrust efficiency as it reduces the distance required to escape eddy currents. Because more induced drag force is created.

The angle between the zero support line and the propeller rotation plane of a section at a distance (r) from the axis of the propeller geometrically represents the propeller pitch. Generally, the geometric pitch varies along the blade of the propeller. For this reason, the geometric pitch of the section at a distance of 70% of the radius from the propeller axis is called the "average geometric pitch" of the propeller. The geometric pitch is a size dependent only on the geometry of the blades and is independent of the flight conditions.

The technical parameters that should be calculated in the propeller design and affect the performance of the system is the propeller angles. There are three different angles in the propellers: pfi(φ), theta(θ) and gamma(γ). The angle pfi(φ) represents the angle between the resultant velocity vector and the propeller plane. Theta(θ) represents the position angle of the local geometric pitch. Gamma(γ) represents that the angle between the lift force and drag force ratio vector with the resultant force. The combination of these angles has a huge impact on propeller performance.

The last technical parameters are resultant velocity, angular velocity and total wing area. The resultant velocity expresses the resultant velocity (rΩ(1-b) acting on the blade element in the propeller plane and the velocity of the current passing the propeller plane(U∞(1+a)). Angular velocity is the amount of angular displacement per second of the propeller depending on the engine speed. The total wing area is the area of the circle, which is the projection of the cross-section point taken at a distance of 70% from the root to the tip of the blade.

Two other important factors to consider in propeller design are “air density and temperature at sea level” and “maximum altitude”. The variation of the thrust and moment gradients of the propeller along the blade can be found by the equations given depending on the density of the air at the altitude where the propeller will operate. It is also possible to calculate the total thrust and torque acting on the propeller with the help of these data. Aerodynamically, the density of air is known as one of the direct parameters affecting flight.

Since atmospheric conditions are very effective in the formation of aerodynamic forces, they directly affect flight performance. Increasing altitude from sea level (sea level conditions accepted by ICEAO) changes the density, temperature, viscosity and pressure of the air. As a result of this situation, the performance of the aircraft changes depending on the altitude. Performance calculations were made using the formulas derived for the troposphere layer because rotary wing aircraft generally fly in the troposphere layer of the atmosphere.

Rotary-wing aircraft are considered for optimal propeller design in this article. There are basically two main expectations from rotary-wing aircraft: stabilization and speed. Among the advantages of rotary-wing aircraft compared to fixed-wing aircraft, the ability to take off-landing vertically and stay in the air can be mentioned first. The component that gives this ability is the propellers. The total take-off weight of the aircraft determines the characteristics of the propeller to be selected. The vehicle propulsion system is selected according to the selected propeller. Thus, the dynamics of the aircraft are determined approximately. For this reason, it is very important to choose the ideal propeller and propulsion system according to the desired characteristics of the aircraft.

3. Solution Methodology

In this paper, a mathematical model based on Multi-Purpose - Nonlinear Mixed Integer Programming has been developed and Simulation Algorithm has been used to solve the problem in Chapter 2. Information on the relevant methods is given below.

3.1. Mathematical Modelling

The mathematical model developed for the article is the Multi Objective-Non-Linear Mixed Integer Programming (MO-NMLP). A standard MO-NMLP consists of two parts, the objective and the constraints, as indicated in the equation below [28].

Objectives

$$max/\min Z = f_1(x,y) + f_2(x,y) + \ldots + f_n(x,y) \quad (1)$$

Constraints

$$g(x,y) = 0 \qquad : g(x,y) = a * x + b * y = 0 \quad (2)$$

$$h(x,y) \geq 0 \qquad : h(x,y) = c * x * y \geq 0 \quad (3)$$

$$x \in R^n \quad (4)$$

$$y \in \{0,1,2,\ldots,m\} \quad (5)$$

The $max/\min Z$ function equation 1 represents the problem's objective function or performance criterion in the model. “x” and “y” are decision variables that are unknown in the problem and must be found in line with the determined purpose and constraints. “a, b and c” represent the parameter values in the problem. It is seen that equation 2 is a linear function since the decision variables are not in the case of multiplication. However, in equation 3, the constraint has a nonlinear structure since the decision variables are multiplications. Finally, equation 4 and 5 in the model represent the types of decision variables “x” and “y” and the range of values they can take. Equation 4 shows that the variable “x” is in the set of real numbers and can take positive/negative/decimal/rational and irrational values. Equation 5 shows that the variables can only take 0 or positive integer values.

The solution architecture developed for the problem in line with the above information is shown in Fig. 2. Information on the optimization model developed to solve the problem stated in this article is given in the tables below. The parameters and variables considered in the problem are shown in Table 2.

As a result of the simulation tests performed in this article, “$cof_1 = 1000$”, “$cof_2 = 1$”, “$cof_3 = 1$” and “$cof_4 = 1$” were determined. In addition, in equation 36, the model was forced to have the system efficiency of 89% and above, thus, it was aimed to obtain the maximum efficiency from the system.

Table 2. Parameters and variables considered in the problem.

Parameters considered in the optimization model.	
g	acceleration of gravity
c_{max}	maximum value of material constant
c_{min}	minimum value of material constant
π	pi number
n_{max}	maximum value of engine revolutions
n_{min}	minimum value of engine revolutions
ro_{sfr}	density of air at sea level
T_{sfr}	temperature of air at sea level
v	aircraft speed
λ	constant coefficient
$altitude$	maximum altitude the aircraft can reach
a_{max}	maximum value of "a"
a_{min}	minimum value of "a"
b_{max}	maximum value of "b"
b_{min}	minimum value of "b"
bl_{min}	mimimum propeller lenght
bl_{max}	maximum propeller lenght
nb_{min}	minimum number of propellers
nb_{max}	maximum number of propellers
rs_{min}	the lower limit of the relative speed
rs_{max}	the upper limit of the relative speed
θ_{max}	maximum value of angle "θ"
θ_{min}	minimum value of angle "θ"
γ_{max}	maximum value of angle "γ"
γ_{min}	minimum value of angle "γ"
φ_{max}	maximum value of angle "φ"
φ_{min}	minimum value of angle "φ"
cof_1	Coefficient of objective 1
cof_2	Coefficient of objective 2
cof_3	Coefficient of objective 3
cof_4	Coefficient of objective 4
Positive continuous variables in the optimization model.	
r	70% of the blade length
$pfi(\varphi)$	Angle between resultant velocity and propeller plane
$sigma(\sigma)$	stiffness ratio of blade element
cd	drag coefficient
cl	lift coefficient
$theta(\theta)$	Seating angle of the propeller profile to the propeller hub at the blade root
bl	blade length
h	pitch
$gamma(\gamma)$	the angle between the lift force vector and the resultant force vector
q	dynamic pressure
s	total wing areas
ro	density of air
T	temperature of the air at altitude
ohm	angular velocity of the propeller
ur	resultant speed
mom	momentum
rs	relative speed
$thrust$	thrust
nu	efficiency
tlf	total lift force
tdf	total drag force
sp	shaft power
pl	propeller length
a	propeller exit plane induced speed
b	propeller current plane induced speed
c	material constant
n	engine revolutions
Positive integer variable in the mathematical model	
nb	number of propellers

The mathematical model developed for the problem is shown in Table 3.

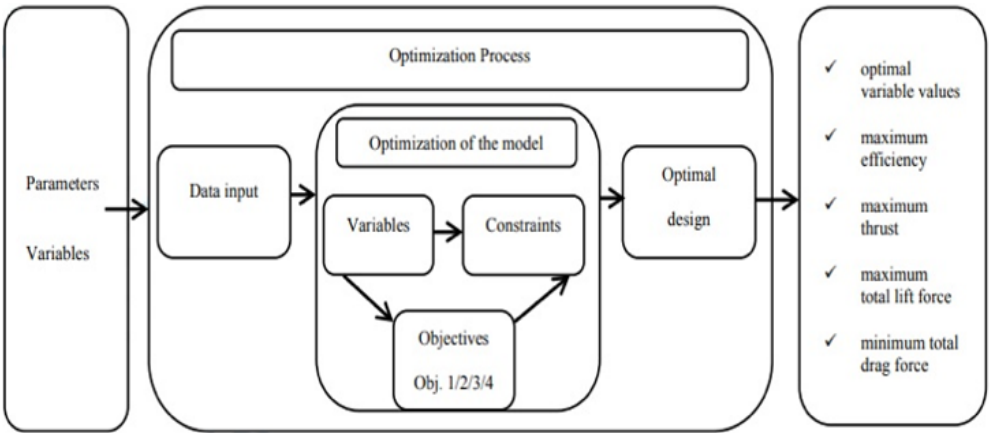

Figure 2. Optimal propeller design process.

Table 3. The objective functions and constraints in the mathematical model.

$makZ = cof_1 * nu + cof_2 * thrust + cof_3 * tlf - cof_4 * tdf$			(6)
$nb \leq nb_{max}$	(7)	$\pi * r^2 = s$	(23)
$nb \geq nb_{min}$	(8)	$2 * \pi * n = ohm$	(24)
$bl \geq bl_{max}$	(9)	$rs * (1 + a) - (1 - b) * (2 * \pi * r * n) * \tan(\varphi) = 0$	(25)
$bl \leq bl_{min}$	(10)	$rs \geq rs_{min}$	(26)
$r = bl * 0.7$	(11)	$rs \leq rs_{max}$	(27)
$\theta \geq \theta_{min}$	(12)	$\gamma \leq \varphi$	(28)
$\theta \leq \theta_{max}$	(13)	$rs * (1 + a) = ur * \sin(\varphi)$	(29)
$2 * \pi * r * tan(\theta) = h$	(14)	$(1 - b) * \tan(\varphi) - \boldsymbol{nu} * 2 * (1 + a) * \tan(\gamma + \varphi) = 0$	(30)
$\sigma * 2 * \pi * r = nb * c$	(15)	$\pi * r * \sigma * ro * ur^2 * cl * \cos(fi + \gamma) = \boldsymbol{thrust}$	(31)
$\gamma \geq \gamma_{min}$	(16)	$\frac{1}{2} * cl * ur^2 * nb * r * c = \boldsymbol{tlf}$	(32)
$\gamma \leq \gamma_{max}$	(17)	$\frac{1}{2} * cd * ur^2 * nb * r * c = \boldsymbol{tdf}$	(33)
$cl * \tan(\gamma) = cd$	(18)	$thrust * r = mom$	(34)
$2 * b * \sin(2 * \varphi) - cl * (1 - b) * \sigma * \sin(\varphi + \gamma) = 0$	(19)	$2 * \pi * n * mom = sp$	(35)
$\frac{1}{2} * ro * v^2 = q$	(20)	$nu \geq 0.89$	(36)
$ro_{sfr} * \left(\frac{T}{T_{sfr}}\right)^{4.259} = ro$	(21)		
$T_{sfr} - \lambda * altitude = T$	(22)		

This optimization model, in equation 6, the objective function of the problem is stated. In this equation, there are four different objectives, three of these objectives are tried to be maximized (efficiency, thrust, tlf) while one of them (tdf) is tried to be minimized. "cof_1", "cof_2", "cof_3" and "cof_4" indicate the balance coefficient of each objective. As a result of the simulation tests performed in this article, "$cof_1 = 1000$", "$cof_2 = 1$", "$cof_3 = 1$" and "$cof_4 = 1$" were determined. In equation 7 and 8, the maximum and minimum integer values that the number of blades can take are expressed, and in equation 9 and equation 10, the maximum and minimum possible lengths of the blade length are specified. In equation 11, the "r" value associated with other formulations is calculated. In equation 12 and 13, lower and upper limits are given for "θ" angle, and in equation 14, "θ" angle is tried to be found for these purposes. In equation 15, the relationships between the number of blades, the material constant, the "r" value and sigma are expressed. In equation 16 and 17, the maximum and minimum values that the gamma variable can take are expressed. In equation 18 and 19, the formulation for the calculation of the variables "cl" and "cd" is indicated. In equation 20, 21, 22 and 23, dynamic pressure (q), total blade areas (q) and ideal air temperature and density at which the propeller will operate at optimal performance are calculated according to the density and temperature of the air at sea level. The omega value was found in equation 24, and the "pfi" angle was determined depending on the relative velocity in equation 25, 26 and 27. In equation 28, the superiority between the fi angle and the gamma angle is expressed, and the "ur" value is calculated in equation 29. In equation 30, the formulation related to efficiency, which is one of our goal variables, is expressed, and in equation 31, the formulas for the

calculation of thrust are specified. The formulations for calculating "tlf" in equation 32 and "tdf" in equation 33 are given. In equation 34 and 35, formulations for determining "shaft power" are shown. In equation 36, the model was forced to have the system efficiency of 89% and above, thus, it was aimed to obtain the maximum efficiency from the system.

3.2. Simulation

Simulation is algorithmic technologies based on statistical foundations that enable the features of systems that cannot be studied, which in case of study bring high costs and risks, or that require a large number of trials, to be studied and tested by transferring them to the computer environment. In the simulation algorithm, the system tries to reach the best values that fulfil the objectives related to the numbers produced according to the uniform distribution within the value range that the relevant variables can take, but the optimal result cannot be guaranteed.

However, this method is used extensively by researchers because it produces suitable solutions for related problems in short solution times. In this study, it has been aimed to simulate the system before the design of the propeller, compare it with the data found for optimization and measure the performance of the system. The simulation study has been carried out using Matlab Simulink software.

The inputs determined for the simulation are "φ" and "γ" angle, blade length, number of blades, "a" and "b" lengths, "c" material constant, "n" engine revolutions, relative and vehicle speed. Thrust, efficiency, total lift force (tlf) and total drag force (tdf) has been calculated as outputs. In the next section, application study will be carried out in line with the defined solution methodologies.

4. Application Study

4.1. Optimization of the Drone System

Application studies have been carried out using Gams Optimization Program and Matlab Simulink program on computers with 16 GB RAM and 3.2 Ghz processor. The features of the "alpha mini drone" have taken into account in the application study and these features are given in Table 4. In this table, in addition to the existing (alpha mini drone) drone information, the value ranges of the variables to be considered in the optimization study are also expressed.

In the direction of parameters in Table 4, the mathematical model, simulation and real data values have been compared in terms of four different objectives. Analysis results and variables values have been shown in Table 5 and Table 6, respectively.

Table 4. Data used in application study.

Symbol	Unit	Real Parameters	Optimization Parameters	Symbol	Unit	Real Parameters	Optimization Parameters
g	m/s^2	9.81	9.81	b_{max}	-------	0.02	0.05
c_{max}	-------	0.16	0.30	b_{min}	-------	0.02	0.01
c_{min}	-------	0.16	0.15	$plmin$	m	0.127	0.762
π	-------	3.14	3.14	$plmax$	m	0.127	0.127
n_{max}	rad/s	282.6	1046.67	$nbmin$	-------	2	6
n_{min}	rad/s	282.6	104.667	$nbmax$	-------	2	2
$rosfr$	kg/m^3	1.225	1.2256	$rsmax$	m/s	8	20
$Tsfr$	^0K	288	288	$rsmin$	m/s	8	8
v_{max}	m/s	8	20	θ_{max}	$degree$	25.2	37
v_{min}	m/s	8	3	θ_{min}	$degree$	25.2	20
λ	-------	0.0065	0.0065	γ_{max}	$degree$	0.01	5
$altitude$	m	3000	3000	γ_{min}	$degree$	0.01	0.01
a_{max}	-------	0.16	0.8	φ_{max}	$degree$	20.63	35
a_{min}	-------	0.16	0.1	φ_{min}	$degree$	20.63	18

When the results in the Table 5 are examined, it is understood that four different objectives have been optimized simultaneously with mathematical modelling and the best result that could be reached under the relevant constraints has been achieved.

Table 5. The best values obtained for each method as a result of the application.

Objective	Existing values	Simulation(Mean)	Mathematical Model
Efficiency	0.8444	0.61066	0.899
Thrust	12.5963	49.9264	49.499
Total lift force	1.3160	5.25022	5.086
Total drag force	0.0002295	0.327	0.000887

Table 6. The values of variables according to analysis results.

Variables	Existing values	Simulation	Optimization
number of propellers (nb)	2	4	2
propeller length (pl)	0.127	0.101584	0.127
engine revolutions (n)	45	96.589167	122.634
material constant (c)	0.16	0.227	0.225
theta(θ)	25.20	28.5	30.894
fpi(φ)	20.63	26.35	18
gamma(γ)	0.01	2.3001	0.01
a	0.16	0.479	0.1
b	0.02	0.03175	0.011
rs (relative speed)	8	13.48	20
v (aircraft speed)	8	13.6	16.624

Table 7. The values of variables according to analysis results.

Objective	Efficiency	Thrust	Tlf	Tdf
The best solution from Efficiency	0.8999	6,186	0.5228	0.00000913
The best solution from Thrust	0.4119	408.2	44.04	3.853
The best solution from Tlf	0.4119	408.2	44.04	3.853
The best solution from Tdf	0.8999	6,186	0.5228	0.00000913

In the Table 5, the average values related to simulation studies have been given. The random numbers have been generated according to normal distribution for the simulation algorithm and the algorithm has been run 1000 times. The detailed analysis of simulation results for each objective has been given in the Table 7.

When Table 6 is examined, it has been determined that while a objective is achieved, very bad results are obtained from other objectives, and it is understood that the simulation method cannot simultaneously optimize the goals. In addition, the normalized percentage graph of the results in Table 6 is shown in Fig. 3.

It can be seen from the Fig. 3 that the parameters affecting the “efficiency maximization” and “tdf” minimization have a linear relationship with each other. In addition, it has been determined that there is a positive relationship between the parameters optimizing “thrust” maximization and “tlf” maximization. As a result, it is understood that “efficiency” and “tdf” have a negative correlation with other purposes.

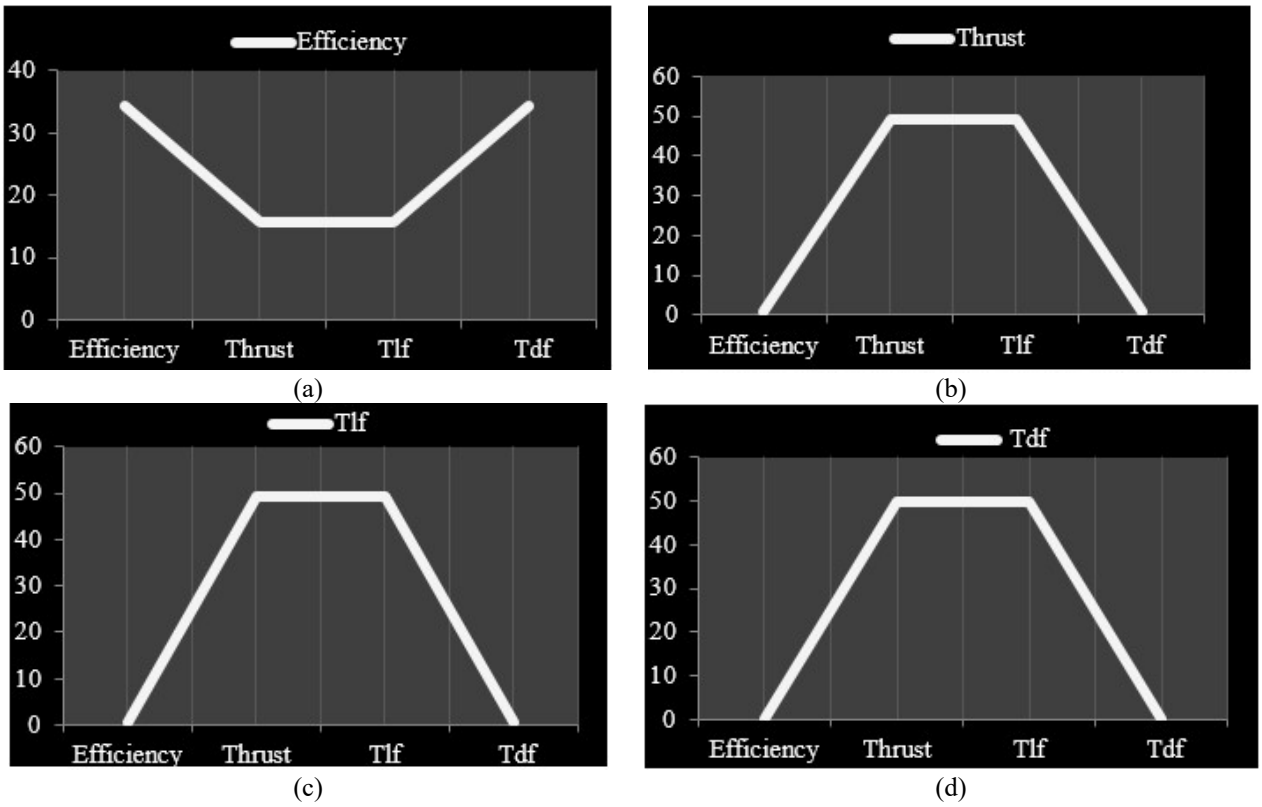

Figure 3. Normalized percentage graph of objective function values. a) Considering only the efficiency objective from the objective function b) Considering only the trust objective from the objective function c) Considering only the tlf objective from the objective function d) Considering only the tdf objective from the objective function

4.2. Analysis of the Simulation Result

In this section, the effects of "pfi", gamma and blade length variables on the propeller design are analyzed in detail based on the simulation results, keeping other parameter values constant, and summarized in the figures below. It is observed that as the "gamma angle" increases, the "tdf" objective increases exponentially to a large extent in Fig. 4. In addition to this, it is seen that "efficiency", "thrust" and "tlf" decrease, although the rate of change is small. It has been stated that the value which maximizes "efficiency", "thrust" and "tdf" and minimizes "tdf" is optimal value.

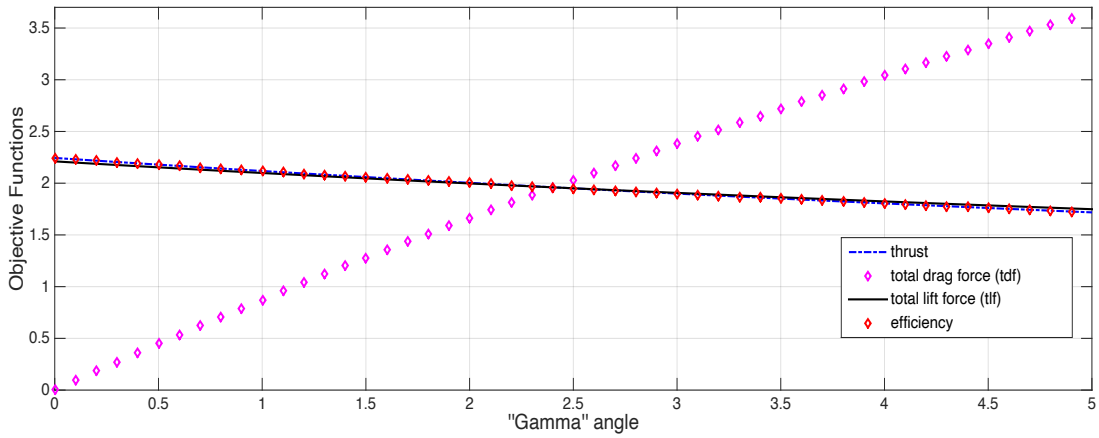

Figure 4. Effect of gamma angle changes on objective functions.

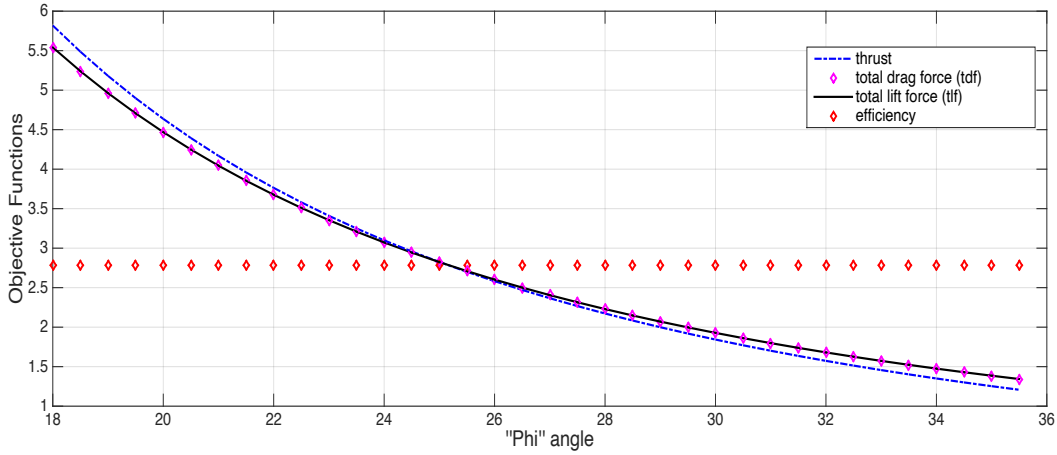

Figure 5. Effect of pfi angle changes on objective functions.

In the Fig. 5, it is understood that as the "pfi" angle increases, the objectives of "thrust", "tlf" and "tdf" decrease significantly, while the aim of "efficiency" remains stable in general. The Fig. 6 shows the effect of change in blade length on objective function values. Accordingly, it is understood that the change in blade length has little effect on "efficiency" and significantly changes other purposes.

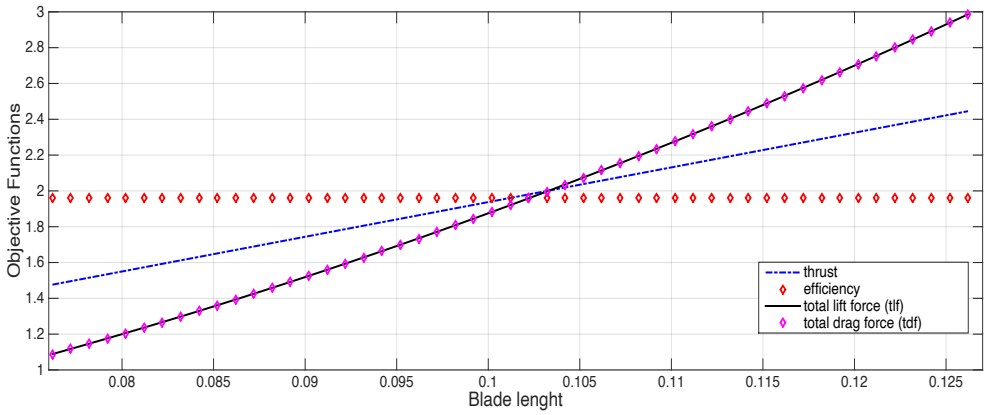

Figure 6. Effect of blade length changes on objective functions.

In the Fig. 5, it is understood that as the "pfi*"* angle increases, the objectives of "thrust", "tlf" and "tdf" decrease significantly, while the aim of "efficiency" remains stable in general. The Fig. 6 shows the effect of change in blade length on objective function values. Accordingly, it is understood that the change in blade length has little effect on "efficiency" and significantly changes other purposes.

4.3. ANSYS Analysis of the Optimization and Existing Values System

In this article, it has been done CFD analysis for the purpose of verification values obtained as a result of optimization and the analysis results have been compared with the existing propeller values. ANSYS SpaceClaim Program has been used in order to propeller design. It is known that the blade, which starts from the center of the propeller and is designed with a length of 127 mm, should be thicker in the root part and thinner towards the tip depending on the twister angle. A combination of four different NACA profiles has been designed in the 5 different points starting from the zero point of the blade length (40%, 50%, 60%, %70 and %100 points of the blade). The used NACA profiles are shown in Fig. 7.

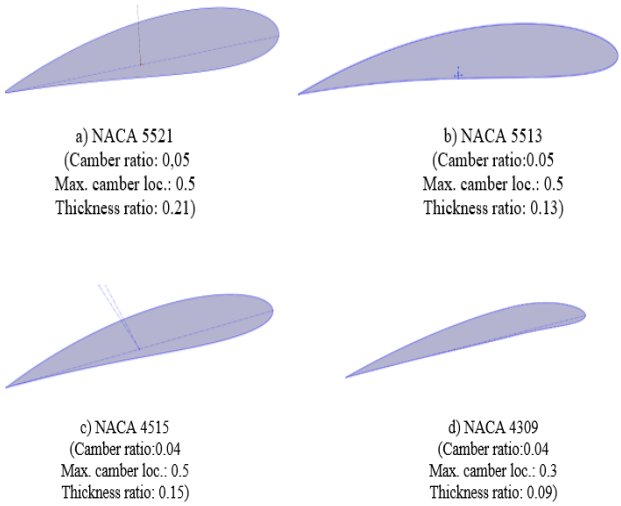

Figure 7. The NACA profiles used for the blade design.

The pitch root angle and wing tip angle have been determined as 25.2 and 10 degrees for the design made taking into account the number of turns of the propeller, the velocity of the fluid entering the propeller, the pitch angle of the propeller in line with the propeller information used in the drone market in real conditions. In the optimal results obtained with the mathematical model, the propeller root angle has been determined as 30,894 degrees and the blade tip angle has been determined as 14 degrees. The current propeller and optimal propeller designs are shown in Fig. 8.

a. The existing blade design. **b.** The optimal blade design.

Figure 8. Blade designs of the propeller

"CFD analysis of the related design", "the pressure values at the 0.7r point referenced for the mathematical model", and "the relations between existing constraints propeller and optimal constraint propeller according to the thrust force values" have been calculated as a percentage (%).

In the results of the analysis made in the real constrained propeller design, the flow lines have been formed properly and maximum flow velocity of 11.293 m/sec has been observed at 2700 rpm propeller speed. In the optimal constrained design, a maximum flow velocity of 35.206 m/sec have been found at 7358 rpm. The flow lines have been given in Fig. 9.

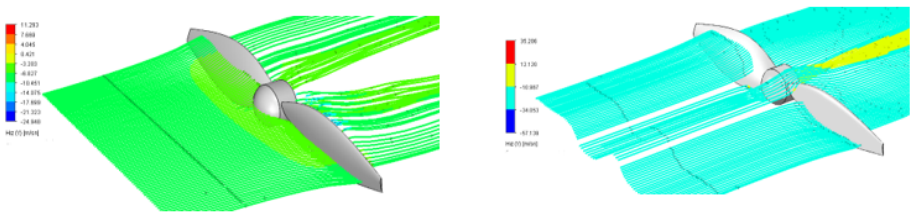

a. Existing constrained propeller design. **b.** Optimal constrained propeller design.

Figure 9. CFD flow velocity profiles.

The difference between the pressure passing under the wing profiles of the propeller blades and the pressure passing over the profile is the main parameter that creates the bearing force of the propeller. The maximum and minimum pressures occurring at 0.7r distance of the blade in both real constrained and optimal constrained propeller designs are shown in Fig. 10.

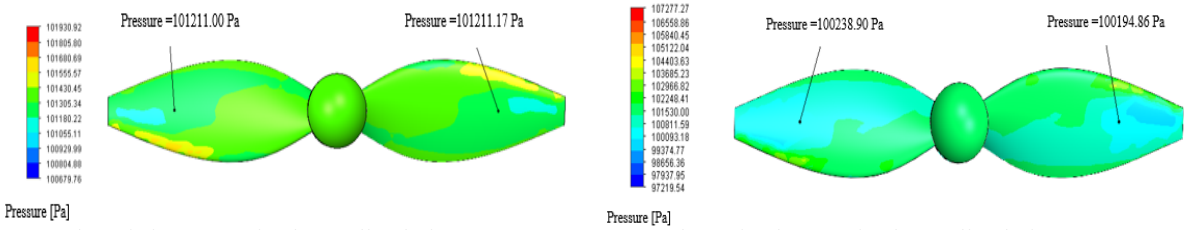

a. The existing constrained propeller design pressure results.

b. The optimal constrained propeller design pressure results.

Figure 10. Optimal and current propeller design comparison.

5. Conclusion

In this paper, the design of the drone propeller systems has been tried to be optimized with a new mathematical modelling used for the first time in the literature. An application study based on real data has been conducted to test the effectiveness of the proposed models. The propeller structure of the alpha mini drone has been considered for the application study. First of all, the optimization process has been carried out using the mathematical modelling method in line with the relevant propeller data. Then, the data obtained as a result of the optimization have been compared with the existing propeller values and simulation results. In consequence of the comparison study, it has been determined that the optimal propeller dimensions have been obtained with the mathematical modelling method and four different objectives have been optimized simultaneously. In addition, according to the analysis study, it has been determined that the simulation algorithm could not optimize the objectives simultaneously. The simulation algorithm found good results for purposes "thrust" and "tlf", while bad results for purposes "efficiency" and "tdf". Comparing the mathematical modelling results with the existing propeller values, it has been determined that quite superior results have been obtained for the purposes of "efficiency", "tlf" and "tdf". Moreover, CFD analysis has been performed using ANSYS program to test the success of optimization results on the real system data. It has been observed that CFD analysis and mathematical model results are parallel to each other.

References

[1] Bacciaglia A, Ceruti A, and Liverani A. Controllable pitch propeller optimization through meta-heuristic algorithm. Eng Comput 2021; 37:2257-2271.
[2] Podsędkowski M, Konopiński R, Obidowski D, and Koter K. Variable pitch propeller for UAV-experimental tests. Energies 2020; 13(5264).
[3] Gur O, and Rosen A. Optimization of propeller based propulsion system, J Aircr 2009; 46(1): 95-106.
[4] Dundar O, Bilici M, and Unler T. Design and performance analyses of a fixed wing battery VTOL UAV. Eng Sci Technol Int J 2020, 23(5): 1182-1193.
[5] ElGhazali AF, and Dol SS. Aerodynamic optimization of unmanned aerial vehicle through propeller improvements. J Appl Fluid Mech 2020; 13(3): 793-803.
[6] Gaggero S, Tani G, Villa D, Viviani M, Ausonio P, Travi P, Bizzarri G. and Serra F. Efficient and multi-objective cavitating propeller optimization: An application to a high-speed craft. Appl Ocean Res 2017; 64: 31-57.
[7] Zhang H, Song B, Li F. and Xuan J. Multidisciplinary design optimization of an electric propulsion system of a hybrid UAV considering wind disturbance rejection capability in the quadrotor mode. Aerosp Sci Technol 2021; 110: 106372.
[8] Zhao A, Zhang J, Li K. and D. Wen. Design and implementation of an innovative airborne electric propulsion measure system of fixed-wing UAV. Aerosp Sci Technol 2021; 109: 106357.
[9] Bayraktar O, and Guldas A. Optimization of Quadrotor's Thrust and Torque Coefficients and Simulation with Matlab/Simulink. J Polytechnic 2020; 23(4): 1197-1204.
[10] Foeth EJ, and Lafeber F. Systematic propeller optimization using an unsteady Boundary Element Method, In Fourth Int Symp on Mar Propulsors (SMP15) Austin; 25 October 2015; TX, USA,

[11] Lee Y, Park E-T, Jeong J, Shi H, Kim J, Kang B-S and Song W. Weight optimization of hydrogen storage vessels for quadcopter UAV using genetic algorithm. Int J Hydrogen Energy 2020; 45: 33939-33947.
[12] Magnussen Ø, Ottestad M and Hovland G, Multicopter design optimization and validation. Modell Identif Control 2015; 36(2): 67-79.
[13] Onay, OK, Khalılov J, Ostovan Y, Cete AR, Açıkyol R, Buzkıran M and Yortucboylu. Developing the design, analysis and testing capabilities of unmanned aerial vehicle propellers. IV. National Aeronaut Space Conf.; 12-14 September 2012; Air Force Academy, İstanbul,
[14] Sinibaldi G, and Marino L. Experimental analysis on the noise of propellers for small UAV. Appl Acoustics 2013; 74(1): 79-88.
[15] Kuantama E, and Tarca R. Quadcopter thrust optimization with ducted-propeller. In MATEC Web of Conf 2017; 126 (01002).
[16] Larocca F, D'ambrosıo D, Raiola L, Tutor, A. and Zamboni, E. F. Topological optimization of a drone propeller using commercial CFD code. Master's Thesis in Aerosp Eng Politecnico Di Torino, Italy, 2019.
[17] Mian HH, Wang G, Zhou H, and Wu X. Optimization of thin electric propeller using physics-based surrogate model with space mapping. Aerosp Sci Technol 2021; 111(106563).
[18] Kapsalis S, Panagiotou P and Yakinthos K. CFD-aided optimization of a tactical Blended-Wing-Body UAV platform using the Taguchi method. Aerosp Sci Technol 2021; 108: 106395.
[19] Dahal C, Dura HB and Poudel L. Design and analysis of propeller for high altitude search and rescue unmanned aerial vehicle. Int J Aerosp Eng 2021; 2021: 1-13.
[20] Delbecq S, Budinger M, Ochotorena A, Reysset A and F Defay. Efficient sizing and optimization of multirotor drones based on scaling laws and similarity models. Aerosp Sci Technol 2020:102105873.
[21] McKay RS, Kingan MJ, Go ST and R Jung. Experimental and analytical investigation of contra-rotating multi-rotor UAV propeller noise. Appl Acoustics 2021; 177: 107850.
[22] Yeong SP and Dol SS. Aerodynamic optimization of micro aerial vehicle. J Appl Fluid Mech 2016; 9(5): 2111-2121.
[23] Andria G, Di Nisio A, Lanzolla AML, Spadevecchia M, Pascazio G, Antonacci F and Sorrentino GM. Design and performance evaluation of drone propellers, In 2018 5th IEEE Int. Workshop on Metrol for AeroSp; 20-22 June 2018; Rome, Italy: pp. 407-412.
[24] Iannace G, Ciaburro G and Trematerra A. Fault diagnosis for UAV blades using artificial neural network. Robotics 2019; 8(59).
[25] Dumitrache A, Pricop, MV, Niculescu ML, Cojocaru MG and Ionescu T. Design and analysis methods for UAV rotor blades. Sci Res & Educ in the Air Force 2017; 19: 115-126.
[26] Wang M, Zhang S, Diepolde J and Holzapfel F. Battery package design optimization for small electric aircraft. Chin J Aeronaut 2020; 33(11):2864–2876.
[27] Raiola L. Topological optimization of a drone propeller using commercial CFD code, Master's Thesis, Politecnico Di Torino, Torino, Italy, 2020.
[28] Guan G., Zhang X, Wang P, and Yang Q. Multi-objective optimization design method of marine propeller based on fluid-structure interaction. Ocean Eng 2022; 252:111222.
[29] Mirjalili S, Lewis A and Mirjalili SAM. Multi-objective optimisation of marine propellers. Procedia Comput Sci 2015; 51: 2247-2256.
[30] Xie G. Optimal preliminary propeller design based on multi-objective optimization approach. Procedia Eng 2011; 16: 278-283.
[31] Gypa I, Jansson M, Wolff K, and Bensow R. Propeller optimization by interactive genetic algorithms and machine learning. Ship Technol Res 2023; 70(1): 56-71.
[32] Rostami M, Chung J and Park HU. Design optimization of multi-objective proportional–integral–derivative controllers for enhanced handling quality of a twin-engine, propeller-driven airplane. Adv Mech Eng 2020; 12(6), 1-15.
[33] Xia X, Ma D, Zhang L, Liu XA and Cong K. Blade shape optimization and analysis of a propeller for VTOL based on an inverse method. Appl Sci 2022; 12(7), 3694.
[34] Kamarlouei M, Ghassemi H, Aslansefat K, and Nematy D. Multi-objective evolutionary optimization technique applied to propeller design. Acta Polytech Hung 2014; 11(9): 163-182.
[35] Schatz ME, Hermanutz A and Baier HJ. Multi-criteria optimization of an aircraft propeller considering manufacturing: Structural design optimization simultaneously considering a knowledge-based manufacturing and a structural model. Struct Multidiscip Optim 2017; 55: 899-911.
[36] Baker SP, Shanahan DF, Haaland W, Brady JE and Li G. Helicopter crashes related to oil and gas operations in the Gulf of Mexico. Aviat Space and Environ Med 2011; 82(9): 885-889.

Turkish Journal of Science & Technology
20(1), 173-184, 2025

Research Paper
https://doi.org/10.55525/tjst.1541073

Assessment of Water Quality and Pollution Load Capacity of the Mmubete Stream in Nigeria

Abiodun Kolawole OYETUNJI[1*], Barry Mark AKATAH[2], Ishmael ONUNGWE[3], Lebabari Choice BARITURE[4]

[1] Department of Estate Management, University of Benin, Nigeria
[1] Lancaster Environment Centre, Lancaster University, United Kingdom
[2,3] Civil Engineering Department, Kenule Beeson Saro-Wiwa Polytechnic, Bori, Rivers State, Nigeria
[3] Department of Civil Engineering, University of Birmingham, United Kingdom
[4] Industrial Safety & Environmental Engineering Department, Kenule Beeson Saro-Wiwa Polytechnic, Bori, Rivers State, Nigeria
[*1] abiodun.oyetunji@uniben.edu, [2] akatah.barry@kenpoly.edu.ng, [3] ixo958@bham.ac.uk, [4] bariturebabari@gmail.com

(Geliş/Received: 31/08/2024; Kabul/Accepted: 15/03/2025)

Abstract: The continuous discharge of waste with high organic content into water bodies causes water pollution. This study evaluates the level of pollution in the Mmubete Stream by focusing on monitoring and evaluating water pollution. The stream is useful for fishing and domestic activities. Water and effluent samples were collected every two months for one year at 12 sampling points covering a total of 1 km stretch of the stream. Seventy-two water samples were collected during the wet and dry seasons covering January, March, May, July, September, and November 2020. Twelve samples were collected in each sampling month and analyzed for twenty parameters: dissolved oxygen, turbidity, total dissolved solids, total suspended solids, biochemical oxygen demand, pH, temperature, electrical conductivity, phosphate, nitrate, copper, lead, iron, manganese, chloride, salinity, nickel, and chemical oxygen demand. The pollution status was evaluated using the modified Water Pollution Index and the National Sanitation Foundation Water Quality Index (NSFWQI) method. The results revealed that Mmubete stream is moderately polluted with water pollution indices for wet and dry seasons as 1.037 and 1.329 respectively and water quality index of 55.87 and 53.22 for dry and wet seasons respectively.

Key words: Stream, waste discharge, water pollution, water quality, wastewater.

Nijerya'daki Mmubete Deresi'nin Su Kalitesi ve Kirlilik Yük Kapasitesinin Değerlendirilmesi

Öz: Su kütlelerine yüksek organik içerikli atıkların sürekli deşarjı su kirliliğine neden olur. Bu çalışma, su kirliliğinin izlenmesi ve değerlendirilmesine odaklanarak Mmubete Deresi'ndeki kirlilik seviyesini değerlendirmektedir. Dere, balıkçılık ve evsel faaliyetler için faydalıdır. Su ve atık su örnekleri, derenin toplam 1 km'lik bölümünü kapsayan 12 örnekleme noktasından bir yıl boyunca her iki ayda bir toplandı. Ocak, Mart, Mayıs, Temmuz, Eylül ve Kasım 2020'yi kapsayan yağışlı ve kurak mevsimlerde yetmiş iki su örneği toplandı. Her örnekleme ayında on iki örnek toplandı ve yirmi parametre açısından analiz edildi: çözünmüş oksijen, bulanıklık, toplam çözünmüş katılar, toplam askıda katılar, biyokimyasal oksijen ihtiyacı, pH, sıcaklık, elektriksel iletkenlik, fosfat, nitrat, bakır, kurşun, demir, manganez, klorür, tuzluluk, nikel ve kimyasal oksijen ihtiyacı. Kirlilik durumu, değiştirilmiş Su Kirliliği Endeksi ve Ulusal Sanitasyon Vakfı Su Kalitesi Endeksi (NSFWQI) yöntemi kullanılarak değerlendirildi. Sonuçlar, Mmubete Deresi'nin orta düzeyde kirli olduğunu, yağışlı ve kurak mevsimlerdeki su kirliliği indekslerinin sırasıyla 1,037 ve 1,329, kurak ve yağışlı mevsimlerdeki su kalitesi indekslerinin ise sırasıyla 55,87 ve 53,22 olduğunu ortaya koymuştur.

Anahtar kelimeler: Akarsu, atık deşarjı, su kirliliği, su kalitesi, atık su.

1. Introduction

The environment has been affected negatively since the creation of the world because of human activities. The negative impact or pollution issues were not a major issue in the early days when population, industrial activities, and technological advancement were minimal. This was so because the effects of human activities were naturally absorbed by the environment without serious negative impact [1]. Pollution of the natural environment became a threat during the era of the Industrial Revolution in Europe and America. Also, population explosion and industrial activities in Africa and other developing countries caused pollution to pose a serious threat to the natural environment [2][3]. In developing countries like Nigeria, there is a growing consciousness of the environmental impact of wastes and wastewater generated from industrial, commercial, agricultural, or domestic activities. In a quest to tackle the menace, several methods have been used to dispose of waste and wastewater

[*] Corresponding author: abiodun.oyetunji@uniben.edu. ORCID Number of authors: [1] 0000-0002-5396-4722, [2] 0000-0002-7245-6547, [3] 0000-0003-3749-3235, [4] 0009-0009-8486-6189

generated from these activities. One of the means of disposing of the wastes or wastewater in Nigeria is by discharging them into surface water bodies such as streams, lakes, rivers, seas, oceans, etc. Rivers and streams are consistently used as the principal route to dispose of wastewater, be it industrial commercial, agricultural, or domestic waste [4]. This may continue for a long time, mostly in developing nations. This is a result of a poor attitude towards environmental sustainability and protection.

Water pollution can be caused by a variety of factors, including the discharge of effluent or solid waste (from commercial and industrial activities), runoff (from agricultural land), untreated waste and sewage from residential areas, chemical contaminants, and other sources into surface waters [5-6]. Most of the freshwater resources that are now available come from surface water (rivers and streams). Unfortunately, rivers and streams are being polluted because of crude oil leakage, discharge of untreated sewage and industrial waste, and several other types of waste that deteriorate water quality [5]. There has been an excessive release of industrial, agricultural, and commercial pollutants into the aquatic environment, which has harmed aquatic lives and people who use the water [7-8].

The quantity of effluent and solid waste that is dumped into streams is so enormous that the reduction of pathogens by natural mechanisms is low to preserve the public's health. In addition, industrial waste changes the pH of the water and makes it easier for bacteria to grow in water bodies by providing an abundance of nutrients. This makes it more difficult for natural systems to rid the water of harmful pathogens [9][10]. The discharge of sewage waste into bodies of water raises the level of biological oxygen demands to a point where it may cause a depletion of dissolved oxygen in the water; consequently, fishes, animals that live at the bottom of the food chain, marine plants, and even humans may be negatively impacted [7-8, 11]. Most Nigeria's fresh water supplies, notably in the Niger Delta region, are polluted, which has resulted in a serious epidemic of diseases that are transmitted through water and those that are associated with water. The chief contributors to stream pollution in the Niger Delta include oil exploration and extraction, industry, economic operations, agricultural activities, and urbanization. According to research, most of the sources of fresh water in Nigeria are polluted, which has led to a rise in waterborne diseases and water-related diseases.

2. Methodology

The Mmubete stream is in Aleto, Eleme Local Government Area of Rivers State, Nigeria. The stream is found on the Atlantic coast in the Southern part of Nigeria. It ends at the Imo River entrance. The stream crosses the East-West Road and is adjacent to the Petrochemical Company within the study location. The stream is freshwater and is located at the coordinates between Latitude 5° 50' 06" N and Longitude 7° 6' 11" E. The stream was selected as the focus of this research due to its significant role as a primary water source for surrounding communities and its vulnerability to anthropogenic activities such as domestic, agricultural, and industrial discharges. The stream is a critical component of the local ecosystem and serves as a key resource for drinking water, irrigation, and fishing, making its water quality a pressing concern for the sustainability and health of the dependent population. Despite its importance, limited studies have comprehensively assessed its pollution load capacity, leaving a gap in data needed for effective water resource management and environmental protection strategies. The map of Eleme LGA showing the stream is presented in Figure 1.

The timing of the sampling was strategically planned to account for seasonal variations in water quality, particularly in a region like Nigeria where the hydrological cycle is heavily influenced by distinct wet and dry seasons. Sampling during both seasons ensures a robust dataset, capturing the fluctuations in pollutant levels caused by rainfall patterns, runoff, and streamflow changes. The wet season typically introduces higher pollution loads due to surface runoff, while the dry season reflects baseline water quality conditions with minimal external inputs. This temporal approach provides a more accurate understanding of the stream's pollution dynamics. The frequency of sampling was chosen to balance logistical feasibility and the need for a detailed temporal resolution of water quality data. Regular sampling over a specified period allows for the detection of short-term variations and trends in water quality, enabling a comprehensive assessment of the stream's pollution load capacity. This systematic approach ensures that the data accurately reflect both natural variations and human-induced impacts, thereby supporting the development of targeted management interventions to mitigate water pollution and protect the stream's ecological integrity.

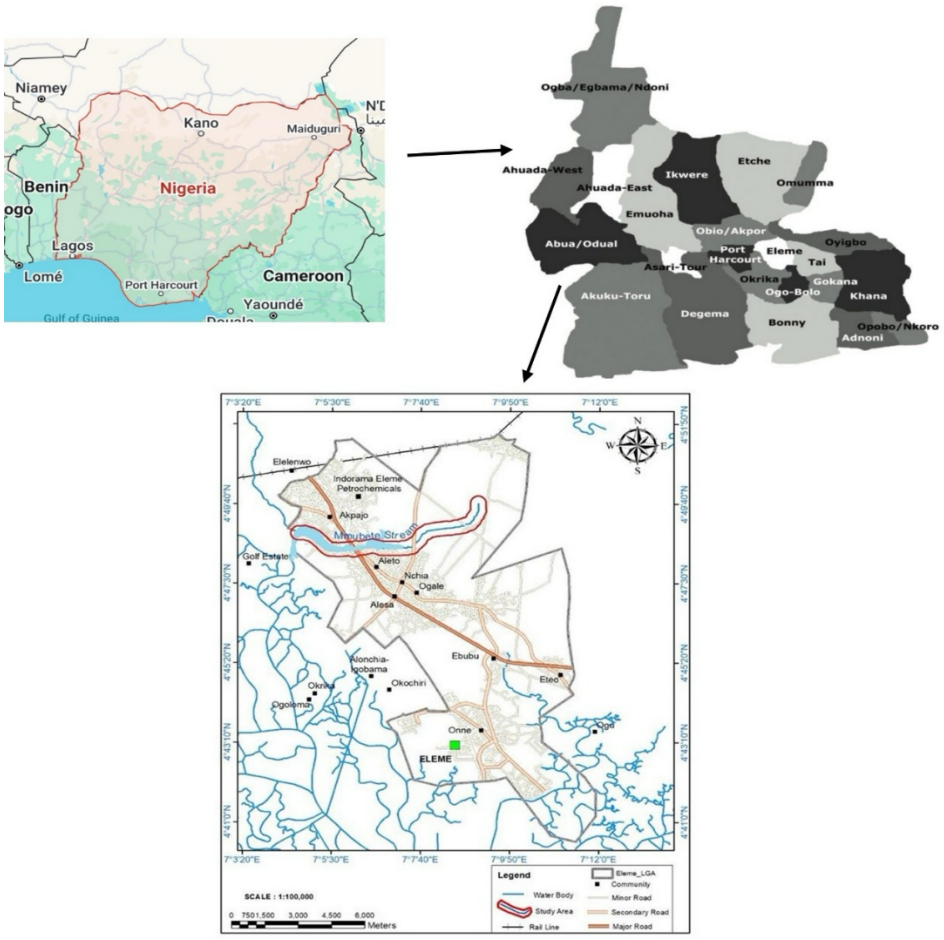

Figure 1. Map of Eleme LGA showing the study stream.

Twelve (12) sampling stations were established for data collection along the stream and pollution sources, including effluent, upstream samples, point of entry samples, and samples collected downstream up to a distance (stretch) of 1000m (1 km). The sampling points were purposively and strategically located to capture potential pollution sources from a petrochemical company, dredging sites and sand mining sites along the stream. The choice of 100m intervals between sampling points was for even distribution of sampling points along the section of the study stream which was 1000m. To achieve the above and accuracy of collection points, wooden pegs painted red were used as location markers and pinned at the locations presented in Figure 2.

The decision to sample every 100 meters along the Mmubete stream is informed by the need to capture spatial variability in water quality and pollution load. Dense sampling ensures that localised pollution hotspots or abrupt changes in water quality caused by point sources such as sewage outlets, industrial discharges, or agricultural runoffs are identified. While some information gathered through dense sampling may appear repetitive, this approach is crucial for a detailed spatial analysis, especially in a stream where pollution sources vary significantly over short distances. The repetition of observations at 100-meter intervals is necessary to ensure that subtle spatial variations in pollutant concentrations are not overlooked. Streams can exhibit significant heterogeneity in water quality due to natural factors like changes in flow dynamics, sediment deposition, and mixing patterns, as well as human activities that vary in intensity and location. Seasonal monitoring is often the most feasible and cost-effective approach for studies focused on capturing the influence of seasonal changes on water quality and pollution dynamics. For the stream, this means sampling during the peak of the wet season, the dry season, and transitional periods between them. This ensures that the dataset reflects the full range of hydrological and pollutant-loading conditions.

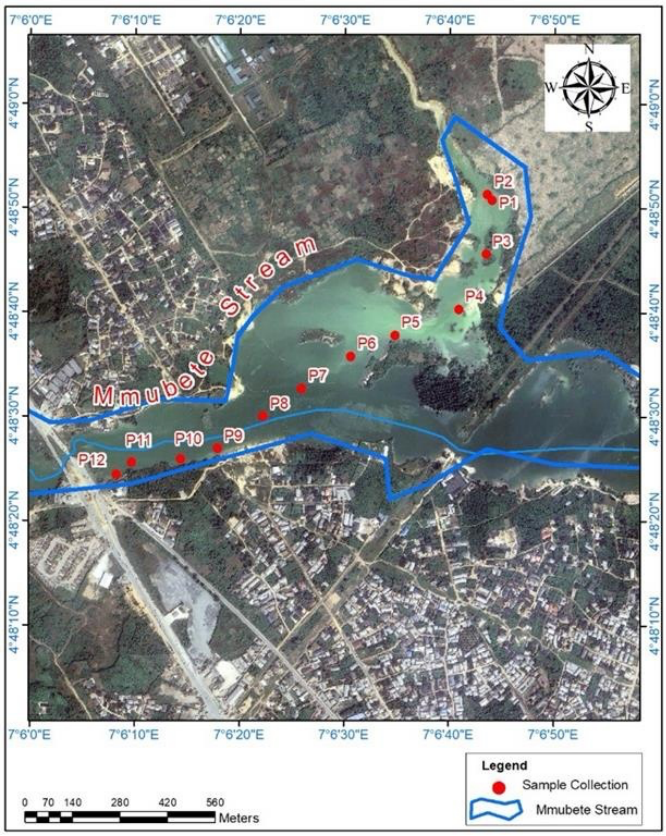

Figure 2. Sampled stations of Mmbute stream.

A denser network of sampling points provides a high-resolution dataset, which is critical for accurately mapping pollution gradients, validating predictive models, and designing targeted intervention strategies. A hand-held eTrex GPS unit was used to obtain the sampling point's coordinates with the sampling stations established every 100 meters. The coordinates are shown in Table 1. The samples were collected at every 100m to capture all other pollution sources (dredging points and sandmining points) along the section of the stream apart from the major pollution source (Petrochemical company).

Table 1. Co-ordinates of sampling stations.

S/N	Easting	Northing	Point
1	290646	532405	P1
2	290632	532422	P2
3	290628	532246	P3
4	290547	532084	P4
5	290359	532007	P5
6	290229	531945	P6
7	290085	531850	P7
8	289971	531769	P8
9	289837	531674	P9
10	289728	531643	P10
11	289584	531634	P11
12	289539	531599	P12

The study on the Mmubete stream considers the influence of land use changes and seasonal agricultural practices, recognising their critical roles in determining water quality dynamics. Over time, land use within the stream's catchment area has undergone significant transformations, including urban expansion, deforestation, and agricultural intensification. These changes have disrupted natural hydrological processes, increased surface runoff and introducing a variety of pollutants into the stream. Urban development, for instance, contributes contaminants

such as heavy metals, hydrocarbons, and untreated domestic wastewater, while deforestation diminishes the natural filtration capacity of the watershed, leading to heightened turbidity and sedimentation. Seasonal agricultural practices within the watershed further exacerbate the water quality challenges faced by the Mmubete stream. During the wet season, heavy rainfall facilitates the transport of fertilisers, pesticides, and herbicides from agricultural fields into the stream, resulting in nutrient enrichment through elevated levels of nitrates and phosphates. This nutrient influx increases the potential for eutrophication and algal blooms. Additionally, the wet season's increased surface runoff and soil disturbance during planting or harvesting activities contribute to higher sediment loads in the water. In contrast, the dry season is characterised by reduced stream flow, which concentrates pollutants and amplifies their impact on water quality. The seasonal nature of these agricultural activities underscores the importance of monitoring water quality across different times of the year to understand the full extent of their effects. Through the analysis of the water quality data that was collected during both wet and dry seasons, the study identifies correlations between key parameters, such as nitrates, phosphates, and turbidity, and human activities within the watershed. Ultimately, the study aims to inform the development of targeted interventions to mitigate the impact of human activities on the stream's ecological balance and ensure the long-term sustainability of its water resources.

2.1 Measurement of water quality parameters

The water quality parameters were determined both in situ and in the laboratory. Temperature, total dissolved solids (TDS), dissolved oxygen (DO), pH, Electrical conductivity, and turbidity were measured in situ using various instruments for their determination. Biochemical Oxygen Demand (BOD), Total Suspended Solids (TSS), Total Petroleum Hydrocarbon (TPH), Nitrate, Nickel, Iron, Manganese, lead, and Phosphate were determined in the laboratory. The analyses were carried out using the following equipment and analytical methods as presented in Table 2.

Table 2. Water quality parameters and analytical methods.

Parameter	**Analytical method**
pH	Electrochemical method
Temperature	Thermometric method
Conductivity	Conductivity method
Turbidity	Nephelometric method
Total suspended solids	Gravimetric method (APHA 2540 D)
Chloride	Argentometric method (APHA4500-Cl^- B)
Total dissolved solids	Conductivity method
Biochemical oxygen demand	Titrimetric method
Dissolved oxygen	Titrimetric method
Chemical oxygen demand	Closed Reflux Titrimetric method (APHA 5220 C)
Total petroleum hydrocarbon	Nonhalogenated organics method (USEPA 8015 C)
Salinity (Mg/l)	Conductivity method
Nitrate	Spectrophotometric method
Phosphate	Colorimetric method
Iron	Direct Air-Acetylene flame method (APHA 3111B)
Manganese	
Copper	
Lead	
Nickel	
Fecal coliform	Membrane filtration

2.2 Sampling months

On account for seasonal variation, samples were collected and analysed for both the dry and rainy seasons. Sample collection was carried out every two months for a year. The sampling months and seasons are presented in Table 3.

Table Error! No text of specified style in document.**.** Sampling months for water samples collection.

S/N	Sampling Month	Sampling Season	Number of Samples	Time of collection
1	January, 2023	Dry	12	12:00 – 2:00pm
2	March, 2023	Dry	12	12:00 – 2:00pm
3	May, 2023	Wet	12	12:00 – 2:00pm
4	July, 2023	Wet	12	12:00 – 2:00pm
5	September, 2023	Wet	12	12:00 – 2:00pm
6	November, 2023	Dry	12	12:00 – 2:00pm

2.3 Determination of water quality and pollution index

Water quality is determined by assessing three classes of attributes: biological, chemical, and physical [12]. The water quality index for the study was determined using the National Sanitation Foundation Water Quality Index (NSFWQI). The NSFWQI technique makes provision for the following parameters to be used for water quality index computation: dissolved oxygen, fecal coliform, pH, BOD5, Temperature, phosphate, nitrate, turbidity, and total solid [13]. The NSFWQI is a 100-point scale index representing the results of nine parameters: BOD, DO, NO3, PO4, Temperature, Turbidity, TS, pH, and FC. NSFWQI presents water quality in general but does not account for water use capacities. Index parameters have exclusive importance, so a weighted average is crucial for calculating the index. The weight scores were obtained using expert judgement and Delphi method [14-16]. In assessing the water quality and pollution load capacity of the Mmubete stream, weightings are applied to different water quality parameters to reflect their relative significance. This ensures that more critical pollutants contribute more substantially to the overall assessment compared to those with lesser impacts. The process begins with the selection of relevant water quality parameters. These typically include physicochemical properties such as pH, temperature, dissolved oxygen (DO), turbidity, and total dissolved solids (TDS). Additionally, nutrient levels, including nitrate, phosphate, and ammonia, are considered, along with the presence of heavy metals such as lead, cadmium, mercury, and iron. Microbial indicators, such as fecal coliforms are also assessed, as they are crucial in determining the safety of the water for human and ecological use.

Once the parameters have been identified, weightings are assigned based on their importance to overall water quality [14]. This is done using expert judgment, regulatory guidelines from bodies such as the World Health Organization (WHO) and the Nigerian Environmental Standards and Regulations Enforcement Agency (NESREA), and statistical methods such as the Delphi technique. Parameters that pose greater risks, such as dissolved oxygen and heavy metal concentrations, are given higher weightings, while those with less severe effects, such as pH, receive moderate weightings.

Since different parameters have varying units of measurement, they must be normalised to a common scale before calculating an overall water quality index. Normalisation is achieved by converting each parameter's value into a standardized quality index using a formula that considers the minimum and maximum permissible limits. This ensures that the values can be meaningfully compared and aggregated. The final water quality index (WQI) is calculated by multiplying the quality index of each parameter by its assigned weight and summing the results for all parameters [13]. The resulting WQI value categorises the river's water quality into different levels, such as excellent, good, poor, very poor, or unfit for use. This classification helps in understanding the overall health of the Mmubete stream and whether it meets acceptable environmental standards.

The Delphi approach employed in this study is a structured and iterative method that gathered expert opinions to reach a consensus on complex issues. This method is valuable in determining the appropriate weightings for different water quality parameters. Since various factors influence water quality, and their impact can differ based on local environmental conditions, expert judgment is necessary to ensure a scientifically sound assessment. The process begins with the selection of a panel of experts with significant knowledge and experience related to water quality and environmental management. However, before the actual Delphi survey, a pilot assessment of the questionnaire was done with university researchers in civil engineering department of University of Benin and Ken Saro Wiwa Polytechnic to ensure the face validity of the research instrument. For the actual survey exercise, the panel of 3 hydrologists, 3 environmental scientists, 3 water resource engineers, 3 pollution control specialists, and 3 government regulators from the Nigerian Environmental Standards and Regulations Enforcement Agency (NESREA) were used.

Once the panel is established, the first round of consultation takes place. Each expert is provided with a structured questionnaire that asks them to assign weightings to various water quality parameters based on their perceived significance to the overall health of the Mmubete stream. These parameters include dissolved oxygen levels, heavy metal concentrations, microbial contaminants, nutrient levels, and physicochemical properties like

pH and turbidity. Experts are required to rank these parameters based on how critically they affect the river's usability for drinking, agriculture, and aquatic life. To prevent any biases and ensure independent judgment, the responses are collected anonymously. The results from the first round are then statistically analysed to determine areas of agreement and disagreement among the experts. A summary of the findings often including the average weightings assigned, the range of values, and areas of divergence is then shared with the panel in a way that keeps individual responses confidential. In cases where there are significant variations in expert opinions, a second round is conducted. Experts are asked to review the summarised responses and consider revising their initial judgments considering the feedback from other experts. They were required to justify their positions or reconsider their weightings based on new insights provided by their peers. This iterative process continued to a third round, until a consensus is reached, meaning that the experts generally agree on the most appropriate weightings for each parameter. At the end of the Delphi process, a final set of agreed-upon weightings is established, which is then used in the computation of the Water Quality Index (WQI) for the Mmubete stream. These weightings help in objectively assessing the pollution level of the river and determining whether it meets regulatory standards. The outcome provides reliable guidance for policymakers, environmental managers, and local authorities in designing appropriate pollution mitigation strategies and ensuring sustainable management of the stream water resources.

The weighted average is presented in Table 4. The water quality index was obtained following the Equation (1) by [17].

$$WQI = \sum_{i=1}^{n} Q_i W_i \quad (1)$$

where, Q_i = sub-index for ith water quality parameter; W_i = weight associated with ith water quality parameter; n = number of water quality parameters.

Table 4. Weight scores of the nine NSF-WQI parameters.

Parameters	Weighted mean
DO, mg/L	0.15
CFU/100mL	0.15
pH	0.12
BOD, mg/L	0.10
Temperature, °C	0.08
NO_3, mg/L	0.12
PO_4, mg/L	0.08
Turbidity, NTU	0.10
TS, mg/L	0.11

The guide for the classification of the water quality index is presented in Table 5.

Table 5. Water quality class and classification of the type of water resource usage.

The index limit	Water quality	Classification of water resources and their usage
90-100	Excellent	No Need for treatment both for drinking water and other uses. It is good for rearing fish and water-resistant species.
70-90	Good	Conventional treatment is required, if usage is for provision of drinking water. It is appropriate for rearing fish and recreative purposes like swimming.
50-70	Moderate	Advanced treatment is required if usage is for provision of drinking water. Appropriate for fish farming and water-resistant plants and animals, and appropriate for domestic animals, as drinking water.
25-50	Bad	Appropriate for irrigation purposes
0-25	Very bad	Not appropriate for any of the above-mentioned uses, and it can support a limited number of aquatic animals.
Source: Authors' compilation, (Adapted from [15])		

The Water Pollution Index (WPI) is a numerical value that indicates the level of pollution in water. It is often calculated using the concentrations of various pollutants. The water pollution index was determined using the modified water pollution index [15]. The WPI is determined by calculating the sum of the ratios of the observed yearly average value (Ai) and the standard threshold values (T) for each parameter and then dividing that total by the number of parameters (n) that were used. This is shown in Equation (2).

$$WPI = \sum_{i=1}^{n} \frac{Ai}{T} x \frac{1}{n} \quad (2)$$

The guide for the classification of the water pollution index is presented in Table 6.

Table 6. Water quality class and water pollution index.

Water Pollution Index Range	Water Quality Class	Description
0–1	Excellent	The water is very clean with no pollution
1-2.5	Good	Slightly polluted but generally clean
2.5–5	Moderate	Moderately polluted
5-7.5	Poor	Heavily polluted
7.5-10	Very Poor	Extremely polluted
>10	Unsuitable for Drinking/Severe	Not fit for human consumption

3. Results and discussion

Table 7. Mmubete water quality parameters during the wet and season.

No	Parameters	Season					WHO Limit	NDW QS
		Wet						
		Min	Max	Mean	S.D	Var		
1	Temperature	23.80	29.30	27.48	0.84	0.70	30	30
2	pH	6.25	6.75	6.54	0.09	0.008	6.5-8.5	8.5
3	TDS (Mg/l)	41.70	49.70	46.43	1.43	2.04	500	500
4	TSS(Mg/l)	10.10	23.90	18.75	2.07	4.30	30	30
5	Chlorides (Mg/l)	5.00	78.00	39.27	17.05	290.70	250	250
6	Salinity (Mg/l)	20.00	29.20	23.97	1.61	2.60	100	100
7	DO (Mg/l)	3.00	5.96	4.96	0.41	0.17	5.0	5
8	EC (µs/cm)	90.00	100.00	94.20	2.26	5.11	1000	
9	COD (Mg/l)	20.10	58.70	37.13	5.25	27.55	40	40
10	BOD (Mg/l)	12.60	37.40	24.56	3.65	13.32	4	4
11	Turbidity (NTU)	15.10	19.10	17.03	0.51	0.26	5	5
12	Nitrate (Mg/l)	10.10	17.80	13.01	1.96	3.85	50	50
13	Copper (Mg/l)	0.00	0.35	0.10	0.02	0.0003	1	1
14	Lead (Pb) (Mg/l)	0.01	0.03	0.02	0.002	0	0.05	0.005
15	Nickel (Mg/l)	0.10	0.34	0.14	0.05	0.002	0.	0.03
16	Phosphate (Mg/l)	0.09	0.45	0.23	0.05	0.003		0.1
17	Iron (Mg/l)	1.45	11.04	0.38	0.16	0.03	0.3	0.03
18	Manganese (Mg/l)	0.01	1.08	0.05	0.08	0.007	0.4	0.1
No	**Parameters**	**WHO Limit**	**NDW QS**	**Season**				
				Dry				
				Min	**Max**	**Mean**	**S.D**	**Var**
1	Temperature	30	30	25.40	29.80	27.99	0.70	0.49
2	pH	6.5-8.5	8.5	6.23	6.74	6.50	0.10	0.01
3	TDS (Mg/l)	500	500	40.00	53.00	46.55	2.23	4.98
4	TSS(Mg/l)	30	30	6.01	162.10	34.59	13.35	178.39
5	Chlorides (Mg/l)	250	250	5.47	215.00	37.89	30.92	955.91
6	Salinity (Mg/l)	100	100	20.10	30.30	24.38	1.60	2.56
7	DO (Mg/l)	5.0	5	4.00	10.20	6.15	0.68	0.46
8	EC (µs/cm)	1000		89.00	101.00	94.70	2.65	7.02
9	COD (Mg/l)	40	40	6.30	38.40	18.52	2.96	8.74
10	BOD (Mg/l)	4	4	2.91	23.00	11.60	1.34	1.81
11	Turbidity (NTU)	5	5	10.40	20.10	16.18	0.54	0.29
12	Nitrate (Mg/l)	50	50	10.20	18.90	13.92	1.80	3.25
13	Copper (Mg/l)	1	1	0.00	0.32	0.10	0.01	0.0001
14	Lead (Pb) (Mg/l)	0.05	0.005	0.01	3.24	0.42	0.26	0.07
15	Nickel (Mg/l)	0.	0.03	0.01	0.41	0.14	0.06	0.003
16	Phosphate (Mg/l)		0.1	0.05	269.00	7.81	25.83	666.95
17	Iron (Mg/l)	0.3	0.03	2.23	13.51	0.26	0.05	0.003
18	Manganese (Mg/l)	0.4	0.1	0.04	0.82	0.06	0.005	0.0

The table presents a comprehensive analysis of various water quality parameters measured in the Mmubete stream during both wet and dry seasons. As shown in Table 7, the data includes the minimum, maximum, mean values, standard deviation (S.D.), and variance (Var) for each parameter. These values are compared against the World Health Organization (WHO) limits and the Nigerian Drinking Water Quality Standards (NDWQS) to assess the water's suitability for consumption and other uses. The temperature during the wet season ranged from 23.80°C to 29.30°C, with a mean of 27.48°C. The standard deviation was 0.84, indicating relatively stable temperatures with minor fluctuations. The variance was 0.70. During the dry season, the temperature ranged from 25.40°C to 29.80°C, with a slightly higher mean of 27.99°C. The standard deviation and variance were lower at 0.70 and 0.49, respectively, suggesting even more stable temperatures. The temperature in both seasons remained below the WHO and NDWQS limits of 30°C, indicating that temperature is not a significant concern regarding water quality in this stream.

The pH ranged between 6.25 and 6.75, with a mean of 6.54, which is within the lower bound of the WHO guideline (6.5-8.5). The standard deviation was 0.09, with a variance of 0.008. The pH during the dry season was slightly more acidic, ranging from 6.23 to 6.74, with a mean of 6.50. The standard deviation was 0.10, and the variance was 0.01. The pH values indicate that the water is slightly acidic during both seasons, with the dry season showing a marginally lower pH, indicating increased acidity. However, the values are within acceptable limits, though require close monitoring. Total Dissolved Solids (TDS) ranged from 41.70 mg/L to 49.70 mg/L, with a mean of 46.43 mg/L during the wet seasons. The standard deviation was 1.43, with a variance of 2.04. TDS values in the dry season varied more, ranging from 40.00 mg/L to 53.00 mg/L, with a mean of 46.55 mg/L. The standard deviation was higher at 2.23, and the variance was 4.98. Both seasons recorded TDS levels far below the WHO and NDWQS limit of 500 mg/L, indicating good water quality concerning dissolved solids. However, the dry season shows a slight increase in TDS, suggesting potential evaporative concentration effects.

Total Suspended Solids (TSS) levels ranged from 10.10 mg/L to 23.90 mg/L, with a mean of 18.75 mg/L during the wet season with a standard deviation of 2.07, and a variance of 4.30. However, TSS levels during the dry season showed a dramatic increase, ranging from 6.01 mg/L to 162.10 mg/L, with a mean of 34.59 mg/L. The standard deviation and variance were much higher at 13.35 and 178.39, respectively. The significant increase in TSS during the dry season could be due to reduced water flow, which allows for the accumulation of suspended particles. Despite this, the mean TSS value during the wet season remains within acceptable limits, while the dry season shows potential concerns.

In the wet season, the Chloride levels ranged from 5.00 mg/L to 78.00 mg/L, with a mean of 39.27 mg/L. The standard deviation was 17.05, with a variance of 290.70. However, the Chloride levels varied more in the dry season, with a range of 5.47 mg/L to 215.00 mg/L and a mean of 37.89 mg/L. The standard deviation was 30.92, and the variance was 955.91. Both seasons recorded chloride levels below the WHO and NDWQS limit of 250 mg/L. However, the wide range and higher variance during the dry season suggest sporadic but significant chloride inputs, possibly from anthropogenic sources or natural mineral dissolution. As for the water Salinity, this ranged from 20.00 mg/L to 29.20 mg/L, with a mean of 23.97 mg/L in the wet season. The standard deviation was 1.61, with a variance of 2.60. During the dry season, salinity ranged from 20.10 mg/L to 30.30 mg/L, with a mean of 24.38 mg/L. The standard deviation was 1.60, and the variance was 2.56. Salinity levels remained consistent across both seasons and well within the acceptable limit of 100 mg/L, indicating that salinity is not a significant issue for the Mmubete stream.

The Dissolved Oxygen (DO) levels in the wet season ranged from 3.00 mg/L to 5.96 mg/L, with a mean of 4.96 mg/L. The standard deviation was 0.41, with a variance of 0.17. In the dry season, DO levels increased, ranging from 4.00 mg/L to 10.20 mg/L, with a mean of 6.15 mg/L. The standard deviation was 0.68, and the variance was 0.46. DO levels are generally within acceptable limits, with the dry season showing higher oxygen levels, likely due to lower temperatures and reduced biological oxygen demand. The wet season's DO is slightly lower but still within acceptable limits for most aquatic life. The values of Electrical Conductivity (EC) in the wet season ranged from 90.00 µs/cm to 100.00 µs/cm, with a mean of 94.20 µs/cm. The standard deviation was 2.26, with a variance of 5.11. EC levels in the dry season ranged from 89.00 µs/cm to 101.00 µs/cm, with a mean of 94.70 µs/cm. The standard deviation was 2.65, and the variance was 7.02. Both seasons show EC levels well below the WHO guideline of 1000 µs/cm, indicating that the water has low mineral content and is unlikely to pose significant risks related to electrical conductivity.

The Chemical Oxygen Demand (COD) values during the wet season range from 20.10 mg/L to 58.70 mg/L, with a mean of 37.13 mg/L. The standard deviation was 5.25, with a variance of 27.55. During the dry season, COD levels dropped significantly, ranging from 6.30 mg/L to 38.40 mg/L, with a mean of 18.52 mg/L. The standard deviation was 2.96, and the variance was 8.74. COD values indicate organic pollution levels, with the wet season showing higher COD values, possibly due to increased organic matter from runoff. The dry season's

lower COD suggests reduced organic loading, likely due to less runoff. The Biological Oxygen Demand (BOD) in the wet season ranges from 12.60 mg/L to 37.40 mg/L, with a mean of 24.56 mg/L. The standard deviation was 3.65, with a variance of 13.32. During the dry season, the BOD values were lower, ranging from 2.91 mg/L to 23.00 mg/L, with a mean of 11.60 mg/L. The standard deviation was 1.34, and the variance was 1.81. BOD levels were significantly higher during the wet season, indicating higher levels of biodegradable organic matter, which could lead to oxygen depletion. In contrast, the dry season recorded lower BOD values, reflecting reduced organic pollution.

The Turbidity values of the stream during the wet season ranged from 15.10 NTU to 19.10 NTU, with a mean of 17.03 NTU. The standard deviation was 0.51, with a variance of 0.26. Turbidity during the dry season ranged from 10.40 NTU to 20.10 NTU, with a mean of 16.18 NTU. The standard deviation was 0.54, and the variance was 0.29. Both seasons recorded turbidity levels above the WHO limit of 5 NTU, indicating that the water is quite murky, which could affect its suitability for drinking without adequate treatment. The slight reduction in turbidity during the dry season might be due to lower runoff, but it remains a concern. As for the Nitrate levels in the wet season, this ranges from 10.10 mg/L to 17.80 mg/L, with a mean of 13.01 mg/L. The standard deviation was 1.96, with a variance of 3.85. Nitrate values during the dry season ranged from 10.20 mg/L to 18.90 mg/L, with a mean of 13.92 mg/L. The standard deviation was 1.80, and the variance was 3.25. Nitrate levels in both seasons were well within the WHO and NDWQS limits of 50 mg/L, indicating that the stream is unlikely to suffer from eutrophication due to nitrate pollution.

The Copper levels in the Mmumbete Stream during the wet season ranged from 0.00 mg/L to 0.35 mg/L, with a mean of 0.10 mg/L. The standard deviation was 0.02, with a variance of 0.0003. During the dry season, copper levels were similar, ranging from 0.00 mg/L to 0.32 mg/L, with a mean of 0.10 mg/L. The standard deviation was 0.01, and the variance was 0.0001. Copper concentrations remained below the WHO and NDWQS limits of 1 mg/L in both seasons, indicating no significant contamination from copper. The Lead levels ranged from 0.01 mg/L to 0.03 mg/L, with a mean of 0.02 mg/L, the standard deviation was 0.002, with a variance of 0 during the wet season. However, the Lead levels increased significantly in the dry season, ranging from 0.01 mg/L to 3.24 mg/L, with a mean of 0.42 mg/L. The standard deviation was 0.26, and the variance was 0.07. Lead levels during the wet season were within safe limits, but the dry season showed a concerning spike, exceeding the WHO limit of 0.05 mg/L. This suggests potential contamination sources that may need to be investigated and mitigated.

In the wet season, Nickel levels ranged from 0.10 mg/L to 0.34 mg/L, with a mean of 0.14 mg/L. The standard deviation was 0.05, with a variance of 0.002. However, during the dry season, it ranged from 0.01 mg/L to 0.41 mg/L, with a mean of 0.14 mg/L. The standard deviation was 0.06, and the variance was 0.003. Nickel levels were generally low and within acceptable limits during both seasons, with no significant variations between wet and dry periods. The Phosphate levels in the wet season ranged from 0.09 mg/L to 0.45 mg/L, with a mean of 0.23 mg/L. The standard deviation was 0.05, with a variance of 0.003. During the dry season, phosphate levels showed a wide range from 0.05 mg/L to 269.00 mg/L, with a mean of 7.81 mg/L. The standard deviation was 25.83, and the variance was 666.95. The dramatic increase in phosphate levels during the dry season is concerning, as it could lead to eutrophication, especially since the maximum value far exceeds typically acceptable limits.

The Iron levels of the stream in the wet season ranged from 1.45 mg/L to 11.04 mg/L, with a mean of 0.38 mg/L. The standard deviation was 0.16, with a variance of 0.03. But during the dry season ranged from 2.23 mg/L to 13.51 mg/L, with a mean of 0.26 mg/L. The standard deviation was 0.05, and the variance was 0.003. Iron levels exceeded the WHO and NDWQS limit of 0.3 mg/L during both seasons, with higher variability and maximum values observed in the dry season, indicating a potential issue with iron contamination in the stream. Manganese levels in the wet season ranged from 0.01 mg/L to 1.08 mg/L, with a mean of 0.05 mg/L. The standard deviation was 0.08, with a variance of 0.007. Manganese levels during the dry season ranged from 0.04 mg/L to 0.82 mg/L, with a mean of 0.06 mg/L. The standard deviation was 0.005, and the variance was 0. Manganese levels remained below the WHO and NDWQS limits of 0.4 mg/L in both seasons, with minimal variations observed.

3.1 Water Quality and Pollution Index

Table 8. Water quality index of Mmubete stream during the wet and dry season.

S/N	Season	Water Index Value		Remark
		Quality	Pollution	
1	Wet	53.22	1.037	Moderate pollution
2	Dry	55.87	1.329	Moderate pollution

The water quality index (WQI) values of the Mmubete Stream for both wet and dry seasons is presented in Table 8. The WQI is a critical indicator that helps in assessing the overall quality of water, integrating multiple parameters to give a singular value that reflects the water's suitability for various uses, such as drinking, agriculture, and recreation. The index values are accompanied by pollution index values, which further categorise the pollution levels in the stream. The data indicates that the stream experiences moderate pollution throughout the year, with minor seasonal variations. The water quality is slightly better during the wet season but worsens slightly during the dry season. This could be due to the balance between increased runoff during the wet season and the reduced dilution capacity of the stream during the dry season.

The WQI during the wet season is recorded as 53.22. This value falls within the range that generally signifies water of fair quality, bordering on good. According to most water quality standards, this index suggests that the water is moderately polluted but still usable for many purposes with basic treatment. The implication here is that the wet season introduces a variety of pollutants into the stream, likely due to runoff, which may carry agricultural chemicals, waste, and other contaminants into the water. During the dry season, the WQI slightly increases to 55.87. This marginal rise suggests a small improvement in water quality, but the stream remains within the category of moderate pollution. The improvement in WQI during the dry season may be attributed to a reduction in surface runoff, which is typically lower when there is less rain. However, despite the lower input of pollutants from runoff, the water quality does not drastically improve, possibly due to reduced flow and higher concentrations of pollutants that persist in the stream.

The practical consequences of the results of the water quality index are on human, environment and socio-economic activities. The environmental consequences include reduction of biodiversity in and around the stream [19], eutrophication risk [14] and alteration of ecosystem balance [12]. From the human health perspective, the stream is unsafe for drinking, hence requires treatment before using [19-20]. It posed recreational hazard and potential disease spread. The economic and social impacts of the WQI results include high cost of water treatment, reduced fisheries yield and declined tourism and recreation [21]

The pollution index during the wet season is 1.037. The value obtained indicates that while the water is not severely polluted, there is a notable presence of pollutants. The wet season typically sees an influx of pollutants from various sources due to higher rainfall and increased surface runoff. These sources can include agricultural runoff, untreated sewage, and other contaminants from urban and rural landscapes. The presence of such pollutants can adversely affect the water quality, resulting in moderate pollution levels as recorded. In the dry season, the pollution index rises to 1.329, indicating a slight increase in the level of pollution compared to the wet season. This increase might seem counterintuitive at first, considering the absence of heavy rainfall that could carry pollutants into the stream. However, during dry periods, the reduced water flow can lead to higher concentrations of existing pollutants, as there is less water to dilute contaminants.

Furthermore, human activities around the stream may continue to introduce pollutants, such as through the disposal of waste, leading to a consistent pollution load. Both seasons are classified as having "moderate pollution", according to the remarks in the Table 5. This classification is critical as it highlights that while the water is not severely polluted, it is still not of optimal quality. The stream's water during both seasons may require some level of treatment before it can be deemed safe for human consumption or other sensitive uses. The consistent classification across seasons suggests that while there are seasonal variations in water quality and pollution, these changes are not significant enough to alter the overall assessment of the stream's health. From an environmental management perspective, these results suggest that efforts to improve the water quality of Mmubete stream should be sustained year-round. During the wet season, controlling runoff and its associated pollutants could be critical, while during the dry season, maintaining flow rates and addressing point-source pollution could help mitigate the concentration of pollutants. Regular monitoring and specific interventions during each season could help in improving the overall water quality, thereby making the stream more suitable for diverse uses. While the water quality in Mmubete stream does not fall into a critical category, the moderate pollution status across both seasons indicates a need for ongoing attention to ensure the water remains usable and does not degrade further, especially in the face of environmental changes and human activities.

4. Conclusion

The Mmubete stream receives the effluent from the abattoir, petrochemical company, and sand dredging and mining activities within the state. Hence, the pollution status of the stream was assessed. The results of the physicochemical analysis revealed that BOD and turbidity of the stream are higher in the rainy season than in the dry season. This is because of the runoff and crude oil from oil spill sites entering the stream during the wet season. The high BOD and turbidity negatively affect the DO and COD. The low DO values, high BOD, and COD values

are indications of pollution of the stream. The DO values fluctuate due to multiple sources of pollution including several points of dredging alongthe studied stretch of the stream and discharge from an abattoir. Also, the results of the water pollution index show that for wet and dry seasons, the values are 1.037 and 1.329 respectively. These indices imply that the stream water is moderately polluted in both the wet and dry seasons. The overall water quality index of the Mmubete stream during the wet and dry seasons are 53.22 and 55.87 respectively. Both the water pollution index and water quality index indicate that the Mmubete stream is moderately polluted. Therefore, regular monitoring of the stream is necessary to mitigate the degradation of water quality.

Acknowledgments

The authors grateful for the contributions of the anonymous reviewers. Their feedback has been invaluable in improving the quality of this manuscript.

References

[1] Amira S, Astono W, Hendrawan D. Study of pollution effect on water quality of Grogal River, DK1 Jarkata. In: The 4th International Seminar on Sustainable Urban Development; 10P Conference Series: Earth and Environmental Science; 2018.
[2] Ugbebor JN. Modelling the variability of water quality of the Oshika Lake. PhD Thesis, University of Nigeria, Nsukka, Nigeria; 2011.
[3] Oguntimehin II, Babatola JO. The pollution status of some selected rivers in Ado-Ekiti, Nigeria. Pak J Sci Ind 2007; 50(1): 22-26.
[4] Ledogo AB, Akatah BM. Assimilative capacity of Khana rivers in present-day Niger Delta, Nigeria. Int J Emp Res Sust Dev 2011; 2(2): 210-217.
[5] Aboyeji OO. Freshwater pollution in some Nigerian local communities, causes, consequences, and probable solutions. Acad J Int Stud 2013.
[6] Asik BB, Ozsoy G. Determination of pollution status of Nitifer river by water and bottom sediment analysis. Water Supply 2023; 001.
[7] Hammer Sr MJ, Hammer Jr MJ. Water quality. In: Hammer MJ, Hammer Jr MJ, editors. Water and Wastewater Technology. 5th ed. London, UK: Pearson; 2004. pp. 139-159.
[8] Galadima A, Garba ZN, Leke L, Almustapha MN, Adam IK. Domestic water pollution among local communities in Nigeria - causes and consequences. Eur J Sci Res 2011; 52(4).
[9] Gerardi MH, Zimmerman MC. Wastewater Pathogens. In: Wastewater Pathogens. 2005.
[10] Grzywna A, Sender J. The assessment of the amount of water pollution and its suitability for drinking of the Tysoniaenica River Basin, Poland. Environ Monit Assess 2021; 315.
[11] Putri MSA, Lou C, Syaiin MO, Oii S, Wang Y. Long-term river water quality trends and pollution source apportionment in Taiwan. Water 2018; 10: 1394.
[12] Sivaranjani S, Rakshit A, Singh S. Water quality assessment with water quality indices. Int J Biores Sci 2015; 2(2).
[13] Zela G, Demiraj E, Marko O, Gjipalaj J, Erebara A, Malltezi J, Zela E, Bani A. Assessment of the Water Quality Index in the Semani River in Albania. J Environ Prot 2020; 11: 998-1013.
[14] Akatah BM. Evaluation and modelling of pollution level and self-purification capacity of Mmubete River, Nigeria. PhD Thesis, University of Benin, Benin City, Edo State, Nigeria; 2023.
[15] Chidiac S, El Najjar P, Ouaini N, El Rayess Y, El Azzi D. A comprehensive review of water quality indices (WQIs): history, models, attempts and perspectives. Rev Environ Sci Biotechnol 2023; 22(2): 349–395.
[16] Mohammed Redha Z, Bu-Ali Q, Janahi AY, AlQahtani MM, Buhindi RA. Development of wastewater quality index as an assessment tool of treated wastewater quality for sea discharge. Water Environ J 2024; 38(3): 450–464.
[17] Jahnig SC, Cai Q. River water quality assessment in selected Yangtze tributaries: background and method development. J Earth Sci 2010; 21(6): 876-881.
[18] Ontiveros HC, Castillo NA, Tristan AC, Cardenas MC, Hernandez CAI, Putri RF. Determination of water quality index (NSFWQI) of water bodies in the Huasteca Potosinna, Mexico. E35 Web Conf 2021; 325: 08002.
[19] Kalagbor IA, Johnny VI, Ogbolokot IE. Application of National Sanitation Foundation and Weighted Arithmetic Water Quality indices for the assessment of Kaani and Kpean Rivers in Nigeria. Am J Water Res 2019; 7(1): 11-50
[20] World Health Organization (WHO). Guidelines for drinking water quality. Geneva, Switzerland: WHO; 2021.
[21] Damo R, Iqbal R. Water quality assessment using WQI and multivariate statistical analysis in Albania. Environ Monit Assess 2018; 190(9): 554.

Turkish Journal of Science & Technology
20(1), 185-192, 2025

Research Paper
https://doi.org/10.55525/tjst.1545362

Enhancing Cost-efficiency Trade-off for Thermoelectric Air Conditioning System in Oyo State, Nigeria

Akeem Lawal SHEU[1*], Olaosebikan Akanni AREMU[2], Kamaldeen Olasunkanmi SULEMAN[3], Ibraheem Abiodun AZEEZ[4], Hakeem Olayinka OYESHOLA[5]

[1,4]Department of Physics, Faculty of Science Education, Emmanuel Alayande University of Education, Oyo, Nigeria
[2] Department of Physics, The Polytechnic, Ibadan, Nigeria
[3] Department of Physics, Maritime University Okerenkoko, Delta State, Nigeria
[5] Department of Physics, Ladoke Akintola University of Technologh, Ogbomoso, Oyo State, Nigeria
[1*] sheuakeemlawal73@gmail.com, [2] aremurichard@yahoo.com, [3] kosuleman@lautech.edu.ng, [4] abeybaba4u@gmail.com, [4]hooyeshola@lautech.edu.ng

(Geliş/Received: 11/09/2024; Kabul/Accepted: 19/02/2025)

Abstract: A variable speed thermoelectric (TE) air conditioner system is developed for efficient power management using intelligent control system. The investigation adopted Variable Voltage Variable Frequency (VVVF) regulator mode of a solid state electronic conversion system with integration of AC–DC and DC–AC Converter method. The system received power from the main 230VAC source and a step-down transformer converted it to 150VAC. The bridge rectifier converted the output voltage varying DCV by regulating the frequency. The DC voltage is transformed back into AC through Pulse Width Modulation (PWM) technique. The sinusoidal waveform is formed automatically by programmed microcontroller (PIC18F4431) Insulated Gate Bipolar Transistor (IGBT) inverter that fed the air conditional compressor motor. The investigational results revealed that as the frequency declines, speed and torque drop which resulted to substantial reduction of power intake. The study reveals that 80,280kWh of energy is expended by a conventional air conditioner (CAC) in a month under steady operation while 15,624kWh is consumed by a thermoelectric air conditioner (TEAC) at the same period. This translates to energy cost of ₦602,100 ($387.51) and ₦18,063,000 ($11625.27) by conventional air conditioner (CAC) daily and monthly respectively while TEAC accounts for ₦117,180 ($75.42) and ₦3,515,400 ($2262.50) at the same period correspondingly. The energy savings cost with the developed TE drive are ₦484,920 ($312.09), ₦14,547,600 ($9362.78) and ₦174,571,200 ($112353.31) averagely on daily, monthly and yearly respectively. The estimated electricity in the study shows that 67% of the energy and cost bill is saved periodically using the developed TE drive likened to traditional climate control system.

Key words: Thermoelectric, variable frequency, inverter, air conditioner, Pulse Width Modulation (PWM), microcontroler.

Oyo Eyaleti, Nijerya'da Termoelektrik Klima Sistemi için Maliyet-Verimlilik Takasının Geliştirilmesi

Öz: Değişken hızlı termoelektrik (TE) klima sistemi, akıllı kontrol sistemi kullanılarak verimli güç yönetimi için geliştirilmiştir. Araştırmada, Değişken Gerilim Değişken Frekans (VVVF) düzenleyici modunu içeren, AC–DC ve DC–AC dönüştürücü yöntemlerinin entegre edildiği katı hal elektronik dönüşüm sistemi kullanılmıştır. Sistem, 230V AC ana güç kaynağından beslenmiş ve bir indirgeme transformatörü yardımıyla 150V AC'ye dönüştürülmüştür. Köprü doğrultucu**,** çıkış gerilimini frekansı düzenleyerek değişken DC gerilime dönüştürmüştür. DC gerilim, Darbe Genişlik Modülasyonu (PWM) tekniğiyle tekrar AC'ye dönüştürülerek izole kapılı bipolar transistörlü (IGBT) inverter tarafından programlanmış bir mikrodenetleyici (PIC18F4431) aracılığıyla sinüzoidal dalga formu oluşturulmuş ve klima kompresör motoruna iletilmiştir. Deneysel sonuçlar, frekans azaldıkça hız ve torkun düştüğünü ve bunun da önemli ölçüde güç tüketimini azalttığını ortaya koymuştur. Çalışma**,** geleneksel bir klima sisteminin (CAC) sabit çalışmada aylık 80.280 kWh enerji tükettiğini**,** buna karşılık termoelektrik klima sisteminin (TEAC) aynı sürede 15.624 kWh enerji tükettiğini göstermiştir. Bu, enerji maliyetlerinin geleneksel klima (CAC) için günlük ₦602.100 ($387.51) ve aylık ₦18.063.000 ($11,625.27) olarak hesaplanmasına karşılık, TEAC sistemi için günlük ₦117.180 ($75.42) ve aylık ₦3.515.400 ($2,262.50) olarak gerçekleştiğini göstermektedir. Geliştirilen TE sürücü sistemi ile günlük ₦484.920 ($312.09), aylık ₦14.547.600 ($9,362.78) ve yıllık ₦174.571.200 ($112,353.31) tasarruf sağlanmıştır**.** Çalışmada tahmin edilen elektrik tüketimi, geleneksel iklimlendirme sistemine kıyasla enerji ve maliyet faturalarında %67'lik tasarruf sağlandığını göstermektedir**.**

Anahtar Kelimeler: Termoelektrik, değişken frekans, invertör, klima, Darbe Genişlik Modülasyonu (PWM),mikrodenetleyici.

[*] Corresponding author: sheuakeemlawal73@gmail.com. ORCID Number of authors: [1] 0000-0003-4877-880X, [2] 0000-0002-6506-609X, [3]0000-0002-9103-1974, [4]0000-0002-6399-8782, [5]0000-0002-1628-1455

1. Introduction

Thermoelectric (TE) climate control is a promising solid-state tool that has the probable to substitute conventional gas compression-based central air conditioning system. It can drive heat from one side of a device to the other by electric current [1]. It possesses many benefits such as no moving parts, noiseless operation, and flexible performance with regulation of current input. Thermoelectric sub-cooling system applies Variable Frequency Drives (VFD) technique to altering the motor speed by varying voltage and frequency of the power supplied to the motor [2,3]. The volts/hertz ratio prototype is conserved to lessen undue heating and sustain appropriate power factor of the motor. VFD control speed of motor by varying output voltage and frequency through sophisticated microprocessor controlled electronics device. The modus operandi of the system consists of rectifier and inverter units. Rectifier transforms Alternating Current (AC) in Direct Current (DC) voltage and inverter changes DC voltage back in AC voltage [4,5]. The temperature rise results in increased energy and saving costs for conventional air-conditioning systems [6].

Thermoelectric cooling air con is a device using power electronics for frequency variations of power to the induction motor, thereby controlling motor speed. It varies the speed of a rotating load, including those that vary the speed of motor and linkage devices that allow constant motor speed while varying the load speed [7-9]. The system is applied to match the speed and torque of a drive to the process requirements and also for energy saving in addition to efficiency improvements. These savings are predominantly perceived with centrifugal pumps and fans, where load force upsurges as the square of the speed and power intake as the cube of the speed (the affinity laws). Substantial cost savings is realizable through this application [10-13].

Air conditioners consume a lot of electricity because the mode of operation involves recurring cycles of compressing a gas to a liquid, which consumes much power. Mechanical control rudiments such as damper and valves used to standardize flow and pressure result in inefficient of operation, great deal of energy loss because of their toggling action. Other challenges include poor efficiency of the machine, high electricity bill costs, occupants discomfort through noise output from fan and compressor, superfluous creation of wear and tear on motors and related components, reduction in equipment life span and high operating costs.

However, universal economic growth as well as imminent hot climates, over the next decades especially in tropical areas will further boost demands for air conditioning system. There is a demand for much more energy efficient way to accomplish space cooling and this is the main goal of this research. This study showcases results of the investigational positioning which proves the conservation of energy in Air Compressors cautiously by adopting TE air cooling system. As a matter of fact, it is imperative for researchers to develop energy efficient air conditioning systems which will significantly reduce the energy and saving costs.

2. Related Works

There are various scholarships thatresearched on the optimizing cost-efficiencytrade-off for thermoelectric sub-cooling climate control system. Most investigators like Kim et al. [14], Saini et al. [15], Tai-feng et al. [16] among others embraced Thermoelectric air conditioning modeling, Thermoelectric Module with Radiative and Convective Processes (TEM-RCP) by mock-up model with an all-out cooling capability, cooling load calculations, capacity estimation, and control for the heavyweight radiant systems related design and control. Some of these researchers observe the effects of convection heat transfer coefficients, air flow rates, and thermoelectric material properties on system performance. The studies relate constant and graded material properties, evaluating their effect on cooling capacity, Coefficient of Performance (COP), and power intake. The discoveries advocate that while graded materials can augment cooling, they may lessen COP equated to constant property materials. The researchers conclude that with appropriate material properties and operating conditions, thermoelectric cooling can be a competitive technology for future air conditioning applications.

The present research is compared with other previous experimental studies. The analysis and comparison are of qualitative observations and devoid of quantitative comparison. By implication, some agreements were attained in the behaviors of the characteristics and the tendency of the curves of the previous researchers. On the other hand there is no concise agreement in the present values with respect to the previous studies. It is observed that the power consumption of developed drive air conditioner is significantly less than the power usage of traditional system. This behavior of average energy consumption, energy efficiency, cooling comfort and motor behavioral characteristics were also mentioned and discussed by previous researchers. The emphasis on the compressor motor beside the blower or the fan by the previous investigators was centered on its ability to control more than 90% of cooling and energy capacity of air conditioner. The adoption of solar system to power the air conditioners by the

previous researchers generated many lapses during the operation of the system. This research consolidates on necessary improvement saving technique required for the available power in the country. The AC motor embraced in the new study enhanced versatile operation of compressor compared to DC motor applied by other researchers.

Again, this study developed an energy efficient air conditioner drive using intelligent control system for effective power and energy cost management. The constant material properties and VFD technique properties are considered for the TE materials, and they are compared in terms of the degree of cooling, COP and power consumption. The available data in Nigeria proved non availability of this kind of research. The study appraising thermoelectric sub-cooling system retrofits opportunities for energy and cost savings of air conditioner by enhancing the motors proficiency.

3. Research Method

3.1. Measuring Materials

The quantifying toolsfor the research are digital multi-meter (DMM), energy meter, mercury-in-glass thermometer and air flow meter. The energy meter processes the consumed power while the air flow meter records the extent of air flows through a tube of both conventional and thermoelectric drive air conditioner. The resistance values, voltages and currents are respectively measured with digital multi-meter.

In this study, an energy meter is applied for monitoring power consumption and overall energy efficiency of the system. Power resolution of 1W and energy resolution of 0.01kWh are adopted for this design for accurate long-term monitoring, detecting minute changes in power consumption and precise energy tracking. Current and voltage resolution of 1mA and 1mV are implemented for better power systems and accurate power calculations respectively. The energy meter also has the capacity of 10ms or <1 second response time for real-time tracking of rapid variations and dynamic changes without significant delays. With these functioning requirements, the energy meter ensures efficient energy management and real-time optimization of the thermoelectric air conditioning system.

Thermometer (temperature sensor) of higher resolution 0.1°C is embraced in this design for more accurate feedback in the control loop, for monitoring and controlling the system's efficiency and reducing energy consumption by preventing overcooling or overheating. Response times of 1-5 seconds are adopted in the research to detect and report a temperature change quickly due to the solid-state nature of thermoelectric modules. A slow thermometer could delay feedback, leading to inefficiencies or instability in the system.

The airflow meter embraced in this design plays a crucial role in ensuring optimal thermal performance. Monitoring and controlling airflow is essential for maintaining system efficiency, managing heat transfer, and achieving desired cooling or heating effects. A resolution of 0.1– 0.5m^3/s is implemented in this study for thermal efficiency**,** system steadiness and energy optimization to improve energy efficiency and system longevity. A response time of 1–2 seconds is required in the research for the airflow meter to register and report a change in airflow. This will enhance rapidly varying cooling loads and ensures real-time feedback for efficient system control (Dynamic Control**).** It also allows fast response to stabilize the system quickly during startup, shutdown, or sudden changes in cooling demand (Transient Conditions**).** Lastly, it enhances filtering or signal processing to lessen more noise in the measurement (Trade-offs).

In this study, a 4½-digit DMM high resolution is applied for measuring critical electrical parameters such as voltage, current, and resistance. These measurements are essential for monitoring the performance of the thermoelectric modules, ensuring proper operation, and diagnosing faults. For Voltage Monitoring, a resolution of 1mV is adopted for precise voltage control to operate efficiently and to ensure accurate monitoring of input voltage. For current measurement, a resolution of 1mA is implemented for precise current measurement and in determining the power consumption and optimizing the system's energy efficiency. For resistance measurement, a resolution of 0.1Ω is applied for diagnosing connection issues or checking the health of thermoelectric modules. A High-speed DMMs with a sampling rate of at least 2–10 Hz for dynamic measurements and response times of >10 readings per second is engaged in the study for dynamic or transient measurements.

3.2. Design Method

The block diagram in Figure 1 designates step-wise process for the invention of thermoelectric central air systems. The variable speed drive is established in this investigation by using Variable Voltage Variable Frequency (VVVF) regulator mode of a solid state electronic conversion system with incorporation of AC–DC and DC–AC Converter expertise. The project plan convoluted the congregation of DC Power Supply Unit, Monitoring & Control Units and Power Unit [16,17]. The incoming power main source of 230VAC is delivered to the entire

system and subsequently converted into 150VAC by a step – down transformer. A bridge rectifier transfigures the transformer output voltage to modifying DC voltage.

The procedure is well-ordered absolutely with current ambient air temperature sampling and correct fine-tuning of compressor speed by a programmed microcontroller (PIC18F4431). Variable frequency Pulse Width Modulation (PWM) signal is produced by the automated microprocessor to confirm the regulation of the functional voltage and significant production of PWM frequency prerequisite at the output of power inverter [18,19]. The sinusoidal waveform is created automatically by microcontroller Insulated Gate Bipolar Transistor (IGBT) inverter that fed the air conditional compressor motor at a regulated frequency. The variable frequency drive efficaciously established in this study is linked with air conditional and set running at different phases in stable power condition. The speeds of the induction motor of air condition are regulated to achieve low energy consumption.

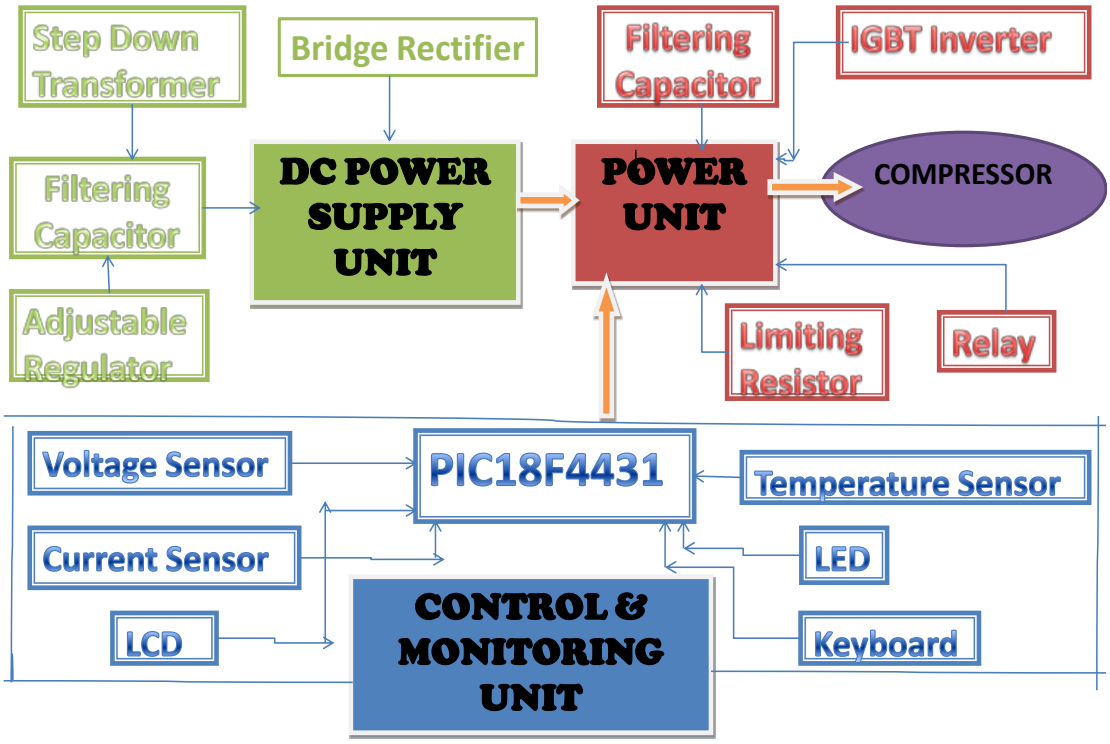

Figure 1. The block diagram of developed thermoelectric drive.

4. Results

The investigational results presenting the resultant frequency – characteristics, air flow, room temperature, power consumption, and actual speeds as observed for days from 7:30am till 6:45pm for the duo of traditional and developed TE air conditioners (Table 1 & Figures 2 – 4). The power consumption rate, cooling output, energy efficiency, estimated electricity costs are also observed for effective power management. Power consumption rate of the system increases as the speed of motor increases for both air conditioners with lesser consumption rate on thermoelectric drive (Figure 3). The rate of air flow for the new TE drive is linearly increasing with the frequency as speed of motor also varies, this result to low consumption of power (Table 1). The conventional air conditioner conversely experienced constant speed and frequency as the air flow increases, this accountable for the excessive power consumption by the device (Table 1). The study reveals that 2,676kWh of energy is consumed by conventional air conditioner in 24 hours under steady operation while 520.8kWh is consumed by thermoelectric system at similar time yielding 67% of energy saving. The estimated electricity shows that 67% of the charge bill is saved periodically using the TE drive compared to traditional system.

Table 1. Results of thermoelectric air conditioner (TEAC) and Conventional Air Conditioner (CAC).

S/N	Time (hr)	Indoor Temperature (°C)	Air Flow (m^3/h)	Energy Meter (kWh)		Motor Speed (rpm)		Frequency (Hz)	
				CAC	TEAC	CAC	TEAC	CAC	TEAC
1.	7:30am	24	50	1.5	1.0	3000	1500	50	25
2.	8:45am	25	100	2.5	1.1	3000	1680	50	28
3.	9:50am	22	150	4.0	1.2	3000	1860	50	31
4.	10:55am	23	200	5.5	1.3	3000	2040	50	34
5.	11:55pm	24	250	7.0	1.4	3000	2160	50	36
6.	12;50pm	30	300	8.5	1.5	3000	2460	50	41
7.	1:45pm	28	350	10.0	1.7	3000	2640	50	44
8.	2:58pm	30	400	11.5	1.9	3000	3060	50	51
9.	3:50pm	26	450	13.0	2.2	3000	3240	50	54
10.	4:45pm	27	500	14.5	2.5	3000	3660	50	61
11.	5:50pm	25	550	16.0	2.8	3000	3840	50	64
12.	6:45pm	26	600	17.5	3.1	3000	4260	50	71

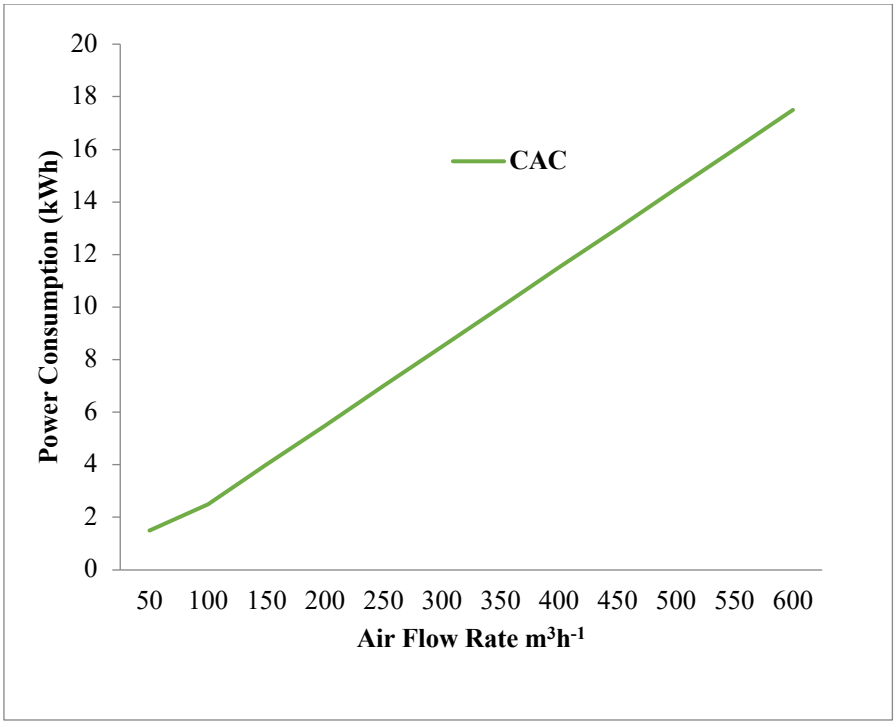

Figure 2. Power Consumption Characteristics of Conventional Air Conditioner (CAC).

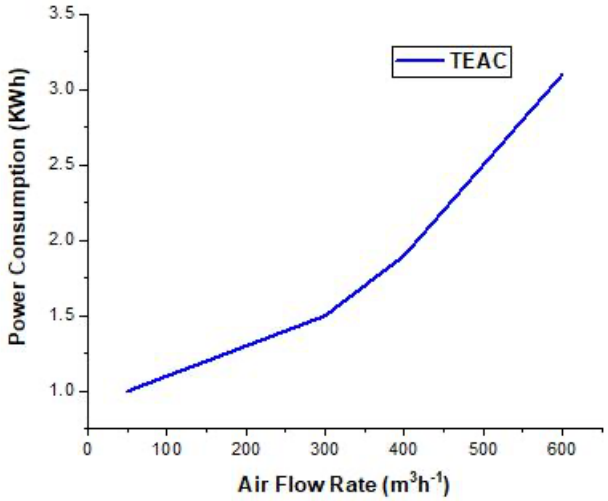

Figure 3. Power Consumption Characteristics of Thermoelectric Air Conditioner (TEAC).

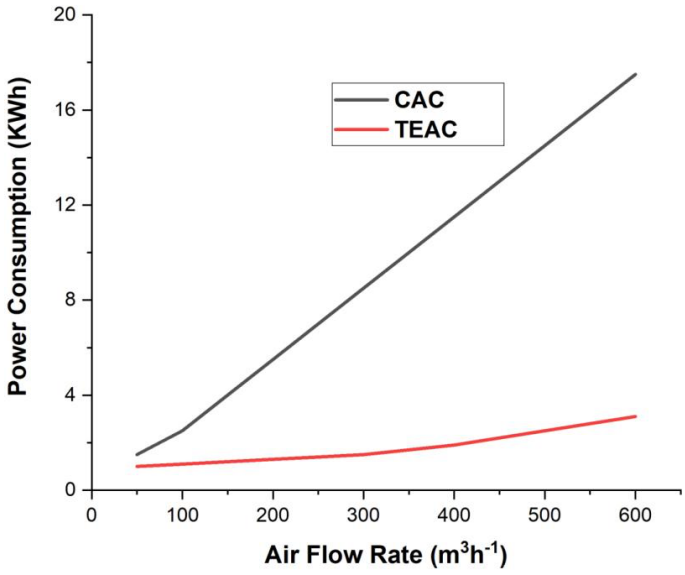

Figure 4. Power Consumption Characteristics of CAC and TEAC.

5. Discussion

The energy efficient drive successfully developed, designed and constructed in this research is connected with a conventional air conditional and set running at different periods under steady power consumption. The developed drive is implemented by a microcontroller (PIC18F4431) based PWM inverter and programmed using C language. The speeds of the induction motor are varied from 1440RPM to 4200RPM at a corresponding frequency range from 24Hz to 70Hz. The developed drive is tested for a 3 phase, 415 Volts, 1.5 H.P. Induction Motor for different frequencies, speeds and load reading.

The application of thermoelectric coordination as demonstrated in the investigation is very essential with the goal of reducing energy cost by optimizing the motors efficiency in the central air system. This is accomplished by change in frequency and speed variation of the motor in the newly invented system. There are extraordinary savings institute in characteristic presentations by using TE drive to run motor of the compressor. To evaluate the prospective savings over time, the actual load/time outline is considered. The load profile specifies the quantity of air flow rate the system necessitates substantial its loads during a typical day, month, and year or time period under study. The energy cost of both conventional and developed TE air conditioner is determined using the present electricity tariff rate of ₦225 per kWh unit by the Nigeria Electricity Regulatory Commission (NERC). Table 3 shows daily/monthly average energy consumption (kWh), energy savings by TEAC (daily/monthly/annually), energy cost by both CAC and TEAC (daily/monthly) and substantial energy savings by the new developed TEAC (daily/monthly/annually).

Table 2. Energy and Cost Analysis of Conventional Air Conditioner (CAC) and Thermoelectric Air Conditioner (TEAC).

DAILY AVERAGE ENERGY CONSUMPTION (kWh)			
CAC		**TEAC**	
80,280kWh		15,624kWh	
ENERGY SAVINGS BY TEAC			
Daily	**Monthly**		**Annually**
2,155.2kWh	64,655.99kWh		786,647.99kWh
ENERGY COST (kWh)			
CAC (Daily)	**CAC (Monthly)**	**TEAC (Daily)**	**TEAC (Monthly)**
₦602,100 ($387.51)	₦18,063,000 ($11625.27)	₦117,180 ($75.42)	₦3,515,400 ($2262.50)
ENERGY SAVINGS BY TEAC			
Daily	**Monthly**		**Annually**
₦484,920 ($312.09)	₦14,547,600 ($9362.78)		₦174,571,200 ($112353.31)

6. Conclusion

The energy efficient drive designed and constructed in this research provides reliable, efficient, cost-effective variable-frequency (V/Hz) control of air conditioner compressor motors. The integration of most recent technologies in Digital Signal Processing (DSP), PWM and IGBTs were implemented in the design to deliver finest motor performance, inclusive programmability, in addition to unfussiness of operation. In the research, an efficient air conditioner drive was realized for efficient power management using intelligent control system that significantly regulates the frequency, speed, voltage, torque, power and reduces the noise output of the fan and compressor for efficient performance at low power consumption.

The economic prominence of this newly developed TE drive is its drastically low power intake and energy cost rate. The study reveals that 80,280kWh (83.7%) of energy is consumed by a conventional air conditioner in a month under steady operation while 15,624kWh (16.29%) at the same period is consumed by a variable speed thermoelectric air conditioner. This translates to energy cost of ₦602,100 ($387.51) and ₦18,063,000 ($11625.27) by CAC daily and monthly respectively while TEAC records ₦117,180 ($75.42) and ₦3,515,400 ($2262.50) at the same period correspondingly. The energy savings cost with the developed drive are ₦484,920 ($312.09), ₦14,547,600 ($9362.78) and ₦174,571,200 ($112353.31) averagely on daily, monthly and yearly respectively. The estimated electricity shows that 67% of the energy as well as cost bill is saved periodically using the TE drive compared to traditional air conditional system.

References

[1] Zuazua-Ros A, Martín-Gómez C, Ibañez-Puy E, Vidaurre-Arbizu M, Gelbstein Y. Investigation of the thermoelectric potential for heating, cooling and ventilation in buildings: characterization options and applications. Renew Energy 2019; 131: 229–239.

[2] Xiaoli Ma, Han Zhao, Xudong Zhao, Guiqiang Li, Samson Shittu. Building integrated thermoelectric air conditioners - a potentially fully environmentally friendly solution in building services. Future Cities Environ 2019; 5(1): 1–13.

[3] Sheu AL, Adagunodo TA. Performance evaluation of inverter-equipped drive to regulate the speed of motor and cooling output of air conditioner. IOP Conference Series: J Phys 2019; 1299: 012029.
[4] Zhang X, Huang Y. Chen Z. A hybrid system integrating photovoltaic module and thermoelectric devices for power and cooling cogeneration. Sol Energy 2022; 239: 350–358.
[5] Adeyanju AA, Manohar K. Design and analysis of a thermoelectric air-conditioning system. J Sci Res 2020; 26 (4): 1–11.
[6] Sheu AL. Design of Energy Efficient Drive for Effective Power Management in Nigeria. South-West Journal of Teacher Education 2017; 8: 103 - 111.
[7] Cai Y, Wang WW, Liu CW, Ding WT, Liu D, Zhao FY. Performance evaluation of a thermoelectric ventilation system driven by the concentrated photovoltaic thermoelectric generators for green building operations. Renew Energ 2020; 147(1): 1565–1583.
[8] Xiao-Xiao Tian, Soheil Asaadi, Hazim Moria, Amr Kaood, Samira Pourhedayat, Kittisak Jermsittiparsert. Proposing tube-bundle arrangement of tubular thermoelectric module as a novel air cooler. Energy 2020; 208: 118428.
[9] Carlo Fanciulli, Hossein Abedi, Adelaide Nespoli, Roberto Dondè, Caterina La Terra, Francesca Migliorini, Francesca Passaretti, Silvana De Iuliis. Additive fabrication and experimental validation of a lightweight thermoelectric generator. Sci Rep 2023; 13(1): 1- 13.
[10] Vián JG, Astrain D, Domínguez M. Numerical modelling and a design of a thermoelectric dehumid. Therm Eng 2002; 22: 407–422.
[11] Dario Narducci, Bruno Lorenzi. Economic convenience of hybrid thermoelectric- photovoltaic solar harvesters. ACS Appl Energy Mater 2021; 4(4): 4029-4037.
[12] Tingrui Gong, Lei Gao, Yongjia Wu, Long Zhang, Shan Yin, Juntao Li, Tingzhen Ming Numerical simulation on 180 a compact thermoelectric cooler for the optimized design. Appl Therm Eng 2019; 146: 815–825.
[13] Sheu AL. Power Management and Regulation of Motor Driven Appliances using Developed Control System. Journal of Pure Science and Science Education 2018; 10: 16 - 21.
[14] Kim M, Kang YK, Joung J, Jeong JW. Cooling performance prediction for hydraulic thermoelectric radiant cooling panels with experimental validation. Sustainability 2022; 14(23): 1 - 17.
[15] Saini A, Watzman SJ, Bahk JH. Cost-performance trade-off in thermoelectric air conditioning system with graded and constant material properties. Energy Build 2021; 240:110931.
[16] Tai-feng Shi, Jing-yuan Zheng, Xia Wang, Peng Zhang, Peng-an Zong, Kafil M. Razeeb. Recent advances of electrodeposition of Bi_2 Te_3 and its thermoelectric applications in miniaturized power generation and cooling. International Materials Review 2023; 68(5): 521-555.
[17] Shoeibi S, Kargarsharifabad H, Sadi M, Arabkoohsar A, Mirjalily SAA. A review on using thermoelectric cooling, heating, and electricity generators in solar energy applications. Sustain Energy Technol Assess 2022; 52: 102105.
[18] Seungho Lee, Kihyun Kim, Deok-Hong Kang, M. Meyyappan, Chang-Ki Baek. Vertical silicon nanowire thermoelectric modules with enhanced thermoelectric properties. Nano Lett 2019; 19(2): 747-755.
[19] Kony Chatterjee, Ankit Negi, Kyunghoon Kim, Jun Liu, Tushar K. Ghosh. In-plane thermoelectric properties of flexible and room-temperature-doped carbon nanotube films. ACS Appl Energy Mater 2020; 3(7): 6929-6936.

Turkish Journal of Science & Technology
20(1), 193-207, 2025

Research Paper
https://doi.org/10.55525/tjst.1555517

Benchmarking Tree-Inspired-Fractal Branching Dendriform Structures From BC to L-System Based Contemporary Structures

Zeynep Gülcan KÖKÇAM[1*], Murat ŞAHİN[2], Ayça GÜLTEN[3]
[1, 2, 3] Department of Architecture, Faculty of Architecture, Fırat University, Elazig, Türkiye
[*1] zeynepgulcankaya@gmail.com, [2] msahin@firat.edu.tr, [3] aycagulten@gmail.com

(Geliş/Received: 24/09/2024; Kabul/Accepted: 19/12/2024)

Abstract: Nature has its own complex geometry, which couldn't be explained using traditional methods until the advent of Fractal Geometry. Nowadays, we can observe and represent almost every geometry using quantitative tools. In this study, the compatibility of geometric compositions, referencing Euclidean geometry from hand-drawing environments to digital drawing and computational Computer-aided design (CAD) tools in the architectural products of complex parametric designs, was observed. Historical structures such as Maison Carrée, The Sakyamuni Pagoda of Fogong Temple, Saint Chapelle, Gloucester Cathedral, King's College Chapel, La Sagrada Familia, and the Stuttgart Airport Terminal, as well as contemporary structures generated by Parametric Design Tools, were examined. Both past and current parametric design examples were benchmarked. The plans and column head views of buildings were analyzed using the Fractal Analysis Method with the FracLac software, which functions as a plug-in within ImageJ. The sophisticated column geometry was created as a dynamic geometry utilizing L-System rules and iteration principles, and then a solid substance was built using a Dynamo-PythonScript node, which acts as an interface command in Autodesk Revit. As a result, contrary to popular belief, dendriform structure geometry behaved unexpectedly and was not complicated than modern times.

Key words: Computational architecture, Computer-aided design (CAD), Fractal geometry, Iterative generation method, Parametric design.

Ağaçtan İlham Alan Fraktal Dallanan Dendriform Yapıların Antik Dönemden L-Sistem Tabanlı Çağdaş Tasarımlara Kadar Karşılaştırılması

Öz: Doğa, Fraktal Geometri ortaya çıkana kadar geleneksel yöntemlerle açıklanamayan kendine özgü karmaşık bir geometriye sahiptir. Günümüzde, hemen hemen her geometriyi niceliksel araçlar kullanarak gözlemleyebilir ve temsil edebiliriz. Bu çalışmada, karmaşık parametrik tasarımların mimari ürünlerindeki el çizimi ortamlarından dijital çizim ve hesaplamalı Bilgisayar destekli tasarım (CAD) araçlarına kadar Öklid geometrisini referans alan geometrik kompozisyonların uyumluluğu gözlemlenmiştir. Maison Carrée, Fogong Tapınağı Sakyamuni Pagodası, Saint Chapelle, Gloucester Katedrali, King's College Şapeli, La Sagrada Familia ve Stuttgart Havaalanı Terminali gibi tarihi yapıların yanı sıra Parametrik Tasarım Araçları ile üretilen çağdaş yapılar incelendi. Hem geçmiş hem de güncel parametrik tasarım örnekleri kıyaslanmıştır. Yapıların planları ve kolon başı görünümleri, ImageJ içinde bir eklenti olarak işlev gören FracLac yazılımı ile Fraktal Analiz Yöntemi kullanılarak analiz edildi. Sofistike kolon geometrisi, L-Sistem kuralları ve iterasyon ilkeleri kullanılarak dinamik bir geometri olarak oluşturuldu ve ardından Autodesk Revit'te bir arayüz komutu olarak işlev gören bir Dynamo-PythonScript düğümü kullanılarak katı bir madde oluşturuldu. Sonuç olarak, sanılanın aksine, dendriform yapı geometrisi beklenmedik şekilde davrandı ve modern zamanlardan daha karmaşık değildi.

Anahtar kelimeler: Hesaplamalı mimari, Bilgisayar destekli tasarım (CAD), Fraktal geometri, Yinelemeli üretim yöntemi, Parametrik tasarım.

1. Introduction

The intricate and inspiring geometric patterns present in nature are more complex than traditional methods of explanation. However, the definition of the concept of fractals, which is contained in Mandelbrot's seminal article "Fractal Geometry" [1], has illuminated this complexity. Fractals are geometric patterns that are generated from repeated forms, and can be observed in natural context such as leaves, waves, and mountains. . From antiquity, the human mind and artisanal skill have not only adeptly imitated these forms but have meticulously integrated their proportions into all elements of construction, decorative elements, and architectural typologies.

Fractal geometry has been an important tool in understanding and modeling complex relationships between natural and artificial structures. Defining fractals and applying them to architecture establishes a bridge between

[*] Corresponding author: zeynepgulcankaya@gmail.com. ORCID Number of authors: [1] 0009-0005-9427-0996, [2] 0000-0001-6733-1136, [3] 0000-0001-9837-8674

aesthetics and functionality [2], [3]. Fractal systems represent an effective method for modelling the complex structure of city centres, encompassing both spatial and temporal dimensions. This is achieved not only at the building scale but also at the urban scale, thereby reflecting the self-similar, hierarchical and dynamic nature of cities. The scale-independent similarity of urban elements, including roads, buildings and green spaces, can be analysed using fractal geometry. The fractal dimension is a measure of the growth, concentration and complexity of urban centres, and also enables the analysis of changes over time. Systems with fractal properties, such as transport networks, can be employed to comprehend and simulate alterations in traffic flows. Moreover, fractal systems facilitate urban planning by elucidating intricate interrelationships between infrastructure, population density and economic activities. When integrated with remote sensing, GIS and agent-based models, this approach can be implemented in domains such as urban growth, land use and infrastructure optimisation to support the design of sustainable and resilient city centres. For several decades, designers have employed fractal geometry to develop innovative architectural forms through the utilisation of parametric modelling tools and the finite element method.

Historical buildings preservation as well as analysis is reliant on computer-aided methods. Image compression, characterization, and recognition techniques are employed in assessing the preservation status of structures [4]. In light of the available case studies, this study compares human cognitive intelligence and ingenuity with both the material and immaterial aspects of the structures obtained through an artificial universe, specifically a computer environment, in the context of fractal geometry, which is often referred to as the geometry of nature.

1.1. Dendriform Structures and Architecture

Natural form adaptation in architecture largely depends on dendriform structures. Innovative structural solutions can be found via L-systems that model such a type of structure [5]. Nouri et al.'s research work [6] discusses how these systems can be used for deriving complex geometries via dendriform structures with consideration to enhancing both form and function. Also Md Rian and Sassone [7] were investigated tree dendriform structures in architectural branching structures. They compared that structures from BC to modern times.

1.2. The application of L-systems and algorithmic generators in Computer-aided design (CAD)

By integrating fractal geometry into the design of architectural structures, a new method has been developed to convert the intriguing and practical principles observed in nature into buildings and structures. A significant advancement in this area is Prusinkiewicz's investigation of the structures of plants using L-Systems [8]. These systems are intended as instruments that generate complex forms that are inspired by the natural world, these forms are created through the use of parametric design tools.

The use of L-Systems in architectural design, and the possibility of parametric design were explored. The investigation by Toussi [9] explains how L-Systems can be used as algorithmic digital generators in architectural design processes. On the other hand, Nouri et al.'s [6] article shows how complex structures can be derived from simple geometric forms through the application of L-Systems. In contrast, Roudavski [10] considered some issues that limit and enable parametric design with emphasis on developing algorithms for handling custom scaling and dynamic properties. This literature review calls for architects to employ L-systems and parametric designs to create innovative and esthetically enriched buildings.

The fractal sorting depends on two main factors. One of them is that knowledge of the nature of fractals must be supported by a straightforward and unalterable method for determining their dimensions. Secondly, unlike mathematical fractals, buildings are not an example of mathematical ones but they bear the characteristics of natural fractals that vary with the scale. This necessitates customized methods for sorting architecture to take into account specificities of different built environments [11].

The use of algorithmic techniques, such as recursion and iteration, has become prevalent in the creation of computer graphics models for fractal objects in a virtual setting. This is due to the self-similarity aspect of fractal geometry. These techniques, which offer efficient model construction, have progressively emerged as the primary means of visually depicting fractal objects in the realm of computer graphics [12].

The use of parametric design enables designers to effortlessly explore and improve shapes by manipulating various parameters. This approach facilitates the seamless connection of the complex and different ways of nature

into architectural designs. Combining parametric design with inspiration from nature offers numerous advantages. These designs have the big potency to be visually fascinating, enhance productivity, and support sustainability. A prime example of this can be seen in the Mercedes-Benz Museum located in Stuttgart, Germany, expertly crafted by Schlaich Bergermann and Partner. The museum's roof draws inspiration from fractal geometry, allowing for the use of natural light and energy conservation [13].

2. Theory/calculation

This study demonstrates the potential use of computer algorithms and parametric design tools for generating and replicating natural geometric shapes. However, it also indicates that architectural products produced prior to the advent of computer-aided design were more successful in capturing natural proportions. This discovery suggests that nature possesses a depth of complexity and aesthetics that cannot be replicated solely through the use of mathematical parameters. The acquisition of artifacts that are proximate to Euclidean geometry, which is regarded as the fractal ratio of natural forms, and the attainment of proximate results from the data derived from the analysis of these artifacts and the data derived from the analysis of computational and low-error-margin geometries generated in the computer environment, reveals the distinction between the structure and vehicle comparison based on the study and the existing fractal analysis studies.

The geometry of natural shapes contains a hidden proportion that can be replicated and easily produced using modern technological methods such as CAD environments, computer algorithms, software application programming interfaces (APIs), and scripts. However, prior to these developments, artisans and other artists were solely reliant on their own abilities to convey ideas. Their designs were meticulously detailed and crafted by hand. The objective of this study is to contrast the profound realm of human cognition with the computational capabilities of computers, thereby emphasizing the significant distinctions between them. In contrast to computers, which are designed solely for computation, humans possess an exceptional capacity to perceive and experience the emotions of nature. Fortunately, humans also possess the ability to achieve results that are computationally similar to those achieved by computers since ancient times (Figure 1).

3. Imitating Natural Geometries

Computer algorithms and parametric design tools are important for mimicking natural forms. However, this research shows that there is a complexity in the natural geometry which cannot be achieved through mathematical parameters alone. There are many geometric shapes that happen to be mathematically precise within nature itself; for instance, the organization of leaves around a stem follows the Fibonacci sequence. The beauty of these geometrical patterns found in Renaissance artworks indicates how artists have been able to utilize natural geometries into human creations. In contrast, current technological advances in architecture and engineering have been driven by the imitation of natural geometric designs, so-called biomimetic design, as evidenced by the creation of structures such as those derived from termite mounds. These developments demonstrate the remarkable capabilities of mathematical laws, which underpin the functioning of both living and non-living entities, across a range of disciplines, including science, technology, and the arts.

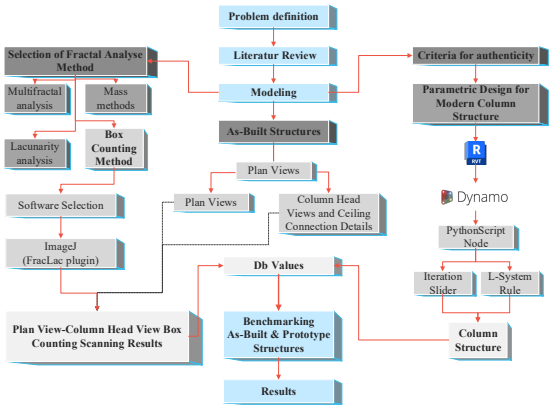

Figure 1. The framework of the study methodology.

3.1. The Role of Human Mind and Skill

In the past, architectural designs were created by humans, rather than computers, which were better able to imitate the natural proportions of architecture. This suggests that the mind can understand the intricacy and beauty of nature through intuitive processes.

In human perception, knowledge about shape, color, texture, and composition, as they relate to one another visually, helps us make sense of our environment. All of these elements combine to form rich patterns that are foundational for how we think. Among these features, it is notable that shape is recognized first and remembered best by the brain, thus serving as a basis for further interpretation. Composition, on the other hand, emerges as key in cognitive processing since it greatly influences our perception. While shape can determine what kind of thing an object belongs to, its uniqueness often gets copied, especially where there are differences in arrangements. Here, different compositions act like catalysts, triggering novel stimuli, leading to personalized visual experiences among individuals [14].

3.2. The Limits of Nature-Inspired Design

The architectural style that employs nature-themed designs is currently a popular trend. However, this study also identifies the limitations of this approach. It asserts that the intricate and beautiful forms of nature cannot be fully replicated through a purely mathematical methodology. This finding has significant implications for environmentally influenced designs in buildings in the future. Architects must not only consider relevant mathematical principles but also the intuitive capacity and skill of humans to imitate the complexity and attractiveness found in natural things.

Biomimicry refers to the design of systems or processes that emulate the functioning of living organisms or their components. These solutions are inspired by the inherent properties of nature, particularly those observed in other species, which are then adapted or proposed as solutions to human aspirations and concerns. An illustrative example is the regulation of bioclimatic conditions in termite nests, the structural stability of spider webs, and the trapping of heat in fur coats among animals. Technological examination of these characteristics of nonhuman nature may have direct practical applications, as well as encouraging appreciation for the cleverness and creativity of other creatures and the natural world [15].

3.3. Tree Branching Form From Historical Times to Present

The architectural design process may benefit from emulating the strength and beauty of natural tree structures. In particular, the manner in which trees branch out can be utilized as a model for increasing stability and longevity in constructions. This organic shape not only leads to a harmonious arrangement in design but also communicates an inherent unity within the system.

With regard to the field of architectural design, an examination of the shapes of trees in relation to their structural roles can result in significant gains through the utilisation of materials' inherent structural capacities and arrangements. While it is widely acknowledged that branches support leaves, which gather sunlight for photosynthesis, it is often overlooked that they are also adept at carrying loads and resisting external forces. From an architectural standpoint, therefore, where durability is a primary concern while ensuring that structures remain stable, tree-like branching strategies could be employed within the design of any given edifice, or even just specific sections thereof. For instance, during load optimization for stability purposes, branches may be employed to distribute weight evenly throughout different sections, thereby ensuring safety while not compromising the structural integrity of the edifice. This is particularly relevant when dealing with heavy items such as those found on roofs. It is possible to make trunks thick enough to bear more vertical loads, thereby enhancing collective strength. This can be done during the planning stages, when necessary, based on specific requirements concerning various elements forming part of the structure. The overall design and intended use must also be considered.

Trees have different mechanisms to cope with external and internal loads. Particularly, when exposed to external factors like wind, they adjust their shapes to withstand strong wind forces and bending moments. Similarly, internal loads such as axial compression due to their own weight are carried by tree stems and trunks. Under wind exposure, stress changes from tensile on the convex side to compressive on the concave side of a component. This highlights how trees utilize their natural engineering abilities and physical properties to interact with external loads [7].

In this study, tree dendriforms which are extended from AD to present examples have been investigated by observing their complex structural generations. The chosen buildings in historical times have almost more complex natural forms then from now. But fractal geometry results from that buildings are lower than modern, simple and non-organic kubic form structures. In other words, “more technology” doesn’t mean “more simplicity”. Literally human brain has been a gift by its creative, productive, handcrafter ways throughout history. Chosen buildings (Table 1) have indicated their potential which had been proved by fractal geometry values.

After fractal geometry is developed, the conscious use of fractal algorithms in constructing building elements emerges. The fractal approach serves as a research method and is widely employed in designing and modeling architectural forms for modern buildings. Utilizing the regularities found in natural structures during the shaping process enables architects to create buildings with fractal characteristics.

In the early 20th century, fractal analysis methods were utilized in urban planning practices. Many architects have applied architectural shaping methods based on fractal geometry and nonlinear Dynamics [16].

Dendriform structures in architecture have ancient roots, possibly stemming from humanity’s fascination with trees and plants, as evidenced by prehistoric cave art. Early architectural examples, such as Egyptian palaces and pyramids, showcased vegetal motifs, including dendriform columns. Luxor Temple’s papyrus-cluster columns (1400 BC) exemplify this, with capitals resembling papyrus plant umbels.

4. Materials and Methods

4.1. Fractal Geometry

The concept of fractals originates from chaos theory and denotes specific behavioral patterns within complex systems. These patterns, rooted in irregularity and uncertainty, enable a deeper comprehension of the intricate structures and arrangements found therein. Mandelbrot’s seminal work, “The Fractal Geometry of Nature” underscores the remarkable semblance between fractals and traditional art forms, as well as architectural compositions. Fractal geometry thus represents a rigorous mathematical endeavor aimed at quantifying and comprehending the inherent complexity and irregularity present in natural phenomena.

In the realm of architecture, fractal geometry offers a systematic approach to examining the similarities and complexities exhibited by architectural forms across varying scales. Notably, architectural designs influenced by fractal principles often display recurring patterns and motifs inspired by natural phenomena, exemplified by the works of Frank Lloyd Wright. Through fractal geometry, architects can conduct detailed analyses of architectural compositions at both micro and macro levels, revealing underlying structural patterns and scale-invariant characteristics. Chaos, contrary to perceptions of randomness or anarchy, is actually concerned with examining the order within disorder. While fractals deal with the geometry of this disorder, chaos theory focuses on the dynamics within it [17], [18].

Mandelbrot’s quote, highlighting the inadequacy of Euclidean geometry in describing natural phenomena such as clouds, mountains, coastlines, and bark due to their rough, irregular structures, underscores the significance of fractals. Fractals demonstrate this irregularity across various scales, commonly observed in natural environments and architecture. As traditional geometric methods prove insufficient in modeling natural shapes, fractal geometry emerges as a more effective tool for modeling natural objects like trees, clouds, mountains, and seaweed (Figure 2).

Furthermore, fractal geometry exerts a profound influence on architectural design processes by guiding the incorporation of geometric principles into various aspects of architectural expression. From the articulation of tectonic movements to the intricacies of spatial planning and detailing, fractal geometry fosters a holistic understanding of architectural form and organization. The recognition of architectural structures as exhibiting fractal formations enables a deeper exploration of their inherent complexity and naturalistic qualities, ultimately enriching the aesthetic and functional aspects of architectural design.

Euclidean geometry has been widely employed for expressing architectural style over an extended period, while another avenue for articulating complexity within a style is directed towards non-Euclidean geometry. Several studies have demonstrated the use of fractal geometry in ancient architecture as a symbol of natural biomimicry [26].

Table 1. Building's chronological identity informations**.**

REFERENCE	NAME	GENERAL VIEW	LOCATION	TIME PERIOD
[7]	THE SAKYAMUNI PAGODA OF FOGONG TEMPLE		China	771 BC - 476 BC
[19]	MAISON CARRÉE		Nîmes, France	16 BC
[20]	SAINT CHAPELLE		Paris, France	1242 AD – 1248 AD
[21]	GLOUCESTER CATHEDRAL		Gloucester, England	1351 AD
[22]	KING'S COLLEGE CHAPEL		Cambridge, England	12th century AD
[23]	LA SAGRADA FAMILIA		Barcelona, Spain	1982 -
[24]	STUTTGART AIRPORT TERMINAL		Stuttgart, Germany	1991
	PARAMETRIC GRIDAL COLUMN PROTOTYPE		Computer Environment	**2024**

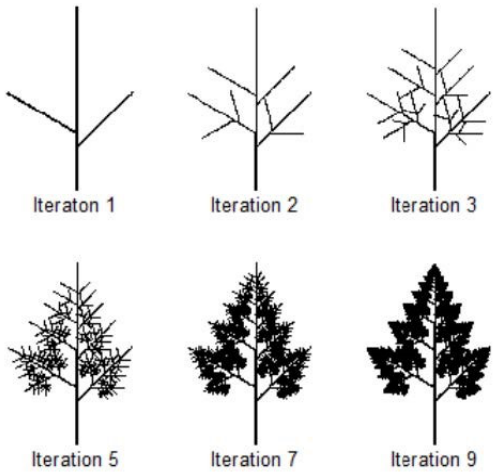

Figure 2. Six iterations of a simulated fern leaf [25].

4.2. Fractal Dimension

Fractal dimension is a mathematical term used to measure the complexity and self-similarity of fractals. Unlike Euclidean dimension, fractal dimension is expressed as a fractional number. A fundamental method for calculating fractal dimension involves examining the number of similar parts of a fractal and how these parts grow proportionally. For example, a fractal like the Koch curve (Figure 3b) divides into three similar parts with each iteration, and the length of each part is divided by three. In this case, the fractal dimension is determined by how the parts are proportioned to each other. While a point is considered dimensionless in Euclidean space, a line has one dimension, a plane has two dimensions, and a cube has three dimensions. However, fractals can have fractional dimensions (e.g., 1.4 or 2.1).

Fractal dimensions can be better understood through mathematical equations. For instance, when you double the length of a line, you get two copies, but when you double the length and width of a square, you get four copies of the original shape, and similarly, for a cube, you get eight copies. This characteristic is used to determine the dimension of a fractal (Figure 3a).

If we we double the sides and get a similar figure, we can write the number of copies as a power of 2 and the exponent will be the dimension. In an another words, if dimension is d then the number of copies or the magnification factor $n = 2^d$. The number of self-similar pieces is 2 (Equation 1) [27].

Therefore it is clear that,

$$Magnification\ factor = (Number\ of\ Self\ similar\ Pieces)^{Dimension} \quad (1)$$

The first iteration for the Koch curve consists of taking four copies of the original line segment, each scaled by **r** = 1/3.Therefore Equation 2 states that,

$$Fractal\ Dimension = \frac{log(\ number\ of\ self-similar\ pieces)}{log\ (\ magnification\ factor)} \quad (2)$$

$$Fractal\ Dimension = \frac{\log(4)}{\log(3)} = 1.262\ \textit{(which is a non-integer)} \quad (3)$$

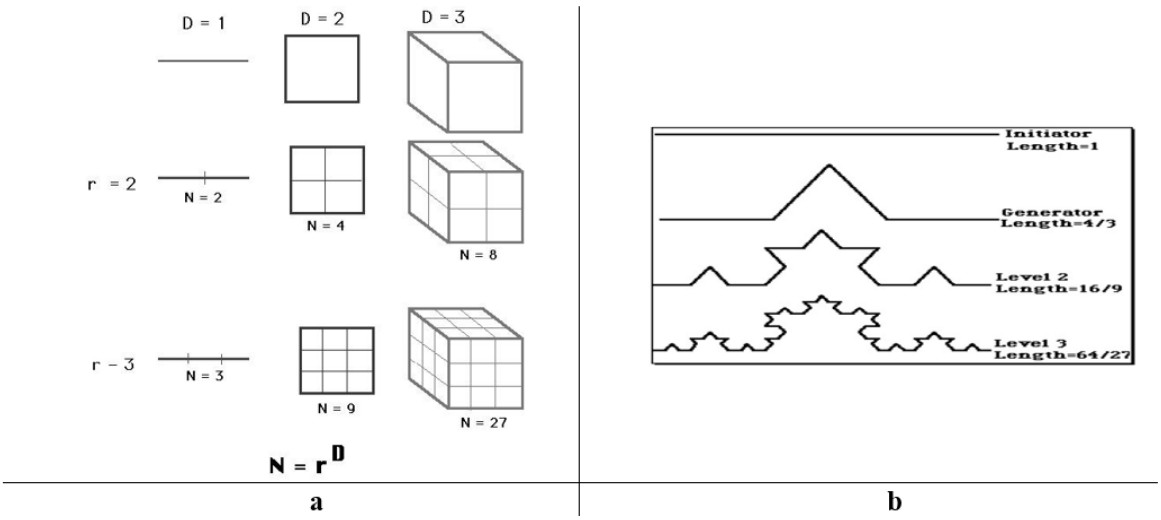

Figure 3. Fractal magnification factor exponential representation. a) Dimensions, b) Koch Curve [27].

To comprehend the notion of a non-integer or fractal dimension, consider the Koch curve as an illustrative example. Initially conceived as a continuous one-dimensional line, the curve undergoes a recursive process wherein each segment is divided into three equal parts, with the middle segment subsequently replaced by the two sides of an equilateral triangle identical in length to the segment removed. This iterative procedure results in the one-dimensional line increasingly occupying a two-dimensional space. Consequently, the fractal dimension (Equation 3) of such a line lies within the interval between 1 and 2, reflecting its complex, self-similar, and non-Euclidean geometric properties [27].

Therefore, fractal dimension is an important tool for mathematically measuring the complexity and self-similarity of fractals. Calculating fractal dimension is a fundamental step in understanding fractal geometry and complex systems. In the end, the fractal dimension of a structure provides a measure of the level of detail within it. A higher fractal dimension indicates a greater degree of intricacy and detail present in the form.

4.3. Box Counting Method

While there are several methods available for measuring fractal dimensions, the box counting method stands out as the most graphical approach for approximate calculations. Although it may not capture intricate details of the base curve as accurately as other methods, its low computational demands make it a recommended choice for obtaining an initial approximation of the fractal dimension.

The method for calculating the fractal dimension of buildings is popular due to its simplicity and effectiveness. It involves the following steps:

a) Place a grid of a specific size (S1) over the elevation of the building.
b) Count the number of occupied grids (C1) containing lines.
c) Double the grid size (S2) and count the occupied grids (C2). Repeat this process and record the results. It's important to note that slight variations in the grid can lead to different values for C (Table 2).

Table 2. Grid Size and Box Count for each iteration [27].

Grid Size	Box Count
S1 -	C1
S2 -	C2
S3 -	C3

d) Utilize a log-log plot of resolution scale versus the number of occupied boxes to ascertain the fractal dimension (D) across scales 2 to 1. The fractal dimension (D) across scales 2 to 1 can be calculated using the formula [27]:

$$\boldsymbol{D}(2to1) = \frac{[\log(C2) - \log(C1)]}{[\log(S2) - \log(S1)]} \quad (4)$$

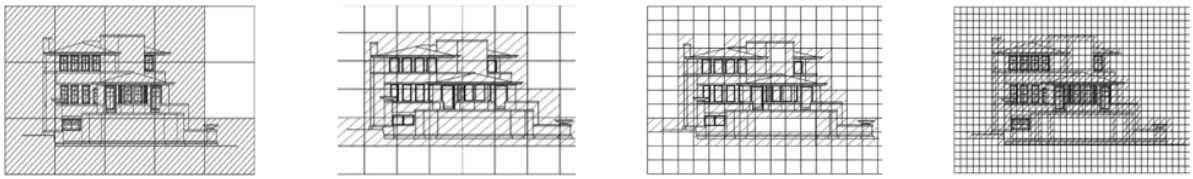

Figure 4. Grid-based calculation of the fractal dimensions of facades a) Grid 1: 5 x 3 grid; the number of boxes is 13 or 1/s1 = 5 and N (s1) = 13, b) Grid 2: 10 x 6 grid; the number of boxes is 29 or 1/s2 = 10 and N (s2) = 29, c) Grid 3: 20 x 12 grid; the number of boxes is 93 or 1/s3 = 20 and N (s3) = 93, d) Grid 4: 40 x 24 grid; the number of boxes is 307 or 1/s4 = 40 and N (s4) = 307 [18].

The obtained *Db* value for Grid 1-2 is 1.156, indicating a relatively low fractal complexity and a uniform distribution (Equation 4). In contrast, for Grid 2–3, the *Db* value increases to 1.681, reflecting a greater degree of fractal density and structural variation. Finally, the *Db* value for Grid 3–4 rises to 1.724, signifying the highest level of fractal complexity among the intervals analyzed. The aggregation of the outcomes from the three box counts yielded an estimation of the fractal dimension, which was calculated as follows: D = 1.520 [18].

The box-counting method is the most common mathematical approach for determining the approximate fractal dimension of an object. In its architectural variant, this method begins with a drawing of the exterior façade of a house. Subsequently, a large grid is placed over the drawing, and the presence of lines in each square is checked. Squares containing detail are recorded. Then, a smaller-scale grid depicting the same façade is placed, and again, the presence of detail within each square is determined. By repeating this process on multiple grids of different scales, an estimate of the fractal dimension of the façade is generated (Figure 4). While this process can be performed manually, the Benoit and Archimage programs automate this operation. Several variations of the method address known deficiencies. Four common variations are associated with balancing the proportion of "white space" and the "starting image" line width, scaling coefficient, and moderating statistically divergent results [28]. In recent years, the software called ImageJ with FracLac (Figure 5) plugin has been used for analyzing the Euclidean geometry value, which varies between 1 and 2, in the box-counting method.

4.4. L-System

The developmental processes are traced using the formalism of L-systems. These systems, introduced by Lindenmayer in 1968, served as a theoretical framework for studying the development of simple multicellular organisms in plants and were subsequently applied to the investigation of more complex plants and plant organs. Following the incorporation of geometric features, plant models expressed through L-systems became sufficiently detailed to allow for realistic visualization of plant structures and developmental processes via computer graphics [29].

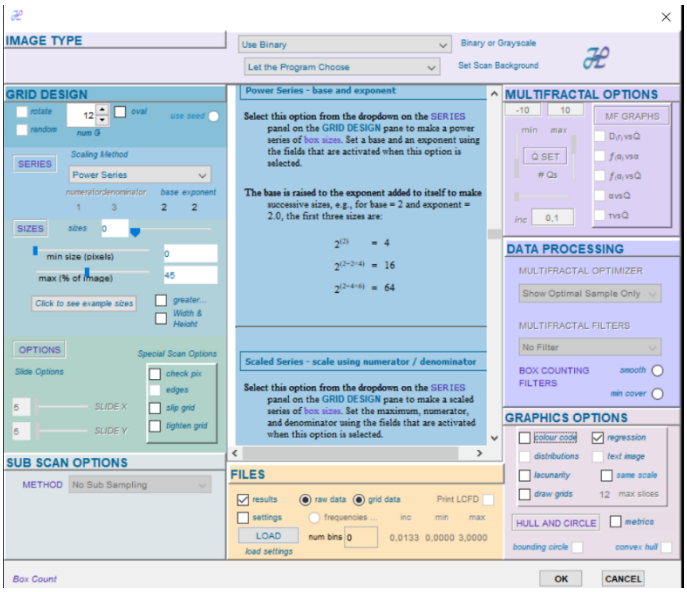

Figure 5. FracLac interface with chosen options and values for each building images.

The computer has played a pivotal role in replicating branching structures akin to those found in natural trees. One such algorithm, known as L-System, has been instrumental in this endeavor by simulating the growth dynamics of plants and generating natural fractals. This system presents architects with a fertile ground for integrating natural forms into architectural designs, thus offering a realm of creative possibilities. A notable illustration of this application is evidenced in the construction of the Tote Restaurant in Mumbai in 2009, where the L-System algorithm was effectively harnessed for architectural form development [7].

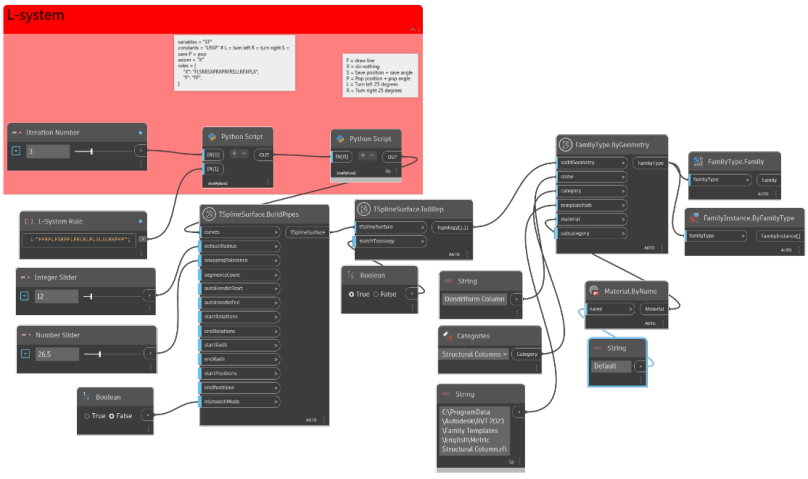

Figure 6. Dynamo interface with node connections.

4.4.1. Parametric Column Structure

As previously mentioned, tree dendriforms can be generated using various techniques in the digital environment, which offers abundant options such as software specifically designed to generate L-System algorithms. In this study, the tree column head, or in other words, the branching structure resembling a tree dendriform, was initially created using a Python code that operates within the Dynamo node (Figure 6). Dynamo

is an visual programming tool located within the Manage tab in Autodesk Revit. The objective was to obtain a parametric column geometry that changes according to manually adjustable rules. Additionally, the geometry should have changed based on the iteration number. As a result, with this prototype, an artificial forest was created (Figure 7). The purpose of this approach is to achieve different variations and produce a grid-like structure with each iteration being unique (Table 3).

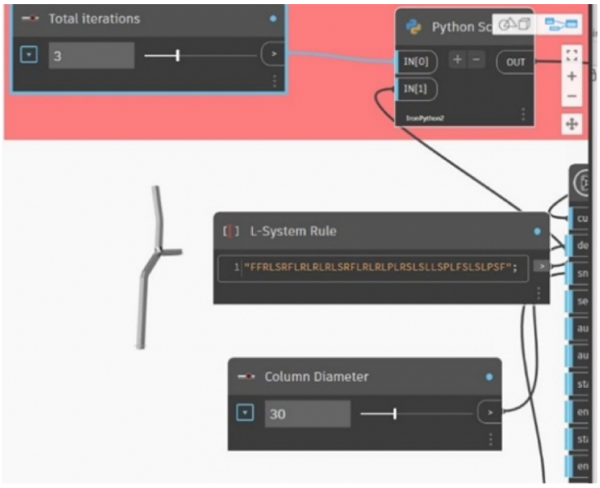

Figure 7. L-System rule for iteration 3 levels.

Table 3. Column geometries for each ıteration prototype and their locations on grid system.

Iteration 1	Iteration 2	Iteration 3	Iteration 4
		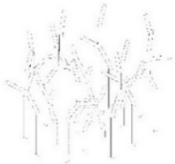	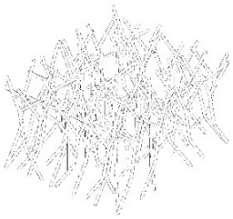
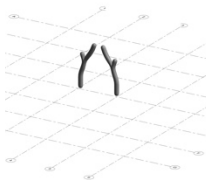	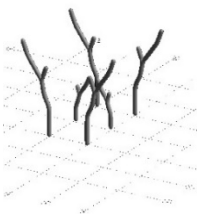	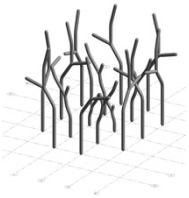	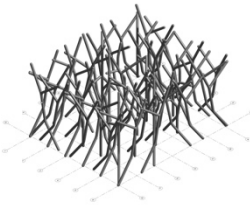

5. Results and Discussion

In the initial stage, plans and column head drawings of historical buildings were analyzed using FracLac. Following the assessment of as-built structures, a new structure generated by an L-System-based rule code was employed to benchmark all structures based on their fractal values.

After analyzing buildings and prototype structure, the results were unexpected. This unexpected outcome can be attributed to the lack of computer-aided design (CAD) systems or any digital tools during that time. For more realistic outcomes, the artificial structure was designed with simple plan and column geometries and orientations.

This decision stemmed from the experience with the previous building, Stuttgart Airport Terminal, which featured a complex plan ratio generated by computational environments (Table 5). Consequently, the plan ratio of the subsequent structure was simplified to allow for a comparative analysis between the two technological products. Other as-built structures exhibited more diverse results due to their organic forms, but this did not account for the high fractal values. Today, we have nearly infinite tools for creating or generating designs from various natural substances and living creatures. However, in the past, people, designers, architects, and craftsmen did not have access to digital devices for drawing or production. The human brain was the sole tool for conceptualizing with all possibilities, while hands were the only means for achieving tangible results.

The perplexing outcomes gained from the initial examination prompt intriguing questions about the planning tactics employed in historical buildings. While models based on L-Systems offer a valuable tool for analyzing complex fractals, they may not fully represent structures designed without computers due to their reliance on recurring motifs. This limitation is further highlighted by the significant difference between the Stuttgart Airport Terminal (complex plan) and its simplified prototype. By further simplifying the model, it would be possible to make a fair comparison. However, this might conceal the architectural achievements of past eras. Certain historical buildings contain natural shapes that suggest different methods employed by architects in achieving high fractal values during ancient times. These techniques, which could be imitative of nature or traditional building, should be investigated further. In ancient times, the geometries of column heads and plans exhibited close resemblances to each other. These structures often mimicked dendriform patterns, resembling various forms found in nature, particularly tree-like shapes.

Table 4. The analysis drawings and Db values of structures dating from 771 BC to 1351 AD.

TIME PERIOD		771 BC - 476 BC	16 BC	1242 AD – 1248 AD	1351 AD
Building Name		THE SAKYAMUNI PAGODA OF FOGONG TEMPLE	MAISON CARRÉE	SAINT CHAPELLE	GLOUCESTER CATHEDRAL
Plan		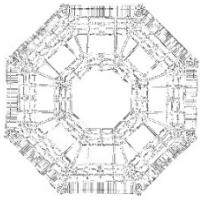	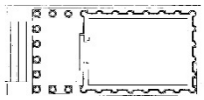	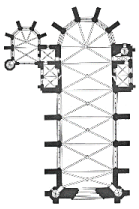	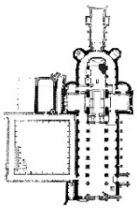
Reference Number		[30]	[31]	[32]	[33]
Column Head		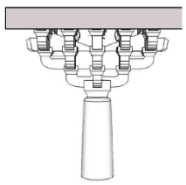			
Reference Number		[7]	[34]	[35]	[33]
Db	**Plan**	**1.6366**	**1.4660**	**1.5602**	**1.6107**
	Column Head	**1.3913**	**1.7500**	**1.7405**	**1.7362**

The geometrical ratios observed in plan views ranged from 1.4660 to 1.6366 Db values (Table 4), indicating a proximity to Euclidean geometry due to the values of the structures. However, the results for column heads were more intricate and higher compared to plan views, owing to their detailed levels and connection points. Interestingly, the column heads generated in computer environments appeared simpler and lower in complexity compared to those from ancient times.

Table 5. The analysis drawings and Db values of structures dating from 12th century AD to 2024.

TIME PERIOD		12th century AD	1982 -	1991	2024
Building Name		KING'S COLLEGE CHAPEL	LA SAGRADA FAMILIA	STUTTGART AIRPORT TERMINAL	PARAMETRIC PROTOTYPE
Plan		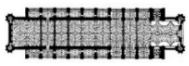	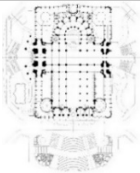	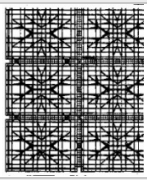	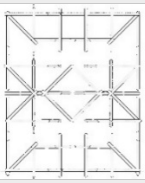
Reference Number		[36]	[37]	[38]	
Column Head				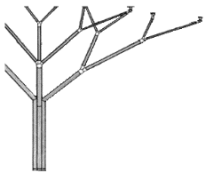	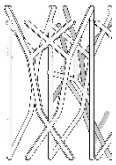
Reference Number		[36]	[39]	[40]	
Db	**Plan**	**1.8511**	**1.3428**	**1.8145**	**1.4529**
	Column Head	**1.7828**	**1.6785**	**1.3710**	**1.4865**

6. Conclusions

The study revealed that design tools are intricately related to the fractal complexity of buildings. While models based on L-systems provide a robust analysis framework, they may lack the capacity to fully capture the nuances of historical computer-less structures. Consequently, it is essential to identify the diverse methodologies employed in the past for designing and their interrelationship with contemporary architecture.

Future research must delve deeply into the L-System rules by integrating biomimicry principles with conventional design philosophies. This approach will enable a more detailed historical evaluation while serving as a foundation for the creation of new architectural styles that integrate both old and new systems. By understanding how people designed without complex tools, we can expand our current limits of architectural design in the digital world. This highlights the significant difference between natural intelligence and artificial intelligence. Feelings, inspirations, and emotions stem from nature for the natural intelligence, whereas the artificial intelligence relies solely on human creation. The geometric proportions of natural forms, while easily replicated by computer software today, have been expertly imitated by human intelligence and craftsmanship since ancient times. This study is distinctive in its focus on architectural design tools and methods from a historical perspective. It compares the nuances of designs created without the aid of computers in the past with those produced using digital tools in the present. Moreover, by integrating the principles of biomimicry with traditional design philosophies, the study proposes an original approach to both enhance the historical evaluation and create new architectural styles that integrate old and new systems.

The distinction between natural intelligence and computer-based design in the architectural domain, the geometric proportions of natural forms in relation to both human expertise and contemporary technology, imbues the study with both philosophical and practical depth. This represents an innovative perspective that not only reconciles past and future, but also demonstrates how the natural and digital realms can coexist in harmony. This approach consistently respects and honors nature, resulting in outcomes that rival modern technology in their precision and harmony with the natural world.

References

[1] Mandelbrot BB. The fractal geometry of nature. Vol. 1. New York: WH Freeman; 1982. Accessed: Apr. 04, 2024. [Online]. Available: http://users.math.yale.edu/~bbm3/web_pdfs/encyclopediaBritannica.pdf

[2] Rian IM, Sassone M, Asayama S. From fractal geometry to architecture: designing a grid-shell-like structure using the Takagi–Landsberg surface. Comput Aided Des. 2018 May;98:40–53.

[3] Yazyeva SB, Mayatskaya IA, Kashina IV, Nesterova AN. The manifestation of fractality in the architecture of buildings and structures. IOP Conf Ser Mater Sci Eng. 2019 Dec;698(3):033046.
[4] Moltedo L, Mortelliti G, Salvetti O, Vitulano D. Computer aided analysis of the buildings. J Cult Herit. 2000 Jan;1(1):59–67.
[5] Aslan N, Saltan M, Demir B. A different construction of the classical fractals via the escape time algorithm. J Abstr Comput Math. 2018;3(4):1–15.
[6] Nouri L, Azari KT, Alaghmandan M. Development of algorithmic applications in architecture: a review and analysis of L-systems. Bagh-e Nazar. 2023 Feb;19(116):5–24.
[7] Md Rian I, Sassone M. Tree-inspired dendriforms and fractal-like branching structures in architecture: a brief historical overview. Front Archit Res. 2014 Sep;3(3):298–323.
[8] Prusinkiewicz P. Applications of L-systems to computer imagery. In: Ehrig H, Nagl M, Rozenberg G, Rosenfeld A, editors. Graph-grammars and their application to computer science. Lecture Notes in Computer Science. Vol. 291. Berlin, Heidelberg: Springer; 1987. p. 534–48.
[9] Toussi H-E. The application of evolutionary, generative, and hybrid approaches in architecture design optimization. 2020;2(2).
[10] Roudavski S. Parametric skinning of complex-graphs: an airborne textile structure test-case. 2018.
[11] Lorenz WE. Fractal geometry of architecture. In: Gruber P, Bruckner D, Hellmich C, Schmiedmayer H-B, Stachelberger H, Gebeshuber IC, editors. Biomimetics—materials, structures and processes. Biological and Medical Physics, Biomedical Engineering. Berlin, Heidelberg: Springer; 2011. p. 179–200.
[12] Zhou T, Li H, Li X, Lange CF, Ma Y. Feature-based modeling for variable fractal geometry design integrated into CAD system. Adv Eng Inform. 2023 Aug;57:102006.
[13] Schlaich J. The Mercedes-Benz Museum. Accessed: Apr. 04, 2024. [Online]. Available: https://www.google.com/search?q=Schlaich%2C+J.+(2009).+The+Mercedes-Benz+Museum.&sourceid=chrome&ie=UTF-8
[14] Hu T, Xie Q, Yuan Q, Lv J, Xiong Q. Design of ethnic patterns based on shape grammar and artificial neural network. Alex Eng J. 2021 Feb;60(1):1601–25.
[15] Kellert S, Calabrese E. The practice of biophilic design. 2015.
[16] Mayatskaya I, Yazyeva S, Gatiev M, Kuznetsov V, Klyuev S, Sabitov L. Application of fractal methods in the design of modern structures. In: Klyuev SV, Vatin NI, Sabitov LS, editors. Industrial and civil construction 2022. Lecture Notes in Civil Engineering. Vol. 436. Cham: Springer Nature Switzerland; 2024. p. 414–22
[17] Degirmenci FB. Fractal geometry and architecture. 2009.
[18] Turan S. Visual analysis of complexity in architecture: fractal analysis. Konya Technical University; 2022.
[19] Fichier:MK54063 Maison Carrée (Nîmes).jpg — Wikipédia. Accessed: May 01, 2024. [Online]. Available: https://commons.wikimedia.org/wiki/File:MK54063_Maison_Carr%C3%A9e_(N%C3%AEmes).jpg
[20] denfr. Plafond chapelle haute. 2015. Accessed: May 01, 2024. [Online]. Available: https://commons.wikimedia.org/wiki/File:PA00086001_-_Sainte-Chapelle_-_7MC_3458%2B3461_-_HDR.jpg
[21] Lacework... intricacies of Gloucester Cathedral cloisters, England. r/architecture. Accessed: May 01, 2024. [Online]. Available: www.reddit.com/r/architecture/comments/ju0koc/lacework_intricacies_of_gloucester_cathedral/
[22] King's College Chapel, Cambridge | Historic Cambridge Guide. Britain Express. Accessed: May 01, 2024. [Online]. Available: https://www.britainexpress.com/counties/cambridgeshire/az/cambridge/kings-college-chapel.htm
[23] Sagrada Familia Interiors | Understanding Gaudi's Architecture. sagradafamilia.barcelona-tickets.com. Accessed: May 01, 2024. [Online]. Available: https://sagradafamilia.barcelona-tickets.com/sagrada-familia-tower-interior/
[24] Stuttgart Airport Structural Case Study. RikySongSu. Accessed: May 01, 2024. [Online]. Available: https://www.rikysongsu.com/blog/2017/4/26/stuttgart-airport
[25] Jiang B, Yin J. Ht-Index for quantifying the fractal or scaling structure of geographic features. *Ann Assoc Am Geogr.* 2014 May;104(3):530–40.
[26] Abdelsalam M. Fractal-based patterns in the Islamic Architecture: Using the fractal dimension of Mameluke Madrasa as an analysis approach and a design generator. 2020.
[27] Kitchley J. Fractals in architecture. *Archit Des.* 2003 Jan;20:42–8.
[28] Ostwald MJ, Vaughan J, Chalup S. A computational analysis of fractal dimensions in the architecture of Eileen Gray. *ACADIA 2008: Silicon + Skin*, Minneapolis (Minnesota), USA, 2008. pp. 256–63.
[29] The Algorithmic Beauty of Plants. Wikipedia. Apr. 10, 2021. Accessed: Apr. 15, 2024. [Online]. Available: https://en.wikipedia.org/w/index.php?title=The_Algorithmic_Beauty_of_Plants&oldid=1017094527
[30] Mi X, Meng X, Yang Q, Li T, Wang J. Analysis of the residual deformation of Yingxian Wood Pagoda. *Adv Civ Eng.* 2020 Mar;2020:1–12.
[31] Spiers RP. Plan of the Maison Carrée at Nîmes. 1911. Accessed: May 01, 2024. [Online]. Available: https://commons.wikimedia.org/wiki/File:Plan_of_the_Maison_Carr%C3%A9e_at_N%C3%AEmes.jpg
[32] File:Plan.sainte.chapelle.Vincenne.png - Wikipedia. Accessed: May 01, 2024. [Online]. Available: https://commons.wikimedia.org/wiki/File:Plan.sainte.chapelle.Vincenne.png
[33] Medieval Gloucester Cathedral - Plans and Drawings. Accessed: May 01, 2024. [Online]. Available: https://www.medart.pitt.edu/image/england/gloucester/cathedral/Plans/mainGlouc-Plans.html

[34] Plan de la Maison-Carrée à Nîmes. La Maison Carrée. Accessed: May 01, 2024. [Online]. Available: https://www.maisoncarree.eu/ressources/catalogue/plan-de-la-maison-carree-a-nimes/
[35] File:Chapiteau.arcature.Sainte.Chapelle.Paris.png - Wikimedia Commons. Accessed: May 01, 2024. [Online]. Available: https://commons.wikimedia.org/wiki/File:Chapiteau.arcature.Sainte.Chapelle.Paris.png
[36] Medieval Cambridge- King's College Chapel - Plans. Accessed: May 01, 2024. [Online]. Available: https://www.medart.pitt.edu/image/england/Cambridge/KingsCollege/Plans/Cambr-kings-Plans.html
[37] Galeria de Clássicos da Arquitetura: La Sagrada Familia / Antoni Gaudi - 38. ArchDaily Brasil. Accessed: May 01, 2024. [Online]. Available: https://www.archdaily.com.br/br/787647/classicos-da-arquitetura-la-sagrada-familia-antoni-gaudi/5255a0e8e8e44e67bf0006ee-ad-classics-la-sagrada-familia-antoni-gaudi-ground-level-plan
[38] plan/detail.jpg (1105×794). Accessed: May 01, 2024. [Online]. Available: https://i.pinimg.com/originals/99/5b/0e/995b0e8d6cbf0bea3bb2698c3436f26c.jpg
[39] Double twist columns. Blog Sagrada Família. Accessed: May 01, 2024. [Online]. Available: https://blog.sagradafamilia.org/en/specialists/double-twist-columns/
[40] Freedom of expression | Mech, Steel structures. Accessed: May 01, 2024. [Online]. Available: https://www.strutture.info/en/freedom-of-expression.html

Turkish Journal of Science & Technology
20(1), 209-224, 2025

Research Paper
https://doi.org/10.55525/tjst.1556618

The Effects of Installation Faults of Air Conditioning Systems on Carbon Emissions

Ruveyda Ergen[1] and Mert Gürtürk[2*]
[1,2]Department of Energy Systems Engineering, Technology Faculty, Fırat University, 23100 Elazig, Turkey
[1]ruveydaergen@gmail.com, [2]m.gurturk@gmail.com

(Geliş/Received: 26/09/2024; Kabul/Accepted: 29/01/2025)

Abstract: In this study, the effects of installation faults of condenser of Air Conditioning (AC) systems on emissions were investigated and Life Cycle Climate Performance (LCCP) analysis was carried out according to the scenario of installation faults of the condenser unit of the AC system for 12 countries. The heat taken by the evaporator units of the ACs is transferred to the condenser unit via the system. This thermal energy is transferred to the surrounding air via condenser. The surrounding air cannot pass through the condenser unit in desired amounts and causes more electricity consumption of the system due to installation faults. The rates of increase of the LCCP values change from 0.02% to 29.6% because of installation faults. The LCCP value was calculated as 19692 – 19858 kg·CO_{2e} with the closing of the air inlet because of installation faults for Turkey. Considering the installation faults of the condenser, the LCCP value was calculated as 21284 - 21505 kg·CO_{2e} for Japan.

Keywords: LCCP, Air-conditioning, Emissions, Global Warming.

Klima Sistemlerinin Montaj Hatalarının Karbon Emisyonlarına Etkileri

Öz: Bu çalışmada, Klima (AC) sistemlerinin yoğuşturucu montaj hatalarının emisyonlara olan etkileri araştırılmış ve 12 ülke için AC sisteminin yoğuşturucu ünitesinin montaj hataları senaryosuna göre Yaşam Döngüsü İklim Performansı (LCCP) analizleri yapılmıştır. Klimaların buharlaştırıcı üniteleri tarafından alınan ısı sistem üzerinden yoğuşturucu ünitesine aktarılır. Bu ısıl enerji yoğuşturucu üzerinden çevre havaya aktarılır. Montaj hataları nedeniyle çevre havası yoğuşturucu ünitesinden istenilen miktarda geçemez ve sistemin daha fazla elektrik tüketmesine neden olur. LCCP değerlerinin artış oranları montaj hataları nedeniyle %0,02 ile %29,6 arasında değişmektedir. Türkiye için montaj hataları nedeniyle hava girişinin kapatılmasıyla LCCP değeri 19692 – 19858 kg·CO_{2e} olarak hesaplanmıştır. Kondenserin montaj hataları da göz önüne alındığında Japonya için LCCP değeri 21284 - 21505 kg·CO_{2e} olarak hesaplanmıştır.

Anahtar Kelimeler: LCCP, Klima, Emisyonlar, Küresel Isınma.

1. Introduction

With global warming, the importance of AC systems has been increasing. Cooling systems are encountered in many application areas such as improvement of comfort conditions in buildings [1] and the transfer or storage of food. The environmental effects of these systems are also important parameters when compared to many studies aimed at increasing the efficiency of these systems [2–5]. Countries and societies taking a more sensitive stance on global warming have researched the effects of many engineering systems on emissions according to The Paris climate agreement [6] and the Glasgow climate summit [7]. In addition, the war between Russia and Ukraine has seriously affected energy prices. Serious price increases due to natural gas prices, especially in the European region, have caused countries to announce a series of measures for energy efficiency and savings. AC systems have a significant share in energy consumption in buildings. Considering the energy performance of Air Conditioning (AC) systems, a review study was carried out with a statistical approach. In that study, when the data obtained from many data centers and the studies in the literature are examined, it is seen that most of the systems do not work at sufficient efficiency values. The electricity consumption rate of those systems is 38% [8]. Considering the articles in the literature examining the effects of cooling systems on emissions, studies examining the effects of refrigerants in particular stand out. In one of those studies, the effects of using five HydroFluoroCarbons (HFC) with low Global Warming Potential (GWP) in AC systems on system efficiency was investigated. Using alternative refrigerants to R410a having high GWP value was evaluated by making thermodynamic analyses [9]. Studies on the effects of HCFs on emissions are dominant in the literature. When the literature is examined, the use of alternative refrigerants to R410a and the effects of the AC system on efficiency and environmental factors were examined [10]. In a similar study, when HFCs having low GWP values were used in the AC system, their effects on emissions were investigated with different analysis methods. It was observed that the review study focused on the results obtained from Total Equivalent Warming Impact (TEWI) and Life

* Corresponding author: m.gurturk@gmail.com. ORCID Number of authors: [1] 0000-0001-7909-7770, [2] 0000-0003-0380-5704

Cycle Climate Performance (LCCP) analyses of different refrigerants. The refrigerant compared as a reference is R410a. As a result, alternative refrigerants have been evaluated to reduce or prevent the use of HFCs having high GWP [11]. Taking into account many factors that affect the operating efficiency of the AC, LCCP and Life Cycle Assessment (LCA) analysis of the system were made by the researchers. The results obtained from the analysis show that the parameters that negatively affect the Seasonal Energy Efficiency (SEER) value have serious effects on the emission values [12]. The AC systems are used for many purposes and application areas. For this reason, some variations can be observed in the designs of the AC. One of them is mobile AC systems. Researchers have studied the effects of different HFCs (R134a, R152a, R1234yf and R744) in mobile AC systems on emissions [13]. Thermodynamic analysis of environmental friendly refrigerants (HFO-1234yf) used in mobil AC systems was carried out [14]. The LCCP analyses of AC systems according to the climate conditions of South Korea were carried out and it is found that the increase in the system efficiency according to the working conditions decreased the emission values [15]. In another study, exergy and environmental assessment analyses of ACs sold in Turkey were carried out. In that study, Exergy Efficiency Factor (EER) and MTEWI value were analyzed. Similar to other studies, the effects of R410a and R22 refrigerants on EER and MTEWI values were investigated [16]. In another study, the Ozone Depletion Potential (ODP) and GWP values of the refrigerants in the AC system, depending on the location, were estimated at a certain time interval. The LCA method was used to estimate ODP and GWP values [17]. The LCCP is the most preferred method today to examine the effects of AC systems on emissions. Successful LCCP analyses of AC systems can be found in the literatüre [18]. Using the LCCP method, the researchers analyzed five different cycle options and seven different low-GWP refrigerants [19]. In another study, life cycle Carbon Footprints (CFP) analyses were performed with the assumption that the AC system was operated for 10 years and 2 hours per day. As a result of the research, the preference for refrigerants having low-greenhouse gas emission values, especially in the destruction process of AC, made a big difference [20]. A review study examining the effects of cooling systems on climate change and global warming focused on refrigerants. The refrigerants have a serious effect on global warming. The effects of refrigerants were examined. That study includes the analyses made within the scope of TEWI [21]. Life Cycle Climate Performance is a method by which HVAC&R (heating, ventilation, AC and refrigeration industry) systems can be evaluated for global warming impact. A lot of valuable studies were examined the environmental effects of refrigerants used in the AC system cycle [20–22]. The literature review described so far consists of studies examining the contribution of air conditioning systems to emissions. Although these studies are very comprehensive and detailed studies, it seems that detailed data are not obtained within the scope of LCCP analysis for installation faults. It is seen that very few studies have been done in the literature examining the effects of installation faults of air conditioners. For example, studies were carried out for air conditioners and heat pumps in the United States for installation faults. Unnecessary energy consumption values caused by the installation faults have been evaluated [23,24].

When the above studies are examined, many academic/scientific studies have been carried out that will improve the performance of AC systems and have positive effects on emissions (CO_2). However, even if today's best technology, equipment or strategy are applied in AC systems, problems caused by the installation faults cause the systems to operate at very low performance. This situation has the potential to contribute significantly to emissions (CO_2) and unnecessary energy consumption due to installation faults. The main purpose of this study is to examine the effects that occur as a result of installation faults of the condenser units of AC systems on LCCP. In the installation of AC systems, researchers have found that there are serious problems. In particular, the air inlets in the condenser section of the AC system are partially or completely closed due to installation faults. This situation makes it difficult to transfer the energy in the refrigerant of the AC system to the environment.

2. Research Methodology

In this part of the study, the installation faults of the air conditioning system is examined experimentally. In the experimental setup, the air inlet sections of the condenser were closed at different rates. Detailed information about the experimental setup is presented in the following lines.

It has been determined by the authors that serious problems occur in the installation of AC systems. Meetings were held with the dealers and technical services of AC systems. The AC manufacturers organize training for their dealers and technical services on the installation of AC systems. In those training, information is shared on how to install to wall the condenser section. However, some of the condenser units of the ACs are not installed according to the information given in those training. The AC manufacturers also inform the AC users with materials such as user guides. When the information on how to install the condenser section of the AC companies is examined, it is stated that a 30 cm space should be left at the back and side (air inlets) in the installation of the condenser units of the ACs. It is stated that 60, 60 and 200 cm spaces should be respectively from the top, right

and finally the front of the condenser. The installation procedure is not taken into account by some dealers and technical services. The main purpose of the installation procedure is that the air inlet and outlet of the condenser are not blocked. This information in the user guide is not read enough by some users. While the AC system is being installed by the dealer or technical service personnel, it is encountered that the trained personnel are not sent to the installation of AC, or the technical personnel who do not participate in the training practices are sent to the installation. At the same time, users can sell the AC system which they purchased for various reasons. It has been observed that the installation of the AC system, which was purchased secondhand, was carried out by untrained technical personnel. Technical service, dealers or the AC manufacturers are not the only responsible for the wrong applications in the installation of the AC. It is also seen that the users force the technical personnel to make the installation faults for various reasons. The authors designed the experimental setup in Fig. (1) to experimentally examine the installation faults of the condenser section. Fig. (1) shows the experimental setup used in this study.

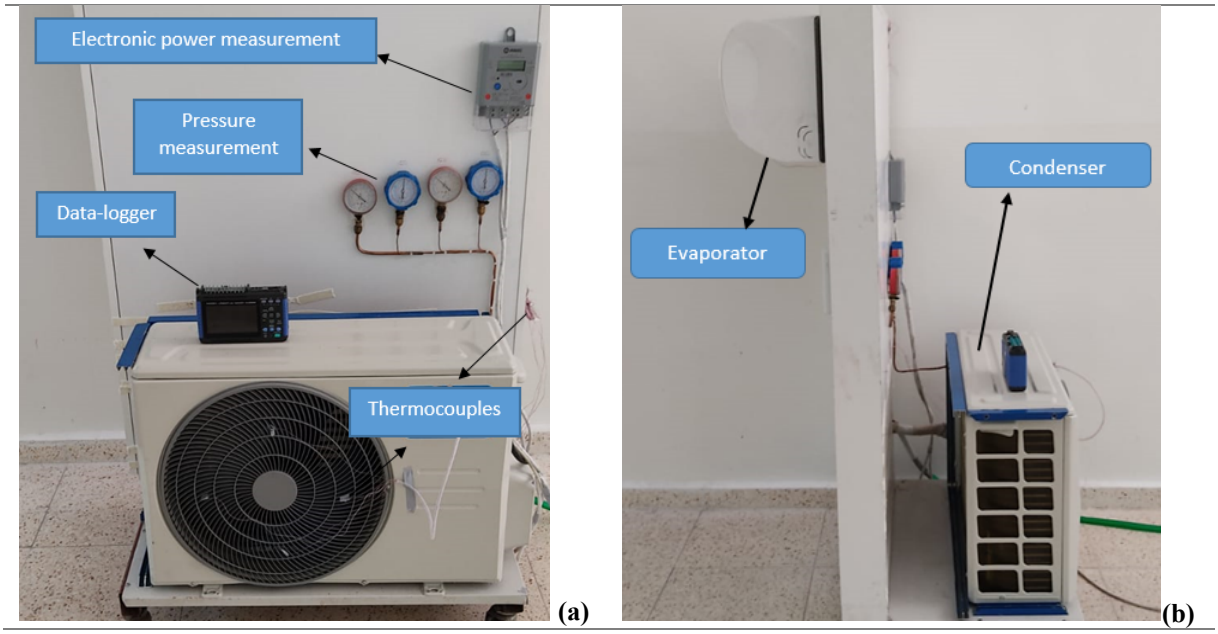

Figure 1. Experimental setup (experiment set view: (a) - front, (b) - side).

Fig. 1-(a) shows the measurement devices used in the experimental study. T-type thermocouples were used in the study. Measurements were made from different points of the air conditioning system with a 10-channel data logger. Pressure measurement and electronic power measurement are also among the measurement devices used. Fig. 1-(b) shows the evaporator and condenser sections of the air conditioning system. They are separated by a partition to prevent the airflow in both units from affecting each other. A split type AC system was used in the experiments. The working fluid used in the cycle of the system is R32. While the cooling capacity of the system is 12000 BTU/h, the seasonal efficiency value is 6.1 in the AC system cooling mode. The experimental process consists of two parts. In the first part, the AC was installed in accordance with the installation procedure of the authorized service and then the system was operated. The energy consumption values of the AC, which was installed in accordance with the installation procedure of the authorized service, were calculated. The values obtained from this analysis are for reference or comparison parameters. In the second part, installation faults was created. Barriers are placed in the air inlets of the condenser section. In the condenser section of the AC, the air is passed from two different sections. The air inlets are made from the back and side of the condenser. The air inputs from the back and side were gradually closed. The stages were formed by closing 25% - 50% - 75% and 94% of the air inlet area. During the experiments, the set value of the AC was kept constant (set value 16 °C). The ambient temperature was taken as 27 °C and the experiments were carried out in the laboratory in summer. The evaporator unit airflow of the AC was worked under different operating conditions. The evaporator unit fan speed was operated at 20%-40%-60%-100% and the measurements were obtained according to this experimental procedure.

Significant studies have been conducted investigating the environmental impact of AC systems. It is very important to examine the effects of cooling systems on climate change. One of the main reasons for this is that the greenhouse gas effect of the refrigerant used in cooling systems is quite high. There are many parameters that contribute to environmental pollution and climate change, such as the gas emission to the atmosphere as a result of leakage, maintenance and repair in 15 years of use, the polluting effects of the production of these gases, the cycle life of the gases, and the disposal of these gases. However, the analyses show that the negative effects of cooling systems on the environment occur especially in the case of use. A lot of valuable studies have been done examining and compiling the environmental effects of gases used in the AC system cycle [20–22]. Discussing the effects of gases on the environment is beyond the scope of this study. Many of the parameters used in LCCP analyzes are obtained from various sources. Among these parameters, it is claimed that the values of Adp.GWP for some gases are controversial [25]. The most challenging parameter in the LCCP analysis of air conditioners is the Annual Energy Consumption (AEC) value of the system and the CO_{2e} value. The AEC value varies according to the climatic conditions of the location where the AC is used, the purpose of use and the structure in which the system is used. Researchers have developed different approaches using different methods for this situation such as field test method, temperature bin method, simulation-based method and data-driven methods. In another review study examining the effects of cooling systems on global warming, TEWI and LCCP analyzes were compared. TEWI and LCCP analyses of domestic refrigeration, supermarket refrigeration, AC systems, mobile AC, heat pumps and transport refrigeration systems were reviewed and compared [26]. Each emission factor is calculated separately. In Fig. (2), the carbon emission categories that affect the system during the LCCP calculation process are shown.

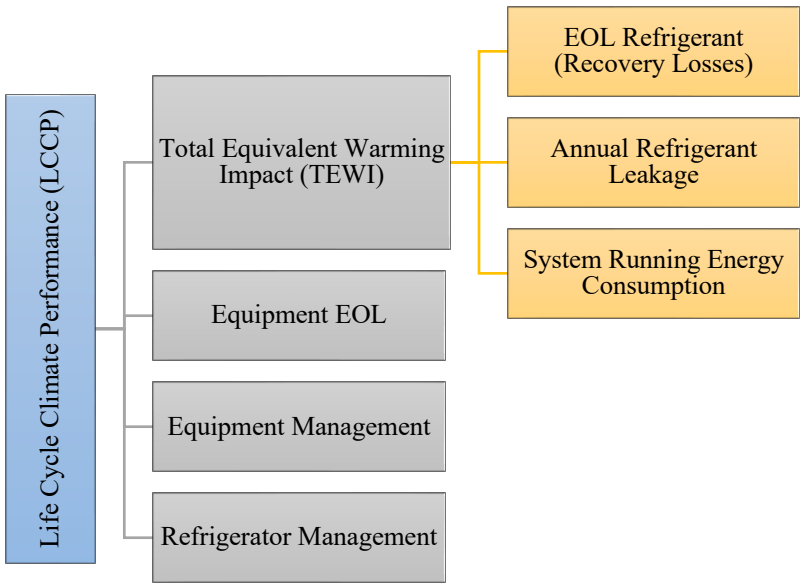

Figure 2. Comparison of the LCCP and TEWI [26].

Fig. (2) shows the comparison of LCCP and TEWI. Another review study examining the effects of cooling systems on climate change and global warming focused on heat transfer or working fluid. The gases used also have a serious effect on global warming. In the study, the effects of gases used in a wide framework were examined. The scope of the study includes the analyzes made within the scope of TEWI [21]. Life Cycle Climate Performance is a method by which HVAC&R (heating, ventilation, AC and refrigeration industry) systems can be evaluated for global warming impact throughout their entire lifecycle. With LCCP analysis is calculated as the sum of the direct and indirect emissions produced over the life of the system. Direct emissions include all effects resulting from the release of refrigerants into the atmosphere over the life of the system. This includes annual leakage and losses during disposal of the unit. Indirect emissions include emissions from the manufacturing process, energy

consumption and disposal of the system [25]. The LCCP consists of direct emissions and indirect emissions. The Eq. (1) is calculated in kg units as [25].

$$\text{LCCP} = \text{Direct Emissions} + \text{Indirect Emissions} \quad (1)$$

Direct emissions consist of refrigerant emission effects released to the atmosphere during and after the life of the unit.

- Annual refrigerant loss due to gradual leaks during use,
- Losses in disposal of the unit at the end of its life,
- Large losses during the operation of the unit,
- Atmospheric reaction products from the decomposition of the refrigerant in the atmosphere

These four categories are calculated using the refrigerant leakage rate multiplied by the refrigerant charge and the global warming potential (GWP) of the refrigerant [25]. Eq. (2) is used to calculate direct emissions.

$$\text{Direct Emissions} = C \times (L \times ALR + EOL) \times (GWP + Adp.GWP) \quad (2)$$

C used in Eq. (2) shows the refrigerant charge amount (kg). L is equipment lifetime (years). ALR is the annual leak rate (%). EOL is the end-of-life refrigerant leakage rate (%). GWP indicates global warming potential (kg CO_{2e}/kg). Adp.GWP shows the GWP of atmospheric degradation products of refrigerant (kg CO_{2e}/kg) [25,27].

Indirect emissions include emissions from energy consumption during AC system operation, materials manufacturing, cooler manufacturing, cooler and system recycling [22]:

• Emissions from electricity generation

• Emissions from the manufacture of materials

• Emissions from the production of refrigerants

• Emissions from the disposal of the unit

$$\text{Indirect Emissions} = L \times AEC \times EM +$$

$$\sum(m \times MM) + \sum(mr \times RM) + C \times (1 + L \times ALR) \times RFM + C \times (1 - EOL) \times RFD \quad (3)$$

Eq. (3) is used to calculate indirect emissions. Here, AEC is annual energy consumption (kWh). EM shows electricity generation emission value (kg CO_{2e}/kg). m is the mass of the refrigeration unit (kg). MM indicates material production emission value (kg CO_{2e}/ kg). mr is mass of recycled material (kg). RM shows the emission value of the recycled material (kg CO_{2e}/ kg). RFM is refrigerant production emission (kg CO_{2e}/kg) and RFD shows the emission value (kg CO_{2e}/ kg) [25]. The fixed parameters used in the above equations were determined by considering the studies in the literature and the characteristics-catalogue values of the air conditioning system used in the experimental study. The parameters used in the LCCP analysis are shown in the Table (1).

The time of AC usage increases in hot climatic conditions. Due to the increase in energy prices, countries announce some measures in the use of ACs. The Spanish government stated that ACs should be used at ambient temperatures above 27 ºC [28]. The authors examined the environmental temperature values in various parts of the world by taking this value as a reference. The capitals of 12 countries were taken into consideration as a location. Table (2) was created by taking the hourly average values of the ambient temperature values in 2019, 2020 and 2021 as a reference to the environmental temperature values taken from NASA POWER Web [29].

Table 1. Fixed parameters used in LCCP analysis [18,20].

Fixed parameters	Values
C (kg)	0.55
GWP (R32)	675
L (year)	10
ALR (%)	2.5
EOL (%)	15
m (kg)	7.9
MM (kg $\mathbf{CO_{2e}}$/kg)	2.25
mr (kg)	3.95
RM (kg $\mathbf{CO_{2e}}$/kg)	0.5
RFM (kg $\mathbf{CO_{2e}}$/kg)	7.2

Table 2. Average hourly values of the capitals of 12 countries in 2019, 2020 and 2021 where the ambient temperature is above 27 ºC [29].

Country	Capital	Annual hourly the AC operation period in which 3-year average ambient temperature values are above 27 ºC (hour)	EM electricity generation emission value (kg CO_{2e}/kWh)
Canada	Ottawa	190	0.029
China	Beijing	1034	0.623
England	London	52	0.269
France	Paris	170	0.055
Germany	Berlin	276	0.301
India	New Delhi	4056	1.4
Japan	Tokyo	860	0.492
Mexican	Mexico City	148	0.423
Spain	Madrid	913	0.019
Sweden	Stockholm	56	0.013
Turkey	Ankara	570	0.555
United States of America	Washinton DC	896	0.373

LCCP analyses were carried out separately for each country by taking into account the values in Table (2). The results of the installation faults of the condenser of the AC are evaluated from different perspectives.

3. Results and Discussions

The results obtained within the scope of the study were examined under several headings. Within the scope of the LCCP analysis, considering the capitals of 12 countries, the effects on emission values were examined with the assumption that similar installation faults was made in these countries. Installation faults causes much more serious problems, especially in countries that use fosil fuel-based energy sources in energy production. Installation faults of the AC system has an effect on indirect emission values. The main reason for this is the variability in electricity consumption values (AEC). This variability is due to the fact that the heat energy taken from the evaporator unit in the cooling cycle cannot be discharged to the environment if the air inlet sections of the condenser unit are blocked. Since the heat energy cannot be discharged to the environment, it is stored in the refrigerant and its elements. In these systems, which work with the inverter system, the compressor power is increased automatically, since the heat in the system cannot be discharged to the environment. This situation increases the electricity consumption values of the AC system and has a negative effect on the indirect emission values. When the results obtained from the analyses for the capitals of the 12 countries considered within the scope

of the study are examined, the contribution of the AC system to carbon emissions due to installation faults of condenser has increased significantly in some countries. Fig. (3) shows the values obtained for Ankara.

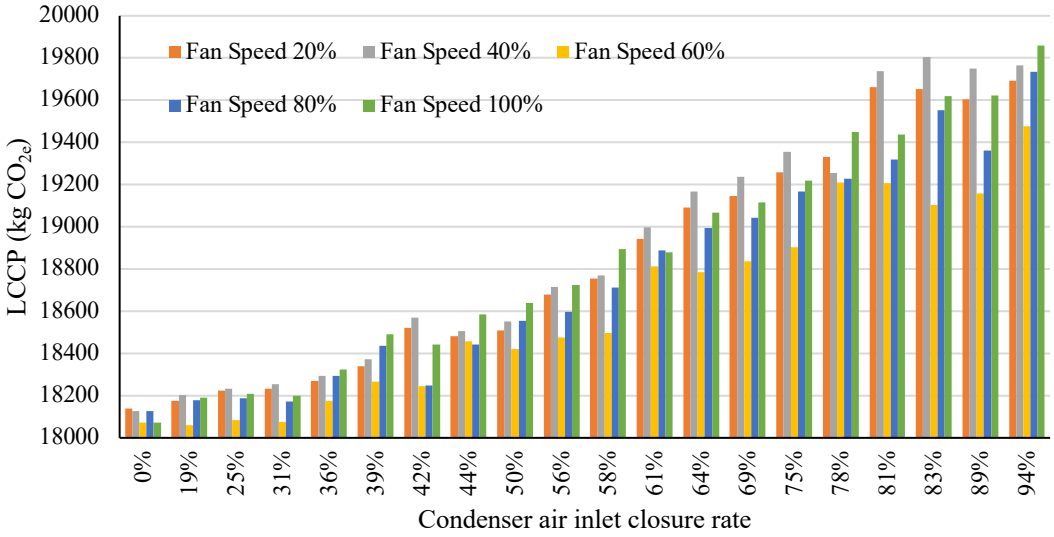

Figure 3. Effect of installation faults on emissions (Ankara).

The capital of Turkey experiences 4 seasons as a location. Locations considered in the analysis: Latitude 39.9659 Longitude 32.9524. It was calculated how many hours the temperatures were above 27 ºC in the relevant location. When the average of the three-year temperature values is taken as 570 hours. This value shows AC usage per year. The LCCP values, which are considered reference values and where the air inlet of the condenser is not blocked, vary between 18073 and 18140 kg·CO_{2e}. According to the installation faults scenario of the condenser, a serious increase in the LCCP value occurs as a result of the gradual closing of the air inlet. The LCCP value increased up to 19692 – 19858 kg·CO_{2e} values with the closing of the air inlet as a result of installation faults. In Fig. (4), the values obtained for Tokyo are presented.

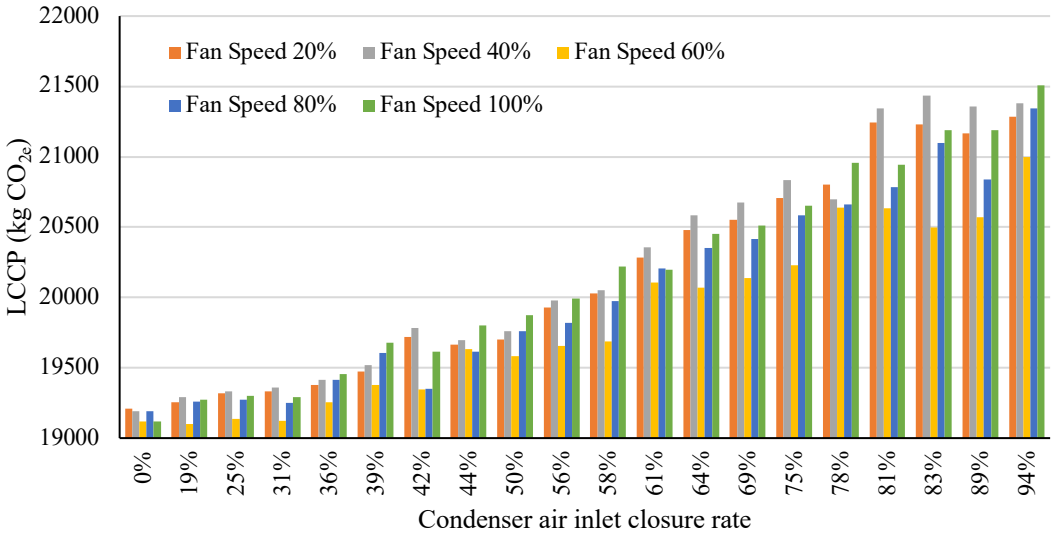

Figure 4. Effect of installation faults on emissions (Tokyo).

Japan is a country where AC usage is intense. Locations considered in the analysis: Latitude 35.7754 Longitude 139.7679. For Tokyo, an average of 860 hours of AC usage per year is taken into account. The LCCP

values considered as reference vary between 19180 and 19208 kg·CO_{2e}. As a result of the gradual closing of the air inlet of the condenser, the LCCP value increases up to 21284 - 21505 kg·CO_{2e} values. The values obtained for Benjing can be examined in Fig. (5).

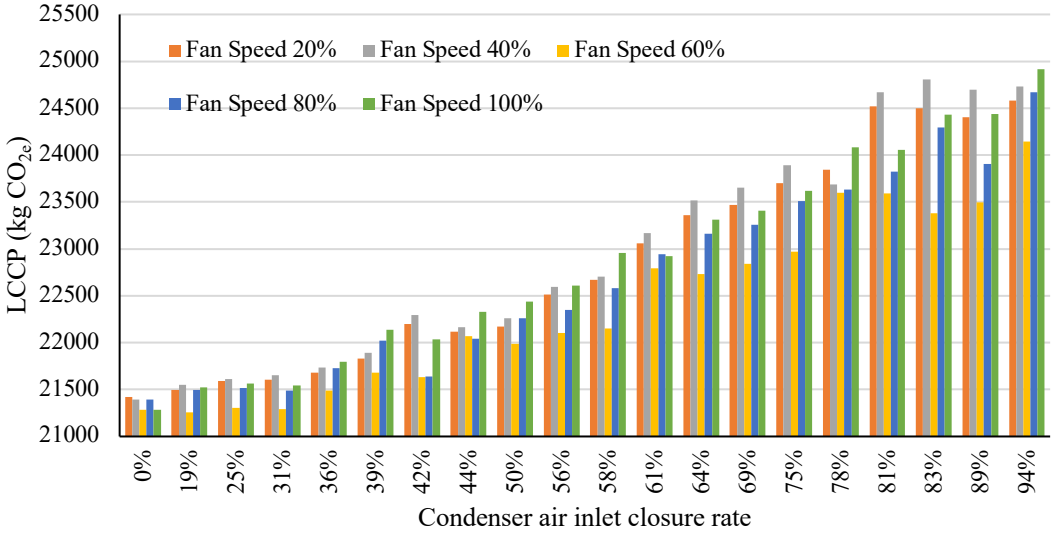

Figure 5. Effect of installation faults on emissions (Benjing).

China is one of the countries where fossil fuel consumption is high in electricity generation. China's EM value has the second highest value among the countries considered in the study. At the same time, assuming that AC is used at an ambient temperature of 27 ºC, China stands out as one of the high hourly value of AC usage. The LCCP values are also quite high in parallel with the high values in the EM value and the AC usage time. An average of 1034 hours of AC usage per year is calculated for Beijing. Reference values for LCCP range from 21420 to 21284 kg·CO_{2e}. As a result of the gradual closing of the air inlet of the condenser, the LCCP value increased to 24581 – 24918 kg·CO_{2e}. The figures obtained for New Delhi are given in Fig. (6).

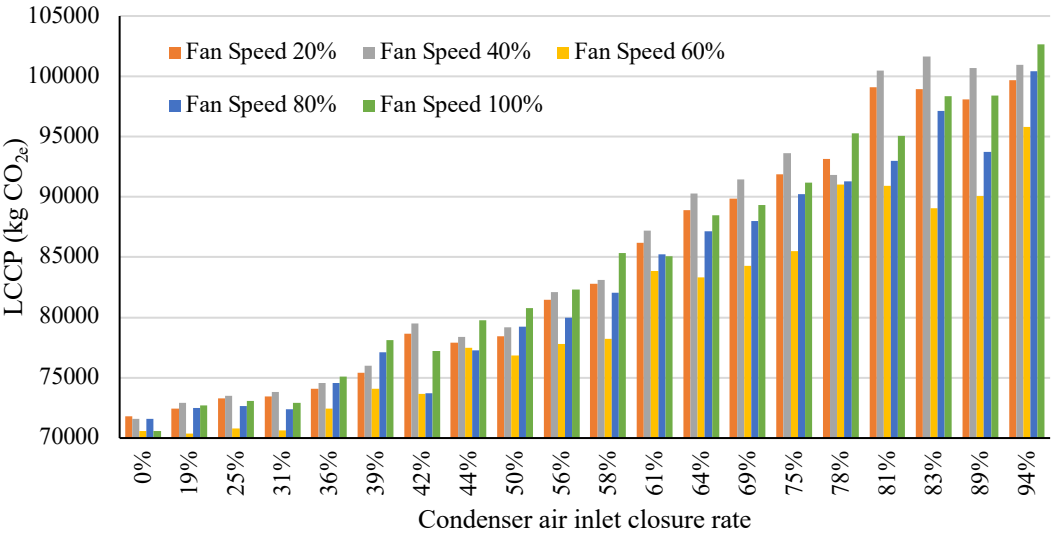

Figure 6. Effect of installation faults on emissions (New Delhi).

India has both the highest EM value and the highest AC usage hours among the countries considered in the study. The main reasons for this are the fact that it has a hot climate as a location, and the use of fossil fuels in

energy production is quite high. India's EM value is 1.4 kg·CO_{2e}/kWh and total the AC usage time is 4056 hours. Locations considered in the analysis: Latitude 28.687 Longitude 77.1719. Reference values for LCCP range from 70601 to 71800 kg·CO_{2e}. According to the scenario of installation faults of the condenser, the LCCP value increased up to 99663-102630 kg·CO_{2e}. When compared by taking the average of the LCCP analyses obtained as a result of the reference and installation faults, there is a 29.6% increase in the LCCP value. In Fig. (7), the values obtained for Madrid are presented.

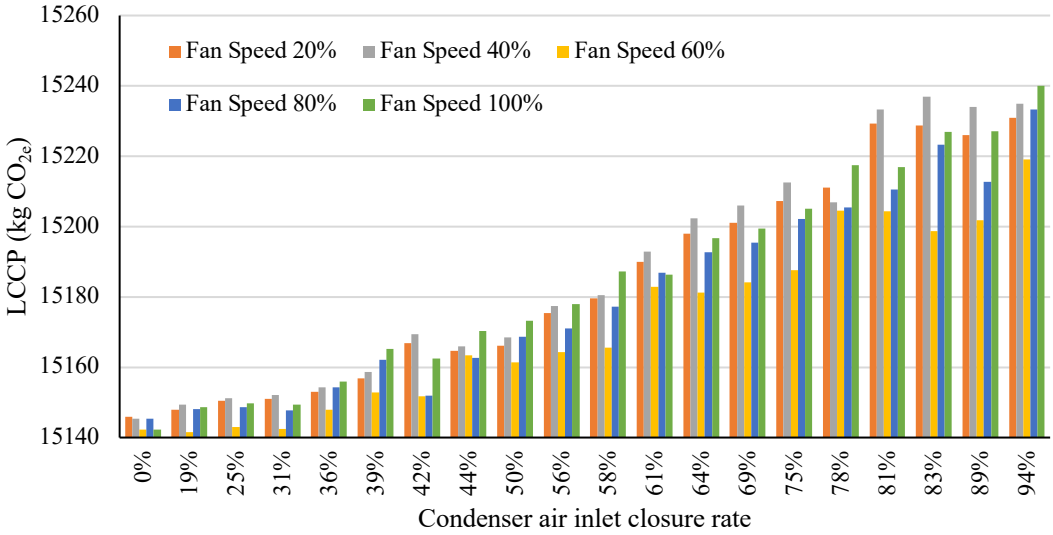

Figure 7. Effect of installation faults on emissions (Madrid).

The EM value for Spain is 0.019 and the total the AC usage time is 913 hours. For Spain, EM and the AC usage time allow good comparison data to be obtained. Spain provides an opportunity to examine the effects of incorrect condenser installation on emissions for a location with low EM but high AC usage. Reference values for LCCP range from 15145 to 15142 kg·CO_{2e}. According to the scenario of installation faults of the condenser, it was calculated that the LCCP value increased to 15239 kg·CO_{2e} by blocking the air inlet. The values obtained for Washington DC are presented in the Fig. (8).

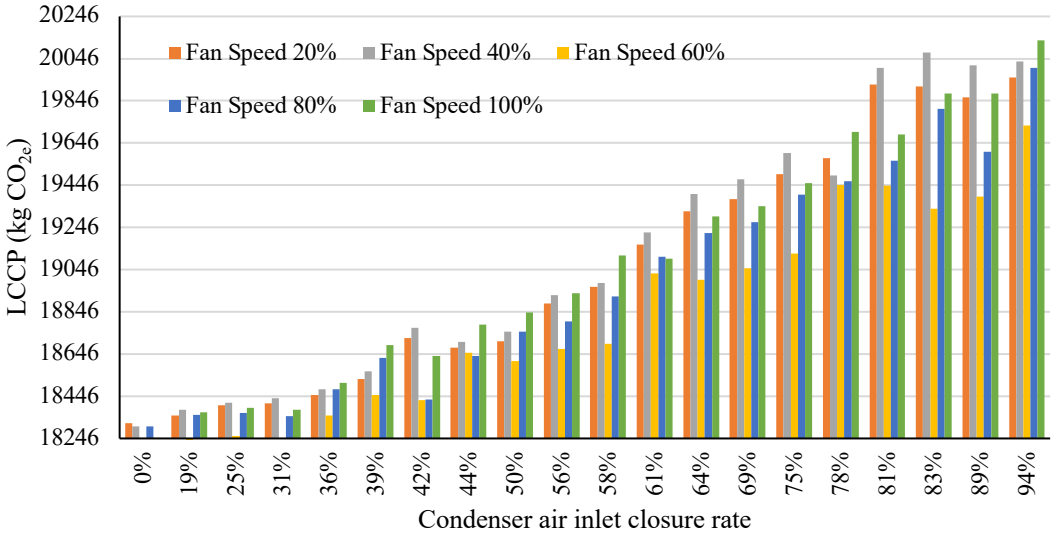

Figure 8. Effect of installation faults on emissions (Washington DC).

The EM value of USA is 0.373 and the total the AC usage time is 896 hours. Reference values for the LCCP range from 18316 to 18246 kg·CO_{2e}. According to the installation faults scenario of the condenser, the LCCP value increased up to 19956- 20131 kg·CO_{2e} values. When compared by taking the average of the LCCP analyses obtained as a result of the reference and installation faults, there is an 8.7% increase in the LCCP value. It can be said that the differences between the values obtained for the other countries covered in the study are very small. The main reason for this is the low air conditioner usage times in these countries. Fig. (9) shows the values obtained for Paris.

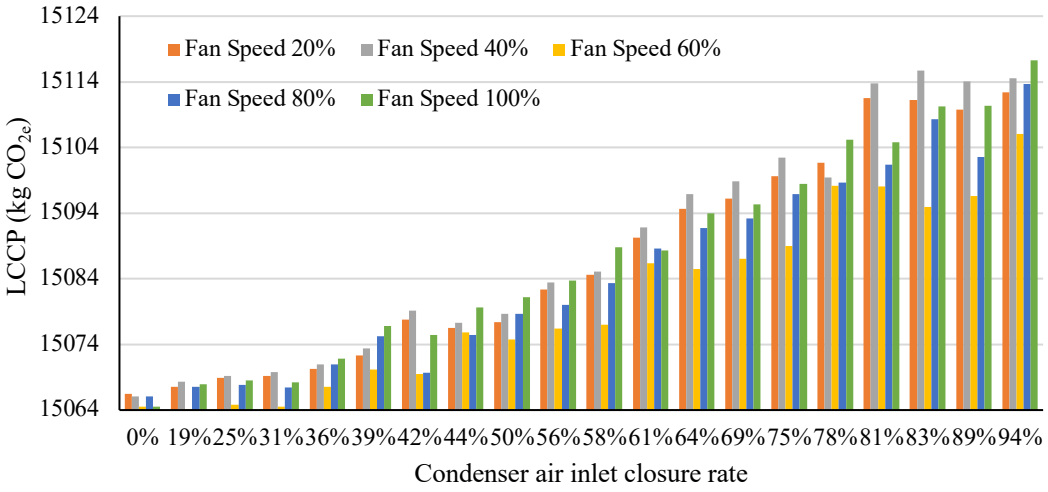

Figure 9. Effect of installation faults on emissions (Paris).

France is a country that heavily benefits from nuclear energy in electricity generation. This situation makes a positive contribution to the EM values of France. It also has a low value in terms of the hourly average of the AC usage. The annual average AC time has been determined as 170 hours. However, with the effects of global warming in Europe, it can be predicted that there will be an increase in the AC usage time. Locations considered in the analysis: Latitude 48.8763 Longitude 2.2868. Reference values for the LCCP range from 15066 to 15064 kg·CO_{2e}. According to the scenario of installation faults of the condenser, the maximum LCCP value is calculated as 15117 kg·CO_{2e}, with the air inlet blocked. The figures obtained for Berlin are given in Fig. (10).

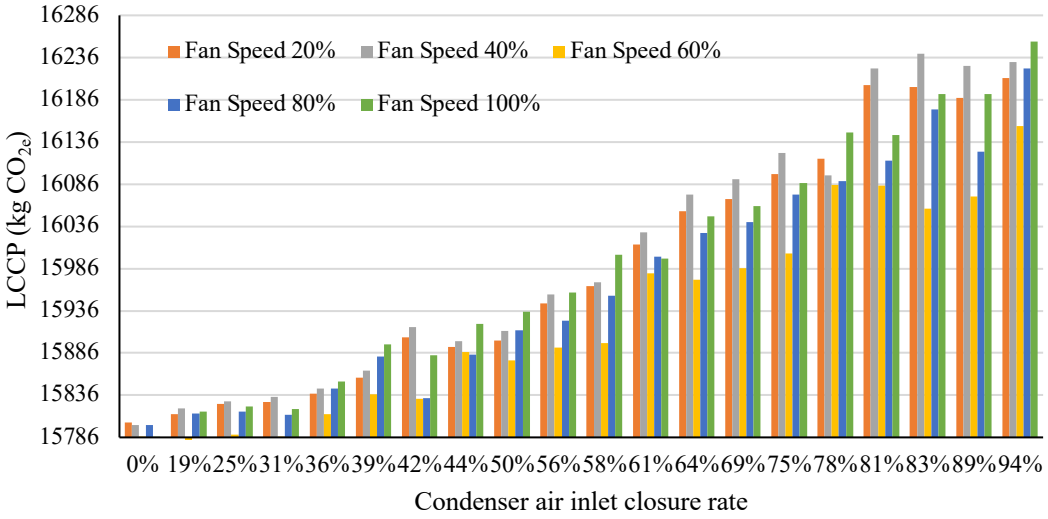

Figure 10. Effect of installation faults on emissions (Berlin).

Locations considered in the analysis: Latitude 52.5203 Longitude 13,383 for Berlin. It was calculated how many hours the temperatures were above 27 ºC in the relevant location. When the average of the three-year temperature values is taken as 276 hours. The LCCP values, which are considered reference values and the air inlet of the condenser is not blocked, vary between 15786 and 15803 kg·CO_{2e}. According to the installation faults scenario of the condenser, a serious increase in the LCCP value occurs as a result of the gradual closing of the air inlet. The LCCP value increases up to 16211 – 16254 kg·CO_{2e} values. In Fig. (11), the values obtained for London are presented.

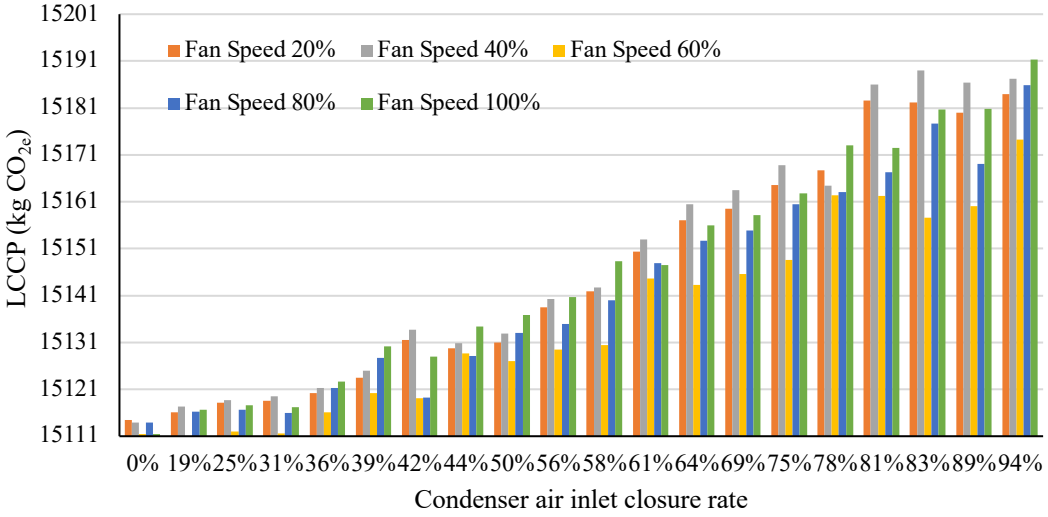

Figure 11. Effect of installation faults on emissions (London).

It cannot be said that England is a country where the use of AC (for cooling) is intense. For London, an average of 52 hours of AC usage per year is taken into account. The LCCP values, where the air inlet of the condenser is not blocked and considered as reference values, vary between 15114 and 15111 kg·CO_{2e}. As a result of the gradual closing of the air inlet of the condenser, the LCCP value increased up to 15191 kg·CO_{2e} values. The values obtained for Stockholm are presented in the Fig. (12).

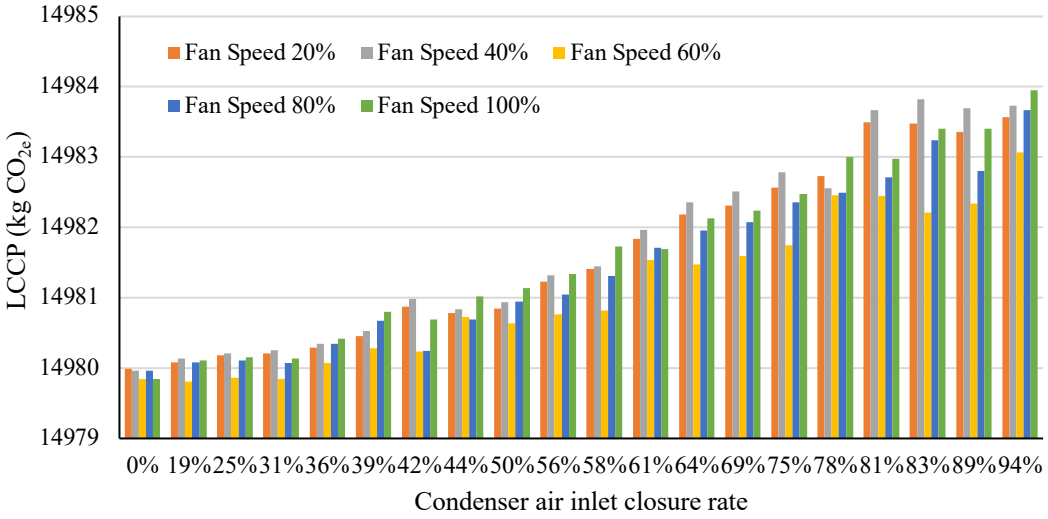

Figure 12. Effect of installation faults on emissions (Stockholm).

Sweden is one of the countries with the lowest fossil fuel consumption in electricity generation. Sweden's EM value has the lowest value among the countries considered in the study. At the same time, Sweden is the second country with the lowest hourly value of AC use, assuming that AC is used at an ambient temperature of 27 °C. Parallel to the low values in EM value and the AC usage time, the LCCP values are also quite low compared to other countries. Locations considered in the analysis: Location: Latitude 59.3863 Longitude 18.0394. An average of 56 hours of AC usage per year is calculated for Stockholm. The reference value for LCCP was calculated as 14979 kg·CO_{2e}. As a result of the gradual closing of the air inlet of the condenser, the LCCP value was calculated to be 14983 kg·CO_{2e}. The values obtained for Ottawa are given in the Fig. (13).

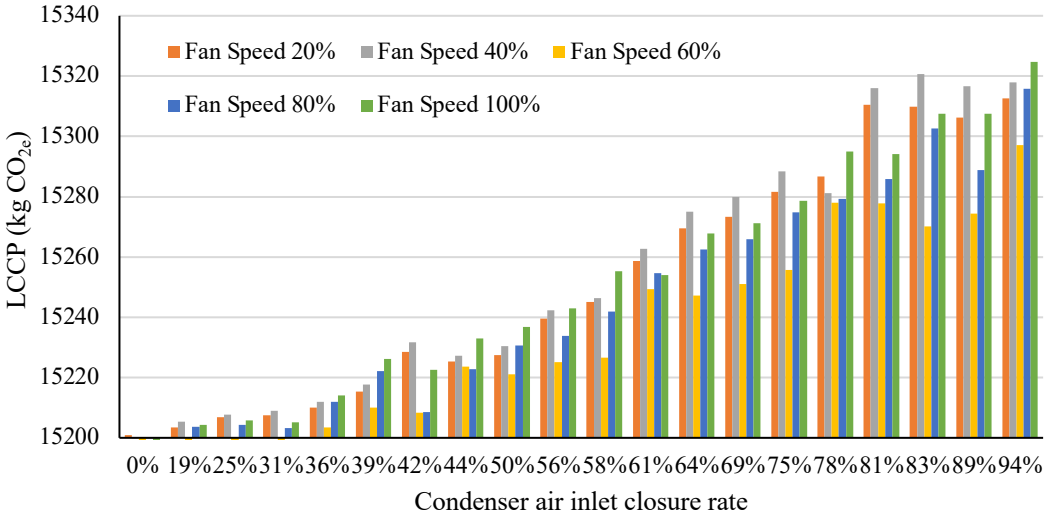

Figure 13. Effect of installation faults on emissions (Ottawa).

The EM value for Canada is 0.029 and the total the AC usage time is 190 hours. When EM and the AC usage time are evaluated for Canada, it can be said that they are relatively low values. Locations considered in the analysis: Location: Latitude 45.3936 Longitude -75.692. Reference values for LCCP range from 15196 to 15200 kg·CO_{2e}. According to the scenario of installation faults of the condenser, it was calculated that the LCCP value increased to 15324 kg·CO_{2e} by blocking the air inlet. The values obtained for Mexico City can be seen in Fig. (14).

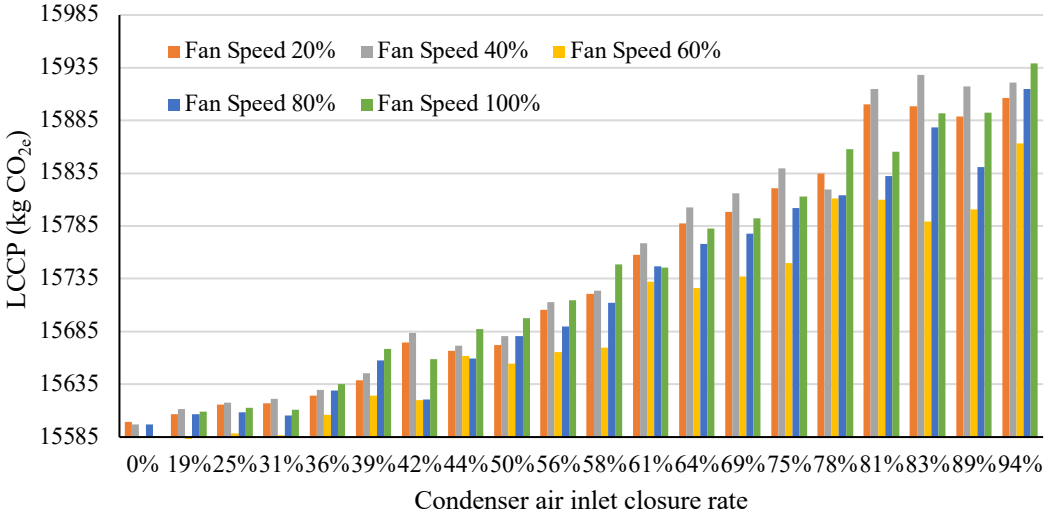

Figure 14. Effect of installation faults on emissions (Mexico City).

For Mexico, the AC has a low value in terms of hourly average usage. The average annual air-conditioning time has been determined as 148 hours. However, with the effects of global warming, it can be predicted that there will be an increase in the AC usage time. Locations considered in the analysis: Location: Latitude 19.4214 Longitude -99.129. Reference values for LCCP range from 15599 to 15585 kg·CO_{2e}. According to the scenario of installation faults of the condenser, the maximum LCCP value is calculated as 15938 kg·CO_{2e} by blocking the air inlet.

LCCP analyses are difficult to compare with results from other studies. The main reason for this is that different approaches are preferred in determining the operating times of the AC system. In addition, it is seen that there are serious differences on the capacity of the AC system considered in the study and the values obtained from the LCCP analysis in the refrigerat - material used. For example, the results obtained from the LCCP analyses of the AC system for an airport and campus in the United States were examined. The study was carried out by considering different refrigerants. According to the results obtained, it is seen that it varies between 60000 and 75000 kg·CO_{2e} [27].

When the graphs above are examined, an increasing trend is seen in the emission values depending on the installation faults. It can be said that the faults made during the installation will contribute to the emissions. In addition to the climatic conditions, the EM values of the countries cause serious variability in emissions. For example, there is no serious AC use in England. It cannot be said at first assessment that the effects of installation faults of the AC system will have serious effects in this country. However, ACs are not only used for the purpose of improving evaporator comfort conditions. ACs are also used to preserve food, medicine and many similar substances in certain temperature environments. In this case, it cannot be assumed that the AC is activated at temperatures above 27 ºC, which is considered within the scope of the study. There will be differences in the LCCP value if the AC is used for the purpose of cooling the warehouses. installation faults of ACs used for the cooling of warehouse environments can have a serious negative impact on the value of the LCCP analysis. For this reason, the operating hour's value of the AC will vary in the storage applications of the AC in countries where the effects of installation faults in the LCCP analysis are low (England, Sweden, Canada, France, Mexico and Germany). Longer operating hours in ACs used for storage will cause a direct increase in the AEC value. In this case, it can be said that there will be serious increases in the LCCP value of these countries presented in the study. The serious effects of installation faults on the LCCP value were seen in the experimental analysis. As a result of installation faults, the rates of increase of the LCCP values change from 0.02% to 29.6% as a result of closing the air inlets of the condenser unit. The effects of installation faults of the AC on the LCCP value increase in direct rate to the usage time of the AC. The effect on emission values can be clearly seen due to the increase in electricity consumption values as a result of installation faults. Installation faults will also have indirect effects on emissions. The maintenance and repair frequency will increase due to the strain of the AC system. At the same time, there will be a case of very frequent break down in the system. This will adversely affect the direct emission values in the LCCP analysis.

The obtained values can also be handled with a statistical approach. The use of air conditioners is intense in Japan, the United States and China [30]. Considering the number of air conditioners used in homes, it can be seen that the values obtained above have serious consequences. While the number of air conditioners used in homes in Japan is 131 million, this number is 331 million in the United States and 336 million in China [30]. The following Table 3 was obtained as a result of comparing the LCCP values obtained according to the closing rate of the condenser air inlet with the reference values. The values in Table 3 were created by considering the characteristics of the air conditioner (12000 Btu) used in this study. When comparing the values obtained for an AC unit in Table 3 according to countries, it can be interpreted that there are no significant differences. For example, the values obtained due to the installation faults of the condenser were compared with the reference values. For Japan, the amount of unnecessary emissions caused by installation faults of the condenser ranges from 15.58 kg·CO_{2e} to 1877,659 kg·CO_{2e}. For the United States, these values range from 12.3 kg·CO_{2e} to 1482.52 kg·CO_{2e}. Finally, the values obtained for China are 23.72 kg·CO_{2e} and 2858,468 kg·CO_{2e}. It cannot be said that these obtained values make a significant difference. However, when the number of air conditioner usage in countries is evaluated, it is revealed that there may be a very serious increase in emissions. When these numbers mentioned above are multiplied by the number of air conditioners, serious emission values are obtained. Considering the number of air conditioners used in Japan, emission values ranging from 2.04E+09 kg·CO_{2e} to 2.46E+11 kg·CO_{2e} are obtained. An optimistic approach can also be adopted. For example, these obtained values by assuming that only 1% of the air conditioners used in Japan are incorrectly installed in the condenser section. When 1% of the air conditioners used in Japan are evaluated, the number of air conditioners is 1.31 million. When this value is multiplied by the values in Table 3, the amount of unnecessary emission varies between 20,417,849

kg·CO_{2e} and 2.46E+09 kg·CO_{2e}. It is seen from the above evaluations that installation faults of condenser units of air conditioners contributes to a serious amount of emissions.

Table 3. Comparison of the values obtained according to the closure ratio of the condenser air inlet (Fan speed %60).

Compared parameters	Japan	US	China
$LCCP_{(Ref^{*}. - 1\ AC\ unite)}$	19118.78 kg·CO_{2e}	18246.28 kg·CO_{2e}	21284.51 kg·CO_{2e}
$LCCP_{(\%25^{**} - 1\ AC\ unite)}$	19134.37 kg·CO_{2e}	18258.59 kg·CO_{2e}	21308.24 kg·CO_{2e}
$LCCP_{(\%50 - 1\ AC\ unite)}$	19582.64 kg·CO_{2e}	18612.52 kg·CO_{2e}	21990.66 kg·CO_{2e}
$LCCP_{(\%75 - 1\ AC\ unite)}$	20227.41 kg·CO_{2e}	19121.61 kg·CO_{2e}	22972.24 kg·CO_{2e}
$LCCP_{(\%94 - 1\ AC\ unite)}$	20996.44 kg·CO_{2e}	19728.81 kg·CO_{2e}	24142.98 kg·CO_{2e}
$LCCP_{(\%25 - 1\ AC\ unite)}$ - $LCCP_{(Ref. - 1\ AC\ unite)}$ amount of unnecessary emissions	15.58614 kg·CO_{2e}	12.30619 kg·CO_{2e}	23.72768 kg·CO_{2e}
$LCCP_{(\%50 - 1\ AC\ unite)}$ - $LCCP_{(Ref. - 1\ AC\ unite)}$ amount of unnecessary emissions	463.8543 kg·CO_{2e}	366.2407 kg·CO_{2e}	706.152 kg·CO_{2e}
$LCCP_{(\%75 - 1\ AC\ unite)}$ - $LCCP_{(Ref. - 1\ AC\ unite)}$ amount of unnecessary emissions	1108.627 kg·CO_{2e}	875.327 kg·CO_{2e}	1687.726 kg·CO_{2e}
$LCCP_{(\%94 - 1\ AC\ unite)}$ - $LCCP_{(Ref. - 1\ AC\ unite)}$ amount of unnecessary emissions	1877.659 kg·CO_{2e}	1482.524 kg·CO_{2e}	2858.468 kg·CO_{2e}
Considering the number of air conditioners used in countries			
$LCCP_{(\%25)}$ - $LCCP_{(Ref)}$ amount of unnecessary emissions	$2.04x10^{9}$ kg·CO_{2e}	4.07x10 kg·CO_{2e}	7.97 x10 kg·CO_{2e}
$LCCP_{(\%50)}$ - $LCCP_{(Ref.)}$ amount of unnecessary emissions	$6.08x10^{10}$ kg·CO_{2e}	$1.21x10^{11}$ kg·CO_{2e}	$2.37x10^{11}$ kg·CO_{2e}
$LCCP_{(\%75)}$ - $LCCP_{(Ref.)}$ amount of unnecessary emissions	$1.45x10^{11}$ kg·CO_{2e}	$2.9x10^{11}$ kg·CO_{2e}	$5.67x10^{11}$ kg·CO_{2e}
$LCCP_{(\%94)}$ - $LCCP_{(Ref.)}$ amount of unnecessary emissions	2.46 $x10^{11}$ kg·CO_{2e}	$4.91x10^{11}$ kg·CO_{2e}	$9.6x10^{11}$ kg·CO_{2e}

(*) Values where condenser air inlets are not closed
(**) Values obtained as a result of closing the air inlets of the condenser at different rates

4. Conclusion

Topics such as rising energy prices and global warming will continue to be hot topics on the agenda of governments and communities for years. Many research and development studies are carried out on systems that consume energy intensively, such as heating and cooling systems. However, the correct use of these systems has been shown to have serious effects on energy efficiency and their contribution to emissions. Within the scope of the study, it was observed that some condenser units of the AC systems were installed incorrectly. The effects of this installation faults on the emission values were examined and the results obtained for 12 different countries were discussed. In the following lines, the results obtained from the study can be summarized.

- When compared by taking the average of the LCCP analyses obtained as a result of the reference and installation faults, there is a 29.6% increase in the LCCP value for India.
- Reference values for LCCP range from 15145 to 15142 kg·CO_{2e}. According to the scenario of installation faults of the condenser, it was calculated that the LCCP value increased to 15239 kg·CO_{2e} by blocking the air inlet for Spain.

- When compared by taking the average of the LCCP analyses obtained as a result of the reference and installation faults, there is an 8.7% increase in the LCCP value for the US.
- For Japan, the amount of unnecessary emissions caused by installation faults of the condenser ranges from 15.58 kg·CO_{2e} to 1877,659 kg·CO_{2e}. For the United States, these values range from 12.3 kg·CO_{2e} to 1482.52 kg·CO_{2e}. Finally, the values obtained for China are 23.72 kg·CO_{2e} and 2858,468 kg·CO_{2e}.
- Considering the number of air conditioners used in Japan, emission values ranging from 2.04E+09 kg·CO_{2e} to 2.46E+11 kg·CO_{2e} are obtained. When 1% of the air conditioners used in Japan are evaluated, the amount of unnecessary emission varies between 20,417,849 kg·CO_{2e} and 2.46E+09 kg·CO_{2e}.

Acknowledgments

This study was produced from the master thesis titled “Investigation of the possible effects of incorrect montage of AC systems on the performance values of the system”. Authors thank to Fırat University Project Support Unit with the project number TEKF.22.07. The historical temperature data used in this study were obtained from the NASA Langley Research Center (LaRC) POWER Project funded through the NASA Earth Science/Applied Science Program.

We undertake that in the article we submitted for publication, no study requiring ethics committee approval, was conducted.

There is no conflict of interest between the authors.

References

[1] Rusen, Eren S, Rusen A. A Sample Study for Determining Energy Consumption Values in Public Buildings: Central Anatolia Region. In: Gökçekuş H, Kassem Y, editors. Clim Chang Nat Resour Sustain Environ Manag, Springer; 2022, p. 100–9.

[2] She X, Cong L, Nie B, Leng G, Peng H, Chen Y, et al. Energy-efficient and -economic technologies for air conditioning with vapor compression refrigeration: A comprehensive review. Appl Energy 2018;232:157–86.

[3] Rușen SE, Koç M. Araştırma Makalesi / Research Article Enerji Tüketim ve CO_2 Salınım Değerlerinin Analizi ; Bir Gıda Fabrikası Örneği Analysis of Energy Consumption and CO_2 Emission Values ; A Case Study of a Food Factory 2019;8:1478–88.

[4] Ener Rüşen S. Elektrik Motorlarının Verimlilik ve CO_2 Emisyon Analizi; Bir Gıda Fabrikası Örneği. Eur J Sci Technol 2019:564–9.

[5] Rüşen Eren S, Rüşen A. Bir Spor Kompleksinin Karbon Ayak İzinin Hesaplanması ve Enerji Kayıplarının Tespiti. 2. Bilsel Int. Korykos Sci. Res. Innov. Congr., Mersin/Türkiye: astana; 2024, p. 145–54.

[6] The Paris Agreement. United Nations Treaty Collect n.d. https://treaties.un.org/pages/ViewDetails.aspx?src=TREATY&mtdsg_no=XXVII-7-d&chapter=27&clang=_en.

[7] Glasgow Climate Change Conference. United Nations Clim Chang n.d. https://unfccc.int/conference/glasgow-climate-change-conference-october-november-2021.

[8] Ni J, Bai X. A review of air conditioning energy performance in data centers. Renew Sustain Energy Rev 2017;67:625–40.

[9] Mishra P, Soni S, Maheshwari G. Exergetic performance analysis of low GWP refrigerants as an alternative to R410A in split air conditioner. Mater Today Proc 2022;63:406–12.

[10] Chen W. A comparative study on the performance and environmental characteristics of R410A and R22 residential air conditioners. Appl Therm Eng 2008;28:1–7.

[11] Guilherme ÍF, Marcucci Pico DF, dos Santos DDO, Bandarra Filho EP. A review on the performance and environmental assessment of R-410A alternative refrigerants. J Build Eng 2022;47.

[12] Li G. Investigations of life cycle climate performance and material life cycle assessment of packaged air conditioners for residential application. Sustain Energy Technol Assessments 2015;11:114–25.

[13] Zhiyi Y, Tianduo P, Xunmin O. Scenario Analysis on CO_2-equivalent Emissions from Alternative Mobile Air Conditioning Refrigerants in China. Energy Procedia 2017;142:2617–23.

[14] Golzari S, Kasaeian A, Daviran S, Mahian O, Wongwises S, Sahin AZ. Analyse selon le second principe d’un système de conditionnement d’air automobile fonctionnant au HFO-1234yf, frigorigène respectueux de l’environnement. Int J Refrig 2017;73:134–43.

[15] Choi S, Oh J, Hwang Y, Lee H. Life cycle climate performance evaluation (LCCP) on cooling and heating systems in South Korea. Appl Therm Eng 2017;120:88–98.

[16] Ziya Sogut M. Exergetic and environmental assessment of room air conditioners in Turkish market. Energy 2012;46:32–41.

[17] Wang Z, Song Q, You Y, Duan H, Yuan W, Li J. Identifying the lifecycle ODP and GWP effects of the refrigerants from household air-conditioners in Macau. Environ Impact Assess Rev 2021;90:106639.

[18] Wan H, Cao T, Hwang Y, Radermacher R, Chin S. Comprehensive investigations on Life Cycle Climate Performance

of unitary air-conditioners. Int J Refrig 2021;129:332–41.
[19] Lee H, Troch S, Hwang Y, Radermacher R. Évaluation du LCCP de diverses options de cycle à compression de vapeur et de frigorigènes à faible GWP. Int J Refrig 2016;70:128–37.
[20] Zhao L, Zeng W, Yuan Z. Reduction of potential greenhouse gas emissions of room air-conditioner refrigerants: A life cycle carbon footprint analysis. J Clean Prod 2015;100:262–8.
[21] Sarbu I. A review on substitution strategy of non-ecological refrigerants from vapour compression-based refrigeration, air-conditioning and heat pump systems. Int J Refrig 2014;46:123–41.
[22] Wan H, Cao T, Hwang Y, Radermacher R, Chin S. Comprehensive investigations on Life Cycle Climate Performance of unitary air-conditioners Études complètes sur les performances climatiques sur le cycle de vie des appareils de conditionnement d ' air monobloc. Int J Refrig 2021;129:332–41.
[23] Winkler J, Das S, Earle L, Burkett L, Robertson J, Roberts D, et al. Impact of installation faults in air conditioners and heat pumps in single-family homes on U.S. energy usage. Appl Energy 2020;278:115533.
[24] Hourahan GC, Baxter VD. Impact of Installation Faults on Heat Pump Performance. IEA Heat Pump Cent Newsl 2015;33:34–8.
[25] Guideline for Life Cycle Climate Performance January 2016, 2016. 1-26. 2016:1–26.
[26] Mota-Babiloni A, Barbosa JR, Makhnatch P, Lozano JA. Assessment of the utilization of equivalent warming impact metrics in refrigeration, air conditioning and heat pump systems. Renew Sustain Energy Rev 2020;129.
[27] Wan H, Cao T, Hwang Y, Radermacher R, Andersen SO, Chin S. A comprehensive review of life cycle climate performance (LCCP) for air conditioning systems. Int J Refrig 2021;130:187–98.
[28] Spanish government to allow flexibility on air-conditioning, but rules out U-turn on decree. Spain in English 2022. https://www.spainenglish.com/2022/08/08/spanish-government-to-allow-flexibility-on-air-conditioning-but-rules-out-u-turn-on-decree/.
[29] NASA. POWER | Data Access Viewer n.d. https://power.larc.nasa.gov/data-access-viewer/.
[30] The International Energy Agency (ıea). Percentage of households equiped with AC in selected countries 2022. https://www.iea.org/data-and-statistics/charts/percentage-of-households-equiped-with-ac-in-selected-countries-2018.

Turkish Journal of Science & Technology
20(1), 225-234, 2025

Research Paper
https://doi.org/10.55525/tjst.1557500

A Novel Two-Dimensional Wind Speed and Direction Measurement Method Based on NTC

Noura SOUKAR[1*], Ayhan YAZGAN[2]
[1] ArGesim Teknoloji A.S., Çorum, Türkiye
[2] Electrical-Electronics Engineering Department, Graduate School of Natural and Applied Sciences, Karadeniz Technical University, Trabzon, Türkiye
[*1] nsoukar@argesim.com.tr, [2] ayhanyazgan@ktu.edu.tr

(Geliş/Received: 28/09/2024; Kabul/Accepted:12/03/2025)

Abstract: Traditional wind sensors, such as cup, hot wire, ultrasonic, and laser Doppler anemometers, often have mechanical parts that limit sensitivity, accuracy, and durability, unlike thermal flow sensors, which detect the wind by measuring the temperature variations using a heater. In addition, the methods reported in the literature have different advantages and disadvantages. In this study, different thermal flow sensor designs reported in the literature are examined and a new method based on the 2-dimensional NTC thermistor is proposed. Simulation results of the proposed method are presented. According to the results actual and calculated wind speed measurements well matched and the maximum wind speed error observed is less than %3. In addition, a simple testbed is presented for wind direction measurement.

Key words: Wind sensor, wind speed, wind direction, anemometer, thermal flow sensor.

NTC Tabanlı Yeni Bir İki-Boyutlu Rüzgar Hızı ve Yönü Ölçüm Yöntemi

Öz: Geleneksel rüzgâr sensörleri, bir ısıtıcı kullanarak sıcaklık değişimlerini ölçerek rüzgârı algılayan termal akış sensörlerinin aksine, kupalı, ultrasonik ve lazer Doppler anemometre gibi, genellikle hassasiyet, doğruluk ve dayanıklılığı sınırlayan mekanik parçalara sahiptir. Bunların yanında, literatürde rapor edilen yöntemlerin farklı avantajları ve dezavantajları bulunmaktadır. Bu çalışmada ise, literatürde rapor edilen farklı termal akış sensörü tasarımları incelenmiş ve 2 boyutlu NTC sensörünü temel alan yeni bir yöntem önerilmiştir. Önerilen yöntemin simülasyon sonuçları sunulmuştur. Sonuçlara göre gerçek ve hesaplanan rüzgâr hızı ölçümleri iyi bir şekilde eşleşmiştir ve gözlenen maksimum rüzgar hızı hatası %3'ten azdır. Ek olarak rüzgâr yönünün tespiti için basit bir düzenek de sunulmuştur.

Anahtar kelimeler: Rüzgâr sensörü, rüzgar hız, rüzgar yön, anemometre, termal akış sensörleri.

1. Introduction

Wind sensors, also known as anemometers, are tools used to measure wind speed and direction. Typically, these sensors include mechanical components that can affect their sensitivity, accuracy, and durability. This study will examine different sensors that measure wind speed and direction through temperature changes.

Wind sensors are commonly utilized in environmental monitoring, meteorology, and energy production to measure wind speed and direction. They come in various models based on different operating principles [1]. Cup Anemometer is known as the most common wind speed sensor in meteorological stations. It consists of three or four cups rotating around a vertical axis. The number of rotations is proportional to wind speed [2]. Ultrasonic Anemometer is based on the operating principle of Ultrasonic Transmitter-Receiver converters. It works by sending a sound wave from the transmitter converter. The microprocessor then measures the time it takes for the signal to be received by the receiver converter. Ultimately, the wind speed is measured by calculating the time it takes for the sound waves to travel between the converters [3]. Laser Doppler Anemometer determines the wind speed using the Doppler effect. It operates by splitting a laser light beam into two beams when these two narrow light beams focus on a stationary object. However, when the object is moving, the returning beam's frequency changes, resulting in a differing transmitted signal. This variance in frequency, known as the Doppler shift, allows for the measurement of wind speed [4]. Hot Wire Anemometer is based on the principle of heat loss. It consists of two probes between which a thin wire is stretched. When the wire is kept at a constant temperature, as the wind blows over the hot wire, it cools down, and its resistance changes. The wire's resistance is directly proportional to the speed of the airflow [5]. Thermistor-Based Anemometer measures wind speed using PTC (Positive Temperature Coefficient) or NTC (Negative Temperature Coefficient) thermistors. As the wind blows, the thermistor cools, causing a change in its resistance. Simple structure, compact size, and fast response are the advantages of this method [6-7].

[*] Corresponding author: nsoukar@argesim.com.tr. ORCID Number of authors: [1] 0000-0003-3876-4551, [2] 0000-0003-2209-2973

Recently, studies have aimed to develop a new wind sensor interface that utilizes thermal flow sensors without any mechanical components [8]. This type of sensor has three basic measurement principles: time-of-flight, hot wire, and calorimetric [6]. Using the hot wire measurement principle, wind speed is calculated by measuring the heat loss brought on by wind. It may operate in either the Constant Power (CP) or Constant Temperature Difference (CTD) modes. The heater's temperature controls the flow rate when operating in the Constant Power Mode, ensuring a steady power supply. On the other hand, the heater's power consumption in the CTD mode indicates the flow speed and maintains the heater's temperature a few degrees above the flow temperature [9-10]. Low-cost silicon sensors for mass flow measurement were also proposed [11]. The calorimetric measurement principle detects variations in heat gradients caused by wind using a central heating source and surrounding thermal sensors. With this information, the wind's direction and speed were calculated and reported in [12]. Furthermore, the Time-of-Flight concept calculates the time it takes for a heat wave to go from the heater to the detector in two specific locations. The benefits of this method include independent data collection regardless of fluid properties, automatic calibration, and multi-parameter measurement. It can also overcome technical obstacles that calorimetric sensors cannot manage [13–14]. One dimensional NTC method is proposed in the literature [6-7]. However, in one-dimensional design, the advantage of the NTC method cannot be utilized efficiently. For this reason, in this study, two-dimensional NTC thermistors are used for the proposed sensor design, and a MATLAB-based simulation of this design is presented in this article. In this simulation, four NTC thermistors are positioned in different orientations (north, south, east, and west) to detect temperature variations caused by wind flow. As the wind cools each thermistor, resistance decreases and the resulting current changes are used to estimate wind speed and direction. A sample of measured temperature values relative to each direction is used in this study. Then, the differences between the calculated and actual wind values are calculated. Finally, the wind direction and wind speed are obtained.

The remainder of this paper is organized as follows: In Section 2, the thermal methods of the wind measurement are given in detail. In Section 3, the proposed method is discussed. The related results are given in Section 4. Section 5 concludes the paper.

2. Thermal Methods of Wind Measurement

2.1. 2-D Thermal flow sensor

As shown in Figure 1, a square silicon device that combines four resistive heaters, a diode, and thermopiles are used to design a 2-D thermal flow sensor. The temperature of the chip is continuously maintained higher than the airflow temperature by a feedback loop and a central diode [15–16]. The airflow asymmetrically cools the chip, creating a slight temperature gradient. The thermopiles detect this gradient, enabling wind direction and speed to be determined. The gradient's direction corresponds to the flow direction. Meanwhile, its magnitude is approximately proportional to the square root of the flow speed [8-17].

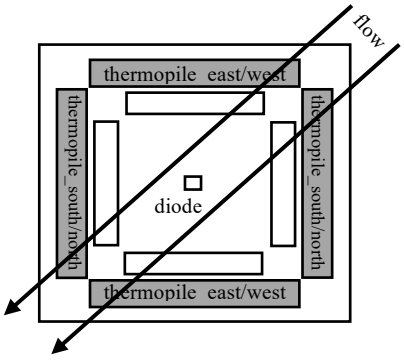

Figure 1. 2-D Thermal Wind Sensor [17].

One aspect of this design is the low-offset instrumentation amplifier that processes microvolt-level signals from thermocouples using a chopper amplifier to reduce noise and thermal offset. The amplifier minimizes thermal offset to 20 μV and provides differential output to reduce common-mode noise.

The system includes wind sensor elements, a multiplexer-connected amplifier, and an analog-to-digital converter (A/D). Tests show accurate results at low wind speeds, with minor deviations at high speeds, and the sensor responds quickly and consistently to wind direction changes [17].

2.2. Micromachined 2-D thermal wind sensor

The thermal wind sensor utilizes MEMS (Micro-Electromechanical Systems) technology to monitor temperature differences and heat dissipation caused by wind, enabling precise wind direction and speed measurements. A semi-empirical temperature model compensates for temperature drift using parameters derived from uncompensated output voltage [18–19–20].

The sensor, as shown in Figure 2, consists of eight self-heating thermistors on a ceramic substrate, arranged symmetrically along East-West and North-South axes to form Wheatstone bridges. One bridge maintains steady heater temperature, while the other adjusts for fluid temperature changes. Voltage differences across the bridges indicate wind direction, and terminal voltage measures wind speed [12–21].

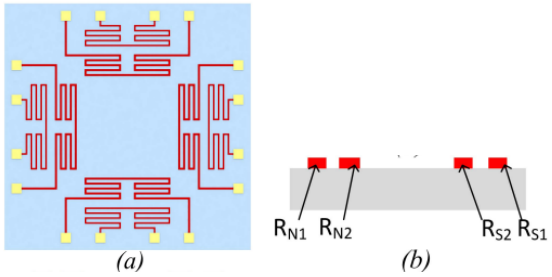

Figure 2. (a) Schematic of a thermal wind sensor, (b) a cross-sectional view [22].

In [12], Temperatures between 270 and 310 K and wind speeds between 0 and 40 m/s were tested on the sensor. With measurement errors of less than ±1.5 m/s, it was observed that the sensor's output voltage decreased as the wind speed increased. Testing revealed that the sensor has a weak temperature dependency when measuring wind direction. These findings imply that the sensor performs accurately and sensitively in various conditions [9–12].

In another study, as given in Figure 3 eight heaters and thermistors, divided into two separate wind-sensing groups (cross-type and saltire-type) are included in the design. The sensor averages the data from these two groups to determine the wind direction and speed. This structure aims to decrease heat conduction and increase measurement accuracy [23–24]. In another study, the sensor uses thermistors positioned all around a central heater to measure temperature fluctuations caused by wind [25–26]. The uneven cooling brought on by the wind blowing across the sensor results in a temperature differential on the chip. This variance is used to determine the direction and speed of the wind. To calculate the final wind speed and direction, the sensor averages the data collected from two different wind sensing groups: cross-type and saltire-type.

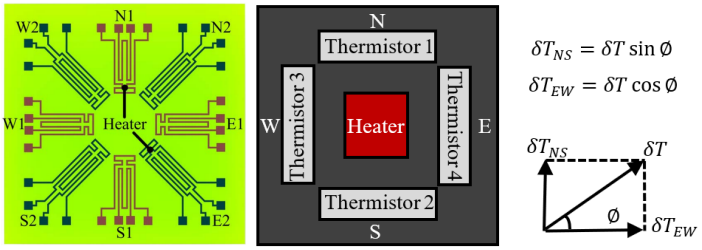

Figure 3. The high-accuracy micromachined thermal wind sensor layout. Includes a red cross-type group (N1-E1-S1-W1) and a blue saltire-type group (N2-E2-S2-W2) and its operating principle [24].

The sensor measures wind speed up to 33 m/s with an error of less than 1% and detect wind direction within a 360° range with a maximum error of ±1.5°. The sensor can rapidly and precisely estimate the wind's direction and speed by using measurements from the cross-type and saltire-type groups. Experimental results indicate that this sensor delivers lower error rates when compared to current 2D MEMS thermal wind sensors [24].

2.3. NTC Segmented thermistor-based anemometer

The sample structure of the NTC Segmented thermistor-based anemometer is given in Figure 4. The uniaxial anemometer is constructed with a sizable wooden structure and is built utilizing thick-film segmented thermistors with a negative temperature coefficient (NTC). It works based on the variable heat loss in the thermistors as a function of airflow speed. A DC constant voltage causes the thermistors to self-heat, and airflow modifies their resistances. This change is used to determine wind direction and speed. A positive difference indicates that the wind is blowing in one direction, while a negative difference indicates it is blowing in the opposite direction [27-28].

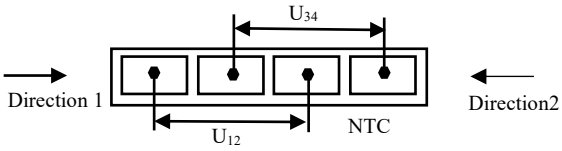

Figure 4. The measurements of voltage variances across the sensor's internal electrodes [28].

As shown in Figure 4, the direction of the wind is ascertained by measuring the voltage difference (dU) where U12 and U34 denote the measured voltage values. The voltage difference is calculated as given in Equation (1).

$$dU = U_{12} - U_{34} \tag{1}$$

The anemometer underwent testing for wind speeds ranging from 1 m/s to 15 m/s at various inlet air temperatures between -20°C and +40°C. When tested at temperatures above 0°C, delays in the cooling and heating processes were observed at specific intervals, with a determined delay time of 180 seconds (3 minutes) for the anemometer with a 1.6 mm aperture. The measurement sensitivity was confirmed to be accurate within ±3% for wind speed and error-free for wind direction [29-30].

2.4. Thermal time-of-flight flow sensor

A Thermal Time-of-Flight (TOF) sensor usually includes one sensing element and one heater. The schematics for the design and the functional block diagram are presented in Figure 5. However, to improve accuracy, it can be designed with three sensing elements. In this configuration, each pair of elements can serve as a TOF sensor. The heater and sensing elements are situated on a thermally insulated membrane.

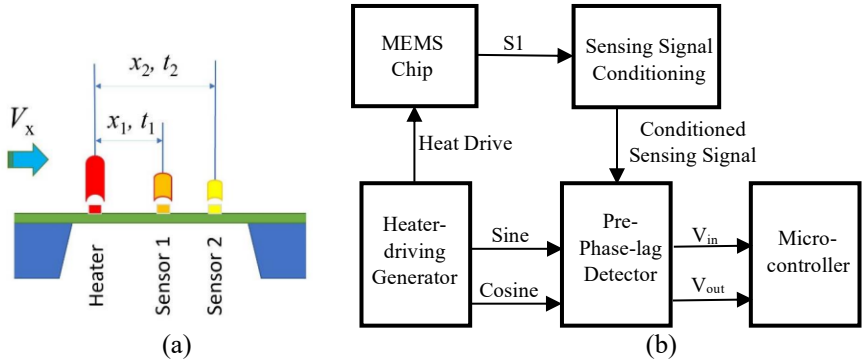

Figure 5. (a) Schematic for the thermal TOF wind sensor [13]
(b) TOF circuit functional block diagram [14].

A single-frequency drive approach is used to measure the phase shift between the heater and sensing element, which is inversely proportional to the flow rate. A heater drive generator excites the heater, a sensing signal conditioner amplifies signals, a Pre-Phase Delay Detector measures phase delay, and a Microprocessor calculates the flow speed based on heat wave travel time.

This method offers high accuracy, noise resistance, and exceptional stability in low flow rate conditions, outperforming other thermal flow sensing technologies in consistency and repeatability [13-14].

3. Proposed 2D NTC Based Wind Measurement Method

Based on the research results obtained from the examination of the designs mentioned in the article, a simulation of the NTC (Negative Temperature Coefficient Thermistor) based wind sensor design was performed as shown in Figure 7. In this design, the wind direction and speed are determined using four NTC thermistors. These sensors are placed in the North (0°), East (90°), South (180°), and West (270°) directions; the analog signals from the NTC sensors are converted to digital data via an ADC and sent to the microprocessor. The microprocessor processes this data to detect the impact of wind on temperature and calculate wind speed and direction. Lateral airflow is greatly reduced by the plus (+) shaped housing covering the 4 sensors (W x H = 1cm x 1cm).

The NTC thermistors are connected to a constant DC voltage source, allowing it to self-heat, with a measuring range of -40°C to 85°C. The resistance R of an NTC thermistor decreases with increasing temperature as given in the Equation (2),

$$\frac{1}{T} = A + B\ln(R) + C\,[\ln(R)]^3 \tag{2}$$

where T is the temperature in Kelvin, R is the thermistor resistance, and A, B, and C are constants derived from measured resistance at different temperatures. Figure 6 shows the temperature-resistance relationship of the NTC thermistor. As the temperature increases, the resistance decreases rapidly.

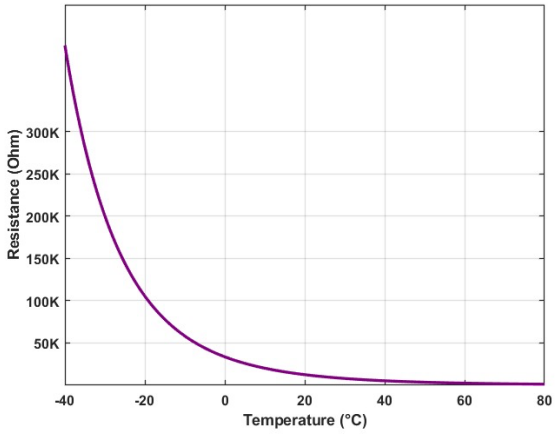

Figure 6. NTC Resistance - Temperature variation.

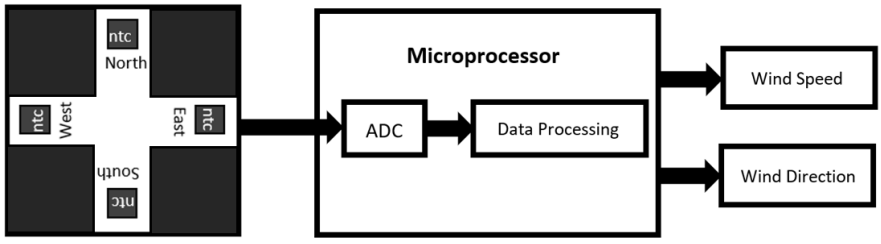

Figure 7. NTC Based wind sensor design.

When wind passes over a thermistor, it cools the thermistor, leading to a decrease in its resistance. As wind speed increases, the thermistor's resistance decreases further, and the current flowing through it increases accordingly. This behavior allows the estimation of wind speed based on current changes. The thermistor with the highest current among the four directions indicates the primary direction of the wind, providing the most accurate data for determining wind speed.

A simulation for this design was performed using MATLAB. Firstly, test data for different wind speeds (from 0 m/s to 30 m/s) and directions (0°, 90°, 180°, and 270°) are created and environmental parameters such as maximum temperature drop and minimum wind speed are defined. For each combination of wind speed and direction, wind speed and direction estimations are completed using temperature data from the four sensors.

Current values obtained from the NTC thermistor, which is selected for measuring wind direction, are converted to wind speed using a pre-established calibration curve. During calibration, Equation (3) is created based on current values (a, b and c) measured at specific wind speeds where I (T,v) The current (mA) depends on wind speed (v) and temperature (T)

$$I(T, v) = a(T).\ln(v + b) + c(T) \tag{3}$$

The constants a, b and c are determined through a calibration process; a is the temperature dependent sensitivity coefficient, b is a constant representing the minimum offset of the velocity and c is the temperature dependent offset current. During calibration, the system is tested at known wind speeds, and the corresponding current values are measured for each speed. For example, a current of 1.2 mA is measured at a wind speed of 2 m/s and 3.5 mA at a wind speed of 10 m/s. These values are used to create an equation. These constants are then used throughout the simulation to accurately estimate wind speed from the measured current values.

Wind direction is determined based on the temperature values of the sensors in the four directions. The sensor in the direction of the wind experiences the most cooling and shows the lowest temperature. Thus, the direction of the sensor with the lowest temperature was accepted as the wind direction. For example, if the sensor in the north shows the lowest temperature, it is concluded that the wind is coming from the north.

For each speed and direction combination, the estimated wind speed and direction is compared with the actual (known) values. The error rate between the estimated and actual wind speed is calculated and results for each wind speed and direction combination are recorded in a table. This table includes actual wind speed, actual direction, estimated wind speed and direction, speed and direction error rates, and temperature values for the four directions.

4. Experimental and Simulation Results

During the simulation, the resistance of the NTC sensors varied in response to temperature changes, and this variation was used to calculate wind speed based on the applied formulation. The simulation was conducted for different temperature and wind speed conditions, yielding the following sample results:

Table 1. Sample values and results of the simulation.

Wind Speed (m/s)	Wind Direction (°)	Computed Wind Speed (m/s)	Computed Wind Direction (°)	Wind Speed Error Rate (%)	Temp. (North) (°C)	Temp. (South) (°C)	Temp. (East) (°C)	Temp. (West) (°C)
2	0	1.99	0	0.05	24.54	24.58	25	25.01
4	90	3.97	90	0.75	23.94	23.87	24.01	23.98
6	180	5.93	180	1.14	22	22.37	21.74	22.2
8	270	7.91	270	1.63	20.89	21.01	21	20.61
10	0	9.85	0	1.42	18.54	18.58	19	19.01
12	90	11.74	90	2.14	16.94	16.86	17.1	17.3
14	180	13.67	180	2.32	16	16.01	15.58	16.02
16	270	15.78	270	1.73	14.89	15.01	15	14.61

Figure 8 (a) illustrates the relationship between actual wind speeds (v_{actual}) and computed wind speeds (v_{computed}) based on Table 1 using the linear model given in Equation (4);

$$v_{computed} = a.v_{actual} + b = (0.9786).v_{actual} + 0.0479 \tag{4}$$

The computed speeds align closely with the ideal line ($v_{computed}$=v_{actual}).

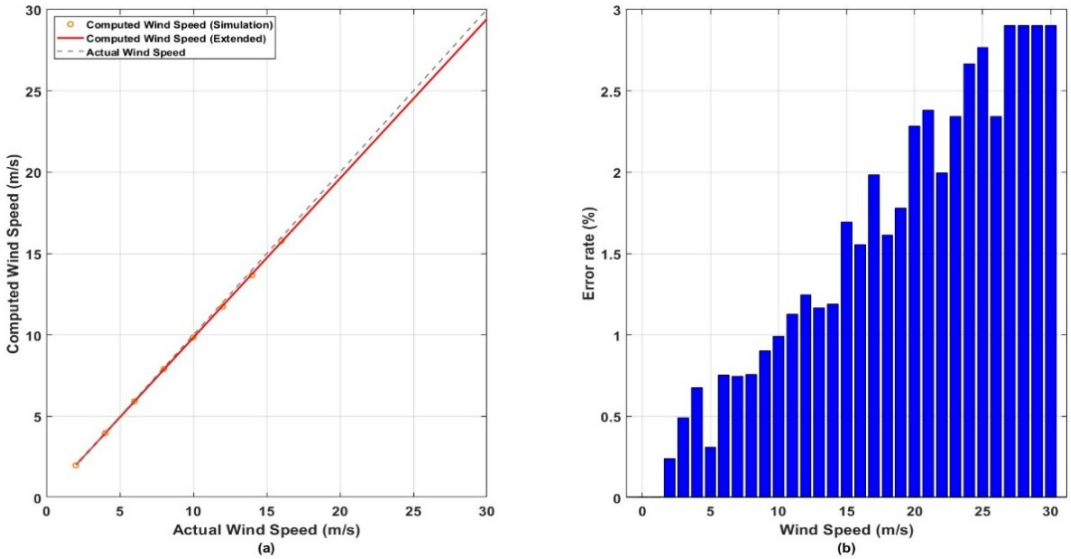

Figure 8. (a) Simulation results for actual and calculated wind speed measurements, (b) Simulation results for wind speed measurements error rates

Considering the variations in Figure 8 (a), the orange points represent the computed wind speeds derived from the system, while the red line extends the computed values to higher wind speeds (up to 30 m/s). The dashed gray line represents the ideal relationship where computed and actual speeds are equal. The close alignment of the orange points and the red line with the ideal line demonstrates the system's accuracy in estimating wind speeds, even at extended ranges. While in Figure 8 (b), the graph highlights the error rates for different wind speeds (1m/s – 30 m/s), represented by blue bars. The error rates remain below 3% across the tested wind speeds, with slight variations. The gradual increase in error rates at higher wind speeds suggests the system maintains reliable performance with only minimal deviations. This consistency reflects the system's robustness and precision in both low and high wind speed conditions.

Figure 9 shows the relationship between wind speed and current at different temperatures. As wind speed increases, current decreases. At higher temperatures, the current is higher, while at lower temperatures, it is lower. This allows for analyzing the system's performance based on wind speed and temperature

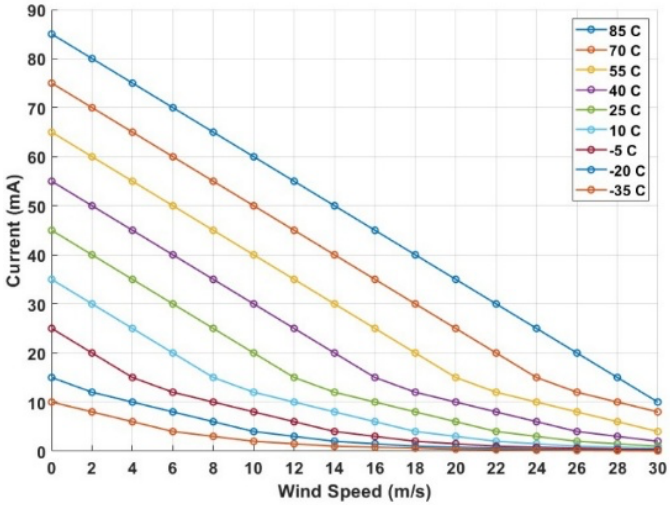

Figure 9. Expected temperature response according to simulation for different temperatures.

Figure 10 shows the test setup of an electronic circuit board, including a power supply, a fan, the circuit board, and a laptop to receive the processed data. The temperature analog data obtained from the 4 NTC thermistors is converted into digital values using the ADC module of the STM32 microcontroller, and then the wind data is processed. The data is transmitted to the computer via the UART protocol using the UART-USB converter.

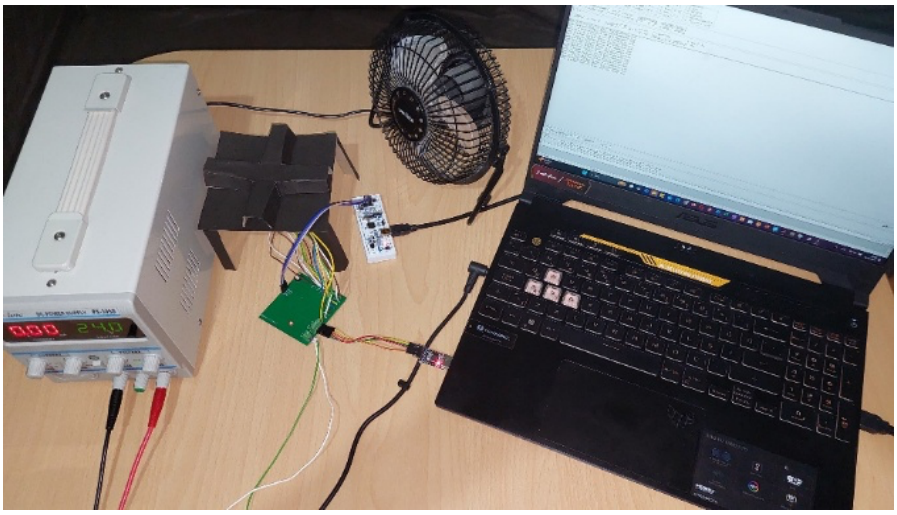

Figure 10. Electronic board and test setup.

The results of the wind direction measurement experiment in Table 2 conducted at a wind speed of 2 m/s, demonstrate that the computed wind direction aligns accurately with the actual wind direction in all instances. The sensor positioned in the direction of the wind consistently records the lowest temperature due to the cooling effect of the wind, with only small temperature differences observed between directions. This highlights effective calibration and reliable performance in detecting wind direction based on temperature variations.

Table 2. Sample values and results of the test (at 3 m/s).

Actual Wind Direction (°)	Computed Wind Direction (°)	Temp. (North) (°C)	Temp. (South) (°C)	Temp. (East) (°C)	Temp. (West) (°C)
0	North (0)	24.44	25	24.53	25.21
90	East (90)	24.89	25	24.79	25.21
180	South (180)	25	24.74	25.93	25.19
270	West (270)	24.96	24.83	25.90	24.61

5. Discussion

This system's low cost and straightforward design offer a solution for applications with limited volume. Unlike typical wind sensors, it doesn't require mechanical components, preventing problems like mechanical wear. Furthermore, NTC sensors are perfect for long-term monitoring applications due to their low energy consumption. More sophisticated algorithms and optimizations can be used to further increase the accuracy of the system. Table 1 summarizes the data obtained from the simulation for different wind speeds and directions. For each test, the actual and calculated wind speed and direction, error rates, and temperature values measured in four directions (north, south, east, west) are presented. The error rate between actual and calculated values generally remained below 3%, indicating that the system operates with high accuracy. According to the table, the sensor in the direction of the wind recorded the lowest temperature, demonstrating the system's ability to accurately determine wind direction. An experimental method was carried out to validate the system at a wind direction of 25° and a speed of 2 m/s. However, testing for different wind speeds and different temperatures would require higher costs and the procurement of necessary testing equipment. Which may be done in the next step. Table 2 summarizes the data obtained from the experiment for different wind directions. The actual and computed wind directions are

consistent, indicating a low error rate. In each case, the sensor facing the wind recorded the lowest temperature, demonstrating the system's ability to accurately detect wind direction. The results confirm that the system operates with high accuracy and precision. A comparison is also conducted between the proposed design and different sensor designs based on parameters in Table 3.

Table 3. Comparison table of the examined sensor designs.

Parameter	2-D Thermal Flow Sensor	MEMS 2-D Thermal Wind Sensor	Octagon-Shaped 2-D Thermal Wind Sensor	NTC Segmented Thermistor-Based Anemometer	Thermal Time-of-Flight (TOF) Flow Sensor	2D NTC-Based Anemometer (proposed work)
Maximum Wind Speed (m/s)	40	40	33	15	30	30
Minimum Wind Speed (m/s)	0	0	0	1	0	1
Error Rate (%)	±3	±2 Speed ±3 Direction	±1 Speed ±1.5 Direction	±3	±2.5	±3

Some positive and negative aspects of all methods are discussed here. The 2-D Thermal Flow Sensor is compact with high sensitivity but struggles at low temperatures and power efficiency. The MEMS 2-D Thermal Wind Sensor offers precision via a double Wheatstone bridge but may face instability at high wind speeds. The Octagon-Shaped 2-D Sensor ensures real-time accuracy but has complex packaging challenges. The NTC Segmented Anemometer is low-cost and simple but experiences heating and cooling delays. The TOF Flow Sensor is reliable and sensitive but affected by humidity. The proposed 2D NTC-Based Anemometer is energy-efficient and cost-effective but may have thermal response delays.

6. Conclusion

Thermal-based flow sensors provide high sensitivity, accuracy, and energy efficiency. However, there is room for improvement in thermal insulation design to enhance its performance at low temperatures. Data obtained using the phase delay detection method showed stability in low flow rate ranges compared to other thermal flow sensing technologies, which experienced significant fluctuations. Implementing new modulation techniques and low-power consumption circuits can help reduce energy consumption. Furthermore, advanced calibration techniques can be developed for more accurate measurements under different environmental conditions. In this study, different thermal flow sensor designs reported in the literature are reviewed, and a novel method based on 2 dimensional NTC sensor is proposed. The sensor operated with a delay of 2-3 minutes at 25°C. During the experiments, wind speed was measured between 1 m/s and 16 m/s, and the minimum measured wind speed was determined as 1 m/s. According to the results, actual and calculated wind speed measurements are well matched, and the maximum wind speed error observed is less than %3. Looking ahead, there is a need for these sensors to be designed to perform reliably over a wider temperature range and be suitable for use in various application areas. New modulation techniques and low-power consumption circuits could be utilized to increase the efficiency. Environmental factors significantly impact the performance of the anemometer, such as temperature, humidity, and heat loss. Temperature variations affect thermistor sensitivity, while heat loss impacts accuracy, particularly at lower temperatures. Design improvements, such as better thermal insulation and optimized thermistor materials, are suggested to enhance performance in extreme conditions.

References

[1] Aleksic SO, Mitrovic NS, Nikolic Z, Lukovic MD, Obradovic NN. Lukovic S. G. Three-Axis' Heat Loss Anemometer Comprising Thick-Film Segmented Thermistors. IEEE Sens J 2019; 19 (22): 10228-10235.

[2] Gutarra JS, Gastelo-Roque JA, Sulluchuco J. A cup anemometer using 3D additive manufacturing. 2020 IEEE 27th Int. Conf. Electron Electr Eng Comput (INTERCON); 03-05 September 2020; Lima, Peru.

[3] Perez del Valle, M, Urbano Castelan JA, Matsumoto Y, Cortes Mateos R. Low Cost Ultrasonic Anemometer. 2007 4th Int Conf Electr Electron Eng (ICEEE); 05-07 September 2007; Mexico City, Mexico. 213-216.

[4] Le Duff A, Plantier G, Gazengel B. Real-Time Particle Detection and Velocity Measurement by Means of Laser Doppler Velocimetry. 2005 IEEE Instrum Meas Technol Conf (IMTC); 16-19 May 2005; Ottawa, ON, Canada. 2222-2225.

[5] Chen J, Liu C. Development and characterization of surface micromachined, out-of-plane hot-wire anemometer. J Microelectromech Syst 2003; 12 (6): 979-988.

[6] Wang, S, Yi Z, Qin M, Huang QA. Temperature effects of a ceramic mems thermal wind sensor based on a temperature-balanced mode. IEEE Sens J 2019; 19 (17): 7254–7260.
[7] Zhu Y, Qin M, Huang J, Yi Z, Huang Q. Sensitivity Improvement of a 2D MEMS Thermal Wind Sensor for Low-Power Applications. IEEE Sens J 2016; 16 (11): 4300-4308.
[8] Makinwa KAA, Huijsing JH. A wind-sensor interface using thermal sigma-delta modulation techniques. Sens Actuators A Phys 2001; 92 (1-3): 280-285.
[9] Sosna C, Buchner R, Lang W. A temperature compensation circuit for thermal flow sensors operated in constant-temperature-difference mode. IEEE Trans Instrum Meas 2010; 59 (6), 1715–1721.
[10] Que RY, Zhu R, Que QZ, Cao Z. Temperature compensation for thermal anemometers using temperature sensors independent of flow sensors. Meas Sci Technol 2011; 22.
[11] Nguyen NT, Kiehnscherf R. Low-cost silicon sensors for mass flow measurement of liquids and gases. Sens Actuators A Phys 1995; 49 (1-2): 17-20.
[12] Gao S, Yi Z, Ye Y, Qin M, Huang QA. Temperature Effect and Its Compensation of a Micromachined 2-D Anemometer. IEEE Sens J 2019; 19 (14): 5454–5459.
[13] Huang L. Micromachined Thermal Time-of-Flight Flow Sensors and Their Applications. Micromachines (Basel). 2022; 13 (10): 1729.
[14] Yao Y, Chen C, Wu X, Huang L. MEMS Thermal Time-of-Flight Flow Meter. 15th Flow Meas Conf (FLOMEKO); 13-15 October 2010; Taipei, Taiwan.
[15] Matova SP, Makinwa KAA, Huijsing JH. Compensation of Packaging Asymmetry in a 2-D Wind Sensor. IEEE SENSORS 2002; 12-14 June 2002; Orlando, FL, USA. 1256-1259.
[16] Nam T, Kim S, Park S. The temperature compensation of a thermal flow sensor by changing the slope and the ratio of resistances. Sens Actuators A Phys 2004; 114 (2-3): 212-218.
[17] Makinwa KAA, Huijsing JH. A wind sensor with an integrated low-offset instrumentation amplifier. 2001 8th IEEE Int Conf Electron., Circuits Syst (ICECS); 02-05 September 2001; Malta, Malta. 1505-1508.
[18] Van Putten AFP, Van Putten MJAM, Van Putten MHPM. Silicon thermal anemometry: developments and applications. Meas Sci Technol 1996; 7: 1360-1377.
[19] Yi Z, Ye Y, Qin M, Huang Q. Modeling of Packaged MEMS Thermal Wind Sensor Operating on CP Mode. IEEE Trans Electron Devices 2019; 66 (5): 2375-2381.
[20] Kim S, Nam T, Park S. Measurement of flow direction and velocity using a micromachined flow sensor. Sens Actuators A Phys 2004; 114 (2-3): 312-318.
[21] Que RY, Zhu R, Wei QZ, Cao Z. Temperature compensation for thermal anemometers using temperature sensors independent of flow sensors. Meas Sci Technol 2011; 22.
[22] Gao S, Yi Z, Ye Y, Qin M, Huang QA. Configuration of a Self-Heated Double Wheatstone Bridge for 2-D Wind Sensors. J Microelectromech Syst 2018; 28 (1): 125-130.
[23] Dong Z, Huang Q, Qin M. Thermal Asymmetry Compensation of a Wind Sensor Fabricated on Ceramic Substrate. IEEE SENSORS 2010; 01-04 November 2010; Waikoloa, HI, USA. 595-599.
[24] Ye Y, Yi Z, Gao S, Qin M, Huang Q. Octagon-Shaped 2-D Micromachined Thermal Wind Sensor for High-Accurate Applications. J Microelectromech Syst 2018; 27 (4): 739-747.
[25] Chen B, Zhu Y, Qin M, Huang Q. Effects of Ambient Humidity on a Micromachined Silicon Thermal Wind Sensor. J Microelectromech Syst 2014; 23 (2): 253-255.
[26] Dong Z, Chen J, Qin Y, Qin M, Huang Q. Fabrication of a Micromachined Two-Dimensional Wind Sensor by Au–Au Wafer Bonding Technology. J. Microelectromech. Syst 2012; 21 (2): 467-475.
[27] Fritsch S, Sarrias J, Brieu M, Couderc JJ, Baudour JL, Snoeck E, Rousset A. Correlation between the structure, the microstructure and the electrical properties of nickel manganite negative temperature coefficient (NTC) thermistors. Solid State Ion 1998; 109 (3-4): 229-237.
[28] Aleksic OS, Maric VD, Zivanov LD, Menicanin AB, A Novel Approach to Modeling and Simulation of NTC Thick-Film Segmented Thermistors for Sensor Applications. IEEE Sens J 2007; 7 (10): 1420-1428.
[29] Menicanin AB, Aleksic OS, Nikolic MV, Savic SM, Radojcic BM. Novel Uniaxial Anemometer Containing NTC Thick Film Segmented Thermistors. 2008 26th Int Conf Microelectron (MIEL); 11-14 May 2008; Nis, Serbia and Montenegro.
[30] Aleksic O, Radojcic B, RamovicR. Electrode Effect on NTC Planar Thermistor Volume Resistivity. 2006 25th Int Conf Microelectron (MIEL); 14-17 May 2006; Belgrade, Serbia.

Turkish Journal of Science & Technology
20(1), 235-248, 2025

Research Paper
https://doi.org/10.55525/tjst.1563258

Dangerous Goods Detection and Warning Approach Based on Image Processing Techniques

Fatma Betül OKUR[1*], Can EYÜPOĞLU[2]

[1] Department of Computer Engineering, Atatürk Strategic Studies and Graduate Institute, National Defence University, İstanbul, Türkiye.

[2] Department of Computer Engineering, Turkish Air Force Academy, National Defence University, İstanbul, Türkiye.

[*1] fbetyildiz@gmail.com, [2] can.eyupoglu@msu.edu.tr, caneyupoglu@gmail.com

(Geliş/Received: 09/10/2024; Kabul/Accepted: 14/02/2025)

Abstract: Hazardous substances are widely used in many sectors such as industry, logistics, agriculture and energy, but they carry potentially serious risks. Accurate identification of these risks before the materials start transportation processes is critical to prevent potential accidents and minimize risks. This study presents an approach to preventing accidents that may occur in the transport of dangerous goods to ensure rapid, effective intervention in case of possible accidents and to take early precautions. Optical Character Recognition (OCR) technology, one of the image processing techniques, is used in the study. Dangerous goods labels were detected with the help of OCR algorithms and the texts on the label were successfully detected. The detected texts, especially the United Nations (UN) numbers specific to hazardous substances, were matched with a previously created database. Based on the UN numbers matched with the database, the properties of the relevant substance, response conditions, precautions to be taken and other critical information were retrieved from the database and presented to the users. This information is matched with visual outputs and transferred to the user through warning systems. In the study, a dataset of 600 images containing hazardous material labels with various background conditions was used. In the tests performed on the dataset, the performance of the system was evaluated by calculating accuracy metrics. The results show the effectiveness of the OCR-based approach in detecting and processing hazardous material labels. This study provides an important contribution for safe transportation and rapid response processes, especially in large-scale logistics operations.

Key words: Image processing, dangerous goods, optical character recognition.

Görüntü İşleme Tekniklerine Dayanan Tehlikeli Madde Tespit ve Uyarı Yaklaşımı

Öz: Tehlikeli maddeler, sanayi, lojistik, tarım ve enerji gibi birçok sektörde yaygın olarak kullanılmakla birlikte, potansiyel olarak ciddi riskler taşımaktadır. Bu risklerin, maddeler taşımacılık süreçlerine başlamadan önce doğru bir şekilde belirlenmesi, olası kazaların önlenmesi ve risklerin minimize edilmesi açısından kritik öneme sahiptir. Bu çalışma, tehlikeli madde taşımacılığında meydana gelebilecek kazaların önlenmesi, olası kaza durumlarında hızlı, etkili müdahale sağlanması ve erken önlem alınmasına yönelik bir yaklaşım sunmaktadır. Çalışmada, görüntü işleme tekniklerinden biri olan Optik Karakter Tanıma (Optical Character Recognition-OCR) teknolojisi kullanılmıştır. Tehlikeli madde etiketleri OCR algoritmaları yardımıyla tespit edilmiş ve etiket üzerindeki metinler başarılı bir şekilde algılanmıştır. Algılanan metinler, özellikle tehlikeli maddelere özgü Birleşmiş Milletler (United Nations-UN) numaraları, önceden oluşturulan bir veri tabanı ile eşleştirilmiştir. Veri tabanı ile eşleştirilen UN numaraları üzerinden, ilgili maddeye ait özellikler, müdahale koşulları, alınması gereken önlemler ve diğer kritik bilgiler veri tabanından alınarak kullanıcılara sunulmuştur. Bu bilgiler, görsel çıktılarla eşleştirilerek uyarı sistemleri aracılığıyla kullanıcıya aktarılmıştır. Çalışmada, tehlikeli madde etiketlerini içeren ve çeşitli arka plan koşullarına sahip 600 adet görselden oluşan bir veri seti kullanılmıştır. Veri seti üzerinde yapılan testlerde, doğruluk metrikleri hesaplanarak sistemin performansı değerlendirilmiştir. Elde edilen sonuçlar, OCR tabanlı yaklaşımın tehlikeli madde etiketlerinin algılanması ve işlenmesindeki etkinliğini göstermiştir. Bu çalışma, özellikle büyük ölçekli lojistik operasyonlarında, güvenli taşıma ve hızlı müdahale süreçleri için önemli bir katkı sunmaktadır.

Anahtar kelimeler: Görüntü işleme, tehlikeli madde, optik karakter tanıma.

1. Introduction

Dangerous goods are encountered in many areas of daily life and are transported to the relevant points through various transport routes. These substances are generally transported by different transport methods such as road, maritime, railway and airway, and urban transport is mostly carried out by road. The vehicles used in the transport of dangerous goods and the materials transported are identified by dangerous goods labels issued in accordance with international standards. These standards are determined depending on the mode of transport and the risks involved in the transported material and require compliance with internationally accepted regulations [1]. Due to the nature of the transported material, potential hazards can pose significant risks to both people and the

* Corresponding author: fbetyildiz@gmail.com. ORCID Number of authors: [1] 0009-0008-6310-4524, [2] 0000-0002-6133-8617

environment. Therefore, many factors such as human factors, organizational processes, equipment used and safety measures taken play a critical role in the transport of dangerous goods. Various analysis methods are used to identify and manage these risks. For example, Quality Function Deployment (QFD) method can be used as an effective tool for the assessment and prioritization of risks in the transport of hazardous materials [2]. In the transport of dangerous goods, the safety of people and property is always considered as a priority issue. All individuals and organizations involved in the transport process are obliged to act in accordance with internationally recognized agreements, applicable laws and regulations. These regulations provide a framework based on detailed provisions to ensure safety and responsibility during transport. An example of a template based on transport-related provisions is presented in Figure 1 [3].

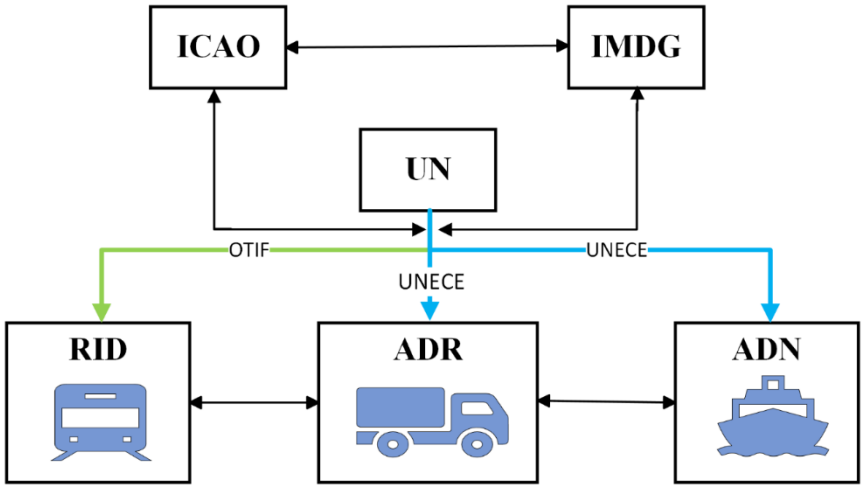

Figure 1. International regulations in the transport of dangerous goods.

The transport of dangerous goods is a critical part of international trade and is controlled by various international regulations to ensure environmental and human safety. These regulations have been developed by different organisations according to the modes of transport. While UNECE (United Nations Economic Commission for Europe) sets the standards for ADR (European Agreement Concerning the International Carriage of Dangerous Goods by Road) for road transport and ADN (European Agreement Concerning the International Carriage of Dangerous Goods by Inland Waterways) for inland waterways transport, OTIF (Intergovernmental Organisation for International Carriage by Rail) establishes the regulations for railway transport within the scope of RID (Regulations Concerning the International Carriage of Dangerous Goods by Rail). The UN provides the basic model regulations for all regulations. UNECE develops both ADR and ADN regulations. The OTIF organisation establishes the RID regulation. ICAO (International Civil Aviation Organization) and IMDG CODE (International Maritime Dangerous Goods Code) develop specialised regulations to implement these rules in air and maritime transport respectively. These regulations aim to minimise risks and promote safe transport by providing common standards for the classification, packaging and transport of dangerous goods. A summary template is presented in Figure 1 within the scope of these regulations.

- UNECE → ADR
- OTIF → RID
- UNECE → ADN
- ICAO → ICAO-TI (Technical Instructions for the Safe Transport of Dangerous Goods by Air)
- IMO (International Maritime Organization) → IMDG

There are many hybrid studies in the literature to reduce the risks during the transportation of hazardous materials and precautions should be taken in advance to reduce these risks [4]. For this purpose, the proposed study detects the UN number of hazardous substances with image processing technique. By matching the detected UN number with the data in the database simultaneously, information such as response actions against the hazardous substance, cleaning of the substance, hazards of the substance, first aid and properties of the substance are obtained. Due to the increase in the demand for hazardous material transportation in recent times, it brings along some risks [5]. In order to prevent accidents, to evaluate and identify some of the basic factors that constitute the risks among

themselves and to prevent accidents in the world from happening again, measures should be taken for hazardous materials within the scope of the purpose [6].

Image processing techniques are used for various purposes according to the topics investigated. Labels identifying the properties of hazardous substances can be detected with an image processing technique. One of the studies on this subject tried to detect hazardous substance labels using two techniques [7]. Hazardous substance label detection has also been done by applying the HND-Net method [8]. At the same time, there are studies in literature that publish large data sets for hazardous substance labels [8]. In this study, the importance of hazardous materials is emphasized. In addition to using image processing methods to detect the labels of hazardous substances, it is also possible to determine what the hazardous substance is [9]. In another study, Optical Character Recognition (OCR) technology was developed in hybrid technology that reads labels using OD technology [10]. In addition, Shahin et al. [11] proposed an MBID-based OCR model to extract label information visible in images captured by a fixed camera in an industrial environment. Their proposed system used an approach to process illumination variations in images including low contrast, distorted, darker and brighter images. Artificial intelligence-based studies are also available in the literature [12]. More comprehensive OCR studies and reviews can be found in the research paper by Memon et al. [13] and other studies published in the literature. According to literature studies, there are gaps in hazardous substances to reduce risks [4]. The proposed approach enables automatic detection of hazardous material labels and simultaneous display of precautionary and response information. It provides an effective approach and instant information for the detection of hazardous substances. A robust and efficient approach for the detection of hazardous substance labels must be created. For this, a warning and prevention approach based on OCR is proposed. Diversification of the dataset and evaluation of the accuracy metrics are crucial for the proposed approach to work efficiently and achieve robust and reliable results. In the field of image processing, hazardous material detection serves several critical purposes, including security and environmental monitoring. Furthermore, the study evaluating the performance of image matching methods for hazardous material detection has contributed to the development and evaluation of this work, providing valuable insights into the effectiveness of such approaches [14]. The main contributions of this study are summarized as follows:

- In existing literature, there is a limited number of studies on automatic detection of hazardous material labels. The application of OCR technologies to this field is rare, especially in hazardous material transport and emergency response. This paper fills this gap and presents a system for both text detection and hazardous material feature identification.
- Tesseract makes an important contribution to literature by demonstrating the use of OCR technologies such as EasyOCR and EAST in a specific application area such as hazardous material detection. Such specific applications extend the potential of OCR in different sectors.
- Many OCR studies in the literature have been tested with images captured under relatively clean and ideal conditions. However, this study examined the detectability and accuracy of hazardous material labels in practical scenarios using a challenging dataset. This gives better validity to the real world.
- Accurate and fast identification of dangerous goods information is vital in emergency situations. The study provides a solution to fulfil this requirement, aiming to reduce response times and increase safety.
- The system offers not only text detection, but also additional functionalities such as the identification of hazardous substances via a database and the provision of warning information. This is a unique solution in the field of industrial safety and logistics.
- This technology has many ready-made libraries and software tools. It is the most suitable and simplest solution method for the detection of a fixed hazardous substance label without requiring any technology. Methods such as deep learning were not preferred since any complex solution proposal would affect the functioning of the system.

This study fills a gap in literature and offers significant original value in areas such as hazardous materials management and emergency response. It also provides a starting point that can contribute to technological progress by providing the infrastructure for future automated systems.

1.1. Review of Label Identification Technologies: Why OCR?

When the studies in the field of OCR are examined in literature, there are other methods used depending on some technologies. When these methods are analyzed in terms of their advantages and disadvantages in Table 1, the reason for the preference of the OCR technology used in the study is clearly seen. Comparisons are available below:

1. **RFID (Radio Frequency Identification):**
   Advantage: Dangerous goods labels can be detected faster if they have RFID tags on them. RFID can be considered more reliable, especially when the physical condition of the labels is poor or the visibility is reduced [15].
   Disadvantage: However, RFID tags may not be available on every hazardous material and installing this system may require higher costs.

2. **Barcode and QR Code Based Identification:**
   Advantage: Barcodes and QR codes enable quick extraction of information from visual data. In addition, the accuracy of these codes is generally high.
   Disadvantage: Hazardous substance labels may not always have these codes. Also, the majority of existing labels are text-only, making the use of OCR more logical.

3. **Image Recognition with Machine Learning:**
   Advantage: With deep learning techniques, elements such as shapes, colors or symbols in tags can be detected at a more complex level. Thus, not only text but also symbols and color coding can be recognized.
   Disadvantage: Machine learning-based image recognition requires large data sets and lengthy training processes. The probability of false positive and negative results is higher than with OCR. OCR is faster and generally more accurate in text-based systems.

4. **Manual Control and Manual Identification:**
   Advantage: Manual checks and identification by the human eye ensure accurate label reading and flexibility in complex situations.
   Disadvantage: This method is time-consuming and prone to human error. Manual control is not sustainable in large-scale operations. Preferring automated methods (such as OCR) over manual identification is more advantageous in terms of speed and accuracy.

5. **Dangerous Goods Labeling Detection with Internet of Things:**
   Internet of Things (IoT) devices enable the detection of hazardous substance labels using wireless technologies such as sensors and radio frequency. Using technologies such as RFID, sensors and smart tags, hazardous materials can be continuously monitored.
   Advantage: IoT devices can continuously monitor the location and condition of hazardous materials from anywhere in the world. Through RFID tags or sensors, environmental conditions such as temperature, humidity, vibration can be monitored, enabling the safe transportation and storage of hazardous materials by controlling businesses with a large supply chain or distribution network. IoT systems continuously collect and analyze data without the need for human intervention. It reduces human error and automates processes.
   Disadvantage: IoT systems often require high hardware and infrastructure costs. Elements such as RFID tags, sensors, network connectivity and data storage solutions are costly. IoT-based systems can be complex to deploy and require constant maintenance and monitoring. Securing networked devices can also create an extra workload. IoT devices can be vulnerable to cyber-attacks. Security vulnerabilities in monitoring and managing hazardous material labels can pose a significant threat.

Table 2 presents comparative performance metrics of methods based on OCR technology used in different studies in the literature. This table provides researchers with information about which methods are more effective in which contexts by evaluating different studies with metrics such as accuracy, success rate, error rate. The table aims to guide research and development in this field by providing a comprehensive comparison of how OCR technology performs in various application areas. This data is an important reference for researchers to identify the strengths and weaknesses of existing methods.

Table 1. Methods used in literature.

Technology	Real-time	Data Types	Accuracy	Scalability	Security	Flexibility
OCR	Not in real time	Text-based data	Medium; good label cleaning and pre-treatment	Limited; difficult at high throughput (our data is fixed)	Low risk; image data only	Limited; restricted to certain text formats
IoT	Real-time data monitoring and notification	Various types of data (sensor data, location data, etc.)	High; dependent on sensor accuracy	High; many devices can be added	High risk; cyber security vulnerabilities	High; adaptable to a wide range of applications
RFID	Real-time, instantaneous data reading	Tag data, location data	High; depends on the condition of the label and the reader	Medium; many objects can be identified	Medium risk; requires physical security	Medium; limited uses
Machine Learning	Not in real time	Various data types (image, audio, text)	High, depending on the training data set	High; continuously updatable with new data	Medium risk; safety of the model is important	High; applicable in different areas
Deep Learning	Often not in real time	Wide range of data types (image, audio, text)	High; better with big data	High; expandable with new data	Medium risk; model security and data privacy are important	High; adaptable to a wide range of applications
Barcode and QR Code	Real time	Text-based and numeric data	Medium; depends on damage condition	Medium; stores a limited amount of data	Low risk; requires physical security	Low; limited to certain code formats

Table 2. Some comparative metric performance values according to studies based on OCR technology in the literature.

Study	Year	Area	Accuracy
[16]	2023	CNN-Based OCR	90.54% accuracy and 2.53% loss value
[17]	2021	Adobe Acrobat, ABBYY FineReader, Tesseract	ABBYY: ~3%, Tesseract: ~5%
[18]	2023	PyTesseract, Microsoft OCR, Google vision, Google Drive OCR, EasyOCR	PyTesseract: ~5%, EasyOCR: ~2%
[19]	2023	Tesseract, Keras-OCR, EasyOCR,kraken	PyTesseract: ~4%, EasyOCR: ~5%
[20]	2022	GoogleOCR, Tesseract, ABBYY Finereader, Transym	ABBYY: ~5%, Tesseract: ~4%
[21]	2024	EAST, Easy OCR, Keras OCR, and Tesseract OCR	Easy OCR: ~5%, Tesseract: ~6%

The content of the paper is organized as follows. In Section 2, a general framework for hazardous material detection is established and the proposed approach is described. The algorithm and schematic of the approach discuss the details of how it is implemented in practice. Section 3 presents the results and discusses the recommendations and the results obtained are shown in tabular form. Section 4 explains the conclusions of the study and future work.

2. Materials and Methods

In this study, image processing techniques are used to detect hazardous material labels. A hybrid structure was created by combining image processing techniques and OCR techniques. Tesseract, EasyOCR and EAST (Efficient and Accurate Scene Text Detector) libraries are preferred in the proposed approach written in Python. In the proposed project, the data used in image processing is preprocessed and cleaned. The images are read and the UN number of the hazardous substance is extracted from the hazardous substance label with image processing. Previously, a database containing warning information was created for use in the study. The UN number extracted from the hazardous substance matches the relevant data in the database and the information of the substance is displayed. Information such as the hazards of the hazardous substance, first aid information, how to intervene in an emergency, and the previous storage status of the substance were displayed on the screen and transferred to the user. Image processing techniques and OCR techniques were used to match the correct information and achieve a good result. The parameters were tested under different images, platforms and conditions to assess their reliability. The best results and values in the parameters were selected. Speeds and image formats were evaluated.

In order to evaluate the metrics used in OCR technology, the input image is read in the software. The UN number is extracted from the read image with OCR and it is checked whether it correctly accesses the relevant data in the database. If the image does not match, error information is returned with control commands. It is very important to evaluate the accuracy of OCR technologies with appropriate metrics. Evaluation metrics such as Character Error Rate (CER) and Word Error Rate (WER) are used here to evaluate the performance within the system. CER is obtained by comparing the results obtained from OCR technology with the rate of erroneous characters compared to all characters. In an excellent OCR performance, the CER value usually takes values between 0% and 1%. WER is obtained by measuring the ratio of incorrectly detected words compared to the whole text [22].

2.1. Proposed Approach

UN numbers of hazardous substance labels were used for the detection of hazardous substances. First, the hazardous substance labels were detected and then the UN number was obtained by extracting the characters from the detected label. The UN number obtained was matched with the database we had previously created and the relevant data of the dangerous substance was displayed. EAST text detector was used for hazardous substance detection. Then, with the help of EasyOCR, the characters were extracted and displayed on the screen. Pre-processing was done to get better results from the images. Text detection and reading was ensured by bringing them to certain sizes. The reason for choosing the EAST text detector in the first stage is that EasyOCR sometimes gives inaccurate results in text detection. EAST was chosen to make this problem more effective. Both are used in image processing to detect and identify text. However, they have different features. With Tesseract, the textual character is detected and a connection to the database is established with the UN number. All this processing is done in Python language. For the accuracy evaluation, the results obtained from the image given as input and the UN numbers matched in the database are considered. If there are non-matching images in the program, the software generates output with the control commands given in the software. Each image was evaluated according to its output and accuracy values were measured. Figure 2 shows the general flowchart of the proposed approach.

Data collected from different sources were used in the study. Images and result outputs were displayed. The database was structured according to the UN number and information on the precautions and characteristics of the hazardous substance was pre-recorded in the database. The UN numbers extracted from the hazardous substance labels were matched with the corresponding UN number in the database and the warnings, recommendations and precautions related to the hazardous substance were displayed.

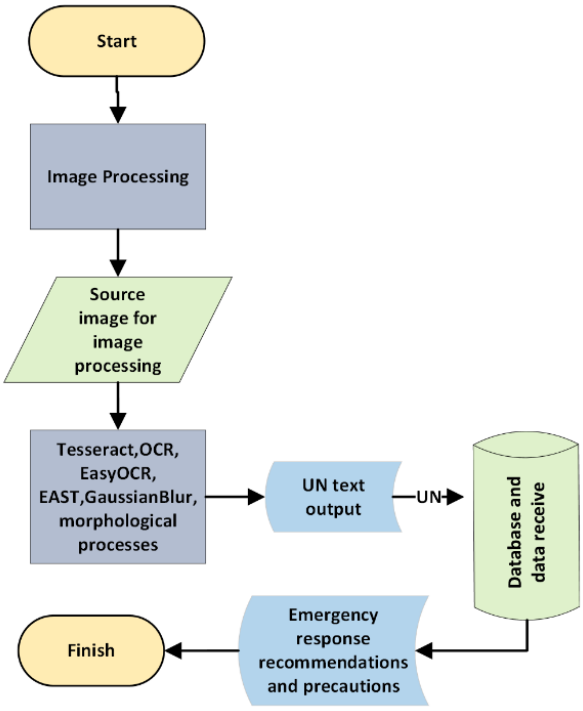

Figure 2. General flowchart of the proposed approach.

2.2. Dataset Description

The dataset used in the study was collected from Google images and websites with datasets [23,24]. The collected dataset was used to match the results for hazardous substance detection and the database created. The data in the database contains similar information such as emergency response situations and substance properties according to the potential risks of the hazardous substance. This study aims to create a warning approach that can produce efficient and reliable results using image processing techniques. After hazardous substance detection, information should be extracted from the database to provide warnings and precautions. In addition, the change in the shape of the images should be determined to be successful on images obtained from bad environmental conditions. The collected data was constructed to fulfil all these requirements and some examples from the dataset are given in Figure 3. The proposed study has made a scientific contribution in terms of the risks of hazardous materials and the precautions to be taken in advance. The dataset consists of 600 images with different backgrounds and taken from different angles [23]. The backgrounds include images of sawdust, wooden floors, images taken in containers, hand-held hazardous material labels and hazardous material labels placed on surfaces such as brick walls. The dataset is based on 8 different combustible materials. Some of the images were obtained in high resolution (5184 x 3456) and in different lighting conditions (dark, bright, blurred). The performance of the presented image processing technique under different conditions is also evaluated.

The images were preprocessed to facilitate hazardous material detection. A series of pre-processing steps were applied to improve the processability of the colour images, which are difficult to read in between. Firstly, the colour images were converted to grayscale (black and white) format so that the analysis is based on intensity information instead of colour information. Gaussian blurring and Otsu thresholding methods were applied on the converted greyscale images. Gaussian blurring reduced the high frequency noise in the image and created a smoother structure. The Otsu thresholding method, on the other hand, allows the detection of prominent objects more easily by determining an automatic threshold according to the intensity values in the image. At this stage, the process was customized by setting manual threshold values. Unnecessary contour areas in the obtained images were filtered and only the areas important for the analysis were left on the image. A resizing step was performed to process the images in a standardized size. In addition, smoothing filters were used to smooth the pixels in certain regions of the images and to obtain a more consistent structure. The removal of noise pixels on the images made certain regions clearer and more distinct. Angular corrections were made for image curvatures to improve

accuracy, especially in edge and contour regions. This helped to remove geometric distortions in the image and provided a more regular structure for analysis. After preprocessing, characters were extracted by image processing. According to the results obtained, the information extracted from the database was displayed.

Figure 3. Sample images from some of the data sets used.

2.3. Image Processing Techniques

In this study, OCR-based image processing techniques are used. OCR is a technology that enables the extraction of text and characters from documents, images or any text-containing sources. It stands out for creating an automated system. Among the OCR-based technologies, EasyOCR, Tesseract and EAST [25] provide different features and outputs. Each model used in OCR technology has its own advantages, disadvantages and differences. However, various challenges such as blurred images, rotated text or images taken from different angles are important factors that can affect the performance of these models. In order to overcome these challenges, OCR models such as Tesseract, EasyOCR and EAST were used to produce image outputs and the results of each step are presented in Figure 4. Figure 4 visualises the preprocessing stages of the image processing and the output of these models during the text extraction process. These results provide an important perspective to understand and compare how different models perform in challenging scenarios. Thus, a more informed assessment of which model is more suitable for a particular application can be made.

Comparative studies of existing models are available. Performance measurements can be analysed through these studies and accuracy values can be examined in detail [26]. Especially by looking at the results presented in Figure 5, the text extraction process and accuracy values can be followed. In Figure 5, the text extraction processes performed using EAST and EasyOCR methods and the accuracy performances of these methods are visualised. This visualisation provides an important reference for understanding the strengths and weaknesses of different OCR models.

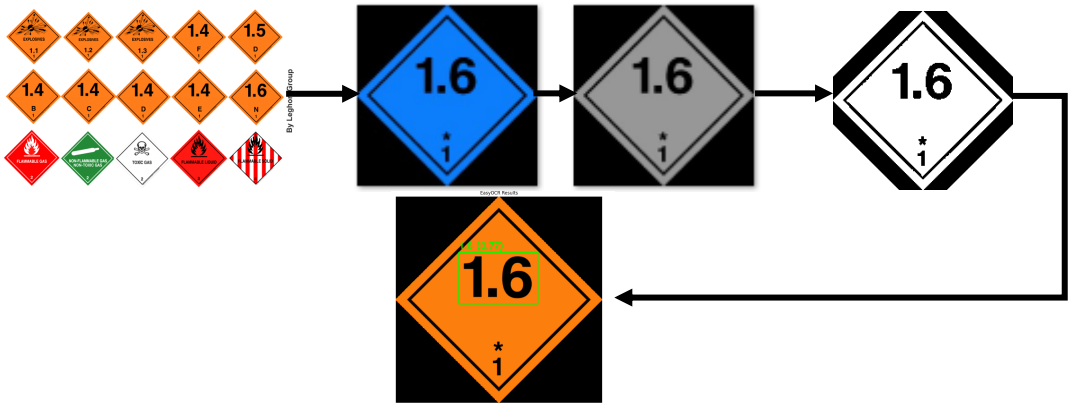

Figure 4. The results of the pre-processing stage of image processing and the image of text extraction using EAST, EasyOCR.

Figure 5. Text extraction and accuracy values using EAST, EasyOCR.

Tesseract OCR is an open-source OCR engine developed by Google. It generally works fast and gives good results in high resolution images. It gives better results in alphabetic character recognition. Some of the hazardous substance labels contain both numeric and textual characters. EasyOCR is Python based and runs under the OpenCV library. In terms of speed, Tesseract runs faster than EasyOCR on CPU, while EasyOCR runs very fast on GPU.

EastOCR works well with noise images. Performance measurements are performed on degraded images [27]. It determines where the text is located. Usually EastOCR is used first, i.e. it detects where the text is on the image. Then the text is recognized using OCR engines (EasyOCR, Tesseract etc.). In this work, detection and recognition are performed separately. In order to achieve better results, the images were resized, blurred according to certain thresholds and some morphological operations were applied.

The relevant image was read in the software. The read image is pre-processed using certain image processing techniques. Image processing techniques were used to output the preprocessed image. The output obtained after image processing is displayed by extracting the relevant data from the database we have created. OCR technologies were created by testing threshold parameters on images. The best threshold values were determined. Figure 6 shows the image processing schematic.

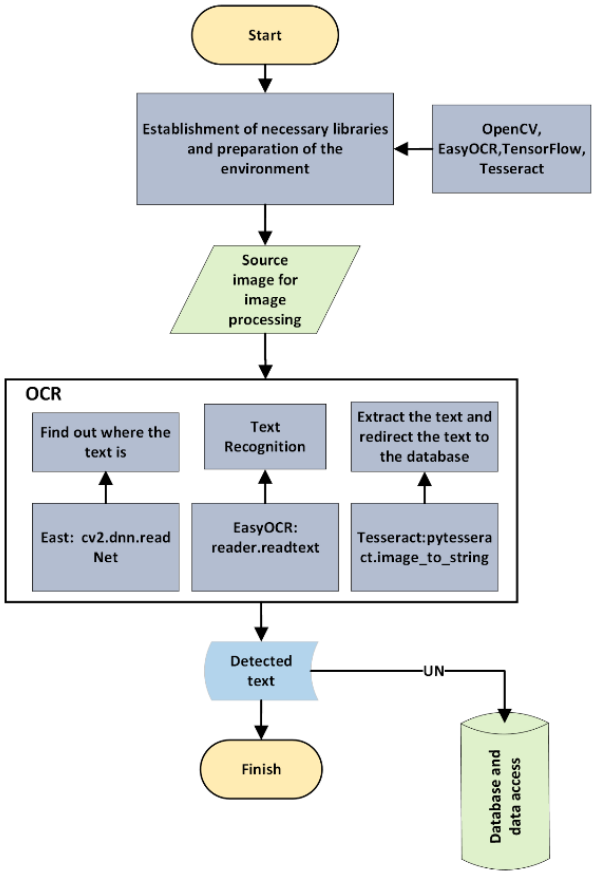

Figure 6. Image processing flowchart.

3. Results and Discussion

OCR technologies are an effective method often used to extract text from images, but they do not always produce perfect results. The accuracy of OCR algorithms is affected by many factors such as image quality, text or characteristic features, image preprocessing techniques and the infrastructural capability of the OCR technology used. For example, OCR systems may have difficulty in finding text in low resolution images, when there is an excess of noise pixels, or when text is skewed, blurred, or on a complex background [28]. Such conditions can lead to misrecognition of characters or word errors in the character recognition process for OCR technologies. This can result in increased character and word error rates, especially when compared to the original texts in the database [29]. Therefore, in OCR-based data extraction systems, it is generally not possible to provide perfect and one hundred per cent accuracy for each data set. However, preparing the collected data in accordance with the same conditions and requirements can increase the consistency and accuracy of the results. For example, significant improvements in OCR accuracy have been observed when preprocessing techniques such as thresholding, noise removal, image resizing and text straightening are used [30]. Research on reducing the error rates of OCR systems is ongoing [31]. In particular, deep learning-based OCR algorithms use more complex network structures and data enrichment techniques to improve text recognition accuracy [32]. However, in order to detect and correct errors that occur during the text extraction process, error analysis methods have been developed that compare OCR outputs with the original texts stored in the database. Such comparisons enable the calculation of character and word-based error rates and the evaluation of system performance. In conclusion, effective preprocessing steps and modern algorithms need to be developed to improve the accuracy of OCR technologies and reduce errors. In particular, when working with data collected and processed at the same thresholds, the results are expected to be more consistent and accurate. In this context, efforts to improve OCR accuracy are ongoing and improvements in the information retrieval process may offer more advanced solutions in the coming years.

The application of OCR technologies to detect the safety precautions and labelling information of dangerous goods has become an important research area in recent years. In this study, EasyOCR, EAST and Tesseract OCR methods are used for the detection of hazardous substance labels and their performances are evaluated. The aim of the study is to improve the accuracy of textual information obtained from visual labels and to contribute to safety measures by matching this information with critical details of hazardous substances in a database. In the study, data was collected from 600 images obtained under different conditions and these images were processed using OCR technologies. The outputs obtained were compared with the real original values and the accuracy and error rates were evaluated. The total CER was used to determine the error rates. This rate is calculated by the following formula (Equation 1):

$$\text{CER} = \frac{\text{number of deleted characters} + \text{number of added characters} + \text{number of modified characters}}{\text{total character counter}} \quad (1)$$

According to the results, 580 out of 600 images were correctly matched, while 20 images were incorrectly matched. The main reasons for the incorrect results are the presence of more than one label in the images and low-resolution conditions. In particular, conditions such as low resolution and blurriness negatively affected the text recognition performance of OCR technologies. In such cases, it has been observed that optimizing the parameters for each image increases the accuracy rates. In the evaluations, it was found that very successful results were obtained when the CER were between 1% and 10% [33]. In particular, EasyOCR and EAST approaches allow more precise parameter settings to minimize error rates in low resolution data, which is one of the prominent advantages of these technologies.

Table 3 presents the detailed results of the correct match rates, while Table 4 summarizes the OCR errors encountered in the images with 20% of incorrect matches. The majority of false matches occurred in cases where there were multiple tags and the resolution was low.

Table 3. Error rate on the image.

Total Number of Images	Number of Images with Incorrect Output	Character Error Rate (%)
600	20	(50 / 1200) * 100 ≈ 4.17

Table 4. Image counts according to OCR technology.

OCR Technology	Number of Images with Incorrect Output
EasyOCR	6
Tesseract	10
EAST	4

The innovations and added value of the study of using Tesseract OCR, EAST OCR and EasyOCR for the detection of hazardous substance labels to show safety measures and label information can be emphasized as follows:

- The combination of three different OCR technologies (Tesseract, EAST, EasyOCR) on the same problem stands out as a methodological innovation. Each OCR algorithm has different advantages; therefore, combining them all in a single framework is an innovative approach.
- Hazardous material labels contain specific safety symbols, classifications and numbers. Digitally recognizing these labels with OCR technologies and then using this data to automatically display safety measures and other information about the label is an innovation that increases speed and safety in business processes and in the event of any danger or accident.
- The use of fast, real-time algorithms such as EAST OCR makes it possible to recognize and process hazardous material labels instantaneously. This is a critical innovation for fast decision-making, especially when transporting or storing hazardous materials. This is very important in the safety and logistics phases.

- Manual inspection and classification of hazardous material labels is a process prone to human error. The integration of OCR technologies automates this process and reduces the error rate.
- Detecting hazardous material labels used in the industry with OCR and instantly checking their compliance with safety standards contributes to automatic reporting and monitoring systems.
- Hazardous material labels detected with OCR technology can be digitally stored and traceable. This adds an additional dimension to the studies on the traceability of hazardous substances in the literature and ensures data security. Digitized data provides a safer way in inspection processes and transportation of dangerous goods.

In conclusion, this work presents important methodological and practical innovations on the detection of hazardous substance labels with OCR technologies and the display of safety precautions and other information. It provides a broad perspective in both academic and industrial environments.

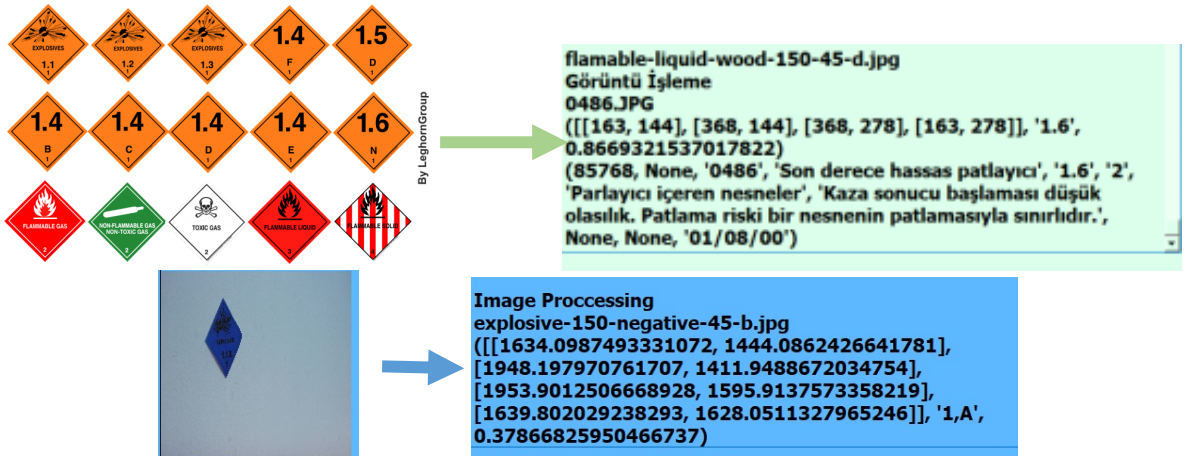

Figure 7. Result values as a result of the image given to the system.

The evaluation of OCR accuracy is commonly assessed using the CER, with thresholds defined as follows: good OCR accuracy corresponds to a CER of 1–2% (i.e., 98–99% accuracy), average OCR accuracy falls within a CER range of 2–10%, and poor OCR accuracy is characterized by a CER exceeding 10% (i.e., below 90% accuracy) [22]. In this study, an OCR performance with a CER of approximately 4.17% was obtained, which aligns with the "average OCR accuracy" category as outlined in the literature. This result is consistent with the CER range of 2–10% and indicates an adequate level of performance according to standard OCR accuracy evaluation criteria. Additionally, it is worth noting that a CER of up to 20% is often considered acceptable for general applications. The findings of this study are closely aligned with those reported in similar works in literature. To further enhance the accuracy, EasyOCR and EAST methods were implemented, yielding improved performance compared to the initial results presented in Table 2. These improvements demonstrate the effectiveness of the proposed methods for applications such as label detection and information extraction. Furthermore, the results highlight the competitive performance of the proposed approach in comparison to existing methods reported in the literature.

4. Conclusion

This study focuses on the automatic detection of labels for hazardous substances, with the aim of managing safety measures and potential risks. The proposed approach enables the rapid detection of which hazardous substance is present, its properties and first response information in the event of an accident. For this purpose, Tesseract, EasyOCR and EAST text detectors were used as image processing methods and effective results were obtained. The study was tested on a large dataset and the hazardous material labels in more than 600 images were successfully detected and the relevant warning information was retrieved from the database. Furthermore, the method proved its effectiveness in terms of both accuracy and processing time, demonstrating its potential to provide a fast and reliable solution, especially for emergency situations. The results of the study are considered as

an important step in the development of warning systems for hazardous substances and offer a practical solution compared to other studies in this field.

In future studies, it is considered to be integrated with barcode technology and transformed into remote controlled robot systems through unmanned vehicles. It is important to minimize the human factor and work efficiently by relying on financially automated systems.

References

[1] Ellena LM, Olampi S, Guarnieri F. Technological risks management: Automatic detection and identification of hazardous material transportation trucks. WIT Trans Ecol Environ 2004; 77: 763-771.

[2] Yang Q, Chin KS, Li YL. A quality function deployment-based framework for the risk management of hazardous material transportation process. Journal of Loss Prevention in the Process Industries 2018; 52: 81-92.

[3] Vojinović N, Sremac S, Zlatanović D. A Novel Integrated Fuzzy-Rough MCDM Model for Evaluation of Companies for Transport of Dangerous Goods. Complexity 2021; 2021(1): 5141611.

[4] Hsu C, Yang J, Chang A, Liu G. A new hybrid MCDM approach for mitigating risks of hazardous material road transportation. Mathematical biosciences and engineering 2024; 21(3): 4210-4240.

[5] Liu Y, Fan LS, Li X, Shi SL, Lu Y. Trends of hazardous material accidents (HMAs) during highway transportation from 2013 to 2018 in China. Journal of Loss Prevention in the Process Industries 2020; 66:104150.

[6] Panke ZH, Fan LU. Evolutionary game analysis on safety supervision of general aviation based on system dynamics simulation. China Safety Science Journal 2019; 29(4): 43.

[7] Parra A, Zhao B, Haddad A, Boutin M, Delp EJ. Hazardous material sign detection and recognition. In: IEEE 2013 International Conference on Image Processing; 15-18 Sep 2013; Melbourne, Australia: IEEE. pp. 2640-2644.

[8] Jia L, Wang J, Wang T, Li X, Yu H, Li Q. HMD-net: a vehicle hazmat marker detection benchmark. Entropy 2022; 24(4): 466-481.

[9] Pramanik A, Sarkar S, Maiti J. Oil spill detection using image processing technique: An occupational safety perspective of a steel plant. Emerging Technologies in Data Mining and Information Security: Proceedings of IEMIS 2018; 3: 247-257).

[10] Monteiro G, Camelo L, Aquino G, Fernandes RD, Gomes R, Printes A, Torné I, Silva H, Oliveira J, Figueiredo C. A Comprehensive Framework for Industrial Sticker Information Recognition Using Advanced OCR and Object Detection Techniques. Applied Sciences 2023; 13(12): 7320-7336.

[11] Shahin M, Chen FF, Hosseinzadeh A. Machine-based identification system via optical character recognition. Flexible Services and Manufacturing Journal 2024; 36(2):453-480.

[12] Tang Q, Lee Y, Jung H. The Industrial Application of Artificial Intelligence-Based Optical Character Recognition in Modern Manufacturing Innovations. Sustainability 2024; 16(5): 2161-2181.

[13] Memon J, Sami M, Khan RA, Uddin M. Handwritten optical character recognition (OCR): A comprehensive systematic literature review (SLR). IEEE access 2020; 8:142642-142668.

[14] Okur FB, Eyüpoğlu C. Image matching based hazardous material detection and warning system. Istanbul Ticaret University Fen Bilimleri Dergisi 2024; 23(46): 271-291.

[15] Application of RFID Technology in Ship Dangerous Goods Transportation Management, JTSpeedwork. https://www.jtspeedwork.com/application-of-rfid-technology-in-ship-dangerous-goods-transportation management_n101. [Accessed: Jan. 25, 2025].

[16] Mishra A, Ram AS. Handwritten Text Recognition Using Convolutional Neural Network. arXiv preprint arXiv:2307.05396 2023.

[17] Olson L, Berry V. Digitization decisions: comparing OCR software for librarian and archivist use. Code4Lib Journal 2021; 22(52).

[18] Santos Y, Silva M, Reis JC. Evaluation of optical character recognition (OCR) systems dealing with misinformation in Portuguese. In: IEEE 2023 36th SIBGRAPI Conference on Graphics, Patterns and Images (SIBGRAPI); 6-9 Nov 2023; Rio Grande, RS, Brazil: IEEE. pp. 223-228.

[19] Palkovič R. Text Recognition in Historic Birth, Death and Marriage Records. Bachelor's Thesis, Masaryk University, Brno, Czechia, 2023

[20] Hukkeri GS, Goudar RH, Janagond P, Patil PS. Machine Learning in OCR Technology: Performance Analysis of Different OCR Methods for Slide-to-Text Conversion in Lecture Videos. International Journal of Advanced Computer Science and Applications 2022; 13(8): 325-332.

[21] Alimovski E, Erdemir G, Kuzucuoglu AE. Text Detection and Recognition in Natural Scenes by Mobile Robot. European Journal of Technique (EJT) 2024; 14(1): 1-7.

[22] OCR Accuracy: What Is It and How to Measure It?, Docsumo, Available: https://www.docsumo.com/blogs/ocr/accuracy#:~:text=Good%20OCR%20accuracy%3A%20CER%201,(i.e.%20below%2090%25%20accurate). [Accessed: Jan. 25, 2025].
[23] Mohamed MA, Tünnermann J, Mertsching B. Seeing Signs of Danger: Attention-Accelerated Hazmat Label Detection. In: IEEE 2018 International Symposium on Safety, Security, and Rescue Robotics (SSRR); 6-8 Aug 2018; Philadelphia, PA, USA: IEEE. pp. 1-6.
[24] Schramm E. Hazmat13 Dataset, Kaggle, 2023. Available: https://www.kaggle.com/datasets/eliasschramm/hazmat13. [Accessed: Jan. 14, 2025]
[25] Zhou X, Yao C, Wen H, Wang Y, Zhou S, He W, Liang J. East: an efficient and accurate scene text detector. In: IEEE 2017 Proceedings of the IEEE conference on Computer Vision and Pattern Recognition; 21-26 Jul 2017; Honolulu, HI, USA: IEEE. pp. 5551-5560.
[26] Vedhaviyassh DR, Sudhan R, Saranya G, Safa M, Arun D. Comparative analysis of easyocr and tesseractocr for automatic license plate recognition using deep learning algorithm. In: IEEE 2022 6th International Conference on Electronics, Communication and Aerospace Technology; 1-3 Dec 2022: Coimbatore, Tamil Nadu, India: IEEE. pp. 966-971).
[27] Salehudin MA, Basah SN, Yazid H, Basaruddin KS, Safar MJ, Som MM, Sidek KA. Analysis of Optical Character Recognition using EasyOCR under Image Degradation. In: IOP Publishing 2023 Journal of Physics: Conference Series; 1 Nov 2023; 2641(1): IOP Publishing. p. 012001.
[28] Hamad K, Kaya M. A detailed analysis of optical character recognition technology. International Journal of Applied Mathematics Electronics and Computers 2016; Sep 1(Special Issue-1):244-249.
[29] Kissos I, Dershowitz N. OCR error correction using character correction and feature-based word classification. In: IEEE 2016 12th IAPR Workshop on Document Analysis Systems (DAS);11-14 Apr 2016; Santorini, Greece: IEEE. pp. 198-203.
[30] Harraj AE, Raissouni N. OCR accuracy improvement on document images through a novel pre-processing approach. Signal & Image Processing: An International Journal 2015; 6(4): 01–18.
[31] de Oliveira LL, Vargas DS, Alexandre AM, Cordeiro FC, Gomes DD, Rodrigues MD, Romeu RK, Moreira VP. Evaluating and mitigating the impact of OCR errors on information retrieval. International Journal on Digital Libraries 2023; 24(1): 45-62.
[32] Subramani N, Matton A, Greaves M, Lam A. A survey of deep learning approaches for ocr and document understanding. arXiv preprint arXiv:2011.13534 2021; Nov 27.
[33] Dölek I, Kurt A. Ottoman Optical Character Recognition with deep neural networks Derin sinir ağlarıyla Osmanlıca optik karakter tanıma. Journal of the Faculty of Engineering and Architecture of Gazi University 2023;38(4): 2579-2593.

Turkish Journal of Science & Technology
20(1), 249-257, 2025

Research Paper
https://doi.org/10.55525/tjst.1589331

An Analysis on YEKDEM Program Implemented in Turkey

Murat ERDEM[1*]
[1]Technical Vocational School, Firat University, Elazığ, Turkey
muratrdm01@gmail.com

(Geliş/Received: 21/11/2024; Kabul/Accepted: 01/02/2025)

Abstract: This study examines the Renewable Energy Resources Support Mechanism (YEKDEM) implemented in Turkey for solar energy. Within this context, the appropriateness of the incentive amounts provided through the YEKDEM application was analyzed. For this purpose, the current formulation calculated the effects of changing the coefficients of the Exchange Rate, PPI, and CPI values in the mathematical equation, as well as the total incentive amounts for certain years. In the study, it was assumed that the weather was entirely sunny when calculating solar radiation. The effects of the incentive amounts, profit-loss scenarios, and the payback period for plant investors were presented. The formula that offers the highest incentive amount for investors is the one with coefficients of 30%-30%-20%-20%. Annual earnings vary between US$ 15,928 and US$ 146,176. Payback periods range from 5.9 to 54 years, depending on the use of credit and equity.

Key words: YEKDEM, Solar energy, Energy economics, Energy policy, Solar power plants.

Türkiye'de Uygulanan YEKDEM Programına İlişkin Bir Analiz

Öz: Bu çalışmada, Türkiye'de güneş enerjisi için uygulanan Yenilenebilir Enerji Kaynakları Destekleme Mekanizması (YEKDEM) incelenmiştir. Bu bağlamda, YEKDEM uygulamasıyla sağlanan teşvik miktarlarının uygunluğu analiz edilmiştir. Bu amaçla, mevcut formülasyon ile matematiksel denklemde Döviz Kuru, ÜFE ve TÜFE değerlerinin katsayılarının değiştirilmesinin etkileri ve belirli yıllar için toplam teşvik miktarları hesaplanmıştır. Çalışmada, güneş radyasyonu hesaplanırken havanın tamamen güneşli olduğu varsayılmıştır. Teşvik miktarlarının etkileri, kar-zarar senaryoları ve santral yatırımcıları için geri ödeme süresi ortaya konulmuştur. Yatırımcılar için en yüksek teşvik miktarını sunan formül, %30-%30-%20-%20 katsayılı olandır. Yıllık kazançlar 15.928 ABD doları ile 146.176 ABD doları arasında değişmektedir. Geri ödeme süreleri, kredi ve öz sermaye kullanımına bağlı olarak 5,9 ila 54 yıl arasında değişmektedir.

Anahtar kelimeler: YEKDEM, Güneş enerjisi, Enerji ekonomisi, Enerji politikası, Güneş enerji santralleri.

1. Introduction

Today, almost all countries still largely use fossil fuels to produce electricity. Using renewable energy instead of fossil fuels is extremely important in terms of leaving a cleaner environment for the future by reducing dependence on fossil fuels. One of these is solar energy, which has drawn significant interest from various sectors and application areas [1–6]. The main areas of focus for researchers are as follows: a) increasing the efficiency of solar thermal collectors or PV/T systems [7], b) producing electricity using solar power using single or hybrid energy systems [8–12], c) producing hydrogen powered by solar energy [12,13], d) using solar energy in zero-energy or sustainable-energy buildings [14,15]. The design and analysis of solar energy systems require an understanding of the distribution of solar radiation worldwide. The energy, energy, and conversion efficiencies as well as the collectors operating circumstances are influenced by numerous factors. The solar irradiation intensity is one of the most crucial factors. It has a direct impact on both the solar irradiance intensity and the thermal collector efficiency. In general calculations, average solar radiation and system efficiency are employed. Nonetheless, it is evident that this approach is unable to forecast results with accuracy. To ensure precise estimations of solar energy, the monthly distribution of solar radiation worldwide should be forecast [1]. Some incentive programs for Renewable Energy Resources are implemented around the World. These are supports such as feed-in tariffs, tax reductions, and discounts based on the power plants institutional capacity and quota. The incentive method used by some countries around the World is given in Table 1.

* Corresponding author: muratrdm01@gmail.com. ORCID Number of authors: 0000-0003-0287-1881

Table 1. Renewable energy resource incentive programs implemented in some countries.

Country	Incentive program
USA [16]	Tax deduction, Financial support for installation
China [17]	Tax deduction
Germany [18, 19]	Tariff guarantees and financial aid instruments
Spain [19]	Inflation-based control of wages and premium
France [20]	Tariff guarantees
Canada [21]	Incentives for solar energy systems, especially for rooftop PV systems
India [22]	Financial aid for maximum 2MW power plants
Malaysia [23,24]	Energy policy supports under the renewable energy program
Ireland [25]	Quota obligation schemes, feed-in-tariff and competitive tendering schemes
Pakistan [26]	Exemption from payment of income tax, exemption from import duties on electricity generation equipment and protection against foreign exchange risks

As mentioned above, Turkey launched an incentive program similar to some of the above countries with a 10-year fixed price guarantee in 2011. However, the program was changed in 2021 and a different application was introduced. According to the program in 2021 [27], a dynamic mathematical formula that changes depending on PPI-CPI-US$-EURO movements was declared, but since the formula did not pose a very positive situation for the investor, this formula was updated again in 2023 by changing the coefficients of the variables in the formula [28, 29]. Today, YEKDEM incentive amount and local contribution amounts are determined with this formula.

The aim of this study is to examine the effects of the YEKDEM program currently implemented by Turkey for certain years and by changing the coefficients in the formula.

2. Material and Methods

The Materials and Methods section is presented under the subheadings of calculations and application conditions of the incentive program and Solar radiation and cost calculations.

2.1. Calculations and application conditions of the incentive program

In the study, analyses of YEKDEM (Renewable Energy Resources Support Mechanism), solar radiation, and GES (Greenhouse Gas Emissions) were conducted. Typically, these analyses are performed independently. However, the critical aspect lies in determining the point at which these separately calculated analyses are integrated. After calculating the YEKDEM rate in Turkish Lira (TL) per kilowatt-hour (kWh), it is converted to US cents (US$/kWh). This value represents the type of monetary incentive that the investor will receive. During the GES analysis, the most recent daily capital cost flow is computed. This value is subsequently utilized to derive the net income for the solar radiation analysis. Similarly, once the YEKDEM calculation is completed

independently, the electricity purchase price is determined by multiplying the US$/kWh value by the power output obtained from the photovoltaic (PV) system. The primary objective is to provide guidance to the investor by determining the most up-to-date annual profit and loss scenario. This integrated approach ensures a comprehensive evaluation of the financial and environmental aspects, enabling informed decision-making for potential investors in renewable energy projects.

The initial YEKDEM values to be used in the formula are 32 TL kuruş/kWh and 106 TL kuruş/kWh for 2021 (old YEKDEM) and 2023 (last YEKDEM), respectively [27,28]. The domestic contribution pricing and application prices for the renewable energy sources support mechanism are revised by Equation 1 for YEK-certified production facilities that go into operation between July 1, 2021, and December 31, 2030.

$$\frac{YEKDEM_{GD}}{YKF_{GD}} = \frac{YEKDEM_{OGD}}{YKF_{GD}} x[\left(\frac{25}{100} x \frac{PPI_{A-2}}{PPI_{A-3}}\right) + \left(\frac{15}{100} x \frac{CPI_{A-2}}{CPI_{A-3}}\right) + \left(\frac{30}{100} x \frac{EXC.RATE_{D-1}}{EXC.RATE_{D-2}}\right) + \left(\frac{30}{100} x \frac{EXC.RATE_{E-1}}{EXC.RATE_{E-2}}\right)] \quad (1)$$

For what these variables mean, please see the following references Refs. [5,29].

2.2. Solar radiation and cost calculations

The methodology for the solar energy estimates utilized in the analysis is summarized below. Further information about the process can be found in the articles listed below [5].
Using Equation 2, the calculation determines the amount of solar radiation at the surface of the PV module at the optimal angle [30].

$$I_s = I \cdot R_B \quad (2)$$

Researchers frequently employ Levelized Cost Analysis (LCOA) as a method in the literature. Consequently, a brief version of the important equations is provided here. For more precise information, please see the Refs. (19,29)

$\dot{Z}$ is the cost flow of capital and is calculated by Equation 3, [19,29].

$$\dot{Z} = \dot{Z}^{CI} + \dot{Z}^{OM} \quad (3)$$

Here, $\dot{Z}^{CI}$,the levelized hourly cost of the capital investment is presented. $\dot{Z}^{OM}$, the levelized hourly maintenance and service costs for the solar power facility are displayed.

The current value (PW) of the studied photovoltaic SPP is calculated by Equation 4, [25,32,33].

$$PW = TCI - S \cdot PWF_{(i_{eff},N)} \quad (4)$$

Total capital investment (TCI) is expressed in US$ in Equation 4, and The letter “S” stands for the solar power plants salvage value (Equation 5) [18,30,31].

$$S = TCI \cdot J \quad (5)$$

Here, J; the salvage value ratio, Equation 6 is used to get the SPPs present value factor (PWF) [18,32].

$$PWF = \frac{1}{(1+i_{eff}{}^{N})} \quad (6)$$

The PWF stands for the single payment present-worth factor [24], N, the systems lifetime, is determined to be 25 years, the effective discount rate is i_{eff} and is calculated by Equation 7, [23,33].

$$i_{eff} = (1 + \frac{i}{p})^p - 1 \quad (7)$$

The compound annual interest rate, or P, is a measure of how much money costs. The total credit amount from all sources plus the interest rates set by each source is added to find the cost of money. The cost of money is equal to the interest rate because this approach considers only one source of funding. These are the annual capital expenses of the studies interest rate analysis, which came under the heading of economic data about PV-module-based solar power facilities. This value is obtained through Equation 8 [37].

$$AC = PW \cdot CRF_{i_{eff},N} \quad (8)$$

Recoverability of capital factor, Equation (9) is used to determine CRF [38].

$$CRF = \frac{\mathrm{i}_{eff}(1+\mathrm{i}_{eff})^N}{(1+\mathrm{i}_{eff})^N - 1} \quad (9)$$

For solar power plants $\dot{Z}^T$, the equipment's annualized cost is calculated as in Equation 10, [38,39].

$$\dot{Z}^T = \frac{\emptyset\, AC}{3600\ (s/h)\ \tau\ (h/year)} \quad (10)$$

Where τ, the estimated number of running system hours per year is found. The SPP based on PV modules has maintenance and operation costs of ϕ. The hourly levelized capital investment $\dot{Z}^{CI}$ cost for the SPP is calculated by Equation 11.

$$\dot{Z}^{CI} = \frac{A\,C}{\tau} \quad (11)$$

Equation 1, taking into account the operating and maintenance economic aspects, it is applied in the estimation process.

$$\dot{Z}^{OM} = \frac{OM}{\tau} \quad (12)$$

3. Results and Discussion

In present study, the incentive amounts given to solar power plant investors by the Republic of Turkey within the scope of the YEKDEM program year 2022 were analyzed. In the literature, the cost of a 1 MW solar power plant varies between US$ 864,517 - US$ 1,158,040 [34,35]. In this study, the cost value of US$ 864,517 was used for the plant cost. Here, the effects obtained by changing the coefficients and the values calculated with the current coefficient are discussed. In the analysis, the year 2022 was chosen because the inflation values in 2022 were very high. Here, domestic contribution amounts and lower and upper limits of the incentive amount were not taken into account. The calculations show the amounts that the investor should receive according to the current calculation through a direct formula. If the investor exceeds the upper limit of the amount given, a fixed monthly fee of 6.05 cents US$/kWh is applied. This shows that the money he will receive will be much lower than this calculation. However, if the GES materials used are preferred domestically, the incentive amount will increase a little more, which will be in favor of the investor.

Economic values according to net profit-loss and capital cost flow are given in Figure 1. Figure 1(a) displays the calculated results based on the applied YEKDEM coefficients. Figures 1(b), 1(c), 1(d), and 1(e) present the results obtained under the conditions where the PPI, CPI, US$, and EURO coefficients are set to 20%, 20%, 30%, and 30%; 15%, 25%, 30%, and 30%; 25%, 25%, 25%, and 25%; and 30%, 30%, 20%, and 20%, respectively.

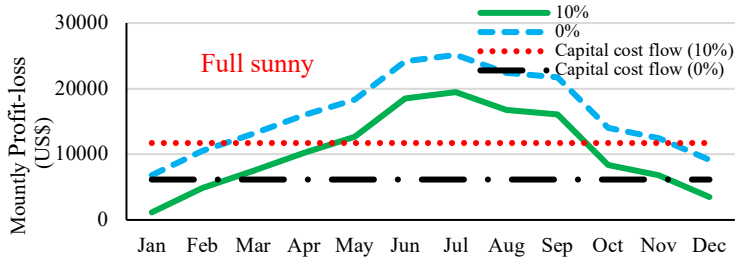

a) PPI, CPI, US$, and EURO coefficient in the valid YEKDEM formula (25, 15, 30, 30%)

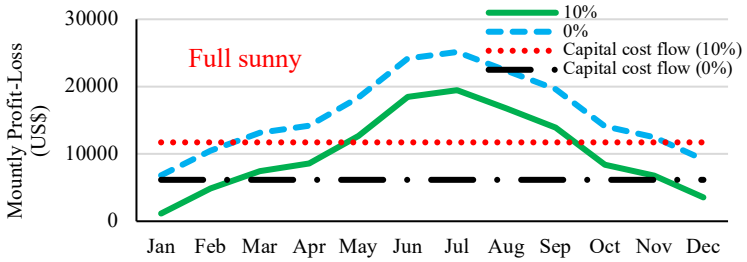

b) PPI, CPI, US$, and EURO coefficient in the YEKDEM formula (20, 20, 30, 30%)

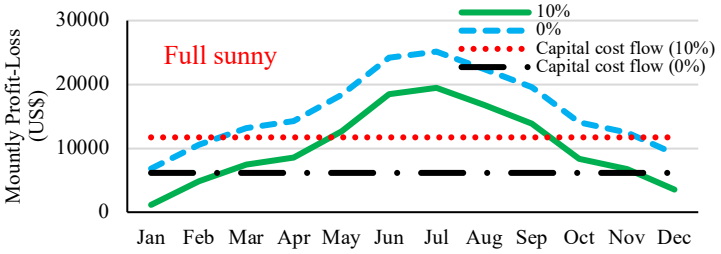

c) PPI, CPI, US$, and EURO coefficient in the YEKDEM formula (15, 25, 30, 30%)

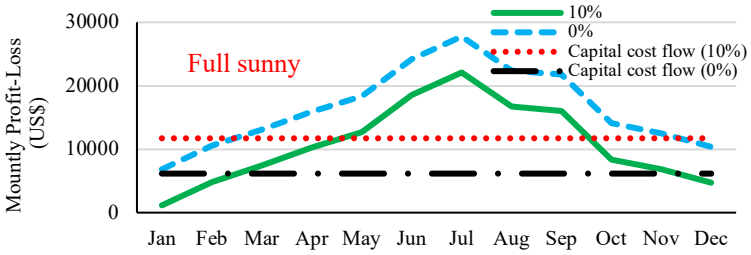

d) PPI, CPI, US$, and EURO coefficient in the YEKDEM formula (25, 25, 25, 25%)

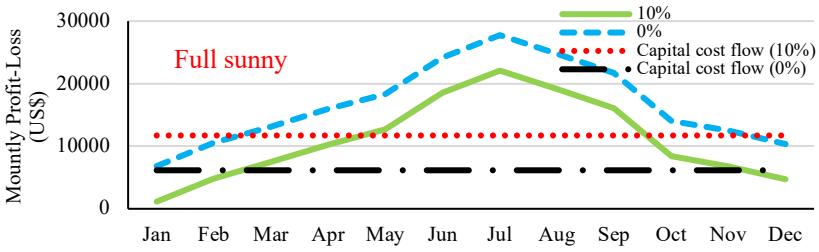

e) PPI, CPI, US$, and EURO coefficient in the YEKDEM formula (30, 30, 20, 20%)

Figure 1. The net profit-loss situation in the coefficient changes for the year 2022.

In Figure 1, calculations were obtained according to capital cost flow, net profit-loss situation and equity and interest rates (10%). If the curve (purchase price) is below the capital cost flow, it shows that the solar power plant investor is losing money, while if it is above it, it shows that the investor is making a profit. Here, it is clear that a power plant established using trade credit costs more to the investor. In other words, the payback period of a power plant established by the investor with his own means is completed in a shorter period of time. It is noticeable from the curves that the investors profit rate is very high in the summer months when solar radiation is high (especially in June, July and August). When a loan is not used, an average profit of almost 10 months is made, while when a loan is used, a profit of only 4-5 months is made. In addition, these profit-loss rates vary according to changes in PPI, CPI, US$, and EURO. The formula that provides the highest total incentive amount to investors is the one with PPI, CPI, US$, and EURO coefficients set at 30%, 30%, 20%, and 20%, respectively (Figure 1(e)).

YEKDEM incentive amounts given between 2018-2023 are given in Fig. 2. The initial application price of YEKDEM was determined by the authorized institution as 106 Turkish lira kuruş/kWh. The incentive amounts to be given without any lower-upper limits (4.95-6.05 cents US$/kWh) are 316.32, 317.57, 302.05, 307.81, 310.59 and 330.83 cents US$/kWh for the years 2018-2023, respectively. The incentive amount given, except for 2020, has increased regularly. This is an expected situation when the formulation variables are taken into account. However, depending on the currency to be given to investors (cents US$/kWh), there may be different reasons for the decrease in 2020. For example, if the incentive was given in TL, this decrease would not have occurred, but the decrease in TL/US$ values together with the sudden increase in the dollar reveals this result. The total incentive amount to be given between these years was found to be 1,885.17 cents US$/kWh. Within the scope of formulation coefficients, the formula that offers the highest incentive amount for investors on a US$/kWh basis is the formula with a coefficient of 30%-30%-20%-20%, while the lowest incentive amount is the formula with a coefficient of 15%-25%-30%-30%. When the lower-upper limit is applied and the incentives are paid in another currency such as TL, there will be some changes in the incentives given with these coefficients. For example, when given in TL, the lowest incentive given is the equation with a coefficient of 20%-20%-30%-30%, while the coefficients giving the highest incentive remain the same as US$. This means that the exchange rate is more dominant than PPI-CPI values. YEKDEM incentive amounts between 2018 and 2023 are given in Figure 2.

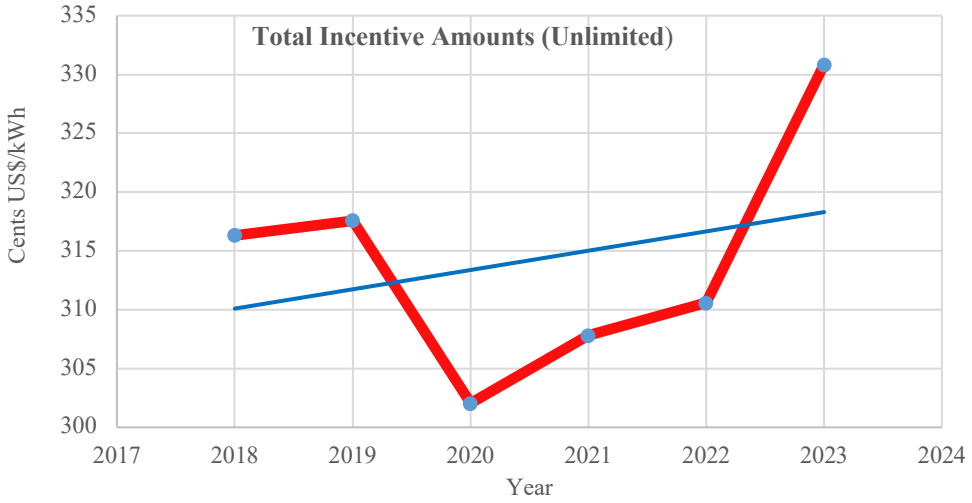

Figure 2. YEKDEM incentive amounts given between 2018-2023.

The total incentive amount to be given between these years (for example, until June 2023) was found to be 1,723.90 cents US$/kWh. This amount is very high compared to the repealed YEKDEM of 2021. According to the YEKDEM of 2021, the total incentive amount to be given between these dates is 180.64 cents US$/kWh. This result shows how correct the removal of the old YEKDEM of 2021 was. In addition, the result of this comparison is shown more clearly in Figure 3 for a better understanding. The reason for such a significant difference between the old YEKDEM and new YEKDEM incentive amounts lies in the effects of the PPI, CPI, Euro, and Dollar coefficients, as well as the differences in YEKDEM application starting prices and payment periods. Investors are now in a more advantageous position compared to the previous YEKDEM.

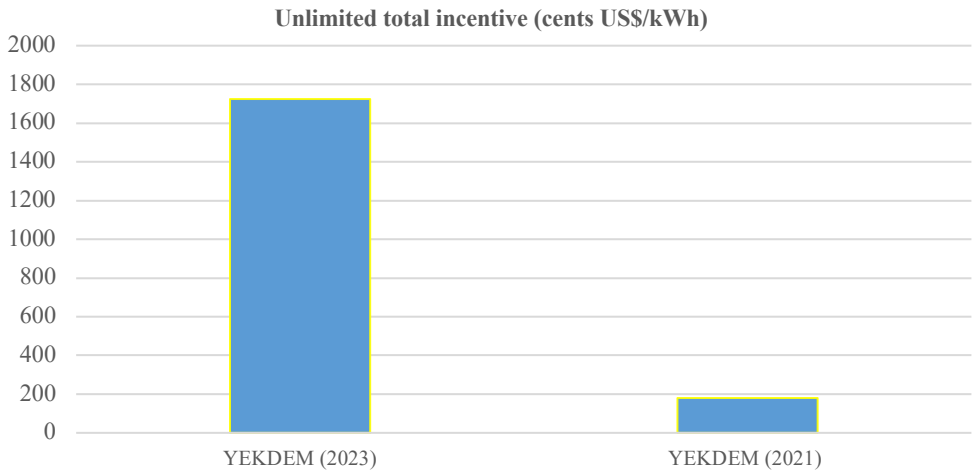

Figure 3. Total incentive amounts to be given between January 2018 and June 2023.

The results of incentive amounts according to the old and new YEKDEM are also reflected in Table 2 data for 2022 (without any lower or upper limits and full sunny).

Table 2. Investment payback period, annual profit-loss situation and total support amounts for 2022.

	YEKDEM (2021)	**YEKDEM (2023)**
Payback period (10%)	54 years	11 years
Payback period (0%)	22.5 years	5.9 years
Yearly profit-loss (10%)	US$ 15,928	US$ 78,229
Yearly profit-loss (0%)	US$ 38,285	US$ 146,176

The difference between the incentive amounts between the two YEKDEMs is striking. It has been understood that the investment payback period is much longer compared to the dated-2021 YEKDEM [27]. For example, the payback periods between the old and last YEKDEM in the non-credit case are 22 years and 6 years. It is seen that the payback period is much longer in credit cases. The payback periods, which are 22.5 and 5.9 years in the credit case, increase to 54 and 11 years. Similarly, the net profit amount in credit and non-credit cases is much higher compared to the last YEKDEM. These rates for credit and non-credit are calculated as US$ 15,928 and US$ 38,285 for YEKDEM dated 2021, and US$ 78,229 and US$ 146,176 for YEKDEM dated 2023, respectively.

4. Conclusions

In this study, a research was conducted on the YEKDEM program currently implemented in Turkey. It was assumed that the weather was completely sunny (cloudless) throughout the year. The data obtained on the implementation of the review program under current conditions in the years 2018-2023, the change of the PPI-CPI-EURO-US$ coefficients in the correlation and the determination of the payback periods of the solar power plant investment were presented. The findings are presented in the form of items.

- Annual earnings vary between US$ 15,928 and US$ 146,176 depending on credit/equity use. But, these values may also change depending on climate and inflation.
- Payback periods are between 5.9 - 54 years depending on credit and equity use. These figures may vary depending on cost and climate conditions.
- The formula that offers the highest incentive amount for investors (the most advantageous to the investor) is the formula with a coefficient of 30%-30%-20%-20%. An update in this direction may be made in the future.

As a result, since the use of commercial credit, the fact that the weather will not be completely sunny, and the negativities caused by inflation will put the investor in a difficult situation, it is recommended to develop a better formula that protects both the investor and the government institutions.

References

[1] Coskun C, Oktay Z, Dincer I. Estimation of monthly solar radiation distribution for solar energy system analysis. Energy 2011; 36: 1319–1323.
[2] Wang RZ, Zhai XQ. Development of solar thermal technologies in China. Energy 2010; 35: 4407–4416.
[3] Badescu V. Optimum size and structure for solar energy collection systems. Energy 2006; 31: 1819–1835.
[4] Gürtürk M. Economic feasibility of solar power plants based on PV module with levelized cost analysis. Energy 2019; 171: 866–878.
[5] Gürtürk M, Ucar F, Erdem M. A novel approach to investigate the effects of global warming and exchange rate on the solar power plants. Energy 2022; 239 (Part D): 122344.
[6] Gürtürk M, Erdem M, Uçar F. Solar energy technical feasibility comparison: an alternative proposal for the Industry. Energy Effic 2024; 17(5): 1-18.
[7] Atkins MJ, Walmsley MRW, Morrison AS. Integration of solar thermal for improved energy efficiency in low-temperature-pinch industrial processes. Energy 2010; 35: 1867–1873.
[8] Erdil E, Ilkan M, Egelioglu F. An experimental study on energy generation with a photovoltaic (PV)-solar thermal hybrid system. Energy 2008; 33: 1241–1245.
[9] Gou C, Cai R, Hong H. A novel hybrid oxy-fuel power cycle utilizing solar thermal energy. Energy 2007; 32: 1707–1714.
[10] Reichling JP, Kulacki FA. Utility scale hybrid wind-solar thermal electrical generation: A case study for Minnesota. Energy 2008; 33: 626–638.
[11] Guo LJ, Zhao L, Jing DW, Lu YJ, Yang HH, Bai BF, et al. Solar hydrogen production and its development in China. Energy 2009; 34: 1073–1090.
[12] Rehman S, Al-Hadhrami LM. Study of a solar PV-diesel-battery hybrid power system for a remotely located population near Rafha, Saudi Arabia. Energy 2010; 35: 4986–4995.
[13] Sarkar J, Bhattacharyya S. Application of graphene and graphene-based materials in clean energy-related devices Minghui. Arch Thermodyn 2012; 33: 23–40.
[14] Kalogirou SA, Bojic M. Artificial neural networks for the prediction of the energy consumption of a passive solar building. Energy 2000; 25: 479–491.
[15] Tiris C, Tiris M, Dincer I. Energy efficiency of a solar drying system. Int J Energy Res 1996; 20: 767–770.
[16] Ding L, Kinnucan HW. This document is discoverable and free to researchers across the globe due to the work of AgEcon Search. Help ensure our sustainability . J Gender, Agric Food Secur 2011; 1: 1–22.
[17] China Institute, Chinas renewable energy & Clean-Tech Market. Univerity of Albetra, Canada: Edmonton, 2016.
[18] Kılıç U, Kekezoğlu B. A review of solar photovoltaic incentives and Policy: Selected countries and Turkey. Ain Shams Eng J 2022; 13(5): 101669.
[19] Mir-Artigues P, Cerdá E, Del Río P. Analyzing the impact of cost-containment mechanisms on the profitability of solar PV plants in Spain. Renew Sustain Energy Rev 2015; 46: 166–177.
[20] Celik AN, Özgür E. Review of Turkeys photovoltaic energy status: Legal structure, existing installed power and comparative analysis. Renew Sustain Energy Rev 2020; 134: 110344.
[21] Kuznetsova E, Anjos MF. Challenges in energy policies for the economic integration of prosumers in electric energy systems: A critical survey with a focus on Ontario (Canada). Energy Policy 2020; 142: 111429.
[22] De La Flor FJS, Cebolla RO, Félix JLM, Domínguez SÁ. Solar radiation calculation methodology for building exterior surfaces. Sol Energy 2005; 79: 513–522.
[23] Rahman Mohamed A, Lee KT. Energy for sustainable development in Malaysia: Energy policy and alternative energy. Energy Policy 2006; 34: 2388–2397.
[24] Wiginton LK, Nguyen HT, Pearce JM. Quantifying rooftop solar photovoltaic potential for regional renewable energy policy. Comput Environ Urban Syst 2010; 34: 345–357.
[25] Huber C, Ryan L, Ó Gallachóir B, Resch G, Polaski K, Bazilian M. Economic modelling of price support mechanisms for renewable energy: Case study on Ireland. Energy Policy 2007; 35: 1172–1185.
[26] Mirza UK, Ahmad N, Harijan K, Majeed T. Identifying and addressing barriers to renewable energy development in Pakistan. Renew Sustain Energy Rev 2009; 13: 927–931.
[27] Gazette of republic of Turkey. Turkish Gov Leg Gaz Repub Turkey, Turkey: 2021.
[28] Gazette of republic of Turkey. Turkish Gov Leg Gaz Repub Turkey, Turkey: 2023.
[29] Lüthi S. Effective renewable energy policy: empirical insights from choice experiments with project developer, Germany: Universität St. Gallen, 2011.
[30] Funkhouser E, Blackburn G, Magee C, Rai V. Business model innovations for deploying distributed generation: The emerging landscape of community solar in the U.S. Energy Res Soc Sci 2015; 10: 90–101.
[31] Muhammed G, Tekbiyik-Ersoy N. Development of renewable energy in china, usa, and brazil: A comparative study on renewable energy policies. Sustain 2020; 12: 1–30.

[32] Zhao X, Luo D. Driving force of rising renewable energy in China: Environment, regulation and employment. Renew Sustain Energy Rev 2017; 68: 48–56.
[33] Lo K. A critical review of Chinas rapidly developing renewable energy and energy efficiency policies. Renew Sustain Energy Rev 2014; 29: 508–516.
[34] Fathi M, Abderrezek M, Grana P. Technical and economic assessment of cleaning protocol for photovoltaic power plants: Case of Algerian Sahara sites. Sol Energy 2017; 147: 358–367.
[35] Erdem M, Gürtürk M. Economic analysis of the impact of Turkeys renewable support mechanism on solar energy investment. Util Policy 2025; 92: 101862.

Turkish Journal of Science & Technology
20(1), 259-268, 2025

Research Paper
https://doi.org/10.55525/tjst.1599173

Biodiesel Production Using Vegetable Oil and Animal Fat Mixtures

Yousef Aziz SHARIF[1], Cevdet AKOSMAN[2*],

[1] Architectural Department, Shaqlawa Technical Collage, Erbil Polytechnic University, Erbil, Iraq
[2] Department of Chemical Engineering, Faculty of Engineering, Fırat University, Elazığ, Türkiye
[1] yousef.luki@gmail.com, [*2] cakosman@firat.edu.tr

(Geliş/Received: 11/12/2024; Kabul/Accepted: 17/02/2025)

Abstract: In this study, the biodiesel samples were produced by using the mixtures of vegetable oils (sunflower and corn oils) and beef tallow. In the experiments, the mixtures of vegetable oils and beef tallow at different ratios were trans esterified in a batch-wise system with methanol by using sodium hydroxide as catalyst. The effects of temperature, time, amount of catalyst and vegetable oil/beef tallow ratio on biodiesel production were studied. The experiments were carried out by using amount of catalyst ranging from 0.125 to 1 wt% of feedstocks by keeping the molar ratio of 1/6 (oil to methanol) at temperatures between 40-70°C for different times ranging from 25 to 80 min. The biodiesel from the mixture of vegetable oils and beef tallow were obtained using the blends containing 0, 5, 10 and 20% of beef tallow by volume. All experiments were conducted at a fixed mixing speed of 600 rpm. The biodiesel conversion increased sharply until 0.75 wt% catalyst amount and slightly between 0.75wt% and 1 wt% with increasing reaction time for all feed stocks. Biodiesel conversions increased with increasing temperature from 40 to 60°C, but there was no significant increase after this temperature. The degree of conversion decreased as the beef tallow content increased in the mixture. The values of density and kinematic viscosity of biodiesel samples increased with an increase of beef tallow amount in vegetable oils. On the other hand, the heat values of biodiesel were similar to sunflower oil and beef tallow from which they were produced.

Key words: Biodiesel, transesterification, vegetable oil, animal fat.

Bitkisel ve Hayvansal Yağ Karışımlarından Biyodizel Üretimi

Öz: Bu çalışmada bitkisel (ayçiçek ve mısır özü) ve sığır iç yağı karışımları kullanılarak kesikli sistemde biyodizel üretimi araştırılmıştır. Deneysel çalışmalar farklı oranlarda hazırlanan bitkisel ve hayvansal yağ karışımlarından metanol kullanılarak sodyum hidroksit katalizörlüğünde gerçekleştirilmiştir. Çalışmada biyodizel üretimine katalizör miktarı, reaksiyon süresi, sıcaklık ve bitkisel/ hayvansal yağ oranı gibi değişkenlerin etkisi araştırılmıştır. Deneylerde kullanılan yağ/metanol oranı 1/6 (mol) olarak sabit tutulmuştur. Katalizör miktarı ise 0,125 ile 1% (ağırlıkça) arasında değişmektedir. Deneyler, 25-80 dakika arasında değişen farklı zamanlarda 40-70 °C arasındaki sıcaklıklarda gerçekleştirilmiştir. Sığır iç yağı bitkisel yağlarla hacimsel olarak 0, 5, 10 ve %20 oranlarında karıştırılarak deneysel çalışmalar yürütülmüştür. Tüm deneyler, 600 rpm'lik sabit bir karıştırma hızında gerçekleştirilmiştir. Bütün karışımlar için biyodizel oluşumu artan reaksiyon süresi ile birlikte katalizör miktarı arttıkça artmaktadır (%0,75' e kadar hızlı ve %0,75 ile %1 arasında yavaş). Biyodizel oluşumu sıcaklık 40 °C'den 60 °C'ye yükseldiğinde artmış, ancak bu sıcaklıktan sonra fazla değişmemiştir. Biyodizel oluşumu bitkisel yağ içerisinde sığır yağı artışıyla azalmaktadır. Biyodizel örneklerinin yoğunluk ve kinematik viskozite değerleri bitkisel yağlardaki sığır yağı içeriğinin artmasıyla artmaktadır. Bununla birlikte, biyodizelin ısı değerleri üretildikleri ayçiçek yağı ve sığır yağına benzerlik göstermektedir.

Anahtar kelimeler: Biyodizel, transesterifikasyon, bitkisel yağ, hayvansal yağ.

1. Introduction

The consuming of fuel in the world, especially in developing countries, has been increasing with an alarming rate. Studies have been concentrated on the searching of alternative energy sources to overcome this crisis. Biomass and biological sources have been used as alternative sources for clean and renewable energy production. Biodiesel and renewable diesel are the fuels gained much attraction among the various biomass-based fuels [1–3]. Although both fuels are biomass-based, they are different type of fuels.

Biodiesel consists of mono-alkyl esters obtained from different sources such as vegetable oils, animal fats, greases, wastes of oil and fats or from the mixture of different feed stocks. It is generally used as a fuel in engines and heating systems. Biodiesel is a nontoxic biodegradable biofuel and it is environmental profitable [4]. Biodiesel is produced from oils, fats or the mixtures of them with an alcohol by using suitable catalysis via transesterification process [1,5–10]. Although the relatively low cost of biodiesel producing process, the high cost of its raw materials is a major holdback for its marketing in wide range; the biodiesel took out from biomass is commonly more

* Corresponding author: cakosman@firat.edu.tr. ORCID Number of authors: [1] 0000-0001-8942-3381, [2] 0000-0001-7507-2613

expensive than diesel gained from petroleum about 10 to 50% [11]. Fortunately, waste frying oils (WFOs) are remained less price feed stocks; as making biodiesel producing more supportable with compare to the production of fossil fuel-based diesel [12,13].

In order to increase the market value of biodiesel, it is necessary to make its production feasible. The use of less valuable raw materials such as solid fats, soap stocks and used frying oils can reduce the cost of biodiesel. However, it is not economically feasible to directly apply the transesterification process to these raw materials due to their high free fatty acid (FFA) content. Because the cold flow properties of biodiesel obtained from such sources, especially animal fats, are unacceptably poor due to their high saturation level [14,15]. Using mixtures obtained by adding animal fats to vegetable oils in certain proportions is an opportunity to produce biodiesel. Altun et al. [16], in their study investigating the physical properties of biodiesel obtained from canola and beef oil mixtures, observed that the kinematic viscosity of biodiesel increased with the increasing of beef fat in the mixture, but its density did not change much. Taravus et al. [17] reported that the physical properties of biodiesel produced from sunflower oil and beef fat mixtures improved significantly as the amount of beef fat in the feedstocks mixture decreased. Similarly, Dawi et al. [18] showed that many physical properties of biodiesel obtained from sunflower oil and beef fat mixtures changed significantly as the amount of beef fat in the mixture increased and these changes were within the standard range of biodiesel for 40% and 60% ratios (beef fat/sunflower oil). Despite several studies on biodiesel from vegetable oil and animal fat mixtures, experimental data on biodiesel production from such mixtures are still insufficient. Therefore, investigation of biodiesel production from vegetable oil and animal fat mixtures may be useful for a better understanding of biodiesel production in terms of utilization of waste animal fats.

The main purpose of this study is to investigate the production of biodiesel by using mixtures of vegetable oils (sunflower and corn oils) with beef tallow, and determine the obtained biodiesel physical properties such as density, kinematic viscosity, acid value, FFA, water content and heat value.

2. Materials and Methods

Sunflower and corn oils were used as vegetable oils while beef tallow was used as animal fat. The refined and winterized food-grade sunflower and corn vegetable oils were collected from local shops. Beef tallow was obtained from a local butcher and melted at 65 °C and filtrated before used in the experiments. Anhydrous grade (99.95 %) methanol (MeOH) was used for methanolysis while grade sodium hydroxide (NaOH) was used as catalysis. AR grade isopropyl alcohol (IPA) were toluene and were used as reagents for FFA measurements.

The transesterification reaction of the mixture of vegetable oils and animal fat was carried out in a batch system in which a 1000 mL three-necked glass reactor was used. A thermometer was placed in the first neck, while the second was equipped with a reflux condenser. The third neck was used as inlet for the reactants. A magnetic stirrer with a hot plate at a constant speed was used to heat the mixture in the reactor.

The parameters such as reaction time, temperature and the ratio of oil to catalyst were studied. In a typical run, first the total 200 mL mixture of oil and fat is charged to reactor. In order to obtain sodium methoxide, a certain amount of catalyst (NaOH) based on weight percent of blend is mixed with MeOH and heated to dissolve at 60°C. The molar ratio of oil to MeOH was1/6 in all experiments. The sodium methoxide is then charged to the reactor containing the oil/fat mixture. The mixture was then stirred continuously at desired temperature maintained by controlling the electrical heating till a required time. After the completion of the transesterification reaction, the mixture in the reactor was kept in a separating funnel for at least 24 hours to separate the fatty acid methyl esters and glycerol phases. After the separation of the phases from each other, the ester phase was washed 3-4 times with warm distilled water to remove excess unreacted methyl alcohol and glycerin. A few drops of 0.1% H_2SO_4 were added to remove trace amounts of catalyst in the ester phase and the washing process was carried out again. The washing process was repeated until a clear water layer with neutral pH was obtained. A rotary evaporator was used to remove excess methanol that might have been carried over during the washing process. The amount of catalyst used varied between 0.125 and 1% of the mixture by weight. The temperatures studied were varied from 40 to 70°C and the times were between 25 and 80 minutes. All experiments were carried out at a fixed mixing speed of 600 rpm. All experiments were conducted at least duplicate for the reproducibility of the process.

The chemical compositions of raw materials and biodiesels were performed by using a GC analyzer (GC- 6C 2010 plus model by Shimadzu Inc., Kyoto, Japan). The capillary column was 0.25 mm in diameter and 100 m long. Each fatty acid methyl ester determination was run in triplicate and average values are used. Molecular weights of sunflower and corn oils, beef tallow, and biodiesel samples were calculated using Equation (1):

$$M_w = \sum M_{Wi} x_i \quad (1)$$

where, M_w is the molecular weight of oil, fat or biodiesel, M_{wi} is the molecular weight of individual methyl esters and x_i is the mole percent of fatty acid methyl ester.

The biodiesel physical properties such as density, kinematic viscosity, acid value, FFA, water content and heat value were determined using appropriate standard test methods. The density of biodiesel samples was determined using a 25 mL density bottle. The density bottle completely filled with sample was weighed on a precision electronic analytical balance and the density was calculated from the weight and volume of the bottle at 15°C. The kinematic viscosities of the samples were measured by Canon Fenske Routine (PSL ASTM-IP 75) viscometer. The test sample was heated to 40 °C in the viscometer. The time elapsed for a certain volume of sample poured from cab of the viscometer was recorded. This value was the converted to kinematic viscosity using the viscosity table. The acid number and FFA content of sunflower oil, corn oil, beef tallow and biodiesel were measured by following ASTM D664. 5 grams of sample was dissolved in 125 mL of 50% toluene and 50% IPA (v/v) solution. The prepared solution was titrated with 0.1 M KOH solution with 1% alcohol as phenolphthalein indicator. The water content of the feedstocks and biodiesel produced was determined using a Mettler Toledo Karl Fischer DL 31 Titrator. The calorific value of the samples was measured by using an oxygen bomb calorimeter (11350 automatic adiabatic model, Julian Peters Co., Moline, IL, USA). All the procedures for measurements of physical properties were repeated three times for process reproducibility.

3. Results and Discussion

3.1. The Characteristics of Feedstocks

The chemical compositions and some properties of vegetable oils and beef tallow are shown in Table 1 and Table 2, respectively. As seen in Table 1, the beef tallow methyl ester's saturated fatty acid amount is 42.57% while saturation degree is 9.79% for sunflower oil methyl ester 14.55% for corn oil. Due to the effect of the degree of saturation in oils and fats on fuel properties, the saturation value in feedstocks can be important when the produced biodiesel is used as fuel in diesel engines.

It can be seen from Table 2 the oils and fat used in the study have typical physical properties as most oils and fats indicate. The data of Table 2 show that sunflower and corn oil samples contained lower percentage FFA of 0.226% and 0.197%, respectively. However, the beef tallow sample contained slightly higher percentage FFA of 0.533%. Feedstocks containing high FFA cause soap formation as side reaction in biodiesel production. Soap formation can cause difficulty in the separation of biodiesel and glycerol phases and thus affect biodiesel conversion and purity.

3.2. Effects Amount of Catalyst and Time on Biodiesel Production

The amount of catalyst and time for the transesterification process are important factors that could affect the biodiesel conversion [19]. In order to examine the effect of catalyst amount on the biodiesel production, experiments were performed for pure sunflower oil and corn oil using 60 °C reaction temperature and 60 min reaction time as a function of different percentage of catalyst. Figure 1 shows the biodiesel conversion as a function of catalyst percentage. It can be seen from Figure 1, the biodiesel conversion increases as the catalyst percentage increases. The Figure also shows that about 97% biodiesel conversion for sunflower oil and 96 % for corn oil were observed when 1 wt% NaOH was used.

The amount of NaOH was in the range of 0.25–1.25 wt% of vegetable oil-tallow mixtures in order to investigate effects of time and catalyst amount. Figure 2 shows the variation of the biodiesel conversion with the reaction time at different catalyst concentration using 10% tallow in sunflower oil at the constant temperature of 60 °C. As can be seen from Figure 2, the biodiesel conversion increased with increasing time for all the catalyst amount used. Similar results were obtained when using corn oil as a feedstock (Figure 3). The optimal conversions for both oils biodiesel and their mixtures with beef tallow were obtained at 60 min reaction time for each catalyst amount. It can be noticed that for reaction times smaller than 60 min the conversions were lower. The results can be explained by the fact that reaction time lower than 60 min is not enough for methanol to complete the transesterification of all the triglycerides contained in oil. When the reaction time exceeded 60 min, there is small increase in the conversions. On the other hand, when increasing the catalyst amount in the reaction mixture, the biodiesel conversion increased sharply until 0.75 wt% catalyst amount and slightly between 0.75 wt% and 1 wt% with increasing reaction time for both oils used (Figures 2 and 3). From these results, it can be said that the

Table 1. Fatty acid methyl ester compositions of oils and fat used in this study.

Ester	Sunflower oil	Corn oil	Beef tallow
Methyl myristate	0	0	3.72
Methyl palmitate	6.54	11.97	23.85
Methyl palmitoleate	0	0	1.56
Methyl stearate	3.25	2.58	14.75
Methyl oleate	27.84	25.12	47.32
Methyl linoleate	60.91	58.72	6.31
Methy linolenate	0.2	0.65	0.2
Methy arachnidate	0	0	0.25
Others	1.26	0.98	2.04
Saturated	9.79	14.55	42.57
Unsaturated	88.75	84.52	55.39

Table 2. Some properties of oils and fat used in this study.

Property	Units	Sunflower oil	Corn oil	Beef tallow
Molecular weight	g/mole	875	869	855
Density (at 15 °C)	g/cm^3	0.92	0.91	0.89
Kinematic viscosity (at 40 °C)	mm^2/s	32.5	33.1	170.1
Acid value	mg KOH/g	0.449	0.393	1.061
% FFA	%	0.226	0.197	0.533
Water content	%	< 0.05	< 0.05	< 0.05
Calorific value	MJ/kg	39.6	39.5	40.5

conversion of biodiesel is strongly dependent on alkali catalyst amount and the optimum amount of NaOH of 1 wt% could be acceptable value for both vegetable oils used. Time and amount of catalyst found in this study were close to the literature values obtained for both oil biodiesel and similar vegetable oil diesel [20–23].

3.3. Effect of Temperature on Biodiesel Production

The effect of temperature on biodiesel production was studied with the mixture of 10% beef tallow in vegetable oils by using catalyst amount of 1 wt%. Figures 4 and 5 show the effect of biodiesel conversion on the reaction temperature in the presence of 1 wt% NaOH amount for sunflower oil-beef tallow mixture and corn oil-beef tallow mixture, respectively. As seen from Figures 4 and 5, increasing the temperatures from 40°C to 60°C increased the biodiesel conversion. However, when temperature increased 70ºC, the methyl esters conversion decreased. This is because high temperature enhances soap formation as side reaction. At 60 min biodiesel conversion of both vegetable oils used were nearly highest values for all temperatures studied. The results are in agreement with those that found in the literature [20,24–27]. It can be concluded that temperature is an important parameters affecting the reaction rate and biodiesel conversion and it can be seen that 60ºC is the optimal temperature for both vegetables studied in this study.

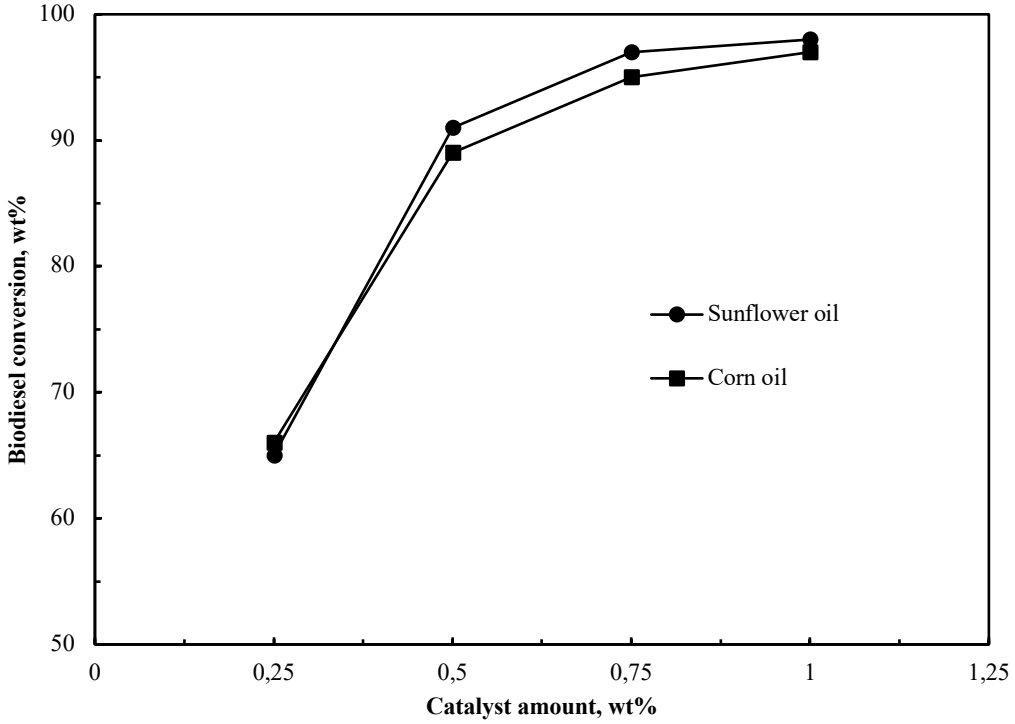

Figure 1. Effect of catalyst amount on biodiesel conversion obtained from pure vegetable oils (60 °C and 60 min).

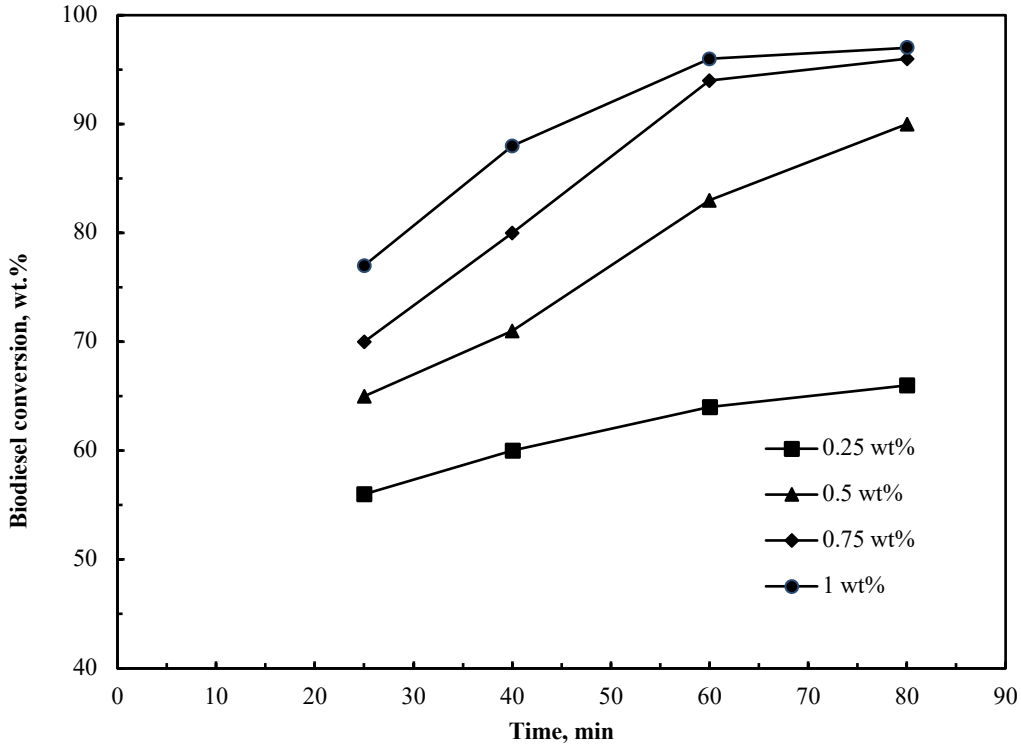

Figure 2. Effect of time on sunflower oil biodiesel conversion at different catalyst amount (60 °C and 10 % beef tallow).

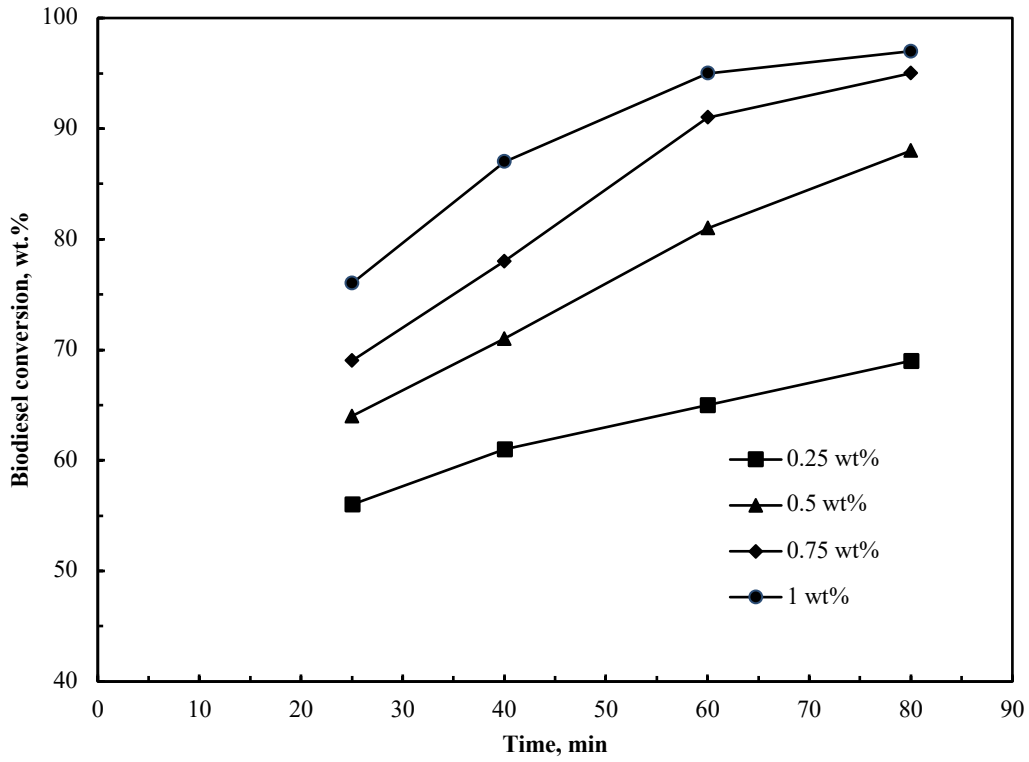

Figure 3. Effect of time on corn oil biodiesel conversion at different catalyst amounts (60 °C and 10 % beef tallow).

3.4. Effect of Beef Tallow Amount on Composition and Physiochemical Properties of Biodiesel

The transesterification of sunflower and corn oils, and their mixtures with beef tallow were carried out using the blends containing 0, 5, 10 and 20% of beef tallow in volume basis to examine effects of beef tallow amount in the mixture on the conversion and properties of biodiesel. The experimental conditions were set up as reaction time of 60 min and 1wt%. Table 3 shows the fatty acid methyl ester compositions, saturation degrees and conversions of biodiesel produced using vegetable oils-beef tallow mixtures. The amounts of methyl esters of oleic acid, palmitic acid, and stearic acid increase with the animal fat content, whereas methyl esters of linoleic acid and linolenic acid decrease as the beef tallow content increases in the sunflower oil (Table 3). Similar results were also seen in Table 3 for corn oil. As can be noted that content and saturation degree of the fatty acid methyl esters in the biodiesel corresponded to the weighted average of its component content in the mixtures. The biodiesel conversion decreases as the beef tallow content increases in the vegetable oils used. This can be attributed to the high FFA content of the beef tallow used (see Table 2). Because the oil samples with high FFA content consume more alkali catalyst to neutralize the FFA in the reaction mixture [14]. The oil samples having high FFA enhance soap formation as side reaction which could cause difficulty in the phase separation of the biodiesel, and affect the yield and the purity of the alkyl esters produced. At the optimum operating conditions, the conversions of biodiesel (methyl esters) from all the mixture of vegetable oil and beef tallow studied varied from 91% to 97.1%. On the other hand, it was observed that the methyl esters conversions obtained for the mixture of sunflower oil and beef tallow are higher than those obtained for the mixtures of corn oil and tallow. Previous studies on the production of biodiesel from the common vegetable oils such as sunflower oil [19,24,28], corn oil [2,29], soybean [2,19,30], canola oil [2,11] and rapeseed [28] gave biodiesel conversions over 90 %. On the other hand, nearly 90% biodiesel conversions were obtained for pure beef tallow [22,31] and for the mixture of vegetable oils and beef tallow [17,18,20]. Considering the studies given above, the conversions obtained in this study are within the range of them.

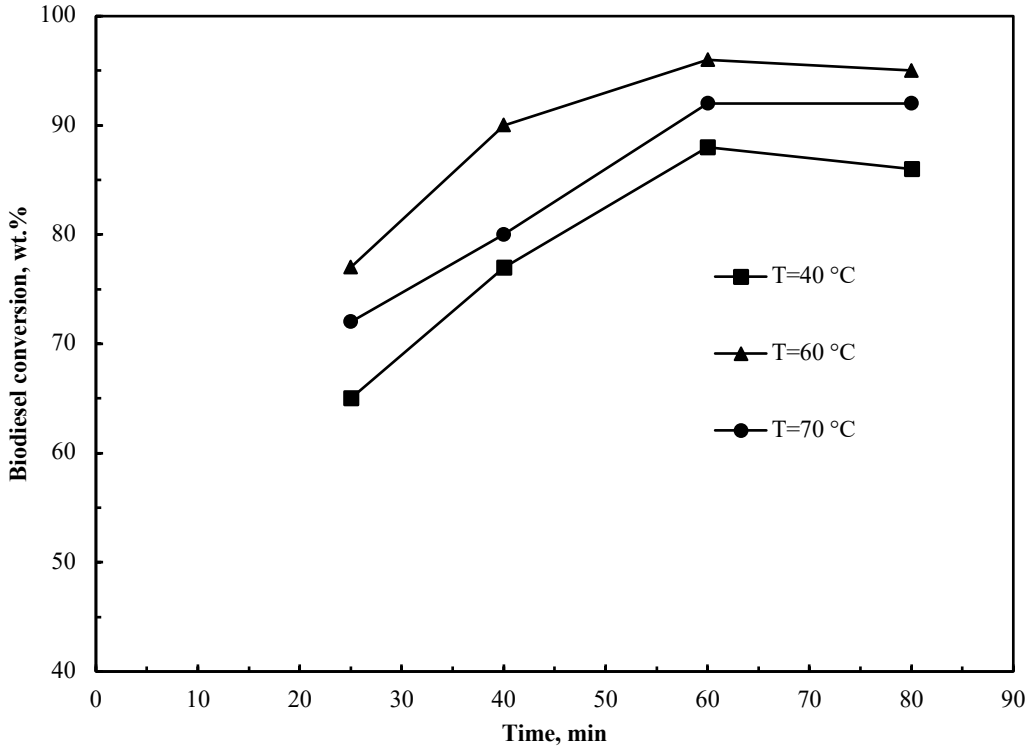

Figure 4. The effect of temperature on conversion of biodiesel obtained from sunflower oil-beef tallow mixture (1 wt% catalyst amount and 10 %beef tallow).

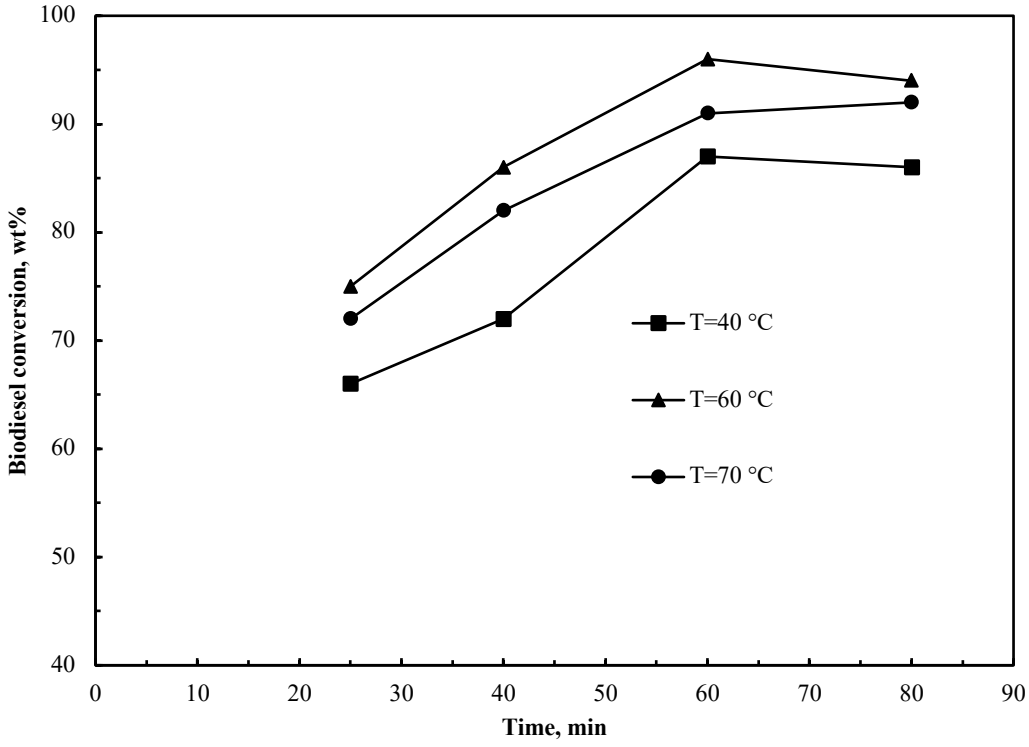

Figure 5. The effect of temperature on conversion of biodiesel obtained from corn oil-beef tallow mixture (1 wt% catalyst amount and 10% beef tallow).

Table 4 summarizes the physical properties of biodiesel produced using the mixtures of sunflower-beef tallow and corn oil-beef tallow. The density has significant effect on the engine combustion system. Because the lower density of fuel breaks up the fuel injected into the combustion. It is known that the density of biodiesel is considerably lower than feedstocks which from it is produced. The density of biodiesel samples produced decreased smoothly with the increase of amount of beef tallow in vegetable oils (Table 4). It was reported that the densities of vegetable oils did not change too much during transesterification process since the densities of methanol and oils are similar to the density of the produced biodiesel and for the blends of vegetable oils with animal fats, the density of methyl ester was reported in the range of 870-890 kg/m^3 [32]. The viscosity is another important property of biodiesel and should be lower than that of its source. The values of viscosity of the biodiesel samples increased with the increasing of beef tallow amount in the vegetable oils. However, the value of kinematic viscosity was slightly high for the mixtures using 20% beef tallow for both vegetable oils to fulfill the standard limits of the standards. This is because of the pure beef tallow as feedstock which have the high viscosity [33,34]. Similar results were reported by Taravus et al. [17] for the mixture of sunflower oil and beef tallow and by Adin et al. [35] for the mixture of canola oil and beef tallow. However, the kinematic viscosity values of the obtained biodiesel for 0, 5 and 10% beef tallow are between the standard limit values [33]. As seen from Table 4, the acid number and acid content decrease with increasing beef tallow content in vegetable oil. The acid content of biodiesel fuel can be come out from FFAs of feedstocks or excess acid that is not used in the biodiesel production process. The acid values and the values of acid contents for all biodiesel samples produced in this study met the standards [33]. The heat values of the biodiesel from vegetable oils-beef tallow mixtures are summarized in Table 4. It is seen from Table 4 that the heat value decreases with increasing beef tallow content in the vegetable oils. On the other hand, the values heat of biodiesel was similar to vegetable oils and beef tallow from which they were produced (see Table 2).

As mentioned above, when comparing both biodiesel conversion and physical properties with literature values, it is seen that biodiesel obtained by blending vegetable oils with low proportions of beef tallow is a suitable fuel. It is reported that the raw material (vegetable oil or animal fat) in biodiesel production constitutes approximately 70–95% of the total cost [9,11,18]. Therefore, it may be economically feasible to obtain high-yield biodiesel by adding animal fats to vegetable oils.

Table 3. Fatty acid methyl ester compositions of biodiesel produced by using mixtures of vegetable oils and beef tallow.

Ester	Sunflower oil				Corn oil			
	Beef tallow (%)				Beef tallow (%)			
	0	5	10	20	0	5	10	20
Methyl myristate	0	0.17	0.39	0.72	0	0.14	0.36	0.73
Methyl palmitate	6.54	7.38	8.17	9.98	11.97	11.95	13.31	14.28
Methyl palmitoleate	0	0.08	0.16	0.3	0	0.079	0.14	0.31
Methyl stearate	3.25	4.05	4.85	5.61	2.58	3.22	3.41	3.52
Methyl oleate	27.84	27.81	29.15	31.5	25.12	26.21	27.52	29.34
Methyl linoleate	60.91	59.18	56.02	50.51	58.72	56.61	53.28	49.94
Methy linolenate	0.2	0.23	0.22	0.21	0.65	0.61	0.58	0.56
Methy arachnidate	0	0.013	0.025	0.05	0	0.013	0.025	0.03
Others	1.26	1.07	1.01	1.12	0.98	1.168	1.375	1.29
Saturated	9.79	11.61	13.43	16.36	14.55	15.32	17.11	18.56
Unsaturated	88.75	87.07	85.32	82.28	87.45	83.51	81.52	80.15
Methyl esters conversion (wt%)	0.971	0.96	0.95	0.93	0.96	0.95	0.93	0.91

Table 4. Some properties of biodiesel produced from mixtures of vegetable oils and beef tallow.

Property	Sunflower oil				Corn oil			
	Beef tallow (%)				Beef tallow (%)			
	0	5	10	20	0	5	10	20
Density at 15 °C, g/cm^3	0.877	0.877	0.874	0.871	0.878	0.877	0.876	0.875
Kinematic viscosity at 40 °C, mm^2/s	4.89	4.92	4.98	5.25	4.53	4.58	4.67	5.32
Acid value, mg KOH/g oil	0.281	0.365	0.224	0.282	0.449	0.331	0.387	0.378
Acid content, %	0.141	0.183	0.113	0.145	0.226	0.166	0.195	0.190
Heat value, MJ/kg	40.18	39.29	38.14	39.86	38.66	38.29	37.14	37.86
Water content, %	<0.05	<0.05	<0.05	<0.05	<0.05	<0.05	<0.05	<0.05

4. Conclusions

The mixtures of vegetable oils and animal fat biodiesels were successfully produced by means of chemical transesterification using MeOH and sodium NaOH. The biodiesel from the mixtures of vegetable oil (sunflower and corn oils) with beef tallow were obtained using the blends containing 0, 5, 10 and 20% of beef tallow in volume basis. It can be concluded from this study that the production of biodiesel from the mixture of vegetable oil sources and beef tallow gave considerable high biodiesel conversions and acceptable physical properties. Although the yield of biodiesel obtained from edible vegetable oils is high, the threat it poses to human food resources makes biodiesel production from these sources unsustainable. For this reason, the addition of unused animal fats to vegetable oils in appropriate amounts can be a reliable and affordable raw material for biodiesel production. It is also necessary to take advantage of these kind of sources to reduce the raw material cost to produce biodiesel. In the view of the results of present study, it is recommended that biodiesel fuel without lowering biodiesel quality can be produced by using different kind of mixture of non-edible oils and relatively less expensive animal fats such as chicken fat, lard and fish oil.

References

[1] Knothe G. Biodiesel and renewable diesel: a comparison. Prog Energy Combust Science 2010; 36(3): 364–373.
[2] Lee SB, Lee JD, Hong IK. Ultrasonic energy effect on vegetable oil based biodiesel synthetic process. J Ind Eng Chem 2011; 17(1):138–143.
[3] Alajmi FSMDA, Hairuddin AA, Adam NM, Abdullah LC. Recent trends in biodiesel production from commonly used animal fats. Int J Energy Res 2018; 42(3): 885–902.
[4] Kumar S, Pal A. A review of bio-diesel as an alternative fuel for vehicles. International Journal of Engineering Technology, Management and Applied Sciences 2014; 2(7):163–177.
[5] Fukuda H, Kond A, Noda H. Biodiesel fuel production by transesterification of oils. Journal of Bioscience and Bioengineering 2001; 92: 405–416.
[6] Ahmad M, Khan MA, Zafar M, Sultana S. Practical handbook on biodiesel production and properties. Boca Raton: CRC Press; 2012.
[7] Hasan N, Ratnam MV. Biodiesel production from waste animal fat by transesterification using H_2SO_4 and KOH catalysts: a study of physiochemical properties. Int J Chem Eng 2022; 2022(1): 6932320.
[8] Binhweel F, Hossain MDS, Ahmad MI. Recent trends, potentials, and challenges of biodiesel production from discarded animal fats: a comprehensive review. Bioenerg Res 2023; 16(2): 778–800.
[9] Azadbakht M, Safieddin Ardebili SM, Rahmani M. A study on biodiesel production using agricultural wastes and animal fats. Biomass Conv Bioref 2023; 13(6): 4893–4899.
[10] Thangthong A, Roschat W, Pholsupho P, Thammayod A, Phewphong S. Physicochemical properties of lard oil and rubber seed oil blends and their comprehensive characterization. Chinese Journal of Chemical Engineering 2024; 75: 1–13.
[11] Leung DYC, Guo Y. Transesterification of neat and used frying oil: Optimization for biodiesel production. Fuel Process Technol 2006; 87(10): 883–890.
[12] González Gómez ME, Howard-Hildige R, Leahy JJ, Rice B. Winterisation of waste cooking oil methyl ester to improve cold temperature fuel properties. Fuel 2002; 81(1): 33–39.
[13] Lamichhane G, Khadka S, Adhikari S, Koirala N, Poudyal DP. Biofuel production from waste cooking oils and its physicochemical properties in comparison to petrodiesel. Nepal Journal of Biotechnology 2020; 8(3): 87–94.
[14] Gerpen JV. Biodiesel processing and production. Fuel Process Technol 2005; 86(10): 1097–1107.

[15] Atadashi IM, Aroua MK, Abdul Aziz AR, Sulaiman NMN. Production of biodiesel using high free fatty acid feedstocks. Renewable Sustainable Energy Rev 2012; 16(5): 3275–3285.
[16] Altun Ş, Yaşar F, Öner C. The fuel properties of methyl esters produced from canola oil- animal tallow blends by basecatalyzed transesterification. The International Journal of Engineering Research and Development 2010; 2(2): 2–5.
[17] Taravus S, Temur H, Yartasi A. Alkali-catalyzed biodiesel production from mixtures of sunflower oil and beef tallow. Energy Fuels 2009; 23(8): 4112–4115.
[18] Dawi H, Muduru I, Abdulkadir B. Evaluation of biodiesel produced from blends of sunflower oil and beef tallow through base catalysis. Am J Polym Sci Technol 2021; 7(2): 23–28.
[19] Dias JM, Alvim-Ferraz MCM, Almeida MF. Comparison of the performance of different homogeneous alkali catalysts during transesterification of waste and virgin oils and evaluation of biodiesel quality. Fuel 2008; 87(17–18): 3572–3578.
[20] Dias JM, Alvim-Ferraz MCM, Almeida MF. Mixtures of vegetable oils and animal fat for biodiesel production: influence on product composition and quality. Energy Fuels 2008; 22(6): 3889–3893.
[21] Baladincz P, Hancsók J. Fuel from waste animal fats. Chem Eng J 2015; 282: 152–160.
[22] Sander A, Antonije Košćak M, Kosir D, Milosavljević N, Parlov Vuković J, Magić J. The influence of animal fat type and purification conditions on biodiesel quality. Renewable Energy 2018; 118: 752–760.
[23] Rosson E, Sgarbossa P, Pedrielli F, Mozzon M, Bertani R. Bioliquids from raw waste animal fats: an alternative renewable energy source. Biomass Conv Bioref 2021; 11(5): 1475–1490.
[24] Rashid U, Anwar F, Moser BR, Ashraf S. Production of sunflower oil methyl esters by optimized alkali-catalyzed methanolysis. Biomass and Bioenergy 2008; 32(12): 1202–1205.
[25] Istiningrum RB, Aprianto T, Pamungkas FLU. Effect of reaction temperature on biodiesel production from waste cooking oil using lipase as biocatalyst. AIP Conference Proceedings 2017; 1911(1): 020031.
[26] Kirubakaran M, Arul Mozhi Selvan V. A comprehensive review of low cost biodiesel production from waste chicken fat. Renewable and Sustainable Energy Rev 2018; 82: 390–401.
[27] Doorı WHA, Alı OM, Ahmed AH, Koten H. Comparative study of biodiesel production from different waste oil sources for optimum operation conditions and better engine performance. Journal of Thermal Engineering 2022; 8(4): 457–465.
[28] Khan E, Ozaltin K, Spagnuolo D, Bernal-Ballen A, Piskunov M, Di Martino A. Biodiesel from rapeseed and sunflower oil: effect of the transesterification conditions and oxidation stability. Energies 2023; 16(2): 657.
[29] Veljković VB, Biberdžić MO, Banković-Ilić IB, Djalović I, Tasić MB, Nježić Z, Stamenković O. Biodiesel production from corn oil: A review. Renewable and Sustainable Energy Rev 2018; 91: 531–548.
[30] Hossain AB, Mazen MA. Effects of catalyst types and concentrations on biodiesel production from waste soybean oil biomass as renewable energy and environmental recycling process. Australian Journal of Crop Science 2010; 4(7): 550–555.
[31] Mata T, Mendes A, Caetano N, Martins A. Properties and sustainability of biodiesel from animal fats and fish oil. Chemical Engineering Transactions 2014; 38: 175–180.
[32] Canakci M. Determination of the density and the viscosities of biodiesel–diesel fuel blends. Renewable Energy 2008; 33: 2623-2630.
[33] Canakci M, Sanli H. Biodiesel production from various feedstocks and their effects on the fuel properties. J Ind Microbiol Biotechnol 2008; 35(5): 431–441.
[34] Canoira L, Rodríguez-Gamero M, Querol E, Alcántara R, Lapuerta M, Oliva F. Biodiesel from low-grade animal fat: production process assessment and biodiesel properties characterization. Ind Eng Chem Res 2008; 47(21): 7997–8004.
[35] Adin H, Altun Ş, Yaşar F. Fuel properties of biodiesels produced from blends of canola oil and animal tallow. Energy Education Science and Technology Part A: Energy Science and Research 2011; 27(1): 199-208.

Turkish Journal of Science & Technology
20(1), 269-279, 2025

Research Paper
https://doi.org/10.55525/tjst.1603517

The Effect of Virtual Reality Images on Artificial Intelligence Classification of Real Environment Images

Nur ÖZBEK[1*], Berna GÜRLER ARI[2], Sevgi ÖZTORUN[3], Ömer Faruk ALÇİN[4]

[1] Software Engineering, Faculty of Technology, Elâzığ, Turkiye
[2]Computer Engineering, National Defense University, Ankara, Turkiye
[3]English Language Teaching, Turkiyem Secondary School, Malatya, Turkiye
[4]Software Engineering, Faculty of Engineering, İnönü University, Malatya, Turkiye

[*1]nurozbek97@gmail.com, [2]berna.gurlerari@msu.edu.tr, [3]oztorun84@gmail.com, [4]omer.alcin@inonu.edu.tr

(Geliş/Received: 18/12/2024; Kabul/Accepted: 25/02/2025)

Abstract: Since virtual reality (VR) is a new and current field of study, it is intensively studied by researchers. Health, education, engineering, culture and tourism, architecture, military fields and many other fields of study have taken steps to support their studies with VR technology and the related subject has become the focus of many researchers. In this thesis, VR technology was used to improve the classification performance of real media images. The proposed approach consists of the classification of real environment images with transfer learning. The transfer learning mentioned in the thesis study can be defined as training an untrained deep architecture with VR images and then retraining the network with real images (fine-tuning). For this purpose, VR scenes are designed in the UNITY environment. A dataset consisting of 15 environments, called V-Env15, was prepared from the designed VR scenes. The proposed approach was tested with the Scene-15 dataset, which is frequently used in environment classification studies. In the thesis, serial and parallel network and GoogLeNet and Inception-ResNet-V2 deep learning architectures were used. In the experimental studies, 0.56% higher accuracy performance increase was achieved in the serial architecture and 4.68% higher accuracy performance increase in parallel architecture. A 4.79% accuracy performance increase was achieved between GoogLeNet and the Serial network, and a 0.44% decrease was achieved between the Parallel network. A 4.47% increase was achieved between Inception-ResNet-V2 and the Serial network, and a 4.57% decrease was achieved between the Parallel network.

Key words: Virtual Reality, Machine Learning, Image Processing, Environment Classification.

Gerçek Ortam Görüntülerinin Yapay Zekâ ile Sınıflandırılmasında Sanal Gerçeklik Görüntülerinin Etkisi

Öz: Sanal gerçeklik (SG) yeni ve güncel bir çalışma alanı olduğundan araştırmacılar tarafından yoğun şekilde çalışılmaktadır. Sağlık, eğitim, mühendislik, kültür ve turizm, mimari, askeri alanlar ve daha birçok çalışma alanı SG teknolojisi ile çalışmalarını destekleyici adımlar atmış ve ilgili konu birçok araştırmacının odağı haline gelmiştir. Bu çalışmada gerçek ortam görüntülerinin sınıflandırma başarımını artırmak için SG teknolojisinden yararlanılmıştır. Önerilen yaklaşım transfer öğrenme ile gerçek ortam görüntülerinin sınıflandırılması işleminden oluşmaktadır. İlgili çalışmada bahsedilen transfer öğrenme, eğitilmemiş bir derin mimarinin SG görüntüleri ile eğitilmesi ardından ağın gerçek görüntülerle yeniden eğitimi (fine-tuning) olarak tanımlanır. UNITY ortamında tasarlanan SG sahnelerinden V-Env15 olarak isimlendirilen ve 15 ortamdan oluşan bir veri seti hazırlanmıştır. Ortam sınıflama çalışmalarında sıklıkla kullanılan Scene-15 veri seti ile önerilen yaklaşım test edilmiştir. Çalışmada tasarlanan Seri ve Paralel ağ ile GoogLeNet ve Inception-ResNet-V2 derin öğrenme mimarileri kullanılmıştır. Deneysel çalışmalarda tasarladığımız seri mimaride %0,56 ve paralel mimaride ise %4,68 daha yüksek doğruluk performans artışı elde edilmiştir. GoogLeNet ile Seri ağ arasında performasn doğruluğu açısından %4,79 artış, Paralel ağ arasında %0,44 azalma elde edilmiştir. Inception-ResNet-V2 ile Seri ağ arasında %4,47 artış, Paralel ağ arasında %4,57 azalma elde edilmiştir.

Anahtar kelimeler: Sanal Gerçeklik, Makine Öğrenmesi, Görüntü İşleme, Ortam Sınıflandırma.

1. Introductıon

Recently, the concept of "Virtual Reality (VR)" has been widely researched. VR concept consists of software and hardware components. In the hardware component, the VR device to be used varies according to the purpose of the

* Corresponding author: nurozbek97@gmail.com ORCID Number of authors: [1]0009-0000-2958-3172, [2]0000-0003-1000-2619,[3]0009-0002-0274-8648, [4]0000-0002-2917-3736

research and the existing infrastructure. Thanks to the sensors whose development has accelerated with the advancement of technology, a large number and variety of data such as audio or image are obtained. Due to the variety of objects in the scenes, there is a deficiency in making sense of scenes with complex backgrounds. As a result of the studies in the field of image processing, scene classification has emerged with the semantic classification of images. Semantic inferences made on the image differ from person to person. Therefore, scene classification is seen as an important problem in image processing. Virtual Reality (VR) technology is widely used in many fields due to the flexibility it provides in the data collection process and its advantage of offering a controlled environment. However, datasets collected from the real world are often costly, time-consuming, and subject to variability due to various environmental factors. This makes it particularly challenging to create large-scale datasets required for training deep learning models. There is a noticeable difference between the low-level features extracted from images and the high-level semantic inferences made by users from images. For this reason, studies on image and video datasets, the number of which increases over time, play an important role in the correct classification of images in terms of semantic information extraction [1,2]. In object detection studies, one can start from images that carry semantic information in scene classification [3]. For example, when identifying the tree object, it is necessary to first examine the forest scene images. Because the number and type of trees in each forest scene should be taught to the classification algorithm. In parallel with the increase in the performance of computer graphics cards in recent years, Deep Neural Networks (DNN) are used to process these data in a shorter time. In the ImageNet competition held in 2012, Krizhevsky et al.'s AlexNet Deep Convolutional Artificial Neural Networks (AlexNet Deep Convolutional Artificial Neural Networks (DPNN) classification performance result increased the use of deep learning methods in the field of artificial intelligence [4]. Deep learning has gained popularity in the field of computer vision and it has been observed that deep learning is used in most of the scientific publications. The topics of these publications are segmentation, object detection, classification and scene classification [5]. Segmentation is the separation of different features in an image into meaningful regions; object detection is the determination of the location and characteristics of each object in an image. Classification is the process of separating each object in an image according to its visual characteristics, while scene classification is the process of analyzing and making sense of the objects in the image as a whole. The main difference between classification and scene classification is that in classification, the objects in an image are analyzed separately, while in scene classification, the image is considered as a whole and the meaning is made in its entirety [6].

In a study by Szummer and Picard [7], they investigated how to infer high-resolution images from the classification of low-resolution images based on the problem of determining whether the environment is indoor or outdoor. In the study, 19 of the 1343 images in the dataset created by Kodak were removed from the dataset due to their ambiguity. Three types of attributes were used in the study: color, frequency and texture. While 75-86% success was achieved in studies using the same dataset, 90.30% success was achieved with the method used in the related study.

In their study [8], Fei-Fei and Perona proposed a new approach for classifying categories of specific areas. They used a dataset with 13 classes: city (308), highway (260), street (292), building (356), residential (241), beach (360), forest (328), mountain (374), bedroom (174), countryside (410), kitchen (151), living room (289) and office (216). Compared to other studies, the researchers emphasized the fact that their work learned the intermediate themes in scenes without any supervision or human intervention. In the Bayesian hierarchical model designed for this purpose, probabilistic frames were first used to learn texture models using code words in the algorithm. Each of the images has an average size of 250×300 pixels and only black and white images were used in the training and testing process. In the complexity matrix used to obtain the performance of the model, the models belonging to the scene category and the basic reality categories of the scenes were compared. The applied method achieved 64% success rate. The classes where the method gave the most errors were bed and living room, kitchen and office. The reason for the method's errors is that these classes have walls and sharp vertical and horizontal edges.

In their study [9], Vailaya et al. aimed to classify holiday image scenes hierarchically. In order to extract features from low-level images based on global features, the scenes were first classified as indoor and outdoor using binary Bayes classifiers. Then, outdoor images were classified as city and landscape, and the landscape was hierarchically classified as sunset, forest, mountain and other natural environments. From 6931 scene images, the classification accuracy was 90.50% for indoor/outdoor, 95.30% for city/landscape, 96.60% for sunset/forest and mountain, and 96% for forest/mountain problems.

In their study [10], Bird et al. aimed to classify the beginning and end scenes of scene images from both virtual and real-world environments with deep learning models. They trained images belonging to six classes on a finely tuned VGG16 on the datasets they created. Transfer Learning (TL) networks trained on virtual data were then compared with real-world data. As a result of the study, it was observed that all transfer learning networks had a higher initial pre-training compared to the others, even showing an average increase of 38.33% in all compared hyperparameter sets. There are 6 class labels in this study. Due to the small number of class labels and the presence of images (doors, walls,

roads, etc.) in the dataset that may be common in many environments, the training error amount is high, which is seen as a gap in the literature.

Herranz et al. [11] emphasized the importance of accurate scene recognition, but also emphasized that this cannot be done only with scene recognition, but also with object recognition. How to effectively combine scene-centered and object-centered knowledge has been the main topic of this research. The scene and object classification on the 397-category SUN397 dataset was performed with CNN architectures. By choosing ImageNet-CNN and Places-CNN combinations, 70.17% success was achieved.

Thanks to the success of studies in the field of pattern recognition, the use of ESA-based architectures has become quite common [20, 21].

The aim of this study is to improve the effect of virtual images prepared using VR technology on the classification performance of real environment images. A dataset containing virtual environment images was created to be used in training the network while classifying real environment images.

2. Material and Method

In this section, information about the deep learning methods used in the study, the datasets, and the environment in which the dataset was prepared are given.

2.1. Convolutional Neural Network (CNN)

In computer vision, feature extraction and classification has been a very common field of study. CNN is a deep feed-forward artificial neural network that performs well in analyzing images. CNN is often used in image processing [12]. CNN architectures consist of input, convolution, pooling, smoothing, fully connected and classification layers. Each of these layers in the architecture performs different tasks and are connected to each other sequentially. While features are extracted in the input, convolution and pooling layers, classification processing is performed in the smoothing, fully connected and classification layers. In CNN architectures, data is divided into parts and a filter is applied to each part. Depending on the size of the filter applied, the image shrinks. When a 16×16 filter is applied to a 16×16 area of the image, the result of this process is reduced to a single pixel. The resulting 1×1 sized output is used for identification [13].

2.2. GoogLeNet

GoogLeNet is a deep learning model with a complex structure consisting of 22 layers and Inception modules. It won the 2014 ImageNet competition with an error rate of 5.70%. The images in the input layer are 224×224×3 [14]. The GoogLeNet architecture does not stack convolution and pooling layers consecutively. This optimizes memory and power usage while minimizing the risk of model memorization. This is because stacking layers and using a large number of filters incurs computational and memory costs. In the GoogLeNet architecture, parallel interconnected modules are used to reduce this cost [15]. The working principle of the GoogLeNet architecture is given in Figure 1.

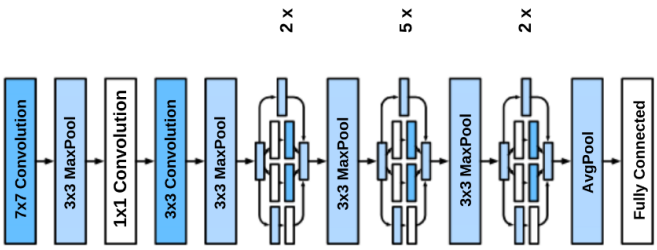

Figure 1. GoogLeNet Architecture.

2.2. Inception-ResNet-V2

The Inception-ResNet-V2 architecture is used in different fields such as image recognition, natural language processing and computer vision. The Inception-ResNet-V2 architecture consists of two main components, Inception and ResNet blocks. Inception blocks combine filters of different sizes to extract more features from the input image. ResNet blocks enable the learning of deeper networks compared to other networks. In this way, it helps in the extraction of

complex features. ResNet blocks use jump connections that add data from the previous layer to the next layer. Figure 2 shows the Inception-ResNetV2 architecture [16].

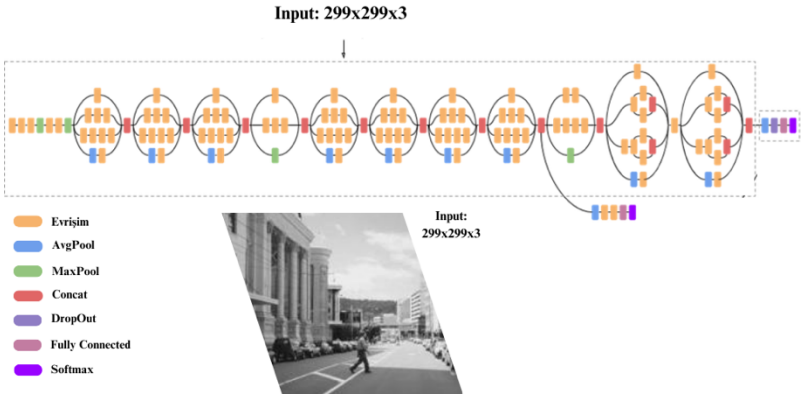

Figure 2. Inception-ResNet-V2 Architecture.

2.3. Serial Network

Serial networks are a very popular type of algorithm in image classification problems due to their simple structure and high accuracy. In this study, an 11-layer Serial network architecture is designed and adapted to image classification. Images of size 80×80×3 were used as the input data of the images in the dataset. The classification, probability and fully connected layers in the last 3 layers of the designed Serial network were removed. After the network trained with V-Env15 prepared within the scope of the study, instead of these 3 layers, the last 3 layers of the trained network, which are fully connected, probability and classification layers, were added. The purpose of this process is fine tuning. Figure 3 shows the Serial network architecture.

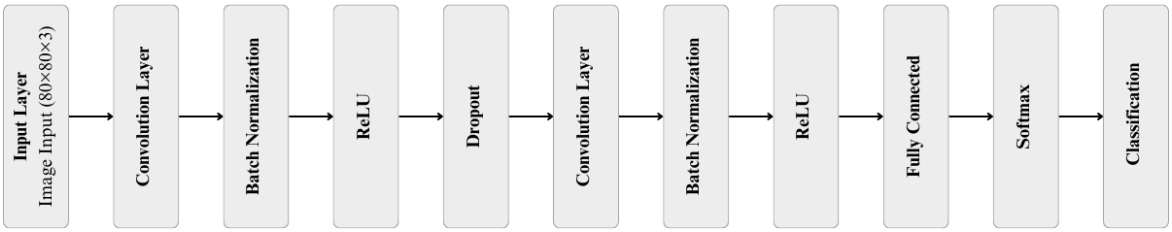

Figure 3. Designed Serial Network Architecture.

2.4. Parallel Network

Parallel network architecture can perform multiple tasks simultaneously. In image classification studies, Parallel networks are used to analyze images in the dataset faster and classify them more accurately. In parallel network approaches, images are divided into parts and each part is analyzed separately on the processor. This approach allows for faster analysis. Because each segmented part is processed in parallel [16]. In addition, Parallel networks provide more feature extraction by taking into account many different aspects of the image and accurate classification is performed. In the parallel network architecture, the last 3 layers of classification, probability and fully connected layers are removed. After the network trained with V-Env15, these 3 layers were replaced with fully connected, probability and classification layers respectively in parallel. This was done for fine tuning. Figure 4 shows the parallel network architecture.

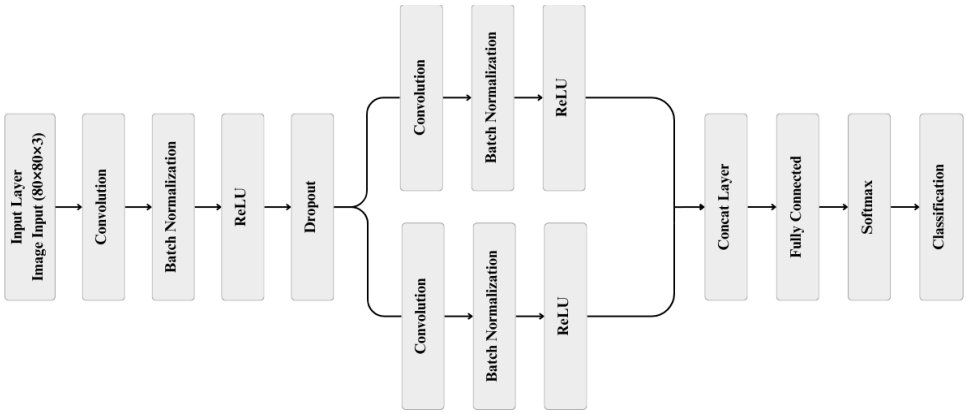

Figure 4. Designed Parallel Network Architecture.

2.5. Dataset

In this study, a transfer learning based approach for image classification is proposed. The dataset consists of real-world and virtual images created in a computer environment using Unity editor. VR environment images are used for training purposes and real environment images are used for testing purposes. In the proposed approach, images obtained from environments created in Unity editor using free assets are used for virtual images and Scene-15 dataset is used for real images.

2.5.1. Scene-15

The images in the Scene-15 dataset, which contains the real images used in the testing process, were collected through Corel and Google images. The first 8 classes in the Scene-15 dataset were added by Oliva and Torralba [17], the next 5 classes by Fei-Fei and Perona [8] and the last 2 classes by Lazebnik et al [18]. There are 15 classes in the dataset: apartment, bedroom, factory, forest, house, kitchen, land, living room, mountain, office, road, sea, market, market, street and skyscraper. The number of images in the classes of the dataset is given in Table 1.

Table 1. Scene-15 dataset image distribution.

	Class Label	Number of Data
Outdoor	Apartment	308
	Factory	311
	Forest	328
	House	241
	Land	410
	Mountain	374
	Path	260
	Sea	360
	Street	292
	Skyscraper	356
Indoor	Bedroom	216
	Kitchen	210
	Sitting room	289
	Office	215
	Market	315
Total		**4485**

2.5.2. V-Env15

The Scene-15 dataset, which contains indoor and outdoor scene images, has been the subject of research in many scientific studies for image classification [8,17,18]. A dataset with the same class labels as the Scene-15 dataset, where virtual images can be used for training, has not been found in the literature. Within the scope of this study, it was aimed to use real and virtual images in the same study by creating labels parallel to these environment labels and there was a need to create a dataset for virtual images. In order to fill the gap in the literature and make a contribution, a new dataset called V-Env15 was created within the scope of the study. The virtual images needed were created with the following steps: In the 3D project created through the Unity editor, the Meta XR Interaction SDK library was included in the project and environments where Oculus Quest 2 can run were prepared. Afterwards, free and publicly available objects from the Unity AssetStore were added to the project. Environments were designed for the class labels created with reference to the Scene-15 dataset. 3D objects, each taken from separate packages, were selected and added to create the relevant scenes in the V-Env15 dataset. The scenes created in Unity were tested on Oculus Quest 2 and video recordings were taken. The video recording was recorded at 1º angles and the images on the screen at each angle change were taken frame-by-frame through the MATLAB program. This process was repeated for each class in the V-Env15 dataset and images were created. As a result of the operations, a total of 40033 images were obtained. In the created dataset, images that are not suitable for use in the research and that may be common to each class label (such as walls, road lines) were excluded. As a result of the excluded images, each class consists of 1000 images. The V-Env15 dataset created for virtual images contains a total of 15,000 images. Table 2 shows the distribution of the media labels of the dataset. Sample images of the V-Env15 dataset are given in Figure 5.

Table 2. V-Env15 dataset image distribution.

	Class Label	Number of Data
Outdoor	Apartment	1000
	Factory	1000
	Forest	1000
	House	1000
	Land	1000
	Mountain	1000
	Path	1000
	Sea	1000
	Street	1000
	Skyscraper	1000
Indoor	Bedroom	1000
	Kitchen	1000
	Sitting room	1000
	Office	1000
	Market	1000
Total		**15000**

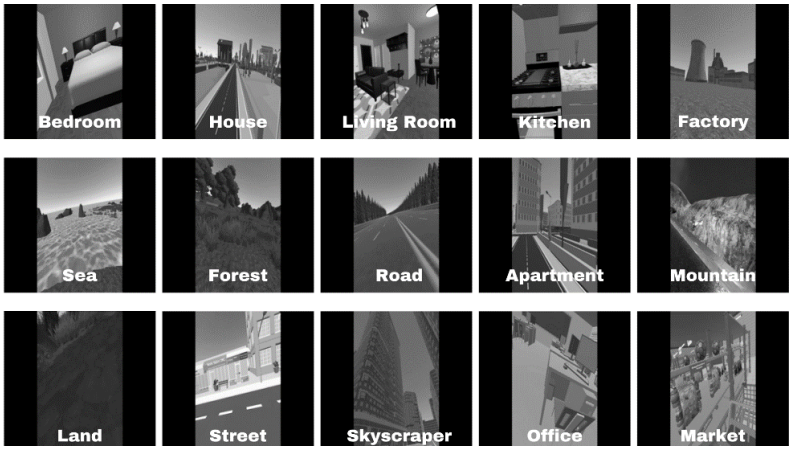

Figure 5. Sample images of the V-Env15 dataset.

2.6. Classification Performance Metrics

Some measurement criteria, such as the complexity matrix, were used to determine the performance of the methods after the classification process. Figure 6 shows a representation of the complexity matrix.

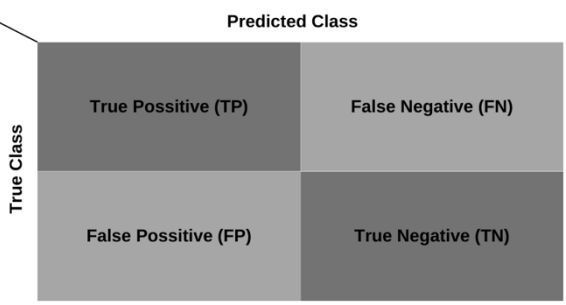

Figure 6. Confusion Matrix.

True Positive (TP): Correctly predicting the predicted class value as class A when the actual class value should be positive A

False Negative (FN): Incorrectly predicting the predicted class value as class A when the actual class value should be negative B

False Positive (FP): The predicted class value is incorrectly predicted as class B when the actual class value should be positive A

True Negative (TN): Correctly predicting the predicted class value as class B when the actual class value should be negative B

When the values in the complexity matrix are analyzed; TP indicates the correct classification value, TN indicates the correct classification of the values in the other class. FP refers to the cases where the values that should actually be in another class are in the relevant class, and FN refers to the cases where the values that should be in the relevant class are in another class [19]. In this study, accuracy, sensitivity, specificity, precision, F1 Score, Mathew Correlation Coefficient (MCC) and Kappa were used. Accuracy is the measurement criterion that shows how much of the predictions of the model are correct. Sensitivity is the measurement criterion that shows how accurately the model classifies positive samples as positive. Specificity is the criterion that shows how much of the negative samples the model classifies as negative. Precision measures how many of the samples predicted as positive are actually positive. The F1 Score is derived from the sensitivity and precision criteria. Mathew Correlation Coefficient (MCC) Accuracy is measured by sensitivity and specificity. Kappa value measures the relationship between different classifier methods. The closer the Kappa value is to 1, the higher the correlation result. The equations for these measurement criteria are given below in Equations 1-6:

$$Accuracy = \frac{TP+TN}{TP+TN+FP+FN} \tag{1}$$

$$Sensivity = \frac{TP}{TP+FN} \tag{2}$$

$$Specificity = \frac{TN}{TN+FP} \tag{3}$$

$$F1\text{-}Score = 2 \times \frac{\text{Sensitivity} \times \text{Precision}}{\text{Sensitivity} + \text{Precision}} \tag{4}$$

$$\text{MCC} = \frac{TP \times TN - FP \times FN}{\sqrt{(TP+FP)(TP+FN)(TN+FP)(TN+FN)}} \tag{5}$$

$$Kappa = 2 \times \frac{TP \times TN - FP \times FN}{(TP \times FN + TP \times FP + 2 \times TP \times TN + FN \times TN + FP \times FP + FP \times TP)} \tag{6}$$

3. Experimental Design

The aim of this study is to classify the images in Scene-15 and V-Env15 datasets as belonging to the indoor or outdoor environment. In this study, two different datasets, Scene-15, which contains real images, and V-Env15, which is prepared by utilizing VR technology within the scope of the study used for transfer learning, were used. There are 4485 images in Scene-15 dataset and 15,000 images in V-Env15 dataset. Of the 15 categories in the datasets, 5 classes consist of indoor environment and 10 classes consist of outdoor environment. All images used were first converted to gray level in MATLAB environment. For the implementation of the method in the study, a computer with Intel (R), @2.30 GHz processor, 6 GB Graphics card and 32 GB RAM was used. In the experimental studies, the hyperparameters of the deep network architectures were obtained empirically. The results section is given under 3 headings for better explanation.

3.1. Serial Network

In the architecture created as a serial network, the Scene-15 dataset was first classified as belonging to the indoor/outdoor environment. In the experimental studies, the dataset was divided into three parts: 70% training, 10% validation and 20% testing. In the experiments, the maximum number of repetitions (Epoch) was fixed as 5 and the optimization method was determined empirically as SGDM (Stochastic Gradient Descent with Momentum). The training time of the serial network was completed in 70 seconds. In Table 3, the Scene-15 row shows the results of applying the Scene-15 dataset to the serial network, the V-Env15 row shows the results of applying the prepared V-Env15 dataset to the serial network, and the TL row shows the results of transfer learning for Scene-15 of the serial network trained with the V-Env15 dataset. This notation is also used in the following subsections.

Table 3. Binary classification results of the architecture created with Serial Network (%).

	Accuracy	Sensivity	Specificity	Precision	F1	MCC	Kappa
Scene-15	95.09	89.58	97.34	93.17	91.34	87.95	87.92
V-Env15	93.20	88.72	95.54	91.20	89.94	84.82	84.81
TL	95.65	89.47	98.26	95.58	92.43	89.48	89.38
ΔF	0.56	-0.11	0.92	2.41	1.09	1.53	1.46

$\Delta \boldsymbol{F}$ shows the difference in the classification performance of the Scene-15 dataset as a result of TL of the Serial network trained with V-Env15. $\Delta \boldsymbol{F}$ will be used to represent the difference in all experimental studies conducted during the study. Table 3 shows that Accuracy improved by 0.56%, Specificity improved by 0.92%, Precision improved by 2.41%, F1 improved by 1.09%, MCC improved by 1.53% and Kappa improved by 1.46%, while Sensitivity improved by 0.11%.

3.2. Parallel Network

In the architecture created as a parallel network, the Scene-15 dataset was first classified as belonging to the indoor/outdoor environment. In the experimental studies, the dataset was divided into three parts: 70% training, 10% validation and 20% testing. In the experiments, the maximum number of repetitions (Epoch) was fixed as 5 and the optimization method was determined empirically as SGDM. The training time of the parallel network was completed in 80 seconds.

Table 4. Binary classification results of the architecture created with Parallel Network (%).

	Accuracy	Sensivity	Specificity	Precision	F1	MCC	Kappa
Scene-15	77.93	61.54	83.28	56.62	57.87	43.13	43.00
V-Env15	87.13	74.00	93.70	85.45	79.31	70.43	70.05
TL	82.61	68.53	88.08	69.08	68.80	56.75	56.74
$\Delta \boldsymbol{F_1}$	4.68	6.99	4.80	12.46	10.93	13.62	13.74

The performance performance resulting from TL realized with the parallel network is given in Table 4. ΔF1 shows the difference in the classification performance of the Scene-15 dataset as a result of TL with V-Env15. When Table 4 is examined, an improvement of 4.68% in Accuracy, 6.99% in Sensitivity, 4.80% in Specificity, 12.46% in Precision, 10.93% in F1, 13.62% in MCC and 13.74% in Kappa.

3.3. Commonly Used Networks

The classification process was repeated with GoogLeNet with 224×224×3 dimensions and Inception with 299×299×3 dimensions. In the experimental studies, the dataset was divided into three parts as 70% training, 10% validation and 20% test. In the experiments, the maximum number of repetitions (Epoch) was fixed as 5 and the optimization method man (ADAptive Moment) was obtained empirically. Table 5 shows the performance performance and increase rates of the TL resulted from the GoogLeNet architecture and Serial and Parallel network architectures. In Table 5, ΔF_2 represents the difference between Serial network and GoogLeNet and ΔF_3 represents the difference between Parallel network and GoogLeNet.

Table 5. Binary classification between GoogLeNet architecture (%).

	Serial Network 80×80×3	Parallel Network 80×80×3	Googlenet 224×224×3	ΔF_2	ΔF_3
TL	95.65	82.61	83.05	+4.79	-0.44

Table 6 shows the performance results of Inception-ResNet-V2 with the Serial and Parallel network architectures and the increase rates. In Table 6, ΔF_4 represents the difference between Serial network and Inception-ResNet-V2, ΔF_5 represents the difference between Parallel network and Inception-ResNet-V2.

Table 6. Binary classification difference between Inception-Resnet-V2 architecture (%).

	Serial Network 80×80×3	Parallel Network 80×80×3	Inception-ResNet-V2 299×299×3	ΔF_4	ΔF_5
TL	95.65	82.61	87.18	+8.47	-4.57

4. Results and Recommendations

In this study, the performance of VR technology in classifying real environment images is investigated. For this purpose, a scene with 15 classes was designed in the Unity editor by taking the Scene-15 dataset as an example. A VR dataset called V-Env15 was prepared by moving 360º at 1º angles from the designed environments. From a network trained using the V-Env-15 dataset, we focused on increasing the classification performance of the environment images in the dataset containing real images called Scene-15 by performing TL. Within the scope of the study, two CNN architectures with serial and parallel structures were designed. First, the Scene-15 dataset was applied to the Serial network and the highest classification accuracy of 95.09% was obtained. Then, after training the Serial network with the V-Env15 dataset, TL was applied and an accuracy of 95.65% was achieved in the environment classification of the Scene-15 dataset. Thus, by applying TL, 0.56% higher accuracy was achieved in the Serial network. Scene-15 dataset was applied to the Parallel network architecture and 77.93% accuracy was achieved in the experiment. Then, by applying TL to the Parallel network architecture trained with the V-Env15 dataset, 82.61% accuracy was achieved in the environment classification of the Scene-15 dataset. TL on the parallel network resulted in an accuracy improvement of 4.68%. Studies were continued with GoogLeNet and Inception-ResNet-V2 architectures, which are widely used in TL applications in image classification. The Scene-15 dataset achieved 83.05% classification accuracy by performing TL with GoogLeNet. Inception-ResNet-V2 network classified the Scene-15 dataset with 87.18% accuracy with TL. In the experiments, binary classification as indoor/outdoor environment was performed on the images in the datasets. In binary classification studies, the highest performance was obtained in the experimental study with the Serial network. Compared to other classification studies, the classification study with Parallel network showed lower performance compared to other architectures.

Experiments were conducted for the case with 15 classes. Classification accuracies for this case are presented in Table 7. When Table 7 is examined, the optimization method rmsprop and the learning rate were changed to 1e-3 for the parameters used in the internal/external classification process in the trained Serial network. SGDM optimization and 1e-4 learning rate in the network trained with parallel network; rmsprop optimization and 1e-3 learning rate in the

network trained with Inception-ResNet-V2 architecture; man optimization and 1e-3 learning rate in the network trained with GoogLeNet architecture.

Table 7. 15 class environment type accuracy results of Scene-15 dataset in different architectures (%).

	Serial Network	Parallel Network	Inception-ResNet-V2	GoogLeNet
TL	83.17	60.00	75.81	82.50

In experimental studies with a 15-class dataset, the classification with the Serial network was 83.17% higher than the other architectures. The lowest classification performance was obtained from the Parallel network with 60% accuracy.

Another study in the literature on environment classification with VR images is given in Table 8. In the study of 6 classes, there are Living room, Staircase, Forest, Land, Computer lab and Bathroom classes. When Table 8 is analyzed, it is seen that the success rate in the study conducted by Bird et al. is 88.27%. However, this performance was obtained in the classification study conducted on only 6 classes. In the study conducted on the 15-class V-Env15 dataset designed within the scope of the study, 83.17% success was achieved.

Table 8. Study on classification with virtual images.

Ref. Name	**Accuracy (%)**	**ΔF_1 (%)**	**Class Number**	**Class Labels**
Paper [10]	88.27	38.33	6	Living Room, Staircase, Forest, Terrain, Computer Laboratory, Bathroom
Proposed Method	**83.17**	**5.36**	**15**	***Apartment, Land, Street, Mountain, Sea, House, Factory, Skyscraper, Market, Kitchen, Office, Forest, Living Room, Bedroom, Road***

When the studies conducted within the scope of the scientific study and the literature are evaluated, the following points are suggested to be taken into consideration in order to increase the classification success in the future studies;

1. In the studies to be conducted with virtual reality images, it is evaluated to create a dataset that does not contain images that may be common in every environment (wall, road, door, chair, etc.) in the data to be created other than the datasets in the literature.
2. In addition to the class labels in the V-Env15 dataset created for use in this study and to contribute to the literature, it is recommended to add real-life environments to the dataset.
3. Serial network, Parallel network, GoogLeNet and Inception architectures were used on Scene-15 and V-Env15 datasets. It is thought that using more up-to-date and complex CNN architectures on the same datasets will contribute to the improvement of the results.
4. It is thought that it would be useful to perform different classification studies on the V-Env15 dataset with 15 class labels (apartment, bedroom, factory, forest, house, kitchen, land, living room, mountain, office, road, sea, market, street and skyscraper) and 40033 images.

Using Scene-15 and V-Env15 datasets, it is suggested to conduct studies on whether malicious computer generated images are real or virtual.

Author Contribution Statement

In the study, Author 1 contributed to the idea, data set creation and methodological analysis; Authors 2 and 4 contributed to the design and analysis; Author 3 contributed to the literature review, spelling check; Authors 1, 2 and 4 contributed to the evaluation of the results, provision of the materials used and examination of the results.

References

[1] Çavuş Ö. Semantic Scene Classification for Content-Based Image Retrieval. Doktora Tezi, Bilkent Üniversitesi, Türkiye, 2008.

[2] Karabulut A. Bayes Tabanlı Sahne Sınıflandırması. Yüksek Lisans Tezi, Hacettepe Üniversitesi, Türkiye, 2006.

[3] Torralba A, Murphy KP, Freeman WT, Rubin MA. Context-based vision system for place and object recognition. Proceedings of the IEEE International Conference on Computer Vision; Ekim 2003; IEEE Computer Society. s. 273-273.

[4] Meldrum D, Glennon A, Herdman S, Murray D, McConn-Walsh R. Virtual reality rehabilitation of balance: assessment of the usability of the Nintendo Wii® Fit Plus. Disabil Rehabil Assist Technol 2012; 7(3): 205-210.

[5] Song H, Chen F, Peng Q, Zhang J, Gu P. Improvement of user experience using virtual reality in open-architecture product design. Proc Inst Mech Eng B J Eng Manuf 2018; 232(13): 2264-2275.

[6] Boas YAGV. Overview of virtual reality technologies. Proceedings of the Interactive Multimedia Conference; Ağustos 2013.

[7] Szummer M, Picard RW. Indoor-outdoor image classification. Proceedings of the IEEE International Workshop on Content-based Access of Image and Video Databases; 1998.

[8] Fei-Fei L, Perona P. A Bayesian hierarchical model for learning natural scene categories. Proceedings of the IEEE Conference on Computer Vision and Pattern Recognition; 2005; Cilt 2. s. 524-531.

[9] Vailaya A, Figueiredo MAT, Jain AK, Zhang HJ. Image classification for content-based indexing. IEEE Trans Image Process 2001; 10(1): 117–130.

[10] Bird JJ, Faria DR, Ekárt A, Ayrosa PP. From simulation to reality: CNN transfer learning for scene classification. Proceedings of the IEEE 10th International Conference on Intelligent Systems; Ağustos 2020. s. 619-625.

[11] Herranz L, Jiang S, Li X. Scene recognition with CNNs: objects, scales and dataset bias. Proceedings of the IEEE Conference on Computer Vision and Pattern Recognition; 2016. s. 571–579.

[12] Karadağ B, Arı A, Karadağ M. Derin öğrenme modellerinin sinirsel stil aktarımı performanslarının karşılaştırılması. Politeknik Dergisi 2021; 24(4): 1611-1622.

[13] Arı B. Kayısı Yapraklarının Evrişimsel Sinir Ağları Kullanılarak Sınıflandırılması. Yüksek Lisans Tezi, Fen Bilimleri Enstitüsü, 2022.

[14] Arı A. Derin Öğrenme Tabanlı Beyin MR Görüntülerinden Beyin Tümörlerinin Tespit Edilmesi ve Sınıflandırılması. Doktora Tezi, İnönü Üniversitesi, Malatya, 2019.

[15] Özküçük M, Alçin ÖF, GENÇOĞLU M. EMG sinyalleri kullanılarak GoogLeNet ve çok seviyeli DPD ile el tutma hareketlerinin sınıflandırılması. Fırat Üniversitesi Mühendislik Bilimleri Dergisi 2022; 34(1): 33-43.

[16] Szegedy C, Vanhoucke V, Ioffe S, Shlens J, Wojna Z. Rethinking the inception architecture for computer vision. Proceedings of the IEEE Conference on Computer Vision and Pattern Recognition; 2016. s. 2818-2826.

[17] Oliva A, Torralba A. Modeling the shape of the scene: A holistic representation of the spatial envelope. Int J Comput Vis 2001.

[18] Lazebnik S, Schmid C, Ponce J. Beyond bags of features: Spatial pyramid matching for recognizing natural scene categories. Proceedings of the IEEE Conference on Computer Vision and Pattern Recognition; 2006.

[19] Arı B. Medikal Veri Setleri için Yeni Bir Aşırı Öğrenme Makinesi Otomatik Kodlayıcı Tasarımı. Doktora Tezi, Fırat Üniversitesi, Elazığ, 2022.

[20] Donuk K, Arı A, Hanbay D. A CNN based real-time eye tracker for web mining applications. Multimed Tools Appl 2022; 81(27): 39103-39120.

[21] Turkoglu M, Aslan M, Arı A, Alçin ZM, Hanbay D. A multi-division convolutional neural network-based plant identification system. PeerJ Comput Sci 2021; 7: e572.

Turkish Journal of Science & Technology
20(1), 281-297, 2025

Research Paper
https://doi.org/10.55525/tjst.1623326

Real-Time Drone Command Processing: A Large Language Model Approach for IoD Systems

Anıl SEZGİN[1*], Aytuğ BOYACI[2]
[1]Research and Development, Siemens A.S, Istanbul, Turkey
[2] Department of Computer Engineering, National Defence University, Air Force Academy, Istanbul, Turkey
[*1] anil.sezgin@siemens.com, [2] aytug.boyaci@msu.edu.tr

(Geliş/Received: 20/01/2025; Kabul/Accepted: 10/03/2025)

Abstract: One of the most critical steps toward autonomous capabilities, where natural language instructions can be successfully converted into executable API calls, is integrating Large Language Models (LLMs) into the ecosystem of the Internet of Drones (IoD). This study introduces an end-to-end LLM-based framework for enhancing real-time drone operation and problem handling in intent recognition, parameter extraction, and ambiguity resolution. It has resorted to a spectrum of methodologies in the form of Retrieval-Augmented Generation (RAG) and customized fine-tuning specific to each domain, towards accurate command interpretation and successful API generation. This paper evaluates the performance of the model on a carefully designed dataset containing 1,500 commands for the different scenarios of IoD with an average BLEU score of 89.6 and a cosine similarity of 0.94. Optimization techniques, such as parallel processing and better query handling, reduced the latency of this system by 15%, with an average query processing time of 0.9 seconds. This work gives considerable importance to the scalability and flexibility of the system, which is quite crucial for applications in domains like disaster response, precision agriculture, and surveillance. Proposed LLM-based framework thus tries to bridge gap between human intent and drone execution for intuitive, reliable, and efficient IoD deployments.

Key words: Large language models, internet of drones, natural language processing, real-time command processing.

Gerçek Zamanlı Drone Komut İşleme: IoD Sistemleri için Büyük Dil Modeli Yaklaşımı

Öz: Doğal dil talimatlarının yürütülebilir API çağrılarına başarıyla dönüştürülebildiği otonom yeteneklere doğru atılan en kritik adımlardan biri, Büyük Dil Modellerinin (LLM) İnsansız Hava Araçları İnterneti (IoD) ekosistemine entegrasyonudur. Bu çalışma, amaç tanıma, parametre çıkarımı ve belirsizlik çözümleme alanlarında gerçek zamanlı drone operasyonlarını ve sorun çözümünü geliştirmek için uçtan uca bir büyük dil modeli tabanlı çerçeve sunmaktadır. Çalışmada, her alana özgü doğru komut yorumlama ve başarılı API oluşturma için Retrieval-Augmented Generation (RAG) yönteminden yararlanılmıştır. Çalışma, IoD'nin farklı senaryolarını kapsayan ve 1.500 komuttan oluşan bir veri kümesi üzerinde modeli değerlendirmiştir. Elde edilen sonuçlara göre, modelin ortalama BLEU skoru 89,6 ve kosinüs benzerliği 0,94 olarak ölçülmüştür. Paralel işlem ve daha iyi sorgu işleme gibi optimizasyon teknikleriyle sistemin gecikme süresi %15 azaltılmış ve ortalama sorgu işleme süresi 0,9 saniye olmuştur. Bu çalışma, özellikle afet müdahalesi, hassas tarım ve gözetim gibi alanlarda uygulamalar için oldukça kritik olan sistemin ölçeklenebilirliğine ve esnekliğine büyük önem vermektedir. Önerilen LLM tabanlı çerçeve, böylece insan amacı ile drone uygulamaları arasında sezgisel, güvenilir ve verimli IoD dağıtımları için bir köprü kurmayı amaçlamaktadır.

Anahtar kelimeler: Büyük dil modelleri, insansız hava araçları interneti, doğal dil işleme, gerçek zamanlı komut işleme.

1. Introduction

The Internet of Drones is one of the advanced technologies today, where drones no longer work in isolation but, rather, in coordination with each other under a single network controlled by centralized systems. Among the many functions such systems make possible are coordinated logistics in the delivery of products, vast monitoring in security uses, and dynamic environmental sensing to gather critical data for better decision-making. IoD systems have revolutionized domains such as disaster management, where drones can be rapidly deployed to aid search and rescue operations; logistics, through route optimization of delivery networks in both urban and rural environments; and precision agriculture, with detailed crop health assessment and efficient application of pesticides.

At the core of this new technology lies the challenge of effective communication between humans and machines. Most often, users give commands in natural language, but it is crucial that such a command is translated into a precise, executable API request so that drones can execute the intended actions. For instance, even the straightforward command “Send Drone A to scan Sector 7” involves finding the right drone, assessing its current status and location, building the appropriate API request, and verifying that the operation satisfies a range of

* Corresponding author: anil.sezgin@siemens.com. ORCID Number of authors: [1] 0000-0002-5754-1380, [2] 0000-0003-1016-3439

constraints, including battery levels, no-fly zones, and task priorities. This task is significantly harder in dynamic environments where the drone networks keep altering, the operational parameters get updated quite often, and user intents change greatly due to the variation of context and applications.

IoD systems, on the other hand, have to cater to a wide range of users, from professional experts to laypersons not necessarily versed in specialized vocabulary. This kind of heterogeneity demands a solution capable of correctly interpreting vague, incomplete, or contextually complex queries while maintaining high levels of accuracy and efficiency. Such is the challenge requiring activation of modern security measures and effective detection systems, discussed in [1], pointing out a number of vulnerabilities in IoD networks while suggesting new methods for data and operational integrity. The increasing sophistication of drone operations and requirements for real-time responsiveness only add another layer of complexity to an already difficult challenge of translating human intent into machine-executable commands. Improvement in the object detection process, as explained in [2], is the key to allowing drones to recognize and react to dynamic objects in their surrounding to accomplish their tasks successfully in different setups.

The focus of this research, by its very nature, integrates large language models in overcoming such challenges—LLMs. These models, through the strengths of advanced generative language capabilities coupled with specialized fine-tuning for specific tasks, are able to analyze user inputs and generate accurate responses that are tailored to specific domains. Methods like Retrieval-Augmented Generation (RAG) and supervised fine-tuning make LLMs very adaptable to perform specialized tasks, like translating natural language instructions into API requests for IoD systems. Besides adaptability in performing different functions, LLMs have proven very efficient in ambiguity resolution and consistency within context; these are factors that further improve performance on incomplete queries or in multi-turn dialog. If fine-tuned carefully, even for the most complex operational settings, LLMs could still come up with quite coherent and stable responses.

The application of Artificial Intelligence (AI) technologies and LLMs in IoD systems is one giant leap toward human-machine interaction and operational efficiency. Similarly, some of the critical IoD challenges, such as resource constraints and scalability, can be overcome by these IoD systems through advanced AI-driven methodologies such as trajectory optimization, intelligent caching, and adaptive edge computing [3]. Simultaneously, LLMs improve the processing of natural languages so that human commands can be correctly translated into executable API requests [4]. The integration follows frameworks investigated in [5], underlining the need for scalable and secure API-driven architectures to enable seamless interactions between humans and machines. It would also enable real-time collaboration in multi-drone environments, ensuring adaptability to dynamic mission requirements and laying the foundations for resilient IoD operations. Exploiting these synergies between AI and LLM offers new solutions for applications in disaster response, smart city, and agriculture [6].

The contribution of LLMs goes beyond command processing to contextual understanding, scalability, and real-time responsiveness of the IoD functionality. In this regard, LLMs have integrated domain-specific retrieval mechanisms with scalable architectures to optimize API generation for mission-specific demands [7]. It will ensure that drones perform complicated tasks with precision, bridging the gap between human intent and machine execution. Furthermore, LLM-based frameworks allow the IoD system to adapt easily in diverse, fast-changing operational contexts, which improves the reliability of the system with less development effort [8]. With advances in artificial intelligence and large language model technologies, simpler, intuitive, and intelligent IoT systems would emerge, enabling larger degrees of innovations on different applications and fields while ensuring that, in themselves, they have roles of promoters for autonomous devices. The capacities of large language models go beyond task completion; they also bring better contextual understanding to the Internet of Things, offer crucial scalability, and make feasible instantaneous responsiveness. Large language models, using retrieval mechanisms focused on given domains combined with flexible architectural designs, enhance the creation of mission-specific APIs. Complex tasks are thus performed with precision by drones, and the gap between the human intent and machine execution is effectively bridged. This will enable the development of LLM-based frameworks to continue, allowing IoD systems to be adaptive under different and dynamic operational contexts with less development effort but increased reliability. With the continuing evolution of AI and LLM technologies, IoD systems are going to be even more accessible, intuitive, and efficient, driving innovation in a lot of fields and further solidifying their position as key enablers of autonomous systems. Another core aspect is that scalability is going to form another cornerstone in our approach: IoD systems frequently demand the simultaneous operation of several drones with very different roles, constraints, and real-time demands. The new framework, based on LLM, is going to efficiently scale up with the incorporation of knowledge-retrieval mechanisms peculiar to a specific domain that adjusts operating parameters for each drone; it ensures API requests are valid and optimized against requirements peculiar to any given context in operation. Hence, this allows perfect integration into each one of the most variable and dynamic situations.

Another core operation of IoD is real-time execution. Any delay in processing and execution of commands could have a tremendous impact on mission outcome, more so in time-critical scenarios involving disaster response or security surveillance. Our system performs advanced indexing techniques along with low-latency retrieval algorithms to reduce delays and ensures that API requests are created and executed within operationally acceptable time frames. This is further complemented by error detection and correction mechanisms, which proactively identify and resolve inconsistencies in generated commands to prevent operational failures.

The potential applications of an IoD command system based on LLM go far beyond the simple execution of tasks. Offering seamless interaction between humans and machines, this technology opens possibilities for much more intuitive and accessible drone operations. As IoD systems will continue to evolve, so must the frameworks to provide support for operation. LLM integration has provided a considerable advance in this aspect by filling the gap between human intent and machine execution in scalable, efficient, and user-friendly solutions for the problems posed by natural language-to-API request conversion. By addressing these issues directly, our research enhances the functionalities of IoD systems and forms a basis for future developments of autonomous systems and intelligent control frameworks.

To better outline the following paper, its structure will be as follows: Section 2 discusses related work on IoT systems, RAG models, and approaches to command generation. Section 3 elaborates on the system architecture with a focus on the retriever and generator components. Section 4 discusses the creation of the dataset and model development. Section 5 evaluates the system using real-world scenarios and benchmarks. Finally, Section 6 concludes with key findings and future directions for advancing IoD command systems.

2. Related Work

2.1. Introduction to AI and large language models

The development of large language models has been a turning point for artificial intelligence, enabling new developments in reasoning, communication, and automation. The core of all this lies in the development of diverse datasets and integration methods that expand these models' abilities. Many research efforts have shed light on some important aspects of LLMs, hence setting the stage for their application in many different domains.

High-quality, diverse datasets are indispensable for large language models. Study [8] classifies datasets into pre-training sources such as Common Crawl, C4, and GitHub repositories, and fine-tuning datasets like Alpaca and InstructGPT, highlighting the importance of dealing with challenges in data duplication, biases, and quality filtering. It calls for open-source initiatives to improve non-English corpora for democratized LLM development and better global utility. The versatility of LLMs is seen even in robotics, as discussed in Study [9], with regard to how models like GPT-4 and LLaMA would impact areas of communication, perception, planning, and control. It highlights zero-shot planning, adaptive control, and robotics-specific prompt engineering, together with challenges in consistencies and computational demands. In a comparable manner, foundational models, including large language models and vision-language models (VLMs), enhance the functionalities of autonomous systems, as indicated in Study [10], by augmenting the comprehension of semantic contexts and facilitating task decomposition, thereby fostering improved robotic autonomy in previously untrained environments. The research highlights progress in semantic scene representation alongside natural language processing, effectively connecting perception with action. Beyond robotics, LLMs revolutionize software development, Study [11] shows how generative AI automates tasks of code generation, debugging, and testing in order to make workflows faster and increase productivity. This paper further stresses balancing automation with human oversight to address ethical and cybersecurity issues, hence showing the transformative role that AI plays in modern software engineering.

2.2. Security and anomaly detection

With the Internet of Things, this increased dependency on interconnected systems and networks has raised the bar for strong security frameworks. Hence, artificial intelligence has come to be among those most significant enablers for addressing the increasingly complex challenges of security in anomaly detection and mechanisms of trust. The modern security environment is now being fundamentally transformed through the use of advanced machine-learning techniques and leading-edge technologies.

Few-shot learning has been promising in the direction of addressing zero-day vulnerabilities by enhancing real-time anomaly detection. Study [12] proposes an unsupervised few-shot learning framework utilizing FastText embeddings and Approximate Nearest Neighbor (ANN) search for API injection attack detection. The methodology proposed has a high accuracy and is flexible, with crucial innovations such as incremental learning

methods and tokenizers tailored for specific APIs, which makes it practical for real-world applications despite the issues regarding dataset representativeness and protocol diversity. The security vulnerabilities associated with Unmanned Aerial Vehicles (UAVs) are thoroughly taxonomized in [13], analyzing susceptibilities present in the hardware, software, and communication layers. The paper discusses AI-driven techniques like federated learning and reinforcement learning, in the context of adaptive security and decentralized processing, which implies the necessity of standardized and scalable benchmarks. Similarly, autonomous vehicles are attacked by adversarial attacks, as addressed in Study [14], which analyzes attack scenarios using ISO 21448. This article synthesizes recent advances in adversarial defenses and robust sensor technologies, thereby offering a roadmap for simulation-based evaluations and enhanced safety. A novel approach to increasing AI trust is introduced by integrating blockchain into LLMs in Study [15]. The BC4LLM framework uses the decentralized and immutable characteristics of blockchain to secure the training and output of LLMs for applications in highly sensitive domains, such as fintech and healthcare. It also addresses the challenges of scalability and energy efficiency. All these studies together present how AI is shaping the future of security across different domains with the help of complementary technologies such as blockchain.

2.3 UAV-enabled wireless networkds and IoT integration

Integration of UAV-enabled wireless networks (UWNs) with the Internet of Things (IoT) systems is one of the modern communication and intelligent infrastructure paradigms. Using artificial intelligence, these networks can respond to key issues of resource management, scalability, and fault tolerance and thus can offer autonomous and adaptive capabilities. In many fields, like smart cities, agriculture, disaster management, etc., UAVs have been indispensable nodes in transmitting real-time data to enhance network efficiency. This integration of artificial intelligence-based systems and new approaches enabled such advancement in these interconnected systems, as could be inferred from the following studies.

The transformative potential of AI in UAV networks and IoT ecosystems is substantiated through the advances in optimization, resource management, and data generation. Study [3] comprehensively reviews the AI applications in UAV networks focusing on trajectory optimization, radio resource management, and edge computing. Techniques such as deep reinforcement learning (DRL) and multi-agent learning have been instrumental in improving resource optimization and adaptability. Practical implementations like intelligent caching and UAV placement address the issues of scalability and energy efficiency, though there is always the computational constraint. The IoIT paradigm further pushes these innovations as Study [16] discusses, for instance, TinyML and 5G in applications of smart cities, healthcare, and military. IoIT, while at the nascent stage, even with interoperability and resource-constrained limitations, shows a future direction with promises of federated learning and adoption of 6G. Enhancing IoT networks further, Study [17] presents the LLM-ENFT framework, where large language models are integrated into edge networks to perform proactive fault diagnosis and decision-making. Simulation results have shown an improvement in throughput and resilience, showing that LLMs will be the cores for autonomous fault management, though challenges remain in computational overhead. In response to the pressing demand for scalable training datasets, Study [18] introduces the ASDA framework, which utilizes procedural generative methods alongside domain randomization (DR) to augment the diversity of datasets pertinent to machine learning in drone-related applications. When combined with the AirSim engine, ASDA markedly enhances both data diversity and efficiency, addressing deficiencies in the availability of real-world data while promoting advancements in aerial autonomy. Together, these studies highlight AI's pivotal role in optimizing UAV networks, IoT systems, and edge computing while addressing scalability and adaptability challenges.

2.4 LLMs for command interpretation and human-robot interaction

Large Language Models, in their development, have revolutionized the way humans can interact with machines by enabling natural language to become a practical interface for understanding and executing commands. This has fostered smooth human-machine collaboration, more so in the complex and dynamic contexts, due to the effectiveness of bridging linguistic input and autonomous responses.

The integration of NLP and LLMs in UAV systems and robotics has greatly enhanced command mechanisms, human-robot interaction (HRI), and industrial automation. Study [4] shows the application of a fine-tuned BERT model for UAV navigation, mapping natural language commands to North-East-Down (NED) coordinates with 89% accuracy. This framework, using Raspberry Pi Zero W and MAVLink protocols, achieves resource-efficient, real-time navigation and shows the potential for integration of multimodal input. Beyond UAVs, Study [6] looks at the applications of LLMs in HRI, with a strong emphasis on planning, contextual reasoning, and ethical decision-

making. The paper classifies the techniques into domains such as education and healthcare, which meet the scalability and safety needs for adaptive and robust robotic systems. Similarly, Study [7] presents LLM-driven advances in humanoid robotics, where these models are used as trajectory planners and reinforcement learning designers to achieve stable locomotion, validated through simulations in Unity. Though the challenges in multi-task integration and computational demands remain, the research shows the transformative potential of LLMs in humanoid robotics. In industrial settings, Study [19] introduces a hierarchical framework leveraging LLMs to translate human commands into precise robotic actions for manufacturing. This line of approach has an 81.88% success rate in tasks such as tool path design and decision-making, thus saving production while addressing scalability challenges in complex 3D tasks. Taken together, these studies show the critical role that LLMs play in advancing UAV navigation, HRI, humanoid robotics, and manufacturing automation, with future directions for improving adaptability, efficiency, and multi-modality.

2.5 Multi-agent systems and collaboration

Integration of Large Language Models in multi-agent systems has revolutionized collaborative workflows in autonomous environments and opened new directions for efficient coordination and decision-making. LLMs help drive these systems with human-like reasoning and interaction, leading to tremendous progress in several domains such as robotics, logistics, and aerial intelligence. This section will cover innovative frameworks and applications where LLMs and AI foster collaboration among agents and outline some of the challenges and future directions that are molding this field.

The integration of large language models and advanced computational techniques has enhanced MAS, UAV coordination, vehicle-drone logistics, and aerial intelligence. Study [20] presents an LLM-based MAS framework with a profile, perception, and mutual interaction module for structured management of complex workflows in industrial and societal simulations. The main contributions of this study are the taxonomy of MAS methodologies and innovative multimodal data integration to improve coordination and efficiency. In UAV coordination, Study [21] presents a linguistics-driven system using SDF and artificial potential field algorithms for real-time swarm geometry adjustments and safe flocking behaviors, with applications ranging from drone shows to VR simulations. Future efforts will focus on improving scalability and aesthetic interactions. The study [22] investigates vehicle-drone cooperative systems for logistics by classifying operational models into single-vehicle single-drone (SVSD) and multiple-vehicle multiple-drone (MVMD) among others, and proposing mathematical formulations such as TSP-D. Focusing on urban and disaster scenarios, the study underlines hybrid models and heterogeneous drones for better synchronization and cost efficiency. Advancing aerial intelligence, Study [23] discusses CNN-based methods for aerial human action recognition and object detection, which overcome challenges such as occlusion and limitations of datasets. The study highlights the potential in multi-modal learning and scalability by combining CNNs with transformers for spatiotemporal analysis, with enhancements in applications in surveillance and urban planning. Taken together, these developments show that LLMs are at the cusp of a transformative role across domains, enabling better adaptability, scalability, and efficiency in collaborative and real-time operations.

2.6 Code generation and API recommendations

The rapid evolution of software ecosystems has created an urgent need for tools able to support code generation and improve API suggestions. Large Language Models have been powerful enablers in this domain, exploiting their understanding of semantics and reasoning capabilities in dealing with ever-increasing complexities of development workflows. The present chapter discusses major LLM-powered code generation and API optimization platforms that could be game-changers across a very broad spectrum of settings.

Improvements in large language models revolutionized graph representation, API usage, conversational agents, software automation, and legacy code modernization. Study [24] introduces the L-MTAR framework, which combines semantic and positional encoding using motifs with a linearizing Transformer architecture, achieving state-of-the-art results in API recommendation tasks where HR@10 exceeds 0.93 on datasets such as ProgrammableWeb, hence showing promising results when dealing with diversity and complexity of APIs. Apart from this, Study [25] proposes the CAPIR framework that solves the problems related to low-resource libraries by decomposing tasks into smaller parts, retrieving and ranking APIs, and directly incorporating APIs into prompts. Showing huge gains in Recall@5 and pass@100, CAPIR is an example of domain-specific adaptability of LLMs. In the healthcare domain, Study [26] explores integrating REST APIs with conversational agents using LLMs for empathetic and personalized health counseling. With a modular design, seamless API integration, and URI-based resource optimization, this framework has great potential in digital healthcare while addressing issues of scalability

and data security. In software automation: Study [27] introduces LLM_GP, an evolutionary algorithm for mutation, crossover, and selection, using LLMs in code generation. LLM_GP, through tokenized code sequences with prompt engineering, is outperforming traditional approaches to symbolic regression, a strong example of the synergy between LLMs and evolutionary algorithms. Study [28] is working on the modernization of legacy code with an LLM-driven type-migration pipeline for the resolution of ambiguities in type conversion, to adapt idiomatic Rust structures. This will significantly lower the effort of developers while preserving maintainability and security in the modernized system. Together, these architectures show the LLM's powerful ability to accelerate automation, scalability, and adaptability within a wide range of software and application domains.

2.7 Environmental monitoring and applications

Integration of such advanced technologies as GIS, large language models (LLMs), and AI-driven tools is revolutionizing workflows in environmental engineering and industrial workflows. Study [29] demonstrates a system that integrates GIS with weather data and GPT-based analysis for the identification of fertile land and crop recommendation with an accuracy of 80% using some techniques like Panchromatic Sharpening and Brovey Transformation. While it highlights its potential to enhance agricultural productivity and sustainability, the study recognizes the limitations in the scope of the datasets and plans to include more expansive datasets and economic factors. In engineering, Study [30] investigates the use of LLMs like GPT-4 in automating multibody system dynamics modeling. Using Python's Exudyn library, the study shows that LLMs can simplify workflows in simulation for simple scenarios. However, challenges in managing complex rigid-body dynamics and a need for multi-modal inputs and domain-specific training data remain. Expanding into industrial applications, Study [31] evaluates the TAPE framework for testing REST API tools like EvoMaster and StarCoder. While these tools do not yet surpass manual test quality, they significantly improve efficiency and usability, providing practical solutions for managing API complexities. Collectively, these advancements underscore the transformative role of LLMs and AI-driven technologies in fostering automation, efficiency, and adaptability across diverse applications while highlighting avenues for future improvements in scalability, accuracy, and dataset integration.

2.8 Emerging frameworks

The development and use of large language models, or LLMs for short, together with associated technologies, have brought profound influence on a wide circle of fields, among them dealing with difficult computational tasks, improving automation, and shrinking perception-action gaps. More recently, it has been explained in the literature how such applications of LLMs revolutionize discrete controller synthesis, server management, robotic assembly, and autonomous operation of systems. A theme common to many of these studies is combining semantic reasoning with feedback mechanisms, enabling iteration to improve efficiency and flexibility.

Recent advances in large language models and foundation models are overcoming the key barriers of computational efficiency, automation, and robotic autonomy in these areas. Study [32] demonstrates that through a structured policy design combined with semantic reasoning in prompt engineering, the computational cost of discrete controller synthesis can be drastically reduced by significantly lowering the need for state and transition analysis. Herein, Research [33] advises using GPT-4-based AI agents for such complicated multitasking in categories that demand a high success rate for the simplification of workflows to reduce the chance of human error in the server management domain. In the field of construction robotics, Research [34] introduces a hierarchical framework that integrates high-level planning with low-level policy development to improve the accuracy and modularity of robot control scripts, consequently enhancing flexibility in intricate assembly operations. Taken together, these studies show the huge impact of LLMs and foundation models on decision process optimization, improvement of automation, and robotic adaptability, while some of the most important challenges remain in scalability and precision.

3. System Architecture

The overall architecture of the system is designed to translate natural language instructions into executable API calls within the IoD ecosystem. This architecture leverages LLMs to understand human intentions and then translates them into suitable IoD functionalities, hence offering a seamless and efficient interface for interaction between humans and drones. The current section provides an end-to-end design consideration in line with its various components, methodologies, and technical aspects in terms of natural language processing and application programming interface integration. LLM processing module is the engine that enables understanding and

processing of user inputs. The module consolidates all the text normalization activities, tokenization, intent recognition, and parameter extraction into a single straightforward workflow. Especially tailored and created for IoD datasets, it ensures correct transformation of the instructions into well-structured API calls to be executed in the IoD operating environment. The LLM is next to be processed, where the natural language input will undergo processing so that it can infer the intent of the user. Extracts actionable parameters—drone IDs, geographical locations, and task-specific goals—via the use of NER, dependency parsing, and semantic analysis. For instance, an instruction such as “Monitor the western sector at sunrise” is converted into a formal request: POST /monitor {“location”: “western sector”, “time”: “sunrise”}.

It also supports real-time ambiguity resolution to enable user interaction. The LLM performs. For instance, if a command lacks essential parameters, such as in the sentence “Send drones to the field” it uses contextual awareness to infer the missing parameters from previous messages or to form clarification questions, like “Which field do you mean?”. This iterative process makes sure that commands are well understood before they are translated into API requests. More of these pre-processing tasks are done in the workflow of the LLM. Typo correction and colloquial handling are a part of these. Thus, it is able to understand instructions like “pls snd drone 2 south” as “Please send a drone to the South” making it truly usable by a wide variety of users. It even remembers follow-up commands, like “Use the same settings as before” with contextual memory—meaning, it recalls and reapplies without having to restate the relevant setting.

In that sense, API Gateway serves as the important middleman in this whole IoD ecosystem, assuring that processed requests are smoothly translated into executable commands. That is what it guarantees for the continuity of operations under standards by IoD, and hence ensures efficiency and reliability between the LLM-driven processing units and drone operation systems. Validation is definitely one of the very basic but most important elements a gateway uses to check API requests for completeness and correctness, and to be compliant with the operation protocols defined in IoD. This way, it does ensure that any such request that is malformed or incomplete is caught well in advance to prevent errors that may arise during execution. For instance, it would ask for more inputs or corrections if any of the key parameters were missing, such as geolocation or drone identifiers.

Dynamic Mapping then enables the API Gateway to route requests efficiently to appropriate endpoints in the IoD ecosystem. Restful APIs or gRPC, whichever are the protocols used in these communications, this mapping mechanism ensures that each request is properly dispatched to its target. Deployment requests are thus broadcast to the fleet management module, while commands from the analytics subsystem concerning data gathering are propagated via a broadcast mechanism. Adaptive routing is bolstered by the fact that the mapping system is context-aware and hence autonomously changes itself as the conditions in which the system is operated change. Most optimization work focuses on reducing payload overhead to increase the efficiency of request execution. The overall system efficiency is improved because the request payload is compressed, unnecessary data transmission is reduced, and API calls are optimized. What's more, this feature assumes greater importance in the case of scenarios with high demand, such as simultaneous drone operations, since it avoids network congestion and assures a quick response.

First of all, validation is the most critical aspect in which a gateway checks API requests for their completeness, correctness, and compliance with operation protocols defined in IoD. In this manner, it makes sure that any such request which is found malformed or incomplete is flagged well in advance before any error in execution could occur. For example, if some necessary parameters are missing, such as geolocation or identifiers of drones, it will ask for more inputs or correction. After that, the mechanism allows for routing requests to endpoints in the IoD ecosystem using Dynamic Mapping, ensuring the process continues uninterrupted. Whatever the communication protocol may be, be it RESTful APIs or gRPC, a mechanism of mapping ensures that the requests are mapped accordingly to their respective destinations. The deployment requests, therefore, reach the fleet management module, whereas the commands aimed at gathering data go to the analytics system. Adaptive routing of the same nature would only be possible using a context-aware mapping system capable of reconfiguring itself in dynamically changing operational conditions.

The primary optimization here is fundamentally to reduce the payload overhead and increase the efficiency of request execution. The gateway can significantly raise the overall performance of the system, mainly by compressing the payload of requests, cutting down the transmission of unrequired data, and optimizing the API calls. This becomes an important aspect in high-demand scenarios with several drones working concurrently, as this helps to lighten the network burden, ensuring quick responses.

Error Handling is another crucial part of the system; it warns users about possible issues that might be generated during operations. For instance, when the user enters the wrong command, near real-time feedback identifies the mistake and corrects it, as is evident from the message, “Invalid location specified. Please provide a valid geolocation”. This functionality not only minimizes the possibility of the system going wrong but also

enables users to rectify their mistakes efficiently, thus promoting an improved interaction experience. There is an adaptive learning process in the system that has a tendency to improve the error handling capacity with time on the basis of learning from the user-specific error trends. This process runs as a two-stage process of error detection and refinement of the adaptive response. Under the error detection stage, errors like invalid commands, incomplete parameters, or wrong identifiers are detected by carrying out rule-based verification processes. When errors are brought to the surface, the system logs such occurrences together with the involved user activity and corrections in a feedback database. The system mines the logs over time to identify recurring patterns of error for a given user or user groups. Machine learning techniques, including clustering techniques or pattern-discovery techniques, are used to identify common issues. For instance, if the user keeps inputting incorrect drone sector IDs (e.g., "Sector X" instead of correct "Zone 5"), the system associates the occurrences and learns to make personalized suggestions like, "Did you mean Zone 5 from past tasks?" or auto-suggest the most likely correct ID from historical data. This adaptive functionality improves efficiency as well as user experience. By minimizing the occurrence of redundant manual corrections, the system lowers command execution latency and enables interaction to be smoother. Adaptive processing is also employed to handle scenarios with sophisticated commands where partial or ambiguous input (e.g., "Send drones to the location") is obtained. In these instances, the system generates contextual memory by drawing on previous interactions and responds with intelligent follow-up questions such as, "What location do you want to survey?".

The Feedback Loop will be a two-way mechanism: on one side, it will provide actionable information and updates to the user so that effective monitoring and control of the activities by the drones are possible; on the other side, it will collect user feedback that can be used in fine-tuning system performance over time. For example, this can be achieved by tuning the performance of the LLM processing module such that better intent recognition and parameter extraction capabilities will be achieved based on trends of user edits.

This is further amplified by advanced analysis methodologies coupled with adaptive learning systems. To a certain degree, the study of user interactions and performance metrics will enable the system to predict and deliver proactive suggestions on potential problems that may arise. In the illustrated example above, repeated delays in one region could enable the system to suggest changes to operating parameters even before a user issues a command.

Furthermore, the Feedback Loop brings in scalability, as the same performance is provided in the face of changing user scenarios. Whether one is controlling a small fleet or managing a large operation, the module will scale dynamically in its communications approaches to meet the needs of the user. In high-pressure situations involving a lot of drones, it will prioritize key updates and push non-critical information into the background in an attempt to reduce the possibility of overwhelming the user with the EMCS.

One of the architecture elements of IoD is the Feedback Loop, which provides for real-time updating, offers complete error management, and is adaptive. The raw data is transformed into actionable intelligence, filling the gap in understanding and building a user-centric framework for interaction. To that end, it assures IoD to be intuitive, responsive, and effective in all feasible operational environments underpinned by the three principles of transparency, efficacy, and continuing improvement.

3.1 Technical Workflow

This architecture shall be cautious from the point of view of data flow so that fluidity and heterogeneity in user directives are handled and, most importantly, such natural language inputs can be concretized. While this architecture design follows a linear progression in itself, it does suit all those complex variations of command patterns for robustness and scalability.

The entire process initiates with the submission of input, wherein, through an interface-directly integrated with the LLM Processing Module-users are able to feed instructions. This may be one of those interaction points which will collect inputs ranging from simple directives to complicated queries such as, "Deploy two drones" or "Survey the eastern field at sunrise and report anomalies". In this context, an interface does very minimal pre-processing of inputs before passing it to the LLM module for deeper analysis.

At the very next step of processing, several levels of analysis are done at a large language model or LLM. The LLM recognizes the intent of the user, extracts the relevant parameters, and contextualizes the command further. State-of-the-art techniques, namely semantic parsing, Named Entity Recognition, and dependency parsing, are utilized while dealing with information that may be either explicit or implicit. Considering a very simple example, parsing of the instruction "Inspect the crop fields tomorrow" identifies "Inspect" as the action verb, "crop fields" as the place identified, and "tomorrow" as the temporal reference and forms an API call like POST /inspect { "location": "crop fields", "time": "2024-01-05"} in structured form. This confirms that the instruction was

understood correctly, even in the case of ambiguity or partial lack of information from the user's original utterance, with iterative clarification in case of need. The structured request is passed further to API Execution through the API Gateway. In this stage, the request gets checked against IoD standards for completeness and correctness. On successful validation, API Gateway forwards the request to a concrete IoD endpoint capable of realizing an action corresponding to one of the three categories: drone deployment, data acquisition, or system calibration. Such a monitoring request is then forwarded to the analytics subsystem, while a deploy command is forwarded to the fleet management module. Dynamic routing depends on changes in drone availability, network conditions, and operational priorities.

During the System Action phase, the core execution of the command is done by the core IoD system. The drones realize programmed actions in the mission, for example, flying to a coordinate, taking photos, or gathering environmental data. Real-time orchestration of multiple drones, using edge computing nodes for localized processing and cloud systems to extend visibility of the mission, will be needed. Mechanisms of feedback are enabled while at this stage, which allows the drones to make out real-time conditions, including obstacle avoidance or recasting of tasks due to unplanned environmental changes.

By any measure, the last phase of the interaction cycle is the User Feedback stage. In such a regard, when raw telemetry data and operational contexts are interpreted into intelligible insights for the users, the Feedback Loop provides actionable updates. For instance, it notifies users: “Mission completed successfully”, “Drone 3 encountered an obstacle and rerouted”, and “Data analysis in progress”. The error alarms, such as “Invalid location specified”, nag the user to make necessary improvements for easier interaction flow. The workflow is visualized in Figure 1.

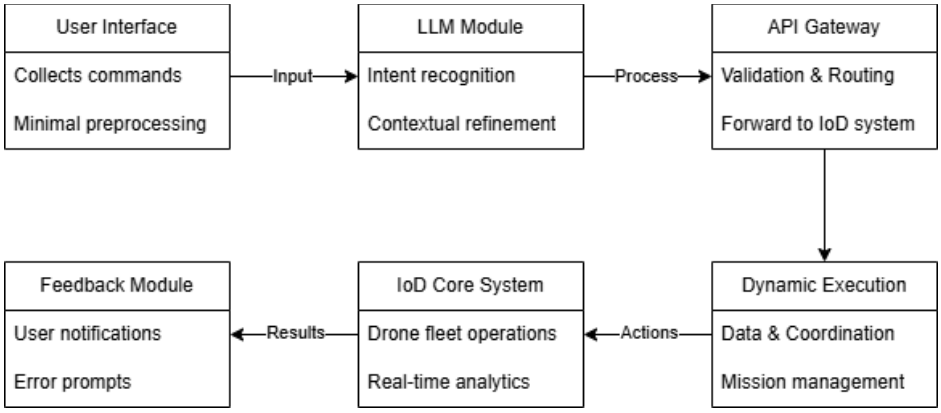

Figure 1. System architecture workflow.

This pseudo code, which can be seen in Table 1, illustrates the core workflow of an LLM-based IoD command processing system that translates natural language commands into executable API requests, ensuring real-time drone operation through systematic input parsing, validation, execution, feedback delivery, and performance optimization.

4. Dataset and Model Development

The creation of an effective system in the conversion of natural language to API calls within the Internet of Drones ecosystem requires well-structured datasets and powerful training methodologies. The subsequent section describes the creation and extension of the IoD application-specific datasets and the training, fine-tuning, and validation methodologies followed for LLM.

The first step towards building a powerful model is the collection of a large dataset. For IoD applications, datasets have to contain various sets of natural language directives, operating scenarios, and their corresponding API mappings. The creation process of the dataset consists of the following big steps: data collection, preprocessing, and augmentation.

Table 1. Pseudo code for LLM-Based IoD command processing system.

Pseudo Code Workflow

```
# Initialize the system
Initialize LLM_Model (fine-tuned for IoD commands)
Initialize API_Gateway
Initialize Feedback_Loop
Initialize Command_Log

# Main processing loop
While system is active:
   Receive user_input_command
   Log user_input_command to Command_Log

   # Step 1: Input Parsing
   parsed_command = LLM_Model.parse(user_input_command)
   If parsed_command is incomplete:
      clarification = LLM_Model.request_clarification(parsed_command)
      Receive user_clarification
      parsed_command = LLM_Model.update_command(parsed_command, user_clarification)

   # Step 2: API Request Generation
   api_request = LLM_Model.generate_API(parsed_command)
   Validate api_request with API_Gateway
   If api_request is invalid:
      Feedback_Loop.notify_error("Invalid API Request. Please check command.")
      Continue

   # Step 3: API Execution
   response = API_Gateway.execute(api_request)
   If response is error:
      Feedback_Loop.notify_error("Execution Failed. Check system logs.")
      Continue

   # Step 4: Feedback Delivery
   Feedback_Loop.send_update(response)

   # Step 5: Performance Monitoring
   Record processing_time, latency
   If processing_time > threshold:
      Optimize system components (parallel processing, query handling)

   # Loop End
End While
```

4.1. Data collection

Initially, the system was bootstrapped using simulated data, which included designing representative scenarios for IoD typical operations—like disaster response, agricultural monitoring, and urban surveillance. The commands were developed manually by experts in the domain and extended by paraphrasing techniques in order to simulate the inputs of different users. For instance, a base instruction like "Survey the northern field" was expanded to variations like "Inspect the northern area", "Deploy drones for surveillance in the north", and "Monitor the field in the north". These artificial conversations made up the core training data for the initial models.

As the system evolved, real-time logging of user interaction became very important in collecting data from active operational contexts, which consists of collecting inputs made by the user, system reactions, and feedback obtained in practical situations. For instance, a logged command like "Deploy two drones to monitor crop health in sector 5" can be traced back to its corresponding API response for model improvement. These logs contain a record of the actual user behavior, colloquial phrasings, unclear instructions, and corrections. For example, a user might enter "Check the area" in a first iteration and then clarify to "Survey the southern zone for anomalies". Iterative logs capture such subtlety present in real-world interactions and are used in model updating. In order to increase dataset diversity further, additional techniques were used. Paraphrasing of commands was done to represent regional and contextual differences. A command "Deploy drones to survey the field" was paraphrased as "Send UAVs for field observation" or "Survey the crop area". Edge cases involving partial directives were added to validate the model's capacity to request clarifications and disambiguate in real-life situations.

Furthermore, the system records exceptional cases and infrequent occurrences, including incomplete directives or instructions involving multiple steps. For example, a directive such as “Inspect the field” may elicit a subsequent clarification from the system: “Which field would you like to inspect?”. The user's reply, “Sector 4” is subsequently integrated into the log, thereby enhancing the dataset with instances of contextual resolution.

Over time, this two-fold approach—simulated and real data combined—ensures the dataset matures to capture both expected and new trends in user engagement. Further, the collected data is enriched with the inclusion of region-specific linguistic patterns like using “patrol” instead of “survey” making it more inclusive and adaptable across different operational environments.

4.2. Augmentation

Augmentation techniques—such as paraphrasing, synonym replacement, and sentence reordering—are applied to increase the size and diversity of the dataset. These make sure that the model generalizes well to varied phrasings like “Send two drones to the northern field at dawn” and “At sunrise, deploy two UAVs for northern field surveillance”. Paraphrasing tools and LLMs are used to generate sentence variants that preserve the original intent but offer linguistic variety. For instance, the phrase “Monitor the southern area” may be rephrased as “Inspect the southern region”, “Survey the south”, or “Deploy drones to observe the southern sector”.

Synonym replacement: It replaces the key terms with synonymous words or phrases. For example, “deploy” can be substituted with “send” or “dispatch”, and “inspect” can be substituted with “examine” or “observe”. In this way, the model understands the commands with different vocabularies but retains semantic correctness. Sentence reordering Similarly, sentence reordering creates structural variations. A fundamental instruction such as “At dawn, deploy drones to the eastern field” can be restructured to “Deploy drones to the eastern field at dawn” or alternatively “Drones should be deployed at dawn for the eastern field”.

Augmentation also contains edge cases such as ambiguous or incomplete commands, including the partial directive “Survey the field” expanding to “Survey the western field”, “Survey the crop fields”, or “Survey the field at 8 AM”. Such edge cases will eventually make the model strong enough to deal with real-world scenarios in which users give very ambiguous or fragmented input. Also, in order to make the model more robust, adversarial examples are included, such as intentionally misspelled or grammatically incorrect commands. The command “Sennd drones 2 west” is mapped to a corrected interpretation, “Send two drones to the west”.

Sophisticated augmentation techniques involve the integration of contextual knowledge to generate domain-specific information. In the agricultural monitoring domain, commands such as “Analyze crop health in sector 4” can be grounded into other alternatives like “Check vegetation health in zone 4”, “Monitor plant conditions in section 4”, or “Survey crops for anomalies in region 4”. In the disaster response domain, commands like “Assess flood damage in the northern area” can be further detailed with, for instance, “Evaluate water levels in the north” or “Inspect flood impact in northern regions.”

With such augmentation strategies, the dataset will not only increase in size but also in representativeness and robustness, meaning the model can generalize well over a large space of user inputs, operational contexts, and unexpected linguistic variations. The diverse and enriched dataset is more able to ensure the model can give accurate API outputs even in complex or unexpected scenarios.

4.3. Model development and fine-tuning

Only after curating such a dataset does developing and fine-tuning an LLM to understand natural language instructions and convert them into API calls come into question. This approach thus fits into model selection, pretraining, fine-tuning, and subsequent evaluation. Because it has been confirmed to work well, especially in cases requiring precise intent identification, fine-tuned versions of BERT are selected to perform IoD. BERT models are pretrained on large corpora and thus capable of capturing the linguistic nuances and semantic relationships important in mapping user intents into structured API requests. In this respect, fine-tuning BERT on IoD-specific datasets optimizes it for certain domain-specific tasks associated with API formatting, such as parameter extraction and intent classification; hence, guaranteeing superior performance in converting natural language commands into actionable output.

It is fine-tuned on the curated IoD-specific dataset by adapting the pre-trained BERT model to the domain-specific tasks. In this step, the model is optimized with task-specific objectives: intent recognition, parameter extraction, and API formatting. The RAG operation is performed over these labeled command-API pairs. This would further solidify the model's capability of extracting relevant data from a structured knowledge base during training and generating outputs that closely match the operational API requirements. The outputs of the model are

then fine-tuned with reinforcement learning using human feedback to achieve high accuracy for diverse input scenarios.

Model performance is assessed on the basis of a set of established metrics, which are tailored to natural language processing in order to guarantee linguistic accuracy as well as functional accuracy by ensuring functional reliability. In the methodology of evaluation, the techniques and their applications include:

Some of the metrics used in measuring the model's ability to correctly classify user intent are accuracy and the F1 score. Taking a command, for example, like “Deploy drones to inspect the northern region”, it should be able to recognize “deploy” as the intent. Accuracy measures the number of correct intentions identified divided by the total number of inputs; the F1 score balances precision and recall in showing a holistic view of performance.

Parameter extraction: Extracting geolocations, timestamps, and action objects from user commands. Precision measures the ratio of correctly identified parameters to all extracted parameters, while recall measures the ratio of correctly identified parameters to all relevant parameters in the input. For example, given the command “Monitor the eastern zone at 6 AM”, it should be able to correctly tag “eastern zone” as the location and “6 AM” as the time. High F1 score here ensures complete parameter extraction.

BLEU is short for Bilingual Evaluation Understudy and a metric to calculate the similarity of generated API requests and reference requests. In our example, it computes how well the model generated POST /monitor request with parameters {“location”: “eastern zone”, “time”: “6 AM”} matches a predefined reference API call. It then uses BLEU for the computation, combined with cosine similarity, to compute the semantic closeness of the generated and reference outputs by comparing vector representations of the commands, ensuring that the underlying intent and semantics are correctly aligned even when syntax differs. Integration of BLEU in assessing syntactic precision with cosine similarity in measuring semantic accuracy forms a complete evaluation framework for assessing API generation quality. Realistic scenarios are simulated in order to exercise the entire system workflow, which includes input commands, execution of the API, and feedback presentation. These are simulated in an attempt to duplicate operational conditions for the purpose of ensuring that the system can, with skill, handle complex and dynamic user inputs. For instance, the system could interpret a directive such as “Survey the southern area and send images by noon”, producing a formatted API request exemplified by POST /survey {“area”: “southern”, “deadline”: “noon”}. Upon execution, the feedback mechanism assesses the results, verifying that the requested images have been accurately captured and transmitted.

All of these scenarios are used by simulations to ensure robustness, from multi-step tasks and ambiguous inputs to high-demand operations. For example, the multi-step instruction “Deploy three drones to inspect the northern field, then report findings to the base” is translated into a series of sequential API requests. The system ensures that each step gets performed in the correct sequence, while the feedback mechanism keeps updating in real-time, such as “Drone 1 deployed successfully” or “Inspection data transmitted to the base”.

Edge cases are also an essential aspect of such simulations. Similarly, ambiguous instructions, such as “Inspect the area”, make the system request more context: “Which area would you like to inspect?”. Through more user-provided context, the system demonstrates dynamic adaptation—how it handles partial inputs. High-load scenarios like managing a number of simultaneous operations in several regions are also tested to validate the scalability and latency of the system. Commands such as “Deploy drones to all sectors for fire monitoring” are processed to have adequate load balancing and an effective execution of tasks.

These simulations include metrics such as success rates, latency assessments, and user feedback evaluations. In a simulated scenario of disaster response, for example, it measures the system's ability to deploy drones within critical time limits and provide actionable updates by comparing the results against set benchmarks. High success rates on these assessments make a strong case for the system's reliability in the face of actual conditions.

Through holistic simulations, this system integrates diverse and challenging situations, giving support to wide examination of its operational processes and therefore emphasizing benefits while highlighting areas for improvement. This iterative process ensures the IoD platform will retain resilience, flexibility, and efficiency in meeting user needs across a large number of applications.

5. Evaluation and Results

The paper evaluates the proposed system by assessing the effectiveness of Llama-3.2-1B-Instruct in producing accurate API requests based on natural language inputs. The evaluation uses Retrieval-Augmented Generation (RAG) methodology to extend the model with an ability to extract and apply relevant information from a structured knowledge base. The evaluation framework consists of metrics such as BLEU score and cosine similarity in order to measure syntactic and semantic accuracy, respectively. The next few sections describe the evaluation methodology, the experimental results, and a detailed analysis of the system's features.

To ensure a solid evaluation, the system was tested with a curated dataset containing 1500 commands representative of diverse IoD scenarios, from simple commands like “Deploy three drones” to complex, multi-step instructions like “Inspect the southern sector and relay images back to the base”. Each command was accompanied by its corresponding ground truth API request for the comparison process. Below are some illustrative pairs (Figures 2–5).

Illustration 1:

- Command: “Deploy three drones to survey the eastern field.”
- API Request:


```
{
    "action": "deploy",
    "number_of_drones": 3,
    "location": {
        "region": "eastern_field",
        "coordinates": {
            "latitude": 39.837128,
            "longitude": 26.241863
        }
    },
    "task": {
        "type": "survey",
        "parameters": {
            "altitude": "300m",
            "coverage": "full"
        }
    },
    "priority": 2,
    "timestamp": "2025-01-10T10:00:00Z"
}
```


Figure 2. API request generated for deploying three drones to survey the eastern field.

Illustration 2:

- Command: “Monitor crop health in sector 7 and send a report by 5 PM.”
- API Request:


```
{
    "action": "monitor",
    "task": {
        "type": "crop_health",
        "parameters": {
            "sensors": ["thermal", "visual"],
            "data_format": "geojson"
        }
    },
    "location": {
        "sector": 7,
        "coordinates": {
            "latitude": 39.837128,
            "longitude": 26.241863
        }
    },
    "deadline": "17:00",
    "notifications": {
        "email": "anil.sezgin@hypersense.dev",
        "sms": "+123456789"
    },
    "priority": 2
}
```


Figure 3. API request for monitoring crop health in sector 7 and sending a report by 5 PM

Illustration 3:

- Command: “Inspect the southern sector for anomalies and relay images back to the base.”
- API Request:


```
{
    "action": "inspect",
    "location": {
        "sector": "southern",
        "coordinates": {
            "latitude": 39.837128,
            "longitude": 26.241863
        }
    },
    "task": {
        "type": "anomaly_detection",
        "parameters": {
            "camera": {
                "type": "infrared",
                "resolution": "4K"
            },
            "detection": {
                "objects": [
                    {
                        "type": "person",
                        "threshold": 0.85
                    },
                    {
                        "type": "vehicle",
                        "threshold": 0.9
                    }
                ]
            }
        }
    },
    "priority": 2,
    "timestamp": "2025-01-10T14:30:00Z"
}
```


Figure 4. API request for inspecting the southern sector and relaying images to the base.

Illustration 4:

- Command: “Return all drones to the base immediately.”
- API Request:


```
{
    "action": "return",
    "target": "all_drones",
    "location": {
        "type": "base",
        "coordinates": {
            "latitude": 39.837128,
            "longitude": 26.241863
        },
        "details": {
            "name": "central_operations_base",
            "capacity": "6_drones"
        }
    },
    "priority": 1,
    "status": {
        "current": "in_progress",
        "estimated_completion_time": "2025-01-10T14:30:00Z"
    },
    "alerts": [
        {
            "type": "notification",
            "method": "email",
            "address": "anil.sezgin@hypersense.dev",
            "message": "All drones are returning to base."
        },
        {
            "type": "log",
            "level": "info",
            "timestamp": "2025-01-10T14:00:00Z"
        }
    ]
}
```


Figure 5. API request for the immediate return of all drones to the base.

Metrics such as the BLEU score and cosine similarity give a holistic framework for evaluating how effective the system is at generating accurate API requests. The BLEU score measures n-gram precision by calculating the amount of overlap between the generated API requests and their reference requests. This ensures the syntactic correspondence of the output to measure how faithful the model is to the expected phrasing. For example, for an instruction such as “Survey the northern region”, if the model generates POST /survey {“region”: “north”}, then a high BLEU score reflects that the generated request is in exact agreement with the expected format.

On the other side, cosine similarity captures semantic similarity by transforming API requests to vector representations and then calculating the cosine of the angle between them. Such an approach catches much better those deeper relationships between input and output, especially where syntax might differ, but the essential meaning remains the same. For instance, the instructions “Inspect the western field at sunrise” and “Survey the west sector early in the morning” may lead to API requests that are structurally distinct; however, they exhibit a cosine similarity score of 0.97, which signifies an almost complete semantic correspondence.

By combining BLEU and cosine similarity, the evaluation model ensures a comprehensive assessment of both syntactic accuracy and semantic correctness. Theoretically, instructions with a BLEU score above 90 and a cosine similarity of more than 0.95 stably reflect good model reliability. For multi-step commands like “Deploy drones to sector 4, inspect for anomalies, and report findings”, discrepancies in timestamp formatting or parameter extraction might reduce the BLEU score to 85, but a cosine similarity of 0.92 would confirm semantic alignment. This dual-metric approach ensures the system's robustness across a variety of IoD command complexities, enabling precise and meaningful API generation.

The testing scenarios were designed to determine how well the model would perform across a variety of complexities and uncertainties. Simple directives were single-intent instructions with very clear parameters—for example, “Deploy two drones to monitor sector 5”. These directives supported basic tests of intent recognition and parameter extraction. In contrast, complex directives examined the model's ability to handle multi-step instructions that require sequential API generation. For instance, a command like “Inspect the southern sector, relay findings to the base, and prepare a status report” demanded the accurate execution of several interdependent tasks. Ambiguous commands presented additional challenges, requiring the model to interpret context or seek clarification. Instructions such as “Survey the area” or “Send drones” were designed to specifically test the system's ability to obtain more information from the users and to adapt its responses in answer to these refinements. The test of those various scenarios sufficiently proved the model's robustness and adaptability in realistic IoD contexts.

6. Conclusion and Future Directions

The development of advanced IoD systems shows the transformative power of large language models in creating a bridge between human intent and machine execution through generation. It achieves a high level of accuracy and adaptation by bringing to bear on a comprehensive dataset for training and a two-metric assessment framework, consisting of BLEU scores and cosine similarity. This allows the human operators to engage drones uninterrupted, bringing in accurate and contextual API generations across vastly complex and diverse operational environments. All the same, despite the high-level achievement attained, there are still quite a number of aspects primed for improvement and further exploration. This research has several important achievements, and perhaps the most prominent among them is the combination of RAG methodologies with the Llama model. This would not only improve the ability of the model to handle complex, multi-step commands but also improve its capacity to retrieve and incorporate relevant contextual information dynamically. The ability of the system to understand ambiguous or incomplete user inputs and produce actionable, precise API calls has made it a robust solution for real-world IoD applications ranging from disaster response to agricultural monitoring. Challenges in high-demand contexts, such as delays, and sporadic errors in command classification, demonstrate that there is always room for improvement. Future research should focus on improving these limitations to ensure both scalability and reliability in large-scale applications. Another important direction is expanding the dataset with more diverse domain-specific scenarios and edge cases. While the existing dataset forms a good base, region-specific language variations, multilingual support, and more real-time data from field operations can only make the system more robust. Similarly, with multimodal data—like images and sensor inputs—the model can learn to generate richer and more contextually relevant API calls, enabling multimodal IoD systems that integrate vision, language, and real-time analytics.

From a technological standpoint, the inclusion of edge computing may be critical in reducing latency and assuring real-time responsiveness. The closer commands are executed to where an operation is being performed, the more edge nodes can offload the central servers from unnecessary computational tasks—especially in applications demanding real-time response, such as wildfire monitoring or disaster relief. Combination of this

approach with lightweight model architecture developments could allow effective deployment even in resource-constrained environments.

The adaptive learning methodologies will be definitely under consideration in integrating with the future versions of this system so that the model itself will keep evolving with new data and interactions from users. For example, RLHF and self-supervised learning can help the model keep pace with the changing operational demands; in reinforcement learning loops, the model could improve the understanding of ambiguous instructions by giving more weight to the cases where successful clarification has happened.

Another hopeful direction is the ethical and secure deployment of such systems. The most central challenges that would need focused attention are data-privacy protection, misuse of information, and dealing with potential biases in command interpretation. Major efforts in security protocols, including encrypting data transmissions and secure API access, could mitigate risks and foster trust among users. Equally importantly, the mechanisms for auditing—that is, those systems that monitor and explain model decisions—may most importantly bring transparency into the system, ensuring it remains accountable and interpretable.

Collaboration with experts in these diverse domains can significantly accelerate the deployment and enhancement of this technology. Alliances with response teams dealing with emergencies, agricultural organizations, or experts in urban development could expose specific problems within an industry and give way to the development of solutions tailor-made for that particular case. Working with disaster response teams could, for example, highlight very concrete operational needs—such as independent control of drone swarms in chaotic environments—that can guide successive feature enhancements.

The real potential of this system lies beyond the traditional applications of IoD. Its use in autonomous shipping, precision forestry, and smart city infrastructure will unlock new opportunities and further drive innovation. These industries are in a good position to harvest the ability of the system in understanding complicated commands and performing precise actions to fully realize the benefits that come with efficiency and automation—hence, wider adoption of IoD platforms. This research has laid a strong foundation that large language models can be integrated into IoD systems with great potential for improving operational efficiency, flexibility, and user experience. Addressing the current limitations and exploring new directions, the system will evolve to become a core technology for IoD platforms and beyond, revolutionizing the way humans interact with autonomous systems.

Acknowledgement

We would like to thank Siemens Turkey for their support in the completion of the study. This study was supported by TUBITAK 1512 Grant, project no: 2220423.

References

[1] Sezgin A, Boyacı A. Securing the Skies: Exploring Privacy and Security Challenges in Internet of Drones. In: 2023 10th International Conference on Recent Advances in Air and Space Technologies (RAST); 2023; Istanbul, Turkiye, pp. 1-6.

[2] Sezgin A, Boyacı A. Advancements in Object Detection for Unmanned Aerial Vehicles: Applications, Challenges, and Future Perspectives. In: 12th International Symposium on Digital Forensics and Security (ISDFS); 2024; San Antonio, TX, USA, pp. 1-6.

[3] Zhou L, Yin H, Zhao H, Wei J, Hu D, Leung VCM. A Comprehensive Survey of Artificial Intelligence Applications in UAV-Enabled Wireless Networks. Digit Commun Netw 2024; 1-26.

[4] Savenko I. Command interpretation for UAV using language models. In: 2024 IEEE 7th International Conference on Actual Problems of Unmanned Aerial Vehicles Development (APUAVD); 2024; Kyiv, Ukraine, pp. 228-231.

[5] Sezgin A, Boyacı A. Rising Threats: Privacy and Security Considerations in the IoD Landscape. Journal of Aeronautics and Space Technologies (JAST) 2024; 17: 219-235.

[6] Zhang C, Chen J, Li J, Peng Y, Mao Z. Large language models for human–robot interaction: A review. Biomim Intell Robot 2023; 3(4): 1-15.

[7] Sun S, Li C, Zhao Z, Huang H, Xu W. Leveraging large language models for comprehensive locomotion control in humanoid robots design. Biomim Intell Robot 2024; 4(4): 1-16.

[8] Du F, Ma X, Yang J, Liu Y, Luo C, Wang X, Jiang H, Jing X. A Survey of LLM Datasets: From Autoregressive Model to AI Chatbot. J Comput Sci Technol 2024; 39: 542-566.

[9] Kim Y, Kim D, Choi J, Park J, Oh N, Park D. A survey on integration of large language models with intelligent robots. Intell Serv Robot 2024; 17: 1091-1107.

[10] Jang D, Cho D, Lee W, Ryu S, Jeong B, Hong M, Jung M, Kim M, Lee M, Lee S, Choi H. Unlocking Robotic Autonomy: A Survey on the Applications of Foundation Models. Int J Control Autom Syst 2024; 22: 2341-2384.

[11] Sauvola J, Tarkoma S, Klemettinen M, Riekki J, Doermann D. Future of software development with generative AI. Autom Softw Eng 2024; 31: 1-8.

[12] Aharon U, Dubin R, Dvir A, Hajaj C. A classification-by-retrieval framework for few-shot anomaly detection to detect API injection. Comput Secur 2025; 150: 1-13.
[13] Tlili F, Ayed S, Fourati LC. Advancing UAV security with artificial intelligence: A comprehensive survey of techniques and future directions. Internet Things 2024; 27: 1-27.
[14] Ibrahum ADM, Hussain M, Hong J. Deep learning adversarial attacks and defenses in autonomous vehicles: a systematic literature review from a safety perspective. Artif Intell Rev 2024; 58: 1-53.
[15] Luo H, Luo J, Vasilakos AV. BC4LLM: A perspective of trusted artificial intelligence when blockchain meets large language models. Neurocomputing 2024; 599: 1-20.
[16] Oliveira F, Costa DG, Assis F, Silva I. Internet of Intelligent Things: A convergence of embedded systems, edge computing and machine learning. Internet Things 2024; 26: 1-20.
[17] Fang H, Zhang D, Tan C, Yu P, Wang Y, Li W. Large Language Model Enhanced Autonomous Agents for Proactive Fault-Tolerant Edge Networks. In: IEEE INFOCOM 2024 - IEEE Conference on Computer Communications Workshops (INFOCOM WKSHPS); 2024; Vancouver, BC, Canada: IEEE. pp. 1-2.
[18] Sabet M, Palanisamy P, Mishra S. Scalable modular synthetic data generation for advancing aerial autonomy. Robot Auton Syst 2023; 166: 1-17.
[19] Fan H, Liu X, Fuh JYH, Lu WF, Li B. Embodied intelligence in manufacturing: leveraging large language models for autonomous industrial robotics. J Intell Manuf 2024; pp. 1-17.
[20] Li X, Wang S, Zeng S, Wu Y, Yang Y. A survey on LLM-based multi-agent systems: workflow, infrastructure, and challenges. Vicinagearth 2024; 1: 1-43.
[21] Lykov A, Karaf S, Martynov M, Serpiva V, Fedoseev A, Konenkov M, Tsetserukou D. FlockGPT: Guiding UAV Flocking with Linguistic Orchestration. In: 2024 IEEE International Symposium on Mixed and Augmented Reality Adjunct (ISMAR-Adjunct); 2024; Bellevue, WA, USA: IEEE. pp. 1-4.
[22] Zhou J, Yi J, Yang Z, Pu H, Li X, Luo J, Gao L. A survey on vehicle–drone cooperative delivery operations optimization: Models, methods, and future research directions. Swarm Evol Comput 2025; 92: 1-29.
[23] Maheriya K, Rahevar M, Mewada H, Parmar M, Patel A. Insights into aerial intelligence: assessing CNN-based algorithms for human action recognition and object detection in diverse environments. Multimed Tools Appl 2024; 1-43.
[24] Zheng X, Wang G, Xu G, Yang J, Han B, Yu J. A LLM-driven and motif-informed linearizing graph transformer for Web API recommendation. Appl Soft Comput 2025; 169: 1-12.
[25] Ma Z, An S, Xie B, Lin Z. Compositional API Recommendation for Library-Oriented Code Generation. In: 2024 IEEE/ACM 32nd International Conference on Program Comprehension (ICPC); 2024; Lisbon, Portugal: IEEE. pp. 1-12.
[26] Park S, Kim A, Lee S, Kamyod C, Kim CG. Design of REST API Client for Conversational Agent using Large Language Model with Open API System. In: 2024 IEEE/ACIS 22nd International Conference on Software Engineering Research, Management and Applications (SERA); 2024; Honolulu, HI, USA: IEEE. pp. 1-4.
[27] Hemberg E, Moskal S, O'Reilly U. Evolving code with a large language model. Genet Program Evolvable Mach 2024; 25: 1-36.
[28] Hong J, Ryu S. Type-migrating C-to-Rust translation using a large language model. Empir Softw Eng 2024; 30: 1-38.
[29] Balasundaram A, Aziz ABA, Gupta A, Shaik A, Kavitha MS. A fusion approach using GIS, green area detection, weather API and GPT for satellite image based fertile land discovery and crop suitability. Sci Rep 2024; 14: 1-16.
[30] Gerstmayr J, Manzl P, Pieber M. Multibody Models Generated from Natural Language. Multibody Syst Dyn 2024; 62: 249-271.
[31] Poth A, Rrjolli O, Arcuri A. Technology adoption performance evaluation applied to testing industrial REST APIs. Autom Softw Eng 2024; 32: 1-34.
[32] Ishimizu Y, Li J, Yamauchi T, Chen S, Cai J, Hirano T, Tei K. Towards Efficient Discrete Controller Synthesis: Semantics-Aware Stepwise Policy Design via LLM. In: 2024 IEEE International Conference on Consumer Electronics-Asia (ICCE-Asia); 2024; Danang, Vietnam: IEEE. pp. 1-4.
[33] Cao C, Wang F, Lindley L, Wang Z. Managing Linux servers with LLM-based AI agents: An empirical evaluation with GPT4. Mach Learn Appl 2024; 17: 1-13.
[34] Luo H, Wu J, Liu J, Antwi-afari MF. Large language model-based code generation for the control of construction assembly robots: A hierarchical generation approach. Dev Built Environ 2024; 19: 1-18.

Turkish Journal of Science & Technology
20(1), 299-307, 2025

Research Paper
https://doi.org/10.55525/tjst.1630246

Risk Detection in Medical Data Using Artificial Afterimage Algorithm

Murat DEMİR[1*]
[1] Department of Software Engineering, Faculty of Engineering-Architecture, Muş Alparslan University, Muş, Türkiye
[*1] m.demir@alparslan.edu.tr

(Geliş/Received: 30/01/2025; Kabul/Accepted: 06/03/2025)

Abstract: Metaheuristic algorithms have become a frequently used methodology in many fields such as genetics, bioinformatics, microbiology, etc. related to human health. Metaheuristic methods provide efficient solutions when classical approaches fail or are computationally expensive. In this study, Artificial Afterimage Algorithm was applied to 4 different medical data sets obtained from Kaggle. There is no previous study in the literature that models the afterimage algorithm as a heuristic method. Its mathematical infrastructure is simpler than many other methods. Using the Artificial Afterimage Algorithm, clusters of test samples taken from healthy individuals and patients were tried to be detected. Accuracy, precision, recall and F1 values of the clusters were calculated. The highest Accuracy value was obtained as 0.85, Precision value as 0.9, Recall value as 1 and F1 score value as 0.86. The study shows that the method can perform a good rate of risk detection in medical data.

Key words: Metaheuristic, Artificial Afterimage Algorithm, Clustering.

Yapay Afterimage Algoritması Kullanarak Medikal Verilerde Risk Tespiti

Öz: Metaheuristic algoritmalar, insan sağlığını ilgilendiren; genetik, biyoinformatik, mikrobiyoloji vb. birçok alanda sıkça kullanılan bir metodoloji olmuştur. Metaheuristic yöntemler, klasik yaklaşımlar başarısız olduğunda veya hesaplama açısından pahalı olduğunda verimli çözümler sunar. Bu çalışmada Yapay Afterimage Algoritması, Kaggle'dan elde edilen 4 ayrı medikal veri seti üzerine uygulanmıştır. Literatürde daha önce Afterimage Algoritmasını sezgisel bir yöntem olarak modelleyen bir çalışma yoktur. Matematiksel alt yapısı diğer birçok yönteme göre daha basittir. Yapay Afterimage Algoritması kullanılarak, sağlıklı kişiler ve hastalardan alınan test örneklerinin kümeleri tespit edilmeye çalışılmıştır. Kümelere ait Accuracy, Precision, Recall ve F1 değerleri hesaplanmıştır. En yüksek Accuracy değeri 0,85, Precision değeri 0,9, Recall değeri 1 ve F1 skor değeri 0,86 olarak elde edilmiştir. Çalışma göstermektedir ki, yöntem medikal verilerde iyi bir oranda risk tespitini gerçekleştirebilmektedir.

Anahtar kelimeler: Metasezgisel, Yapay Afterimage Algoritması, Kümeleme.

1. Introduction

The development of technology has increased the use of digital devices in all areas. The spread of digital technologies has made this technology a driving factor in innovation and transformation in the scientific world. The digital tools that information technologies provide to the digital world form the basis for this situation [1]. In parallel with these developments, a very critical increase in data density has emerged. Big data is being recorded in many areas day by day.

One of the most important areas that has made significant progress in the field of digital technologies is artificial intelligence technology. Artificial intelligence, which affects every area of life in daily life, is gaining more and more importance every day. Apart from daily activities and business life activities, it also significantly affects our perspective on problems, our understanding of entertainment and our lifestyles [2].

Artificial intelligence was first presented as a proposal letter by John McCarthy, Marvin L. Minsky, Nathaniel Rochester and Claude E. Shannon at the Dortmund Conference in 1956 [3]. However, John McCarthy is considered the inventor of artificial intelligence. McCarthy [4] defined artificial intelligence as "the science and engineering of creating human-like intelligent machines, especially intelligent computer programs."

As in every field, very critical volumes of data are generated in studies concerning the field of health. A digital health system that integrates with traditional methods is being tried to be put forward in health technologies. Since this development is very rapid, the volume of investment in digital technologies in the health sector is also increasing [5]. Artificial intelligence accelerates many processes such as diagnosis, treatment and preventive health services in the field of health [6].

[*] Corresponding author: m.demir@alparslan.edu.tr ORCID Number of author: [1] 0000-0001-7362-0401

1.1. Metaheuristic Methods

This field of study, known as metaheuristic methods, is actually artificial learning studies. They try to product solutions to problems by imitating systems, events and living things in nature. It is expressed as inspired by nature [7]. Although there are many types; evolutionary algorithms, physics-based algorithms, swarm-based algorithms and human-based algorithms are the four most studied types of metaheuristic algorithms [8].

Metaheuristic algorithms act on the principle of creating a solution set and continuing on their way by selecting the best solution candidate from among them. When creating new solution values, the values of the best solution are acted upon. Each metaheuristic method has mathematical formulas that it uses to produce new values. The method uses a mathematical infrastructure in such a way that it imitates the living being/system that is inherent in the method and imitates it. In general, the solution space is initially generated randomly. However, it is later generated in a way that approaches the best solutions using these equations.

1.2. Afterimage and Artificial Afterimage Algorithm

The Artificial Afterimage Algorithm [9] is an algorithm that has recently entered the literature of heuristic methods. Even if the eyes are closed after looking at light emitting objects for a certain period of time, negative or positive afterimage reflections continue to be created by our brain for a while. The structure on which the algorithm is based is the mathematical substructure in the creation of this image.

1.2.1. Afterimage

When we look at a lighted object for a certain period of time, the brain continues to create an image for a while even if our eyes are closed. This phenomenon is called afterimage. Even if our eyes do not see the original object, the chemical effect caused by the light in the eye continues for a while. These images are also called ghost images. Afterimages can also be colored. After a while, this image becomes clear and disappears [10-12]. If we continue to see the same color but less clearly even when our eyes are not open, this is positive afterimage. When the object we are looking at is colored, if we turn our eyes to a neutral surface, we continue to see it with complementary colors. This is called negative afterimage [13]. Figure 1 is an example of a positive afterimage and Figure 2 is an example of a positive afterimage.

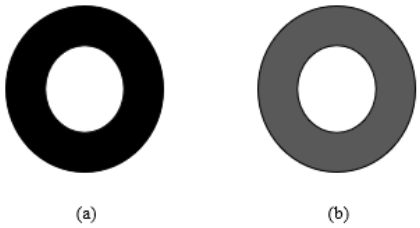

Figure 1. Example of positive afterimage: (a) original image, (b) reflection image.

Figure 1 (a) represents the original image, and (b) represents the reflection image in the eye. Although the reflection image will be the same color as the original, its brightness will be less.

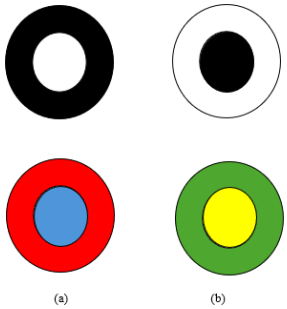

Figure 2. Example of negative afterimage: (a) original image, (b) reflection image.

Figure 2 the negative reflections of the images in (a) will appear as in (b). The colors will appear different, as the reflection colors.

1.2.2. Visual Angle and Perceptual Size

The rays reflected from our eyes pass through the top and bottom of an object to create a viewing angle. This is called the Visual Angle. The size of the image formed on the retina is determined by this angle. The image size is proportional to the size of this Visual Angle. Figure 3 shows the representation of the viewing angle.

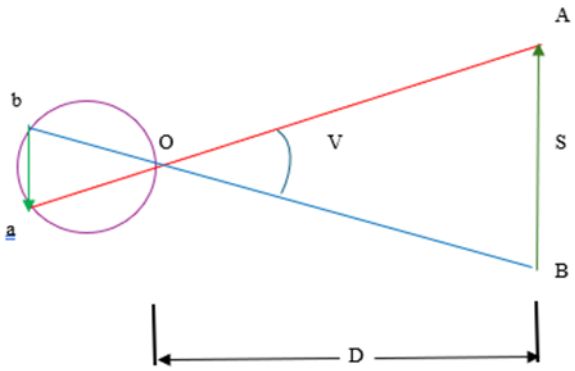

Figure 3. Visual Angle.

Visual Angle is calculated by the expression in Equation (1) [14].

$$V = 2 * \arctan\left(\frac{object\ size}{2 * object\ distance}\right) \quad (1)$$

When calculating the visual angle (V), 2 values are used. The first is the size of the object. Its real size is the distance between A and B. The second is the D value. It is the distance between the object and the eye. This value also shows the distance between O and B.

Perceptual size is the size perceived by the eye. It is expressed by Equation (2) [14].

$$S = V * D \quad (2)$$

1.3. Artificial Afterimage Algorithm

The algorithm that uses the concepts of afterimage, visual angle and perceptual size is a new algorithm in literature. Since this study is applied to data clustering, the value of the candidate solution is used instead of the concept of object size, and the distance of the object from the eye is used instead of the distance from the best solution. Equations (3) and (4) [9] show the visual angle (V), perceptual size (S) equations of the Artificial Afterimage Algorithm adapted to data clustering. Equation (5) [9] shows the formula to be used when generating new solution values. V is the AAIA adapted version of the visual angle. In fact, it is the result of the ratio of the values of the solution population to the difference between them and the best values. $S_{i,j}$ is the value obtained by multiplying the distance of a solution from the best by the visual angle after obtaining the visual angle value. $New\ pop_{i,j}$ is the step in which new candidate solutions are obtained using the obtained V and S(i,j) values.

$$V = 2 * \text{atan}\left(\frac{pop_{i,j}}{2 * pop_{i,j} - best_{1,j}}\right) \quad (3)$$

$$S_{i,j} = V * (pop_{i,j} - best_{1,j}) \quad (4)$$

$$New\ pop_{i,j} = S_{i,j} + (|\ S_{i,j-}(best_{1,j} - |(worst_{i,j} - pop_{i,j})|) * rand) \quad (5)$$

The matrix expressed as best represents the solution with the best fitness value and worst represents the solution with the worst fitness value. After these updates are made, the resulting pseudo code is as in Algorithm 1 [9]. Figure 4 shows the flow chart of the Artificial Afterimage Algorithm.

Algorithm 1: Pseudo code of Artifical Afterimage Algorithm

1. **Begin**
2. Create initial population
3. Create initial best solution
4. **while**(count⩽iteration)
5. Specify Object size
6. Specify Object distance
7. V←$2 * \text{atan}\ (\frac{pop_{i,j}}{2*pop_{i,j}-best_{1,j}})$
8. S←$V * (pop_{i,j} - best_{1,j})$
9. Local best values←determine current best values
10. **if** fitness value of local best value < fitness value of best value **then**
11. best←local best
12. **end if**
13. Compute $new\ pop_{i,j} = S_{i,j} + (|\ S_{i,j-}(best_{1,j} - |(worst_{i,j} - pop_{i,j})|) * rand)$
14. **End while**
15. Print best values
16. e**nd begin**

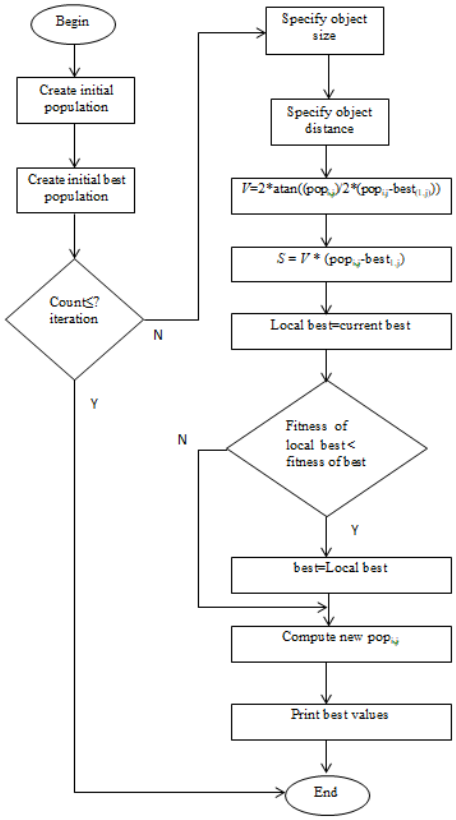

Figure 4. Flowchart of the Artificial Afterimage Algorithm.

2. Data Clustering

The name of the analysis technique that tries to group a group of data according to the similarities of their attributes is clustering. This grouping process is carried out according to the criteria we have determined beforehand [15]. Since the similarities of the existing data are tried to be grouped, a similarity measurement criterion is needed. Distance and similarity measurements are used for this task [16]. There are some distance measurement methods in the literature. In this study, the Manhattan distance measurement method is used.

Machine learning algorithms are basically divided into three different classes: supervised learning, unsupervised learning and reinforcement learning. In supervised learning, a labeled training set is used for output. The data in the training set consists of binary input objects and output values in a vector format. Unsupervised learning uses unlabeled data. Grouping is done according to the distance relationship between the attributes [17].

Clustering is unsupervised learning. Thanks to this feature, it manages to find hidden patterns in the data. In this respect, it has been the subject of important research in many fields such as pattern recognition, signal processing, bioinformatics, image processing and data mining [16]. Figure 5 is given as a representative example of the clustering process.

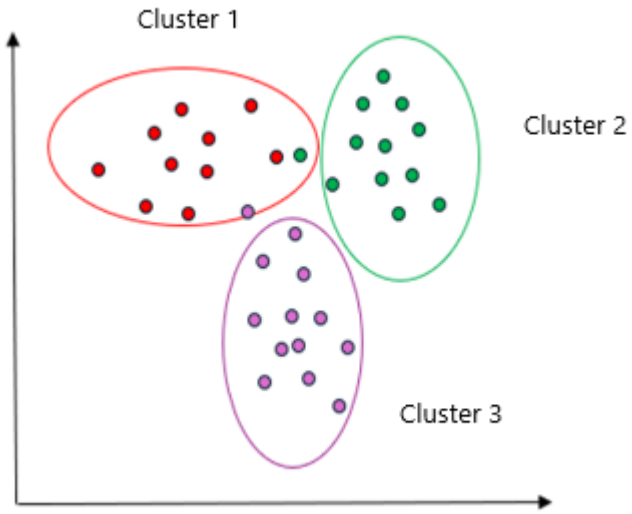

Figure 5. Visual representation of the clustering process.

In Figure 5, some data are not in the cluster they should be in. These data are detected as errors. In other words, they are not detected in the cluster they should be in. Points other than this are considered to be detected correctly.

2.1. Confusion Matrix and Performance Metrics

Confusion matrix is an important concept in the evaluation of machine learning classification and clustering. For performance evaluation, accuracy calculation is the basis. Confusion matrix is used when evaluating accuracy. In fact, confusion matrix is a summary of the prediction results in a classification problem [18]. We have 4 different values in the confusion matrix [19].

TP (True Positive): Cases where the predicted positive class overlaps with the true value
TN (True Negative): Cases where the predicted negative class overlaps with the true value
FP (False Positive): Cases where the predicted positive class does not overlap with the true value
FN (False Negative): Cases where the predicted negative class does not overlap with the true value

Figure 6 shows a representation of the confusion matrix.

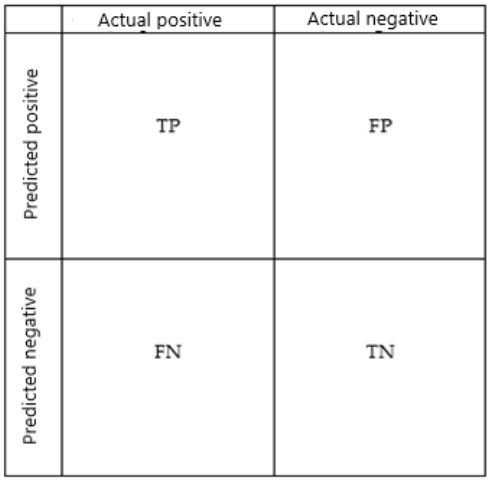

Figure 6. Confusion matrix representation.

Performance evaluation metrics are obtained from this matrix using the formulas in Equations 6-9 [20].

$$Accuracy = \frac{\mathrm{TP+TN}}{\mathrm{TP+TN+FP+FN}} \tag{6}$$

Accuracy is obtained by dividing the correctly predicted values by the total value in the data set.

$$\mathrm{Precision} = \frac{\mathrm{TP}}{\mathrm{TP+FP}} \tag{7}$$

Precision is obtained by dividing the true positives by the total positives.

$$\mathrm{Recall} = \frac{\mathrm{TP}}{\mathrm{TP+FN}} \tag{8}$$

Recall is obtained by dividing the true positives by the sum of the true positives and false negatives.

$$\mathrm{F1\ score} = 2 * \frac{\mathrm{Precision*Recall}}{\mathrm{Precision+Recall}} \tag{9}$$

The F1 score is the harmonic mean value of Precision and Recall.

3. Experimental Results

In this study, clustering operations of Artificial Afterimage Algorithm were performed on disease data obtained from Kaggle database [21-24]. Thus, risk factor assessment of diseases could be successfully presented with Artificial Afterimage Algorithm which is newly introduced to the literature.

Risk detection in medical data is of critical importance for the diagnosis of the disease. Because it can be very difficult to detect risk, especially in large-scale disease data or in data where the number of parameters affecting the disease is high. Although the Artificial Afterimage Algorithm has recently entered the literature; it was able to successfully perform risk detection on the data in this study. Thanks to the simple mathematical infrastructure it uses, the Artificial Afterimage Algorithm can reach a result without causing too much complexity. In this respect, it has an advantageous infrastructure.

Table 1 shows the best, worst and V values obtained by the algorithm for clustering process. V value was obtained with Equation (3) and perceptual angle was calculated with Equation (4). Finally, new candidate solutions of the solution set were calculated with Equation (5). While some of the data sets were used for train process, some were separated for testing.

Table 1. Experimental results of Datasets.

Colon Cancer Dataset						
best	0.424	0.789	0.168	0.318	0.09	0.524
	0.72	1.198E+14	0.310	0.397	0.362	0.524
worst	2.445E+260	0.669	1.704E+259	6.730E+260	5.87E+260	0.417
	8.603E+260	0.815	5.937E+260	1.182E+260	6.148E+260	8.864E+260
V	1.358					
Coronary Heart Disease Dataset						
best	2.053E+14	1.149E+14	3.456E+14	0.710	0.171	
	0.422	0.439	4.635E+14	2.094E+14		
worst	0.916	4.343E+251	3.126E+14	0.505	3.179E+252	
	0.310	2.315E+252	1.419E+252	3.688E+252		
V	0.999					
Indian Liver Patient Records Dataset						
best	3.940E+14	1.140E+14	6.804E+14	0.1623	2.320E+14	
	0.168	3.754E+14	0.0464	0.178	0.270	
worst	3.017E+14	1.673E+257	1.086E+257	1.993E+257	1.018E+14	
	8.249E+256	1.745E+14	4.669E+256	3.053E+257	4.986E+257	
V	3.123					
Prostate Cancer Dataset						
best	0.458	3.284E+14	0.536	0.681	1.339E+14	
	0.385	0.071	0.199			
worst	3.330E+251	1.852E+14	0.222	0.513	3.58E+250	
	2.328E+251	2.188E+251	4.011E+251			
V	1.497					

According to the results obtained, the confusion matrices of each data set are as shown in Figure 7.

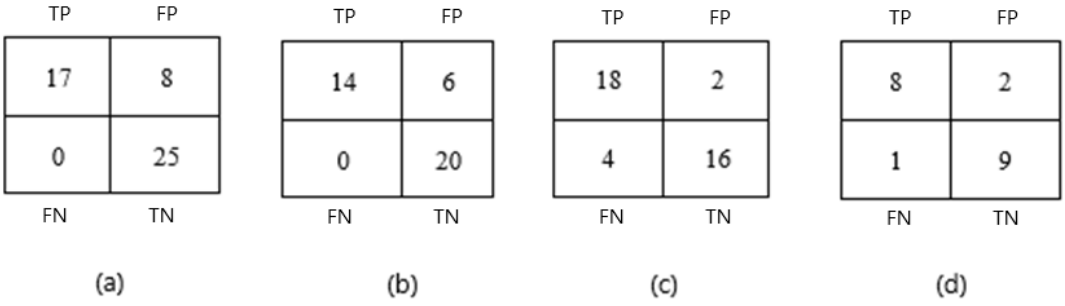

Figure 7. Confusion matrices for the evaluated datasets: (a) Colon Cancer Dataset, (b) Coronary Heart Disease Dataset, (c) Indian Liver Patient Records Dataset, (d) Prostate Cancer Dataset

Table 2 shows the performance metrics of the experimental results.

Table 2. Performance metrics of AAIA on four medical datasets

	Accuracy	Precision	Recall	F1
Colon Cancer Dataset	0.84	0.68	**1**	0.81
Coronary Heart Disease Dataset	**0.85**	0.7	**1**	0.82
Indian Liver Patient Records Dataset	**0.85**	**0.9**	0.82	**0.86**
Prostate Cancer Dataset	**0.85**	0.8	0.89	0.84

Figure 8 shows the graphical representation of performance metrics.

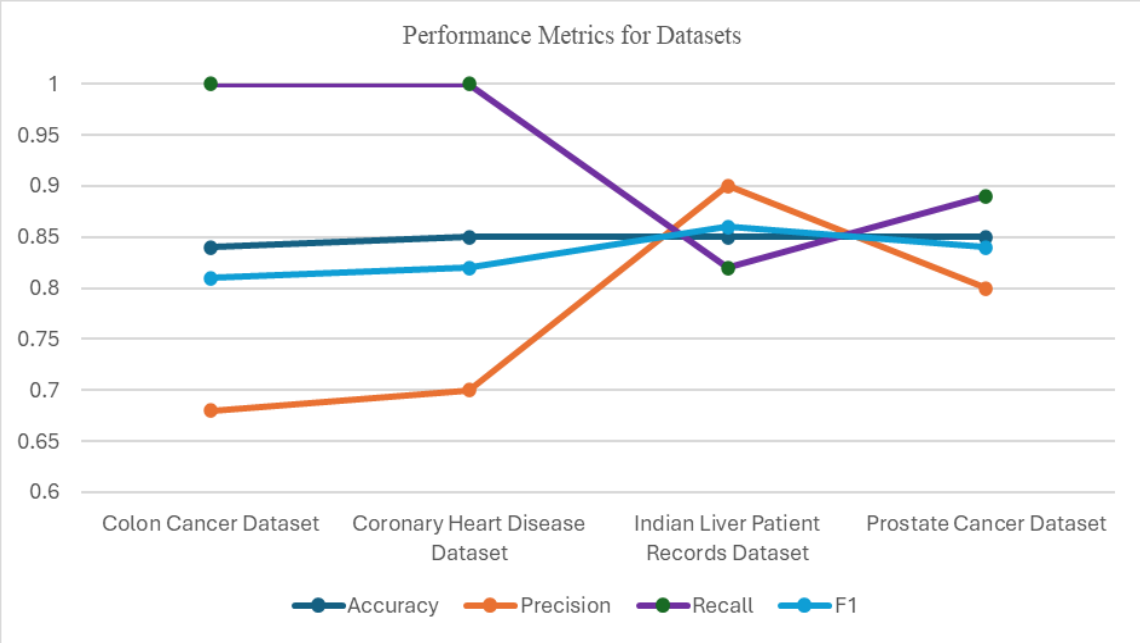

Figure 8. Graphical representation of performance metrics.

4. Discussion and Conclusion

Metaheuristic algorithms are frequently preferred methods, especially in problems where a solution cannot be found with analytical methods or where the solution time may be a problem even if it is found. In this study, the Artificial Afterimage Algorithm was applied to medical data. The Artificial Afterimage Algorithm clustering metrics were examined for disease risk analysis detection.

Although the Artificial Afterimage Algorithm is a new algorithm in the literature; It has obtained significant results in terms of Accuracy, Precision, Recall and F1 metrics. A distance-based evaluation measure was used in the clustering method. In this methodology, the distribution of values in the datasets greatly affects the clustering performance. Therefore, this situation should be taken into account when selecting the data to be worked on. The distribution of the data should be examined and then worked on. In addition, disadvantageous situations in terms of time may occur in very large datasets. The Artificial Afterimage Algorithm has a distance-based infrastructure. Grid-based and hierarchical-based versions can be developed; how they will behave on data sets with different distributions may be the aspects waiting to be studied.

References

[1] Ersöz B, Özmen M. Dijitalleşme ve Bilişim Teknolojilerinin Çalışanlar Üzerindeki Etkileri. AJIT-e: 2020; 11(42): 170-179.

[2] Aydın A. Devlet erkinin yönetim paradigmasının yapay zeka bağlamında dönüşümü. G. Telli (Ed.), Yapay Zeka ve Gelecek içinde İstanbul: Doğu Kitapevi; 2019.

[3] McCarthy J, Minsky ML, Rochester N, Shannon CE. "A proposal for the Dartmouth summer research project on artificial intelligence" https://www-formal.stanford.edu/jmc/history/dartmouth/dartmouth.html(accessed Nov 15, 2024).

[4] McCarthy J. "What is artificial intelligence?" http://www-formal.stanford.edu/jmc/whatisai/(accessed Nov 18, 2024).

[5] Şimşir İ, Mete B. Sağlık Hizmetlerinin Geleceği: Dijital Sağlık Teknolojileri. JOINIHP 2021; 2(1): 33-39.

[6] Yorgancıoğlu Tarcan G, Yalçın Balçık, P, Sebik, NB. Türkiye ve Dünyada Sağlık Hizmetlerinde Yapay Zekâ. MEÜ Tıp Fakültesi Tıp Tarihi ve Folklorik Tıp Dergisi 2024; 14(1):50-60.

[7] Rajwar K, Deep K, Das S. An exhaustive review of the metaheuristic algorithms for search and optimization: taxonomy, applications, and open challenges. Artif Intell Rev 2023; 56: 13187–13257.

[8] Faramarzi A, Heidarinejad M, Stephens B, Mirjalili S. Equilibrium optimizer: A novel optimization algorithm. Knowl Based Syst 2020; 191.
[9] Demir M. Artificial Afterimage Algorithm: A New Bio-Inspired Metaheuristic Algorithm and Its Clustering Application. Appl Sci (Basel) 2025; 15(3): 1359.
[10] Bender, MB, Feldman M, Sobin AJ. Palinopsia. Brain 1968; 91(2): 321–338.
[11] Gersztenkorn D, Lee AG. Palinopsia revamped: A systematic review of the literatüre. Surv Ophthalmol 2014; 60: 1–35.
[12] L″orinc G, András H. Analyzing afterimage strength and duration test results with k-means clustering. In Szemelvények a BGE Kutatásaiból (II. Kötet) Budapest; 2023.
[13] Lee HC. Introduction to Color Imaging Science Cambridge University Press: Cambridge; 2005.
[14] Visual Angle-Wikipedia. Available online: https://en.wikipedia.org/wiki/Visual_angle(accessed Nov 20, 2024).
[15] Taşkın Ç, Emel, GG. Clustering Approaches in Data Mining and an Application with Kohonen Networks in Retailing Sector. Süleyman Demirel University the Journal of Faculty of Economics and Administrative Sciences 2010; 15(3): 395-409.
[16] Avşar İİ. Clustering of Türkiye and European Union Countries by Length of Railroad Lines. Journal of The Faculty of Applied Sciences of Tarsus University 2023; 3(1): 13-25.
[17] Çatak FÖ. Development of data mining software framework by using map/reduce method in cloud computing systems. Phd. Thesis, İstanbul University Institute of Science, Department of Electronics, Informatics Program, İstanbul, 2014.
[18] Chen RC, Dewi C, Huang SW, Caraka RE. Selecting critical features for data classification based on machine learning methods. J Big Data 2020; 7:52.
[19] Yeşildal G. Diagnosing COVID-19 Disease through Medical Images. MSc, Ankara University Institute of Science, Department of Computer Engineering, Ankara, 2022.
[20] Aslanyürek M, Mesut A. A New Method to Measure Clustering Performance and its Evaluation for Text Clustering. Eur J Sci Technol 2021; 27:, 53-65.
[21] Colon Cancer, https://www.kaggle.com/datasets/lakshmi25npathi/colon-cancer(accessed Dec 10, 2024).
[22] Prostate Cancer, https://www.kaggle.com/datasets/sajidsaifi/prostate-cancer(accessed Dec 10, 2024).
[23] Indian Liver Patient Records, https://www.kaggle.com/datasets/uciml/indian-liver-patient-records(accessed Dec 10, 2024).
[24] Coronary Heart Disease, https://www.kaggle.com/datasets/billbasener/coronary-heart-disease?resource=download (accessed Dec 10, 2024).

Turkish Journal of Science & Technology
20(1), 309-325, 2025

Research Paper
https://doi.org/10.55525/tjst.1633962

An Effective Algorithm for Edge Coloring: Malatya Edge Coloring Algorithm

Furkan ÖZTEMİZ[1*]
Software Engineering Department, Engineering of Faculty, Inonu University, Malatya, Türkiye
[*] furkan.oztemiz@inonu.edu.tr

(Geliş/Received: 05/02/2025; **Kabul/Accepted: 12/03/2025)**

Abstract: In this research, an algorithm offering effective and robust solutions for the edge coloring problem in graph theory is proposed. The edge coloring problem is identified as an NP-hard problem, known for its extensive resolution time and inability to be resolved within polynomial time. The proposed edge coloring algorithm emerges as an efficient greedy method that delivers effective solutions within polynomial time constraints. This developed algorithm employs Malatya centrality values as a decisive factor in the edge coloring process. The Malatya centrality algorithm, a current centrality method, has achieved successful outcomes in various graph problems in the literature. In this study, the algorithm is named the Malatya Edge Coloring Algorithm (MECA). To highlight the success of MECA, its analytical proof has been computationally verified on well-known graphs. Additionally, MECA has been tested on 40 unweighted and undirected lattices, 36 bipartite, 24 multipartite, 8 random, and social network graphs. The results obtained indicate that MECA provides optimal solutions for lattice, bipartite, and complete multipartite graphs while offering optimal or near-optimal solutions for any multipartite, random, and social networks. These findings emphasize the applicability and solution efficiency of the edge coloring problem in various scenarios within graph theory.

Keywords: Edge coloring algorithm, minimum edge coloring, Malatya centrality, Matching approach.

Kenar Renklendirme için Etkili bir Algoritma: Malatya Kenar Renklendirme Algoritması

Öz: Bu çalışmada çizge teorisinde kenar renklendirme problemi için etkili ve sağlam çözümler sunan bir algoritma önerilmektedir. Kenar renklendirme problemi, çözüm süresinin uzunluğu ve polinomsal zamanda çözülememesi ile bilinen NP-zor bir problem olarak tanımlanmaktadır. Önerilen kenar renklendirme algoritması, polinomsal zaman kısıtları içinde etkili çözümler sunan verimli bir açgözlü (greedy) yöntem olarak ortaya çıkmaktadır. Geliştirilen bu algoritma, kenar renklendirme sürecinde belirleyici bir faktör olarak Malatya merkezilik (centrality) değerlerini kullanmaktadır. Güncel bir merkezilik yöntemi olan Malatya merkezilik algoritması, literatürde çeşitli çizge problemlerinde başarılı sonuçlar elde etmiştir. Bu çalışmada, algoritma Malatya Kenar Renklendirme Algoritması (MECA) olarak adlandırılmıştır. MECA'nın başarısını vurgulamak amacıyla, analitik kanıtları iyi bilinen grafikler üzerinde hesaplamalı olarak doğrulanmıştır. Ayrıca, MECA; 40 ağırlıksız ve yönsüz örgü (lattice) çizge, 36 iki parçalı (bipartite), 24 çok parçalı (multipartite), 8 rastgele ve sosyal ağ çizge üzerinde test edilmiştir. Elde edilen sonuçlar, MECA'nın örgü, iki parçalı ve tam çok parçalı çizgeler için optimal çözümler sağladığını, çok parçalı, rastgele ve sosyal ağ grafiklerinde ise optimal veya optimal'e yakın çözümler sunduğunu göstermektedir. Bu bulgular, MECA'nın çizge teorisi bağlamında çeşitli senaryolarda kenar renklendirme probleminin uygulanabilirliği ve çözüm etkinliği açısından önemli bir katkı sunduğunu vurgulamaktadır.

Anahtar kelimeler: Kenar renklendirme algoritması, minimum kenar renklendirme, Malatya merkezlilik, eşleştirme yaklaşımı.

1. Introduction

Graph theory encompasses a wide range of problem types, many of which are complex to solve. Among these problem types, minimum edge coloring stands out as one of the more popular problems. The minimum edge coloring problem, in brief, aims to color the edges connected to the same vertex with different colors [1]. In other words, edges of the same color should not intersect at the same vertex. To briefly mention its applications, examples include telecommunications networks, graphic mapping, resource allocation, schedule planning, and scheduling problems, among others [2]. In the literature, there is no method yet that guarantees optimal results in polynomial time for all types of graphs. The Minimum Edge Coloring (MEC) problem in any type of graph has been defined as an NP-hard [3] problem. While there are efficient methods that offer polynomial-time solutions specific to certain graph types, generally, methods that yield successful outcomes across all graph types are considerably limited. The limited methods in the literature can have a complex structure in terms of applicability and require significant performance. This study proposes a robust method that produces optimal or near-optimum results in polynomial time across all graph types. The suggested method has been tested on graph types with known

[*] Corresponding author: furkan.oztemiz@inonu.edu.tr. ORCID Number of authors: [1]0000-0001-5425-3474

analytical proofs, such as bipartite graphs, and computational validations have been conducted. Based on these validations, it is believed that the proposed method will not only be successful in specific graphs but across all graph types. To substantiate this claim, numerous testing processes have been carried out. Additionally, due to its simple structure, the proposed method requires low system resources, thereby producing successful results even in large graphs. The proposed algorithm consists of three fundamental stages. In the first stage, the Malatya centrality (MC) value is calculated. In the second stage, matching sets are formed using the MC. In the third stage, the coloring process is performed on these matching sets. The MC (Malatya Centrality) algorithm has previously been utilized in solving significant graph theory problems such as the maximum independent set [4], minimum vertex cover [5], and maximum flow [6]. For the first time in this study, it will be used to solve the minimum edge color problem. The method proposed in the study has been named the Malatya Edge Coloring Algorithm (MECA). To determine the success of MECA, test procedures have been conducted on a wide variety of graph types, both with and without polynomial-time solutions. These graph types include bipartite, multipartite, lattice, random, and social networks.

To briefly touch upon the contribution of this study to the literature; the Malatya Centrality algorithm, which possesses an original approach, has been used for the first time in this work to solve the minimum edge coloring problem. The proposed Malatya Edge Coloring Algorithm (MECA) is characterized by its comprehensibility, ease of application, and high performance. The study emphasizes the success of MECA by including numerous visual and numerical contents.

1.1. Motivation for proposed method

The primary objective of the presented study is to develop an algorithm that achieves optimal or near-optimum results in polynomial time for the minimum edge color problem, which is defined as an NP-Hard problem in the literature, across all graph types. Thanks to MECA, which provides a robust solution in polynomial time, solutions can be reached with low memory consumption even for large graph types. The proposed method will demonstrate the success of the Malatya Centrality algorithm, which has been used in numerous studies in recent literature, in facing the edge coloring problem. MECA, which is developed based on the Malatya Centrality algorithm and has a greedy approach, possesses a unique methodology. The presented method produces optimum results for all types of bipartite, lattice, and complete multipartite graphs, while it achieves optimal or near-optimum results for other graph types. When compared with other different methods, MECA, with its effective greedy approach, is seen to significantly stand out in the literature, where brute force and weighted optimization methods hold an important place. Brute force algorithms, which operate on the principle of testing all possibilities, are typically low-performance yet comprehensive solution methods. As the graph structure becomes complex and larger, obtaining results through brute force methods becomes increasingly difficult. When examining the solution process with optimization methods, the number of iterations is subjected to certain limits. These limitations prevent reaching a better set of solutions. The uncertainties found in brute force and optimization methods can be eliminated with clear and definite steps. These methods offer solutions without considering the structure and properties of the graph. Since not all nodes and edges in a graph possess similar characteristics, solution methods produced using all graph parameters (structure and properties etc) will yield more successful results. The method presented in this study produces optimal or near-optimum solutions as a robust algorithm.

2. Related Word

In graph theory, edge coloring problems are widely addressed in the literature. However, solution strategies in this area are often focused on specific types of graphs, and a general solution strategy is lacking. Therefore, the edge coloring problem remains an NP-Hard problem. In these studies, the information in the literature is primarily classified according to graph types. Studies on bipartite graphs include examples specific to graph types such as planar bipartite [7], regular bipartite [8], and complete bipartite [9, 10]. These studies have focused on solving the edge coloring problem by taking into account the special properties of bipartite graphs in particular. On the other hand, the edge coloring problem in simple and finite graphs [11] has been addressed in a more limited context, with solutions developed for special cases such as acyclic edge coloring [12] and injective edge coloring [13,14]. From a general perspective, looking at studies on other graph types, it is observed that various solution strategies have been developed for the edge coloring problem under different special cases and constraints. Successful studies have been conducted for graph types such as Cubic [15], Path [16], Halin [17], Regular [18], Complete [19], Oriented [20], Sparse [21], Simple Vague [22], and Degenerate [23]. However, a general solution strategy is lacking, and therefore, these studies make significant contributions to understanding the properties of various graph

types in graph theory and producing optimized solutions in specific situations. Among the studies in the edge coloring literature, different approaches can be found. Some methods have been developed through approaches such as cutting [24], Petersen coloring conjecture [25], Local and Congest model [26], Matching [27], Entropy [28], Maximum Degree [29], and Local Search [30]. These approaches sometimes focus on the results in graph types, and other times on the solution time. For example, alongside studies that offer approximate solutions in polynomial time for complete graphs [31], exact algorithms have also been developed for planar graphs [32]. In methods developed based on Matching, studies offering approximate solutions [33] and solutions in exponential time [34] have been carried out. Additionally, parallel programming-based methods have also been developed using parallel computations models for massive graphs [35]. In studies that tackle the edge coloring problem from different angles, focus has been given to problems such as Locally irregular edge-coloring [36], which considers irregularities among a node's neighbors; Distributed edge-coloring [37], where edges in each node's vicinity are assigned a specific color; and Cost Edge-Coloring [38], which aims for minimum edge costs in coloring.

When examining the studies in the literature, it is observed that most of the studies have been developed for specific types of graphs. While some studies aim for approximate solutions in polynomial time, other methods target optimal solutions in exponential time. The correct use of a method generally requires having significant information about the graph. The proposed Malatya Edge Coloring Algorithm (MECA), on the other hand, produces successful results in all types of graphs independently of the graph type. Verified through numerous tests, MECA provides optimal solutions for bipartite and lattice graphs and either optimal or near-optimal solutions for all other types of graphs in polynomial time.

Table 1. Comparison of MECA with other algorithmic approaches.

Algorithmic approaches	Robust	Deterministic	Time complexity	Space complexity	Optimum	The same outcome for all executions
Statistical	N	N	N-A	P/ Ex.	Although optimal, it is not stable.	N
Heuristic	N	N	N-A	P	Although optimal, it is not stable.	N
Greedy	Y	Y	P	P	Approximation	Y
Exact	Y	Y	Ex	Ex. in recursion case	Optimum	Y
MECA	Y	Y	P	P	Optimum for bipartite and lattice, Optimal or near optimum for any graph	Y
P(Polynomial), Ex(Exponential), Y(Yes), N(No)						

Table 1 presents a comparison of the Malatya Edge Coloring Algorithm (MECA) with other algorithmic approaches. Statistical methods can offer different solutions in each iteration. Algorithms with a heuristic approach are not stable, thus they can also provide different solutions with each run. Methods with a greedy approach are capable of producing robust solutions in polynomial time, but they do not guarantee the optimal result. Methods with an exact approach produce optimal results and have exponential time complexity, making their use costly and problematic for large graphs. MECA stands out among these approaches as an effective and robust greedy method.

3. Material and Methods

The proposed Malatya Edge Coloring Algorithm (MECA) undergoes two critical processes for edge coloring tasks. These processes involve calculating the Malatya centrality values of the nodes and obtaining the matching results identified using these values. As indicated in Figure 1, the edge coloring process with MECA can generally be summarized in five stages. MECA is an algorithm that works with all types of graphs. In Stage 1, an input of any type of graph is made. The example in Stage 1 is performed on a cubic graph that is both bipartite and lattice. In Stage 2, the line graph of the input graph is created. This enables the Malatya centrality algorithm, which operates on vertices, to be applied on the edges of the graph. Applying the Malatya centrality algorithm on vertices solves problems such as the minimum vertex cover [5] and the maximum independent set [4], while its application on edges solves maximum matching [6] problems. The Malatya centrality (MC) algorithm is applied on the created line graph, and the matching members are selected with the Malatya Matching Algorithm (MMA). The matching members identified with MMA represent independent edge relations in the graph. In Stage 3, the matching

members on the original graph are shown. The first matching members are colored with the same color (the red edges in the visual) and removed from the graph. After updating the graph, the matching process is applied again, and the matching members selected in this iteration are colored with the same color (the green edges in the visual) and again removed from the graph. Finally, the remaining graph is completed with matching processes and colored purple. In Stage 4, the edges colored during the matching are combined to form the results of MECA.

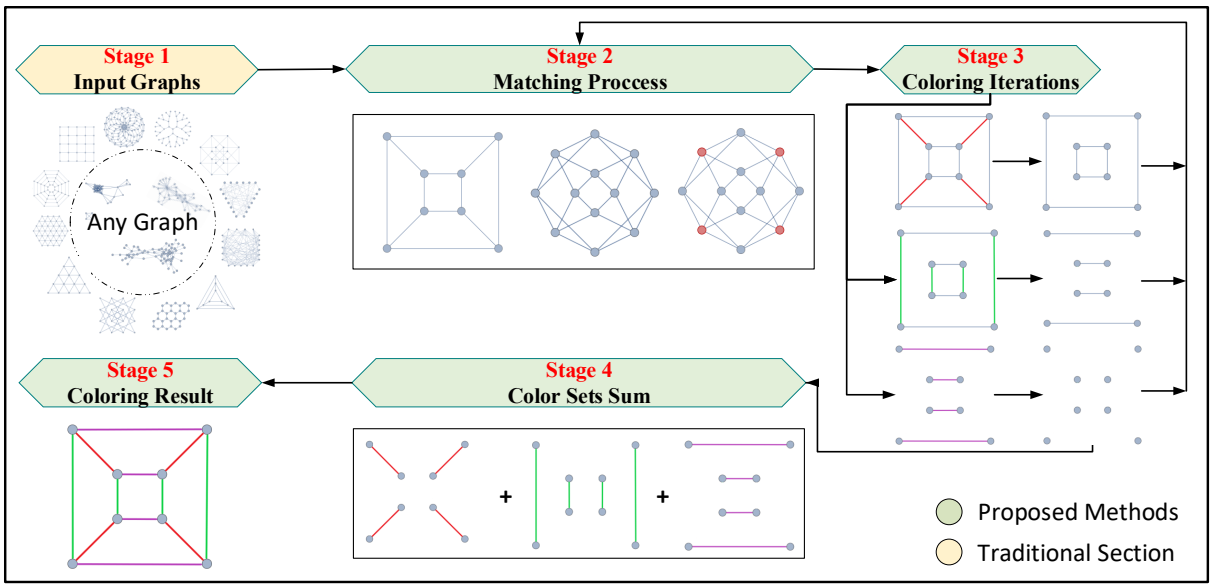

Figure 1. MECA graphical abstract.

3.1. Minimum Edge Coloring

Edge coloring is one of the important concepts in graph theory. The primary goal is to ensure that edges sharing a common vertex are not represented with the same color [1]. During the edge coloring process, the aim is to assign different colors to adjacent edges. Minimum edge coloring seeks to color the edges of a graph with the fewest number of colors accurately. Determining the fewest number of colors is referred to as the graph's edge chromatic index [39]. The objective of the edge coloring problem is to color the edges of the graph with the least possible number of colors. The number of colors used determines the chromatic index. According to Vizing's theorem [40], the chromatic index of a graph is either equal to the graph's maximum degree or one more than the maximum degree.

The chromatic index of a graph *G is denoted* $X_e(G)$ or $X'(G)$. It is defined as $X_e(G)$ veya $X'(G)$ = min{k: the edges of graph G can be colored with k colors}. The maximum degree of a graph represents the highest degree of the nodes in the graph and is denoted by Δ(G) [41]. The degree of a node indicates the number of edges connected to that node, typically represented by d(v). Vizing's theorem articulates the relationship between a graph's chromatic index and its maximum degree as expressed in Equation 1 [41].

$$\Delta(G) \leq X'(G) \leq \Delta(G) + 1 \quad (1)$$

3.2. Matching Process

For a graph G=(V,E), a matching process involves selecting a set of edges where no two edges share a common vertex. In other words, a matching set M in the graph G refers to a set of edges that are non-looping and non-adjacent to each other [42]. A matching that contains the largest possible number of edges is called a maximum matching [42]. Multiple maximum matchings can be identified within a graph. The term v(G) denotes the size of the maximum matching in the graph G. To discuss the relationship between matching and maximum matching, let M be any matching set and M′ denote a set of maximum size matching. Based on these terms, the size of set M, or the number of matchings, should be equal to or greater than |M|>= |M'|. Another important concept is perfect

matching. Perfect matching describes a situation where every vertex in the graph intersects with an edge of the matching. If the condition |E| = |V|/2 is met, then the matching is considered perfect [43].

In this study, the matching process constitutes a significant phase of the proposed edge coloring algorithm. For determining matching sets, an approach based on Malatya centrality has been utilized. This approach has previously been employed in solving the maximum flow problem in bipartite networks using edge matchings [6]. However, in this study, it is used for the first time in an original matching approach to contribute to solving the edge coloring problem across all types of graphs.

The pseudocode of the matching algorithm implemented in Algorithm 1 is provided.

Algorithm 1. Matching Algorithm Pseudo Code [6]

Maximum Matching Algorithm(A, $\boldsymbol{\Psi_1}$)

Input: Adjacency matrix of G is A and G = (V, E) // G Graph

G = Line (Current Graph) The G graph is the current graph converted to a line graph.

Output: $V_{ind} \subseteq V$, Vind is a set of nodes and it is a solution for the independent vertex set problem

1. $V_{ind} \leftarrow \varnothing$
2. While $E \neq \varnothing$ do
3. i←1, …, |V|
4. $\boldsymbol{\Psi_1(v_i)} = \sum_{\forall v_j \in N(v_i)} \frac{\boldsymbol{d(v_i)}}{\boldsymbol{d(v_j)}}$
5. $\boldsymbol{V_{ind} = V_{ind} \cup \{\arg\min(\Psi_1(v_i))\}}$
6. V=V-{vi}, and E=E-∀(vi, vj)∈E
7. V=V-{ $\boldsymbol{N(v_i)}$}, and E=E-∀($\boldsymbol{N(v_i)}$, vj)∈E
8. Output=V_{ind}
9. MatchingSet = Edge($Output_{id}$)

3.3. Malatya Centrality

The Malatya Centrality (MC) algorithm is a successful algorithm that calculates the dominance values of nodes in a graph in polynomial time [44]. In other words, it determines the importance rankings of the nodes. The MC algorithm was initially used for solving the Maximum Independent Set (MIS) and the Minimum Vertex Cover (MVC) problems. The successful outcomes in solving MIS, MVC, and Maximum Flow problems have made the MC algorithm an attractive solution parameter for other types of problems as well. In calculating a node's Malatya centrality value, the ratio of the given node's degree to each neighboring node's degree is determined. Subsequently, these proportional values are summed up to calculate the Malatya centrality value of the relevant node. The mathematical formula of the MC algorithm is provided in Equation 2 [5,44].

$$\Psi_1(v_i) = \sum_{\forall v_j \in N(v_i)} \frac{d(v_i)}{d(v_j)}, 1 \leq i \leq |V| \; and \; 1 \leq i \leq |V|, i \neq j \tag{2}$$

3.4. Malatya Edge Coloring Algorithm (Proposed Algorithm)

In this study, the proposed Malatya Edge Coloring Algorithm (MECA) is based on an original matching approach. Figure 2 explains all stages of MECA on an example graph, which is chosen to be a Q (4)-Hypercube. The Hypercube is selected because being both a bipartite and a lattice graph, it more clearly demonstrates the success of the proposed method. In Stage 1, an input graph with 16 vertices and 32 edges is created. The Malatya centrality algorithm, designed to work on vertices, requires determining the dominance values of edges to identify matching members. For this purpose, in Stage 2, the line graph of the input graph is created. The line graph of the Q (4)-Hypercube in Stage 2 consists of 32 vertices and 96 edges. The MC algorithm is applied on the line graph to determine the 1st matching set. The vertex with the smallest degree is chosen as the first member of the 1st matching set. Table 2 provides the MC values for matching sets in all stages. In the original line graph, the MC

value is determined to be 6 for all vertices. Hence, the first vertex in index order is chosen as a matching member. Subsequently, the selected vertex and its neighboring vertices are removed from the graph along with their edge connections. The MC algorithm is applied again, and the vertex with the minimum MC value is selected as the 2nd member of the 1st matching set. The 2nd member and its neighboring vertices are removed from the graph, and the graph is updated. This process continues until all vertices in the graph are exhausted. The vertices selected on the line graph represent edges in the original graph. Thus, the members of the 1st matching set are identified and colored with the same color. In Stage 3, the members of the 1st matching set are shown in red. The 1st matching members are removed from the original graph in Stage 3, and the graph is updated, restarting the process from Stage 2. At this stage, the MC value of the current line graph is determined to be 4. Again, starting with the vertex with the lowest index, the same steps are followed. The independent vertices selected on the line graph, which correspond to edges in the original graph, are colored green as indicated in Stage 4. The green-colored edges represent the members of the 2nd matching set.

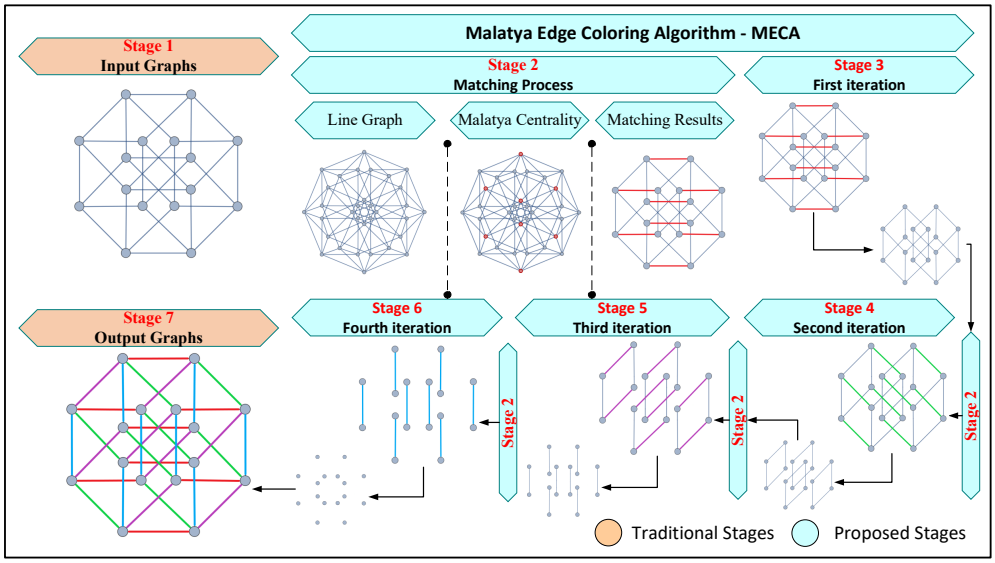

Figure 2. MECA edge coloring stages.

As demonstrated in Stage 4, edges colored green are removed from the graph, and the graph is updated. The updated graph is then subjected to the process described in Stage 2, resulting in the formation of the 3rd matching set, which is colored purple. Following Stage 5, the edges colored purple are removed from the graph, which is then updated, and the process returns to Stage 2. In Stage 6, the 4th matching set is identified and colored blue. At this point, the blue-colored edges are removed from the graph, and since no other edges remain, the edge coloring process of the algorithm is completed. By this stage, the members (edges) of all matching sets have been colored. In Stage 7, the colored matching sets are combined, culminating in the edge coloring of the Q (4)-Hypercube.

Table 2. Malatya centrality values for line graph of Q (5) Hypercube.

Iterations	Node Number	Malatya Centrality Values
1. iteration (Stage 3 in Figure 2)	32	6
2. iteration (Stage 4 in Figure 2)	24	4
3. iteration (Stage 5 in Figure 2)	16	2
4. iteration (Stage 6 in Figure 2)	8	0

The flow chart depicting all the stages of the proposed MECA is shown in Figure 3.

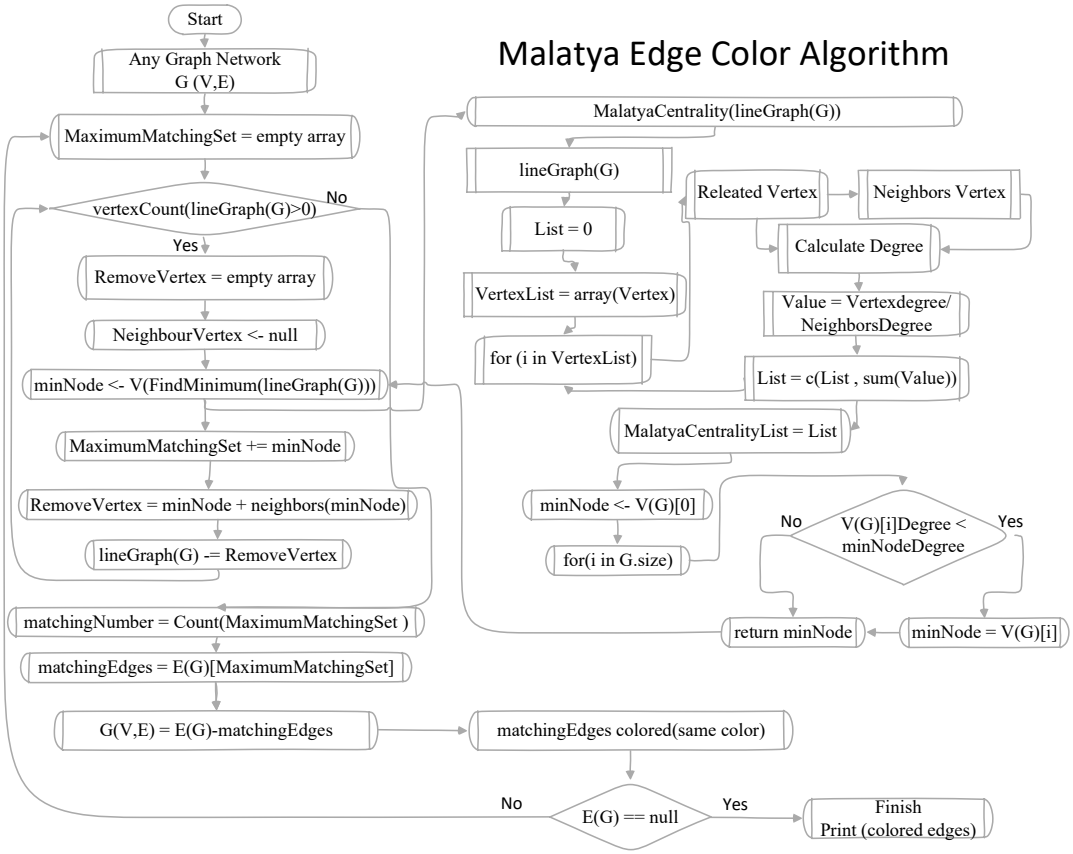

Figure 3. MECA Flow Chart.

The pseudocode for the MECA is provided in Algorithm 2.

To prove the success of MECA, computational proofs have been carried out on graph types whose analytical proofs are known.

Theorem 1: For complete bipartite graphs, the proposed algorithm finds the optimum solutions.
Proof: To prove the theorem, we begin with any complete bipartite graph.
Step: G(V, E), $V = V_1 \cup V_2, V_1 \cap V_2 = \emptyset$, m: vertex number in bottom vertex set, n: vertex number in top vertex set, V_1: Bottom vertices, V_2: Top vertices.

$\forall_v$ = m+n

$\forall_{V_i} \in V_1, \Psi(V_i) = \frac{n}{m}.n = \frac{n^2}{m}$

$\forall_{V_j} \in V_2, \Psi(V_j) = \frac{m}{n}.m = \frac{m^2}{n}$

for $\boldsymbol{m > n}$

$\frac{m^2}{n} > \frac{n^2}{m}, V_j > V_i$, The Maximum Independent Set(MIS) member is chosen from the vertex with the lowest MC value. The first MIS member is chosen from V_i in this situation.

$$Neighbour(V_i) = V_2 = n;$$

$\forall_v$ - V_i – n = m-1 (Since the graph is complete bipartite, the remaining vertices after deletion are isolated vertices.)

The $m-1$ isolated vertex represents the other members of the MIS.

$MIS = 1(first\ member) +$ m-1(isolated vertex) = m

* As a result of this proof, in complete bipartite graphs, the MIS set is expressed as the set that is larger than the bottom and top vertex sets. Maximum matching is achieved up to the cluster with the smallest number of vertexes among the bottom and top vertex clusters. In other words, the matching number is equal to the number of elements in the cluster with fewer vertices. In complete bipartite graphs, the neighboring set of the MIS set gives the matching number.

Matching number = Neighbour(m) = n

* In complete bipartite graphs, the number of edges is m*n. The algorithm colors the edges with different colors as many as the matching number. For this reason, all edges in the graph are colored with (m*n)/n different colors.

$X'(G) =$ Chromatic index = **m**

for m < n

The process steps are the inverse of 'for m>n'.

Therefore;

$X'(G) =$ Chromatic index = **n**

Algorithm 2. MECA Pseudocode

Malatya Edge Color Algorithm

```
G : (V,E)            : Any Graph
G_original<- G

FindMinimum <- function(G){
    centralities <- MalatyaCentrality(G)
    return(which.min(centralities))
}
FindMatching <- function(G){
    linegraph <- line.graph(G)    // The line graph of the graph G has been constructed.
    MatchingSet = c()
    while(vcount(linegraph) > 0 ){      // vertex number of linegraph
        RemoveVertex =c()
        neighborVertex <- NULL
        minNode <- V(linegraph)[FindMinimum(linegraph)]
        MatchingSet <- append(MatchingSet,minNode)
        neighborVertex <- neighbors(linegraph,v = minNode)
        RemoveVertex <- (neighborVertex ∪ minNode)
        linegraph <- delete_vertices(linegraph,RemoveVertex )
    }
    MatchingEdgeSet  <- E(G)[MatchingSet]      //matching edges
}
FindMinimumEdgeColor(G_original, MatchingEdgeSet ){
    G_original  = -   MatchingEdgeSet
    MatchingEdgeSet <- colored with the same color
        If ( E(G_original) == null){
         Print (Distinct MatchingEdgeSet colors)
         }else{
         G <- G_original
         FindMatching(G)
    }
}
```

for m = n

$\frac{n^2}{m} = \frac{m^2}{n}$, $\Psi(V_i) = \Psi(V_j)$, In this case, if the first choice is from (V_i), the solution is the same as "**m>n**", if it is from (V_j), it is the same as "**m<n**"

Matching number = **m** = **n**

$X'(G)$ = Chromatic index = **m** =**n** ■

Theorem 2: For regular lattice (Hypercube or Cubical) graphs, the proposed algorithm finds the optimum solutions.

Proof: We use the Q(3) hypercube graph to prove the theorem.
Step: Q(3) Hypercube

Q(x), H_x = (V, E), and | V |=2^x and | E |=$x2^{x-1}$.

Q(3), |V|=2^3 and |E|=$3*2^{3-1}$

$\forall_v = m + n, m = n = 4$

In Hypercube graphs, since they are bipartite graphs, m and n denote the top and bottom vertex sets, respectively.

$\forall_{V_i} \in V_1, \Psi(V_i) = \frac{n}{m}.n = \frac{n^2}{m}$

$\forall_{V_j} \in V_2, \Psi(V_j) = \frac{m}{n}.m = \frac{m^2}{n}$

Since $\Psi(V_i) = \Psi(V_j)$ one can be selected.

If the first vertex V_i is selected for MIS, the centrality values in the second iteration;

$\Psi(V_i) = \frac{n-3}{m-1}$, $\Psi(V_j) = \frac{m-1}{n-3}$,$\Psi(V_i) < \Psi(V_j)$

Since $\Psi(V_i)$ is small, selection is made from V_1. Next iteration;

$\Psi(V_i) = \frac{n-4}{m-2} = 0$, $\Psi(V_j) = \frac{m-2}{n-4}$ = undefined. In this case, since V_j is undefined, there is no vertex left in V_2. Since V_i value is 0, isolated vertices remain in V_1. All remaining isolated vertices are added to the MIS.

$MIS = (first\ member)\ 1 + (second\ member)\ 1$ +(isolated vertices) m-2 = **m**

* Each independent set member is linked to at most one matching member. Indepedent set üyelerinin çizgenin line'ında matching değerlerini verdiği bilinmektedir. Therefore, in regular lattice graphs, the number of independent vertex sets is equal to the number of matching numbers.

Matching number = m

* The total number of edges in the graph is m*x. m edges determined by Matching can be colored with the same color. As a result, coloring will be done with (m*x)/m different colors.

$X'(G)$ = Chromatic index = x ■

For example;

Q (3) hypercube, |V|=2^3 and |E|= $3*2^{3-1}$, $\forall_v = m + n, m = n = 4$ $X'(G)$ = (4*3)/4 = **3**

Q(4) hypercube, |V|=2^4 and |E|= $4*2^{4-1}$, $\forall_v = m + n, m = n = 8$ $X'(G)$ = (8*4)/8 = **4**

Q(5) hypercube, |V|=2^5 and |E|= 5*2^{5-1}, $\forall_v = m + n, m = n = 16$ $X'(G) = (16*5)/19 = \mathbf{5}$

.

.

.

4. Experimental Results

For the testing procedures of the proposed Malatya Edge Coloring algorithm, a multitude of diverse graph types has been utilized. These graphs comprise lattice, bipartite, multipartite, random, and social networks, and they have been evaluated under three different headings in the study. The chromatic index values and representative visuals for the graphs have been included in this section following all testing procedures.

4.1. Lattice Graphs

During the testing phase of the Malatya Edge Coloring Algorithm (MECA), 40 different lattice graphs were utilized. Among these graphs were grid, king, square, triangular, bethe, hexagonal mesh, rook, torus graphs, and various combinations of these graphs. The characteristics of all lattice graphs used in the testing phase, along with visual and numerical analysis results, are displayed in Figure 4. Additionally, MECA was applied to different combinations of the graphs shown in Figure 4, and the results are presented in Table 3. For instance, when the King (4,4) graph is examined, it consists of 16 vertices and 42 edges. After applying MECA, the chromatic index was determined to be 8, indicating that the edges of the graph could be colored with a minimum of 8 different colors. Upon examining the Square (5*4*3) graph, it was found to have 60 vertices and 133 edge connections. After the application of MECA, the chromatic index was identified as 6.

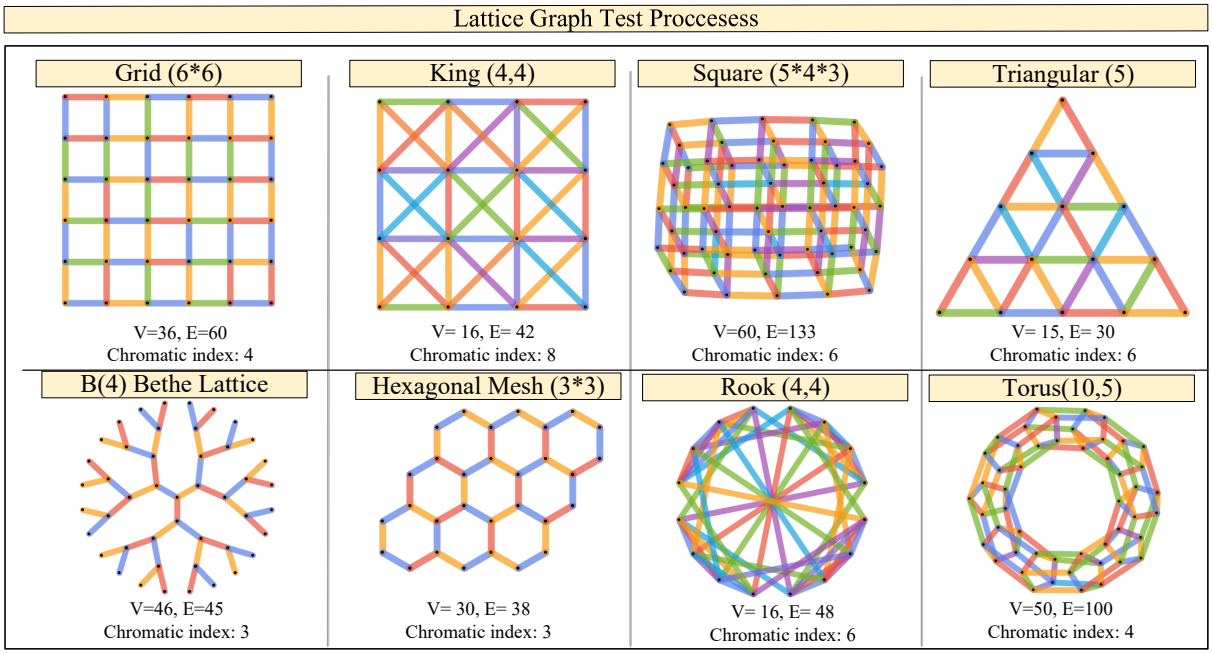

Figure 4. MECA lattice graph analysis.

In Table 3, other combinations of the lattice graphs, whose visuals are provided, are included. For example, the King (4*5) graph comprises 20 vertices and 55 edge connections. Following the application of the Malatya Edge Coloring Algorithm (MECA), the chromatic index was determined to be 8. Additionally, upon examining another example, the King (8*8) graph, it is found to possess 64 vertices and 210 edges. After the application of MECA, the minimum number of edge colorings was identified as 8.

Table 3. Lattice graph test results.

Lattice Graphs	Parameter	V	E	MECA chromatic index	Optimum chromatic index
Grid	7*7	49	84	4*	4
	8*8	64	112	4*	4
	9*10	90	161	4*	4
	10*10	100	180	4*	4
King	4*5	20	55	8*	8
	5*5	25	72	8*	8
	7*7	49	156	8*	8
	8*8	64	210	8*	8
Triangular	6	21	45	6*	6
	7	28	63	6*	6
	8	36	84	6*	6
	9	45	108	6*	6
Bethe	5	46	45	3*	3
	6	94	93	3*	3
	7	190	189	3*	3
	8	382	381	3*	3
Rook	2*4	8	16	4*	4
	2*10	20	100	10*	10
	3*5	15	45	6*	6
	3*8	24	108	9*	9
Torus	4*6	24	48	4*	4
	6*8	48	96	4*	4
	8*8	64	128	4*	4
	10*10	100	200	4*	4
Square	4*4*4	64	144	6*	6
	5*5*5	125	300	6*	6
	5*6*7	210	523	6*	6
	6*6*6	216	540	6*	6
Hexagonal Mesh	4*4	63	48	3*	3
	5*5	70	94	3*	3
	6*6	96	131	3*	3
	7*7	126	174	3*	3

Among popular lattice graphs, the grid (8*8) possesses 64 vertices and 112 edge relations. This graph has been determined to have a chromatic index of 4. Upon examination of the grid (10*10) graph, it is found to contain 100 vertices and 180 edge relations. Following the application of MECA, the chromatic index has been identified as 4. When examining the test results conducted on various types of lattice graphs, it is observed that MECA yields optimum outcomes for lattice graphs.

4.2. Bipartite and Multipartite graphs

In this section, MECA was tested on bipartite and multipartite graphs. The analysis results conducted on 36 bipartite and 24 multipartite graphs are presented in Figure 5 and Table 4. Figure 5 displays the visuals of the relevant graphs, including the number of vertices, the number of edges, and the chromatic index values determined after the application of MECA. For instance, upon examining the Hoffman graph, it is found to have 16 vertices and 32 edge relations. Following the application of MECA, the chromatic index value has been identified as 4. Another specific bipartite graph, the B (10) Book graph, when examined, possesses 22 vertices and 31 edge relations. After the analysis process, the chromatic index has been determined to be 11. In addition to these analysis results, Table 4 includes some of the bipartite graphs presented in Figure 5 that have been produced with different parameter values and incorporated into the analysis.

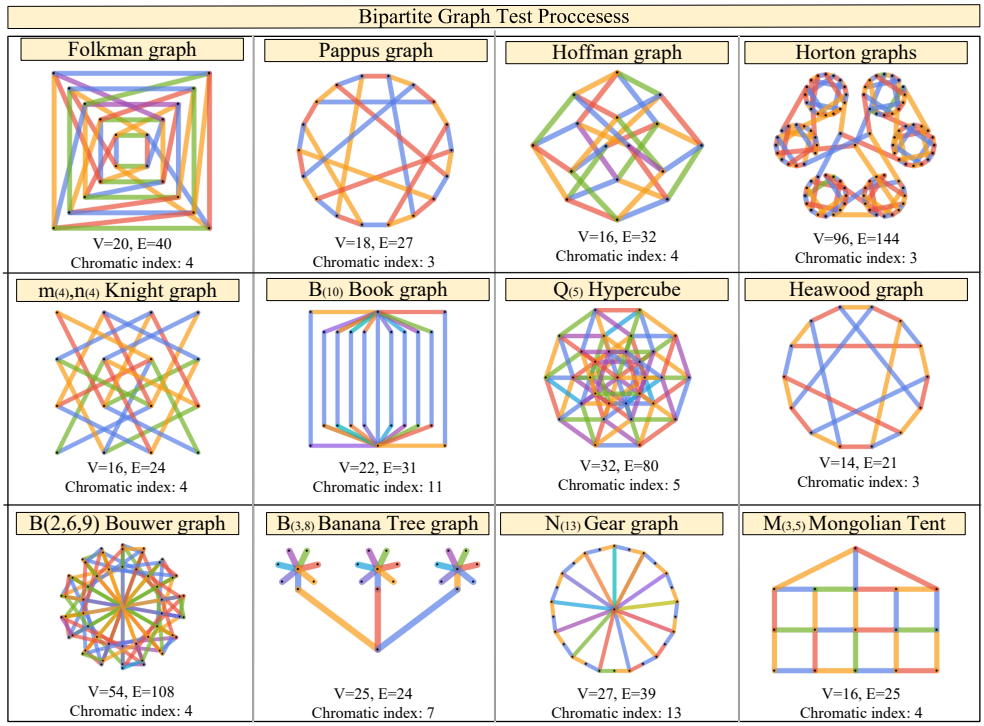

Figure 5. MECA bipartite graph analysis.

For example, the Book (3) graph consists of 8 vertices and 10 edges. Following the application of MECA, the chromatic index has been identified as 4. In the case of Book (15), the chromatic index is 16. When examining the gear(10) graph, which is one of the special types of bipartite graphs, it is found to have 21 vertices and 30 edges. After the application of MECA, the chromatic index has been determined to be 10.

Table 4. Bipartite graphs MECA results.

Bipartite Graphs	Parameter	V	E	MECA chromatic index	Optimum chromatic index
Hypercube	Q(5)	32	80	5*	5
	Q(6)	64	192	6*	6
	Q(7)	128	448	7*	7
	Q(8)	256	1024	8*	8
Knight	4*5	20	34	6*	6
	5*5	25	48	8*	8
	5*6	30	62	8*	8
	6*6	36	80	8*	8
Banana Tree	3*6	19	18	5*	5
	4*6	25	24	5*	5
	4*8	33	32	7*	7
	5*4	21	20	5*	5
Book	3	8	10	4*	4
	6	14	19	7*	7
	12	26	37	13*	13
	15	32	46	16*	16
Gear	5	15	11	5*	5
	8	17	24	8*	8
	9	19	27	9*	9
	10	21	30	10*	10
Mongolian Tent	2*5	11	16	4*	4
	3*3	10	14	4*	4
	4*5	21	34	4*	4
	5*5	26	43	4*	4

Upon examining the results of the Modified Edge Coloring Algorithm (MECA) on bipartite graphs, it is observed that the minimum edge coloring outcomes are optimal. Additionally, MECA has been tested on 24 different multipartite graphs to analyze the situation in multilayered graphs. In Figure 6, examples of randomly generated 2, 3, 4-partite graphs along with a Complete Multipartite graph are presented. The Erdos-Renyi model has been utilized as the random graph generator [45]. When these graphs are examined, it is found that the 2-partite graph has 10 vertices and 10 edge relations, and its chromatic index has been determined to be 4 following the application of MECA. The randomly generated 3-partite graph has 20 vertices and 30 edges, and its chromatic number has been identified as 6. For the graph produced as a Complete multipartite, the chromatic index has been determined to be 7. A Complete graph is named for graphs in which all vertices are connected to each other [46]. Table 5 presents analysis results for graphs with different numbers of partites, both complete and incomplete.

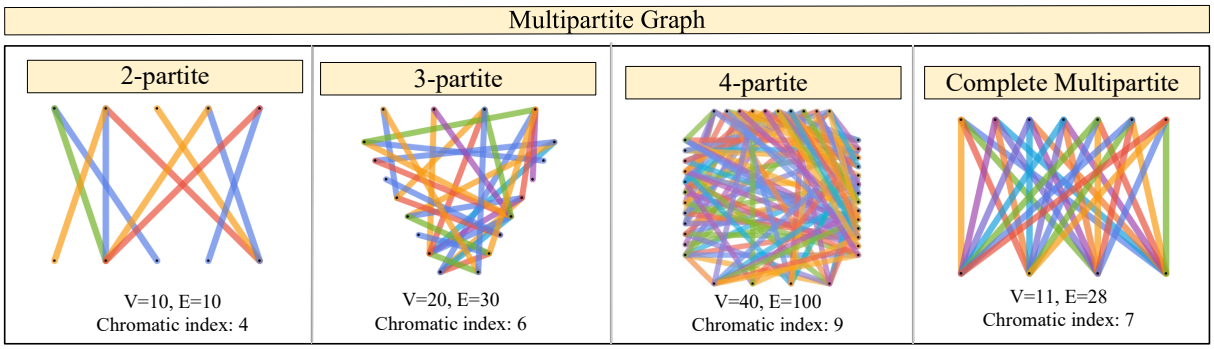

Figure 6. MECA multipartite graph analysis.

In Table 5, information about the number of layers in the generated graph, along with the number of vertices, edges, and the chromatic index as identified by the MECA, is provided. Upon examination of the table, it is found that a 3-partite graph with 12 vertices and 16 edges has a chromatic index of 5. For a graph possessing 14 vertices and 18 edges, the chromatic index has been determined to be 6. When analyzing a more complex 8-partite graph, which comprises 50 vertices and 500 edge connections, MECA has determined the chromatic index to be 28. These findings underscore MECA's capability to effectively analyze and determine the chromatic index across graphs with varying degrees of complexity and multipartite structures, showcasing its utility in graph coloring challenges.

Table 5. Multipartite graphs MECA results.

Multipartite Graphs	Partite Number	V	E	MECA chromatic index	Optimum chromatic index
Partites Graphs	2	8	8	4*	4
		12	12	3*	3
		14	14	5*	5
		15	15	4*	4
	3	10	10	4*	4
		12	16	5*	5
		14	18	6*	6
		15	22	5*	5
	4	15	30	7*	7
		20	40	7*	7
		25	50	8*	8
		25	60	8*	8
	5	30	120	15*	15
	6	30	150	16*	16
	7	40	300	21*	21
	8	50	500	28*	28
Complete n-partite layer	(3,4)	7	12	4*	4
	(3,4,5,7)	19	131	16*	16
	(4,6,3,6,8,5)	32	419	29*	29
	(5,10,7,3,5,7, 9,4)	50	1073	47*	47

When examining the results related to Complete n-partite graphs, four different testing procedures have been conducted. The notation (3,4) in the table signifies that the graph consists of two layers, with the first layer comprising 3 vertices and the second layer comprising 4 vertices, resulting in a total of 7 vertices and 12 edge relations. Following the application of the MECA, the chromatic index has been determined to be 4. Another example of a complete bipartite graph, denoted as '(3,4,5,7)', consists of four layers. The first layer contains 3 vertices, the second layer contains 4, the third layer has 5, and the fourth layer comprises 7 vertices, totaling 19 vertices and 131 edge relations. After the application of MECA, the chromatic index has been identified as 16. The analysis results indicate that the proposed MECA provides optimum results for complete multipartite graphs, while producing optimal or near-optimal outcomes for any multipartite graph.

4.3. Random and Special Graphs

In this section, the Malatya Edge Coloring Algorithm (MECA) has been applied to real-world social networks known in the literature, as well as to randomly generated graphs using different algorithms. For social networks, the Zachary Karate Club, Dolphin, Zebra, and complex network models have been chosen. As for random graph generators, the Erdos-Renyi, Forest Fire, Watts Strogatz, and Regular models have been utilized. MECA has been tested on 8 different examples as shown in Figure 7. Upon examining the Zachary Karate Club network, it is found to consist of 34 vertices and 78 edge relations. Following the application of MECA, the chromatic index has been determined to be 17. In another example of a social network, the Dolphin network, with 62 vertices and 159 edge relations, has been found to have a chromatic index of 12.

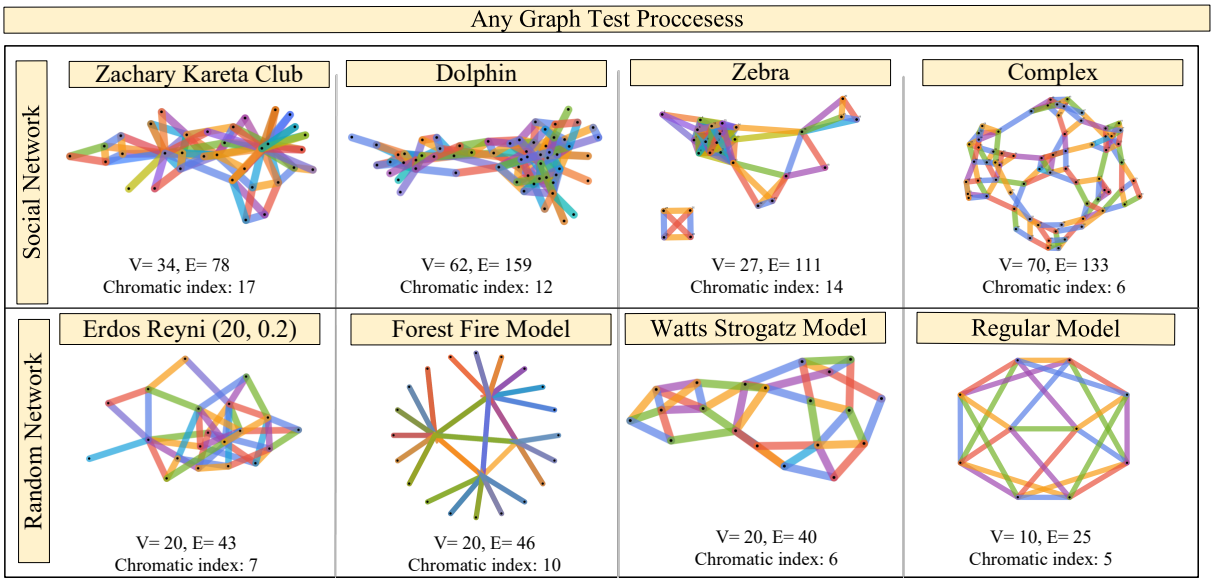

Figure 7. MECA social and random graph analysis.

When examining randomly generated graphs, for the Erdos-Renyi Model with parameters p=20 and q=0.2, a graph consisting of 20 vertices and 43 edges was produced, for which the MECA has determined the chromatic index to be 7. In another example, using the Regular model, a graph with 10 vertices and 25 edges was generated, and its chromatic index was identified as 5. Upon reviewing the test results, it is evident that MECA provides optimal or near-optimum results for both real-world social networks and any type of randomly generated graph. This underscores MECA's robustness and effectiveness in addressing edge coloring challenges across a diverse range of graph types.

The proposed method has also been tested on 10 random graphs with varying densities. All random graphs were generated using the Erdős-Rényi model. The relevant test results are presented in Table 6. Upon examining the table results, it is observed that as the density of the graph increases, the number of edge colors also increases. The identified MECA chromatic index represents the number of matching sets determined within the graph. For instance, in a random graph with a density of 0.20, 28 distinct matching sets were generated. Since the matching

set generated in each iteration is removed from the graph, the identified 28 matching sets are completely distinct from one another, with unique members.

Table 6. MECA results based on densities

~Density	V	E	MECA chromatic index
0.10	100	506	17
0.15	100	753	21
0.20	100	1011	28
0.25	100	1206	35
0.30	100	1529	42
0.35	100	1674	41
0.40	100	1973	48
0.45	100	2273	53
0.50	100	2473	58
0.55	100	2713	69

5. Conclusion

This study proposes a robust method that solves the minimum edge coloring problem in polynomial time for any type of graph. Named the Malatya Edge Coloring Algorithm (MECA), this method has been extensively tested across various graph types. Testing processes have been conducted under the categories of Lattice, Bipartite, Multipartite, Random, and social networks. The proposed method's steps have been elaborately explained on the hypercube, which is both lattice and bipartite. Additionally, the pseudo-code and flowchart of the proposed method are detailed within the study. Computational proofs have been conducted for graphs whose analytical proofs are known, thereby demonstrating that the proposed method yields optimum results for known bipartite and complete multipartite graphs. The success of MECA in these graphs suggests that it could exhibit similar success across all graph types. Care was taken to use well-known graphs in the literature during the testing process. Under the Lattice category, 40 different tests were conducted on grids, kings, squares, triangular, bethe lattices, hexagonal meshes, rooks, and tori. Under the Bipartite and Multipartite categories, 60 different tests were performed on knights, hypercubes, gears, books, folkman, and numerous n-partite graphs. The analysis shows that MECA provides optimum results for all lattice, bipartite, and complete multipartite graphs while offering Optimal or Near Optimum results for other multipartite graph types. Additionally, MECA conducted 8 different tests under the Random and Special Graphs category, utilizing popular social networks such as the Zachary Karate Club, Dolphin, Zebra, and complex networks, and using random graph generators like the Erdos-Renyi, Forest Fire, Watts Strogatz, and Regular models. MECA offers optimal or near-optimum results for random and social networks. Throughout all conducted tests, the chromatic index results obtained from the Malatya Edge Coloring Algorithm (MECA) comply with Vizing's Theorem. Vizing's Theorem is a fundamental result in graph theory that classifies graphs into two classes based on their chromatic index: Class 1, where the chromatic index equals the maximum degree of the graph, and Class 2, where the chromatic index is $\Delta+1$. The theorem asserts that for any simple, undirected graph, the chromatic index is either $\Delta+1$. The adherence of MECA's results to Vizing's Theorem underlines the algorithm's efficacy and accuracy in determining the edge coloring of a wide array of graphs. This includes various types such as lattice, bipartite, multipartite, random, and social networks. The algorithm's ability to consistently align with a foundational theory of graph coloring emphasizes its reliability and potential applicability in solving practical problems related to graph coloring, network design, scheduling, and other areas where edge coloring is relevant.

The results of MECA are presented in Tables 3, 4, and 5 in comparison with the optimal outcomes. MECA has been introduced as an effective greedy approach. Thanks to its robust methodology, MECA produces same results in every run, making it a stable method. Consequently, it can be successfully implemented in real-time systems. In deep learning methods, the challenges during the network training phase, the inability to achieve results at a fixed iteration in heuristic methods, and the need for multiple runs to achieve the best outcome are notable. In this context, MECA generates results with a single iteration. The comparative analysis of different algorithmic approaches proposed by the method is presented in Table 1.

The analysis processes pertaining to the proposed method have been incorporated into the study both visually and numerically. The complete codes of the Malatya Edge Coloring Algorithm (MECA), written in the R programming language, can be accessed at https://github.com/furkanoztemiz. Additionally, this website also contains data on the random multipartite graphs generated during the test process. The sharing of these codes is

anticipated to expand the usage of the proposed algorithm and contribute significantly to the literature. This open-source approach not only facilitates the replication of the study's results by other researchers but also enables the continuous improvement and adaptation of MECA for different applications and graph types, thereby enhancing its utility and impact in the field of graph theory and network analysis.

References

[1] Plantholt MJ, Shan S. Edge coloring graphs with large minimum degree. J Graph Theory 2023; 102: 611–632.
[2] Badoni RP, Gupta DK. A graph edge colouring approach for school timetabling problems. Int J Math Oper Res 2014; 7(2): 123-138.
[3] Bellitto T, Li S, Okrasa K, et al. The complexity of routing problems in forbidden-transition graphs and edge-colored graphs. Algorithmica 2023; 85: 1202–1250.
[4] Yakut S, Öztemiz F, Karci A. A new approach based on centrality value in solving the maximum independent set problem: Malatya centrality algorithm. Comput Sci 2023; 8(1): 16-23.
[5] Yakut S, Öztemiz F, Karci A. A new robust approach to solve minimum vertex cover problem: Malatya vertex-cover algorithm. J Supercomput 2023; 79: 19746–19769.
[6] Öztemiz F. İki parçalı eşleştirme ile maksimum akış. Comput Sci 2023; 8(2): 102-109.
[7] Foucaud F, Hocquard H, Lajou D. Complexity and algorithms for injective edge-coloring in graphs. Inf Process Lett 2021; 170: 106121.
[8] Furmańczyk H, Kosowski A, Ries B, Żyliński P. Mixed graph edge coloring. Discrete Math 2009; 309(12): 4027-4036.
[9] Basavaraju M, Chandran LS. A note on acyclic edge coloring of complete bipartite graphs. Discrete Math 2009; 309(13): 4646-4648.
[10] Venkateswarlu A, Sarkar S, Ananthanarayanan SM. On acyclic edge-coloring of complete bipartite graphs. Discrete Math 2017; 340(3): 481-493.
[11] Plantholt MJ, Shan S. Edge coloring graphs with large minimum degree. J Graph Theory 2023; 102: 611–632.
[12] Basavaraju M, Chandran LS. Acyclic edge coloring of graphs with maximum degree 4. J Graph Theory 2009; 61: 192-209.
[13] Junlei Z. Injective edge coloring of graphs with maximum degree 5. Discrete Appl Math 2023; 334: 119-126.
[14] Cardoso DM, Cerdeira OJ, Dominicc C, Cruz PJ. Injective edge coloring of graphs. Filomat 2019; 33(19): 6411-6423.
[15] Andersen LD, Máčajová E, Mazák J. Optimal acyclic edge-coloring of cubic graphs. J Graph Theory 2012; 71: 353-364.
[16] Kano M, Li X. Monochromatic and heterochromatic subgraphs in edge-colored graphs: A survey. Graphs Combin 2008; 24: 237–263.
[17] Miao Z, Song Y, Wang T, Yu X. List star edge coloring of generalized Halin graphs. Discrete Math 2023; 346(1): 113204.
[18] Balister PN, Riordan OM, Schelp RH. Vertex-distinguishing edge colorings of graphs. J Graph Theory 2003; 42: 95-109.
[19] Fabrício S, Benevides CH, Rudini MS. Edge-colorings of graphs avoiding complete graphs with a prescribed coloring. Discrete Math 2017; 340(9): 2143-2160.
[20] Wdowinski R. Orientation-based edge-colorings and linear arboricity of multigraphs. J Graph Theory 2023; 102: 633–647.
[21] Li X, Li Y, Lv JB, Wang T. Strong edge-colorings of sparse graphs with 3Δ−1 colors. Inf Process Lett 2023; 179: 106313.
[22] Dey A, Son LH, Kumar PKK, Selvachandran G, Quek SG. New concepts on vertex and edge coloring of simple vague graphs. Symmetry 2018; 10(9): 373.
[23] Basavaraju M, Chandran LS. Acyclic edge coloring of 2-degenerate graphs. J Graph Theory 2012; 69: 1-27.
[24] Dey A, Ghosh D, Pal A. Edge coloring of a complement fuzzy graph. Int J Mod Eng Res (IJMER) 2012; 2: 1929-1933.
[25] Mazzuoccolo G, Mkrtchyan V. Normal edge-colorings of cubic graphs. J Graph Theory 2020; 94: 75–91.
[26] Halldórsson MM, Nolin A. Superfast coloring in CONGEST via efficient color sampling. Theor Comput Sci 2023; 948: 113711.
[27] Akbari S, Beikmohammadi A, Brešar B, Dravec T, Habibollahi MM, Movarraei N. On the chromatic edge stability index of graphs. Eur J Comb 2023; 111: 103690.
[28] Esperet L, Parreau A. Acyclic edge-coloring using entropy compression. Eur J Comb 2013; 34(6): 1019-1027.
[29] Kostochka A, Raspaud A, Xu J. Injective edge-coloring of graphs with given maximum degree. Eur J Comb 2021; 96: 103355.
[30] Januario T, Urrutia S, Ribeiro CC. Edge coloring: A natural model for sports scheduling. Eur J Oper Res 2016; 254(1): 1-8.
[31] Feng W, Zhang L, Wang H. Approximation algorithm for maximum edge coloring. Theor Comput Sci 2009; 410(11): 1022-1029.
[32] Ito T, Kato A, Zhou X, Nishizeki T. Algorithms for finding distance-edge-colorings of graphs. J Discrete Algorithms 2007; 5(2): 304-322.
[33] Ghaffari M, Kuhn F, Maus Y, Uitto J. Deterministic distributed edge-coloring with fewer colors. In: Proceedings of the 50th Annual ACM SIGACT Symposium on Theory of Computing (STOC 2018); Association for Computing Machinery; New York, NY, USA, 2018. pp. 418–430.

[34] Kowalik Ł. Improved edge-coloring with three colors. Theor Comput Sci 2009; 410(38–40): 3733-3742.
[35] Behnezhad S, Derakhshan M, Hajiaghayi M, Knittel M, Saleh H. Streaming and massively parallel algorithms for edge coloring. In: 27th Annual European Symposium on Algorithms (ESA 2019); Leibniz International Proceedings in Informatics (LIPIcs), 2019. pp. 15:1-15:14.
[36] Lužar B, Maceková M, Rindošová S, Soták R, Sroková K, Štorgel K. Locally irregular edge-coloring of subcubic graphs. Discrete Appl Math 2023; 339: 136-148.
[37] Gandham S, Dawande M, Prakash R. Link scheduling in wireless sensor networks: Distributed edge-coloring revisited. J Parallel Distrib Comput 2008; 68(8): 1122-1134.
[38] Zhou X, Nishizeki T. Algorithm for the cost edge-coloring of trees. J Comb Optim 2004; 8: 97–108.
[39] Akbari S, Haslegrave J, Javadi M, Nahvi N, Niaparast H. Tight bounds on the chromatic edge stability index of graphs. Discrete Math 2024; 347(4): 113850.
[40] Bernshteyn A. A fast distributed algorithm for (Δ+1)-edge-coloring. J Comb Theory Ser B 2022; 152: 319-352.
[41] Chen G, Hao Y. On the coequal values of total chromatic number and chromatic index. J Comb Theory Ser B 2023; 158(2): 286-304
[42] Abrahamyan S. On maximum matchings in 5-regular and 6-regular multigraphs. Discrete Math 2023; 346(2): 113243.
[43] Le VB, Telle JA. The perfect matching cut problem revisited. Theor Comput Sci 2022; 931: 117-130.
[44] Karci A, Yakut S, Öztemiz F. A new approach based on centrality value in solving the minimum vertex cover problem: Malatya centrality algorithm. Comput Sci 2022; 7(2): 81-88.
[45] Mohd-Zaid F, Kabban SC, Deckro RF, Shamp W. Network characterization and simulation via mixed properties of the Barabási–Albert and Erdös–Rényi degree distribution. J Def Model Simul 2024; 21(1): 87-102.
[46] Akbari S, Alipour A. Multicolored trees in complete graphs. J Graph Theory 2007; 54: 221-232.

Turkish Journal of Science & Technology
20(1), 327-337, 2025

Research Paper
https://doi.org/10.55525/tjst.1637713

Exploring the Impact of Model Capacity and Parameter Tuning on 3D Semantic Segmentation

Furkan KARAMAN[1*], Fatma GUMUS[2]
[1] Department of Computer Engineering, ATASAREN, National Defence University, İstanbul, Türkiye
[2] Department of Computer Engineering, National Defence University, İstanbul, Türkiye
[*1] furkan09karaman@gmail.com, [2] fatma.gumus@msu.edu.tr

(Geliş/Received: 11/02/2025; Kabul/Accepted: 18/03/2025)

Abstract: 3D semantic segmentation, the process of assigning semantic labels to every point in a 3D space, is critical for numerous applications, including autonomous driving, robotics, medical imaging, and urban mapping. Despite significant progress, challenges such as data imbalance, scalability, and real-time processing constraints persist. This study addresses the real-time processing issue by comparing Tiny, Medium, and Large PointNet-inspired models utilizing the ShapeNetCore dataset. The models incorporate the T-Net module for pose normalization to maintain robustness against geometric transformations. Class-specific segmentation is explored by training separate models for the Airplane, Motorbike, and Car classes, allowing custom optimizations for each class. The Tiny model with 512 sampled points where the batch size is 16 and trained for 40 epochs with a starting learning rate of 1×10^{-3} achieved an average training accuracy of 86.18% and an average validation accuracy of 83.50%, making it optimal for real-time applications due to its fast inference speed and high accuracy.

Key words: 3D semantic segmentation, point cloud processing, scalability, real-time processing.

3B Semantik Bölütleme Performansı Üzerinde Model Kapasitesi ve Parametre Ayarının Etkisinin Araştırılması

Öz: 3B semantik bölütleme, üç boyutlu uzaydaki her noktaya anlamsal etiketler atama sürecidir ve otonom sürüş, robotik, tıbbi görüntüleme ve kentsel haritalama dahil olmak üzere çok sayıda uygulama için kritik öneme sahiptir. Önemli ilerlemeye rağmen, veri dengesizliği, ölçeklenebilirlik ve gerçek zamanlı işleme kısıtlamaları gibi zorluklar devam etmektedir. Bu çalışma, ShapeNetCore veri setini kullanan Tiny, Medium ve Large olarak PointNet'ten esinlenen modelleri karşılaştırmak suretiyle gerçek zamanlı işleme sorununu ele almaktadır. Modeller, geometrik dönüşümlere karşı gürbüzlüğü korumak üzere poz normalizasyonu için T-Net modülünü içerir. Uçak, Motosiklet ve Araba sınıfları için ayrı modeller eğitilerek sınıf-özel segmentasyon çalışılmış ve her sınıf için özel optimizasyon değerlendirilmiştir. Küme büyüklüğünün 16 olduğu ve 1×10^{-3} başlangıç öğrenme oranıyla 40 epok boyunca eğitilen 512 örneklenmiş noktaya sahip Tiny modeli, %86,18 ortalama eğitim doğruluğu ve %83,50 ortalama doğrulama doğruluğu elde etti ve test hızı ve yüksek doğruluğu nedeniyle gerçek zamanlı uygulamalar için ideal olduğu değerlendirilmiştir.

Anahtar kelimeler: 3B semantik bölütleme, nokta bulutu işleme, ölçeklenebilirlik, gerçek zamanlı işleme.

1. Introduction

The rapid advancements in 3D semantic segmentation have significantly improved the ability to analyze and interpret point cloud data. Applications such as autonomous navigation, medical imaging, and remote sensing rely on robust segmentation models to classify and segment objects in complex 3D environments. Despite notable progress, achieving high segmentation accuracy while maintaining computational efficiency remains a critical challenge, particularly for real-time applications. A deep learning model PointNet [1] and its derivatives such as [2] leverage hierarchical feature extraction to capture both local and global geometric properties, enabling precise object classification and segmentation. Voxel-based approaches, on the other hand, convert point clouds into structured 3D grids, enabling the use of convolutional operations [3-5]. Hybrid approaches combine both point cloud and voxel-based methods [6-8].

In contrast to voxel-based and hybrid methods, which introduce quantization artifacts and impose high memory requirements, PointNet operates directly on point clouds, preserving geometric details while maintaining efficiency. This study systematically investigates the influence of architectural and hyperparameter decisions on the segmentation performance of a PointNet inspired architecture. It examines how sampling density affects accuracy, the role of batch size in convergence speed, and the trade-offs between model capacity and segmentation

[*] Corresponding author: furkan09karaman@gmail.com. ORCID Number of authors: [1] 0009-0009-1304-8103, [2] 0000-0001-5191-0037

quality. The paper also emphasizes the importance of real-time applicability, shedding light on a frequently overlooked but crucial factor in 3D segmentation methodologies. This work shares results on class-specific segmentation where a separate segmentation model was trained for each class independently. This approach of segmentation allows custom optimization such that each class can have its architecture, hyperparameters, and loss function. This is also better for imbalanced data; since each model only focuses on one class, it can be better suited for handling rare classes. There are some downsides to this approach, such as if multiple models predict the same pixel, conflict resolution might be required. This paper does not address the approach but presents fine-tuned results for models with different capacities (Tiny, Medium, Large) and three sets of hyper-parameters.

The remainder of this paper is structured as follows: Section 2 provides a comprehensive literature review, summarizing key developments in 3D semantic segmentation, including deep learning-based methodologies, benchmark datasets, and open challenges. Section 3 presents the material and methods. Section 4 presents our experimental results, detailing the dataset, preprocessing steps, and PointNet parameter tuning strategy. Section 5 discusses challenges and open issues in the field, such as data imbalance, scalability, and annotation costs.

2. Literature Review

Point cloud-based methods operate directly on unstructured 3D point clouds, allowing for flexible and efficient data processing. PointNet [1] was a pioneering architecture that employed permutation-invariant networks to process unordered point clouds to perform three major tasks: classification, part segmentation, and semantic segmentation (Figure 1). To prevent sensitivity to point ordering, it uses max pooling. Each point is processed via Multi-Layer Perceptrons (MLPs), and the maximum is computed across all points to learn the global features of the scene. The method's primary advantage is its ability to directly handle raw point cloud data with high speed. PointNet struggled to capture local geometric features, which was addressed by PointNet++ [2]. Instead of using a fixed grid (like CNNs in images), PointNet++ dynamically groups points based on their geometric proximity using a radius threshold. This allows it to adaptively learn geometric details at different scales, preserving local curvature and surface variations. While it excelled in handling complex geometries, it required higher computational costs and processing time. Dynamic Graph CNNs (DGCNN) [9] further expanded on this concept by introducing dynamic graph construction, which updates the neighborhood connections during training. Despite its success, the method required significant computational resources, limiting its scalability for large datasets.

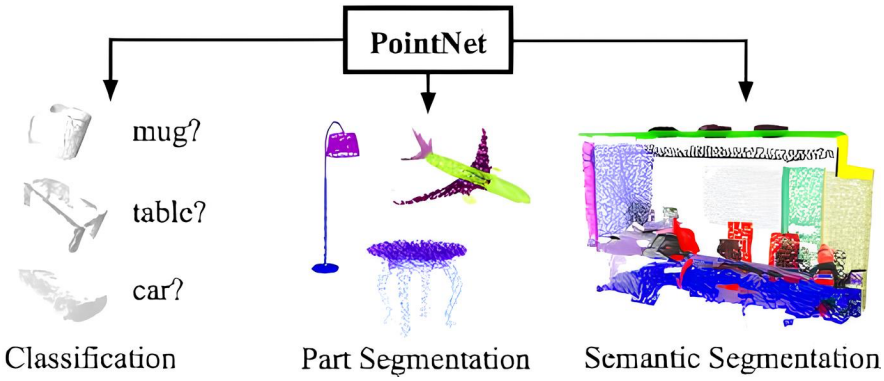

Figure 1. PointNet tasks [1].

Sub-manifold Sparse Convolutional Networks (SSCN) [10] utilized sparse convolutions for more efficient processing of 3D grids. MinkowskiNet [3] extended this concept by using sparse convolutions in 4D spatio-temporal networks. However, voxelization leads to quantization errors, which may degrade segmentation performance at high resolutions. It employs 4D sparse convolutions to optimize time and memory usage for large-scale datasets. Sparse convolutions operate only on active voxels, enhancing memory efficiency.

PolarNet [5] introduced a polar grid representation to improve the processing of LiDAR data, especially when dealing with uneven data distributions. This method demonstrated notable improvements in datasets such as SemanticKITTI [4]. However, it faced challenges related to memory consumption and computational complexity, particularly for large-scale applications. PolarNet processed LiDAR data using polar grid representations. It aimed to understand the global context of the data. The model processed each cell to learn the global features of the scene.

KPConv [11] achieved high accuracy in complex scenes by leveraging deformable convolutions that adapt to irregular geometries. It defines learnable kernel points between points, and filters are automatically shaped based on the density of the data. While it was highly effective in detailed local feature learning, it required substantial computational resources and a complex training process.

Hybrid methods aim to combine the strengths of point-based and voxel-based techniques. SalsaNext [6] is such a model that integrates point-wise uncertainty estimation with voxel-based representations. It achieved real-time performance for applications like autonomous driving. Using an encoder-decoder architecture, it learned features from LiDAR inputs. The model optimized computations with polar grid representations and enhanced reliability through uncertainty estimation in segmentation predictions. This method is particularly effective for real-time applications, such as environmental sensing in autonomous vehicles. PVCNN [12] is another hybrid approach that integrates the computational efficiency of voxel grids with the flexibility of point-level representations. It offered a balanced approach for real-time applications. SPVConv [7] merged sparse voxel processing with high-resolution point features, resulting in enhanced segmentation accuracy while maintaining computational efficiency. These hybrid models are well-suited for real-world applications that require both precision and high throughput.

SASSNet [8], a semi-supervised learning approach, demonstrated state-of-the-art performance in kidney tumor segmentation. The KiTS19 challenge [13] highlighted the potential of automated 3D segmentation techniques for kidney tumor analysis, showcasing the effectiveness of these methods when annotated data is scarce and expensive to obtain.

The field of 3D segmentation has been extensively reviewed in the literature. Vinodkumar et.al.[14] extensively explored deep learning-based methodologies for 3D object segmentation, detection, and classification. Their work categorized methods based on data modalities, such as LiDAR-based approaches, point cloud techniques, and hybrid models, providing insights into their relative strengths and limitations. Moreover, the study offered an analysis of benchmark datasets like SemanticKITTI and ModelNet, enabling comparative evaluations of various methods. Similarly, He et al. [15] conducted an in-depth survey focusing on three primary segmentation tasks: semantic segmentation, instance segmentation, and part segmentation.

3. Material and Methods

For this study, we utilize ShapeNetCore [16], a subset of the ShapeNet dataset, which is a large-scale, richly annotated repository of 3D shapes. ShapeNetCore includes 55 common object categories with 3D models, providing a reliable benchmark for 3D semantic segmentation. The experiments focused on the three vehicle categories, which are also included as part of the PASCAL 3D+ [17] dataset. The experiments were conducted on the classes: airplane, car, and motorbike, each segmented into specific parts (Table 1). The dataset consists of point cloud representations of 3D models along with manually verified category and alignment annotations (Figure 2). A class-specific segmentation method was used, where each class had its model trained separately. This allows the model to optimize for the unique features of each class.

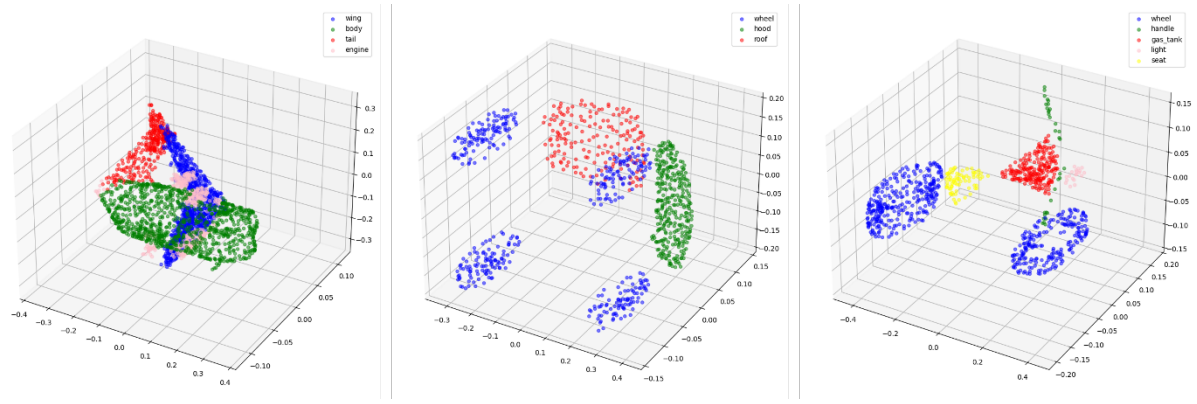

(a) (b) (c)

Figure 2. Samples from the dataset: a)Airplane b)Car c)Motorbike.

Table 1. Data distribution.

Class	Segmentation parts	Training size	Validation size
Airplane	wing, body, tail, engine	2955	739
Car	wheel, hood, roof	5420	1356
Motorbike	wheel, handle, gas tank, light, seat	187	47

3.1. Preprocessing

One of the key challenges in handling point cloud data is that different 3D scans contain a variable number of points. This variability makes batch processing difficult. To ensure uniformity, we perform the following preprocessing steps:

1) Fixed-size Sampling: We randomly sample a fixed number of points from each point cloud, choosing from $\{256, 512, 1024\}$ to analyze its impact on performance.

2) Normalization: The point clouds are normalized to ensure scale invariance, making the model robust to different object sizes.

3.2. Model variants and hyperparameters

We employ a PointNet-inspired architecture. The proposed model processes unstructured 3D point cloud data to classify each point into predefined segment categories. The architecture consists of three main components: an input transformation block, a hierarchical feature extraction network, and a segmentation head.

Segmentation outputs should remain unchanged under geometric transformations (e.g., translation or scaling). To achieve pose normalization, we apply rigid or affine transformations to input point clouds. This is done using a Spatial Transformer Network (STN) [18], implemented as the T-Net module in PointNet. The T-Net learns a 3×3 transformation matrix using a multi-layer perceptron (MLP), max-pooling, and fully connected layers. This matrix is then applied to the input before feature extraction, ensuring transformation invariance. While global features are sufficient for classification, segmentation requires capturing both local and global contexts. PointNet integrates local point features with global shape descriptors, ensuring fine-grained segmentation. To systematically explore the parameter space, we experiment with the three sets of hyper-parameters in Table 2 and the learning rate scheduled for decay by half every 5 epochs.

Table 2. Hyper-parameter sets.

Parameter set	Number of sampled points	Batch size	Training epochs	Initial learning rate
Set-0	256	8	20	1×10^{-2}
Set-1	512	16	40	1×10^{-3}
Set-2	1024	32	60	1×10^{-4}

We evaluate three different model capacities (Table 3): The large model serves as an upper bound for computational complexity, while the tiny model allows efficient benchmarking with minimal hardware requirements. We ran the experiments on NVIDIA L4 Tensor Core GPU for each hyper-parameter set in Table 2 and the models in Table 3.

Table 3. Number of filters in T-net and segmentation-net convolutions and network size.

Model Variant	Transformation-net	Segmentation-net	Network size (Total parameters / Model Size)
Tiny	16, 32, 256, 128, 64	16, 32, 32, 32, 128, 512	~344K / 1.31 MB
Medium	64, 128, 1024, 512, 256	64, 128, 128, 128, 512, 2048	~7M /28.11 MB
Large	128, 256, 2048, 1024, 512	128, 256, 256, 256, 1024, 4096	~45M /173.22 MB

3.3. The architecture

The segmentation pipeline consists of three main components: input transformation, hierarchical feature extraction, and segmentation output (Figure 3). To ensure pose invariance, an affine transformation was applied to the input point clouds using a Spatial Transformer Network (STN). This module learns a transformation matrix via a multi-layer perceptron (MLP), max-pooling, and fully connected layers. This transformation matrix normalizes point positions, reducing sensitivity to spatial distortions.

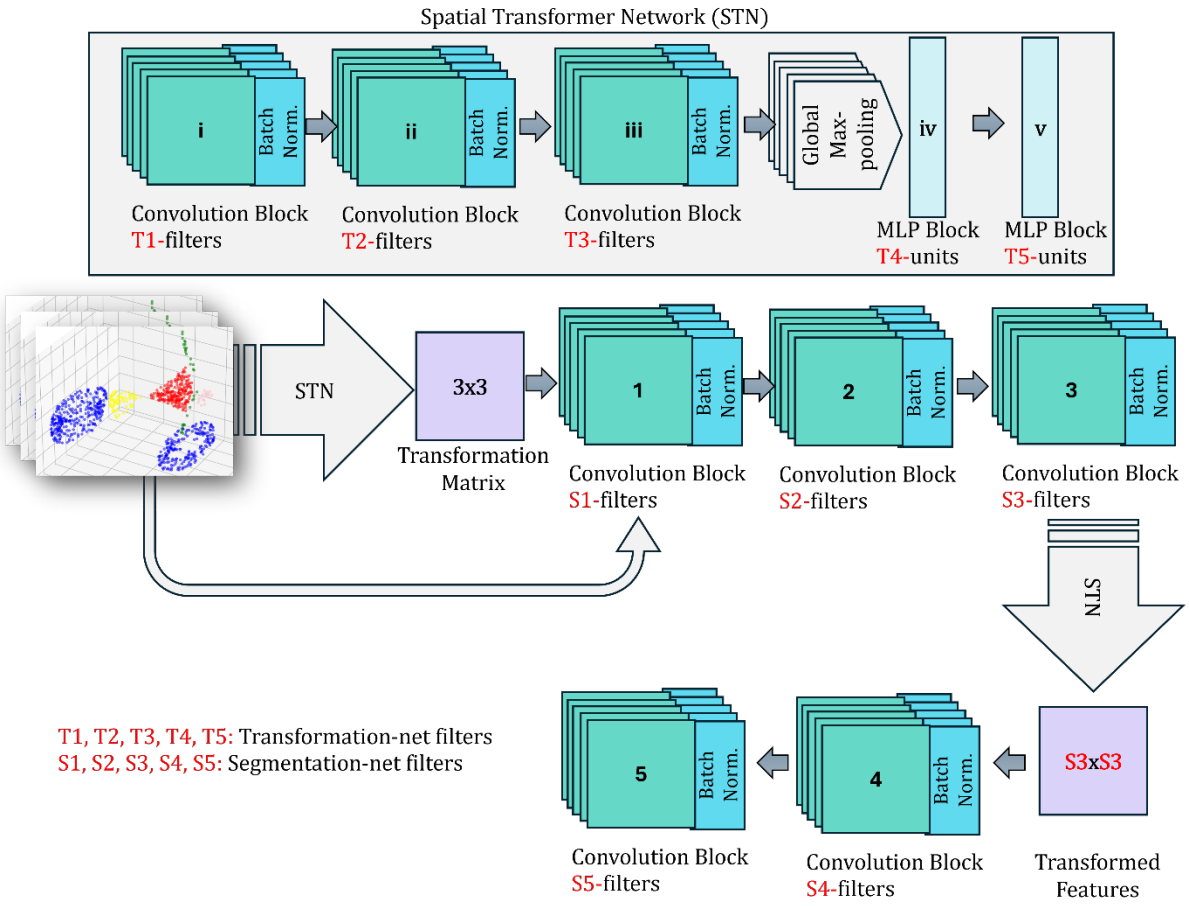

Figure 3. The segmentation pipeline.

The model extracts feature through multiple convolutional layers, progressively capturing local and global geometric structures. The key steps in this pipeline are point-wise feature learning, feature propagation, and global feature aggregation. A series of 1D convolutional layers with ReLU activation map each point to a higher-dimensional feature space. Intermediate features are aggregated across different scales, allowing for both local and global context preservation. Using a max-pooling operation, a global shape descriptor is generated, summarizing the overall object structure while retaining permutation invariance.

The extracted hierarchical features are concatenated and passed through a final segmentation head, which consists of 1D convolutional layers followed by a softmax activation function. This module assigns a class label to each point in the input cloud, completing the segmentation process.

4. Experimental Results

The results in Tables 4-7 highlight the trade-offs between model size, training time, inference speed, and segmentation accuracy. Before class specific insights, a general overview is presented. Tiny models (Table 4) demonstrate the lowest computational overhead, with training times per epoch under 7 seconds and inference times per sample below 2 seconds across all hyperparameter sets. These models provide a fast and lightweight solution while maintaining competitive accuracy.

Table 4. Results for model Tiny.

Class	Hyper-parameters	Training time per epoch (Sec.s)	Inference time per sample (Sec.s)	Training loss	Validation loss	Training accuracy	Validation Accuracy
Airplane	**Set-0**	4.1349	1.7620	2.3877	2.4146	0.8780	0.8698
Airplane	**Set-1**	2.3104	1.7696	8.6765	8.6967	0.8840	0.8740*
Airplane	**Set-2**	2.4414	1.8607	34.0441	34.0239	0.8712	0.8708
Car	**Set-0**	6.8611	1.8447	2.2676	2.3316	0.9157	0.8872
Car	**Set-1**	3.1754	1.6191	8.5696	8.5645	0.9204	0.9153*
Car	**Set-2**	3.7116	1.8042	33.9594	33.7699	0.9095	0.9091
Motorbike	**Set-0**	2.0226	1.8694	2.4935	2.6193	0.8071	0.7603*
Motorbike	**Set-1**	1.2687	1.9001	8.5986	8.7146	0.8039	0.7519
Motorbike	**Set-2**	0.9450	1.9736	33.1477	29.3361	0.7664	0.6769
Average		**2.9857**	**1.8226**	**14.9050**	**14.4968**	**0.8618**	**0.8350**

Medium models (Table 5) increase the parameter count significantly, leading to longer training times (up to 14 s/epoch) and inference times exceeding 2 seconds. In addition to the increased computational cost, the Medium model achieves worse validation accuracy in Set-1 for Airplane (87.40%→86.31%), Car (91.53%→89.14%), and Motorbike (75.19%→71.38%) compared to the Tiny model.

Table 5. Results for model Medium.

Class	Hyper-parameters	Training time per epoch (Sec.s)	Inference time per sample (Sec.s)	Training loss	Validation loss	Training accuracy	Validation Accuracy
Airplane	**Set-0**	1.8816	2.2174	8.5226	8.4514	0.8385	0.8457
Airplane	**Set-1**	3.5018	2.0405	32.9312	32.8586	0.8593	0.8631*
Airplane	**Set-2**	8.5038	2.0583	132.2373	131.8697	0.8130	0.8191
Car	**Set-0**	9.1773	3.1154	15.1606	19.3051	0.8218	0.8126
Car	**Set-1**	8.2329	2.2342	32.8249	34,8191	0.8971	0.8914*
Car	**Set-2**	14.1265	2.1972	131.6679	131.4640	0.8797	0.8840
Motorbike	**Set-0**	3.1759	2.9597	8.7785	23.2788	0.7758	0.6799
Motorbike	**Set-1**	1.6189	2.0418	37.5718	107.0709	0.7741	0.7138*
Motorbike	**Set-2**	1.6044	2.1266	221.6887	9.722.6299	0.7405	0.7093
Average		**6.3708**	**2.3323**	**69.0426**	**1.134.6386**	**0.8222**	**0.8021**

Large models (Table 6) introduce a major computational burden, requiring 12 to 33 s/epoch of training for the large sets of Airplane and Car classes. Validation accuracy drops yet again for most cases, except Set-2 of Airplane. In short, the increased network size and parameter count bring diminishing returns across most of the experiments. As for the Motorbike class, validation accuracy remains inconsistent and sometimes higher than for the Tiny model. This inconsistent behavior is best observed in terms of validation loss.

Table 6. Results for model Large.

Class	Hyper-parameters	Training time per epoch (Sec.s)	Inference time per sample (Sec.s)	Training loss	Validation loss	Training accuracy	Validation Accuracy
Airplane	**Set-0**	12.5527	1.9552	16.6900	16.6852	0.8040	0.8027
Airplane	**Set-1**	13.2459	2.0164	70.2028	73.5573	0.8146	0.8151
Airplane	**Set-2**	19.8034	0.1301	337.5113	322.4445	0.8311	0.8377*
Car	**Set-0**	18.8614	2.2012	16.6593	18.9986	0.8238	0.8058
Car	**Set-1**	21.1859	2.1274	65.7322	70.3808	0.8334	0.8385*
Car	**Set-2**	33.2247	2.3344	275.3770	287.1585	0.8240	0.8240
Motorbike	**Set-0**	4.8082	2.0731	62.1769	9503.0341	0.7364	0.6749*
Motorbike	**Set-1**	2.3329	2.0818	217.9921	675.8121	0.7580	0.6280
Motorbike	**Set-2**	2.7758	3.1757	1080.8776	170735.4062	0.7384	0.6785*
Average		**14.3101**	**2.0106**	**238.1355**	**20189.2753**	**0.7960**	**0.7672**

4.1. Segmentation of Airplane

Hyperparameter Set-0 indicates a small point cloud with a high learning rate, Set-1 moderate point cloud with reduced learning rate, and Set-2 largest point cloud with the lowest learning rate. Set-0 has the shortest training time across all model sizes as expected. However, higher training and validation loss values indicate potential convergence issues. Set-1 achieves the best balance between training time and segmentation accuracy. The medium model in Set-1 reaches 86.31% validation accuracy, making it a strong candidate for practical deployment. Set-2 shows stability with lower training loss but at a significantly higher computational cost. The large model in Set-2 reaches 83.77% accuracy but suffers from extreme inference latency (337.51s per sample), making it impractical for real-time scenarios.

The Large Models show a notable increase in computational time and memory usage but do not achieve the highest accuracy when compared to the Tiny and Medium Models. In Set-1, the Large Model has a validation accuracy of 81.51%, which is lower than both the Tiny Model (87.40%) and the Medium Model (86.31%). This suggests that, despite the larger model capacity, it may not be as well-optimized for the task at hand, likely due to overfitting or the challenges of efficiently capturing the relevant features with a larger network.

Figure 4 shows the segmentation results on medium models under each parameter set. The qualitative results indicate that Set-1 achieves a well-balanced trade-off between segmentation accuracy and computational efficiency. While Set-0 exhibits faster training times, its segmentation outputs show slightly less refined boundaries, particularly in complex regions of airplane models. In contrast, Set-2, which uses the highest number of sampled points and training epochs, produces finer segmentation but at the cost of significantly increased training time and inference delay. Set-1 provides a middle ground, capturing sufficient local and global features while maintaining reasonable training and inference efficiency. These findings align with the quantitative results in Table 4, where Set-1 consistently achieves high validation accuracy with lower training loss compared to Set-0, without the excessive computational burden of Set-2.

The Tiny model with Set-1 hyper-parameters (512 sampled points, batch size of 16, 40 training epochs, and an initial learning rate of 1×10^{-3}) demonstrates a promising balance between computational efficiency and segmentation accuracy. The total training time for Set-1 is 1.54 minutes, which is only slightly higher than Set-0 (1.38 minutes) but significantly lower than Set-2 (2.44 minutes). This increase in training time is justified by the observed improvement in segmentation accuracy. The validation accuracy reaches 87.40%, surpassing both Set-0 (86.98%) and Set-2 (87.08%). The inference time per sample is 1.77 seconds, which is similar to Set-0 at 1.76s and faster than Set-2 at 1.86s. This suggests that Set-1 maintains efficient real-time performance while benefiting from improved model stability and accuracy. The choice of 512 points ensures that the model captures more geometric details than Set-0 with 256 points while avoiding the computational overhead of Set-2 with 1024 points.

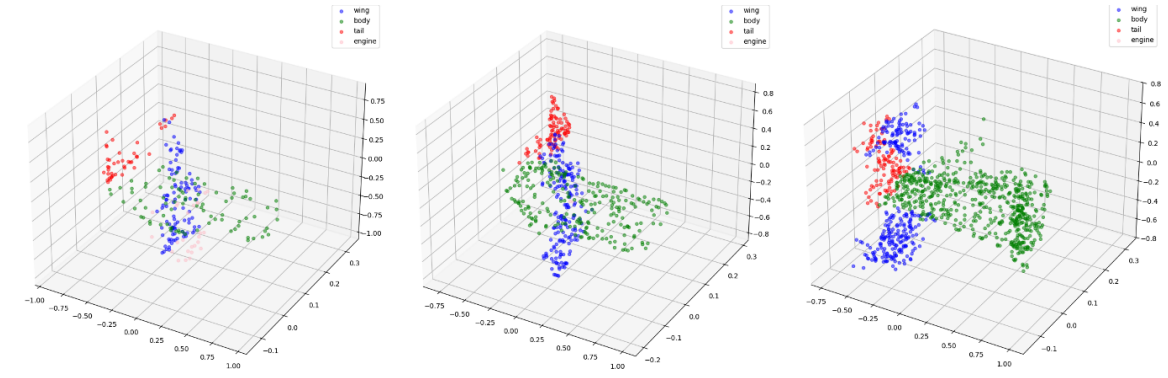

(a) (b) (c)

Figure 4. Medium model inference for airplane: a)Set-0 b)Set-1 c)Set-2.

4.2. Segmentation of Car

Training time per epoch is significantly higher with Set-2: 3.71s (Tiny) → 14.13s (Medium) → 33.22s (Large), making the Large model computationally expensive. Inference time per sample is stable in Set-1 and-2, however, it varies for Set-2, with the Large model performing inference the fastest (0.13s), possibly due to improved internal representations. The results for Set-1 portray better results in terms of validation accuracy. However, training and validation loss increase across models (8.56 – 8.56 for Tiny, 32.82 – 34.81 for Medium, 65.73 – 70.38 for Large), showing a higher complexity in optimization as model size increases. For Set-2 experiments, loss values skyrocket in the Medium and Large models (131.67 – 131.46 for Medium, 337.51 – 322.44 for Large), indicating overfitting and unstable training dynamics at this learning rate.

As seen in Table 5 and Figure 4, Set-1 achieves a well-balanced trade-off between segmentation accuracy and computational efficiency for the Car category. While Set-0 provides the shortest training time, it falls behind in accuracy. On the other hand, Set-2 produces detailed segmentation but comes with significantly increased training time and high training loss, especially in the Large model. Set-1 successfully captures both local and global features, making it the most practical choice.

Tiny model configurations struggle with overfitting and training stability, especially as batch size increases and the learning rate decreases in higher sets. Overall, the Tiny model's validation accuracy peaks in Set-1 (91.53%), indicating that a moderate batch size (16), increased training epochs (40), and lower learning rate (1×10^{-3}) provide the best generalization. Training and validation loss increase significantly from Set-0 (2.26 / 2.33) to Set-2 (33.96 / 33.77) on the Tiny model, suggesting that a higher learning rate (1×10^{-2}) in Set-0 helps maintain stable optimization. In terms of hyper-parameters sets, Set-1 strikes a balance, providing good validation accuracy with reasonable training efficiency. Set-0 offers fast performance but with limitations in terms of generalization for more complex models. Set-2 requires addressing the high training loss and the slow learning speed for the models.

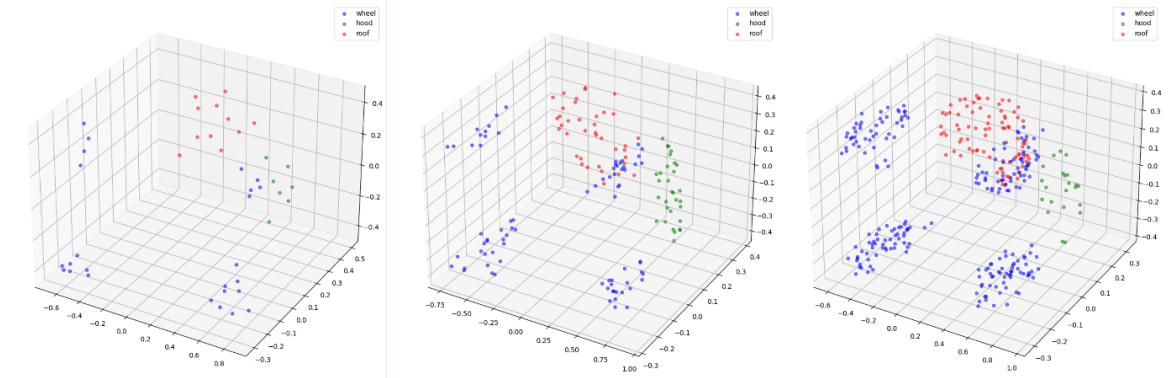

(a) (b) (c)

Figure 5. Medium model inference for car: a)Set-0 b)Set-1 c) Set-2.

4.3. Segmentation of Motorbike

The Tiny model in Set-0 exhibits a relatively decent training accuracy (80.71%), but the validation accuracy (76.03%) is notably lower, suggesting some overfitting. This indicates that while the model performs well on the training data, it struggles to generalize effectively to unseen data. The training loss (2.4935) and validation loss (2.6193) are also on the lower side, indicating that the model is not overly complex. The Medium model in Set-0 demonstrates training accuracy (77.58%) and validation accuracy (67.99%), which is lower than expected (based on the results of the other classes). The training loss (8.7785) and validation loss (23.2788) show that the model could benefit from better hyperparameter tuning, as it might not be training efficiently with this configuration.

The Tiny model in Set-1 shows a small drop in both training accuracy (80.39%) and validation accuracy (75.19%), which may be a result of the higher training loss (8.5986) and validation loss (8.7146). The performance deterioration indicates a potential issue with the larger batch size and smaller learning rate, as it might have caused the model to struggle with the small number of samples. The Medium model in Set-1 performs slightly better with training accuracy (77.41%) and the best validation accuracy (71.38%), which indicates that the model is slightly more generalizable compared to its Set-0 counterpart. Validation loss (107.0709) is significantly higher than Set-0, but the improvement in validation accuracy suggests that the model has improved its performance with the new hyperparameters, particularly the batch size and learning rate.

The segmentation results obtained from the Medium dataset in Figure 6 show that Set-0 produces less refined segmentation boundaries, particularly in complex car models. In contrast, Set-2 generates more detailed segmentation but comes at the cost of significantly increased training time and inference delay. These findings align with the quantitative results in Table 5, where Set-1 consistently achieves high validation accuracy with lower training loss compared to Set-0 while avoiding the excessive computational burden of Set-2.

The Large model with Set-0 parameters shows train accuracy (73.64%) and validation accuracy (67.49%), with significantly higher train and validation loss compared to smaller models. With Set-1, the Large model shows a noticeable drop in validation accuracy (62.80%) compared to Set-0, with train accuracy (75.80%) still decent. The training loss (217.9921) and validation loss (675.8121) increase substantially, suggesting that the model's larger capacity is not necessarily translating to better generalization for the Motorbike class. This insight is confirmed in Set-1 experiments indicating that this model struggles with overfitting and does not generalize well on the Motorbike class data.

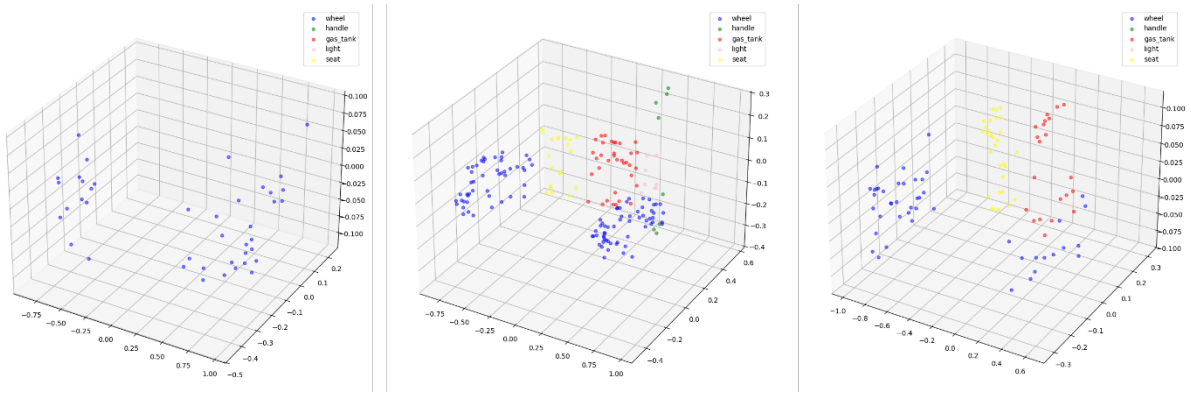

(a) (b) (c)

Figure 6. Medium model inference for motorbike: a)Set-0 b)Set-1 c)Set-2.

5. Discussion

Our findings demonstrated how architectural choices and hyper-parameter tuning impact segmentation accuracy, computational efficiency, and real-world usability. Choosing the appropriate model size and hyper-parameter configuration is crucial for practical applications. The Tiny Model with the Set-1 configuration, featuring a moderate batch size of 16, 512 sampled points, and an initial learning rate of 1×10^{-3}, provided the best balance between fast convergence, stable learning, and segmentation accuracy. Figure 7 summarizes the results in validation accuracy. The Tiny model across all the hyper-parameter sets achieves reasonably competitive performance, especially in the Car class where it attains the highest validation accuracy at Set-1 (91.53%).

However, the validation accuracy for Motorbike (around 75%) shows a significant drop when compared to the other classes. This may suggest that the model struggles more with the smaller dataset.

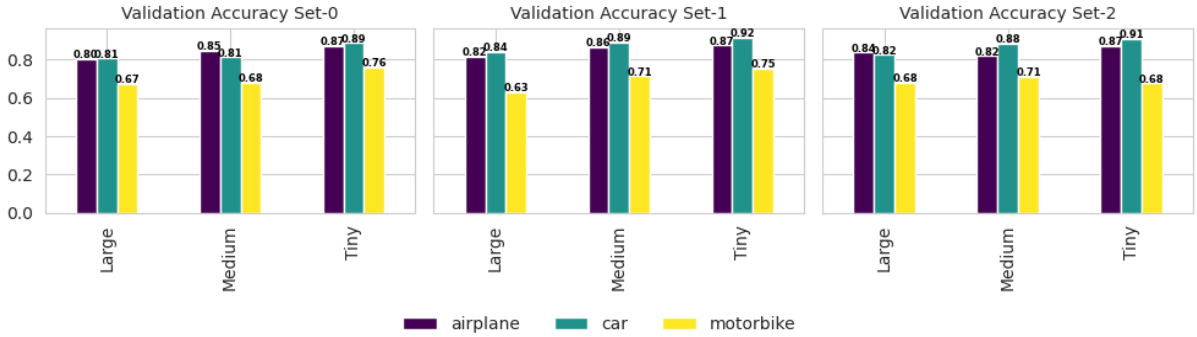

Figure 7. Validation accuracy across models and hyper-parameter sets.

The Airplane class and the Set-2 configuration of the Large Model, with larger sampled points (1024) and an extended training period (60 epochs), led to higher accuracy but at the expense of computational efficiency. However, it is computationally expensive, making it more practical for offline processing. For Car segmentation, the Tiny Model (Set-1) offers the best trade-off between accuracy and computational efficiency. Larger models introduce a higher computational burden without significant performance gains, making them less ideal for practical use. For the Motorbike class, with the smallest number of samples, Set-1 offers the best performance for both Medium and Large models, providing the most balanced trade-off between training time and validation accuracy. Set-2 needs careful adjustment to prevent overfitting and high loss, especially with Tiny and Medium models. Additionally, it is important to note that Tiny models may require further tuning, particularly in Set-2, to improve both training and validation accuracies. The observed trade-offs suggest that hyper-parameter selection should be tailored to the specific deployment constraints rather than simply optimizing for accuracy alone.

Our experimental results demonstrated that different model architectures exhibit distinct trade-offs between computational efficiency and segmentation accuracy. The Tiny model, with its shallower architecture, achieves competitive accuracy while maintaining low computational cost. This is primarily due to its ability to capture essential features efficiently without excessive parameter overhead. In our experiments, the Large model showed a higher risk of overfitting, particularly in the Motorbike class, where the dataset size was significantly smaller. This suggests that while deeper networks have greater capacity, they require careful regularization when handling limited data. Increasing the number of sampled points and batch size influences both convergence speed and generalization ability. The Set-1 configuration (512 sampled points, batch size of 16) provided the best balance, leading to stable learning dynamics and improved segmentation accuracy.

Future studies will explore the integration of semantic, instance, and panoptic segmentation into a unified model. This would enhance the adaptability of segmentation systems across diverse applications, particularly for autonomous perception tasks in autonomous vehicles, robotics, and geospatial analysis [7, 8]. Extending training datasets to include more diverse scenarios, such as adverse environmental conditions, varying object densities, and occlusions, will further improve model robustness [9, 19]. The ability to generalize across different real-world settings remains a key challenge in 3D vision research. Although this study briefly explored efficiency concerns, future research will focus on optimizing neural architectures to improve computational complexity without sacrificing segmentation accuracy. Approaches such as sparse convolutions, knowledge distillation, and quantization will be explored to enable faster and more efficient inference on edge devices [3, 7].

References

[1] Qi CR, Su H, Mo K, Guibas LJ. PointNet: Deep Learning on Point Sets for 3D Classification and Segmentation. Proc IEEE Conf Comput Vis Pattern Recognit (CVPR), 2017; Honolulu, HI, USA. 652-660.

[2] Qi CR, Su H, Yi L, Guibas LJ. PointNet++: Deep Hierarchical Feature Learning on Point Sets in a Metric Space. Adv Neural Inf Process Syst (NIPS), 2017; Long Beach, CA, USA. 30.

[3] Choy C, Gwak JY, Savarese S. 4D Spatio-Temporal ConvNets: Minkowski Convolutional Neural Networks. Proc IEEE/CVF Conf Comput Vis Pattern Recognit (CVPR), 2019; Long Beach, CA, USA. 3075-3084.

[4] Behley J, Garbade M, Milioto A, Quenzel J, Behnke S, Stachniss C, Gall J. SemanticKITTI: A Dataset for Semantic Scene Understanding of LiDAR Sequences. Proc IEEE/CVF Conf Comput Vis Pattern Recognit (CVPR), 2019; Long Beach, CA, USA. 9297-9307.
[5] Zhang Y, Zhou Z, David P, Yue X, Xi Z, Gong B, Foroosh H. PolarNet: An Improved Grid Representation for Online LiDAR Point Clouds Semantic Segmentation. Proc. IEEE/CVF Conf Comput Vis Pattern Recognit (CVPR), 2020; Virtual. 9601-9610.
[6] Cortinhal T, Tzelepis G, Aksoy EE. SalsaNext: Fast, Uncertainty-aware Semantic Segmentation of LiDAR Point Clouds for Autonomous Driving Int Symp Vis Comput., 2020; San Diego, CA, USA. 207-222.
[7] Tang H, Liu Z, Zhao S, Lin Y, Lin J, Wang H, Han S. Searching Efficient 3D Architectures with Sparse Point-Voxel Convolution Eur Conf Comput Vis (ECCV), 2020; Glasgow, UK. 685-702.
[8] Li S, Zhang C, He X. Shape-aware Semi-supervised 3D Semantic Segmentation for Medical Images. Med Image Comput Comput Assist Interv (MICCAI), 2020; Lima, Peru. 552–561.
[9] Wang Y, Sun Y, Liu Z, Sarma SE, Bronstein MM, Solomon JM. Dynamic Graph CNN for Learning on Point Clouds. ACM Trans Graph (TOG), 2019; 38 (5): 1-12.
[10] Graham B, Engelcke M, van der Maaten L. 3D Semantic Segmentation with Submanifold Sparse Convolutional Networks. Proc IEEE Conf Comput Vis Pattern Recognit (CVPR), 2018; Salt Lake City, UT, USA. 9224-9232.
[11] Thomas H, Qi CR, Deschaud JE, Marcotegui B, Goulette F, Guibas LJ. KPConv: Flexible and Deformable Convolution for Point Clouds. Proc. IEEE/CVF Int Conf Comput. Vis. (ICCV), 2019; Seoul, Korea (South). 6410-6419.
[12] Liu Z, Tang H, Lin Y, Han S. Point-Voxel CNN for Efficient 3D Deep Learning. Adv. Neural Inf. Process. Syst. (NeurIPS), 2019; Vancouver, Canada. 32.
[13] Heller N, Isensee F, Maier-Hein KH, Hou X, Xie C, Li F, Nan Y, Mu G, et al. The state of the art in kidney and kidney tumor segmentation in contrast-enhanced CT imaging: Results of the KiTS19 Challenge. Med Image Anal 2021; 67: 101821.
[14] Vinodkumar PK, Karabulut D, Avots E, Ozçınar C, Anbarjafari G. A Survey on Deep Learning Based Segmentation, Detection and Classification for 3D Point Clouds. Entropy, 2023; 25 (4): 635.
[15] He Y, Yu H, Liu X, Yang Z, Sun W, Anwar S, Mian A. Deep Learning Based 3D Segmentation: A Survey Inf Fusion 2025; 115: 102722.
[16] Chang AX, Funkhouser T, Guibas L, Hanrahan P, Huang Q, Li Z, Savarese S, Savva M, Song S, et al. ShapeNet: An Information-Rich 3D Model Repository. arXiv. 2015; 1512.03012.
[17] Xiang Y, Mottaghi R., Savarese S. Beyond PASCAL: A Benchmark for 3D Object Detection in the Wild. Proc. IEEE Winter Conf. Appl. Comput. Vis. (WACV), 2014; Steamboat Springs, CO, USA. 75-82.
[18] Jaderberg M, Simonyan K, Zisserman A, Kavukcuoglu K. Spatial Transformer Networks. Adv Neural Inf Process Syst (NIPS), 2015; Montreal, Canada. 29.
[19] Zhao H, Jiang L, Jia J, Torr P, Koltun V. Point Transformer. Proc. IEEE/CVF Int Conf Comput Vis (ICCV), 2021; Montreal, Canada. 16239-16248.

Turkish Journal of Science & Technology
20(1), 339-354, 2025

Research Paper
https://doi.org/10.55525/tjst.1623887

Thinner Induced Multiple Organ Toxicities in Wistar Rats: Ameliorative Role of Vitamin E (Alpha-Tocopherol)

Rachael Oluwabusayo FOLARIN[1], Jamiu Oyewole OMIRINDE[2*], Taidinda Tashara GILBERT[3], Adam Moyosore AFODUN[4]

[1]Department of Biomedical Laboratory Science, University of Ibadan, Ibadan, Nigeria.
[*2]Department of Veterinary Anatomy, University of Jos, Jos, Nigeria.
[3]Department of Veterinary Anatomy, University of Ibadan, Ibadan, Nigeria.
[4]Department of Anatomy and Cell Biology, Faculty of Health Sciences, Busitema University, Uganda.
[1]oluwabusayoracheal@gmail.com,[*2]omirindejamiu66@gmail.com,[3]taigiltas@gmail.com, [4]afodunadam@yahoo.com

(Geliş/Received: 21/01/2025; Kabul/Accepted: 09/03/2025)

Abstract: Thinner, a common industrial solvent, is a popular choice for recreational self-intoxication, leading to potential serious health consequences. This study delves into the acute toxicity of thinner, focusing on its impact on various organ systems and the potential ameliorative ability of Vitamin E as an antioxidant. Four experimental groups of Wistar rats (n-12) were established as follow: control, Vitamin E only, thinner only and thinner + Vitamin E. The rats were subjected to a 3week inhalation protocol, and various parameters such as body weight, biochemical markers (aspartate aminotransferase (AST), alanine aminotransferase (ALT), alkaline phosphatase (ALP), total bilirubin (TBIL), blood urea nitrogen (BUN) and creatinine levels), oxidative stress markers (malondialdehyde, nitrites, glutathione, catalase and superoxide dismutase), and histopathological examinations were assessed using standard procedures. The results revealed a significant reduction in body weight in the thinner-exposed group. However, the group exposed to both thinner and Vitamin E exhibited marked increase in body weight. Biochemical parameters (AST, ALT, ALP, TBIL, BUN and creatinine) were significantly elevated ($p<0.05$) in thinner only exposed rats. Conversely, the parameters were markedly reduced in the rats co-administered with thinner and vitamin E. The different tissue oxidative stress marker profiles were significantly altered in the thinner only treated rats. Interestingly, vitamin E supplementation significantly reversed the alterations to the markers. Thinner exposure precipitated severe histomorphological disruptions in the liver, kidneys, lungs and spleen. Remarkably, vitamin E co-administration with thinner markedly ameliorate the structural damage to the organs. This study emphasizes the potential therapeutic role of Vitamin E in mitigating the adverse effects of thinner-induced toxicity, suggesting its importance as an antioxidant strategy in managing solvent abuse-related health complications.

Key words: Thinner, toxicity, vitamin E, antioxidant, histopathology.

Wistar Sıçanlarında Tinerin Neden Olduğu Çoklu Organ Toksisiteleri: E Vitamininin (Alfa-Tokoferol) İyileştirici Rolü

Öz: Yaygın bir endüstriyel çözücü olan tiner, keyfi amaçlı kendi kendine zehirlenme için yaygın bir seçimdir ve potansiyel ciddi sağlık sonuçlarına yol açmaktadır. Bu çalışma, tinerin akut toksisitesini, çeşitli organ sistemleri üzerindeki etkisine ve bir antioksidan olarak E Vitamininin potansiyel iyileştirici yeteneğine odaklanarak incelemektedir. Wistar sıçanlardan oluşan dört deney grubu (n-12) şu şekilde oluşturulmuştur: kontrol, sadece E Vitamini, sadece tiner ve tiner + E Vitamini. Sıçanlar 3 haftalık bir inhalasyon protokolüne tabi tutulmuş ve vücut ağırlığı, biyokimyasal belirteçler (aspartat aminotransferaz (AST), alanin aminotransferaz (ALT), alkalin fosfataz (ALP), total bilirubin (TBIL) gibi çeşitli parametreler ölçülmüştür, kan üre azotu (BUN) ve kreatinin seviyeleri), oksidatif stres belirteçleri (malondialdehit, nitritler, glutatyon, katalaz ve süperoksit dismutaz) ve histopatolojik incelemeler standart prosedürler kullanılarak değerlendirilmiştir. Sonuçlar, tiner maruz kalan grupta vücut ağırlığında önemli bir azalma olduğunu ortaya koymuştur. Bununla birlikte, hem tiner hem de E Vitaminine maruz kalan grupta vücut ağırlığında belirgin bir artış görülmüştür. Biyokimyasal parametreler (AST, ALT, ALP, TBIL, BUN ve kreatinin) sadece tinere maruz kalan sıçanlarda önemli ölçüde yükselmiştir ($p<0,05$). Tersine, tiner ve E vitamini birlikte uygulanan sıçanlarda parametreler belirgin şekilde azalmıştır. Farklı doku oksidatif stres belirteç profilleri sadece tinerle tedavi edilen sıçanlarda önemli ölçüde değişmiştir. İlginç bir şekilde, E vitamini takviyesi belirteçlerdeki değişiklikleri önemli ölçüde tersine çevirmiştir. Tiner maruziyeti karaciğer, böbrekler, akciğerler ve dalakta ciddi histomorfolojik bozulmalara yol açmıştır. Dikkat çekici bir şekilde, E vitamininin tiner ile birlikte uygulanması organlardaki yapısal hasarı belirgin bir şekilde iyileştirmiştir. Bu çalışma, tiner kaynaklı toksisitenin olumsuz etkilerini hafifletmede E Vitamininin potansiyel terapötik rolünü vurgulamakta ve solvent kullanımına bağlı sağlık komplikasyonlarının yönetiminde antioksidan bir strateji olarak önemini ortaya koymaktadır.

Anahtar kelimeler: İnceltici, toksisite, E vitamini, antioksidan, histopatoloji.

[*]Corresponding author: omirindejamiu66@gmail.com. ORCID Number of authors: [1]0000-0002-8790-2343, [*2]0000--0002-2952-9376, [3]0001-7396-2591, [4]0000-0002-9262-1175

1. Introduction

Intentional abuse of solvent is a popular form of inhalant abuse common among children and adolescent age [1, 2]. This involves sniffing (nasally inhaled), huffing (orally inhaled) or bagging of thinner solvent for recreational self-intoxication [3]. It is a habit found most appealing among adolescents due to easy accessibility, inexpensiveness and legal acceptability in some part of the world [4, 5]. Thinner is an industrial solvent that is composed of volatile solvents such as toluene, acetone, methanol, benzene, hexane and other substances with the toluene constituting the greatest proportion [6]. A study using a gas chromatography has confirmed toluene, as the major components found in commercial thinner samples, making up to 60-70% of the solution [7].

Evidences have shown that prolonged or regular use or over-exposure to thinner can affect the body and induce serious toxicity resulting in organ system dysfunction and sudden death [7]. Since thinner solvent (toluene and benzene) is volatile; hence, it may be sniffed (nasally inhaled), huffed (orally inhaled) or bagged by abusers. Following inhalation, a potential user reported a pleasurable or euphoric effects, which may be intoxicating [6]. This effect which occurs rapidly and disappears fairly quickly create a sober attitude in individual abusers that makes early detection more difficult [8], thus creating the possibility of continuous abuse which may persist into adulthood and subsequently, may lead to medical complications. Consistent inhalation of thinner can serve as a gateway to the abuse of more addictive substances [9].

Toluene, the major component of thinner is a well-known organo-toxins, mostly implicated in oxidative damage of several body organs including the brain, lung, liver, kidney, testes and ovaries [7, 10]. In recent time, most of the research on inhalant abused is primarily focused on central nervous system, however, solvent abuse also exerts effects on other organ systems and cellular processes. Organ defects associated with prolonged or regular use or over-exposure to toluene-based solvent includes bone-marrow depression [11], cardiac dysrhythmias, liver and kidney disorders. Gastrointestinal effects include nausea, vomiting, diarrhea, abdominal cramps and loss of appetite [12]. Some of the systemic pathologies recorded from examination of individuals constantly exposed to toluene include renal tubular acidosis [13], renal calculi, haematuria, hypovitaminosis, hypertension and glomerulonephritis [14]. Myocardial infarctions have been attributed to inhalation of toluene-based solvent, with the production of reactive oxygen species (ROS) and increased oxidative stress [15]. Hepatotoxicity with toluene-based solvents results to ascites, jaundice, hepatomegaly and liver failure [16]. Other clinical symptoms associated with thinner exposure includes acute respiratory failure, cardiac arrhythmias, heart failure, choking, kidney damage, weight loss, hearing loss, skin rashes and sudden death [12, 17]. Leukemia, lymphoma, multiple myeloma and aplastic anaemia are also haematological malignancy associated with chronic inhalant abuse [18].

Although the mechanism underlying thinner toxicity has not been clearly elucidated [19]. Some evidences have implicated oxidative stress as the main etiology of thinner intoxication [7, 10]. Toluene being the principal component of thinner, also induce oxidative stress effect [15]. Some of the proposed mechanisms by which thinner induced cellular damages in biological tissue includes production of toxic end product of oxidative metabolism (toluene and benzene) which generates free radicals [20], cytosolic NADH [21] and cytotoxic ROS [22], which subsequently disrupt cellular redox system. The other mechanisms include upregulation of agents of inflammation (TNF-α, NF-κB) and oxidative stress markers (NO) produced in the organ tissue in response to thinner induced toxicity. Cellular oxidative damages linked with thinner toxicity are peroxidation of macro molecules, reduction of antioxidant enzymes and upregulation of inflammatory mediators [23, 24]. A recent study found increased levels of thiobarbituric acid reactive substances (TBARS), glutathione reductase (GR), glutathione disulfide (GSSG) and superoxide dismutase (SOD) in various rat organs after chronic toluene inhalation [25]. Rats exposed to toluene also exhibited elevated lipid peroxidation products and evidence of oxidative damage to the DNA [26].

Since the induction of oxidative stress has been proposed as the fundamental mechanism of toxic substances [27], potent antioxidants can antagonize toxic effect elicited by free radicals generated by toxic chemicals in the body [7]. Vitamin E (Alpha-tocopherol) is a fat-soluble compound with distinctive antioxidant activities [28, 29]. It stops the production of reactive oxygen species (ROS) formed during oxidative processes and thus delays oxidative damage in the tissue [30]. Vitamin E exists in eight chemical forms: α-, β-, γ-, and δ-tocopherols, along with their corresponding tocotrienols [31]. Among these, α-tocopherol is the most biologically active form, playing a crucial role in neutralizing reactive oxygen species (ROS). It achieves this by donating phenolic hydrogen to unstable lipid radicals (such as peroxyl radicals and singlet oxygen), thereby inhibiting the lipid peroxidation chain reaction. This process results in the formation of a relatively stable tocopheroxyl radical, which does not readily propagate further oxidative damage within the cell [32, 33, 34]. The tocopheroxyl radical can be recycled back to its active form through interactions with other antioxidants, including Vitamin C (ascorbic acid) and glutathione (GSH) [35, 36]. Additionally, Vitamin E enhances cellular antioxidant defense by upregulating superoxide dismutase (SOD) [37], which converts superoxide radicals ($O_2^{\bullet-}$) into hydrogen peroxide (H_2O_2), and by supporting glutathione peroxidase (GPx) in detoxifying hydrogen peroxide and lipid peroxides [38].

The ameliorative effect of vitamin E against chemical toxicity has been explored in several epidemiological and clinical studies [39]. Cellular damage of toluene via the formation of ROS was effectively ameliorated with the use of vitamin E [40]. Therefore, antioxidant therapy may be an important strategy for managing thinner-induced toxicity. Despite the plethora of works on the influence of thinner on central nervous system disruption [7, 41-42], there is still scanty information on the high possibility of thinner abuse impacting other organs. Therefore, this study was designed to extensively evaluate thinner-induced multiple organ damage in Wistar rats and the ameliorative potential of vitamin E.

2. Materials and Methods Chemicals

ABRO # 11 nitrocellulose Thinner (Part. No. #11-4-5L) (was obtained from ABRO Industries, International. (Court South Bend, USA), while all other reagents, of analytical grade, were sourced from the British Drug Houses (Poole, Dorset, UK).

Animal Protocol and Ethical Considerations

A total of 48 juvenile male Wistar rats (100g) were acquired and bred in the Central Animal House at the College of Medicine, University of Ibadan, Ibadan, Nigeria. The rats were housed under standardized lighting conditions with food and tap water available ad libitum. All procedures were conducted under the Institutional Animal Care and Use Committee (IACUC) protocol of the Institute of Health, United States of America. Every effort was made to minimize animal suffering, ensuring the study met ethical standards.

Experimental Design

The study design is as follows:

Group 1 (Control): Rats were unexposed to thinner fumes via inhalation throughout the treatment
Group 2 (Vitamin E only): Rats were orally administered with vitamin E 500mg/kg body weight 72 hourly for 3 weeks after being acclimatized for 3 weeks.
Group 3 (Thinner): Rats were exposed to thinner fumes via inhalation at 3000ppm, 1 hour per day for 3 weeks following a 3-week acclimatization period.
Group 4 (Thinner + Vitamin E): Rats were exposed to thinner fumes via inhalation at 3000ppm, 1 hour per day for 3 weeks and orally administered with 500mg/kg body weight of Vit. E 72 hourly in the same period.

Inhalation Protocol

The inhalant used in this study was paint thinner, commonly sold in cans and typically used to thin oil-based paints and also to clean excess paint from work surfaces or application tools. The experimental animals were divided into four groups (n=12 per group): Control, Vitamin E only, Thinner, and Thinner + Vitamin E. The amount of inhalant used was modified based on a preliminary study by Baydas et al. [43] and Fifel et al. [44]. The conversion factor used was (1 µl≈1.5 ppm). Specifically, 1.5-2.0ml of liquid thinner was applied to a filter paper placed on a glass Petri dish, which was covered with a wire mesh and positioned on the floor of the inhalation chamber, achieving an estimated thinner concentration of 3000 ppm. To examine the effects of acute thinner exposure, Thinner, and Thinner + Vitamin E groups rats were exposed to 3000 ppm thinner inhalation (1 h/day) between 1700 and 1800 h [43], for 21 days in the whole inhalation chamber. The exposure to thinner was performed in whole-body inhalation as described by Fifel et al., [44], while the control and Vitamin E-only groups had no thinner exposure. The potential mitigating effects of Vitamin E following 21 days of thinner exposure were tested in the Thinner + Vitamin E group, with oral administration of 500 mg/kg body weight of Vitamin E every 72 hours for 21 days.

Body Weight Assessment

Each of the animals were weighed at the commencement of the experiments, during the time of experiment, body weight of the animals was measured two times in a week for all groups using a standard electronic weighing balance. The data obtained was documented for further analysis such as relative organ and body weight.

Biochemical Assays.

Blood samples were collected into lithium heparin bottles and centrifuged at 3500 rpm to obtain plasma, which was then stored at -20ºC until analysis. Biochemical values were measured using an automatic chemistry analyzer, Cobas® Integra 400 plus (Roche Diagnostics Ltd., Switzerland). The parameters assayed included serum

creatinine, blood urea nitrogen, alkaline phosphatase (ALP), alanine transaminase (ALT), aspartate transaminase (AST), and total bilirubin (TBIL).

Antioxidant Assay

Following treatment, rats from each group were sacrificed by rapid decapitation on ice. Organs (liver, kidney, lungs, and spleen) were removed using the method described by Folarin et al. [35 45]. The tissues were homogenized in eight volumes of 50 mM phosphate buffer, and the homogenate was centrifuged at 10,000×g for 15 minutes at 4 °C. The supernatant (post-mitochondrial fraction) was collected and stored at −20 °C for biochemical analysis. Oxidative stress in organ homogenates was assessed by measuring malondialdehyde (MDA) levels. Antioxidant enzyme activities were evaluated by measuring superoxide dismutase (SOD), glutathione peroxidase (GPx), reduced glutathione (GSH), and glutathione transferase (GST) using commercially available kits from Northwest Life Sciences Specialties, Washington, USA. The activity of catalase (CAT) was determined using kits from Oxford Biomedical Research, Michigan, USA.

Histopathological Preparations of the Tissues

Immediately after sacrifice, the liver, kidney, lungs, and spleen were excised and fixed in 10% buffered formalin. The tissues underwent conventional processing techniques, including dehydration, clearing, and infiltration, before being embedded in paraffin wax. Sections of 5 μm were cut using a Leica RM 2115 rotary microtome. These sections were stained with hematoxylin and eosin for light microscopy. Photomicrographs were captured at ×100 magnification using a spinning disc laser confocal system (Nikon Eclipse 80i) with Nikon Microphotography system (DS-Fi1, NIS-Elements BR 3.2 software). Histopathological examination was conducted to identify the presence of lesions in the organs.

Statistical Analysis

Data on body weight, relative organ weight, biochemical, and antioxidant analyses were analyzed using one-way analysis of variance (ANOVA), with post hoc comparisons made using the Tukey test. Results are presented as means ± standard error of the mean, and significance was determined at $p < 0.05$.

3. Results Examination of Body Weight

The study involved an examination of the body weights of animals over the course of exposure to the toxicant (thinner). Notably, there was a progressive increased bodyweight in rats exposed to thinner only from week 1 to 4. However, there was a marked decline in bodyweight from week 4 downwards when compared to the control and Vitamin E (Figure 1). Conversely, rats exposed to thinner and Vitamin E displayed a noticeable increase in body weights from week 1 – 4 then followed by a decrease between week 4-5 and a steady progressive increase from week 5 to 6.

Biochemical Examination

The results on biochemical assays are presented in Tables 1 & 2. The liver function marker [aspartate aminotransferase (AST), alanine aminotransferase (ALT), alkaline phosphatase (ALP) and total bilirubin (TBIL)] levels were significantly higher in the rats exposed to thinner only compared to the control. However, co-administration of vitamin E with thinner markedly reduced the serum level of AST, ALT, ALP and TBIL when compared to the group exposed to acute thinner only (Table 1). Regarding the renal function markers, rats exposed to acute thinner showed significantly higher creatinine and blood urea nitrogen when compared to the control. Similarly, the level of the renal markers was significantly reduced in rats treated with co-administration of thinner +Vit E compared to thinner only (Table 2).

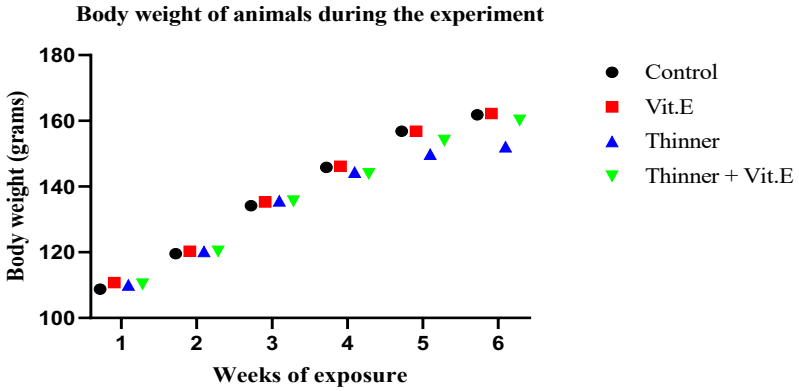

Figure 1. Profile of body weight of rats during the course of the study. There was reduction in body weights during the period of exposure for toxicity group when compared with the control. However, Toxicity+ Vit. E group showed increase in weight during recovery period with treatment with Vit.E when compared with the Toxicity Group.

Table 1. Effect of acute thinner inhalation (500ppm) on liver function markers in male Wistar rats.

Treatments	AST (U/L)	ALT (U/L)	ALP (U/L)	TBIL (µmol/L)
Control	11.2 ± 0.58	12.2 ± 0.37	48.4 ± 1.27	0.48 ± 0.06
Thinner	28.0 ± 0.71 [a]	31.0 ± 0.71 [a]	77.6 ± 1.81 [a]	1.44 ± 0.12 [a]
Thinner + Vit. E	17.2 ± 0.86[d]	23.6 ± 0.51 [d]	52.2 ± 0.86 [d]	0.88 ± 0.06[c]
Vit. E	8.6 ± 0.51	9.6 ± 0.51	42.6 ± 1.08	0.62 ± 0.06

AST: aspartate aminotransferase; ALT: alanine aminotransferase; ALP: alkaline phosphatase; TBIL: total bilirubin; Values with different superscripts are significantly different; *p*-values ([a]p<0.001: Thinner compared with normal control); ([b]p<0.05, [c]p<0.01, and [d]p<0.001: Thinner compared with Thinner +Vit. E); Vit.E vs Control: not significantly different (ns).

Table 2. Serum creatinine and Blood Urea Nitrogen levels after acute thinner inhalation (500ppm) in male Wistar rats

Treatments	CR (µmol/L)	BUN (mg/dL)
Control	0.58 ± 0.004	36.20 ± 1.36
Thinner	2.58 ± 0.007 [a]	101.4.4 ± 1.6 [a]
Thinner + Vit.E	1.4 ± 0.007[d]	62.60 ± 2.79 [d]
Vit.E	0.62 ± 0.06	42.6 ± 0.93

CR: Creatinine; BUN: Blood Urea Nitrogen. Values with different superscripts are significantly different; *p*-values: ([a] p<0.0001: Thinner compared with normal control); ([b]p<0.05, [c]p<0.01, and [d]p<0.001: Thinner+ Vit. E compared with Thinner); [Vit.E vs Control: not significantly different (ns)].

Oxidative Stress Marker Profiles in the Liver, Lungs, Kidneys, Spleens and Testes of Rats Exposed to Thinner

There was a marked increase in hepatic MDA level of thinner only exposed rats compared to the control and Vit. E groups (Figure 2). However, the MDA level was significantly reduced in thinner + Vit E group when compared to thinner only group. With the exception of the non-significant difference (p>0.05) in the hepatic nitrites levels across the different treatment groups, the levels of the hepatic endogenous antioxidant (GSH, SOD, GST and CAT) enzymes were significantly decreased (p<0.05) in the thinner only treated rats when compared to the control. On the other hand, co-administration of thinner and Vit E elicited significantly elevated (p<0.05) level when compared to thinner only (Figure 2).

The trend in the changes in the oxidative stress markers observed in other organs (lungs, kidneys, spleen and testes) seemed to be similar to the profile recorded for liver (Figures 3, 4, 5 and 6). The MDA and nitrite levels in the lung, renal, splenic and testicular tissues were significantly elevated ($p<0.05$) in the thinner only treated rats when compared to the control and Vit E. Interestingly, the MDA and nitrite profiles were significantly reduced ($p<0.05$) in thinner + Vit E group relative to thinner only. With respect to the endogenous enzymes (GSH, SOD, GST and CAT) in the four tissues, the thinner only treated rats displayed markedly reduced levels when compared to the control. However, the endogenous antioxidant levels were remarkably elevated in rats co-administered with thinner and Vit E when compared to thinner only.

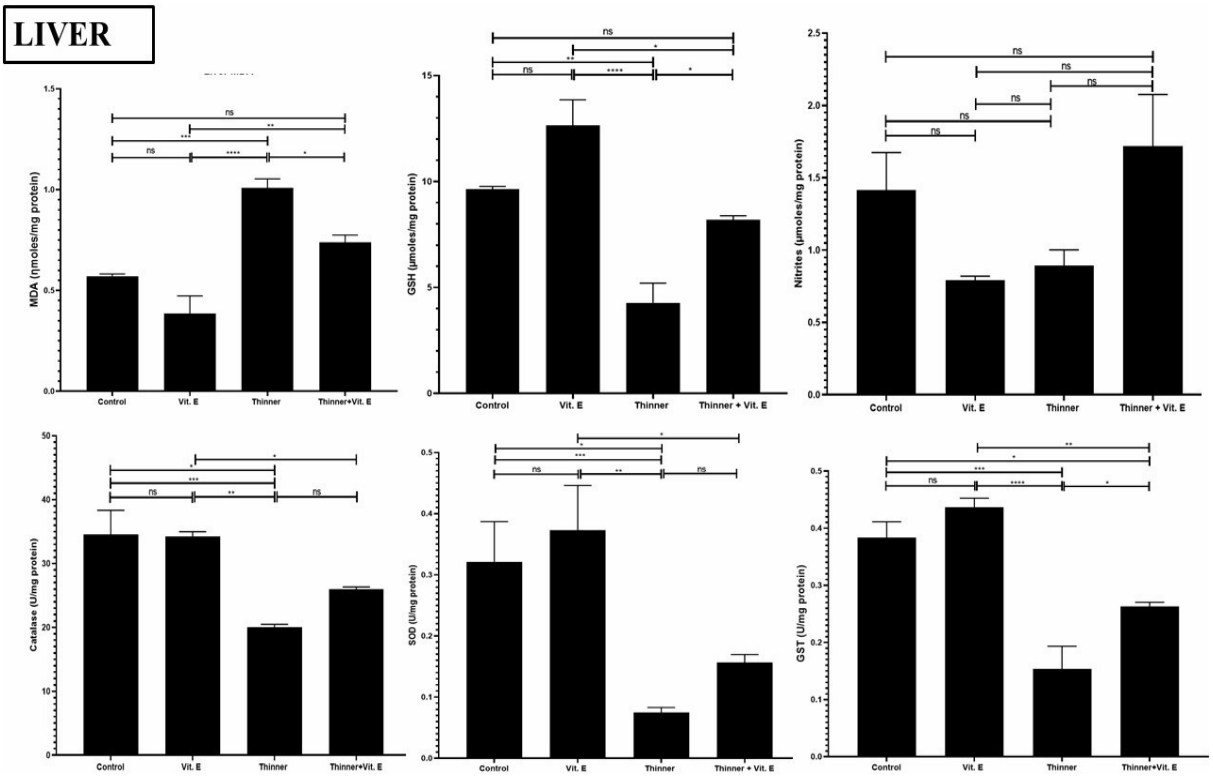

Figure 2. Changes in the oxidative stress markers profile in the liver of rats exposed to acute thinner inhalation (500ppm). Bars with different asterisks are significantly different; *p*-values ($^{*}p<0.05$, $^{**}p<0.01$, $^{***}p<0.001$, $^{****}p<0.001$ & ns (not significantly different) were established between the experimental groups.

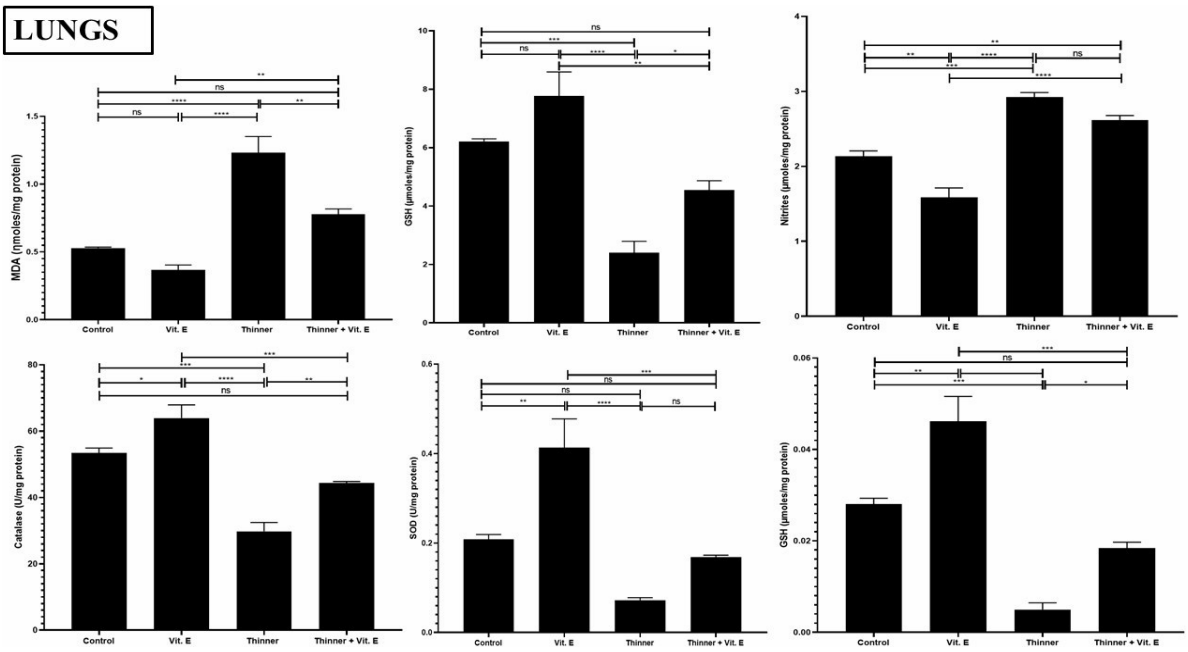

Figure 3. Changes in the oxidative stress markers profile in the lungs of rats exposed to acute thinner inhalation (500ppm). Bars with different asterisks are significantly different; *p*-values ($^{*}p<0.05$, $^{**}p<0.01$, $^{***}p<0.001$, $^{****}p<0.001$ & ns (not significantly different) were established between the experimental groups.

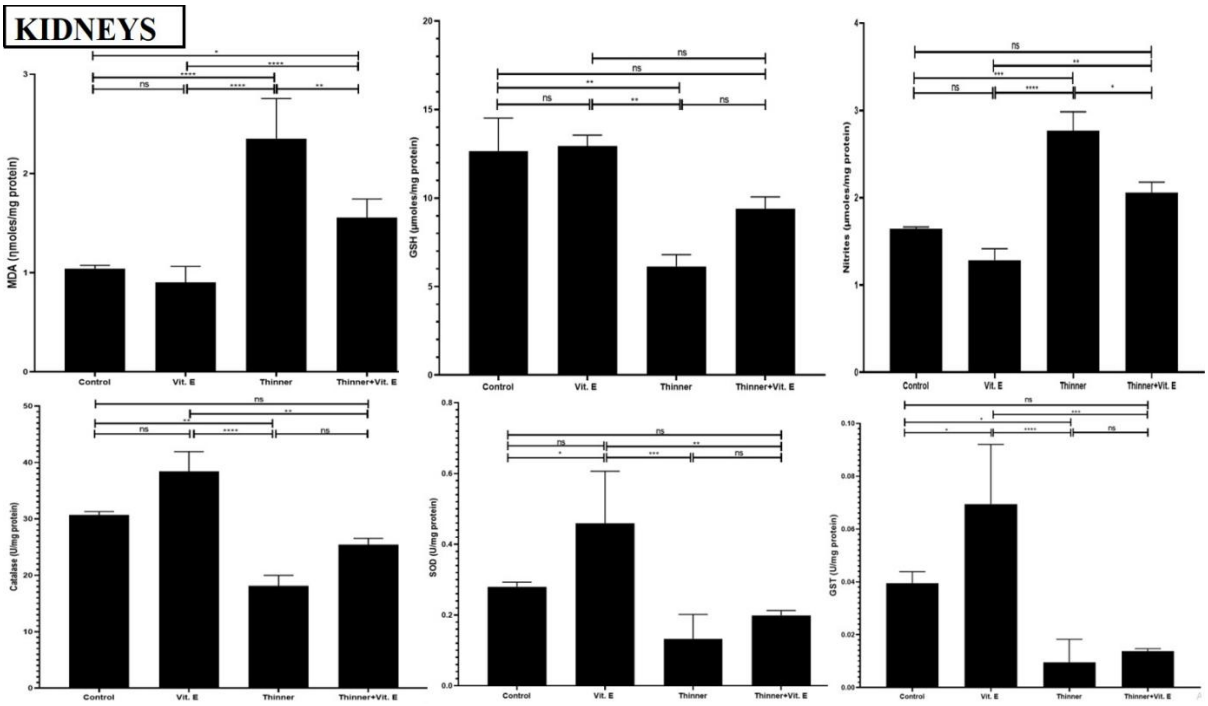

Figure 4. Changes in the oxidative stress markers profile in the kidneys of rats exposed to acute thinner inhalation (500ppm). Bars with different asterisks are significantly different; *p*-values ($^{*}p<0.05$, $^{**}p<0.01$, $^{***}p<0.001$, $^{****}p<0.001$ & ns (not significantly different) were established between the experimental groups.

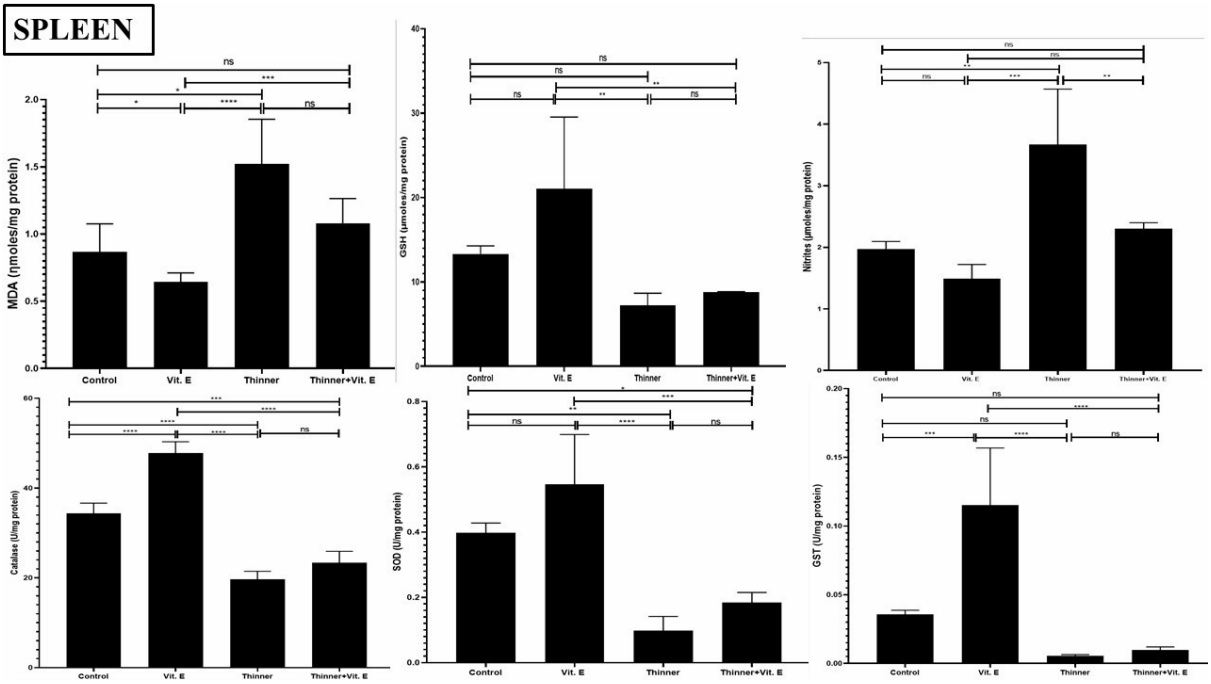

Figure 5. Changes in the oxidative stress markers profile in the spleen of rats exposed to acute thinner inhalation (500ppm). Bars with different asterisks are significantly different; *p*-values ($^{*}p<0.05$, $^{**}p<0.01$, $^{***}p<0.001$, $^{****}p<0.001$ & ns (not significantly different) were established between the experimental groups.

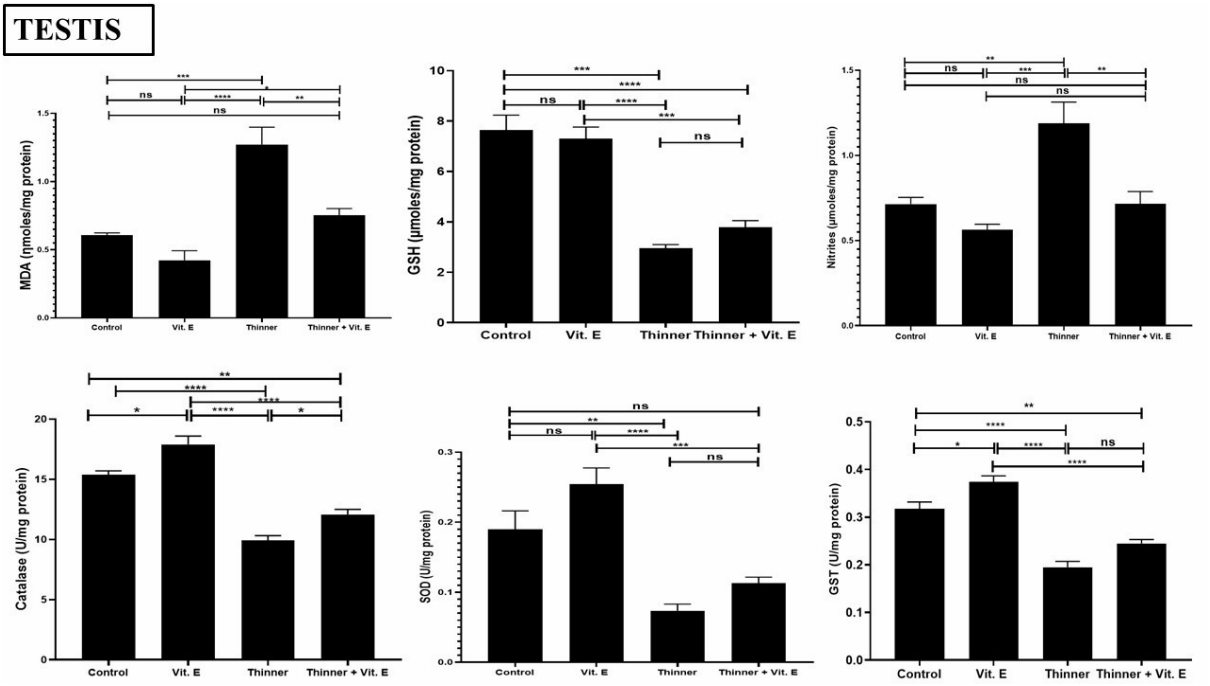

Figure 6. Changes in the oxidative stress markers profile in the testis of rats exposed to acute thinner inhalation (500ppm). Bars with different asterisks are significantly different; *p*-values ($^{*}p<0.05$, $^{**}p<0.01$, $^{***}p<0.001$, $^{****}p<0.001$ & ns (not significantly different) were established between the experimental groups.

Histopathological Examination

The histopathological results from this study were presented in Figures 7-11. The hepatic parenchyma was devoid of lesions in rats treated with Vit. E only and the control rats (Figure 7A & B). However, moderate to severe hepatic histo-architectural alterations (hepatocellular degeneration and sinusoidal congestion) were observed in Vit. E + thinner (Figure 7D) and thinner only group (Figure 7C) respectively.

The lung tissue parenchyma was intact in the control, Vit E only and thinner +Vit E treated rats (Figure 8A, B & D). On the contrary, the lung histomorphological integrity was markedly disrupted in the thinner only exposed rats when compared to others (Figure 8C).

With regard to the renal tissue histological integrity, the kidneys of the control, Vit. E only and thinner +Vit E treated rats were devoid of histo-architectural alterations (Figure 9A, B & D). Conversely, there was a marked renal interstitial congestion (arrowhead) (Figure 9C) in the thinner only rat.

The splenic histo-architecture was not altered in the control and Vit E only treated as typified by the presence of intact white and red pulp (Figure 10A & B). However, moderate to severe splenic histomorphological disruptions (congestion of red pulp) were observed in thinner + Vit E (Figure 10D) and thinner only (Figure 10C) respectively.

The testicular seminiferous tubules in the control and Vit. E exposed rats bear normal histo-architectural organization characterized by distinct seminiferous tubular germinal epithelium, considerable luminal contents and intact interstium (Figure 11A & B). However, rats exclusively given thinner and those co-administered thinner and vitamin E (Figure 11 C & D) showed only mild focal germinal epithelial depletion when compared to the control rats.

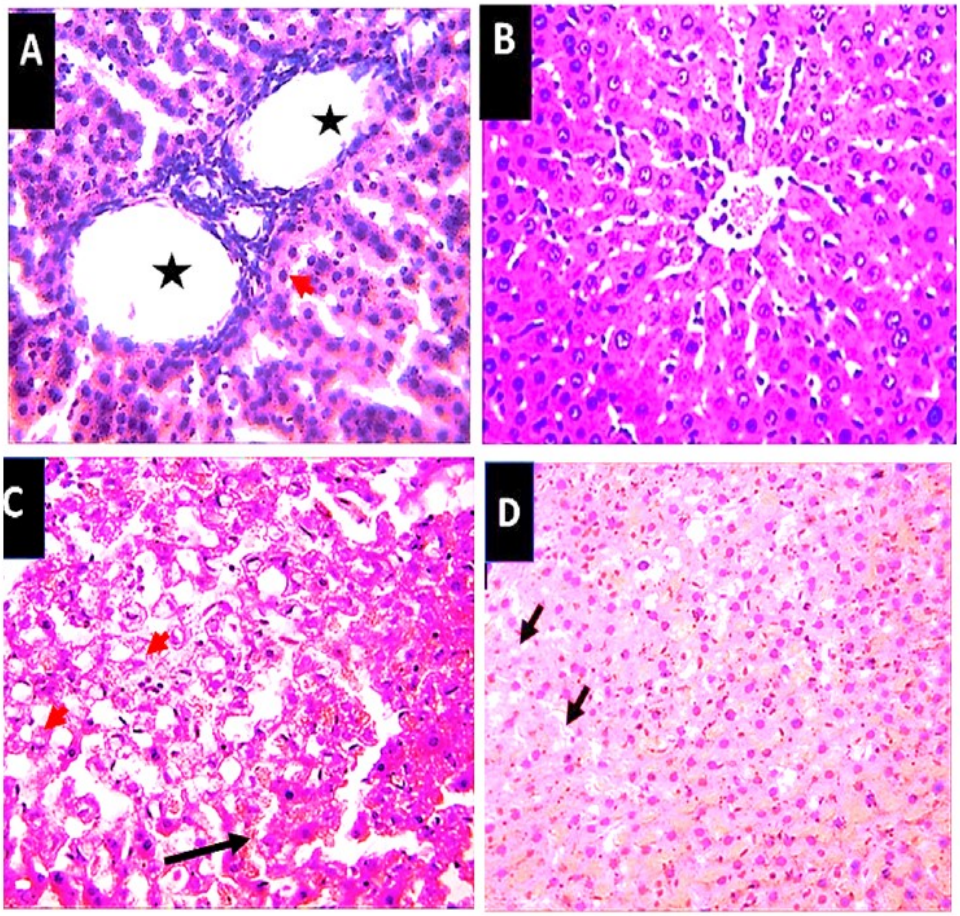

Figure 7. Histopathology of the liver of rats exposed to acute thinner inhalation (500ppm) from 3 weeks of exposure: A (Control) & B (Vit. E only): showed normal liver histoarchitecture as evidenced by intact hepatocytes (red arrowhead) and portal vessels (star). C (Toxicity): showed severe sinusoidal congestion (black arrow) with marked hepatocellular degeneration (red arrowhead). D (Toxicity + Vit. E): showed moderately diffused sinusoidal congestion (black arrow) Magnification: X400; Stain: Haematoxylin-eosin.

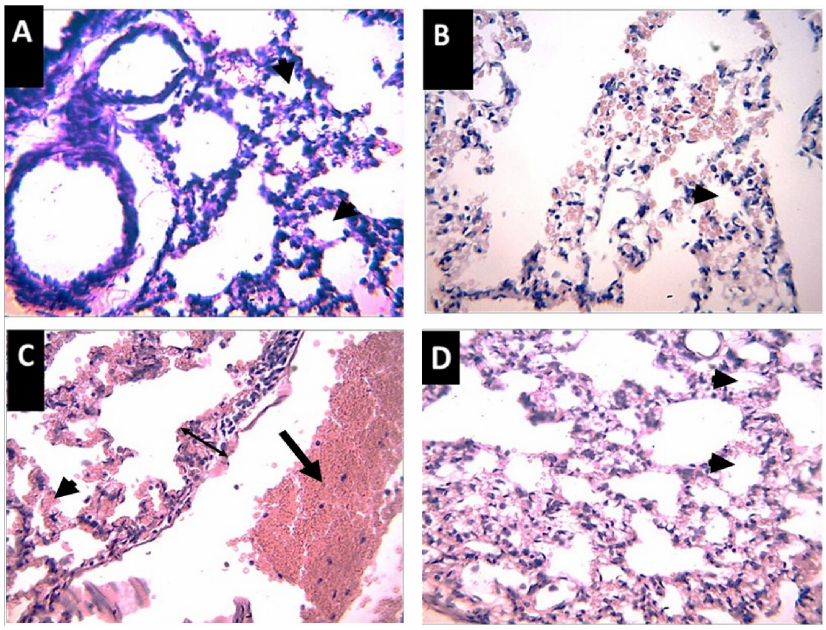

Figure 8. Histopathology of the lungs of rats exposed to acute thinner inhalation (500ppm) from 3 weeks of exposure: A (Control), B (Vit E only) & D (Toxicity + Vit E): showed normal histoarchitecture of the lungs including intact alveoli (arrowhead). C (Toxicity): showed peribronchiolar hemorrhage (black arrow), interstitial congestion with hemorrhagic foci in the alveoli (black arrowhead) and pneumocytes proliferation. Magnification: X400; Stain: Haematoxylin-eosin.

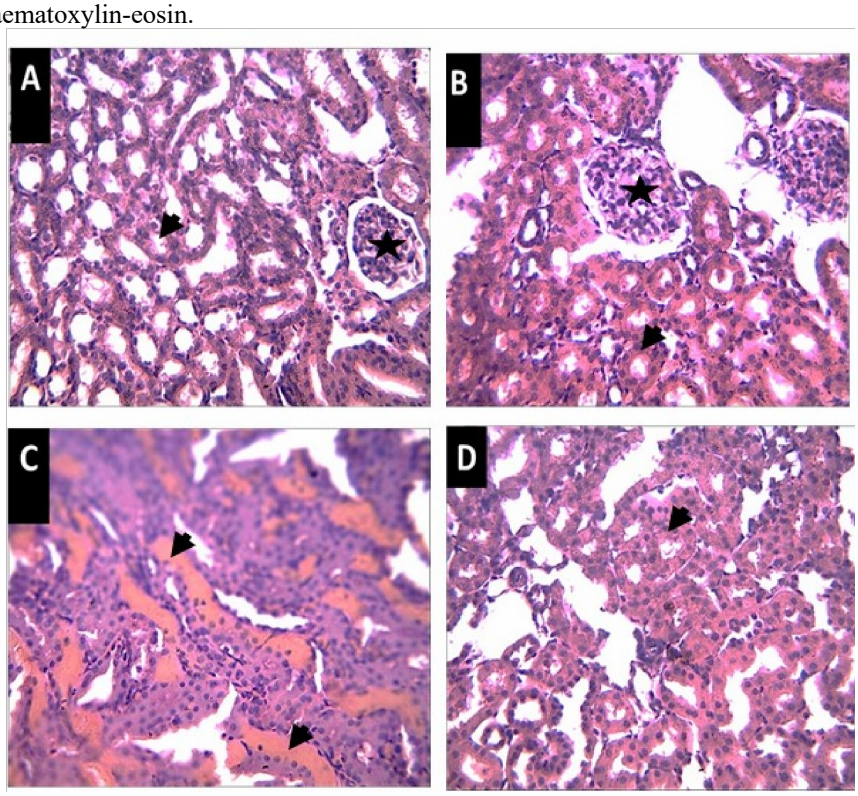

Figure 9. Histopathology of the kidney of rats exposed to acute thinner inhalation (500ppm) from 3 weeks of exposure: A (Control), B (Vit E only) & D (Toxicity + Vit E): showed normal histoarchitecture as evidenced by intact glomerulus (star) and renal tubular epithelium (black arrowhead). C (Toxicity): showed very severe renal interstitial congestion (arrowhead). Magnification: X400; Stain: Haematoxylin-eosin.

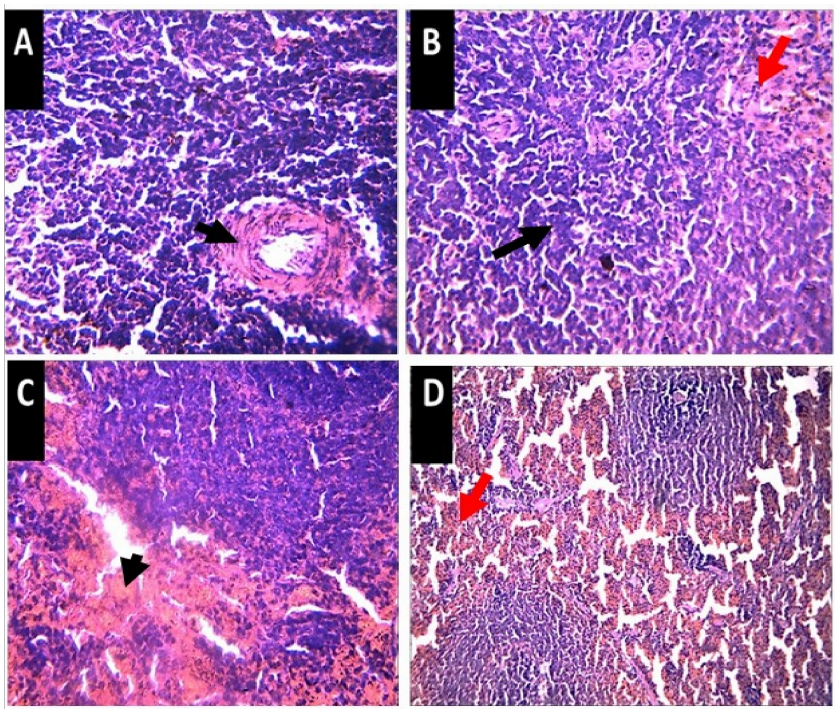

Figure 10: Histopathology of the spleen of rats exposed to thinner inhalation (500ppm) from 3 weeks of exposure: A (Control) & B (Vit E only): splenic parenchyma is devoid of lesion as revealed by intact white pulp (black arrow), red pulp (red arrow) and splenic arteriole (arrowhead) C (Toxicity): severed generalized congestion of red pulp (black arrowhead). D (Toxicity + Vit E): showed moderate congestion of red pulp (red arrow). Magnification: X400; Stain: Haematoxylin-eosin.

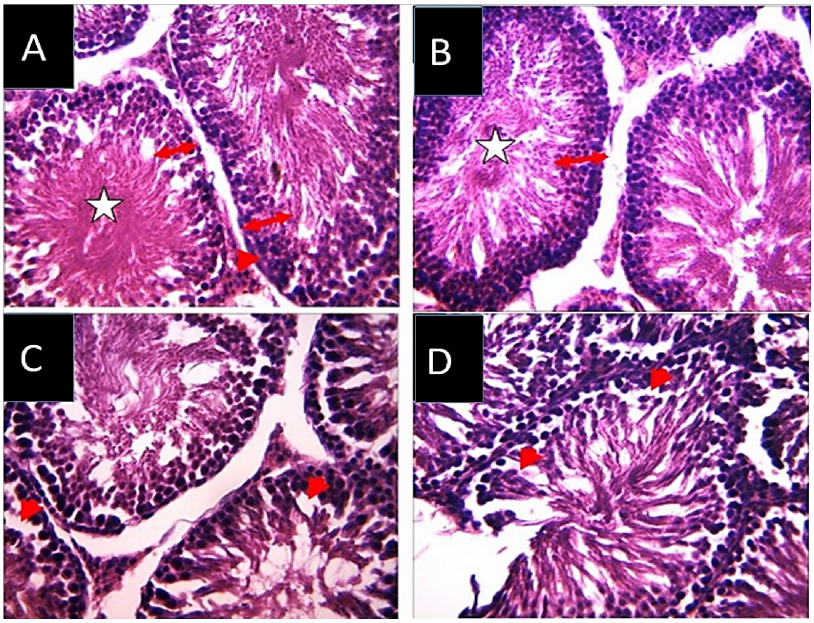

Figure 11. Photomicrographs of the testes of rats exposed to thinner inhalation (500ppm) and exposed to Vitamin E. **A. Control**; **B. Vitamin E only:** There is no visible histo-architectural alterations as evidenced by intact seminiferous germinal epithelium (double arrow-head), substantial luminal contents (star) **C. Thinner only; D. Thinner + Vit E:** With the exception of mild germinal epithelial focal depletion (arrowhead), there was no visible histo-architectural alterations to the testes. (H & E: X 100).

4. Discussion

This study demonstrated that thinner, a toluene rich solvent, intoxication resulted in some multiple organ toxicities as reflected in significant increase in biochemical parameters (AST, ALT, ALP, total bilirubin, BUN and creatinine), deranged antioxidant marker profiles and marked histomorphological alterations. Remarkably, vitamin E co-administration with thinner strikingly ameliorated the perturbed biochemical and antioxidant profiles as well as improved the compromised histo-architectural integrity.

The body weight of laboratory animals is a crucial indicator of distress and can independently signify pain and discomfort [46 – 48]. Therefore, the significant decrease in body weight observed in rats exposed to acute thinner inhalation compared to the control rats seemed to be in tandem with reports of consistent gradual decline in body weights and appetite in rats exposed to acute thinner inhalation as previously documented by MartínezAlfaro et al. [49] and Malloul et al. [50]. The validation for the decrease in the body weight sequel to gum sniffling has been suggested by Brohi et al. [51] and Fialkow et al. [24] to be due to progressive muscle weakness, nerve denervation and loss of functions potentially emanating from increased tissue free radical production leading to lipid and protein degradation. Interestingly, rats co-administered with vitamin E and thinner showed a significant improvement in body weight loss. This finding on improved body weight following acute toluene intoxication and treatment with vitamin E is consistent with report of Muti et al. [40].

Hepatic function tests or markers consist of arrays of blood tests that are usually performed for the assessment of the preclinical studies and understanding of the liver health [52]. Bearing this in mind, the increased levels of hepatic function markers such as AST (aspartate aminotransferase), ALT (alanine aminotransferase), ALP (alkaline phosphatase), and TBIL (total bilirubin) in rats treated solely with thinner indicated significant hepatocellular damage. These findings further underscore the toxic nature of thinner, as previously documented in the literature by Rahimi et al. [53] and Lala et al. [54]. Vitamin E is well-known for its potent antioxidant properties as documented by Rizvi et al. [55]. It functions by neutralizing reactive oxygen species generated during oxidative stress. Therefore, it is reasonable to suggest that the markedly reduced serum levels of hepatic markers observed in rats co-administered with thinner and Vitamin E may stem from the antioxidative actions of Vitamin E. In essence, Vitamin E likely mitigates the hepatocellular damage induced by thinner exposure through its ability to scavenge free radicals and protect cells from oxidative stress. This suggests a potential therapeutic role for Vitamin E in attenuating liver injury associated with toxic exposures such as thinner. The observed liver markers findings in our study concurs with the report of Sekihashi et al [56] and Upperman et al. [57].

The renal function markers, including serum creatinine and blood urea nitrogen (BUN), provide valuable insights into the health status of the kidneys. In the context of rats exclusively treated with thinner, these markers markedly deranged and the elevated levels of serum BUN and urea nitrogen primarily indicate severe renal morpho-physiological alterations that are detrimental to the normal functioning of the kidneys. These findings suggest renal dysfunction, possibly resulting from the toxic effects of thinner on renal tissue. Interestingly, the improved renal function markers observed in rats treated with both thinner and vitamin E lend credence to the potential protective effect of vitamin E against thinner-induced renal damage. The amelioration of renal function markers in the presence of vitamin E suggests that vitamin E may mitigate the adverse effects of thinner on kidney function, possibly through its antioxidant properties. The renal function marker profile recorded in this study agree with report of Latief et al. [58].

Lipid peroxidation is a process wherein free radicals attack lipids containing carbon-carbon double bonds, leading to the formation of reactive lipid peroxides. The remarkable increase in malondialdehyde (MDA) levels across all the visceral organs (liver, lungs, kidneys, and spleen) of rats exposed only to thinner could be attributed to the reactive oxygen generating potential of thinner. This signifies the heightened oxidative stress induced by thinner exposure. On the other hand, the decrease in MDA levels in the visceral organs resulting from the co-administration of Vitamin E with thinner appeared to mitigate the oxidative damage to the organs caused by thinner treatment. This observation further reinforces the antioxidant properties of Vitamin E in combating oxidative stress. In similar manner, the nitrite composition in the tissues is also indicative of increased oxidative stress. Therefore, the elevated nitrite levels in the various organs of rats treated solely with thinner, as measured in this study, further confirms the oxidative damage caused by thinner exposure. The observation of a remarkable reduction in nitrite levels in the various tissues of rats exposed to both thinner and Vitamin E lends support to the notion that Vitamin E effectively mitigates oxidative stress induced by thinner exposure. These findings from our study on nitrite levels in the internal organs corroborate with the work of Sekihashi et al. [56].

Endogenous antioxidants refer to the body's natural defense mechanisms against oxidative stress. These include Glutathione (GSH), Superoxide Dismutase (SOD), Glutathione-S-Transferase (GST), and Catalase (CAT). The observed decline in the levels of endogenous antioxidants (GSH, SOD, GST, CAT) enzymes in the different visceral organs of rats exposed solely to thinner suggests a depletion of the body's antioxidant defense mechanisms in response to oxidative stress. However, Pajaro-Castro et al. [59] reported increased in GST gene

expression after thinner and toluene exposure. Conversely, the significantly elevated levels of endogenous enzymes observed in rats exposed to both thinner and co-administered Vitamin E indicated the protective effect of Vitamin E in preserving the antioxidant defense mechanisms against thinner-induced oxidative stress.

The observed severely damaged hepatic parenchyma in rats exclusively exposed to thinner, characterized by marked hepatocellular degeneration and sinusoidal congestion, confirms the potential toxic nature of thinner which align with previous report by Tas et al. [60]. These histomorphological alterations align with the biochemical and antioxidant derangements recorded for this category of rats in the study. The histological results provide further evidence of the adverse effects of thinner on liver health. However, the co-administration of thinner and Vitamin E noticeably improved the severe histo-architectural disruptions elicited by thinner. This observation aligned with the histological findings reported by Bansal et al. [61] in a similar study that investigated the protective role of N-nitrosodiethylamine induced oxidative stress in rat liver. Thus, it suffices to suggest that Vitamin E may have a protective effect against the hepatic damage induced by thinner exposure, as evidenced by the restoration of liver histology towards normalcy.

The distinct histo-architectural disruptions observed in the lungs of rats exclusively exposed to thinner, such as peri-bronchiolar hemorrhage, interstitial congestion, and pneumocyte proliferation, further substantiate the toxic potential of thinner on lung health which mirrors observations by Fujimaki et al. [24] and Muti et al. [40]. On the other hand, the moderate distortion of lung parenchyma histomorphology noticed in rats treated with Vitamin E in addition to thinner, relative to rats exposed solely to thinner, suggests that Vitamin E supplementation may provide a partial protection against lung damage induced by thinner. In addition, the renal histological alterations, particularly parenchymal interstitial congestion, observed in rats treated exclusively with thinner, further establish the nephrotoxic potential of thinner which correspond with reports of Martinez-Alfaro et al. [7] and Latief et al. [58]. Conversely, the marked renal histomorphological amelioration observed in the form of visibly intact renal histo-architecture in rats treated with both thinner and Vitamin E suggests that coadministration of Vitamin E may protect against renal damage induced by thinner exposure. The findings on ameliorative potential effect of Vitamin E on kidney tissue in this study corroborate the reports of Baltusnikiene et al. [62].

The respective histological variations, ranging from moderate to severe, in splenic histo-morphological integrity of rats treated with thinner + Vitamin E and thinner only, depict the slight mitigating potential of Vitamin E against the inherent toxic effect of thinner on splenic morphology. These lesions observed as red pulp congestion and hemorrhagic foci in the spleen, are consistent with a previous work [63]. The moderate splenic histological disruption observed could be attributed to the antioxidant properties of Vitamin E, which might have helped in counteracting some of the damage caused by thinner exposure. Multi-organ toxicity recorded in this study appeared to further validate the previous documentation on paint thinner fumes inhalation reported by Zaidi et al. [64].

The observed apparently intact testicular histomorphological integrity in both thinner only and thinner + Vit. E treated rats implies that testicular tissues markedly tolerate thinner toxicity relative to other visceral organs. Though, the data on oxidative stress markers in this study contradicts the histological results as the former established the toxic potential of thinner. It is envisaged that if the exposure time is prolonged beyond the 21 days used in study, there is great chances of presentation of thinner induced testicular histological alterations. The testicular results from this study is at variance with the report of precipitation of testicular histological lesions by Kanter [65].

5. Conclusion

The study suggests that exposure to thinner induces oxidative stress and organ damage, particularly in the liver, lungs, kidneys, spleen and testes. Vitamin E supplementation shows promise in mitigating thinner-induced toxicity by reducing oxidative stress, preserving organ function and ameliorating histopathological alterations. These findings underscore the importance of antioxidant therapy in mitigating the adverse effects of toxicant exposure and highlight Vitamin E as a potential therapeutic agent against thinner toxicity. However, further research, including dose-response studies and investigation of underlying mechanisms, is warranted to fully understand the protective effects of Vitamin E and its potential clinical applications in toxicant-induced organ damage.

Ethics

The study was approved by the University of Ibadan Animal Care and Use Research Ethics Committee (UIACUREC), under ethical code number UI-ACUREC/APP/21/133.

References

[1] McGarvey EL, Clavet GJ, Mason W, Waite D. Adolescent inhalant abuse: environments of use. AJDAA 1999; 25(4): 731–741.

[2] Jayanth S, Hugar BS, Praveen S, Girish Chandra Y. Glue sniffing. Med Leg J 2016; 85(1): 38-42.

[3] Patrick ME, Collins LM, Smith E, Caldwell L, Flisher A, Wegner L. A prospective longitudinal model of substance use onset among South African adolescents. Subst. Use & Misuse 2009; 44(5): 647–662.
[4] Young SJ, Longstaffe S, Tenenbein M. Inhalant abuse and the abuse of other drugs. AJDAA 1999; 25(2): 371–375.
[5] Howard MO, Bowen SE, Garland EL, Perron BE, Vaughn MG. Inhalant use and inhalant use disorders in the United States. Addict Sci & Clin Pract 2011; 6(1): 18–31.
[6] Sato H, Bottle SE, Blinco JP, Micallef AS, Eaton GR, Eaton SS. Electron spin-lattice relaxation of nitroxyl radicals in temperature ranges that span glassy solutions to low viscosity liquids. J Magn Reson 2008;191: 66–77.
[7] Martínez-Alfaro M, Alcaraz-Contreras Y, Cárabez-Trejo A, Leo-Amador, GE. Oxidative stress effects of thinner inhalation. Indian J. Occup and Environ Med 2011; 15(3): 87–92.
[8] Cruz SL, Armenta-Reséndiz M, Carranza-Aguilar CJ, Galván EJ. Minocycline prevents neuronal hyperexcitability and neuroinflammation in medial prefrontal cortex, as well as memory impairment caused by repeated toluene inhalation in adolescent rats. Toxicol and Appl Pharmacol 2020; 395: 114980.
[9] Bennett ME, Walters ST, Miller JH, Woodall WG. Relationship of early inhalant use to substance use in college students. J Subst Abuse 2000; 12(3): 227–240.
[10] Crossin R, Qama A, Andrews ZB, Lawrence AJ, Duncan JR. The effect of adolescent inhalant abuse on energy balance and growth. Pharmacol. Res. & Perspect 2019;7(4): e00498.
[11] Schikler KN, Seitz K, Rice JF, Strader T. Solvent abuse associated cortical atrophy. J. Adolesc. Health Care: Official Publication of the Society for Adolescent Medicine 1982; *3*(1): 37-39.
[12] Camara-Lemarroy CR, Rodríguez-Gutiérrez R, Monreal-Robles R, González-González JG. Acute toluene intoxication--clinical presentation, management and prognosis: a prospective observational study. BMC Emerg. Med 2015; 1*5*: 19.
[13] Taher SM, Anderson RJ, McCartney R, Popovtzer MM, Schrier RW. Renal tubular acidosis associated with toluene "sniffing". N Engl J Med 1974; 290(14): 765-768.
[14] Kaneko T, Koizumi T, Takezaki T, Sato A. Urinary calculi associated with solvent abuse. Urol J 1992;147(5): 1365–1366.
[15] Dündarz MR, Türkbay T, Akay C, Sarici SU, Aydin A, Denli M, Gökçay E. Antioxidant enzymes and lipid peroxidation in adolescents with inhalant abuse. Turk J Pediatr 2003;45(1): 43–45.
[16] Yurtseven A, Türksoylu M, Yazıcı P, Karapınar B, Saz EU. A `glue sniffer` teenager with anuric renal failure and hepatitis. Turk J Pediatr 2018; 60(2): 206–209.
[17] Arslan Ş, Uzunhasan I, Kocas BB, Cetinkal G, Arslan Ş, Kocas C., Abaci O, Yildiz M, Celiker C, Turkoglu C. Effect of chronic toluene exposure on heart rhythm parameters. Pacing Clin Electrophysiol 2018; 41(7): 783-787.
[18] Snyder R. Benzene and leukemia. Crit. Rev in Toxicol 2002;32(3): 155–210.
[19] Win-Shwe TT, Fujimaki H. Neurotoxicity of toluene. Toxicol. Lett. 2012; 198(2): 93-99.
[20] Backes WL, Sequeira DJ, Cawley GF, Eyer CS. Relationship between hydrocarbon structure and induction of P450: effects on protein levels and enzyme activities. Xenobiotica; The Fate of Foreign Compounds in Biological Systems 1993; 23(12): 1353–1366.
[21] Roberts RA, Laskin DL, Smith CV, Robertson FM, Allen EM, Doorn JA, Slikker W. Nitrative and oxidative stress in toxicology and disease. Toxicol Sci: An Official Journal of the Society of Toxicology 2009; 112(1): 4–16.
[22] Ayoubi M, Naserzadeh P, Hashemi MT, Reza Rostami M, Tamjid E, Tavakoli MM, Simchi A. Biochemical mechanisms of dose-dependent cytotoxicity and ROS-mediated apoptosis induced by lead sulfide/graphene oxide quantum dots for potential bioimaging applications. Sci Rep 2017; 7(1): 12896.
[23] Victor VM, De la Fuente M. Immune cells redox state from mice with endotoxin-induced oxidative stress. Involvement of NF-kappaB. Free Radic Res 2003; 37(1): 19–27.
[24] Fialkow L, Wang Y, Downey GP. Reactive oxygen and nitrogen species as signaling molecules regulating neutrophil function. Free Radic Biol & Med 2007; 42(2): 153–164.
[25] El-Nabi Kamel, MA, Shehata M. Effect of toluene exposure on the antioxidant status and apoptotic pathway in organs of the rat. Br J Biomed Sci 2008; 65(2): 75–79.
[26] Anyanwu BO, Orish CN, Ezejiofor AN, Nwaogazie IL, Akaranta O, Orisakwe OE. Multi-organ protective effect of *Costus afer* on low concentration toxic metal mixture in albino rats. Int J Physiol Pathophysiol & Pharmacol 2021; 13(2): 52–68.
[27] Nygren J, Cedervall B, Eriksson S, Dusinská M, Kolman A. Induction of DNA strand breaks by ethylene oxide in human diploid fibroblasts. Environ. and Mol. Mutagen 1994; 24(3), 161–167.
[28] Traber MG, Head B. Vitamin E: How much is enough, too much and why!. Free Radic. Biol. Med. 2021; 177 212-225.
[29] Gupta, S, Kumar, D, Rauthan, JVS, Kamal, B (2022). Hepatoprotective Effect of Vitamin-E (α-Tocopherol) on Trichloroethylene and Toluene Induce Liver Damage in Rats. J. Mountain Res 17(2), 199-204.
[30] Dewry, RKr, Deka, BC, Biswas RK, Bhuyan D, Borah, P, Mahanta, N, Kurmi, N (2020). Effect of butylated hydroxy toluene and vitamin e on the cryosurvivability of buck semen. CryoLetters 41 (2), 68-74.
[31] Szymańska, R., Nowicka, B., Trela, A. and Kruk, J., 2020. Vitamin E: Structure and forms. In Molecular nutrition. Academic Press. 67-90 p.
[32] Ali, S.S., Ahsan, H., Zia, M.K., Siddiqui, T. and Khan, F.H., 2020. Understanding oxidants and antioxidants: Classical team with new players. J Food Biochem, 44(3), p.e13145.
[33] Valgimigli, L. Lipid peroxidation and antioxidant protection. Biomolecules 2023; 13(9): 1291.
[34] Tyuryaeva, I. and Lyublinskaya, O. Expected and unexpected effects of pharmacological antioxidants. Int J Mol Sci 2023; 24(11): 9303.

[35] Liao, S., Omage, S.O., Börmel, L., Kluge, S., Schubert, M., Wallert, M., Lorkowski, S. Vitamin E and Metabolic Health: Relevance of Interactions with Other Micronutrients. Antioxidants (Basel, Switzerland) 2022; 11(9), 1785.
[36] Zheng, H., Xu, Y., Liehn, E.A. and Rusu, M. Vitamin C as scavenger of reactive oxygen species during healing after myocardial infarction. International Journal of Molecular Sciences 2024; 25(6): 3114.
[37] Islam, M.N., Rauf, A., Fahad, F.I., Emran, T.B., Mitra, S., Olatunde, A., Shariati, M.A., Rebezov, M., Rengasamy, K.R. and Mubarak, M.S. Superoxide dismutase: an updated review on its health benefits and industrial applications. Crit Rev in Food Sci and Nutr 2022; 62(26): 7282-7300.
[38] Sarıkaya, E. and Doğan, S. Glutathione Peroxidase in Health. Glutathione system and oxidative stress in health and disease. IntechOpen. 49 p.
[39] Kamat CD, Gadal S, Mhatre M, Williamson KS, Pye QN, Hensley K. Antioxidants in central nervous system diseases: preclinical promise and translational challenges. J. Alzheimer's Dis: JAD 2008;15(3), 473–493.
[40] Muti AD, Pârvu AE, Muti LA, Moldovan R, Mureşan A. Vitamin E effect in a rat model of toluene diisocyanate-induced asthma. Clujul Medical 2016; 89(4): 499–505.
[41] Demır M, Cicek M, Eser N, Yoldaş A, Sısman T. "Effects of Acute Toluene Toxicity on Different Regions of Rabbit Brain". Anal Cell Pathol 2017; 6.
[42] Soares MV, Mesadri J, Gonçalves DF, Cordeiro LM, Franzen da Silva A, Baptista FBO, Wagner R, Corte CLD, Soares FAA, Ávila DS. Neurotoxicity induced by toluene: In silico and in vivo evidences of mitochondrial dysfunction and dopaminergic neurodegeneration. *Environ Pollut* 2022; 298.
[43] Baydas, G., Ozveren, F., Tuzcu, M. and Yasar, A. Effects of thinner exposure on the expression pattern of neural cell adhesion molecules, level of lipid peroxidation in the brain and cognitive function in rats. Eur J Pharmacol 2005; 512(2-3): 181-187.
[44] Fifel, K., Bennis, M. and Ba-M'hamed, S., 2014. Effects of acute and chronic inhalation of paint thinner in mice: behavioral and immunohistochemical study. Metab brain dis 2014; 29: 471-482.
[45] Folarin RO, Omirinde JO, Gilbert TT, Igbeneghu C. Acute and Sub-chronic Toxicity of Aqueous Extract of Roots of Khaya senegalensis (Desr.) A. Juss. in Mice and Rats Respectively. Annu. Res Rev Biol 2023; 38(8): 33–46.
[46] Morton DB, Griffiths PH. Guidelines on the recognition of pain, distress and discomfort in experimental animals and an hypothesis for assessment. Veter Rec. 1985;116: 431–436.
[47] Baumans V, Brain PF, Brugere H, Clausing P, Jeneskog T, Perretta G. Pain and distress in laboratory rodents and lagomorphs. Report of the Federation of European Laboratory Animal Science Associations (FELASA) Working Group on Pain and Distress accepted by the FELASA Board of Management November 1992. Lab Anim 1994; 28:97–112.
[48] Talbot SR, Biernot S, Bleich A. Defining body-weight reduction as a humane endpoint: a critical appraisal. Lab Anim. 2020; 54(1):99–110.
[49] Martínez-Alfaro M, Cárabez-Trejo A, Gallegos-Corona MA, Pedraza-Aboytes G, Hernández-Chan NG, Leo-Amador GE. Thinner inhalation effects on oxidative stress and DNA repair in a rat model of abuse. J of Appl Toxicol: JAT 2010; 30(3): 226–232.
[50] Malloul H, Mahdani FM, Bennis M, Ba-M'hamed S. Prenatal Exposure to Paint Thinner Alters Postnatal Development and Behavior in Mice. Front. Behav. Neurosci 2017; 11: 171.
[51] Brohi, HA, Saeed A, Shams O, Al Jundi, EZ, Alreshi MN, Abualela H, Khotani A, Babakkor M. "glue sniffing neuropathy and review of literature," Pak J Neurol Sci 2013; 8(1)3: 8 -11.
[52] Lopez-Lopez V, Garcia-Carrillo N, de Gea D, Oltra L, González-Bermúdez CA, *et al.* Assessment of hepatic function, perfusion and parenchyma attenuation with indocyanine green, ultrasound and computed tomography in a healthy rat model: Preliminary determination of baseline parameters in a healthy liver. PLOS ONE 2021;16(12): e0261447.
[53] Rahimi HR, Agin K, Shadnia S, Hassanian-Moghaddam H, Oghazian MB. Clinical and biochemical analysis of acute paint thinner intoxication in adults: a retrospective descriptive study. Toxicol Mech Methods 2015; 25(1): 42–47.
[54] Lala V, Zubair M, Minter DA. Liver function tests. [Updated 2023 Jul 30]. In: StatPearls [Internet]. Treasure Island (FL): StatPearls Publishing; 2024 Jan-. Available from https://www.ncbi.nlm.nih.gov/books/NBK482489/
[55] Rizvi S, Raza ST, Ahmed F, Ahmad A, Abbas S, Mahdi F. The role of vitamin E in human health and some diseases. SQUMJ 2014; 14(2): e157–e165.
[56] Sekihashi K, Yamamoto A, Matsumura Y, Ueno S, Watanabe-Akanuma M, Kassie F, Knasmüller S, Tsuda S, Sasaki YF. Comparative investigation of multiple organs of mice and rats in the comet assay. Mutation Res 2002; 517(1-2): 53–75.
[57] Upperman JS, Bucuvalas JC, Williams FN, Cairns BA, Cox CS Jr, Doctor A, Tamburro RF. Specific etiologies associated with the multiple organ dysfunction syndrome in children: Part 2. Pediatr Crit Care Med 2017; 18(3 Suppl 1): 58–66.
[58] Latief M, Hassan Z, Wani ML, Abbas F, Farooq S. Automobile paint reducer induced acute kidney injury: A case series. JRENHEP 2021; 5(2): 10–13.
[59] Pajaro-Castro N, Caballero-Gallardo K, Olivero-Verbel J. Toxicity and expression of oxidative stress genes in Tribolium castaneum induced by toluene, xylene, and thinner. J Toxicol Environ Health. Part A 2019; 82(1): 28–36.
[60] Tas U, Ogeturk M, Meydan S, et al. Hepatotoxic activity of toluene inhalation and protective role of melatonin. Toxicology and Industrial Health. 2011; 27(5):465–473.
[61] Bansal AK, Bansal M, Soni G, Bhatnagar D. Protective role of Vitamin E pre-treatment on Nnitrosodiethylamine induced oxidative stress in rat liver. Chem Biol Interact 2005; 156(2-3): 101–111.

[62] Baltusnikiene A, Staneviciene I, Jansen E. Beneficial and adverse effects of vitamin E on the kidney. Front Physiol, 2023; 14: 1145216.
[63] Voloshin VN, Koveshnikov VG, Voloshina IS. Morphology of the spleen in adult albino rats after wholebody exposure to low-level of toluene. Int J Anat Res 2014; 2: 421–430.
[64] Zaidi SA, Shaw AN, Patel MN, Shah VV, Rajendran D, Shah BP, Sinha SN, Gandhi SJ, Saiyed HN. Multiorgan toxicity and death following acute unintentional inhalation of paint thinner fumes. Clin Toxicol 2007; 45(3): 287–289.
[65] Kanter, M. Thymoquinone attenuates lung injury induced by chronic toluene exposure in rats. Toxicol Ind Health 2011; 27: 387-395.

C O P Y R I G H T R E L E A S E F O R M

TURKISH JOURNAL OF SCIENCE AND TECHNOLOGY (TJST)
Published by Firat University

Firat University, Fen Bilimleri Enstitüsü Müdürlüğü
Turkish Journal of Science & Technology Editörlüğü
Elazığ-TURKEY,
Manuscript title: .....
.....
.....
Full names of all authors (in order to appear on manuscript): .....
.....
Name, address etc. of corresponding author: .....
.....
.....
ID Number: ..... Telephone: .....
E-mail: ..... Mobile phone: .....

The author(s) warrant(s) that:
a) the manuscript submitted is his/her/their own original work;
b) all authors participated in the work in a substantive way and are prepared to take public responsibility for the work;
c) all authors have seen and approved the manuscript as submitted;
d) the manuscript has not been published and is not being submitted or considered for publication elsewhere;
e) the text, illustrations, and any other materials included in the manuscript do not infringe upon any existing copyright or other rights of anyone. Notwithstanding the above, the Contributor(s) or, if applicable the Contributor's Employer, retain(s) all proprietary rights other than copyright, such as
a) patent rights;
b) to use, free of charge, all parts of this article for the author's future works in books, lectures, classroom teaching or oral presentations;
c) the right to reproduce the article for their own purposes provided the copies are not offered for sale.
However, reproduction, posting, transmission or other distribution or use of the article or any material contained therein, in any medium as permitted hereunder, requires a citation to the Journal and appropriate credit to Firat University as publisher, suitable in form and content as follows:
Title of article, author(s), journal title and volume/issue, Copyright© year.
All materials related to manuscripts, accepted or rejected, including photographs, original figures etc., will be kept by Turkish Journal of Science and Technology editority for one year following the editor's decision. These materials will then be destroyed.
I/We indemnify Firat University and the Editors of the Journals, and hold them harmless from any loss, expense or damage occasioned by a claim or suit by a third party for copyright infringement, or any suit arising out of any breach of the foregoing warranties as a result of publication of my/our article. I/We also warrant that the article contains no libelous or unlawful statements and does not contain material or instructions that might cause harm or injury.
This copyright form must be signed by all authors. Separate copies of the form (completed in full) may be submitted by authors located at different institutions; however, all signatures must be original.

ID number: ..... ID number: .....
Full name (block letters) ..... Full name (block letters) .....
Signature ..... Date ..... Signature ..... Date .....
ID number: ..... ID number: .....
Full name (block letters) ..... Full name (block letters) .....
Signature ..... Date ..... Signature ..... Date .....
ID number: ..... ID number: .....

Turkish authors must supply their ID card number; foreign authors must supply their passport number (if possible)